

Neuroscience Bulletin

The Official Journal of The Chinese Neuroscience Society

神经科学通报

Volume 36
Number 12
December 2020



 **SIBS**  Springer
www.neurosci.cn

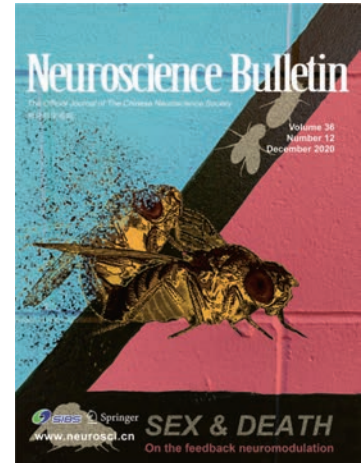
SEX & DEATH

On the feedback neuromodulation

About the Cover

The animal nature to pursue more sex and the possible fatal consequence by excessive sex must be orchestrated by negative feedback signals. In this issue, Gao *et al.*, investigated how continuous sexual activity could kill male flies and identified feedback neuromodulatory signals that could balance reproduction and survival. The cover image shows a critical decision in the corner for flies to pursue sex or not, and the possible fatal consequence if faces (burning into ashes during mating). See page 1429-1440. (Cover image provided by Dr. Yufeng Pan).

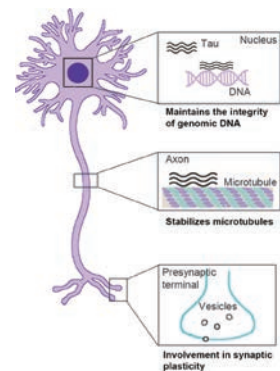
Volume 36 Number 12
December 2020



Editorial

1411 Tau Accumulation and Defective Autophagy: A Common Pathological Mechanism Underlying Repeat-Expansion-Induced Neurodegenerative Diseases?

Li Song · Luoying Zhang



p 1412

Original Articles

1414 Tau Accumulation via Reduced Autophagy Mediates GGGGCC Repeat Expansion-Induced Neurodegeneration in *Drosophila* Model of ALS

Xue Wen · Ping An · Hexuan Li · Zijian Zhou · Yimin Sun · Jian Wang · Lixiang Ma · Boxun Lu

1429 Sex and Death: Identification of Feedback Neuromodulation Balancing Reproduction and Survival

Can Gao · Chao Guo · Qionglin Peng · Jie Cao · Galit Shohat-Ophir · Dong Liu · Yufeng Pan



p 1432

1441 Spinal Cord Stimulation Enhances Microglial Activation in the Spinal Cord of Nerve-Injured Rats

Bin Shu · Shao-Qiu He · Yun Guan

1454 Fine-Grained Topography and Modularity of the Macaque Frontal Pole Cortex Revealed by Anatomical Connectivity Profiles

Bin He · Long Cao · Xiaoluan Xia · Baogui Zhang · Dan Zhang · Bo You · Lingzhong Fan · Tianzi Jiang

1474 Genetic Evidence that Dorsal Spinal Oligodendrocyte Progenitor Cells are Capable of Myelinating Ventral Axons Effectively in Mice

Minxi Fang · Qian Yu · Baiyan Ou · Hao Huang · Min Yi · Binghua Xie · Aifen Yang · Mengsheng Qiu · Xiaofeng Xu

1484 Connexin 36 Mediates Orofacial Pain Hypersensitivity Through GluK2 and TRPA1

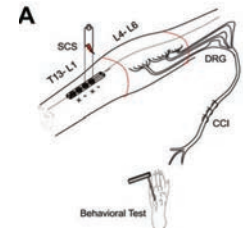
Qian Li · Tian-Le Ma · You-Qi Qiu · Wen-Qiang Cui · Teng Chen · Wen-Wen Zhang · Jing Wang · Qi-Liang Mao-Ying · Wen-Li Mi · Yan-Qing Wang · Yu-Xia Chu

1500 Dual Oxidase Mutant Retards Mauthner-Cell Axon Regeneration at an Early Stage via Modulating Mitochondrial Dynamics in Zebrafish

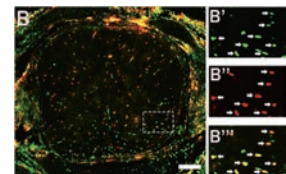
Lei-Qing Yang · Min Chen · Da-Long Ren · Bing Hu

1513 Dynamic Variations in Brain Glycogen are Involved in Modulating Isoflurane Anesthesia in Mice

Ze Fan · Zhihao Zhang · Shiyi Zhao · Yuanyuan Zhu · Dong Guo · Bo Yang · Lixia Zhuo · Jiao Han · Rui Wang · Zongping Fang · Hailong Dong · Yan Li · Lize Xiong



p 1443

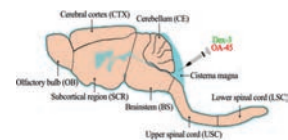


p 1479

Method

1524 Quantitative Determination of Glymphatic Flow Using Spectrophotofluorometry

Yu Zhang · Jian Song · Xu-Zhong He · Jian Xiong · Rong Xue · Jia-Hao Ge · Shi-Yu Lu · Die Hu · Guo-Xing Zhang · Guang-Yin Xu · Lin-Hui Wang



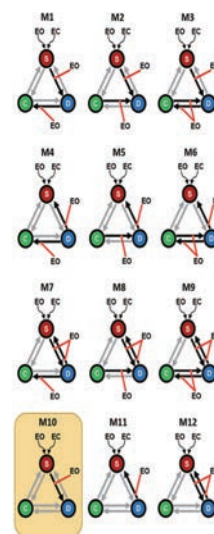
p 1527

Letters to the Editor

1538 Synaptic Adaptation Contributes to Stimulus-Specific Adaptation in the Thalamic Reticular Nucleus

Yu-Ying Zhai · Ryszard Aukstulewicz · Pei-Run Song · Zhi-Hai Sun · Yu-Mei Gong · Xin-Yu Du · Jie He · Xiongjie Yu

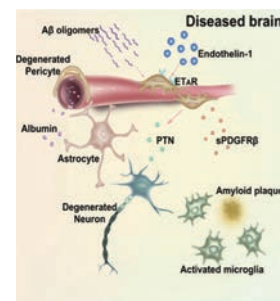
- 1542 Iron Aggravates the Depressive Phenotype of Stressed Mice by Compromising the Glymphatic System**
Shanshan Liang · Yan Lu · Zexiong Li · Shuai Li · Beina Chen · Manman Zhang · Binjie Chen · Ming Ji · Wenliang Gong · Maosheng Xia · Alexei Verkhratsky · Xu Wu · Baoman Li
- 1547 Eye-Opening Alters the Interaction Between the Salience Network and the Default-Mode Network**
Junrong Han · Xuehai Wu · Hang Wu · Dong Wang · Xuan She · Musi Xie · Fang Zhang · Delong Zhang · Xilin Zhang · Pengmin Qin
- 1552 Pgan4 and Tango1 Mediate Anoxia and Reoxygenation Injury**
Qingqing Du · Nastasia K.H. Lim · Yiling Xia · Wangchao Xu · Qichao Zhang · Liyao Zhang · Fude Huang · Wenan Wang
- 1558 Complement Factor H Displays Opposite Expression Patterns Under Two Situations of Methamphetamine Administration: Acute Exposure and Chronic Dependence**
Ming Lin · Jiamin Xu · Zhimin Liu · Liang Qin · Xiaodong Wang · Xiaoping Pu
- 1563 Image-Forming Visual Basis of Empathy for Pain in Mice**
Kai-Wen Geng · Rui Du · Na Wei · Chun-Li Li · Yan Wang · Wei Sun · Tao Chen · Dong-Yu Wei · Yang Yu · Ting He · Wen-Jun Luo · Rui-Rui Wang · Zhou-Feng Chen · Jun Chen



p 1550

Research Highlights

- 1570 New Insights into the Dysfunctions of Pericytes and Neurovascular Units in Neurodegenerative Diseases**
Qiang Liu · Wei-Jye Lin · Yamei Tang
- 1573 A Novel Potassium Nanosensor Powers up the Detection of Extracellular K⁺ Dynamics in Neuroscience**
Ying Wang · Qingyu Wang · Xia Zhang
- 1576 SCGN-regulated Stage-wise SNARE Assembly: Novel Insight into Synaptic Exocytosis**
Ying Lv · Sunmin Xiang · Renxian Cao · Li Wu · Jing Yang



p 1571



Tau Accumulation and Defective Autophagy: A Common Pathological Mechanism Underlying Repeat-Expansion-Induced Neurodegenerative Diseases?

Li Song¹ · Luoying Zhang^{1,2}

Received: 15 May 2020 / Accepted: 3 June 2020 / Published online: 5 November 2020
© Shanghai Institutes for Biological Sciences, CAS 2020

Repetitive DNA tracts (microsatellites) occur thousands of times throughout the human genome, and their expansion is known to cause many diseases. Expansion of CAG repeats encoding polyglutamine (polyQ) tracts is a pathological cause of nine neurodegenerative diseases: spinal and bulbar muscular atrophy, Huntington's disease, dentatorubropallidolusian atrophy, and six autosomal dominant forms of spinocerebellar ataxia (SCA1, 2, 3, 6, 7, and 17) [1]. In 2011, two independent groups found an intronic GGGGCC (G4C2) expansion mutant in *C9orf12* as the most common genetic cause of both amyotrophic lateral sclerosis (ALS) and frontotemporal dementia (FTD) [2, 3]. Evidence from these studies supports the idea that both loss-of-function and gain-of-function mechanisms contribute to these diseases. Bidirectional transcription of mutant *C9orf12* produces sense and antisense hexanucleotide repeat expansions. These RNA tracts can undergo repeat-associated non-AUG translation to produce aggregated dipeptides. The aggregated substances can lead to nuclear dysfunction, affecting RNA splicing and transcription as well as causing DNA damage. Proteostasis pathways have also been implicated in disease pathology, including impairments in autophagy and lysosomal function, the unfolded protein response, and the endoplasmic reticulum [4], as well as the ubiquitin–proteasome system [5]. Besides gain-of-function

mechanisms, the G4C2 repeats (G4C2r) also interfere with the expression of the *C9orf12* gene product, leading to a decreased protein level. Therefore, both *C9orf12* deficiency and toxic gain-of-function mechanisms can lead to various disruptions of nucleotides and proteins, although the pathological mechanisms remain largely unclear (Fig. 1).

Tau, a microtubule-associated protein first discovered in 1975 and encoded by *MAPT*, functions in microtubule assembly and stabilization (Fig. 2). Aggregation of tau is a defining pathological feature of several neurodegenerative diseases that are collectively known as tauopathies, including Alzheimer's disease, progressive supranuclear palsy, corticobasal degeneration, Huntington's disease, and frontotemporal dementia with parkinsonism-17 [6]. Under pathological conditions, the altered modification of tau can result in detachment of tau from microtubules, leading to defects in microtubule stabilization. Neurofibrillary tangles, which consist of hyper-phosphorylated tau acting in a toxic gain-of-function manner, interfere with the transport of vesicles and other cargos [7].

Previous studies implied a synergistic interaction between G4C2r expansion and tau that leads to neurodegeneration-related pathological features in both humans and flies. Moreover, the protein and phosphorylation levels of tau are increased by G4C2r expansion [8]. Hyperphosphorylated tau that tends to aggregate into insoluble neurofibrillary tangles are found in tauopathy patients. A new finding published in this issue of *Neuroscience Bulletin* demonstrates a potential role of tau in the development of G4C2r expansion-induced neurodegenerative diseases [9].

In this study by Wen and colleagues, overexpression of $(GGGGCC)_{30}$ repeats $[(G4C2r)_{30}]$ induced ALS-related phenotypes in flies, including neurodegeneration, motor

✉ Luoying Zhang
zhangluoying@hust.edu.cn

¹ Key Laboratory of Molecular Biophysics of the Ministry of Education, College of Life Science and Technology, Huazhong University of Science and Technology, Wuhan 430074, China

² Institute of Brain Research, Huazhong University of Science and Technology, Wuhan 430074, China

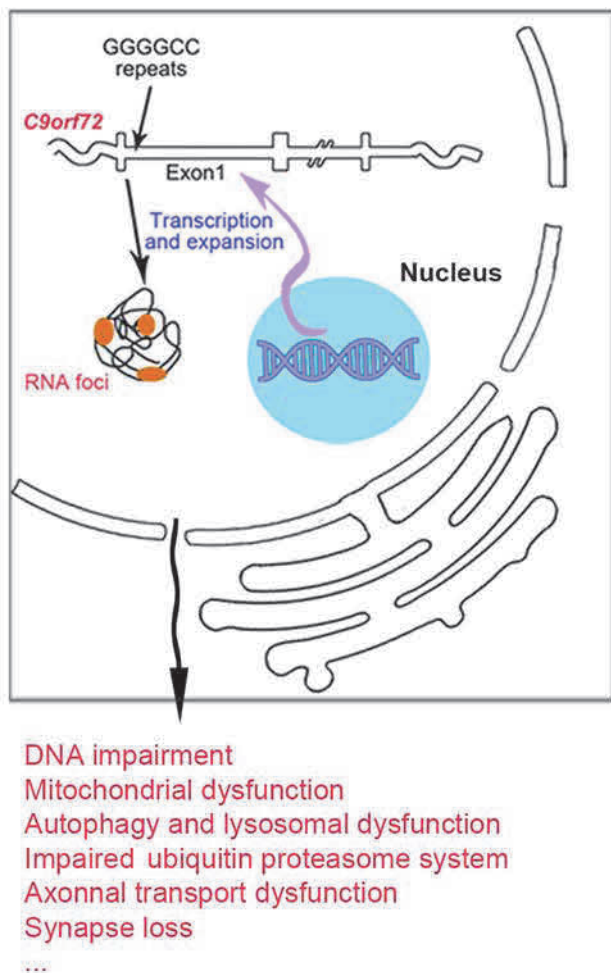


Fig. 1 Cellular processes implicated in FTD and ALS associated with G4C2 repeat expansion

deficits, and shortened life span, indicating that the fly model recapitulates some of the major symptoms in human ALS patients [9]. Importantly, *dtau* homozygous (*dtau* $-/-$) or heterozygous knockout (*dtau* $+/-$) successfully rescued the ALS-related phenotypes in flies overexpressing (*G4C2r*)₃₀, implying that tau mediates the neurological perturbations caused by G4C2r expansion [9]. Consistent with the findings at the cellular and behavioral levels, expanded G4C2r increases the tau protein levels and phosphorylated-tau levels in both fly and human cells, further suggesting a key role of tau in the expanded G4C2r-induced neurodegeneration [9].

In ALS patients with C9ORF72 expansion, cytoplasmic p62/sequestosome-1 (SQSTM1)-positive inclusions have been observed in neurons of the cerebellum, hippocampus, and neocortex. Given that SQSTM1/p62 functions as an autophagy receptor, this suggests autophagy deficits in these patients. Molecular characterizations in cell lines and primary neurons indicate that C9ORF72 regulates the initiation of autophagy by interacting with the Rab1a and

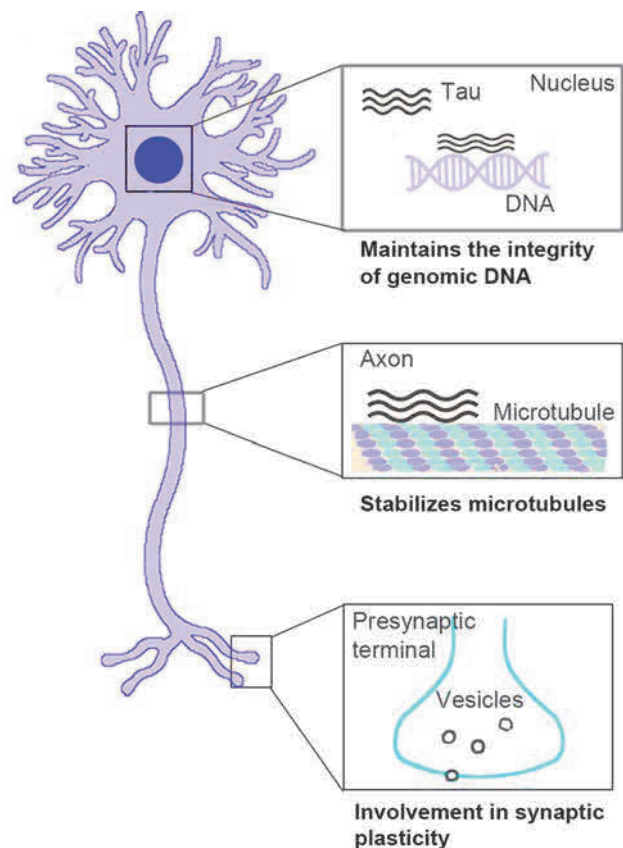


Fig. 2 Potential roles of tau in different subcellular compartments

ULK1 autophagy initiation complex. Depletion of *C9orf72* leads to p62/SQSTM1-positive inclusions in these cells [10]. In the current study, on the other hand, the authors found that expansion of G4C2r in both fly and human cells impaired autophagic flux by inhibiting autophagosome-autolysosome fusion, which contributes to tau aggregation [9]. Bcl2-associated athanogene 3 (BAG3) is a member of the BAG family of co-chaperones and interacts with heat shock protein (Hsp) 70. As an autophagy regulator, BAG3 can cooperate with the autophagy receptor SQSTM1/p62 to mediate the clearance of soluble tau and its phosphorylated forms. During this degradation process, BAG3 regulates autophagic flux through interaction with the post-synaptic cytoskeletal protein synaptopodin in mature neurons [11]. In this study, the authors showed that expanded G4C2r expression reduced *BAG3/starvin* mRNA levels and overexpression of *BAG3* rescued the impaired autophagic flux [9]. Taken together, these results reveal a potential pathological mechanism underlying neurological diseases caused by G4C2 expansion: the expanded G4C2r expression decreases *BAG3* expression, leading to reduced autophagic flux and tau accumulation. Given that tau also appears to mediate HTT-induced neurodegeneration, alterations in the BAG3-autophagy-tau pathway may contribute to the pathological processes in Huntington's disease and

perhaps other repeat-expansion-induced neurodegenerative diseases as well. Further explorations are needed to validate this, as well as to determine whether these findings in flies hold true in mammals. Nonetheless, the current work offers new hope for possible therapeutic targets for these devastating neurodegenerative diseases.

References

1. Lieberman AP, Shakkottai VG, Albin RL. Polyglutamine repeats in neurodegenerative diseases. *Annu Rev Pathol* 2019, 14: 1–27.
2. DeJesus-Hernandez M, Mackenzie IR, Boeve BF, Boxer AL, Baker M, Rutherford NJ, *et al.* Expanded GGGGCC hexanucleotide repeat in noncoding region of C9ORF72 causes chromosome 9p-linked FTD and ALS. *Neuron* 2011, 72: 245–256.
3. Renton AE ME, Waite A, Simon-Sanchez J, Rollinson S, Gibbs JR, *et al.* A hexanucleotide repeat expansion in C9ORF72 is the cause of chromosome 9p21-linked ALS-FTD. *Neuron* 2011: 245–256.
4. Wang R, Xu X, Hao Z, Zhang S, Wu D, Sun H, *et al.* Poly-PR in C9ORF72-related amyotrophic lateral sclerosis/frontotemporal dementia causes neurotoxicity by clathrin-dependent endocytosis. *Neurosci Bull* 2019, 35: 889–900.
5. Haeusler AR, Donnelly CJ, Rothstein JD. The expanding biology of the C9orf72 nucleotide repeat expansion in neurodegenerative disease. *Nat Rev Neurosci* 2016, 17: 383–395.
6. Wang Y, Mandelkew E. Tau in physiology and pathology. *Nat Rev Neurosci* 2016, 17: 5–21.
7. Ballatore C, Lee VM, Trojanowski JQ. Tau-mediated neurodegeneration in Alzheimer's disease and related disorders. *Nat Rev Neurosci* 2007, 8: 663–672.
8. He H, Huang W, Wang R, Lin Y, Guo Y, Deng J, *et al.* Amyotrophic lateral sclerosis-associated GGGGCC repeat expansion promotes Tau phosphorylation and toxicity. *Neurobiol Dis* 2019, 130: 104493.
9. Wen X, An P, Li H, Zhou Z, Sun Y, Wang J, *et al.* Tau accumulation via reduced autophagy mediates GGGGCC repeat expansion-induced neurodegeneration in *Drosophila* ALS models. *Neurosci Bull* 2020. <https://doi.org/10.1007/s12264-020-00518-2>.
10. Webster CP, Smith EF, Grierson AJ, De Vos KJ. C9orf72 plays a central role in Rab GTPase-dependent regulation of autophagy. *Small GTPases* 2018, 9: 399–408.
11. Ji C, Tang M, Zeidler C, Hohfeld J, Johnson GV. BAG3 and SYNPO (synaptopodin) facilitate phospho-MAPT/Tau degradation via autophagy in neuronal processes. *Autophagy* 2019, 15: 1199–1213.



Dynamic Variations in Brain Glycogen are Involved in Modulating Isoflurane Anesthesia in Mice

Ze Fan¹ · Zhihao Zhang² · Shiyi Zhao¹ · Yuanyuan Zhu³ · Dong Guo² ·
Bo Yang¹ · Lixia Zhuo⁴ · Jiao Han⁴ · Rui Wang³ · Zongping Fang¹ ·
Hailong Dong¹ · Yan Li⁴ · Lize Xiong^{1,5} 

Received: 23 December 2019 / Accepted: 20 May 2020 / Published online: 13 October 2020
© The Author(s) 2020

Abstract General anesthesia severely affects the metabolites in the brain. Glycogen, principally stored in astrocytes and providing the short-term delivery of substrates to neurons, has been implicated as an affected molecule. However, whether glycogen plays a pivotal role in modulating anesthesia–arousal remains unclear. Here, we demonstrated that isoflurane-anesthetized mice exhibited dynamic changes in the glycogen levels in various brain regions. Glycogen synthase (GS) and glycogen

phosphorylase (GP), key enzymes of glycogen metabolism, showed increased activity after isoflurane exposure. Upon blocking glycogenolysis with 1,4-dideoxy-1,4-imino-D-arabinitol (DAB), a GP antagonist, we found a prolonged time of emergence from anesthesia and an enhanced δ frequency in the EEG (electroencephalogram). In addition, augmented expression of glycogenolysis genes in glycogen phosphorylase, brain (Pygb) knock-in (Pygb^{H11/H11}) mice resulted in delayed induction of anesthesia, a shortened emergence time, and a lower ratio of EEG- δ . Our findings revealed a role of brain glycogen in regulating anesthesia–arousal, providing a potential target for modulating anesthesia.

Ze Fan, Zhihao Zhang and Shiyi Zhao have contributed equally to this work.

Electronic supplementary material The online version of this article (<https://doi.org/10.1007/s12264-020-00587-3>) contains supplementary material, which is available to authorized users.

✉ Yan Li
liyanxjtu@xjtu.edu.cn

✉ Lize Xiong
mzkxlz@126.com; lizexiong@tongji.edu.cn

¹ Department of Anesthesiology and Perioperative Medicine, Xijing Hospital, Fourth Military Medical University, Xi'an 710032, Shaanxi, China

² College of Basic Medicine, Fourth Military Medical University, Xi'an 710032, Shaanxi, China

³ Department of Neurobiology, Fourth Military Medical University, Xi'an 710032, Shaanxi, China

⁴ Center for Brain Science and Department of Anesthesiology, The First Affiliated Hospital of Xi'an Jiaotong University, Xi'an 710061, Shaanxi, China

⁵ Translational Research Institute of Brain and Brain-Like Intelligence, Department of Anesthesiology and Perioperative Medicine, Shanghai Fourth People's Hospital Affiliated to Tongji University School of Medicine, Shanghai 200081, China

Keywords Anesthesia-arousal · Brain glycogen · General anesthesia · Glycogen phosphorylase · Glycogen synthetase · Isoflurane

Introduction

General anesthetics are widely used clinically. However, the mechanisms through which general anesthetics induce quiescent neuronal activity and cause unconsciousness remain largely unknown [1–6]. In recent decades, the role of cerebral energy metabolism has attracted increasing attention [7, 8]. It has been revealed that mutations in complex I of mitochondria increase the sensitivity of *Caenorhabditis elegans* to volatile anesthetics [9–12]. Recently, emerging evidence has indicated that a reduction in cellular adenosine triphosphate (ATP) levels is associated with a delay in isoflurane-induced loss of the righting reflex (LORR) in mice [13], suggesting that changes in available cerebral energy might regulate anesthetic effects [11–13].

Brain glycogen, principally stored in astrocytes rather than in neurons, is considered to be the largest on-demand energy source in the brain [14–17]. Glycogen can be metabolized into phosphorylated glucose and subsequently produce pyruvate, which is eventually converted to lactate [15]. According to the “lactate shuttle” hypothesis, the lactate derived from astrocytic glycogen is transferred into neighboring neurons to fuel the tricarboxylic acid cycle [18–20]. In addition, a growing body of evidence indicates that astrocytic glycogenolysis and the subsequent lactate transport play a crucial role in memory formation, long-term potentiation of synapses, and other physiological and pathological events in the brain [17, 21–23]. Although general anesthetics such as ether and pentobarbital have been reported to induce increased levels of brain glycogen [24–26], dynamic changes in brain glycogen throughout anesthesia and their association with anesthetic effects remain unclear. Moreover, since the amount of brain glycogen is steadily and dynamically maintained due to the balance between glycogenesis and glycogenolysis, two key enzymes – glycogen synthase (GS) and glycogen phosphorylase (GP) – are responsible for the regulation of brain glycogen levels [15]. However, much less attention has been directed toward the effects of anesthetic agents on glycogen metabolic enzymes.

In this study, we investigated changes in the brain glycogen levels and key enzymes of glycogen metabolism in the cortex, hippocampus, thalamus, and striatum during isoflurane anesthesia in mice. Furthermore, an inhibitor of GP (DAB) and transgenic *Pygb* knock-in (*Pygb*^{H11/H11}) mice were used to test the hypothesis that brain glycogen plays a crucial role in modulating anesthesia–arousal.

Materials and Methods

Animals and Experimental Protocols

Male C57BL/6 mice (8 weeks old) weighing 22 g–25 g were purchased from the Animal Experimental Center of the Fourth Military Medical University (Xi’an, China), and all experiments were conducted with the approval of the Ethics Committee for Animal Experimentation of the Fourth Military Medical University. Mice were housed in an environment with a temperature of 22°C–24°C, humidity 38%–42%, and a light–dark cycle of 12 h/12 h. Standard rodent chow and tap water were available *ad libitum*. Mice with *Pygb* knocked in at the H11 locus on chromosome 11 (heterozygous: *Pygb*^{H11/+}; from Cyagen Biosciences Inc., Guangzhou, China) were housed in a specific pathogen-free environment and were interbred to obtain homozygous *Pygb*^{H11/H11} mice and wild-type (WT) littermates.

Experiment 1: To investigate whether brain glycogen levels change during isoflurane anesthesia, 12 mice were randomly divided into two groups ($n = 6$ per group): a control group and an isoflurane exposure group (2 h of exposure). Then, the levels of brain glycogen in the cortex (CTX), hippocampus (HIPPO), thalamus (THAL) and striatum (STRIAT) were measured. To further evaluate the dynamic variations in brain glycogen during isoflurane anesthesia, the glycogen levels in the mice exposed to 1.4% isoflurane for different durations (0.5, 1, 2, or 4 h; $n = 6$ per duration) and in control mice were measured. We also assessed the glycogen levels under both control conditions and the following anesthetic states: LORR, isoflurane exposure for 2 h, recovery of righting reflex (RORR), and 2 h after isoflurane exposure ($n = 8$ per group).

Experiment 2: The effects of isoflurane exposure on key glycogen metabolic enzymes were examined. 8 mice were randomly divided into two groups ($n = 4$ per group): a control group and an isoflurane exposure group (2 h of exposure). The levels of phosphorylated GS and GP and their activities were measured in the indicated brain regions as described previously.

Experiment 3: To determine the role of brain glycogen in the induction of, maintenance of, and recovery from isoflurane anesthesia, 16 mice were randomly divided into two groups ($n = 8$ per group): intracerebroventricular injection of DAB (2 μ L, 300 pmol) 15 min before isoflurane exposure and a saline injection group [23, 27]. *Pygb*^{H11/H11} mice and WT littermates were also used ($n = 8$ per group). For these mice, the time to LORR and to RORR under 1.4% isoflurane exposure as well as the total percentage of power in the EEG under 0.8% isoflurane exposure were recorded.

Isoflurane Exposure

Mice were exposed to 1.4% isoflurane (R510-22, RWD Life Science, Shenzhen, China) in 98.6% oxygen (oxygen flow, 1 L/min) in a chamber with an air intake and exhaust system (20×10×11 cm³). The temperature was controlled at 37°C during anesthesia. The oxygen, carbon dioxide, and isoflurane levels were continuously monitored (MP-60, Phillips Medical Systems, Best, The Netherlands), and post-anesthesia care was carried out. All instances of isoflurane exposure were performed at 08:00–12:00 to avoid the influence of circadian rhythms. The control mice were administered 100% oxygen.

Brain Tissue Preparation and Glycogen Measurement

A focused microwave irradiation system (ORW1.5S-Focus, Orient Microwave, Nanjing, China) was used to

rapidly fix brain tissue and prevent glycogen breakdown [28]. Briefly, a mouse was confined in a specialized animal containment device. A high-energy microwave (1 kW) was focused on the head for 5 s, after which the brain was immediately removed and different regions were dissected under a stereomicroscope (SZ51, Olympus, Tokyo, Japan). For staining experiments, the brain was fixed in and incubated with 4% paraformaldehyde prior to paraffinization and sectioning. The glycogen levels in these samples were assessed with a glycogen assay kit (K648, BioVision, Milpitas, USA) or a periodic acid-Schiff (PAS) staining kit (ab150680, Abcam, Cambridge, MA, USA).

Enzyme Activity Assay

GS and GP activities were determined with assay kits (GMS50500.2 for GS and GMS50092.2 for GP, Genmed Scientifics, Shanghai, China). Relative activity was calculated by measuring the absorbance at 340 nm on a microplate reader (infinite M200, Tecan, Männedorf, Switzerland) and then by normalizing the value to that of the total protein levels in similar samples.

Immunoblotting

The brain tissue of mice was homogenized in RIPA lysis buffer (Beyotime, Nantong, China) containing a complete protease inhibitor and phosphatase inhibitor cocktail (1%, Thermo Fisher Scientific, Waltham, MA, USA). The protein concentration was determined with a BCA protein assay kit (23225, Thermo Fisher Scientific). Equivalent amounts of protein (30 μg per lane) were loaded and separated on SDS-PAGE gels and then transferred to 0.22- μm PVDF membranes (10600021, GE Healthcare, Munich, Germany) for 2 h. After the membranes were blocked with 5% skim milk, they were incubated overnight at 4°C with the following primary rabbit antibodies (Table S1): anti-PYGB (ab154969, 1:1000, Abcam), anti-GYS1 (ab40867, 1:1000, Abcam), anti-pSer641-GS (3891, 1:1000, CST), anti-pSer15-PYGB (synthesized by Genecreate Biological Engineering Co., Ltd, Wuhan, China), anti-AGL (ab133720, 1:1000, Abcam), anti-GBE1 (ab180596, 1:1000, Abcam), and anti- β -actin (ab119716, 1:1000, Abcam). After three washes, the membranes were incubated with goat anti-rabbit secondary antibody conjugated to horseradish peroxidase (ab6721, 1:5000, Abcam) for 2 h at room temperature. The membranes were washed again, and the bands were detected using a chemiluminescent horseradish peroxidase substrate (1812401, Millipore, MA, USA). The optical density of each band was analyzed using Quantity One software 5.0 (Bio-Rad, La Jolla, CA, USA).

Immunohistochemical/Immunofluorescent Staining

After brain sections were deparaffinized, endogenous peroxidase activity was blocked by immersion in hydrogen peroxide for 10 min. Then, the sections were incubated with 5% normal donkey serum for 1 h to block non-specific binding. Subsequently, the sections were incubated at 4°C overnight with the following primary antibodies as appropriate (Table S1): rabbit anti-PYGB (HPA031067, 1:50, Atlas), rabbit anti-GYS1 (1:25, Abcam), mouse anti-NeuN (MAB377, 1:200, Millipore), chicken anti-GFAP (GTX85454, 1:500, GeneTex), and goat anti-Iba1 (ab5076, 1:300, Abcam). The sections were then treated with fluorescent secondary antibodies as follows: AlexaFluor 488 (green)-conjugated goat anti-rabbit (A32731, 1:500), AlexaFluor 594 (red)-conjugated goat anti-chicken (A32759, 1:500), AlexaFluor 594-conjugated donkey anti-mouse (A32744, 1:500), and AlexaFluor 594-conjugated donkey anti-goat (A11058, 1:500) (all from Thermo Fisher Scientific). Nuclei were stained with DAPI (4',6-diamidino-2-phenylindole; 1:1000; Sigma-Aldrich, St Louis, MO, USA). Biotinylated secondary antibody (ab6721, 1:5000, Abcam) and peroxidase-conjugated streptavidin followed by chromogenic reaction with 3,3'-diaminobenzidine were added to sections for immunohistochemical staining, which were counterstained with hematoxylin.

Blood Glucose Analysis

The blood glucose levels were determined using a blood glucose meter (OneTouch Ultra, Johnson & Johnson, New Brunswick, NJ, USA).

Intracerebroventricular Injection

DAB (2 μL , 300 pmol, D1542, Sigma-Aldrich) or saline was injected into the lateral ventricle through a cannula (62003, RWD Life Science) placed 1 week before the experiment (0.22 mm posterior to bregma, 1.0 mm lateral, 1.5 mm deep).

Analysis of Anesthesia Induction and Emergence

Each mouse was placed in a rotating cylinder and then exposed to 1.4% isoflurane. The induction time was defined as the interval from the beginning of anesthesia to the LORR. Similarly, the emergence time was defined as the interval from the termination of anesthesia to the RORR.

EEG Recording and Analysis

For EEG recording, electrodes were implanted 7 days before experiments. After 0.8% isoflurane exposure for 30

min, EEG signals were digitized at 1 kHz by a PowerLab and LabChart system (AD Instruments, Dunedin, New Zealand) and were bandpass filtered at 0.3 Hz–50 Hz. The analysis of the percentage total power and construction of spectra were completed in MatLab (MathWorks, Natick, MA). EEG changes in the frequency bands δ (0.3 Hz–4 Hz), θ (4 Hz–10 Hz), α (10 Hz–15 Hz), β (15 Hz–25 Hz), and γ (25 Hz–50 Hz) were used to estimate the wake/anesthesia states.

Statistical Analysis

GraphPad Prism 7.0 (GraphPad Software, San Diego, CA) was used for statistical analysis. All results are shown as the mean \pm SEM. Comparisons between two groups were made using an unpaired *t*-test, and comparisons between multiple groups were made using one-way ANOVA with Tukey-Kramer's *post hoc* test. To determine statistically significant differences among groups at different time points throughout anesthesia delivery, one-way ANOVA with Sidak's multiple comparisons was used. $P < 0.05$ was considered statistically significant.

Results

Elevated Brain Glycogen Levels After Isoflurane Exposure

Mice were exposed to 1.4% isoflurane in 98.6% oxygen. Glycogen levels were measured in the CTX, HIPPO, THAL, and STRIAT. PAS staining revealed that after isoflurane exposure for 2 h, more intense signals were observed in the analyzed regions compared to those in the control group (Fig. 1A, B). Consistent with these data, the glycogen assay kit revealed higher glycogen levels in the homogenates of the CTX, HIPPO, THAL, and STRIAT after 2 h of isoflurane exposure (Fig. 1C). These data suggested that isoflurane anesthesia increases the glycogen levels in various brain regions, including the CTX, HIPPO, THAL, and STRIAT.

Dynamic Variations in Glycogen Levels Under Isoflurane Anesthesia

Next, we evaluated the temporal changes in glycogen levels during extended exposure to isoflurane (Fig. 2A). We noted that the degree of glycogen increase in the four regions was positively related to the duration of isoflurane anesthesia (Fig. 2D). We then assessed the glycogen levels under different anesthetic states according to the righting reflex behavior: no anesthesia (control), LORR, isoflurane exposure for 2 h, RORR, and 2 h after isoflurane exposure

(Fig. 2B, C). Generally, in the analyzed regions, the glycogen levels were elevated during anesthesia but reduced during arousal. Notably, the THAL displayed remarkable sensitivity to changes in anesthetic state because each state showed significant differences in glycogen levels in the THAL, while other regions did not show this pattern (Fig. 2E). Collectively, these results revealed a changing pattern of glycogen in specific brain regions under isoflurane anesthesia.

Glycogen Metabolism is Activated After Isoflurane Exposure

As glycogen levels are maintained in a balance between glycogenesis and glycogenolysis, we examined the key enzymes of glycogen metabolism. First, we used immunofluorescence to localize GS and GP. We found that GP was predominately co-localized with GFAP rather than with NeuN or Iba1, and GS co-localized with both GFAP and NeuN (Fig. 3A, B). These results indicated that both neurons and astrocytes are able to synthesize glycogen. However, most relevant to the role of brain glycogen as an energy source is the putative role of astrocytes in regulating glycogenolysis. Next, to verify the effects of isoflurane anesthesia on glycogen metabolism, we assessed the expression of key enzymes in the CTX, HIPPO, THAL and STRIAT. No significant differences were found after isoflurane exposure for 2 h (Fig. S1). However, the level of phosphorylated GS at Ser641 (p641-GS), which represents the inactivated form, was lower in various brain regions in the isoflurane-treated group than that in the control group, although there were no significant differences in these levels in the HIPPO and THAL (Fig. 3C). Concurrently, increased GS activity was also found (Fig. 3E). Similarly, the levels of phosphorylated GP at Ser15 (p15-GP) showed increased trends in the CTX, THAL, and STRIAT (Fig. 3D), which was consistent with the increased GP activity in these regions (Fig. 3F). Notably, GP activity and the phosphorylation level in the HIPPO showed no significant differences between the two groups (Fig. 3D, F). Therefore, these results demonstrated that isoflurane exposure enhances both the anabolism and catabolism of brain glycogen, although there is heterogeneity among regions.

Inhibition of Glycogenolysis Enhances EEG- δ Frequency and Delays Emergence from Anesthesia

To explore whether the variations in brain glycogen affect the isoflurane-induced EEG spectrum and anesthesia–arousal, DAB (2 μ L, 300 pmol), a GP antagonist, was injected into the lateral ventricle (Fig. 4A). DAB injection led to a significant decrease in GP activity in the HIPPO,

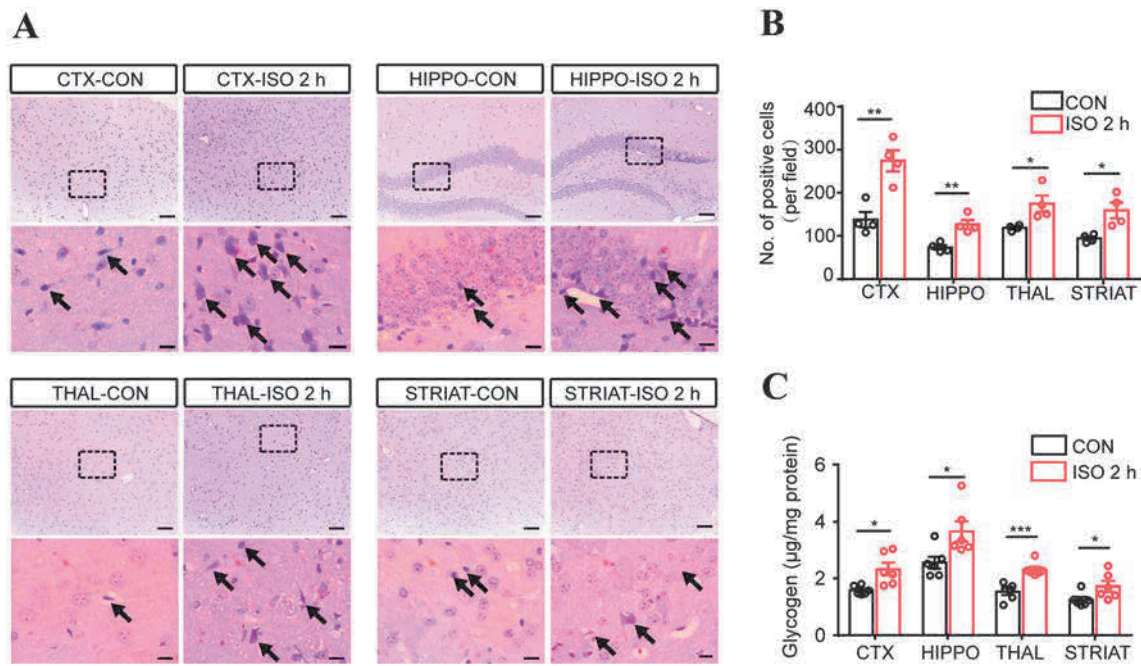


Fig. 1 Brain glycogen levels increase in mice under isoflurane anesthesia. **A** Representative PAS staining of sections in the four brain regions. (arrows, cells with abundant glycogen; scale bars, 100 µm in upper panels, 20 µm in lower panels). **B** Numbers of PAS-positive cells per field under 20× magnification ($n = 4$ per group).

C Glycogen levels ($n = 6$ per group). * $P < 0.05$, ** $P < 0.01$, *** $P < 0.001$ vs control. CON, oxygen control; ISO 2 h, isoflurane exposure for 2 h; CTX, cortex; HIPPO, hippocampus; THAL, thalamus; STRIAT, striatum.

Fig. 2 Dynamic variations in glycogen levels in mice under isoflurane anesthesia.

A Schematic of the different time points at which brain glycogen levels during administration of isoflurane anesthesia were measured. **B** Schematic of brain glycogen at key time points during isoflurane anesthesia. **C** Cartoon of observation of righting reflex behavior. **D** Brain glycogen slowly accumulates in a time-dependent manner in different brain regions ($n = 6$ per group). **E** Patterns of regional changes in brain glycogen during isoflurane anesthesia ($n = 8$ per group). * $P < 0.05$, ** $P < 0.01$, *** $P < 0.001$, and **** $P < 0.0001$. ISO 2 h-R 2 h, 2 h after isoflurane exposure; LORR, loss of righting reflex; RORR, recovery of righting reflex.

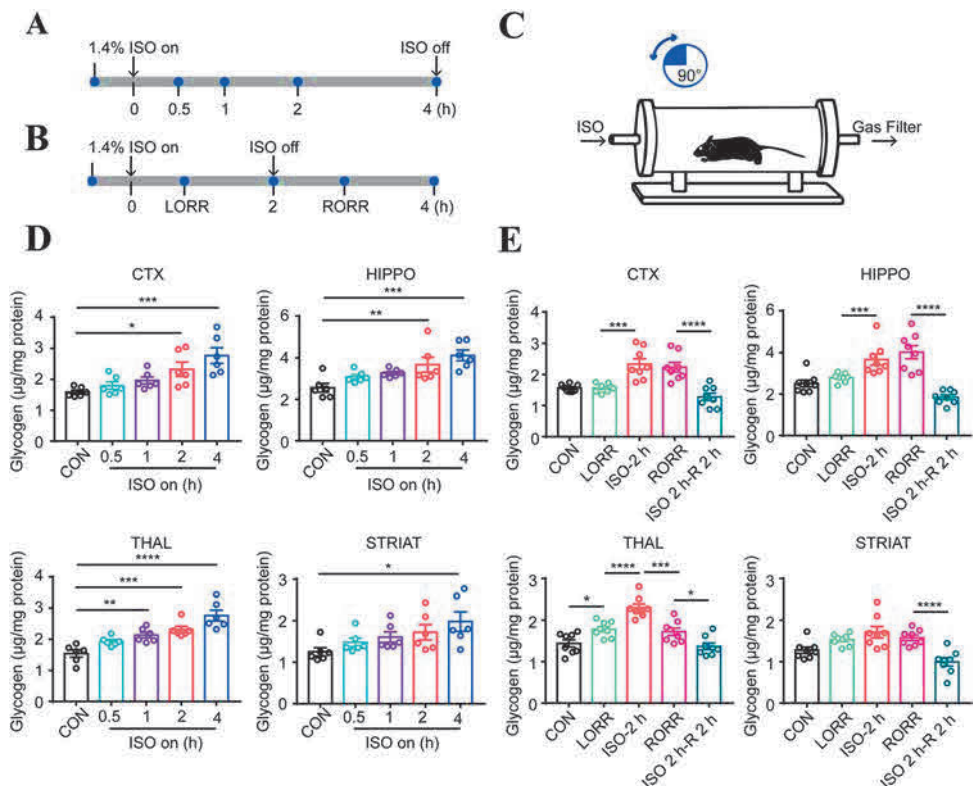
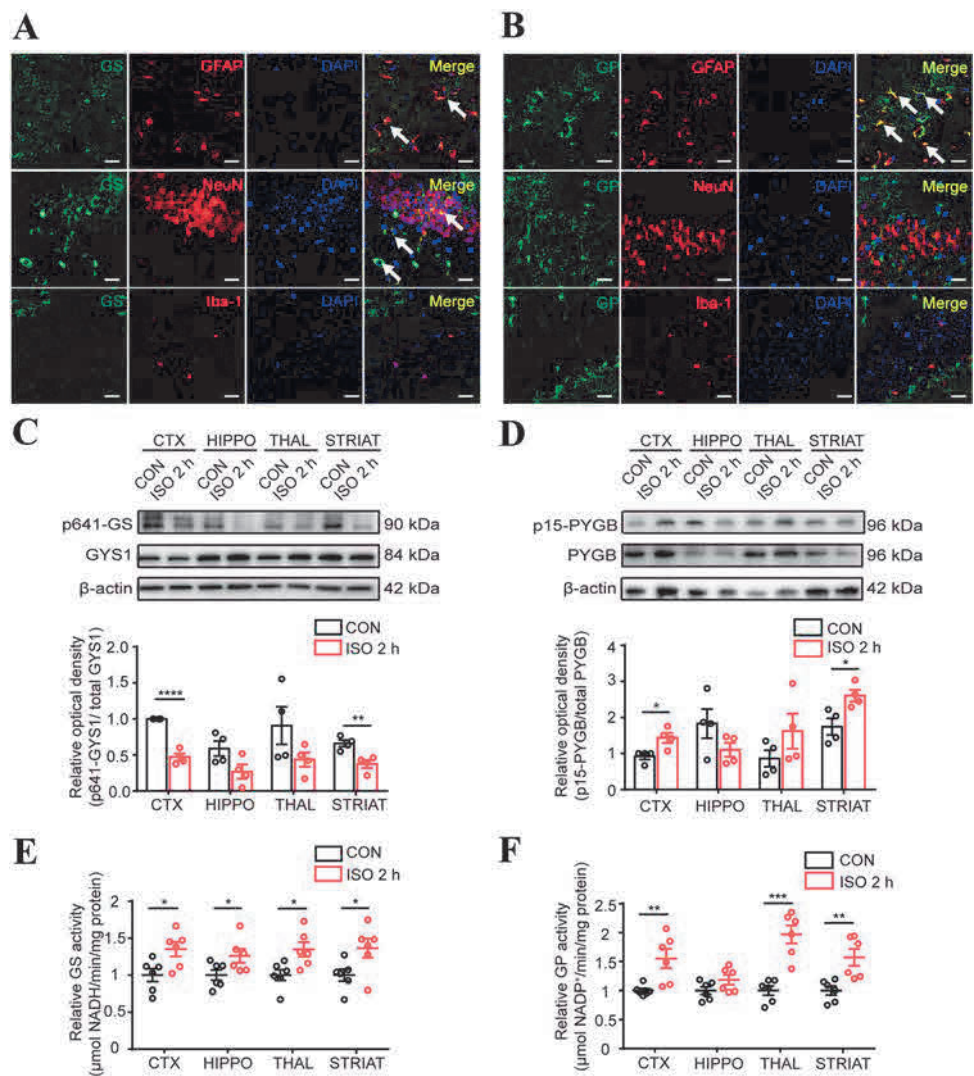


Fig. 3 Effects of isoflurane on enzymes related to glycogen metabolism. **A, B** Representative images of immunofluorescent staining of GS (**A**) and GP (**B**) with GFAP, NeuN and Iba-1 (arrows, co-labeled cells; scale bars, 20 μ m). **C, D** Levels of phosphorylated GS at Ser641 (**C**) and phosphorylated GP at Ser15 (**D**) ($n = 4$ per group). **E, F** Activity of GS (**E**) and GP (**F**) in the presence or absence of isoflurane exposure ($n = 6$ per group). * $P < 0.05$, ** $P < 0.01$, *** $P < 0.001$, **** $P < 0.0001$ vs control.



THAL, and STRIAT (Fig. 4B). GP activity in the CTX was also down-regulated, but there were no significant differences between the DAB and saline groups (Fig. 4B). At 15 min after DAB administration, mice were exposed to isoflurane (Fig. 4C). The glycogen levels were higher in the DAB injection group than in the saline group after isoflurane exposure for 2 h (Fig. 4D). Despite a declining trend, there were no significant differences in the LORR time between the two groups (Fig. 4E), but the RORR time was markedly delayed in the mice receiving DAB compared with those receiving saline (Fig. 4F). The total percentage power of the EEG spectrum under 0.8% isoflurane exposure showed that the ratio of the δ band increased after DAB injection, and no significant differences in the other bands were found between the two groups (Fig. 4G–I). Hence, we concluded that blocking glycogenolysis by DAB has an anesthesia-promoting effect.

Augmentation of Glycogenolysis Reduces EEG- δ Frequency, Prolongs Anesthesia Induction, and Facilitates Emergence from Anesthesia

To further corroborate the role of glycogenolysis in isoflurane anesthesia, we generated GFAP-specific Pygb knock-in mice by using CRISPR/Cas-mediated genome editing to insert the “GFAP-mouse Pygb CDS-Poly A” cassette into the H11 locus on mouse chromosome 11 (Fig. S2A). Genotypes were identified by PCR, and homozygous Pygb^{H11/H11} mice (747 bp/747 bp) and WT littermates (519 bp/519 bp) were used in the experiments (Fig. S2B). Immunocytochemistry and immunoblotting were used to evaluate the gene-targeting efficiency of Pygb overexpression, both of which demonstrated a significant increase in PYGB expression compared to that in WT littermates (Fig. S2C, D). Under isoflurane anesthesia, the glycogen levels in the four assessed regions were markedly higher in Pygb^{H11/H11} mice than in WT littermates

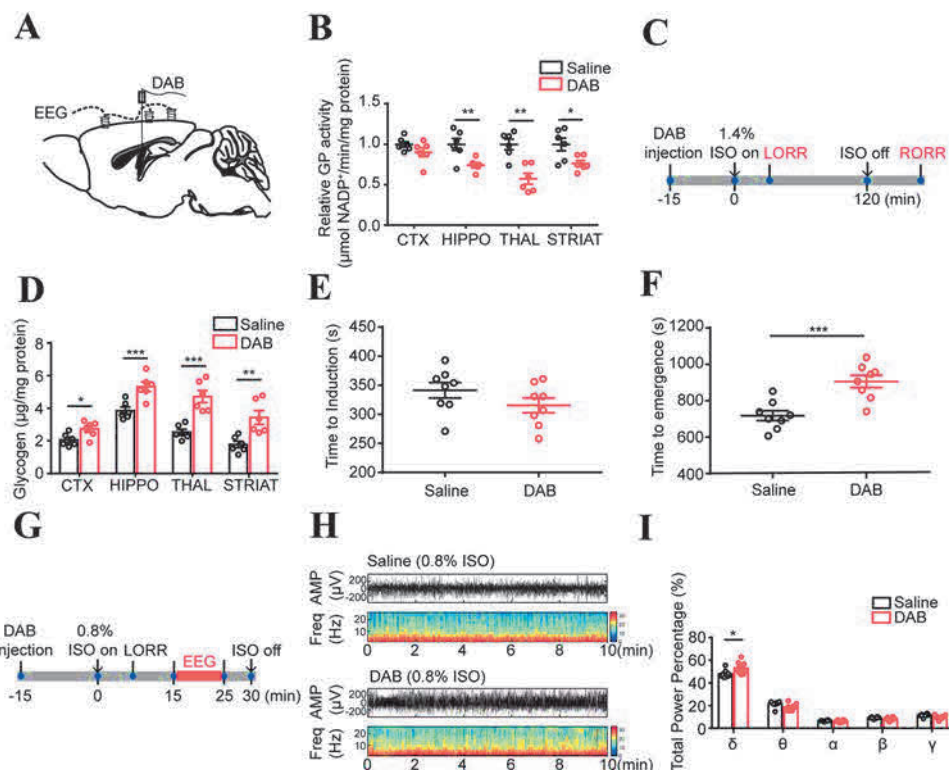


Fig. 4 Inhibiting glycogenolysis with DAB accelerates induction of isoflurane anesthesia in mice. **A** Diagram of the intracerebroventricular injection site. **B** GP activity in the brain regions 2 h after DAB injection ($n = 6$ per group). **C** Protocol for recording the LORR and RORR times of mice under 1.4% isoflurane anesthesia. **D** Brain glycogen levels in the selected regions under isoflurane anesthesia for 2 h after DAB or saline injection ($n = 6$ per group). **E**, **F** The LORR

(**E**) and RORR (**F**) times in the DAB and saline injection groups after 2 h of isoflurane exposure ($n = 8$ per group). **G** Protocol for recording the EEG in mice under 0.8% isoflurane anesthesia. EEG recording for 10 min began at 15 min after initial administration of isoflurane. **H** Representative EEG traces and heat maps. (**I**) Total percentage power of the EEG in mice under 0.8% isoflurane exposure ($n = 8$ per group). * $P < 0.05$, ** $P < 0.01$, *** $P < 0.001$.

(Fig. 5A). Compared with WT littermates, $Pygb^{H11/H11}$ mice exhibited an increased time to LORR (Fig. 5B) and a reduced time to RORR (Fig. 5C). EEG signals showed that the δ -band ratio was significantly decreased. In addition, there were no significant differences in the other EEG bands between the two groups (Fig. 5D–F). Taken together, these results suggested that the enhanced capacity for glycogenolysis in $Pygb^{H11/H11}$ mice leads to an arousal-promoting effect.

Discussion

In the current study, we demonstrated that exposure to the inhalational anesthetic isoflurane increased the levels of glycogen in various brain regions: the CTX, HIPPO, THAL, and STRIAT. Decreased phosphorylation of GS at Ser641 and increased phosphorylation of GP at Ser15, which were accompanied by increased activity of the two rate-limiting enzymes in glycogen metabolism, occurred after 2 h of isoflurane anesthesia. Interventions targeting brain glycogen changed anesthesia-associated behaviors,

such as the latency of the LORR and RORR and the EEG spectrum. We conclude that the availability of brain glycogen is critical in the regulation of recovery from isoflurane anesthesia.

Brain glycogen, which is regarded as an advantageous form for glucose storage in astrocytes [15], has been implicated in various physiological and pathological events, such as memory formation, sleep, aging, exercise, migraine, and stroke [23, 29–32]. Brain glycogen levels have also been proposed to increase during general anesthesia, and the degree of increase is related to both the depth and duration of general anesthesia and the type of anesthetic used [24–26]. However, whether brain glycogen can be manipulated to regulate the effects of anesthesia remains unknown. Here, we found that the glycogen levels in the CTX, HIPPO, THAL, and STRIAT mildly increased during isoflurane exposure in a time-dependent manner, in agreement with previous studies [26]. Furthermore, we refined the correlation between the changing pattern of brain glycogen levels and anesthetic status: the induction of, maintenance of, and emergence from anesthesia. We concluded that brain glycogen levels increase as anesthesia

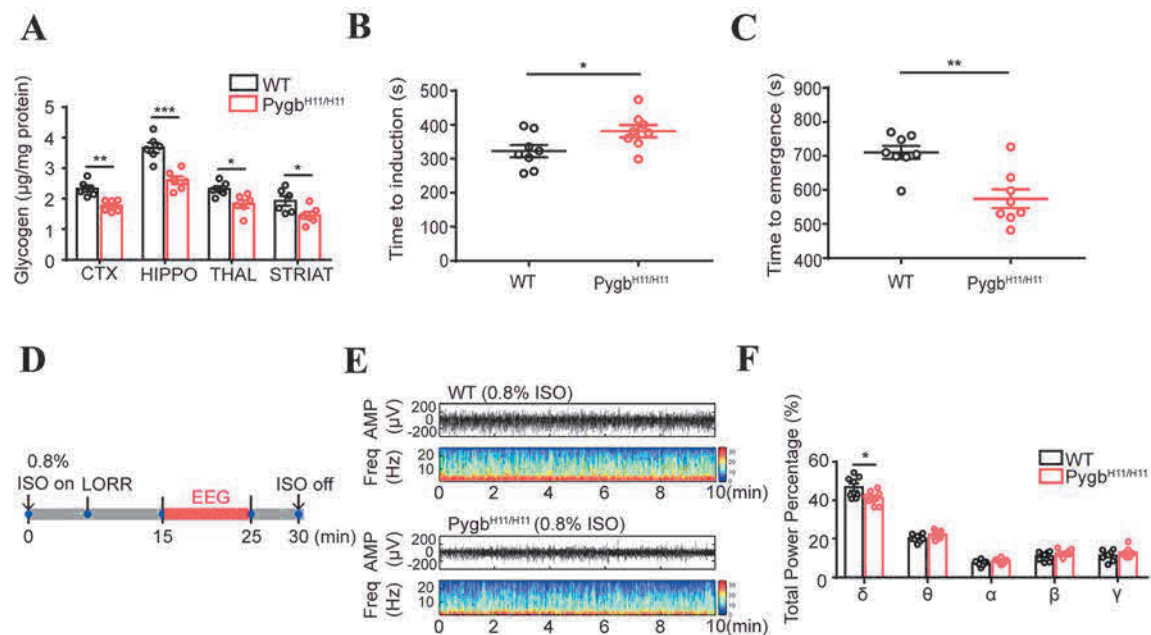


Fig. 5 $Pygb^{H11/H11}$ mice exhibit a decreased arousal time from isoflurane anesthesia. **A** Comparison of glycogen levels in several brain regions of $PyGB^{H11/H11}$ mice and their WT littermates after exposure to isoflurane for 2 h ($n = 6$ per group). **B**, **C** The LORR (**B**) and RORR (**C**) times of $PyGB^{H11/H11}$ and WT mice exposed to isoflurane for 2 h ($n = 8$ per group). **D** Protocol for recording EEG

frequency in mice under 0.8% isoflurane anesthesia for 10 min, beginning 15 min after initial administration of isoflurane. **E** Representative EEG traces and heat maps. **F** Total percentage power of the EEG bands in mice under 0.8% isoflurane anesthesia ($n = 8$ per group). * $P < 0.05$, ** $P < 0.01$, *** $P < 0.001$.

progresses and decrease as arousal progresses. Among the analyzed regions, the THAL showed strikingly sensitive changes in glycogen levels in response to the changes in anesthetic status, suggesting that glycogen in the THAL might play a distinctly important role in the regulation of anesthesia.

Since glycogen synthesis and degradation occur simultaneously, glycogen content varies depending upon the immediate energy needs of the tissue [33, 34]. Two rate-limiting enzymes, GS and GP, are involved in the regulation of glycogen metabolism [35]. According to our immunofluorescent staining results, GP is exclusively expressed in astrocytes, while GS is localized to both neurons and astrocytes in adult mice. The results are also supported by previous studies [36]. GS exists in two forms: the inactive phosphorylated form and active dephosphorylated form; its activity is controlled by glycogen synthase kinase-3 (GSK-3) and protein kinase A (PKA) [37]. GP, by contrast, exists in an active phosphorylated state and inactive dephosphorylated state; its activity in the brain is regulated by phosphorylase kinase (PhK) and the allosteric binding of AMP and glucose [38, 39]. Our previous study demonstrated that sevoflurane exposure induces the hyperphosphorylation of GSK-3 β [40], resulting in a shift towards GS dephosphorylation. Here, we provide evidence that isoflurane exposure results in decreased phosphorylation of GS at Ser641 (p641-GS), in accordance with the

increased GS activity found in the biochemical assay. Notably, isoflurane exposure also elicited hyperphosphorylation of GP at Ser15 (p15-GP) and increased GP activity in the CTX, THAL, and STRIAT. However, the levels of phosphorylated GP in the HIPPO showed no detectable change in our study. Additional studies are needed to clarify the heterogeneity of brain glycogen metabolism among brain regions.

The biosynthesis of brain glycogen depends heavily on the supply of blood glucose [41, 42], the levels of which tend to correlate with brain glycogen levels [43]. It has been reported that blood glucose levels are elevated after isoflurane anesthesia [44]. However, the relationship between blood glucose levels and brain glycogen under isoflurane anesthesia were still unclear. In this study, we investigated the pattern of blood glucose changes under different stages of isoflurane anesthesia (Fig. 2A, B), and found that the level began to increase significantly 30 min after 1.4% isoflurane anesthesia, then remained at the peak level (~ 14 mmol/L) for at least 4 h (Fig. S3A). The dynamic variations in blood glucose at different stages of isoflurane anesthesia were similar to those in brain glycogen shown in Fig. 2E (Fig. S3B). Considering the effect of brain glycogen and its underlying mechanism on anesthetic status is not totally understood, one possibility is that the effect might be induced by blood glucose levels [45]. Therefore, these levels were manipulated in mice by

intraperitoneal injection of exogenous glucose (2 g/kg) or glucose starvation with extended fasting (24 h) under isoflurane exposure [46, 47] (Fig. S4A, B). The results showed that the glycogen levels in the CTX, HIPPO, THAL, and STRIAT were significantly increased after glucose injection and decreased after extended fasting (Fig. S4C), in accordance with previous studies [48]. Besides, a low blood glucose level significantly delayed the time to RORR, while a high blood glucose level did not change the time to RORR (Fig. S4D). Since our pharmacological intervention targeting glycogenolysis only affected RORR (Fig. 4E, F), and in the interest of the clinical value of arousal modulation [49], in this experiment, we paid more attention to the effects of blood glucose level on RORR rather than on LORR. We speculate that the underlying mechanism that the extended fasting-induced delayed RORR is associated with the abnormal metabolism and dysfunction of neuronal cells under conditions of hypoglycemia, such as mitochondrial damage and oxidative stress [50, 51]. In addition, one explanation why glucose injection did not affect the time to RORR is that isoflurane anesthesia itself induces hyperglycemia [44], additional glucose feeding might not change the arousal from anesthesia. The mechanism underlying the arousal-modulating effect of brain glycogen after general anesthesia deserves further investigation.

Glycogenolysis in astrocytes is strictly associated with the fate of glucose as described by the astrocyte–neuron lactate shuttle (ANLS) hypothesis, which states that astrocyte-derived lactate supports neuronal metabolism and plasticity [30, 52]. To date, controversies about the existence and significance of the ANLS continue [53]. The “energetic” explanation is that the glycogen stored in astrocytes is rapidly converted to pyruvate/lactate *via* glycolysis. As a predominant energy substrate, lactate is transferred from astrocytes to neurons and metabolized in the tricarboxylic acid cycle for ATP synthesis during functional activation [18]. The rates of oxidative phosphorylation and changes in ATP concentrations alter the sensitivity of *C. elegans* and rodents to volatile anesthetics [11, 54, 55]. We found that DAB treatment resulted in significant amelioration of glycogenolysis and consequently induced an increase in the ratio of the δ band in the EEG spectrum and delayed emergence from anesthesia. By contrast, compared with WT littermates, transgenic $\text{Pygb}^{\text{H11/H11}}$ mice showed a lengthened induction time and reduced emergence time from anesthesia and the δ ratio in the EEG spectrum. Besides, a low blood glucose level induced by 24 h fasting significantly delayed the time to RORR, accompanied by reduced brain glycogen levels. These consolidated results suggested that changes in energy levels, particularly those produced by glycogen

degradation, modulate the effects of general anesthesia by isoflurane.

A previous study based on ^{13}C magnetic resonance spectroscopy *in vivo* proposed that lactate, a product of glycogenolysis, might be used as an alternative metabolic substrate under thiopental anesthesia [56]. Here, we found increased GP activity in the CTX, THAL, and STRIAT after isoflurane exposure for 2 h, indicating that isoflurane has an energy metabolism pattern similar to that of thiopental anesthesia to some degree. We speculate that the elevated GP activity is attributable to a compensatory reaction following the elevated glycogen level. Additional studies, such as investigating the time course of GS and GP activity, might uncover the mechanism.

A main limitation of our study is that we did not evaluate metabolites of glycogenolysis, such as lactate and ATP. Cell-based experiments could be designed to explore the energy network, especially the ANLS hypothesis, between astrocytes and neurons in the future. In addition, since the levels of blood glucose in the glucose injection group were already decreased after 2 h of isoflurane exposure compared with the beginning of anesthesia (Fig. S4B), persistent perfusion or different doses of glucose should be used to determine the effect of hyperglycemia on RORR under isoflurane anesthesia.

In conclusion, our results show that the dynamic variations in brain glycogen levels during general anesthesia are crucial to anesthesia–arousal modulation. Developing novel drugs targeting the degradation of brain glycogen may offer a promising strategy to modulate arousal during general anesthesia.

Acknowledgements We thank Dr. Bairen Wang (Department of Anesthesiology and Perioperative Medicine, Xijing Hospital, Fourth Military Medical University) for critical evaluation of the manuscript. This work was supported by the Major Program of the National Natural Science Foundation of China (81590954), the International Cooperation and Exchange of the National Natural Science Foundation of China (81420108013), and the State Key Program of National Natural Science Foundation of China (81730032).

Compliance with Ethical Standards

Conflict of interest The authors claim that there are no conflicts of interest.

Open Access This article is licensed under a Creative Commons Attribution 4.0 International License, which permits use, sharing, adaptation, distribution and reproduction in any medium or format, as long as you give appropriate credit to the original author(s) and the source, provide a link to the Creative Commons licence, and indicate if changes were made. The images or other third party material in this article are included in the article’s Creative Commons licence, unless indicated otherwise in a credit line to the material. If material is not included in the article’s Creative Commons licence and your intended use is not permitted by statutory regulation or exceeds the permitted use, you will need to obtain permission directly from the copyright

holder. To view a copy of this licence, visit <http://creativecommons.org/licenses/by/4.0/>.

References

- Kennedy D, Norman C. What don't we know? *Science* 2005, 309: 75.
- Brown EN, Lydic R, Schiff ND. General anesthesia, sleep, and coma. *N Engl J Med* 2010, 363: 2638–2650.
- Campagna JA, Miller KW, Forman SA. Mechanisms of actions of inhaled anesthetics. *N Engl J Med* 2003, 348: 2110–2124.
- Urban BW. Current assessment of targets and theories of anaesthesia. *Br J Anaesth* 2002, 89: 167–183.
- Li Y, Xu J, Xu Y, Zhao X, Liu Y, Wang J, *et al.* Regulatory effect of general anesthetics on activity of potassium channels. *Neurosci Bull* 2018, 34: 887–900.
- Ou M, Zhao W, Liu J, Liang P, Huang H, Yu H, *et al.* The general anesthetic isoflurane bilaterally modulates neuronal excitability. *iScience* 2020, 23: 100760.
- Hanley PJ, Ray J, Brandt U, Daut J. Halothane, isoflurane and sevoflurane inhibit NADH:ubiquinone oxidoreductase (complex I) of cardiac mitochondria. *J Physiol* 2002, 544: 687–693.
- Kayser EB, Suthammarak W, Morgan PG, Sedensky MM. Isoflurane selectively inhibits distal mitochondrial complex I in *Caenorhabditis elegans*. *Anesth Analg* 2011, 112: 1321–1329.
- Kayser EB, Morgan PG, Sedensky MM. GAS-1: a mitochondrial protein controls sensitivity to volatile anesthetics in the nematode *Caenorhabditis elegans*. *Anesthesiology* 1999, 90: 545–554.
- Cohen PJ. Effect of anesthetics on mitochondrial function. *Anesthesiology* 1973, 39: 153–164.
- Kayser EB, Sedensky MM, Morgan PG. The effects of complex I function and oxidative damage on lifespan and anesthetic sensitivity in *Caenorhabditis elegans*. *Mech Ageing Dev* 2004, 125: 455–464.
- Morgan PG, Hoppel CL, Sedensky MM. Mitochondrial defects and anesthetic sensitivity. *Anesthesiology* 2002, 96: 1268–1270.
- Wang H, Xu Z, Wu A, Dong Y, Zhang Y, Yue Y, *et al.* 2-deoxy-D-glucose enhances anesthetic effects in mice. *Anesth Analg* 2015, 120: 312–319.
- Brown AM, Ransom BR. Astrocyte glycogen and brain energy metabolism. *Glia* 2007, 55: 1263–1271.
- Brown AM. Brain glycogen re-awakened. *J Neurochem* 2004, 89: 537–552.
- Cataldo AM, Broadwell RD. Cytochemical identification of cerebral glycogen and glucose-6-phosphatase activity under normal and experimental conditions. II. Choroid plexus and ependymal epithelia, endothelia and pericytes. *J Neurocytol* 1986, 15: 511–524.
- Duran J, Guinovart JJ. Brain glycogen in health and disease. *Mol Aspects Med* 2015, 46: 70–77.
- Brooks GA. The science and translation of lactate shuttle theory. *Cell Metab* 2018, 27: 757–785.
- Belanger M, Allaman I, Magistretti PJ. Brain energy metabolism: focus on astrocyte-neuron metabolic cooperation. *Cell Metab* 2011, 14: 724–738.
- Pellerin L, Bouzier-Sore AK, Aubert A, Serres S, Merle M, Costalat R, *et al.* Activity-dependent regulation of energy metabolism by astrocytes: an update. *Glia* 2007, 55: 1251–1262.
- Gibbs ME, Anderson DG, Hertz L. Inhibition of glycogenolysis in astrocytes interrupts memory consolidation in young chickens. *Glia* 2006, 54: 214–222.
- Newman LA, Korol DL, Gold PE. Lactate produced by glycogenolysis in astrocytes regulates memory processing. *PLoS One* 2011, 6: e28427.
- Suzuki A, Stern SA, Bozdagi O, Huntley GW, Walker RH, Magistretti PJ, *et al.* Astrocyte-neuron lactate transport is required for long-term memory formation. *Cell* 2011, 144: 810–823.
- Nelson SR, Schulz DW, Passonneau JV, Lowry OH. Control of glycogen levels in brain. *J Neurochem* 1968, 15: 1271–1279.
- Rosengarten H. Glycogen level and oxygen consumption of rabbit brain tissue slices under ethyl ether and halothane anesthesia. *Agressologie* 1970, 11: 159–162.
- Hutchins DA, Rogers KJ. Physiological and drug-induced changes in the glycogen content of mouse brain. *Br J Pharmacol* 1970, 39: 9–25.
- Walls AB, Sickmann HM, Brown A, Bouman SD, Ransom B, Schousboe A, *et al.* Characterization of 1,4-dideoxy-1,4-imino-D-arabinitol (DAB) as an inhibitor of brain glycogen shunt activity. *J Neurochem* 2008, 105: 1462–1470.
- Oe Y, Baba O, Ashida H, Nakamura KC. Glycogen distribution in the microwave-fixed mouse brain reveals heterogeneous astrocytic patterns. *Glia* 2016, 64: 1532–1545.
- Kilic K, Karatas H, Donmez-Demir B, Eren-Kocak E, Gursoy-Ozdemir Y, Can A, *et al.* Inadequate brain glycogen or sleep increases spreading depression susceptibility. *Ann Neurol* 2018, 83: 61–73.
- Drulis-Fajdasz D, Gizak A, Wojtowicz T, Wisniewski JR, Rakus D. Aging-associated changes in hippocampal glycogen metabolism in mice. Evidence for and against astrocyte-to-neuron lactate shuttle. *Glia* 2018, 66: 1481–1495.
- Hossain MI, Roulston CL, Stapleton DI. Molecular basis of impaired glycogen metabolism during ischemic stroke and hypoxia. *PLoS One* 2014, 9: e97570.
- Matsui T, Soya S, Okamoto M, Ichitani Y, Kawanaka K, Soya H. Brain glycogen decreases during prolonged exercise. *J Physiol* 2011, 589: 3383–3393.
- Prats C, Graham TE, Shearer J. The dynamic life of the glycogen granule. *J Biol Chem* 2018, 293: 7089–7098.
- Hosokawa M, Takeuchi A, Tanihata J, Iida K, Takeda S, Hagiwara M. Loss of RNA-binding protein sfpq causes long-gene transcriptopathy in skeletal muscle and severe muscle mass reduction with metabolic myopathy. *iScience* 2019, 13: 229–242.
- Roach PJ, Depaoli-Roach AA, Hurley TD, Tagliabracci VS. Glycogen and its metabolism: some new developments and old themes. *Biochem J* 2012, 441: 763–787.
- Pellegrini G, Rossier C, Magistretti PJ, Martin JL. Cloning, localization and induction of mouse brain glycogen synthase. *Brain Res Mol Brain Res* 1996, 38: 191–199.
- Zois CE, Harris AL. Glycogen metabolism has a key role in the cancer microenvironment and provides new targets for cancer therapy. *J Mol Med (Berl)* 2016, 94: 137–154.
- Ferrer JC, Favre C, Gomis RR, Fernandez-Novell JM, Garcia-Rocha M, de la Iglesia N, *et al.* Control of glycogen deposition. *FEBS Lett* 2003, 546: 127–132.
- Mathieu C, Li de la Sierra-Gallay I, Duval R, Xu X, Coccagn A, Leger T, *et al.* Insights into brain glycogen metabolism: The structure of human brain glycogen phosphorylase. *J Biol Chem* 2016, 291: 18072–18083.
- Chen Y, Nie H, Tian L, Tong L, Deng J, Zhang Y, *et al.* Sevoflurane preconditioning-induced neuroprotection is associated with Akt activation via carboxy-terminal modulator protein inhibition. *Br J Anaesth* 2015, 114: 327–335.
- McEwen BS, Reagan LP. Glucose transporter expression in the central nervous system: relationship to synaptic function. *Eur J Pharmacol* 2004, 490: 13–24.

42. Vannucci SJ, Maher F, Simpson IA. Glucose transporter proteins in brain: delivery of glucose to neurons and glia. *Glia* 1997, 21: 2–21.
43. Poiry-Yamate C, Lei H, Gruetter R. The rate-limiting step for glucose transport into the hypothalamus is across the blood-hypothalamus interface. *J Neurochem* 2009: 38–45.
44. Pomplun D, Möhlig M, Spranger J, Pfeiffer AFH, Istow M. Elevation of blood glucose following anaesthetic treatment in C57BL/6 mice. *Horm Metab Res* 2004, 36: 67–69.
45. Garriga J, Cussó R. Effect of starvation on glycogen and glucose metabolism in different areas of the rat brain. *Brain Res* 1992, 591: 277–282.
46. Bowyer JF, Tranter KM, Sarkar S, George NI, Hanig JP, Kelly KA, *et al.* Corticosterone and exogenous glucose alter blood glucose levels, neurotoxicity, and vascular toxicity produced by methamphetamine. *J Neurochem* 2017, 143: 198–213.
47. Pitchaimani V, Arumugam S, Thandavarayan RA, Karuppagounder V, Afrin MR, Sreedhar R, *et al.* Hypothalamic glucagon signaling in fasting hypoglycemia. *Life Sci* 2016, 153: 118–123.
48. Choi IY, Seaquist ER, Gruetter R. Effect of hypoglycemia on brain glycogen metabolism in vivo. *J Neurosci Res* 2003, 72: 25–32.
49. Zhong H, Tong L, Gu N, Gao F, Lu Y, Xie R, *et al.* Endocannabinoid signaling in hypothalamic circuits regulates arousal from general anesthesia in mice. *J Clin Invest* 2017, 127: 2295–2309.
50. Cryer PE. Hypoglycemia, functional brain failure, and brain death. *J Clin Invest* 2007, 117: 868–870.
51. Herzog RI, Jiang L, Herman P, Zhao C, Sanganahalli BG, Mason GF, *et al.* Lactate preserves neuronal metabolism and function following antecedent recurrent hypoglycemia. *J Clin Invest* 2013, 123: 1988–1998.
52. Magistretti PJ, Allaman I. Lactate in the brain: from metabolic end-product to signalling molecule. *Nat Rev Neurosci* 2018, 19: 235–249.
53. Diaz-Garcia CM, Mongeon R, Lahmann C, Koveal D, Zucker H, Yellen G. Neuronal stimulation triggers neuronal glycolysis and not lactate uptake. *Cell Metab* 2017, 26: 361–374.
54. Kayser EB, Morgan PG, Sedensky MM. Mitochondrial complex I function affects halothane sensitivity in *Caenorhabditis elegans*. *Anesthesiology* 2004, 101: 365–372.
55. Ramadasan-Nair R, Hui J, Itsara LS, Morgan PG, Sedensky MM. Mitochondrial function in astrocytes is essential for normal emergence from anesthesia in mice. *Anesthesiology* 2019, 130: 423–434.
56. Sonnay S, Duarte JMN, Just N, Gruetter R. Energy metabolism in the rat cortex under thiopental anaesthesia measured In Vivo by ¹³C MRS. *J Neurosci Res* 2017, 95: 2297–2306.



Tau Accumulation *via* Reduced Autophagy Mediates GGGGCC Repeat Expansion-Induced Neurodegeneration in *Drosophila* Model of ALS

Xue Wen¹ · Ping An¹ · Hexuan Li¹ · Zijian Zhou¹ · Yimin Sun¹ · Jian Wang¹ · Lixiang Ma² · Boxun Lu¹

Received: 13 February 2020 / Accepted: 21 March 2020 / Published online: 4 June 2020
© Shanghai Institutes for Biological Sciences, CAS 2020

Abstract Expansions of trinucleotide or hexanucleotide repeats lead to several neurodegenerative disorders, including Huntington disease [caused by expanded CAG repeats (CAGr) in the *HTT* gene], and amyotrophic lateral sclerosis [ALS, possibly caused by expanded GGGGCC repeats (G4C2r) in the *C9ORF72* gene], of which the molecular mechanisms remain unclear. Here, we demonstrated that lowering the *Drosophila* homologue of tau protein (dtau) significantly rescued *in vivo* neurodegeneration, motor performance impairments, and the shortened life-span in *Drosophila* expressing expanded CAGr or expanded G4C2r. Expression of human tau (htau4R) restored the disease-related phenotypes that had been mitigated by the loss of dtau, suggesting an evolutionarily-conserved role of tau in neurodegeneration. We further revealed that G4C2r expression increased tau accumulation by inhibiting

autophagosome–lysosome fusion, possibly due to lowering the level of BAG3, a regulator of autophagy and tau. Taken together, our results reveal a novel mechanism by which expanded G4C2r causes neurodegeneration *via* an evolutionarily-conserved mechanism. Our findings provide novel autophagy-related mechanistic insights into *C9ORF72*-ALS and possible entry points to disease treatment.

Keywords ALS · *C9orf72* · *G4C2* · Huntington disease

Introduction

An expansion of the GGGGCC repeat (G4C2r) in intron 1 of *C9ORF72* is a common mutation associated with sporadic amyotrophic lateral sclerosis (ALS) and frontotemporal dementia (FTD) [1, 2]. ALS is a fatal neurodegenerative disorder primarily affecting motor neurons, whereas FTD is caused by neurodegeneration primarily in the frontal, insular, and anterior temporal cortex. The aggregation-prone dipeptides synthesized from the expanded G4C2 *via* repeat-associated non-ATG translation and/or G4C2 RNA foci/membraneless granules originating *via* phase separation are likely the major cause of neurodegeneration, but the downstream molecular mechanisms remain unclear [1–7]. Abnormalities of the microtubule-binding protein tau play a central role in several neurodegenerative diseases termed tauopathies, including Alzheimer’s disease (AD), progressive supranuclear palsy (PSP), and tau-positive FTD with parkinsonism (FTD with parkinsonism-17). Among these, FTD with parkinsonism-17 is caused by aberrant splicing of tau, and similar mechanisms may contribute to the pathology in Huntington’s disease (HD) [8], another disease caused by nucleotide repeat expansion (CAG repeat expansion in

Electronic supplementary material The online version of this article (<https://doi.org/10.1007/s12264-020-00518-2>) contains supplementary material, which is available to authorized users.

Xue Wen and Ping An have contributed equally to this work.

✉ Jian Wang
wangjian_hs@fudan.edu.cn

✉ Lixiang Ma
lxma@fudan.edu.cn

✉ Boxun Lu
luboxun@fudan.edu.cn

¹ Neurology Department at Huashan Hospital, State Key Laboratory of Medical Neurobiology and Ministry of Education Frontiers Center for Brain Science, School of Life Sciences, Fudan University, Shanghai 200438, China

² Department of Anatomy, Histology and Embryology, School of Basic Medical Sciences, Fudan University, Shanghai 200032, China

exon 1 of the HTT gene) [9]. Abnormal phosphorylation and aggregation of tau has also been reported in patients with *C9ORF72*-ALS [10]. Thus, we investigated whether tau mediates expanded G4C2r-induced neurotoxicity, which may share molecular commonalities in the pathological mechanisms with CAG repeat expansion diseases.

Tau is the key protein in several neurodegenerative diseases such as AD and other tauopathies. The tau-related toxicity in neurodegenerative disorders may be a mixture of both loss-of-function of normal tau and gain-of-function of aggregation-prone tau caused by abnormal splicing and post-translational modification under pathological conditions. Loss of normal tau may have an impact on axonal transport and thus contribute to synaptic dysfunction and neurodegeneration [11]. Meanwhile, aggregated tau can be generated by hyperphosphorylation [12, 13] and/or an altered isoform ratio [14]. Hyperphosphorylated tau detaching from microtubules usually misfolds and sequesters normal tau and other related proteins to produce large insoluble tau aggregates, which may impair the cellular clearance machinery [15, 16], axonal transport [17], mitochondrial function [18, 19], and other cellular processes.

Drosophila models have been widely used to study genetic neurodegenerative disorders, especially CAG expansion and G4C2 expansion diseases, probably because of their monogenetic nature [20, 21]. Many of the genetic and chemical modifiers identified in these models have been validated in patient cells and mammalian models [22–25]. In this study, we first characterized the pathophysiological action of the *Drosophila* homologue of tau (dtau) in a model of HD. We confirmed an evolutionarily-conserved role of dtau in HD neurotoxicity by showing that the loss of dtau significantly rescued phenotypes in the *Drosophila* HD model expressing an exon 1 fragment of human mutant HTT protein, consistent with the report in a mouse model of HD expressing this fragment [8]. We then investigated the potential role of dtau in the expanded G4C2r-induced neurotoxicity in the *Drosophila* model, and explored tau-related pathogenic mechanisms, in which autophagy plays a key role.

Materials and Methods

Fly Stocks and Genetics

Fly cultures and crosses were maintained on standard food according to standard procedures and raised at 25 °C. The *elav(c115)-GAL4* (*elav(I)-GAL4*) (no. 458), *elav(II)-GAL4* (no. 8765), *elav(III)-GAL4* (no. 8760), *OK371-GAL4* (no. 26160), and *UAS-GFP-mCherry-atg8a* (no. 37749) were from the Bloomington *Drosophila* Stock Center at Indiana

University (Bloomington, Indiana). The *dtau*^{-/-} stock was as described previously [26]. *GMR61G12-GAL4* was from the FlyLight *GAL4* collection organization (<http://flweb.janelia.org/cgi-bin/flew.cgi>). The *UAS-(G4C2)₃₀-EGFP* and *UAS-(G4C2)₃-EGFP* lines were as described previously [27]. The transgenic *Drosophila* line expressing human wild-type was as described previously [28]. The expression of *(G4C2)₃₀* in all cells of the peripheral and central nervous systems using *elav(I)-GAL4* caused lethality in early development as described previously [27]. As the pupal lethality of *(G4C2)₃₀* driven by *elav(I)-GAL4* precluded studies in mature neurons of the adult brain, we used *elav(II)-GAL4* or *elav(III)-GAL4* as a substitute. *UAS-HTT.ex1.Q25* and *UAS-HTT.ex1.Q72* were generated by injecting *pUAST-HTT.ex1.Q25* or *pUAST-HTT.ex1.Q72* plasmid with helper-plasmids named $\Delta 2-3$ into *w1118*.

Behavioral and Lifespan Experiments

In behavioral experiments (climbing assay), we placed 15 age-matched virgin female flies in an empty vial and tapped them down. The percentage of flies that climbed past a 9-cm line after 15 s was recorded. The mean of five observations was plotted for each vial on each day, and data from multiple vials containing different batches of flies were plotted and analyzed using two-way ANOVA. Flies were randomly placed into each tube. For lifespan measurements, we placed ≥ 60 age-matched virgin females in an empty plastic vial and recorded the survival in each vial on each day. In both behavioral and lifespan measurement experiments, the investigator who performed the experiments was blind to the genotypes until data analysis. The survival distribution of the two genotypic groups were compared using the log-rank (Mantel-Cox) test.

Plasmids Used for Fly Strain Generation and Mammalian Cell Transfection

The HTT.ex1.Q25 and HTT.ex1.Q72 cDNA were obtained by PCR amplification from pcDNA- HTT.ex1.Q25 and pcDNA- HTT.ex1.Q72 plasmid, and they were cloned into the pUAST vector. The tau-snap plasmid was generated by inserting the cDNA expressing one transcript of human tau (0N4R, cloned by PCR amplification from the *UAS-htau4R* *Drosophila* strain) into a snap-tag vector (P9312S, New England Biolabs, CA). *(G4C2)₃* and *(G4C2)₂₅* plasmids were generated by inserting *(G4C2)₃* or *(G4C2)₂₅* repeats into the pTT-sfGFP vector. The *(G4C2)₃* repeats were generated by the primer-annealing process and *(G4C2)₂₅* repeats were generated using an enzyme to cut the plasmid named pHR-Tre3G-29xGGGGCC-12xMS2 (cat.no. #99149, Addgene, MA). The BAG3 (BAG family

molecular chaperone regulator 3) vector was constructed by cloning the human BAG3 cDNA sequence from PUC57_BAG3wt-eGFP (cat.no. #98182, Addgene, MA) into the pTT-sfGFP vector. As the end of the BAG3 gene PCR product was a termination codon, GFP protein in the vector was not expressed with BAG3 protein. The mRFP-GFP-LC3B vector was from Addgene (cat.no. #21074, Addgene, MA). The Lamp1-mcherry vector was a gift from Prof. Shouqing Luo (Peninsula School of Medicine and Dentistry, University of Plymouth, UK).

SiRNA Treatment

The siRNAs were reverse-transfected into HEK293T cells with Lipofectamine 2000 (11668027, ThermoFisher, MA). All transfections were performed according to the manufacturer's protocol. Cells were collected 3 days after siRNA transfection for western blots. The siRNAs were validated by qPCR and/or western blots for target knock-down. The siRNA target sequence was 5'-AAGGUUCA-GACCAUCUUGGAA-3'.

Immunostaining

For immunofluorescence studies (Figs. 2D, 5A and 6C), cultured HeLa cells were fixed in 4% paraformaldehyde (PFA) at room temperature for 10 min after washing three times with 1× PBS (20 min each), and then washed again and permeabilized in 0.5% (v/v) TritonX-100 for 10 min. The cells were then blocked in blocking buffer [4% bovine serum albumin + 0.1% (v/v) Triton X-100 in 1× PBS] for 30 min, incubated overnight at 4 °C with the primary antibody (clone 5A6, P10636, Developmental Studies Hybridoma Bank, IA), and then washed three times with blocking buffer and incubated with secondary antibody at room temperature for 1 h. The cells on coverslips were then washed three times, stained with 0.5 mg/mL DAPI for 5 min at room temperature, and then mounted in Vectashield mounting medium (H-1002, Vector Laboratories, CA). Images were captured on a Zeiss Axio Vert A1 confocal microscope (H1009664-1, Zeiss, Oberkochen, Germany) and the number of htau puncta in each cell was analyzed blindly using ImageJ (ImageJ 1.52a, Wayne Rasband National Institutes of Health, CA).

For immunofluorescence of cultured HEK293T cells (Fig. 5C–E), all the procedures for immunostaining were the same as for HeLa cells, except for LysoTracker and cathepsin D (CTSD) immunostaining, for which LysoTracker dye (1:1000; L7526, ThermoFisher, MA) or BODIPY-FL-pepstatin A dye (1:500; P12271, ThermoFisher, MA) was added to live cells and incubated for 1 h; after which the cells were immediately sealed on slides with nail polish. Images were captured on a Zeiss Axio

Vert A1 confocal microscope and the number of puncta per cell was analyzed blindly using ImageJ.

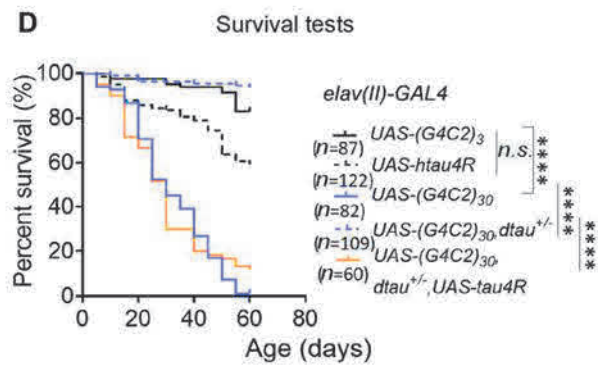
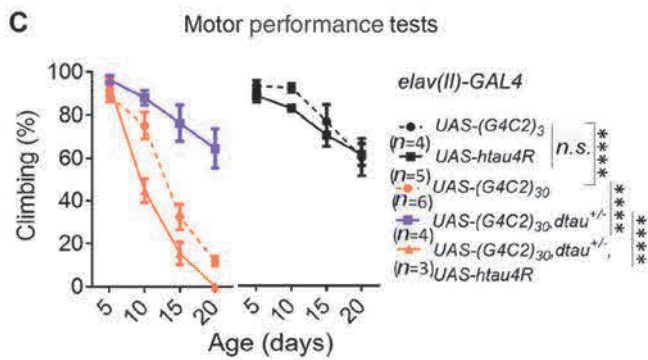
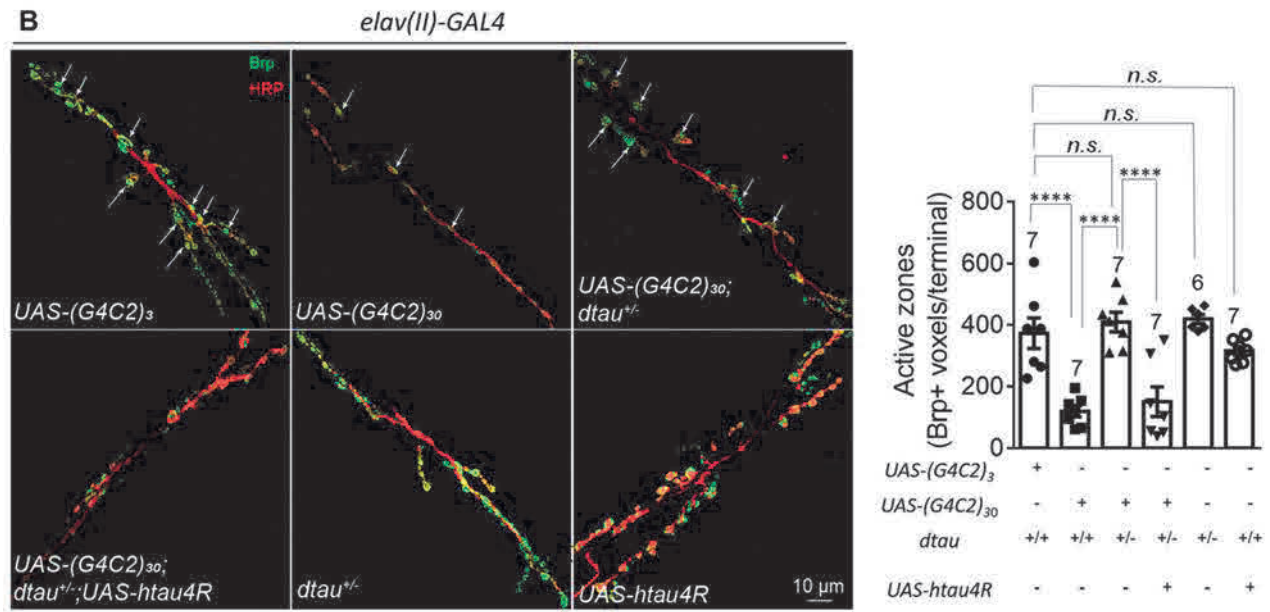
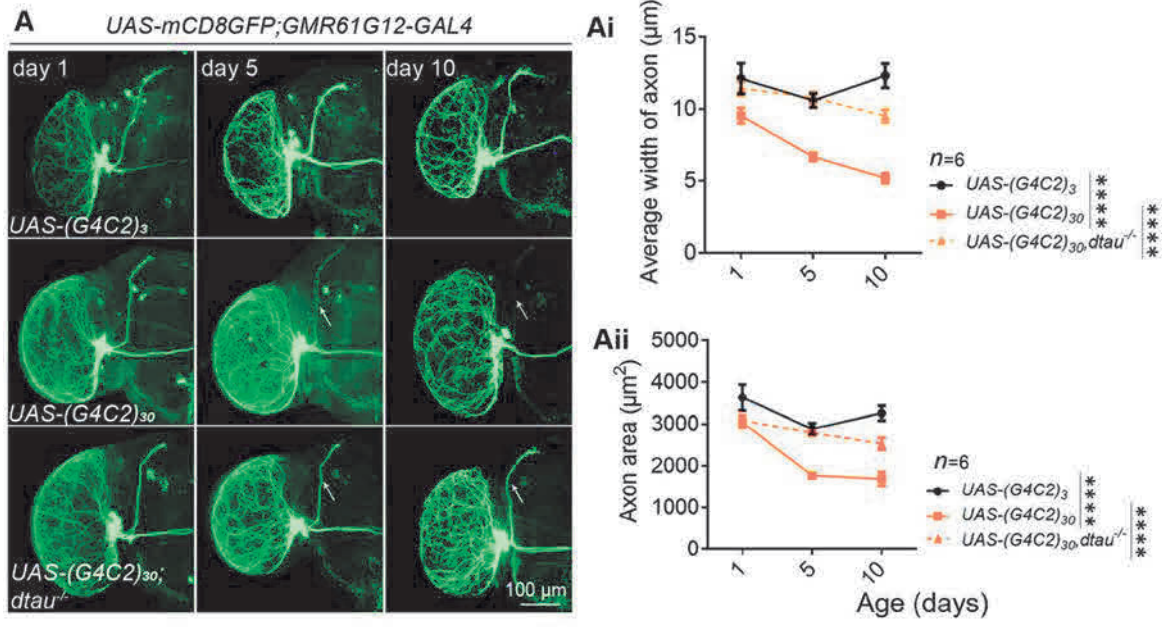
To image neurodegeneration in the fly brain (Figs. 1A, S1A, B, and S2), the whole brains of adult flies at the indicated ages were dissected on ice and then fixed in 4% PFA on ice for 20 min. Immunostaining was then performed in the same way as for cultured HeLa cells. The primary antibody used was anti-GFP (50430-2-AP, ProteinTech, Wuhan, China). The red fluorescence signals of DenMarker (Fig. S2) were imaged directly without antibody staining.

To immunostain neuromuscular junctions (NMJs; Fig. 1B), muscle tissue was isolated by dissection of third stage larvae. The dissected samples were fixed in 4% PFA at room temperature for 30 min, and then washed 3 times in 0.5% PBST (~ 20 min each time). Immunostaining was then performed as for cells. The primary anti-Brp antibody nc82 (AB 2314866, Developmental Studies Hybridoma Bank, IA) was then added to the samples at 1:20 for incubation at 4 °C overnight. The samples were washed 3 times (20 min each), then incubated with the fluorophore-labeled primary anti-HRP antibody Cy3-HRP (1:200; 123-165-021, Jackson ImmunoResearch, PA) and the secondary antibody (goat anti-mouse, 633 nm) for 1 h at room temperature. The samples were then washed three times and mounted in Vectashield mounting medium (H-1002, Vector Laboratories, CA). Images were captured on the Zeiss Axio Vert A1 confocal microscope and analyzed blindly using ImageJ. The NMJs in muscles 6/7 of segment A2 or A3 were chosen for analysis.

The immunostaining process for neurons driven by *OK371-GALA* (Fig. 4D) was the same as for NMJ immunostaining but without the antibody staining. Images of neurons in the ventral nerve cord of each larva were captured and analyzed blindly using ImageJ.

Western Blot Experiments

To extract proteins from fly tissues, samples (brains or whole bodies) were dissected on ice and homogenized with a tissue grinder for 5 min at 60 Hz and lysed on ice for 60 min in 1× RIPA buffer (P0013B, Beyotime, Shanghai, China) and 1× complete protease inhibitor (4693159001, Sigma, MO). The samples were then sonicated for 10 cycles of 15 s on and 20 s off. The whole lysates were then loaded onto a 4%–12% bis-tris gradient gel for western blots. For western blots of ref(2)P (Fig. 4B, C), the lysates were centrifuged at > 20,000 g at 4 °C for 30 min. The precipitates were then collected and loaded for western blots. To extract proteins from cells, the cell pellets were lysed on ice for 30 min in 2% SDS [in 1× PBS + 1× complete protease inhibitor (4693159001, Sigma, MO)]



◀ **Fig. 1** Homozygous (*dtau*^{-/-}) and heterozygous (*dtau*^{+/-}) knockout rescue the neurodegeneration, motor deficits, and shortened lifespan in flies expressing (*G4C2*)₃₀. **A** Representative immunofluorescence images of whole-mount brains from flies of the indicated genotypes at the indicated ages showing neuronal degeneration. The small ventral lateral (sLNv) clock neurons were labeled by mCD8GFP protein, which was driven by *GMR61G12-GALA* (scale bar, 100 μm). *Dtau*^{-/-} significantly rescued the neuronal degeneration induced by (*G4C2*)₃₀ expression, using (*G4C2*)₃ as the control (**Ai, Aii**; *n*, number of flies tested; statistical analysis, two-way ANOVA with Turkey's *post-hoc* test). **B** Representative images and quantification of neuronal degeneration in the neuromuscular junctions (NMJs) of flies with the indicated genotypes. NMJs of muscle 6/7 in abdominal segments A2 and A3 of third instar larvae were stained with anti-HRP (neuronal axon marker, red) and anti-Bruchpilot (Brp) (active zone marker, green) (arrows, boutons of NMJs; scale bar, 10 μm). The Brp-positive active zones were reduced by (*G4C2*)₃₀ expression, and rescued by *dtau*^{+/-} (numbers above bars, numbers of flies tested; statistical analysis, one-way ANOVA with Turkey's *post-hoc* test). **C** Motor performance (climbing) of flies with the indicated genotypes and ages. *Dtau*^{+/-} rescued the motor deficits induced by (*G4C2*)₃₀ expression (*n*, number of tested vials, each containing 15 virgin females; statistical analysis, two-way ANOVA with Dunnett's *post-hoc* test). **D** Lifespans of flies with indicated genotypes. *Dtau*^{+/-} rescued the shortened life-span induced by (*G4C2*)₃₀ expression (*n*, number of flies; statistical analysis, log-rank test). For all plots in **A–D**, error bars indicate mean ± SEM; *n.s.* *P* > 0.05, *****P* ≤ 0.0001).

and sonicated for 10 cycles, 15 s on and 20 s off. The whole lysates were then loaded for western blots.

Antibodies for Western Blots and Immunostaining

The antibodies used were: anti-Brp (ab2314866, Developmental Studies Hybridoma Bank, IA); anti-htau (clone 5A6, P10636, Developmental Studies Hybridoma Bank, IA); anti-actin (Millipore, cat. no. 92590); anti-β-tubulin (ab6046, Abcam, Cambridge, UK); anti-ref(2)P (ab178440, Abcam, Cambridge, UK); anti-GFP (50430-2-AP, Protein-Tech, Wuhan, China); anti-BAG3 (10599-1-AP, Protein-Tech, Wuhan, China); AT8 [detects phosphorylated tau (phospho-tau), MN1020, ThermoFisher, MA]; pS262 (detects Ser262 phospho-tau, OPA1-03142, ThermoFisher, MA); and pS199 (detects Ser199 phospho-tau, 701054, ThermoFisher, MA). The specificity of each antibody has been validated in this study (Fig. S4) or in the literature (*e.g.*, as cited or indexed in Antibodypedia).

Bafilomycin A1 (bafA), chloroquine (CQ), and MG132 Treatment

To assess the LC3B-II protein levels in HEK293T cells expressing (*G4C2*)₂₅ (Fig. 5B), after the cells were transfected with (*G4C2*)₃ or (*G4C2*)₂₅ for 48 h, they were incubated with the autophagy inhibitor bafA (100 mmol/L; S1413, Selleck, TX) or CQ (10 μmol/L; C6628, Sigma, MO) for another 24 h, then collected for western blots.

To determine the htau protein levels in HEK293T cells expressing (*G4C2*)₂₅ (Fig. 5F), after they were transfected with (*G4C2*)₃ or (*G4C2*)₂₅ plus snap-tau vectors for 24 h, they were incubated with CQ (10 μmol/L; C6628, Sigma, MO) for another 48 h. Since MG132 (S2619, Selleck, TX) is highly toxic to HEK293T cells, we used a concentration of 2 μmol/L and the treatment time was ~15 h. Then cells were collected for western blots.

RNA Extraction and RT-qPCR

RNA was extracted from fly tissues or cells using an RNAPrep kit (DP419, Tiangen, Beijing, China) followed by purification using an RNA-clean kit (DP412, Tiangen, Beijing, China) to remove proteins, and RNase-free DNase I (RT411, Tiangen) to break down the genomic DNA. cDNA was obtained by reverse transcription using the FastQuant RT Kit with the oligo (dT) primer (RR047A, Takara, Japan). qPCR was then performed using SYBR Green Realtime PCR Master Mix (QPK-201, Toyobo, Japan). All the primers have been published, validated, and further tested using standard and melting curves. Amplification efficiency was 95%–105% and the *R*² for a linear relationship was >0.999 for all primers. No reverse-transcriptase controls were used to ensure the specificity of the signals. The qPCR primer sequences were as follows:

3R + 4R-F 5'-GGCGGCGAGAAGAAGATA-3',
 3R + 4R-R 5'-GCGAACCGATTTTGGACTT-3'; 4R-F
 5'-TGGGCTCGACGGCCAATGTGAAACA-3', 4R-R 5'-
 CCGCCACCGGGCTTGTGCTTTACA-3'; 3R-PI-F 5'-
 AAGGACAAGGCCAAGCCGAAGGTG-3', 3R-PI-R 5'-
 GGTGCCTTCCAATACTTGATGTCTCCGC-3'; 3R-PJ-F
 5'-AAGGACAAGGCCAAGCCGAAGGTG-3', 3R-PJ-R
 5'-TGGACTCTTGATGTCTCCGCCACCC-3'; EGFP-F
 5'-TATATCATGGCCGACAAGCA-3', EGFP-R 5'-GTTG
 TGGCGGATCTTGAAGT-3'; Upstream-F 5'-TCAAT-
 TAAAAGTAACCAGCAACCA-3', and Upstream-R 5'-
 TCCCTATTCAGAGTTCTTCTTGTGA-3'.

The process for testing standard curves was as follows. The fly or cellular cDNA was diluted 5 times step-by-step until 5 different concentration gradients were achieved. Then the samples, including the 5 concentration gradients, were subjected to qPCR. The results of qPCR for the samples had amplification efficiency 95%–105% and an *R*² for linear relationship > 0.999.

Statistical Analysis

Statistical comparisons between two groups were assessed with unpaired two-tailed *t* tests; for comparisons among multiple groups with one-way ANOVA and *post-hoc* tests (Turkey's tests); and for comparisons of series of data

collected at different times with two-way ANOVA tests. The similarity of variances between groups to be compared was tested using GraphPad Prism 7 and Microsoft Excel 2016. Normality of data sets was assumed for ANOVA and *t* tests, and was assessed by Shapiro-Wilk tests. When the data were significantly different from a normal distribution, nonparametric tests were used. All statistical tests were unpaired and two-tailed.

Results

Homozygous or Heterozygous dtau-Knockout Rescues HD-Related Phenotypes in the *Drosophila* Model of HD

In order to capture the neuronal morphology in the *Drosophila* brain clearly, we used a simple GAL4-UAS system to express a membrane GFP marker (mCD8GFP) in a very small group of neurons using *GMR61G12-GAL4*, so that their morphology could be clearly observed. We assessed the HD-related neurodegeneration by observing the loss of major axon bundles from neurons labeled with GFP induced by the expression of the human mHTT but not the wild-type HTT exon1 fragment (HTT.ex1.Q72 *versus* HTT.ex1.Q25; Fig. S1A). The neurodegeneration in both dendrites and axons was detected by fluorescent protein-tagged marker proteins (Fig. S2).

At the whole-animal level, flies expressing mutant HTT exon1 (HTT.ex1.Q72) by the pan-neural driver *elav-GAL4* caused motor impairments and shortened the life-span compared to flies expressing the wild-type version (HTT.ex1.Q25, Fig. S1C, D), recapitulating certain aspects of the HD-related phenotypes in patients.

We then investigated the potential role of tau in HD by testing knockout of the *Drosophila tau* gene (*dtau*, the homologue of human *MAPT*) to eliminate the expression of dtau proteins. The *dtau* knockout line we used was previously reported to present a specific deletion of the genetic region spanning exon 2 to exon 6, which codes for the microtubule-binding region of dtau [26]. Interestingly, homozygous knockout (*dtau*^{-/-}) or heterozygous knockout (*dtau*^{+/-}) significantly rescued the HD-related neurodegeneration, behavioral deficits, and shortened life-span phenotypes, suggesting that dtau mediates mHTT neurotoxicity, at least partially (Fig. S1B–D). These findings are consistent with a study using the mouse R6/2 HD model, confirming an evolutionarily-conserved role of dtau in neurodegeneration. To further demonstrate this, we expressed human tau (htau4R) in these flies and found that it restored the HD-related phenotypes in *dtau*^{+/-} *Drosophila* (Fig. S1C, D).

Homozygous or Heterozygous dtau-Knockout Rescues the Expanded G4C2r-Induced ALS-Related Neurodegeneration, Behavioral Deficits, and Shortened Life-Span

We next investigated the potential functions of dtau in the expanded G4C2r-induced neurotoxicity in a well-characterized and widely-used *Drosophila* model expressing 30 repeats of G4C2 [(G4C2)₃₀] [27]. Similar to the *Drosophila* model of HD, the *GMR61G12-GAL4*-driven *UAS-mCD8GFP* and *UAS-(G4C2)₃₀* expression led to neurodegeneration (Fig. 1A). In addition, (G4C2)₃₀ expression in the neurons driven by *elav-GAL4* led to a significantly reduced number of active zones in NMJs, as detected by the NMJ marker Brp and the axon marker HRP (Fig. 1B). At the animal level, neuronal expression of (G4C2)₃₀ driven by *elav-GAL4* led to motor performance impairments and a shortened life-span (Fig. 1C, D). Homozygous *dtau*-knockout (*dtau*^{-/-}) or heterozygous knockout (*dtau*^{+/-}) significantly mitigated all of these disease-related phenotypes (Fig. 1A–D), suggesting that dtau mediates the neurotoxicity induced by expanded G4C2r as well.

We then determined whether dtau and human tau are evolutionarily-conserved in mediating the expanded G4C2r-induced toxicity by expressing htau4R in the neurons driven by *elav-GAL4*. The expression of htau4R restored the (G4C2)₃₀-induced neurodegeneration, deficient motor performance, and the shortened life-span in the *dtau*^{+/-} flies (Fig. 1C, D), confirming that dtau plays a role in the expanded G4C2r-induced neurodegeneration.

Expanded G4C2r Increases Total Tau and Phospho-Tau Protein Levels in *Drosophila* and Human Cells

We then explored potential mechanisms through which dtau influenced the expanded G4C2r-induced toxicity, since the mechanisms had not yet been revealed. There were two major possibilities: (1) dtau is an upstream regulator of expanded G4C2r expression; and (2) dtau is a downstream factor that is modulated by the expanded G4C2r and mediates its neurotoxicity. To distinguish these possibilities, we first determined whether dtau-knockout lowered the expanded G4C2r RNA, which is likely the fundamental source of neurotoxicity in this model [27]. Since it is extremely difficult to amplify the G4C2 repeat region *per se* by quantitative PCR (qPCR), we chose the upstream and downstream sequences for qPCR measurements (Fig. S3A). We found no significant changes in the expanded G4C2r mRNA levels in the *dtau*^{+/-} flies, suggesting that dtau is not an upstream regulator of expanded G4C2r expression (Fig. S3B).

The above evidence suggested that *dtau* is likely a downstream mediator of the expanded *G4C2r*-induced toxicity. We thus investigated the potential mis-splicing of tau transcripts, which is known to cause neurodegeneration [29–31]. Alternative splicing of exon 10 of the *MAPT* gene results in tau isoforms containing either three or four microtubule-binding repeats (3R and 4R) [30, 32]. Similar to human tau, *dtau* proteins expressed from different tau transcripts (Fig. S3C) contained either three or four putative microtubule-binding domains (MTBDs) that are homologous with those of mammals [32, 33]. In addition, all *dtau* proteins had an extra MTBD that is homologous with *Caenorhabditis elegans* but not mammals. Thus, *dtau* had the 4R *versus* the 3R isoform due to alternative splicing (or 5R *versus* 4R if considering the extra MTBD), corresponding to the 4R *versus* 3R isoforms in human tau. We thus measured the different *dtau* transcript levels and the 4R/3R ratio in fly brains with $(G4C2)_{30}$ expression *versus* the control [$(G4C2)_3$], and found no significant changes in either the transcript levels or the 4R/3R ratio (Fig. S3D), suggesting that the expanded *G4C2r* does not induce *dtau* mis-splicing.

An increased level of tau protein and/or phospho-tau is another possible driver of neurodegeneration [34–45]. We

thus investigated whether the tau or phospho-tau protein levels are increased by expressing the expanded *G4C2r* in *Drosophila*. Expression of $(G4C2)_{30}$ led to increased total tau protein levels in tissue samples from third-stage larvae and adult *Drosophila* (Fig. 2A, B), suggesting that the expanded *G4C2r* expression increases tau accumulation. Consistent with the finding in *Drosophila*, the exogenous expression of expanded *G4C2r* [$(G4C2)_{25}$] in HEK293T cells also resulted in tau protein accumulation (Fig. 2C), as suggested by western blots using a tau-specific antibody (Fig. S4). We further investigated the levels of tau aggregates, which are likely to be a biomarker associated with toxic tau accumulation [46]. While tau aggregates were hardly observable in *Drosophila* and HEK293T cells with *htau* transgene expression [consistent with previous reports (not shown)] [28, 47], HeLa cells expressing $(G4C2)_{25}$ showed a drastic increase of tau aggregates by both kinds of imaging (Fig. 2D), suggesting that expanded *G4C2r* is capable of enhancing the aggregated form of tau as well.

We further investigated the levels of phospho-tau, which is considered to be a major toxic species that causes neurodegeneration [37, 48]. Western blots of the brains of adult *Drosophila* expressing $(G4C2)_{30}$ showed an increase

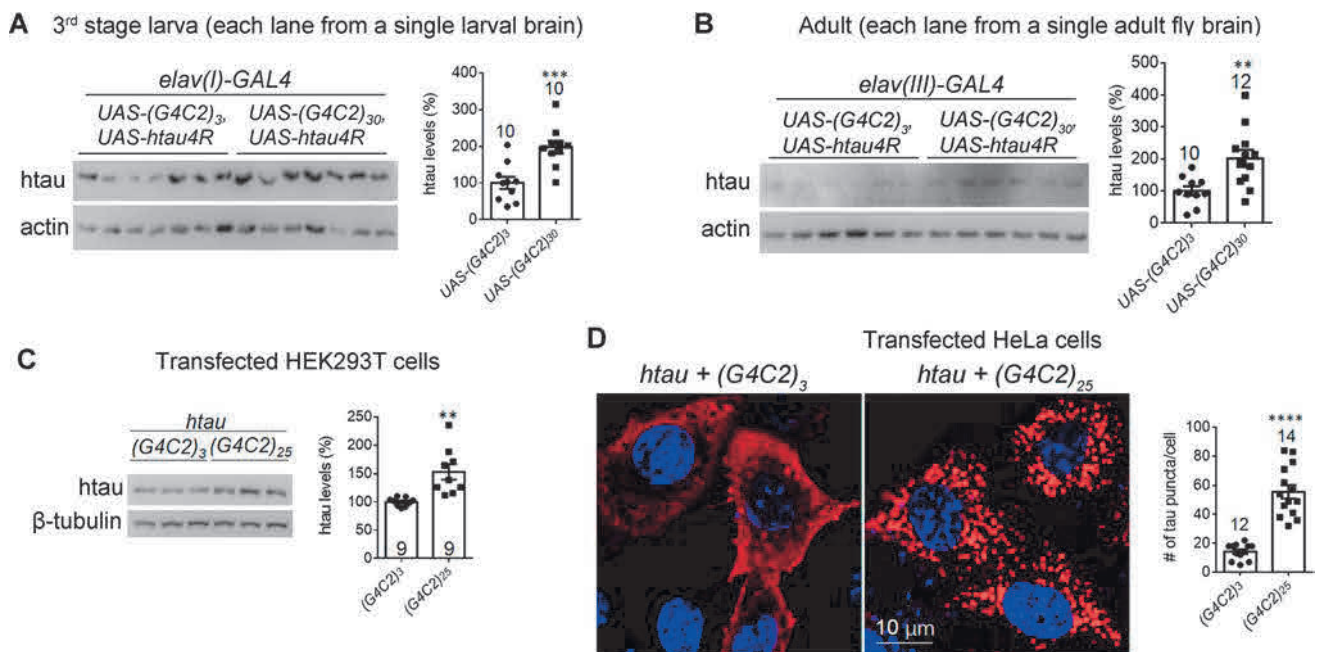


Fig. 2 Expanded *G4C2r* expression increases tau protein levels or aggregation in *Drosophila* and in human cells. **A**, **B** Representative western blots and quantification of *htau* in brain lysates of the indicated genotypes showing that the total tau levels were increased by $(G4C2)_{30}$ expression in the third instar larva (**A**) and adult (**B**) flies, compared to the controls expressing $(G4C2)_3$ (numbers above bars, numbers of flies tested; statistical analysis, two-tailed unpaired *t* test). **C** Representative western blots and quantification showing that total *htau* levels were increased by $(G4C2)_{25}$ compared

to $(G4C2)_3$ controls in transfected HEK293T cells (statistical analysis, two-tailed unpaired *t* test). **D** Representative immunofluorescence images and quantification (numbers of tau puncta per cell) showing that $(G4C2)_{25}$ expression increased tau aggregates in HeLa cells compared to controls expressing $(G4C2)_3$ (statistical analysis, two-tailed unpaired *t* tests). Note: aggregates were tested in HeLa cells because tau aggregates were hardly visible in HEK293T cells. In all plots, bars indicate the mean ± SEM; ***P* ≤ 0.01, ****P* ≤ 0.001, *****P* ≤ 0.0001.

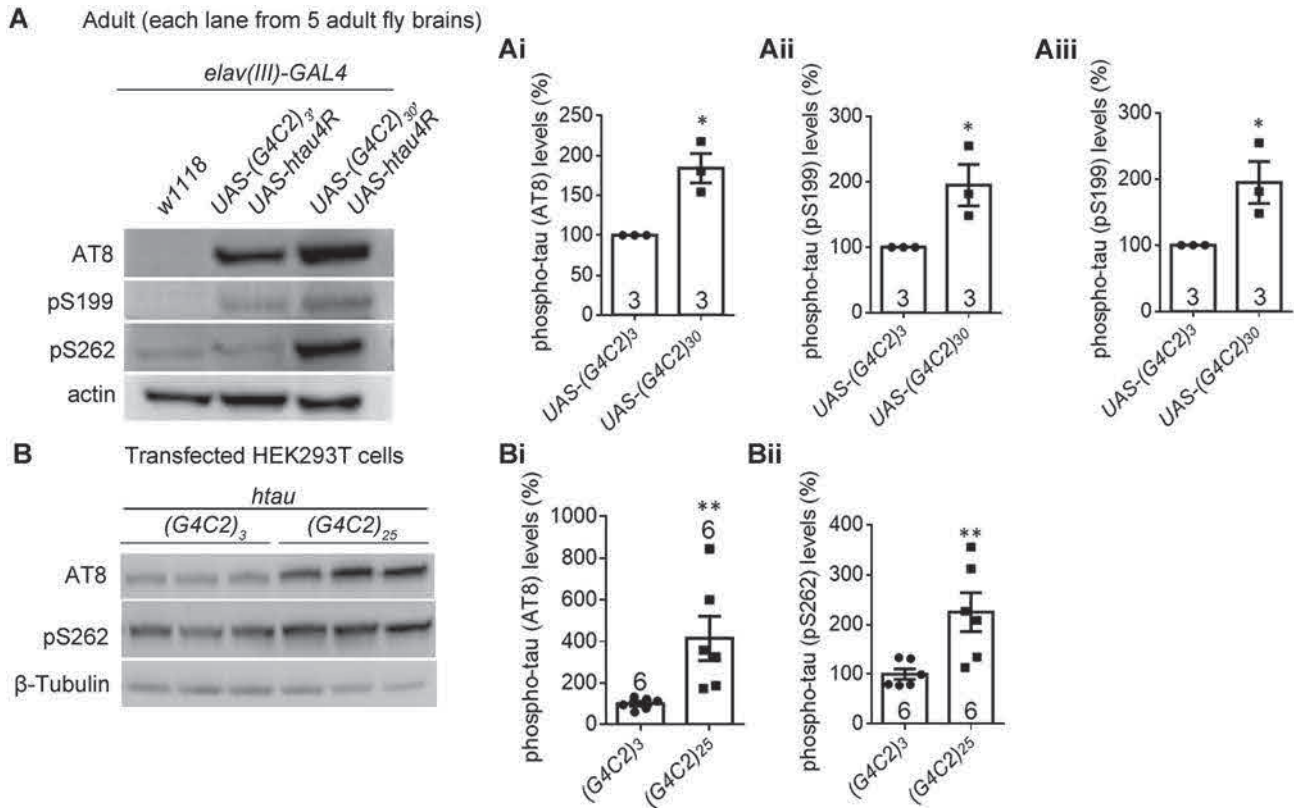


Fig. 3 Expanded *G4C2r* expression increases the levels of specific forms of phosphorylated tau protein in *Drosophila* and in human cells. **A** Representative western blots and quantification of brain lysate samples from indicated genotypes showing that the phosphorylated tau levels detected by the antibodies AT8, pS262, and pS199

were increased by $(G4C2)_{30}$ expression in the adult fly head, compared to controls expressing $(G4C2)_3$ (**i**, **ii**, **iii**) (numbers in bars, numbers of biological replicates; statistical analysis, two-tailed unpaired *t* test). **B** As in **A**, but in transfected HEK293T cells. In all plots, bars indicate the mean \pm SEM; **P* \leq 0.05, ***P* \leq 0.01.

of certain forms of phospho-tau as detected by the phospho-tau antibody AT8, pS199, or pS262 (Fig. 3A, Ai–Aiii). Consistent with this, the phospho-tau increase by $(G4C2)_{25}$ expression was also found in HEK293T cells (Fig. 3B, Bi, Bii). The phospho-tau increase is likely a consequence of increased tau accumulation (Fig. 2A–C), and may also contribute to the neurotoxicity induced by expanded G4C2r expression.

Expanded G4C2r Expression Impairs Autophagic Flux by Inhibiting Autophagosome–Autolysosome Fusion in Flies

The tau protein is known to be degraded *via* autophagy in cells [35], so we hypothesized that the expanded G4C2r expression may impair autophagy, resulting in tau accumulation. We assayed the autophagic flux by assessing the cleavage of GFP-mCherry-atg8a (autophagy-related protein 8a). Atg8a in *Drosophila* is the homologue of the mammalian protein LC3, which is the key autophagosome protein that is cleaved in lysosomes. Thus, GFP-atg8a or GFP-LC3 cleavage is a widely used assay for

measurements of autophagic flux [49, 50]. By expressing GFP-mCherry-atg8a driven by *OK371-GAL4* in *Drosophila*, we measured the autophagic flux in motor neurons by the levels of free GFP [51], the cleaved product of the GFP-mCherry-atg8a protein. The free GFP band essentially disappeared in all the $(G4C2)_{30}$ -expressing *Drosophila* brains tested compared to those expressing $(G4C2)_3$ (Fig. 4A, Ai, Aii), indicating an impairment of autophagic flux. Consistent with this, the ref(2)P protein (the *Drosophila* homologue of SQSTM1/p62 [52]) was significantly increased by $(G4C2)_{30}$ expression at larval and pupal stages, compared to those expressing $(G4C2)_3$ (Fig. 4B, C), further demonstrating that autophagic flux was impaired by the expanded G4C2r expression.

The major causes of impaired autophagic flux include decreased autophagosome formation, deficient autophagosome–autolysosome fusion, and defects of lysosome functions. To distinguish these possibilities, we measured the autophagosome–autolysosome fusion using GFP-mCherry-atg8a, which labels autophagosomes with both red and green fluorescence and autolysosomes with only red fluorescence because of the quenching of green

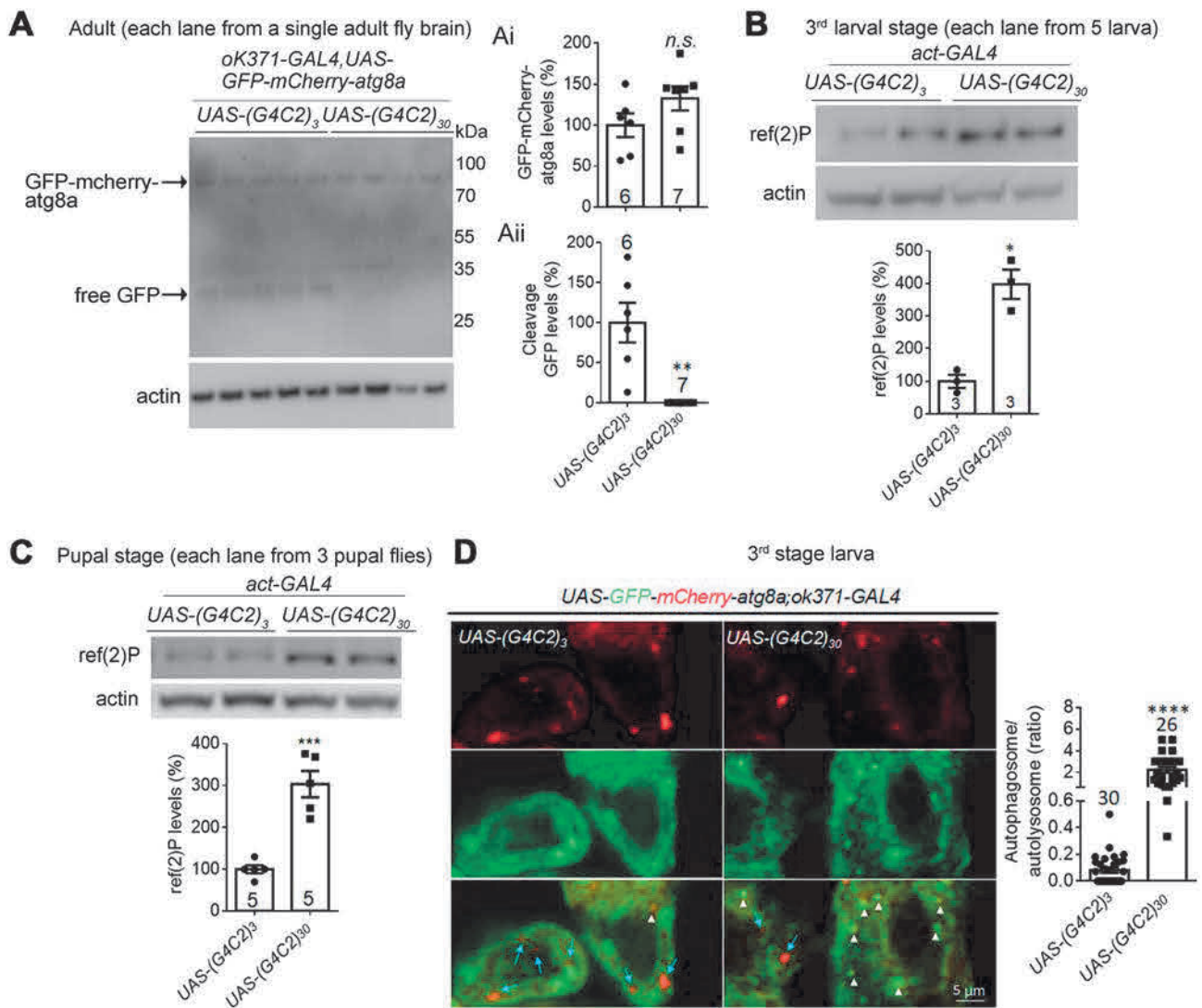


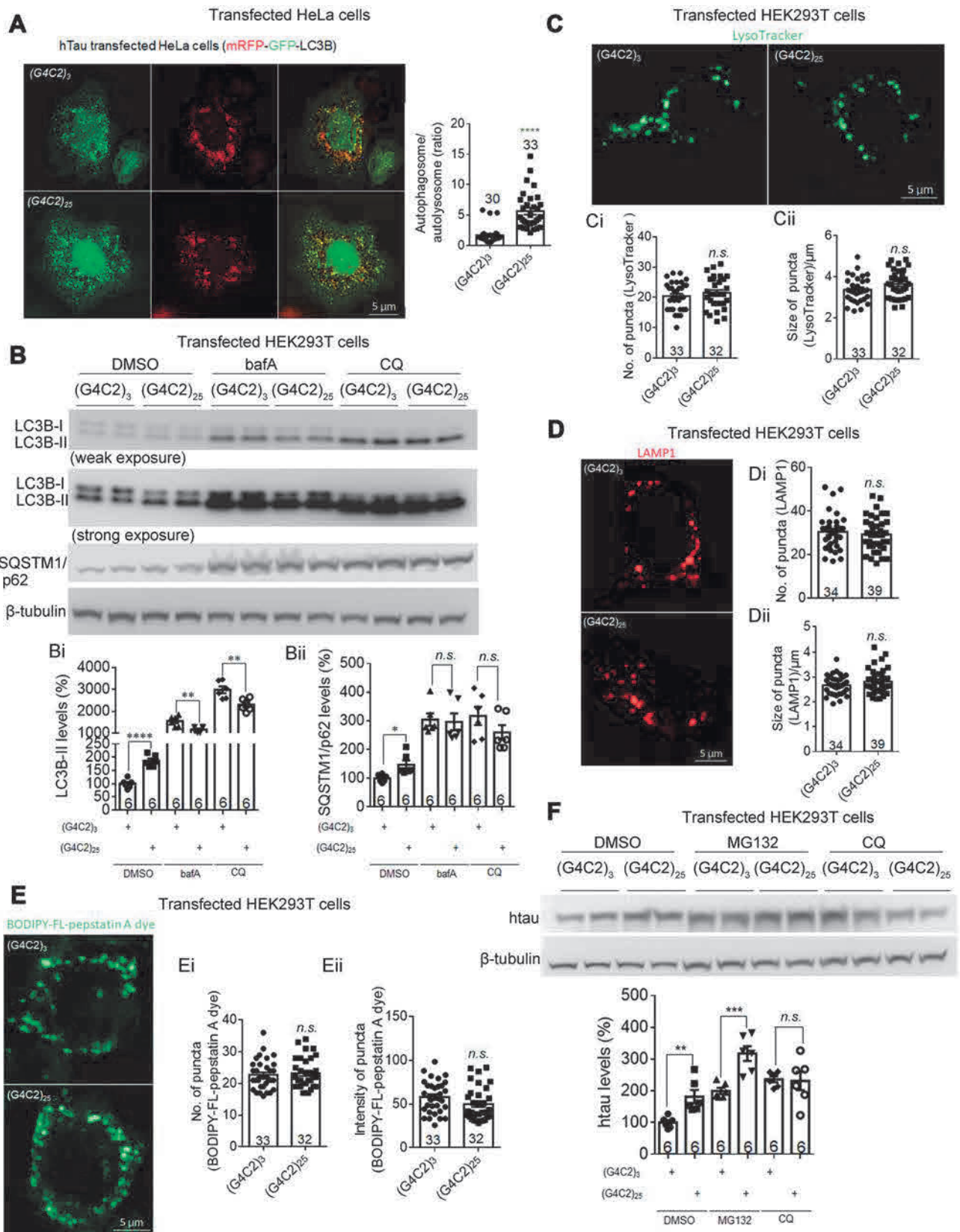
Fig. 4 Expanded *G4C2r* expression impairs autophagic flux by inhibiting autophagosome–lysosome fusion in flies. **A** Representative western blots and quantification of fly brain lysates of indicated genotypes showing that the cleaved product band (free GFP cleaved from GFP-mCherry-atg8) is largely missing from motor neurons expressing *(G4C2)₃₀* driven by *OK371-GAL4* (**i**, **ii**), suggesting an inhibition of autophagy activity in these neurons (numbers above bars, numbers of flies; statistical analysis, two-tailed unpaired *t* test). Note: each lane is loaded with the lysate from a single fly brain, and the cleaved product may be too low to detect in samples expressing *(G4C2)₃₀*. **B**, **C** Representative western blots of the ref(2)P protein

fluorescence by the low pH in autolysosomes. By expressing GFP-mCherry-atg8a driven by *OK371-GAL4* in *Drosophila* larvae, we found significantly more yellow puncta in *Drosophila* brains expressing *(G4C2)₃₀* than in those expressing *(G4C2)₃* (Fig. 4D), suggesting a reduction of autolysosome numbers and a likely inhibition of autophagosome–autolysosome fusion.

(homologue of human SQSTM1/p62) showing an increased level in larvae expressing *(G4C2)₃₀* (**B**) and pupae (**C**) (numbers in bars, numbers of flies; statistical analysis, two-tailed unpaired *t* test). **D** Representative immunofluorescence images of GFP-mCherry-atg8 puncta and quantification of the autophagosome/autolysosome ratio (red + green + puncta : red + green – puncta) in fly larvae (arrows, putative autolysosomes; arrowheads, putative autophagosomes; *n*, number of individual cells in >20 flies per group; statistical analysis, two-tailed unpaired *t* test). In all plots, bars indicate the mean ± SEM; *n.s.* *P* > 0.05, ***P* ≤ 0.01, ****P* ≤ 0.001, *****P* ≤ 0.0001).

Expanded *G4C2r* Expression Impairs Autophagic Flux by Inhibiting Autophagosome–Autolysosome Fusion in Human Cells

Consistent with the results in *Drosophila*, in HeLa cells transfected with mRFP-GFP-LC3B, *(G4C2)₂₅* expression increased the autophagosome/autolysosome ratio compared to *(G4C2)₃* (Fig. 5A), further demonstrating deficient autophagosome–autolysosome fusion induced by expanded



◀ **Fig. 5** Expanded *G4C2r* expression impairs autophagic flux by inhibiting autophagosome–lysosome fusion in human cells. **A** Representative immunofluorescence images of mRFP-GFP-LC3B puncta and quantification of the autophagosome /autolysosome ratio (red + green + puncta : red + green – puncta). (*G4C2*)₂₅ expression significantly decreased autophagosome–lysosome fusion in HeLa cells compared to controls expressing (*G4C2*)₃ (*n*, number of individual flies; statistical analysis, two-tailed unpaired *t* test). **B** Representative Western blots and quantification showing that (*G4C2*)₂₅ expression significantly increased LC3B-II and SQSTM1/p62 protein levels in HEK293T cells, compared to controls expressing (*G4C2*)₃. **Bi, Bii** After the treatment with lysosome inhibitors bafilomycin A1 (bafA, 100 nmol/L) or chloroquine (CQ, 10 μmol/L), (*G4C2*)₂₅ expression mildly decreased LC3B-II levels and did not change the SQSTM1/p62 levels in HEK293T cells, compared to controls expressing (*G4C2*)₃ (*n*, number of biological replicates; statistical analysis, two-tailed unpaired *t* test). **C** Representative immunofluorescence images labeled by LysoTracker and quantifications of lysosomes (**Ci, Cii**) showing that (*G4C2*)₂₅ expression did not change the number or size of lysosomes in HEK293T cells, compared to controls expressing (*G4C2*)₃ (*n*, number of cells; statistical analysis, two-tailed unpaired *t* test). **D** As in **C**, but measured by the number and the averaged size of mCherry-LAMP1 puncta per cell in transfected HEK293T cells. **E** As in **C**, but measured by BODIPY-FL-pepstatin A, which specifically binds to and inhibits active CTSD (a key protease in the lysosome) at low pH (number, active lysosomes; intensity, level of active CTSD). **F** Representative western-blots and quantification of htau protein levels in HEK293T cells transfected with the indicated plasmids and treated with the indicated compounds (2 μmol/L MG132; 10 μmol/L CQ; *n*, number of independently plated and treated wells; statistical analysis, two-tailed unpaired *t* test). In all plots, bars indicate the mean ± SEM; *n.s.* *P* > 0.05, ***P* ≤ 0.01, ****P* ≤ 0.001, *****P* ≤ 0.0001.

G4C2r expression. Consistent with this, the LC3B-II and SQSTM1/p62 protein levels were significantly higher in HEK293T cells expressing (*G4C2*)₂₅ than in controls (Fig. 5B, Bi, Bii). The increased LC3-II levels could be an indication of increased autophagosome formation, decreased autophagosome–lysosome fusion, or decreased lysosome functions. To distinguish among these possibilities, we treated the cells with the lysosome inhibitors bafA and CQ, which block autophagosome–lysosome fusion and lysosome functions. If (*G4C2*)₂₅ expression increased the LC3-II levels by activating autophagosome formation, the increase would persist in the presence of these inhibitors. Contradicting this prediction, the (*G4C2*)₂₅-induced increase of LC3B-II and SQSTM1/p62 protein levels was ameliorated or even reversed in cells treated with bafA or CQ (Fig. 5B, Bi, Bii), suggesting defective autophagosome–lysosome fusion or lysosome functions in HEK293T cells expressing (*G4C2*)₂₅. To measure potential changes in lysosomes, we labeled them with LysoTracker or LAMP1-mCherry and quantified the numbers and sizes of puncta. We found no significant difference between HEK293T cells expressing (*G4C2*)₂₅ and (*G4C2*)₃ in these parameters (Fig. 5C, Ci, Cii, D, Di, Dii), suggesting that the lysosomes were not influenced. We further measured lysosome

functions using BODIPY-FL-pepstatin A, which specifically binds to active CTSD under low pH conditions [53]. The functional lysosomes were labeled by this dye and when we quantified the number and intensity of puncta, they showed no significant difference between HEK293T cells expressing (*G4C2*)₂₅ and (*G4C2*)₃ (Fig. 5E, Ei, Eii), suggesting that the lysosomes were not influenced. Taken together, the expanded *G4C2r* most likely impairs autophagosome–lysosome fusion.

Since tau protein may be degraded by proteasomes in addition to autophagy, we tested the effects of the proteasome inhibitor MG132 *versus* the autophagy inhibitor CQ on (*G4C2*)₂₅-induced tau accumulation. The effects were not significantly influenced by MG132, but were largely abolished by CQ (Fig. 5F), confirming that the expanded *G4C2r*-induced tau accumulation is largely due to deficient autophagy.

Taken together, expanded *G4C2r* expression impaired autophagic flux by inhibiting autophagosome–autolysosome fusion, leading to tau accumulation.

Expanded *G4C2r* Expression Decreases BAG3 (starvin) mRNA Levels, Contributing to Deficient Autophagosome–Autolysosome Fusion and Tau Accumulation

We then explored the potential molecular mechanisms of autophagy impairment. Studies have shown that BAG3 (BAG family molecular chaperone regulator 3), a key modulator of autophagy [54, 55], is negatively associated with tau protein levels [56, 57]. We thus hypothesized that the expanded *G4C2r* expression may reduce BAG3 levels, leading to impaired autophagy and tau accumulation. Consistent with this hypothesis, (*G4C2*)₃₀ expression in *Drosophila* neurons significantly reduced the mRNA levels of *starvin* (*stv*), the *Drosophila* homologue of BAG3 [58], compared to controls expressing (*G4C2*)₃ (Fig. 6A, Ai, Aii). Due to a lack of anti-starvin antibody, we examined potential BAG3 protein level changes in HEK293T cells and found consistent BAG3 lowering by expanded *G4C2r* expression (Fig. 6B).

To confirm that deficient autophagosome–autolysosome fusion is due to the decreased BAG3 level, we overexpressed BAG3 in HeLa cells expressing (*G4C2*)₂₅ and investigated fusion using the mRFP-GFP-LC3 marker. Compared to controls with (*G4C2*)₂₅ expression alone, BAG3 overexpression significantly rescued the deficient autophagosome–autolysosome fusion (Fig. 6C), suggesting a role of reduced BAG3 levels.

Given that reduced BAG3 levels contribute to the impairment of autophagy and that tau is degraded by autophagy, it is likely that reduced BAG3 leads to tau accumulation. This is also consistent with the previously-

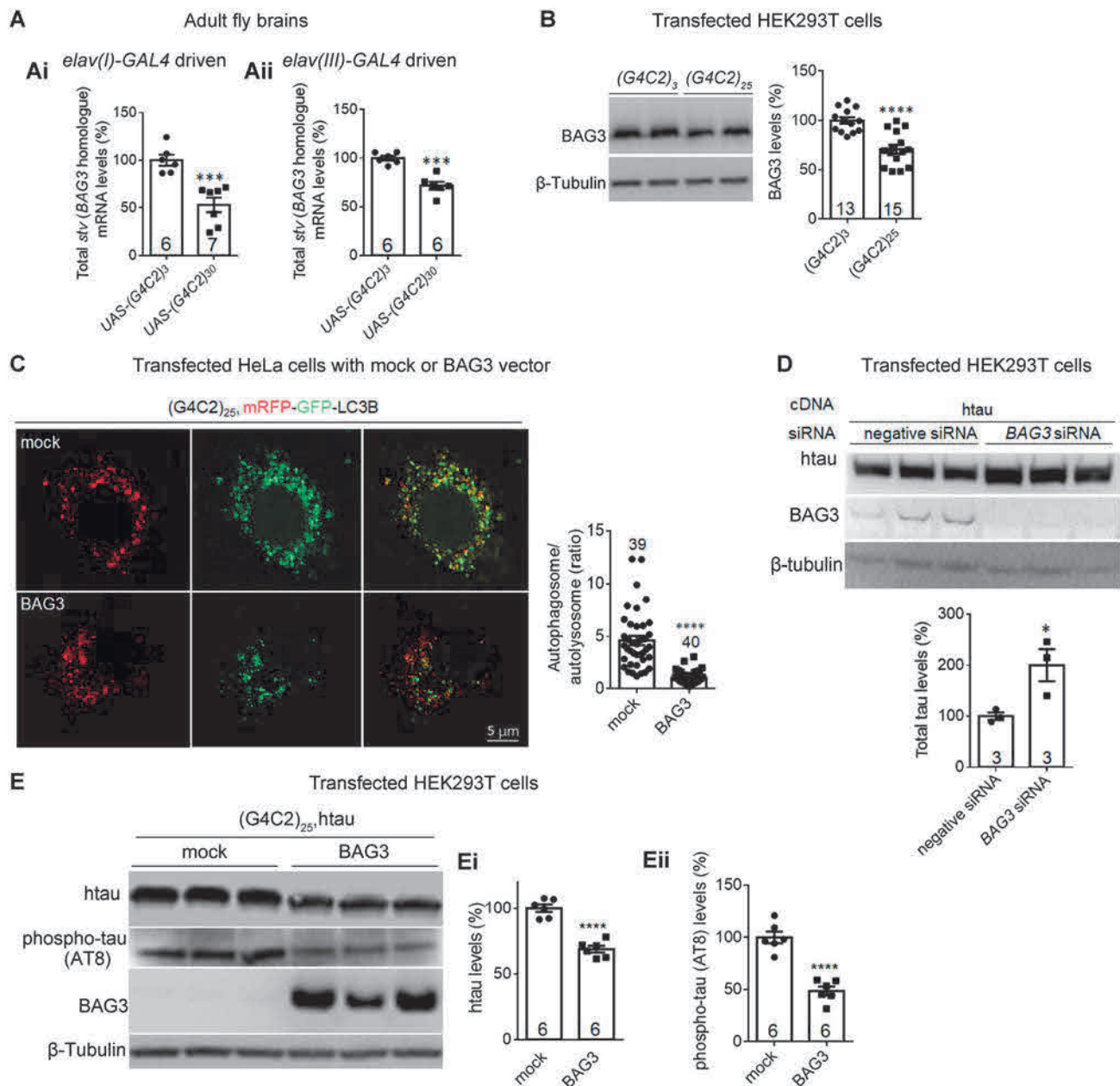


Fig. 6 Expanded *G4C2r* expression decreases BAG3 (starvin) levels, contributing to the decreased autophagosome–lysosome fusion and increased tau accumulation. **Ai**, **Aii** qPCR quantification of the *starvin* (*stv*, the *BAG3* homologue in *Drosophila*) mRNA levels in adult fly brains expressing (*G4C2*)₃₀ versus (*G4C2*)₃. **B** Representative western blots and quantification of lysates from HEK293T cells transfected with the indicated plasmids showing decreased endogenous BAG3 protein levels with (*G4C2*)₂₅ expression. **C** Representative immunofluorescence images of mRFP-GFP-LC3B puncta and quantification of autophagosome/autolysosome ratio (red+green+ puncta :

red+green- puncta) in HeLa cells transfected with the indicated plasmids (*n*, number of cells; statistical analysis, two-tailed unpaired *t* test). **D**, **E** Representative western blots and quantification of lysates from HEK293T cells transfected with the indicated cDNA plasmids and/or siRNAs. **Ei**, **Eii** Total tau and phospho-tau levels decreased with the expression of BAG3 protein in HEK293T cells expressing (*G4C2*)₂₅ compared to mock controls (*n*, number of biological replicates; statistical analysis, two-tailed unpaired *t* test). In all plots, bars indicate the mean \pm SEM; **P* \leq 0.05, ****P* \leq 0.001, *****P* \leq 0.0001.

reported negative association between BAG3 and tau protein levels [56, 57]. We thus investigated whether BAG3 functionally modulates tau protein levels by knocking down BAG3 in HEK293T cells co-expressing (*G4C2*)₂₅ and tau, and found that lowering BAG3

expression increased the tau level (Fig. 6D). In the reverse direction, overexpressing BAG3 reduced the tau level (Fig. 6E, Ei, Eii).

Taken together, expanded G4C2r expression decreased BAG3 levels, leading to reduced autophagic flux and tau accumulation.

Discussion

Our study revealed a functional role of tau in the expanded G4C2r-mediated neurotoxicity. While some of the previous studies have suggested a potential link between tau and G4C2r expansion [10, 59], including a recent report showing synergistic neurotoxicity induced by htau and (*G4C2*)₃₀ over-expression in *Drosophila* [60], there have been no loss-of-function experiments to demonstrate tau as a potential mediator of neurotoxicity in these flies. Our data revealed a novel pathogenic role of tau in mediating the expanded G4C2r-induced neurotoxicity by showing that *dtau*^{+/-} and *dtau*^{-/-} mitigated the neuronal degeneration, motor performance deficits, and a shortened lifespan in the *Drosophila* (*G4C2*)₃₀ model (Fig. 1).

While our study mainly used the *Drosophila* model, the pathogenic action of tau in mediating the expanded G4C2r-induced neurotoxicity is likely to be evolutionarily conserved between humans and flies. Dtau has been cloned and demonstrated to have microtubule-binding properties [33], but its potential role in neuronal degeneration has been controversial. Studies using either *Drosophila* RNAi lines or tau hypomorphic/deficient lines led to contradictory results regarding the potential detrimental or beneficial effects of dtau removal [61], possibly because of off-target effects or incomplete removal of dtau, and there were no disease phenotype “restoration” experiments expressing human tau (htau) to test the functional similarity between dtau and htau. Meanwhile, dtau knockout did not trigger major effects on fly survival and climbing ability in the wild-type background (Figs 1 and S1), and it did not influence the toxic effects on fly survival associated with the expression of toxic human A β [26], suggesting that dtau mediates neurodegeneration in a specific context, not generally.

On the other hand, our results demonstrated that expression of htau restored most of the phenotypes that were ameliorated by *dtau*^{+/-} or *dtau*^{-/-} (Figs. 1B–D and S1C–D). In addition, the expanded G4C2r expression increased the tau levels in both *Drosophila* and mammalian cells (Fig. 2A–C). Finally, *dtau*^{+/-} and *dtau*^{-/-} rescued the HD-related phenotypes in *Drosophila* expressing mHTT protein (Fig. S1), consistent with the report in a mouse model [8]. These pieces of cross-species evidence suggest an evolutionarily conserved role of dtau in mediating neuronal degeneration, and justify using dtau for mechanistic studies of tauopathies, providing a much faster and

more convenient model for research in this field compared to mouse models.

In neurodegenerative mouse and cellular models, different tau protein species including non-phosphorylated tau and phosphorylated tau have different turnover rates [62–64]. The short-lived and misfolded tau protein species are degraded through the ubiquitination–proteasome system [65, 66], while the long-lived and aggregated proteins are preferentially degraded through the autophagy pathway [67, 68]. Consistent with this, the level of tau without expanded G4C2r co-transfection was increased more by MG132 treatment than by CQ treatment, suggesting that the proteasome system is more involved. The likely explanation is that the transient transfection leads to comparatively higher levels of proteasome-sensitive short-lived tau species than autophagy-sensitive long-lived species, because of the limited expression time. Meanwhile, this does not affect our conclusion that the expanded G4C2r-induced tau increase is mediated by inhibition of autophagy, because this increase was insensitive to MG132 treatment.

BAG3-mediated autophagy may play a key role in maintaining cellular homeostasis under stress as well as during aging (reviewed in [69]), when the increased demand for protein degradation enhances BAG3 expression, followed by a functional switch from the BAG1-mediated proteasomal to BAG3-mediated autophagic pathway. Meanwhile, the potential changes or functional roles of BAG3 in G4C2r models were previously unknown, and it was unclear which specific process in autophagy is influenced by BAG3. Our study revealed that BAG3 influences autophagosome–autolysosome fusion, at least in cells expressing expanded G4C2r (Fig. 6C). In addition, we demonstrated a potential role of the BAG3–autophagy pathway in the neurotoxicity induced by expanded G4C2r. However, the molecular mechanism by which expanded G4C2r expression causes BAG3 reduction is yet to be elucidated.

In summary, our study reveals a possible functional role of tau and BAG3-mediated autophagy in the neuronal degeneration caused by expanded G4C2r, providing entry points for targeting *C9ORF72*-ALS.

Acknowledgements We thank Prof. Peng Jin and Ranhui Duan for providing the G4C2 *Drosophila*, Prof. L. Partridge, Haihui He, and Peng Lei for providing the dtau-knockout *Drosophila*, Prof. Yongqin Zhang for providing related tool *Drosophila* stocks and *UAS-htau4R* [28], and Prof. Shouqing Luo for providing the Lamp1-mcherry vector. This work was supported by the National Natural Science Foundation of China (81925012 and 31961130379) and a Newton Advanced Fellowship (NAF_R1_191045).

Conflict of interest The authors claim no conflict of interest.

References

- DeJesus-Hernandez M, Mackenzie IR, Boeve BF, Boxer AL, Baker M, Rutherford NJ, *et al.* Expanded GGGGCC hexanucleotide repeat in noncoding region of C9ORF72 causes chromosome 9p-linked FTD and ALS. *Neuron* 2011, 72: 245–256.
- Renton AE, Majounie E, Waite A, Simon-Sanchez J, Rollinson S, Gibbs JR, *et al.* A hexanucleotide repeat expansion in C9ORF72 is the cause of chromosome 9p21-linked ALS-FTD. *Neuron* 2011, 72: 257–268.
- Mizielinska S, Gronke S, Niccoli T, Ridler CE, Clayton EL, Devoy A, *et al.* C9orf72 repeat expansions cause neurodegeneration in *Drosophila* through arginine-rich proteins. *Science* 2014, 345: 1192–1194.
- Mori K, Weng SM, Arzberger T, May S, Rentzsch K, Kremmer E, *et al.* The C9orf72 GGGGCC repeat is translated into aggregating dipeptide-repeat proteins in FTL/ALS. *Science* 2013, 339: 1335–1338.
- Zhang K, Daigle JG, Cunningham KM, Coyne AN, Ruan K, Grima JC, *et al.* Stress granule assembly disrupts nucleocytoplasmic transport. *Cell* 2018, 173: 958–971 e917.
- Fay MM, Anderson PJ, Ivanov P. ALS/FTD-associated C9ORF72 repeat RNA promotes phase transitions *in vitro* and in cells. *Cell Rep* 2017, 21: 3573–3584.
- Lee YB, Chen HJ, Peres JN, Gomez-Deza J, Attig J, Stalekar M, *et al.* Hexanucleotide repeats in ALS/FTD form length-dependent RNA foci, sequester RNA binding proteins, and are neurotoxic. *Cell Rep* 2013, 5: 1178–1186.
- Fernandez-Nogales M, Cabrera JR, Santos-Galindo M, Hoozemans JJ, Ferrer I, Rozemuller AJ, *et al.* Huntington's disease is a four-repeat tauopathy with tau nuclear rods. *Nat Med* 2014, 20: 881–885.
- TheHuntington'sDiseaseCollaborativeResearchGroup. A novel gene containing a trinucleotide repeat that is expanded and unstable on Huntington's disease chromosomes. *Cell* 1993, 72: 971–983.
- King A, Al-Sarraj S, Troakes C, Smith BN, Maekawa S, Iovino M, *et al.* Mixed tau, TDP-43 and p62 pathology in FTL associated with a C9ORF72 repeat expansion and p.Ala239Thr MAPT (tau) variant. *Acta Neuropathol* 2013, 125: 303–310.
- Ballatore C, Lee VM, Trojanowski JQ. Tau-mediated neurodegeneration in Alzheimer's disease and related disorders. *Nat Rev Neurosci* 2007, 8: 663–672.
- Andorfer C, Kress Y, Espinoza M, de Silva R, Tucker KL, Barde YA, *et al.* Hyperphosphorylation and aggregation of tau in mice expressing normal human tau isoforms. *J Neurochem* 2003, 86: 582–590.
- Li C, Gotz J. Tau-based therapies in neurodegeneration: opportunities and challenges. *Nat Rev Drug Discov* 2017, 16: 863–883.
- Schoch KM, DeVos SL, Miller RL, Chun SJ, Norrbom M, Wozniak DF, *et al.* Increased 4R-Tau induces pathological changes in a Human-Tau mouse model. *Neuron* 2016, 90: 941–947.
- Guo JL, Buist A, Soares A, Callaerts K, Calafate S, Stevenaert F, *et al.* The dynamics and turnover of Tau aggregates in cultured cells: Insights into therapies for tauopathies. *J Biol Chem* 2016, 291: 13175–13193.
- Jo C, Gundemir S, Pritchard S, Jin YN, Rahman I, Johnson GV. Nrf2 reduces levels of phosphorylated tau protein by inducing autophagy adaptor protein NDP52. *Nat Commun* 2014, 5: 3496.
- Ittner LM, Fath T, Ke YD, Bi M, van Eersel J, Li KM, *et al.* Parkinsonism and impaired axonal transport in a mouse model of frontotemporal dementia. *Proc Natl Acad Sci U S A* 2008, 105: 15997–16002.
- Reddy PH. Abnormal tau, mitochondrial dysfunction, impaired axonal transport of mitochondria, and synaptic deprivation in Alzheimer's disease. *Brain Res* 2011, 1415: 136–148.
- Lu MH, Zhao XY, Yao PP, Xu DE, Ma QH. The mitochondrion: A potential therapeutic target for Alzheimer's disease. *Neurosci Bull* 2018, 34: 1127–1130.
- Ito K, Sass H, Urban J, Hofbauer A, Schneuwly S. GAL4-responsive UAS-tau as a tool for studying the anatomy and development of the *Drosophila* central nervous system. *Cell Tissue Res* 1997, 290: 1–10.
- Guo C, Pan Y, Gong Z. Correction to: Recent advances in the genetic dissection of neural circuits in *Drosophila*. *Neurosci Bull* 2019, 35: 1138.
- Lu B, Al-Ramahi I, Valencia A, Wang Q, Berenshteyn F, Yang H, *et al.* Identification of NUB1 as a suppressor of mutant Huntingtin toxicity via enhanced protein clearance. *Nat Neurosci* 2013, 16: 562–570.
- Yao Y, Cui X, Al-Ramahi I, Sun X, Li B, Hou J, *et al.* A striatal-enriched intronic GPCR modulates huntingtin levels and toxicity. *Elife* 2015, 4.
- Yu M, Fu Y, Liang Y, Song H, Yao Y, Wu P, *et al.* Suppression of MAPK11 or HIPK3 reduces mutant Huntingtin levels in Huntington's disease models. *Cell Res* 2017, 27: 1441–1465.
- Al-Ramahi I, Giridharan SSP, Chen YC, Patnaik S, Safren N, Hasegawa J, *et al.* Inhibition of PIP4Kgamma ameliorates the pathological effects of mutant huntingtin protein. *Elife* 2017, 6.
- Burnouf S, Gronke S, Augustin H, Dols J, Gorsky MK, Werner J, *et al.* Deletion of endogenous Tau proteins is not detrimental in *Drosophila*. *Sci Rep* 2016, 6: 23102.
- Xu Z, Poidevin M, Li X, Li Y, Shu L, Nelson DL, *et al.* Expanded GGGGCC repeat RNA associated with amyotrophic lateral sclerosis and frontotemporal dementia causes neurodegeneration. *Proc Natl Acad Sci U S A* 2013, 110: 7778–7783.
- Wittmann CW, Wszolek MF, Shulman JM, Salvaterra PM, Lewis J, Hutton M, *et al.* Tauopathy in *Drosophila*: neurodegeneration without neurofibrillary tangles. *Science* 2001, 293: 711–714.
- Hutton M, Lendon CL, Rizzu P, Baker M, Froelich S, Houlden H, *et al.* Association of missense and 5'-splice-site mutations in tau with the inherited dementia FTDP-17. *Nature* 1998, 393: 702–705.
- Liu F, Gong CX. Tau exon 10 alternative splicing and tauopathies. *Mol Neurodegener* 2008, 3: 8.
- Himmler A. Structure of the bovine tau gene: alternatively spliced transcripts generate a protein family. *Mol Cell Biol* 1989, 9: 1389–1396.
- Himmler A, Drechsel D, Kirschner MW, Martin DW, Jr. Tau consists of a set of proteins with repeated C-terminal microtubule-binding domains and variable N-terminal domains. *Mol Cell Biol* 1989, 9: 1381–1388.
- Heidary G, Fortini ME. Identification and characterization of the *Drosophila* tau homolog. *Mech Dev* 2001, 108: 171–178.
- Adams SJ, Crook RJ, Deture M, Randle SJ, Innes AE, Yu XZ, *et al.* Overexpression of wild-type murine tau results in progressive tauopathy and neurodegeneration. *Am J Pathol* 2009, 175: 1598–1609.
- Zhu M, Zhang S, Tian X, Wu C. Mask mitigates MAPT- and FUS-induced degeneration by enhancing autophagy through lysosomal acidification. *Autophagy* 2017, 13: 1924–1938.
- Roberson ED, Halabisky B, Yoo JW, Yao J, Chin J, Yan F, *et al.* Amyloid-beta/Fyn-induced synaptic, network, and cognitive impairments depend on tau levels in multiple mouse models of Alzheimer's disease. *J Neurosci* 2011, 31: 700–711.
- Alonso AC, Grundke-Iqbal I, Iqbal K. Alzheimer's disease hyperphosphorylated tau sequesters normal tau into tangles of filaments and disassembles microtubules. *Nat Med* 1996, 2: 783–787.

38. Lasagna-Reeves CA, de Haro M, Hao S, Park J, Rousseaux MW, Al-Ramahi I, *et al.* Reduction of Nuak1 decreases Tau and reverses phenotypes in a tauopathy mouse model. *Neuron* 2016, 92: 407–418.
39. Iijima-Ando K, Sekiya M, Maruko-Otake A, Ohtake Y, Suzuki E, Lu B, *et al.* Loss of axonal mitochondria promotes tau-mediated neurodegeneration and Alzheimer's disease-related tau phosphorylation via PAR-1. *PLoS Genet* 2012, 8: e1002918.
40. Rapoport M, Dawson HN, Binder LI, Vitek MP, Ferreira A. Tau is essential to beta -amyloid-induced neurotoxicity. *Proc Natl Acad Sci U S A* 2002, 99: 6364–6369.
41. Roberson ED, Searce-Levie K, Palop JJ, Yan F, Cheng IH, Wu T, *et al.* Reducing endogenous tau ameliorates amyloid beta-induced deficits in an Alzheimer's disease mouse model. *Science* 2007, 316: 750–754.
42. Vossel KA, Zhang K, Brodbeck J, Daub AC, Sharma P, Finkbeiner S, *et al.* Tau reduction prevents Abeta-induced defects in axonal transport. *Science* 2010, 330: 198.
43. Lee S, Wang JW, Yu W, Lu B. Phospho-dependent ubiquitination and degradation of PAR-1 regulates synaptic morphology and tau-mediated Abeta toxicity in *Drosophila*. *Nat Commun* 2012, 3: 1312.
44. Fu H, Possenti A, Freer R, Nakano Y, Villegas NCH, Tang M, *et al.* A tau homeostasis signature is linked with the cellular and regional vulnerability of excitatory neurons to tau pathology. *Nat Neurosci* 2019, 22: 47–56.
45. Jackson GR, Wiedau-Pazos M, Sang TK, Wagle N, Brown CA, Massachi S, *et al.* Human wild-type tau interacts with wingless pathway components and produces neurofibrillary pathology in *Drosophila*. *Neuron* 2002, 34: 509–519.
46. Wang Y, Mandelkow E. Tau in physiology and pathology. *Nat Rev Neurosci* 2016, 17: 5–21.
47. Guthrie CR, Kraemer BC. Proteasome inhibition drives HDAC6-dependent recruitment of tau to aggresomes. *J Mol Neurosci* 2011, 45: 32–41.
48. Feuillet S, Miguel L, Frebourg T, Campion D, Lecourtis M. *Drosophila* models of human tauopathies indicate that Tau protein toxicity in vivo is mediated by soluble cytosolic phosphorylated forms of the protein. *J Neurochem* 2010, 113: 895–903.
49. Kimura S, Noda T, Yoshimori T. Dissection of the autophagosome maturation process by a novel reporter protein, tandem fluorescent-tagged LC3. *Autophagy* 2007, 3: 452–460.
50. Li Z, Wang C, Wang Z, Zhu C, Li J, Sha T, *et al.* Allele-selective lowering of mutant HTT protein by HTT-LC3 linker compounds. *Nature* 2019, 575: 203–209.
51. Mahr A, Aberle H. The expression pattern of the *Drosophila* vesicular glutamate transporter: a marker protein for motoneurons and glutamatergic centers in the brain. *Gene Expr Patterns* 2006, 6: 299–309.
52. DeVorkin L, Gorski SM. Monitoring autophagic flux using Ref(2)P, the *Drosophila* p62 ortholog. *Cold Spring Harb Protoc* 2014, 2014: 959–966.
53. Chen CS, Chen WN, Zhou M, Arttamangkul S, Haugland RP. Probing the cathepsin D using a BODIPY FL-pepstatin A: applications in fluorescence polarization and microscopy. *J Biochem Biophys Methods* 2000, 42: 137–151.
54. Gamerding M, Hajieva P, Kaya AM, Wolfrum U, Hartl FU, Behl C. Protein quality control during aging involves recruitment of the macroautophagy pathway by BAG3. *EMBO J* 2009, 28: 889–901.
55. Kathage B, Gehlert S, Ulbricht A, Ludecke L, Tapia VE, Orfanos Z, *et al.* The cochaperone BAG3 coordinates protein synthesis and autophagy under mechanical strain through spatial regulation of mTORC1. *Biochim Biophys Acta Mol Cell Res* 2017, 1864: 62–75.
56. Ji C, Tang M, Zeidler C, Hohfeld J, Johnson GV. BAG3 and SYNPO (synaptopodin) facilitate phospho-MAPT/Tau degradation via autophagy in neuronal processes. *Autophagy* 2019, 15: 1199–1213.
57. Lei Z, Brizzee C, Johnson GV. BAG3 facilitates the clearance of endogenous tau in primary neurons. *Neurobiol Aging* 2015, 36: 241–248.
58. Arndt V, Dick N, Tawo R, Dreiseidler M, Wenzel D, Hesse M, *et al.* Chaperone-assisted selective autophagy is essential for muscle maintenance. *Curr Biol* 2010, 20: 143–148.
59. Bieniek KF, Murray ME, Rutherford NJ, Castanedes-Casey M, DeJesus-Hernandez M, Liesinger AM, *et al.* Tau pathology in frontotemporal lobar degeneration with C9ORF72 hexanucleotide repeat expansion. *Acta Neuropathol* 2013, 125: 289–302.
60. He H, Huang W, Wang R, Lin Y, Guo Y, Deng J, *et al.* Amyotrophic Lateral Sclerosis-associated GGGGCC repeat expansion promotes Tau phosphorylation and toxicity. *Neurobiol Dis* 2019, 130: 104493.
61. Bolkan BJ, Kretschmar D. Loss of Tau results in defects in photoreceptor development and progressive neuronal degeneration in *Drosophila*. *Dev Neurobiol* 2014, 74: 1210–1225.
62. Berger Z, Roder H, Hanna A, Carlson A, Rangachari V, Yue M, *et al.* Accumulation of pathological tau species and memory loss in a conditional model of tauopathy. *J Neurosci* 2007, 27: 3650–3662.
63. Yamada K, Patel TK, Hochgrafe K, Mahan TE, Jiang H, Stewart FR, *et al.* Analysis of *in vivo* turnover of tau in a mouse model of tauopathy. *Mol Neurodegener* 2015, 10: 55.
64. Khlistunova I, Biernat J, Wang Y, Pickhardt M, von Bergen M, Gazova Z, *et al.* Inducible expression of Tau repeat domain in cell models of tauopathy: aggregation is toxic to cells but can be reversed by inhibitor drugs. *J Biol Chem* 2006, 281: 1205–1214.
65. Rock KL, Gramm C, Rothstein L, Clark K, Stein R, Dick L, *et al.* Inhibitors of the proteasome block the degradation of most cell proteins and the generation of peptides presented on MHC class I molecules. *Cell* 1994, 78: 761–771.
66. Wong E, Cuervo AM. Integration of clearance mechanisms: the proteasome and autophagy. *Cold Spring Harb Perspect Biol* 2010, 2: a006734.
67. Saitoh T, Fujita N, Jang MH, Uematsu S, Yang BG, Satoh T, *et al.* Loss of the autophagy protein Atg16L1 enhances endotoxin-induced IL-1beta production. *Nature* 2008, 456: 264–268.
68. Lee MJ, Lee JH, Rubinsztein DC. Tau degradation: the ubiquitin-proteasome system versus the autophagy-lysosome system. *Prog Neurobiol* 2013, 105: 49–59.
69. Behl C. Breaking BAG: The co-chaperone BAG3 in health and disease. *Trends Pharmacol Sci* 2016, 37: 672–688.



Sex and Death: Identification of Feedback Neuromodulation Balancing Reproduction and Survival

Can Gao¹ · Chao Guo² · Qionglin Peng¹ · Jie Cao¹ · Galit Shohat-Ophir³ · Dong Liu^{2,4} · Yufeng Pan^{1,4} 

Received: 15 April 2020 / Accepted: 31 May 2020 / Published online: 11 November 2020
© Shanghai Institutes for Biological Sciences, CAS 2020

Abstract Some semelparous organisms in nature mate as many times as they can in a single reproductive episode before death, while most iteroparous species including humans avoid such suicidal reproductive behavior. Animals naturally pursue more sex and the possible fatal consequence of excessive sex must be orchestrated by negative feedback signals in iteroparous species, yet very little is known about the regulatory mechanisms. Here we used *Drosophila* male sexual behavior as a model system to study how excessive sex may kill males and how the nervous system reacts to prevent death by sex. We found that continuous sexual activity by activating the *fruitless*-expressing neurons induced a fixed multi-step behavioral pattern ending with male death. We further found negative feedback in the fly brain to prevent suicidal sexual behavior by expression changes of the neurotransmitters acetylcholine and gamma-aminobutyric acid, and neuropeptide

F. These findings are crucial to understand the molecular underpinnings of how different organisms choose reproductive strategies and balance reproduction and survival.

Keywords *Drosophila* · Reproduction · Survival · NPF · GABA · Acetylcholine

Introduction

Most species, including humans, balance sexual behaviors and survival, avoiding excessive sexual activity based on their past experience and internal physiological state [1–3]; however, there are some semelparous organisms, such as the insectivorous marsupials, that mate as many times as they can in a single reproductive episode that eventually kills them [4]. While the evolutionary mechanism of suicidal reproduction in semelparous animals is of much interest, it is hard to study the molecular and neuronal mechanisms underlying such behavior due to the very limited genetic and neurological tools in these animals.

Drosophila melanogaster is iteroparous with survival and reproduction well balanced [2]. Male courtship in *Drosophila* is a well-studied innate behavior, which is largely controlled by the sex-specific transcription factors (FRUM and DSXM in males, and DSXF in females) encoded by the *fruitless* (*fru*) and *doublesex* (*dsx*) genes [5–7]. FRUM is responsible for most aspects of male courtship [8–10], and is expressed in a dispersed subset of ~2000 neurons including sensory neurons, interneurons, and motor neurons that are interconnected to form sex circuitry [9–12]. Recently, much progress has been made on how sensory cues are integrated by the male-specific P1 neurons that initiate male courtship, and how experiences may alter P1 excitability to modulate courtship [13–20]. In

Electronic supplementary material The online version of this article (<https://doi.org/10.1007/s12264-020-00604-5>) contains supplementary material, which is available to authorized users.

Can Gao and Chao Guo are contributed equally to this work.

✉ Yufeng Pan
pany@seu.edu.cn

¹ The Key Laboratory of Developmental Genes and Human Disease, School of Life Science and Technology, Southeast University, Nanjing 210096, China

² School of Life Sciences, Nantong University, Nantong 226019, China

³ The Mina & Everard Goodman Faculty of Life Sciences and Susan Gonda Multidisciplinary Brain Research Center, Bar-Ilan University, Ramat-Gan 5290002, Israel

⁴ Co-innovation Center of Neuroregeneration, Nantong University, Nantong 226019, China

particular, mating experience decreases further courtship through dopamine modulation of P1 neurons [2, 21, 22], providing a potential mechanism to avoid excessive sexual behavior in male flies. However, there is no evidence that sexual activity *per se* in male flies perturbs their survival, although exposure to female pheromones does [23, 24], making it hard to study the molecular and neuronal mechanisms underlying suicidal reproduction despite the advanced genetic tools in this species [25].

We previously showed that mild activation of all *fruM* neurons induces courtship behaviors in solitary males, which perform courtship behaviors until death [26]. In this study, we used two genetic models, one in the above males with *fruM* neurons activated that are semelparous, and the other in wild-type males that are iteroparous. Combining these two genetic models, we investigated how excessive sexual activity accelerates death in male flies, and how the central nervous system reacts to prevent such behaviors. We found that continuous performance of sexual behaviors induces a fixed behavioral pattern ending with male death. We further found a negative feedback in the fly brain involving acetylcholine, gamma-aminobutyric acid (GABA) and neuropeptide F (NPF) to prevent suicidal sexual behavior.

Materials and Methods

Fly Stocks

Flies were maintained at 22°C or 25°C in a 12h:12h light:dark cycle. Canton-S flies were used as the wild-type strain. *fruGAL4* [10], *fruLexA* [27], *UAS-dTrpA1* (II) [28], *UAS-CsChrimson* (attp2) [29], *UAS-fruMi* (attp2) [30], *UAS-fruMiScr* (attp2) [30], *R19B03-Gal4* (attp2) [31], *NPF-GAL4* (BDSC#25682), and *Crz-GAL4* (BDSC#51976) have been described previously. RNAi lines (*UAS-GABA-B-R3-RNAi*, *UAS-Dsk-RNAi*, *UAS-CCKLR-17D3-RNAi*, *UAS-Oct-beta-2R-RNAi*, *UAS-NPF-RNAi*, *UAS-NPFRI-RNAi*, *UAS-Trh-RNAi*, and *UAS-Dop1RI-RNAi* all at attp2, and *UAS-Gad1-RNAi* and *UAS-ChAT-RNAi* at attp40) have been described previously [32] and were from Tsinghua Fly Center at Tsinghua University.

Male Courtship Assay

In courtship assays for Fig. 4, 4–8-day-old wild-type virgin females were loaded individually into cylindrical chambers (diameter: 1 cm; height: 3 mm per layer) as courtship targets, and 4–6-day-old test males were then gently loaded into the chambers after cold anesthesia and separated from target females by a transparent film. The chambers were warmed at 27°C for 4 h allowing dTRPA1-mediated

neuronal activation, and transferred to 22°C for 30 min, 1 h, or 2 h before the 10-min courtship test. The courtship index (CI), which is the percentage of observation time a male fly performs courtship, was used to measure courtship towards female targets, and measured manually using LifeSongX software.

In the courtship assays for Fig. 5, 4–8-day-old wild-type virgin females were loaded into large cylindrical chambers (diameter: 4 cm; height: 3 mm per layer) as courtship targets (10 females per chamber), and 4–6 day-old-test males were then individually loaded into chambers after cold anesthesia, and separated from target females by a transparent film until courtship testing for 5 h continuously at 25°C.

Feeding Assay

Feeding was assayed using food with a blue dye. In brief, in a regular feeding assay test (Fig. 2C), flies were starved for 24 h on 1% aqueous agar food at 22°C, then transferred to 1% FD & C Blue 1 food (2.5% sucrose, 2.5% yeast extract, and 0.5% agar; Sigma-Aldrich, St. Louis, MO) at 27°C for 30 min (the food was pre-warmed at 27°C for 3 h). The feeding test shown in Fig. 2A was the same but used non-starved males; that in Fig. 2B used non-starved males and allowed feeding at 27°C for 12 h. To quantify food intake, the absorbance of the ingested blue dye was measured at 630 nm using a 96-well microplate spectrophotometer.

Survival Assay

Adult male flies were collected within 12 h after eclosion and group housed (10–15 males) for 3–4 days before the survival test. In the survival assay for Figs 1A, B, and 5I, individual test males were loaded with a certain number of virgin females (1M+1F, 1M+4F, 1M+7F, or 1M+10F) into empty vials without food, and controls with the same group size of males (2M, 5M, 8M, or 11M). The survival of males was scored every 6 h at 25°C. Only the 1M+10F condition was used for the survival assays shown the Figs 1B and 5I. The sample size for all experiments was 10, and each sample contained 8–11 males. For all M+F groups (1M+1F, 1M+4F, 1M+7F or 1M+10F), 10 vials were used as one sample, thus there were 100 males in each group. For the 2M group, 5 vials were used as one sample (100 males; for the 5M group, 2 vials were used as one sample (100 males; and for the 8M and 11M groups, each vial was a sample (80 and 110 males).

The survival assay shown in the Fig. S1 was almost the same as above, but 1% agar + 1% sugar medium in vials at 22°C was provided. The number of dead males was scored

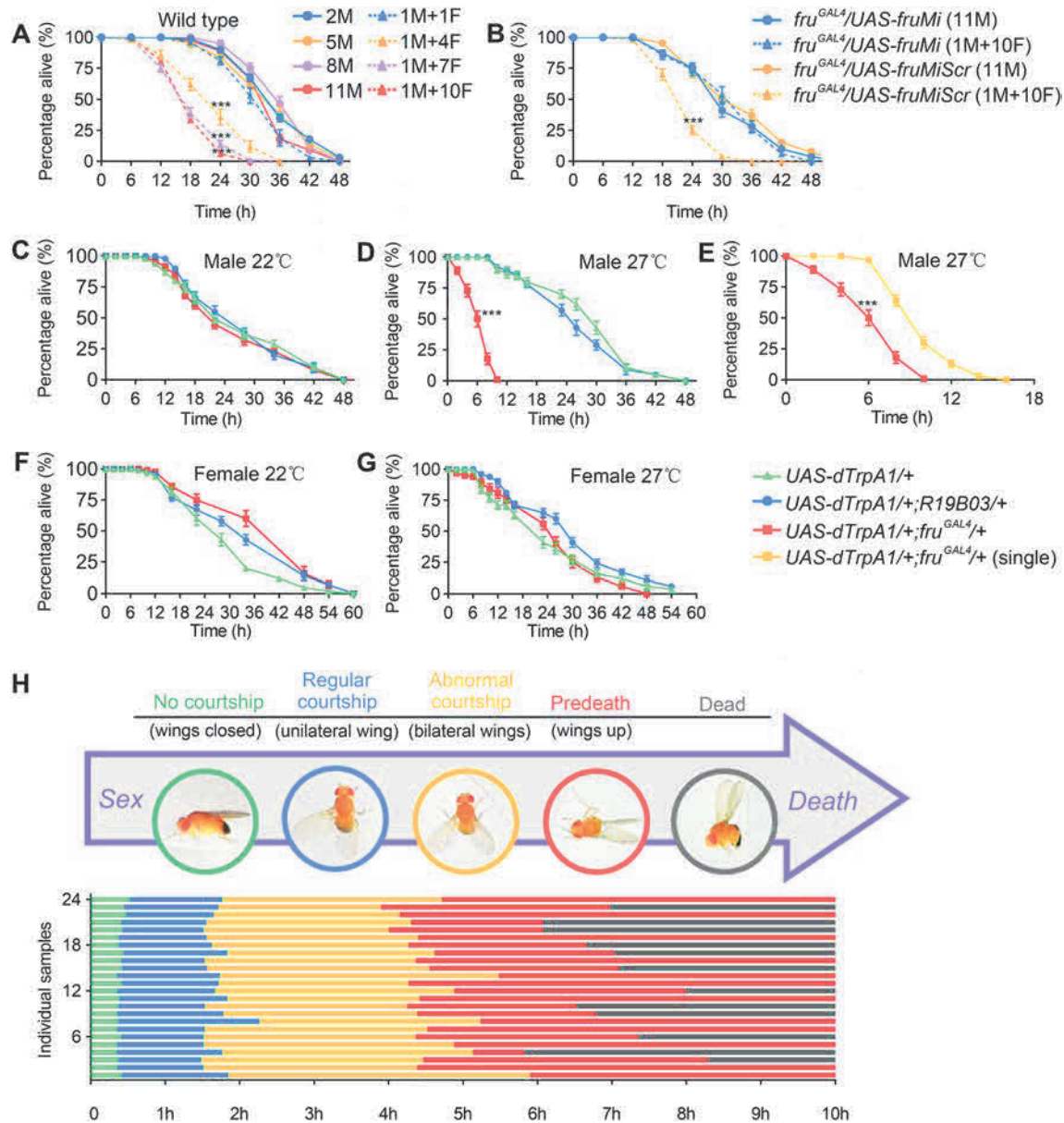


Fig. 1 Coupling sex and death in *Drosophila* males. **A** Survival rates of wild-type males under conditions allowing different levels of sexual activity. Males die much sooner when group-housed with increasing numbers of virgin females (M, males; F, virgin females). Flies were housed in vials without food and assayed at 25°C. *N* = 10 for each. Each *n* consists of 10 vials of 1M+1F, 1M+4F, 1M+7F, 1M+10F, 5 vials of 2M, 2 vials of 5M, or one vial of 8M or 11M. ****P* < 0.001 for 1M+4F vs 5M, 1M+7F vs 8M, or 1M+10F vs 11M at the 24-h time point, Mann Whitney U test. **B** Males with *fru^M* knocked down survive similarly when grouped with 10 virgin females or in groups of 11 males. *n* = 10 for each. Each *n* consists of 10 vials of 1M+10F or one vial of 11M. ****P* < 0.001, Mann Whitney U test. **C, D** Mildly activating all *fru^M* neurons at 27°C induces continuous

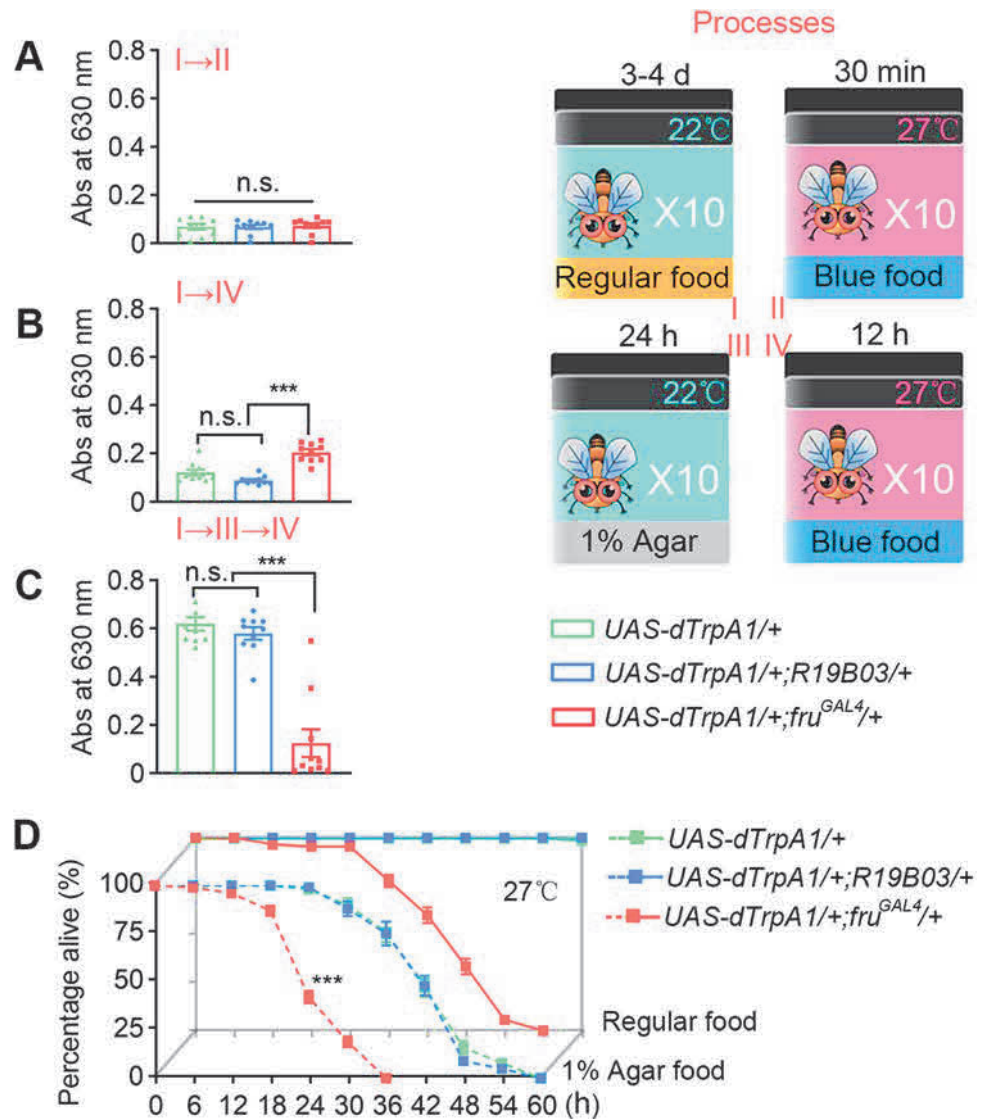
courtship and accelerates male death. All males were housed in groups of 10 without food. *n* = 10 for each. ****P* < 0.001 at 6 h, Mann Whitney U test. **E** Males with *fru^M* neurons activated die much more quickly in groups of 10 males than in isolation. *n* = 10 for each. Each *n* consists of one vial of 10 males or 10 vials of single-housed males. ****P* < 0.001 at 6 h, Mann Whitney U test. **F, G** Activating *fru^M* counterpart neurons in females does not accelerate female death. *n* = 10 (10 females/group) for each. **H** Activating *fru^M* neurons induces a series of stereotypical behavior patterns from regular courtship display to male death. Flies were individually housed in round chambers without food and recorded at 27°C. *n* = 24. Error bars indicate SEM.

twice a day. Flies were transferred to new vials with medium every 2 days.

In the survival assays for Figs 1C–G, 2D, and 3E, I: groups of 10 males (or 10 females in Fig. 1F, G) were

housed in vials without food (Fig. 1C–G), or in a nutritional environment (1% agar for the 3 agar groups in Fig. 2D; regular food for the other 3 groups in Figs 2D and 3E, I) at specified temperatures. Flies housed in vials with

Fig. 2 Abnormal feeding in continuously courting males. **A–C** Males with activated *fru^M* neurons eat more in the short term, but much less in the long term. Feeding assays are illustrated on the right. *n* = 10 (10 flies/group) for each. n.s., not significant, ****P* < 0.001, Kruskal–Wallis test, post hoc Dunn’s multiple comparisons test. **D** Feeding alleviates but does not prevent death in males with activated *fru^M* neurons. *n* = 10 (10 flies/group) for each. ****P* < 0.001 at 24 h, Mann–Whitney U test. Error bars indicate SEM.



food were transferred to new food vials every 2 days, and dead flies were removed and counted. Ten replicate vials were established for each group, a total of 100 flies.

In the survival assays for Fig. 3H, flies were raised on regular food or food with 0.2 mmol/L ATR (all-trans-retinal, MFCD00001550, Sigma-Aldrich, St. Louis, MO) throughout development and adulthood in the dark. Test males were group-housed (10 flies per vial) and exposed to 620-nm red light (40 Hz, 8 ms duration, 0.071 mW/mm²). Flies were transferred to new vials containing fresh food every 2 days, and dead flies were removed and counted. Ten replicate vials were established for each group (total, 100 males).

Ejaculation Assay

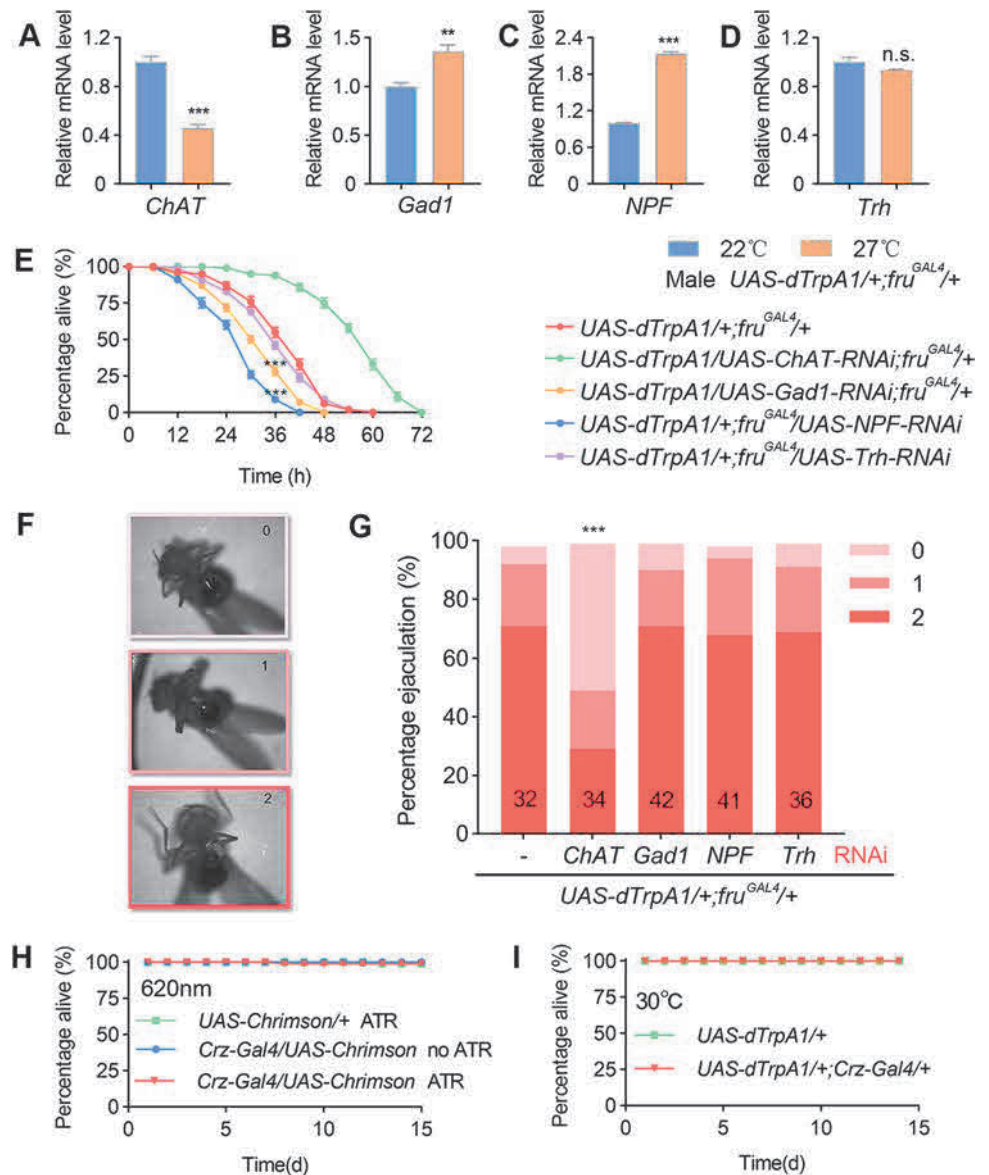
To evaluate ejaculation, males were loaded individually into cylindrical chambers (diameter, 2 cm; height, 3 mm)

after ice anesthesia, and allowed to recover at 22°C for 30 min, then transferred to 27°C for 30 min. Ejaculation levels (0, 1, or 2; see Fig. 3F) were manually scored under a microscope.

Body Weight

A few 1.5-mL centrifugal tubes were numbered and each weighed as M_0 . Then 20 males were loaded into each tube after CO₂ anesthesia, and weighed as M_1 . The same 20 males were transferred from the centrifugal tube to an empty vial, transferred to 27°C for 6 h, and then returned to the original centrifugal tube and weighed as M_2 . The percentage weight loss was $(M_2 - M_1)/(M_1 - M_0) \times 100\%$. Five replicates were measured for each group.

Fig. 3 Counterbalancing molecular changes induced by excessive sexual output. **A–D** Continuous activation of *fru^M* neurons decreases *chat* expression and increases *Gad1* and *NPF* expression in male brains. Groups of 10 males were housed in food vials for 12 h at 27°C. *n* = 3 per group. n.s., not significant, ***P* < 0.01, ****P* < 0.001, unpaired *t*-test. **E** Knocking down *chat* alleviates, while knocking down *Gad1* or *NPF* further accelerates, the fatal effect of *fru^M* neuronal activation in males. All test males were housed in food vials in groups of 10 at 27°C. *n* = 10 (10 flies/group) for each. ****P* < 0.001 at 36 h, Mann Whitney U test. **F** Evaluation of ejaculation in individual males. 0 refers to no ejaculation, 1 and 2 refer to ejaculation with different volumes. **G** Knocking down *chat* significantly reduces the level of ejaculation in males with activated *fru^M* neurons. *n* as indicated inside bars. ****P* < 0.001, χ^2 test. **H, I** Activation of *Crz* neurons via light-sensitive CsChrimson (**H**) or temperature-sensitive dTrpA1 (**I**) does not affect mortality over a 15-day period on regular food or food with ATR. *n* = 10 each, each *n* consists of 10 flies. Error bars indicate SEM.



Quantitative Real-time PCR

Fly samples from neuronal activation and mating experiments were frozen in liquid nitrogen and decapitated by vigorous vortexing. The heads were then separated from the bodies using metal sieves. Each sample, consisting of 30 frozen heads, was used for total RNA using TRIzol reagent (15596026, Thermo Fisher Scientific, Waltham, MA). We purified total RNA using a DNA-freeTM Kit (AM1906, Thermo Fisher Scientific, Waltham, MA) and performed reverse transcription using SuperScriptTM IV (18091050, Thermo Fisher Scientific, Waltham, MA) to obtain cDNA used for templates. Quantitative PCR was performed on the Roche LightCycler® 96 Real-Time PCR machine using AceQ qPCR SYBR Green Master Mix (Q121-02, Vazyme, Nanjing). Transcript levels were

analyzed by the $2^{-\Delta\Delta CT}$ method using *Actin* as an internal control. Each sample was run in triplicate. Each experiment was repeated three times using independent sets of genetic crosses. Primers used for RT-PCR quantification were:

<i>Actin</i> Forward	5'-GTCGCGATTTAACCGAC-TACCTGA-3'
<i>Actin</i> Reverse	5'-TCTTGCTT CGAGATCCACATCTGC-3'
<i>ChAT</i> Forward	5'-TGAATATGCCTTGAGCTGTGC-3'
<i>ChAT</i> Reverse	5'-TCGTGCGAGAATTCCGCAAAC-3'
<i>Gad1</i> Forward	5'-GTGCCACCACATTGAAGTACC-3'
<i>Gad1</i> Reverse	5'-AGACCGTTGGACAGCTGATTG-3'

<i>Trh</i> Forward	5'-TCCATTCTACACACCAGAACCG-3'
<i>Trh</i> Reverse	5'-ACTGGGCAAACTGGAGTTG-3'
<i>NPF</i> Forward	5'-CCTCATTAACCGCGAGCAAAT-3'
<i>NPF</i> Reverse	5'-ATCGCTGATGGATATCCTGAGG-3'

Tissue Dissection, Staining, and Imaging

Brains of 4–6 day-old males and females were dissected in Schneider's insect medium (S2) and fixed in 4% paraformaldehyde in 0.5% Triton X-100 and 0.5% bovine serum albumin in phosphate-buffered saline (PAT) for 30 min at room temperature. After 4 × 10-min washes, tissues were blocked in 3% normal goat serum (NGS) for 60 min, then incubated in primary antibodies diluted in 3% NGS for 4 h at room temperature and 1–2 days at 4°C, then washed in PAT, and incubated in secondary antibodies diluted in 3% NGS for 4 h at room temperature and 1–2 days at 4°C. The tissues were then washed thoroughly in PAT and mounted for imaging. The antibodies used were rabbit anti-NPF (1:500; RB-19-0001, RayBiotech, Norcross, GA), rabbit anti-GFP (1:1000; A11122, Invitrogen, Waltham, MA), and secondary Alexa Fluor 488 antibodies (1:500, A21206, Invitrogen, Waltham, MA). Samples were imaged at ×20 magnification on Zeiss 710 confocal microscopes using ZEN (<https://www.zeiss.com/microscopy/int/products/microscope-software/zen.html>) and processed with Fiji software (<https://imagej.net/Fiji/Downloads>).

Statistics

Experimental flies and genetic controls were tested under the same conditions, and data are collected from at least two independent experiments. Statistical analysis was performed using GraphPad Prism 8 (<https://www.graphpad.com/scientific-software/prism/>) as indicated in each figure legend. Data were first verified for normal distribution by the D'Agostino–Pearson normality test. For normally-distributed data, Student's *t* test was used for pairwise comparisons, and one-way ANOVA was used for comparisons among multiple groups, followed by Tukey's multiple comparisons. For data not normally-distributed, the Mann-Whitney U test was used for pairwise comparisons, and the Kruskal–Wallis test was used for comparison among multiple groups, followed by Dunn's multiple comparisons. For RT-PCR experiments, the average relative expression of three independent experiments was analyzed using the unpaired *t*-test. The χ^2 test was used to compare two groups in the male ejaculation assay.

Results

Coupling Sex and Death: A *Drosophila* Model

Previous studies revealed that male courtship behavior *per se* does not affect life span in male *Drosophila* [23, 24]. We wondered if the excessive expression of courtship behaviors (successive mating in a short period of time) would be costly, and tested the survival rate of individual wild-type *Canton-S* (*wtcs*) males housed with increasing numbers of virgin females (1M+1F, 1M+4F, 1M+7F, or 1M+10F). We also tested the survival rates of groups of males with the same group size as above (2M, 5M, 8M, or 11M). We found that male flies grouped with 4, 7, or 10 virgin females died more quickly than those grouped with males or with only one female, if no food was provided (Fig. 1A). To confirm that this effect was induced by sexual activity, we used male flies with *fru*^M knockdown by expressing RNAi targeting *fru*^M [30] using *fru*^{GAL4}, which rarely showed any courtship behavior when grouped with females during the 2-day test period. We found that such males had the same survival rates when grouped with 10 virgin females or in groups of 11 males (Fig. 1B). We also tested groups of *wtcs* flies (1M+10F, or 11M) under low nutrition conditions (1% agar + 1% sugar), and found that individual males housed with 10 females died more quickly than groups of 11 males (Fig. S1). However, we did not find a survival difference in males housed with females (1M+10F) or males (11M) within a 30-day period if regular food was provided. These results indicate that excessive sexual activity with multiple females is costly to male survival under low nutrition conditions but has no effect on survival if fed on regular food.

Although the above results revealed an effect of excessive sexual activity on survival, wild-type male flies would not court until death. We previously showed that activation of ~2,000 *fru*^M-expressing neurons at 29°C using the warmth-activated cation channel dTRPA1 [28] induces continuous courtship behaviors and eventually kills males [26]. Thus we used such a model to couple sex and death in male flies, and study how excessive sexual activity would be fatal and how flies avoid such behavior. We tested the survival rate of groups of 11 males without food, and found that all showed similar survival rates at the permissive temperature (22°C, Fig. 1C); however, half of the *UAS-dTrpA1/+; fru*^{GAL4/+} males at 27°C performing continuous courtship behaviors died in ~6 h, much more quickly than control *UAS-dTrpA1/+* males (Fig. 1D). We used 27°C, rather than the 29°C previously used [26], as it allowed much longer survival of *UAS-dTrpA1/+; fru*^{GAL4/+} males, suitable for further genetic manipulations (see below). We also tested the survival rate of male flies in

which ~2,000 mushroom body (MB) neurons (labeled by *R19B03*) were activated at 27°C, and did not find any survival deficit (Fig. 1D). Furthermore, individual *UAS-dTrpA1/+; fru^{GAL4}/+* males survived longer than groups of such males, probably due to the lack of energy-consuming chasing behaviors that were only found in groups of such males (Fig. 1E). We found no survival deficit in *UAS-dTrpA1/+; fru^{GAL4}/+* females at 27°C with all *fru^{GAL4}* neurons activated (Fig. 1F, G). These results indicated that it is the continuous output of sexual behaviors, but not the continuous activation of a large number of neurons (MB neurons in males and females; *fru^{GAL4}* neurons in females), that kills flies in hours.

To reveal how continuous sexual activity results in quick death in males, we recorded individual *UAS-dTrpA1/+; fru^{GAL4}/+* males at 27°C for 10 h, and found a stereotypic behavioral expression from sex to death in all males: initially they closed their wings and did not show any courtship in the first few minutes after transfer to 27°C, and performed intensive courtship behaviors including unilateral wing extension and abdominal bending for 1–2 h. Later, all males began to extend and vibrate the wings bilaterally, indicating abnormal courtship, for 2–3 h, followed by a pre-death phase when males stopped walking, raised both wings, and bent their abdomen to attempt copulation, until motionless and dead (Figs 1H and S2).

As sexual activity is energy-consuming, we tested how 6-h continuous expression of courtship behaviors might change body weight. We found that after 6-h activation of *fru^M* neurons at 27°C, males lost ~20% of their body weight, while 6-h activation of *fru^M* neurons in females, or 6-h activation of MB neurons in males or females, like control *UAS-dTrpA1/+* males or females, lost <10% of their body weight (Fig. S3A–D), which may be due to dehydration during this period. That 6-h activation of *fru^M* neurons induces ~10% more weight loss in males than control flies indicates that continuous sexual activity is associated with energy expenditure that burns ~10% of their body weight in 6 h.

Feeding Alleviates but Does not Prevents Death From Sex

The above results show how continuous activation of *fru^M* neurons accelerates male death if food is not provided, and we next tested whether these males could eat, and if so, if feeding could prevent death. We first transferred fed males to 27°C, allowing feeding on blue food for 30 min. Males with activated *fru^M* neurons or MB neurons, or control *UAS-dTrpA1/+* males, all showed similarly low levels of feeding (Fig. 2A). However, when we transferred fed males to 27°C and allowed 12-h feeding on blue food, we

found that males with activated *fru^M* neurons ate more than males with activated MB neurons or control *UAS-dTrpA1/+* males (Fig. 2B), which may be due to the higher energy consumption and need for food in males with activated *fru^M* neurons. In contrast, when starved males were allowed 12-h feeding on blue food at 27°C, those with activated *fru^M* neurons ate significantly less than males with activated MB neurons or control *UAS-dTrpA1/+* males (Fig. 2C). These results demonstrate that while performing intensive courtship behaviors, males with activated *fru^M* neurons can eat, so feeding and courtship behaviors are not exclusive at least in this context, although the level of feeding is much lower than control males over 12 h. Indeed, males with activated *fru^M* neurons at 27°C survived much longer if provided food [Fig. 2D, 50% of males survived for >36 h with regular food, and ~18 h with 1% agar, compared to ~6 h without any food (Fig. 1D)]. Thus males with activated *fru^M* neurons have a lower level of feeding, and such feeding alleviates but does not prevent death.

Altered Neural Transmission Upon Excessive Sexual Activity

As flies, like most animals, do not court and mate until death, we reasoned that there must be feedback signals upon excessive sexual activity to inhibit further such behaviors. We first used real-time PCR to assess changes in the mRNA expression of major neurotransmitters, as well as neuropeptide F (NPF) that is a reward signal for mating [33, 34], in the brains of *UAS-dTrpA1/+; fru^{GAL4}/+* males after 12-h at 27°C. We found reduced expression of *choline acetyltransferase (ChAT)*, increased expression of the GABA synthesis enzyme *glutamic acid decarboxylase 1 (Gad1)*, and *NPF*, and unaltered expression of *tryptophan hydroxylase (Trh)* (Fig. 3A–D). These results indicated that continuous sexual activity resulted in reduced excitatory acetylcholine (ACh) signaling, and enhanced inhibitory GABA signaling, as well as elevated NPF signaling. To test if these expression changes play a role in survival during the activation of *fru^M* neurons, we knocked down *ChAT*, *Gad1*, *NPF*, or *Trh* in *UAS-dTrpA1/+; fru^{GAL4}/+* males using RNAi [32], and assayed their survival rates at 27°C on food. We found that the lethal effect of activating *fru^M* neurons was alleviated by knockdown of *ChAT*, but accelerated by knockdown of *Gad1* or *NPF* (Fig. 3E). Together, these results indicate that feedback neuromodulation (reduced ACh and increased GABA and NPF) by continuous sexual activity is protective and enhances male survival.

We noted that all the above males at 27°C performed intensive courtship behaviors in groups of 10 males, and found no difference, so we further tested the ejaculation

rates of individual males at 27°C. We found that knock-down of *ChAT*, but not *Gad1*, *NPF*, or *Trh*, significantly decreased the ejaculation rates of *UAS-dTrpA1/+; fru^{GAL4}/+* males (Fig. 3F, G), suggesting a role of ACh-dependent ejaculation in the mortality of these males. To test if excessive ejaculation alone kills males, we activated *Corazonin* (*Crz*) neurons, which induce ejaculation but no other courtship behaviors in isolated males [34, 35], and found no survival deficit during the 15-day test period using either optogenetic (Fig. 3H) or thermogenetic activators (Fig. 3I). Together, these results suggest that continuous display of courtship behaviors other than ejaculation (wing extension and abdominal bending) is more fatal to males, although ejaculation might enhance this fatal effect.

Negative Feedback Prevents Continuous Sexual Activity

To test if prior experience of excessive sexual activity inhibits further courtship behaviors, we first kept individually-housed *UAS-dTrpA1/+; fru^{GAL4}/+* males at 27°C for 4 h, allowing continuous courtship expression, then

transferred them to 22°C for 30 min, 1 h, or 2 h, during which all males stopped courting. We then introduced virgin females to test male courtship behavior after the above experience (Fig. 4A). We found that males with 4-h experience of *fru^M* neuronal activation, even after 0.5–2 h recovery, showed much reduced courtship of virgin females (Fig. 4B–D; the percentage of time males displayed any courtship behavior was ~13% after 1 h of recovery, compared to ~85% in control males). We reasoned that the altered neural transmission described above might be involved in courtship inhibition after continuous courtship expression, so we separately knocked down *ChAT*, *Gad1*, *NPF*, *Trh*, and some other transmission related genes in *UAS-dTrpA1/+; fru^{GAL4}/+* males. All males tested showed reduced courtship levels (compared to the control CI of ~85%) after 4-h continuous courtship expression and 1-h recovery; however, we found that knocking down *NPF* in *fru^M*-expressing neurons significantly alleviated the courtship inhibition effect (Fig. 4E; the CI was ~40% with *NPF* knockdown, and ~10% with intact *NPF*). Together, these results indicate that excessive sexual activity induces expression changes of certain

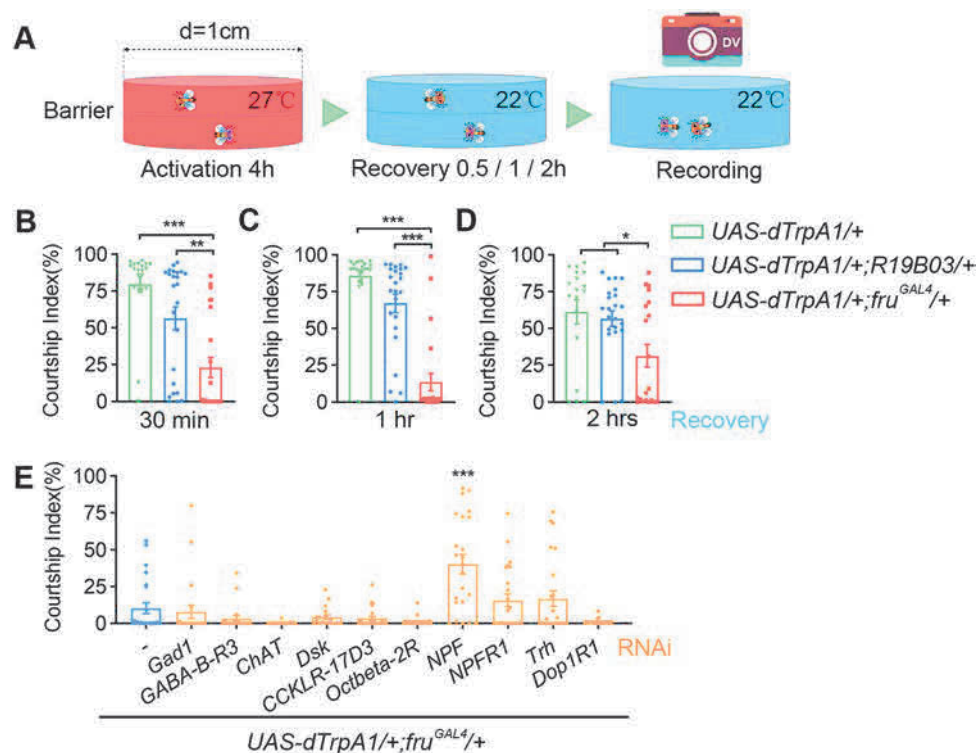


Fig. 4 NPF represses courtship after excessive sexual output. **A** Schematic for experiments assaying courtship inhibition after 4 h of continuous sexual output. **B–D** Reduced male courtship toward virgin females after 4 h of continuous activation of *fru^M* neurons. For 0.5 h recovery, $n = 21, 24, \text{ and } 23, P < 0.001$, Kruskal-Wallis test. $^{**}P < 0.01$, $^{***}P < 0.001$, *post hoc* Dunn's multiple comparisons test. For 1 h recovery, $n = 22, 24, \text{ and } 23, P < 0.001$, Kruskal-Wallis test.

$^{***}P < 0.001$, *post hoc* Dunn's multiple comparisons test. For 2 h recovery, $n = 18, 23, \text{ and } 20, P = 0.032$, Kruskal-Wallis test. $^{*}P < 0.05$, *post hoc* Dunn's multiple comparisons test. **E** Knocking down *NPF* partially restores male courtship that was suppressed by 4-h activation of *fru^M* neurons. $n = 24, 22, 20, 24, 18, 23, 22, 23, 24, 24, \text{ and } 22. ^{***}P < 0.001$, Mann-Whitney U test compared with control without RNAi (blue). Error bars indicate SEM.

transmission genes including *NPF*, which in turn inhibit further courtship behaviors.

The above results used males with *fru^M* neurons forcefully activated for 4 h, but whether this applied to regular males without artificial neuronal activation was uncertain. Thus we placed individual males with 10 virgin females, and recorded their courtship behaviors for 5 h (Fig. 5A). We found that control *fru^{GAL4/+}* males, as well as males with *Gad1*, *NPF*, or *Trh* knocked down, mated multiple times; however, males with *ChAT* knocked down in *fru^M* neurons rarely courted and never mated (Fig. 5B). Further analysis of their courtship behaviors showed that

control *fru^{GAL4/+}* males, as well as those with *Trh* knocked down, reduced their further courtship after each mating, such that their CI was $\sim 15\%$ after 4 successive matings (Fig. 5C, CI-5). Although males with *Gad1* knocked down reduced their courtship after mating, this reduction was not as severe as in control males (Fig. 5C, CI-5; $\sim 48\%$ after 4 successive matings). Surprisingly, males with *NPF* knocked down displayed indistinguishable levels of courtship even after 4 successive matings (Fig. 5C; initial CI-1 $\sim 83\%$, and CI-5 after 4 matings $\sim 73\%$, not significantly different). Furthermore, while control *fru^{GAL4/+}* males and those with *Trh* knocked down had an average of ~ 4

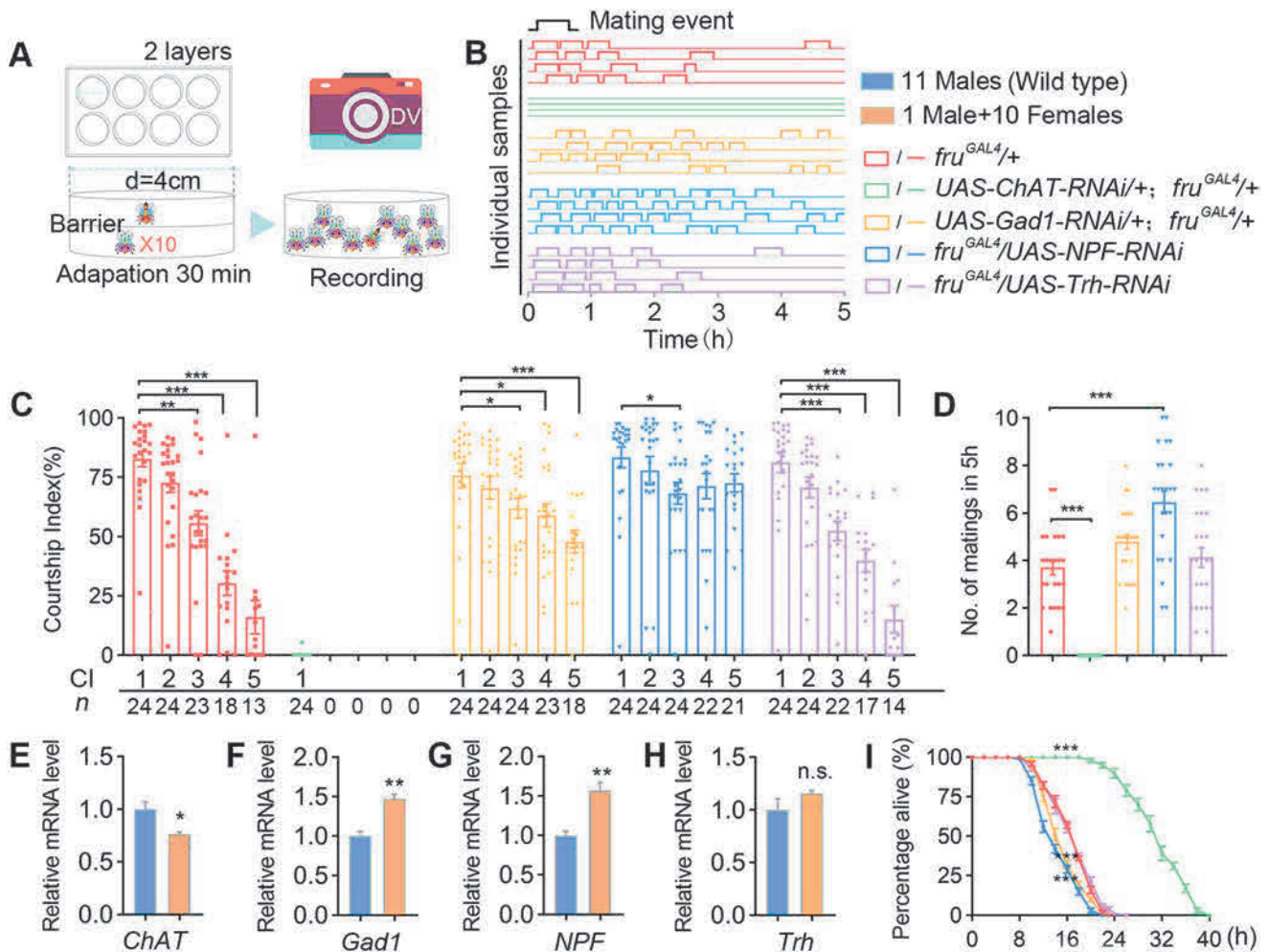


Fig. 5 GABA and NPF inhibit excessive sexual activity in wild-type males. **A** Behavioral setup allowing up to 10 matings (1M+10F) in a 5-h test. **B** Examples of male mating activity in 5 h. Genotypes as indicated by colors below. **C** Courtship indices of males in the 1M+10F environment. CI-1 indicates courtship in the first 10 min after the male and females are introduced; CI-2, CI-3, CI-4, and CI-5 indicate 10-min courtship after the 1st, 2nd, 3rd, and 4th matings, respectively. Kruskal-Wallis test, * $P < 0.05$, ** $P < 0.01$, *** $P < 0.001$, *post hoc* Dunn's multiple comparisons test. *N* as indicated below. **D** Numbers of matings by males during the 5-h test. Knockdown of *NPF* significantly increases the number of matings.

$n = 24$ per group, $P < 0.001$, one-way ANOVA, *** $P < 0.001$, *post hoc* Tukey's multiple comparisons test. **E–H** Wild-type males housed with 10 virgin females have reduced *chat* expression and elevated *Gad1* and *NPF* expression in their brains compared with groups of 11 males. Flies were housed in vials without food for 12 h at 25°C. $N = 3$ per group. n.s., not significant, * $P < 0.05$, ** $P < 0.01$, unpaired *t*-test. **I** Knocking down *Gad1* or *NPF* accelerates, while knocking down *ChAT* slows down death in males housed with 10 virgin females without food. $n = 10$ for each. Each n consists of 10 vials of 1M+10F. *** $P < 0.001$ at 16 h, Mann Whitney U test. Error bars indicate SEM.

successive matings with 10 virgin females within 5 h (3.7 ± 0.3 and 4.1 ± 0.4 , respectively), males with *NPF* knocked down showed more successive matings (6.5 ± 0.5 , Fig. 5D). Males with *Gad1* knocked down showed slightly more successive matings (4.8 ± 0.3), but not significantly different from controls (Fig. 5D). Together, these results reveal crucial roles of GABA and NPF in inhibiting further sex after excessive sexual experiences.

As we showed that knockdown of *NPF* in *fru^M* neurons eliminated the courtship inhibition effect after excessive sexual activity, we tried to identify the specific *NPF* and *fru^M* co-expressing neurons involved in courtship inhibition. Anti-NPF staining in male and female brains revealed three pairs of male-specific *NPF* neurons (Fig. S4A, B). These neurons were also faithfully labeled through genetic intersectional labelling between *fru^{LexA}* and *NPF-GAL4* (Fig. S4C, D). Consistent with our findings, a recent study uncovered the role of these male-specific *NPF* neurons in inhibiting courtship [36].

We further found that, after 5 h of experience with 10 virgin females, the mRNA level of *ChAT* decreased, while those of *Gad1* and *NPF* increased in the brains of wild-type males (Fig. 5E–H), which is consistent with our previous findings in males with activated *fru^M* neurons. We then measured the survival rate of males housed in the 1M+10F environment, and found that males with *ChAT* knocked down that rarely courted survived much longer than control *fru^{GAL4}/+* males, while males with *Gad1* or *NPF* knocked down died slightly quicker (Fig. 5I), probably due to their continuously high level of courtship and mating. Thus, using two independent genetic models, we showed that ACh, GABA, and NPF are key modulators that respond to excessive sexual activity, and prevent continuous sex that may result in male death.

Discussion

In this study, we established a model in which *Drosophila* males perform continuous sexual behaviors until death, mimicking the behavior of semelparous animals during the mating season. We also identified ACh, GABA, and NPF as key feedback modulators in the brain that respond to excessive sexual activity and prevent semelparous mating.

Previous studies imply that mating does not affect lifespan in *Drosophila* [23, 24]. We showed that while single mating (1M+1F) does not affect survival, multiple matings (1M+4F, 1M+7F, and 1M+10F) do affect male survival, at least under lower nutrition conditions, and this is probably due to the energy expenditure incurred during courtship display and mating. In an extreme example, males with activated *fru^M* neurons performed intense courtship behaviors for 6 h and lost $\sim 10\%$ of their body

weight, compared to males that did not perform courtship behaviors. However, whether this effect is specific to sexual behaviors or could also be caused by other kinds of strenuous physical activity still needs further investigation.

A striking phenomenon was that while males with activated *fru^M* neurons at 27°C performed intensive courtship behaviors, they were able to eat, although significantly less, consistent with a previous finding that sexually-aroused males with ~ 23 pairs of male-specific P1 neurons activated have reduced feeding [37]. This phenomenon indicates that sexual and feeding behaviors are not mutually exclusive. Indeed, males with activated *fru^M* neurons at 27°C survived ~ 30 h longer if provided food (median survival time ~ 36 h with food, and 6 h without food).

Males of most species decrease further sexual activity after mating to prevent excessive sex; such a process must evolve feedback signals that respond to mating, or changes in metabolism or immunity, and decrease sexual drive through the nervous system. Indeed, we found a spontaneous negative feedback mechanism used by male flies to protect them from excessive sex. On one hand, the enzyme for the generally excitatory neurotransmitter ACh, *ChAT*, was lower and the enzyme for the inhibitory neurotransmitter GABA, *Gad1*, was higher in males with activated *fru^M* neurons or experienced with 10 virgin females. On the other hand, knockdown of *ChAT* in *fru^M* neurons alleviated, and knockdown of *Gad1* in *fru^M* neurons accelerated death in the above males. These results reveal how the nervous system responds to excessive sexual activity by rebalancing the excitatory and inhibitory signals.

We also found that the neuropeptide NPF as an important modulator that prevents excessive sexual activity. First, *NPF* expression was increased in males with activated *fru^M* neurons or males housed with 10 virgin females, consistent with previous notions that NPF is a reward signal for mating [33, 34]. Second, knockdown of *NPF* partially restored courtship behaviors in males with *fru^M* neurons activated for 4 h. Furthermore, wild-type males with *NPF* knocked down failed to decrease courtship even after 4 successive matings, such that they could mate up to 10 times (the maximum, as there were 10 females in total) in 5 h. Third, knockdown of *NPF* accelerated the deaths caused by *fru^M* neuronal activation or grouping with 10 females. Thus, while *NPF* functions as a reward signal for mating, its cumulative increase after mating experiences inhibits further sex. Recently, Liu and colleagues found that disrupting *NPF* signaling increases sexual activity, and identified subsets of *NPF* and *fru^M* co-expressing male-specific neurons that inhibit courtship [36]. Meanwhile, another recent study by Zhang and colleagues found *NPF* signaling to be courtship-promoting, although they were involved in recurrent circuitry for

sexual satiety [22]. Our results are generally consistent with the former study that NPF functions as a repressor of courtship, at least when it becomes excessive, although these studies used different behavioral protocols. Future study of how NPF possesses dual roles, first as a reward signal, then an inhibitor for further sex, probably through distinct NPF and/or NPFR neurons, would help to interpret these discrepancies.

Acknowledgements We thank the Tsinghua Fly Center and Bloomington Stock Center for the fly stocks. This work was supported by grants from the National Key R&D Program of China (2019YFA0802400), the National Natural Science Foundation of China (31970943, 31622028, and 31700920), and the Jiangsu Innovation and Entrepreneurship Team Program.

Conflict of interest All authors claim that there are no conflicts of interest.

References

- Rodriguez-Manzo G. Glutamatergic transmission is involved in the long lasting sexual inhibition of sexually exhausted male rats. *Pharmacol Biochem Behav* 2015, 131: 64–70.
- Zhang SX, Rogulja D, Crickmore MA. Dopaminergic circuitry underlying mating drive. *Neuron* 2016, 91: 168–181.
- Phoenix CH, Chambers KC. Old age and sexual exhaustion in male rhesus macaques. *Physiol Behav* 1988, 44: 157–163.
- Fisher DO, Dickman CR, Jones ME, Blomberg SP. Sperm competition drives the evolution of suicidal reproduction in mammals. *Proc Natl Acad Sci U S A* 2013, 110: 17910.
- Burtis KC, Baker BS. *Drosophila* doublesex gene controls somatic sexual differentiation by producing alternatively spliced mRNAs encoding related sex-specific polypeptides. *Cell* 1989, 56: 997–1010.
- Ryner LC, Goodwin SF, Castrillon DH, Anand A, Vilella A, Baker BS, *et al.* Control of male sexual behavior and sexual orientation in *Drosophila* by the fruitless gene. *Cell* 1996, 87: 1079–1089.
- Ito H, Fujitani K, Usui K, Shimizu-Nishikawa K, Tanaka S, Yamamoto D. Sexual orientation in *Drosophila* is altered by the satori mutation in the sex-determination gene fruitless that encodes a zinc finger protein with a BTB domain. *Proc Natl Acad Sci U S A* 1996, 93: 9687–9692.
- Demir E, Dickson BJ. Fruitless splicing specifies male courtship behavior in *Drosophila*. *Cell* 2005, 121: 785–794.
- Manoli DS, Foss M, Vilella A, Taylor BJ, Hall JC, Baker BS. Male-specific fruitless specifies the neural substrates of *Drosophila* courtship behaviour. *Nature* 2005, 436: 395–400.
- Stockinger P, Kvitsiani D, Rotkopf S, Tirian L, Dickson BJ. Neural circuitry that governs *Drosophila* male courtship behavior. *Cell* 2005, 121: 795–807.
- Cachero S, Ostrovsky AD, Yu JY, Dickson BJ, Jefferis GS. Sexual dimorphism in the fly brain. *Curr Biol* 2010, 20: 1589–1601.
- Yu JY, Kanai MI, Demir E, Jefferis GS, Dickson BJ. Cellular organization of the neural circuit that drives *Drosophila* courtship behavior. *Curr Biol* 2010, 20: 1602–1614.
- Inagaki HK, Jung Y, Hoopfer ED, Wong AM, Mishra N, Lin JY, *et al.* Optogenetic control of *Drosophila* using a red-shifted channelrhodopsin reveals experience-dependent influences on courtship. *Nat Methods* 2014, 11: 325–332.
- Clowney EJ, Iguchi S, Bussell JJ, Scheer E, Ruta V. Multimodal chemosensory circuits controlling male courtship in *Drosophila*. *Neuron* 2015, 87: 1036–1049.
- Kallman BR, Kim H, Scott K. Excitation and inhibition onto central courtship neurons biases *Drosophila* mate choice. *Elife* 2015, 4: e11188.
- Chen D, Sitaraman D, Chen N, Jin X, Han C, Chen J, *et al.* Genetic and neuronal mechanisms governing the sex-specific interaction between sleep and sexual behaviors in *Drosophila*. *Nat Commun* 2017, 8: 154.
- Pan Y, Meissner GW, Baker BS. Joint control of *Drosophila* male courtship behavior by motion cues and activation of male-specific P1 neurons. *Proc Natl Acad Sci U S A* 2012, 109: 10065–10070.
- Wu S, Guo C, Zhao H, Sun M, Chen J, Han C, *et al.* Drosulfakinin signaling in fruitless circuitry antagonizes P1 neurons to regulate sexual arousal in *Drosophila*. *Nat Commun* 2019, 10: 4770.
- Kimura K, Hachiya T, Koganezawa M, Tazawa T, Yamamoto D. Fruitless and doublesex coordinate to generate male-specific neurons that can initiate courtship. *Neuron* 2008, 59: 759–769.
- Ho MS. A shared neural node for multiple innate behaviors in *Drosophila*. *Neurosci Bull* 2018, 34: 1103–1104.
- Zhang SX, Miner LE, Boutros CL, Rogulja D, Crickmore MA. Motivation, perception, and chance converge to make a binary decision. *Neuron* 2018, 99: 376–388.e376.
- Zhang SX, Rogulja D, Crickmore MA. Recurrent circuitry sustains *Drosophila* courtship drive while priming itself for satiety. *Curr Biol* 2019, 29: 3216–3228.e3219.
- Harvanek ZM, Lyu Y, Gendron CM, Johnson JC, Kondo S, Promislow DEL, *et al.* Perceptive costs of reproduction drive ageing and physiology in male *Drosophila*. *Nat Ecol Evol* 2017, 1: 152.
- Flintham EO, Yoshida T, Smith S, Pavlou HJ, Goodwin SF, Carazo P, *et al.* Interactions between the sexual identity of the nervous system and the social environment mediate lifespan in *Drosophila melanogaster*. *Proc Biol Sci* 2018, 285: 20181450.
- Guo C, Pan Y, Gong Z. Recent advances in the genetic dissection of neural circuits in *Drosophila*. *Neurosci Bull* 2019, 35: 1058–1072.
- Pan Y, Robinett CC, Baker BS. Turning males on: activation of male courtship behavior in *Drosophila melanogaster*. *PLoS One* 2011, 6: e21144.
- Pan Y, Baker BS. Genetic identification and separation of innate and experience-dependent courtship behaviors in *Drosophila*. *Cell* 2014, 156: 236–248.
- Hamada FN, Rosenzweig M, Kang K, Pulver SR, Ghezzi A, Jegla TJ, *et al.* An internal thermal sensor controlling temperature preference in *Drosophila*. *Nature* 2008, 454: 217–220.
- Klapoetke NC, Murata Y, Kim SS, Pulver SR, Birdsey-Benson A, Cho YK, *et al.* Independent optical excitation of distinct neural populations. *Nat Methods* 2014, 11: 338–346.
- Meissner GW, Luo SD, Dias BG, Texada MJ, Baker BS. Sex-specific regulation of Lgr3 in *Drosophila* neurons. *Proc Natl Acad Sci U S A* 2016, 113: E1256–1265.
- Jenett A, Rubin GM, Ngo TT, Shepherd D, Murphy C, Dionne H, *et al.* A GAL4-driver line resource for *Drosophila* neurobiology. *Cell Rep* 2012, 2: 991–1001.
- Ni JQ, Liu LP, Binari R, Hardy R, Shim HS, Cavallaro A, *et al.* A *Drosophila* resource of transgenic RNAi lines for neurogenetics. *Genetics* 2009, 182: 1089–1100.
- Shohat-Ophir G, Kaun KR, Azanchi R, Mohammed H, Heberlein U. Sexual deprivation increases ethanol intake in *Drosophila*. *Science* 2012, 335: 1351–1355.

34. Zer-Krispil S, Zak H, Shao L, Ben-Shaanan S, Tordjman L, Bentzur A, *et al.* Ejaculation induced by the activation of Crz neurons is rewarding to *Drosophila* Males. *Curr Biol* 2018, 28: 1445–1452 e1443.
35. Tayler TD, Pacheco DA, Hergarden AC, Murthy M, Anderson DJ. A neuropeptide circuit that coordinates sperm transfer and copulation duration in *Drosophila*. *Proc Natl Acad Sci U S A* 2012, 109: 20697–20702.
36. Liu WW, Ganguly A, Huang J, Wang YJ, Ni JFD, Gurav AS, *et al.* Neuropeptide F regulates courtship in *Drosophila* through a male-specific neuronal circuit. *Elife* 2019, 8: 29.
37. Zhang W, Guo C, Chen D, Peng Q, Pan Y. Hierarchical control of *Drosophila* sleep, courtship, and feeding behaviors by male-specific P1 neurons. *Neurosci Bull* 2018, 34:1105–1110.



Spinal Cord Stimulation Enhances Microglial Activation in the Spinal Cord of Nerve-Injured Rats

Bin Shu^{1,2} · Shao-Qiu He¹ · Yun Guan^{1,3}

Received: 30 April 2020 / Accepted: 23 July 2020 / Published online: 5 September 2020
© Shanghai Institutes for Biological Sciences, CAS 2020

Abstract Microglia can modulate spinal nociceptive transmission. Yet, their role in spinal cord stimulation (SCS)-induced pain inhibition is unclear. Here, we examined how SCS affects microglial activation in the lumbar cord of rats with chronic constriction injury (CCI) of the sciatic nerve. Male rats received conventional SCS (50 Hz, 80% motor threshold, 180 min, 2 sessions/day) or sham stimulation on days 18–20 post-CCI. SCS transiently attenuated the mechanical hypersensitivity in the ipsilateral hind paw and increased OX-42 immunoreactivity in the bilateral dorsal horns. SCS also upregulated the mRNAs of M1-like markers, but not M2-like markers. Inducible NOS protein expression was increased, but brain-derived neurotrophic factor was decreased after SCS. Intrathecal minocycline (1 µg–100 µg), which inhibits microglial activation, dose-dependently attenuated the mechanical hypersensitivity. Pretreatment with low-dose minocycline (1 µg, 30 min) prolonged the SCS-induced pain inhibition. These findings suggest that conventional SCS may paradoxically increase spinal M1-like microglial activity and thereby compromise its own ability to inhibit pain.

Keywords Spinal cord stimulation · Microglia · Neuropathic pain · Spinal cord · Rat

Introduction

Glial cells, including both macroglia and microglia, account for ~70% of the cells in the central nervous system (CNS) [1]. These cells play important roles in maintaining homeostasis, supporting and protecting neurons, and synthesizing and releasing various neuromodulators that affect neuronal excitability. Microglia, the resident innate immune cells of the CNS, show remarkable morphological and functional plasticity to environmental changes, injuries, and neurologic disorders [2–4]. Both quiescent and activated microglia have been isolated from the CNS by immunomagnetic separation [3]. The isolated microglia retain properties similar to those *in vivo*, and hence are suitable for use in *ex vivo* investigations [2, 3]. The phenotypes of isolated microglia also correlate with two major phenotypic profiles characterized mostly by *in vitro* studies. The classically activated M1-like state is associated with the release of pro-inflammatory cytokines [e.g., tumor necrosis factor (TNF)- α , interleukin (IL)-1 β , and IL-6], which are thought to enhance pain transmission and exacerbate neurological injury [4–6]. The alternative anti-inflammatory M2-like state mediates neuronal repair, neurogenesis, and protection against neurotoxicity and is associated with the release of anti-inflammatory cytokines (e.g., IL-10 and IL-4) [4]. Mounting evidence suggests that activation of microglia and astrocytes in the spinal cord contributes to pain facilitation and exacerbation, such as that experienced after tissue and nerve injury [4, 5, 7, 8].

An important strategy for treating pain when pharmacotherapies fail or cause intolerable side-effects is spinal cord stimulation (SCS) [9]. Conventional SCS, which has

✉ Yun Guan
yguan1@jhmi.edu

¹ Department of Anesthesiology and Critical Care Medicine, School of Medicine, Johns Hopkins University, Baltimore, MD 21205, USA

² Present Address: Department of Anesthesiology, Tongji Hospital, Tongji Medical College, Huazhong University of Science and Technology, Wuhan 430030, China

³ Department of Neurological Surgery, School of Medicine, Johns Hopkins University, Baltimore, MD 21205, USA

been used for over 50 years, activates low-threshold A β -fibers in the dorsal columns and induces pain inhibition through both spinal and supraspinal neuronal mechanisms [10–13]. Although it is useful, conventional SCS is associated with suboptimal clinical efficacy and short-lived pain relief [14]. Until recently, attempts to improve SCS have focused primarily on neuronal effects [11, 13–17]. Intriguingly, a new SCS paradigm with differential target multiplexed programming (DTMP) produced better pain inhibition than conventional SCS, and more effectively modulated glia-related genes and pain-relevant biological processes associated with neuron-glia interactions in nerve-injured rats [18]. Despite the ability of glial cells to initiate signaling cascades that modulate neuronal excitability and pain processing, glial mechanisms have often been overlooked in the study of SCS.

A previous study showed that conventional SCS decreases glial cell reactivity markers in the spinal cord of nerve-injured rats, indicating glial suppression [19]. Yet, recent genome-wide microarray and RNA-sequencing studies have suggested that SCS may increase immune responses and promote glial activation in the spinal cord of neuropathic rats [20–22]. Microarray and RNA-sequencing studies are useful for identifying gene networks that are altered by SCS, but they reveal changes in gene expression only at the transcriptional level. Accordingly, the effects of conventional SCS on activation of spinal glial cells in neuropathic pain are still unknown. By conducting animal behavioral tests, immunocytochemistry, real-time polymerase chain reaction (RT-PCR), and western blot analysis, we endeavored to determine how conventional SCS affects microglial activation and alters the expression of pro-inflammatory (M1-like) and anti-inflammatory (M2-like) phenotypic markers in the lumbar spinal cord after sciatic nerve injury in male rats.

Materials and Methods

All procedures were approved by the Johns Hopkins University Animal Care and Use Committee (Baltimore, MD, USA) as consistent with the National Institutes of Health Guide for the Care and Use of Laboratory Animals to ensure minimal animal use and discomfort. Animals received food and water *ad libitum* and were maintained on a 12-h day–night cycle in isolator cages.

Animals and Surgery

Animals

Adult, male Sprague-Dawley rats (2–3 months old, Harlan Bioproducts for Science, Indianapolis, IN) were

administered SCS and drug treatment for behavioral tests and molecular biological studies.

Chronic Constriction Injury (CCI) of Sciatic Nerve

A neuropathic pain model of CCI was made as described previously [23]. Briefly, animals were anesthetized with 2.0% isoflurane (Abbott Laboratories, North Chicago, IL). The left sciatic nerve was loosely ligated with a 6–0 silk suture. The animals were monitored after surgery for signs of wound infection, inadequate food and water intake, or weight loss until the surgical site had healed.

Behavioral Tests

Mechanical Hypersensitivity Test

Hypersensitivity to punctuate mechanical stimulation was determined with the up-down method by using a series of von Frey filaments (0.38 g, 0.57 g, 1.23 g, 1.83 g, 3.66 g, 5.93 g, 9.13 g, and 13.1 g) [24]. Briefly, the von Frey filaments were applied to the test area between the footpads on the plantar surface of the hind paw for 4 s to 6 s. If a positive response occurred (abrupt paw withdrawal, licking, and shaking), the next smaller von Frey hair was used; if a negative response was observed, the next higher force was used. The test was continued until (1) the responses to five stimuli were assessed after the first crossing of the withdrawal threshold or (2) the upper/lower end of the von Frey hair set was reached before a positive/negative response had been obtained. The paw withdrawal threshold (PWT) was determined according to the formula provided by Dixon [25]. Rats that showed impaired motor function after surgery or that failed to develop mechanical hypersensitivity (mechanical allodynia, >50% reduction from pre-CCI PWT) on the hind paw ipsilateral (left) to the nerve injury by day 5 post-injury were excluded from subsequent study.

SCS in CCI Rats

One week after CCI, a custom-made quadripolar electrode (contact diameter, 0.9 mm–1.0 mm; center spacing, 2.0 mm; Medtronic Inc., Minneapolis, MN) that provided bipolar SCS (“twin-pairs” stimulation) was placed epidurally through a small laminectomy at the T13 vertebra (Fig. 1A), as described in our previous studies [16, 21]. The sterilized lead was placed at the T10–12 levels, which correspond to the T13–L1 spinal cord region. A subcutaneous tunnel was used to position the proximal end of the electrode in the upper thoracic region, where it exited the skin and connected to an external stimulator (Model 2100, A-M Systems, Sequim, WA). Animals were allowed to

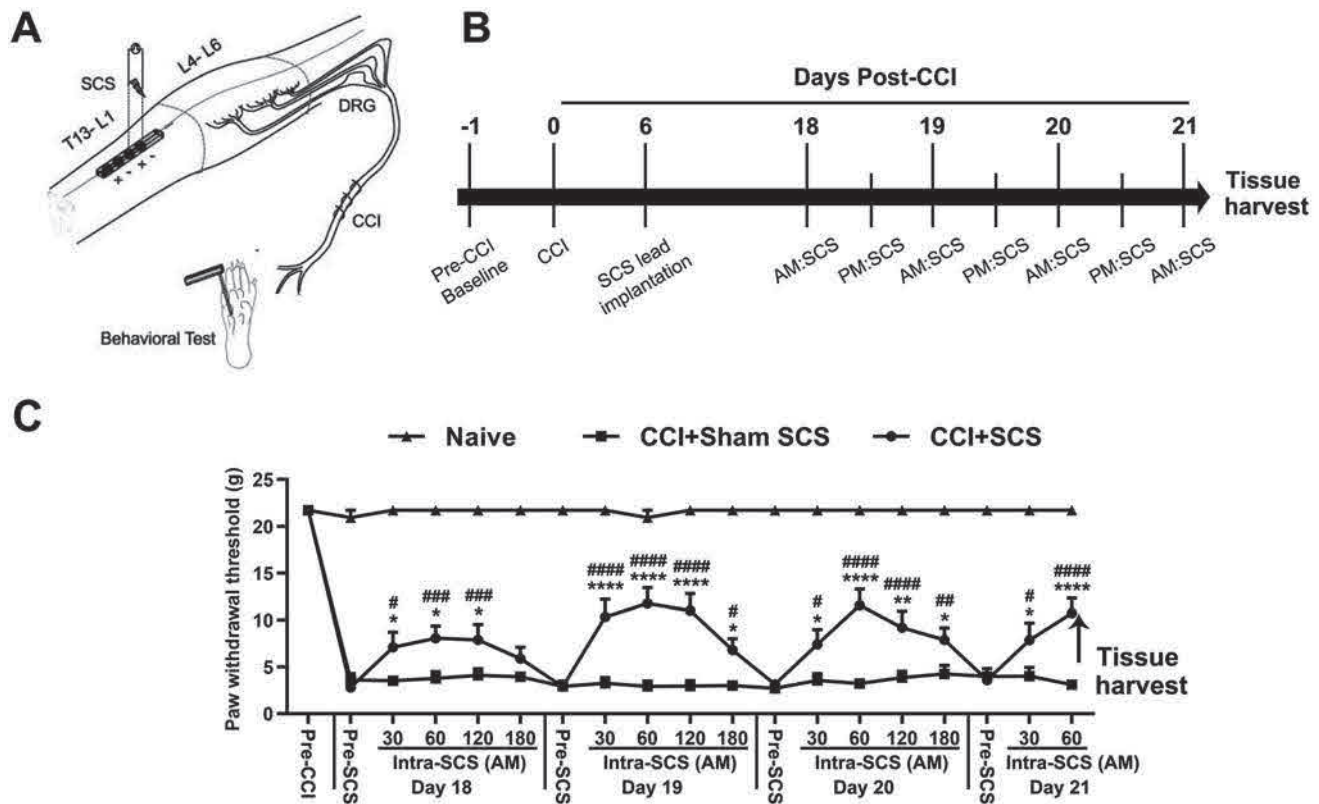


Fig. 1 Repeated SCS induces short-term inhibition of mechanical hypersensitivity in CCI rats. **A** Schematic illustrating the experimental setup for repeated SCS in rats with CCI of the left sciatic nerve. Lumbar spinal cord tissue (L4–L6, marked with dotted lines) ipsilateral to the side of nerve injury was harvested after the last SCS treatment on day 21 post-injury. **B** Experimental timeline. CCI rats received repeated SCS (50 Hz, 0.2 ms, biphasic, 80% motor threshold, 180 min/session, $n = 15$) or sham stimulation ($n = 10$) from

days 18 to 21 post-injury. Naïve rats ($n = 8$) received no treatment. **C** Paw withdrawal thresholds were measured before injury (Pre-CCI), before stimulation (Pre-SCS), and during the morning (AM) session of SCS (Intra-SCS) on days 18 to 21 post-injury. Data are shown as the mean \pm SEM. Two-way mixed model ANOVA, with Bonferroni *post hoc* test. * $P < 0.05$, ** $P < 0.01$, **** $P < 0.0001$ versus CCI+Sham SCS; # $P < 0.05$, ## $P < 0.01$, ### $P < 0.001$, #### $P < 0.0001$ vs Pre-SCS of the same day.

recover from surgery for >1 week. SCS and mechanical pain hypersensitivity were examined at 7 days–14 days after lead implantation (Fig. 1B).

CCI rats were randomized to receive SCS ($n = 15$) or sham stimulation ($n = 10$). On each test day, rats were acclimated for 30 min before we measured the pre-SCS PWT. Motor threshold (MoT), which ranged from 0.1 mA to 0.5 mA, was determined first by slowly increasing the amplitude of 4 Hz electrical stimulation from zero until muscle contraction was observed in mid-lower trunk or hind limbs. On days 18, 19, and 20 post-CCI, rats received SCS (50 Hz, 0.2 ms, biphasic, constant current, 80% MoT, 180 min) or sham stimulation (0 mA) in two sessions per day, and on day 21, they received one session in the morning. We measured PWT before applying SCS and at 30 min, 60 min, 120 min, and 180 min during SCS (intra-SCS) on days 18 to 20 in the morning session, and at 30 min and 60 min during SCS on day 21 (Fig. 1B). We used 80% MoT because it represents the maximum intensity of SCS that can be applied without causing discomfort in

awake animals and has been used in previous studies [16, 20, 26]. Naïve rats ($n = 8$) received neither CCI nor SCS treatment and were handled and tested in parallel with other groups of rats.

Immunocytochemistry

Rats were deeply anesthetized with isoflurane (2%–3%) at 1–2 h after the last SCS treatment and perfused intracardially with 0.1 mol/L phosphate-buffered saline (PBS; pH 7.4, 4°C) followed by fixative (4% formaldehyde and 14% [v/v] saturated picric acid in PBS, 4°C). Lumbar (L4–L6) spinal cord tissue was cryoprotected in 20% sucrose for 24 h before being serially cut into 15- μ m sections and placed on slides. The slides were incubated overnight at 4°C in the primary antibodies mouse antibody to glial fibrillary acidic protein (GFAP; MAB-360, 1:500, Millipore, Temecula, CA) and mouse OX-42 antibody (CBL-1512, 1:500, Millipore). Slides were incubated in secondary antibody at room temperature for 45 min. The secondary antibody,

donkey antibody to mouse (715-095-151, FITC-conjugated, Jackson ImmunoResearch, West Grove, PA), was diluted 1:100 in PBS. Tissues from different experimental groups were processed and analyzed simultaneously. The images of immunostained tissue were analyzed with ImageJ 1.46a (NIH, Bethesda, MD). Areas that contained positive immunoreactivity are expressed as percentage of total dorsal horn on each side.

Real-Time PCR

The dorsal aspect of the lumbar (L4–L6) spinal cord was collected from naïve and CCI rats at 1 h–2 h after the last SCS. Tissues ipsilateral and contralateral to the nerve injury were then separated. Half of the tissue on each side was used for RT-PCR, and the other half was processed for western blot analysis. RNA and protein were isolated using TRIzol reagent (Invitrogen, Carlsbad, CA) according to the manufacturer's protocols. After measuring the concentration of RNA on a Nanodrop 2000c (Thermo Fisher, Waltham, MA), we prepared cDNA from 1 µg of total RNA using an oligo(dT) primer and reverse transcriptase (SuperScript III First-Strand Synthesis SuperMix for qRT-PCR, 11752-050, Invitrogen, CA) according to the kit instructions. PowerUp SYBR Green Master Mix (A25741, Applied Biosystems, Waltham, MA) was used to perform real-time PCR on the StepOnePlus Real-Time PCR system (Applied Biosystems). Each PCR mixture contained 500 nmol/L forward and reverse primers, 5 µL of PowerUp SYBR Green Master Mix (2X), 1 µL of cDNA, and 2 µL of nuclease-free water for a total volume of 10 µL. PCR was carried out with the following steps: uracil-DNA glycosylase activation at 50°C for 2 min, Dual-Lock DNA polymerase at 95°C for 2 min, denature at 95°C for 15 s, anneal at 55°C–60°C for 15 s, and extend at 72°C for 1 min. All PCRs were performed in triplicate; β-actin was used as an endogenous control and to normalize the mRNA expression data. Relative expression was calculated by the $2^{-\Delta\Delta C_t}$ method. Primer sequences are listed in Table 1.

Western Blot Analysis

Protein was isolated using a TRIzol reagent kit and concentration determined by the bicinchoninic acid method (Thermo Fisher). After protein concentrations were equalized with 1% sodium dodecyl sulfate (SDS), 4X Bolt lithium dodecyl sulfate sample buffer (Thermo Fisher) and 10X Bolt sample reducing agent (Thermo Fisher) were added to the samples in a ratio of 1 to 1. Finally, the samples were heated at 70°C for 10 min and separated by electrophoresis on 4%–12% Bis-Tris Plus SDS-polyacrylamide gels at a constant voltage for ~35 min in Bolt 2-(N-morpholino) ethanesulfonic acid SDS running buffer.

Protein was transferred to a polyvinylidene difluoride membrane (Bio-Rad, Berkeley, CA) and blocked in a solution of tris-buffered saline and 0.1% Tween 20 containing 5% nonfat dry milk (Bio-Rad). Membranes were incubated with mouse anti-inducible nitric oxide synthase (iNOS) antibody (1:1000, BD Biosciences, San Jose, CA), rabbit anti-TNF-α antibody (1:1000, Abcam, Cambridge, UK), goat anti-arginase 1 (Arg1) antibody (1:1000, Santa Cruz Biotechnology, Dallas, TX), rabbit anti-IL10 antibody (1:1000, Abcam), rabbit anti-phosphorylated extracellular signal-regulated kinase (p-ERK1/2) antibody (1:2000, Cell Signaling Technology, Danvers, MA), rabbit anti-c-Fos antibody (1:1000, Abcam), rabbit anti-protein kinase C (PKC)-γ antibody (1:1000, Santa Cruz Biotechnology), rabbit anti-brain derived neurotrophic factor (BDNF) antibody (1:800, Santa Cruz Biotechnology), rabbit anti-phosphorylated glutamate receptor (p-GluR) subunit 1 at serine 831 residue (p-GluR1^{ser831}) antibody (1:1000, Millipore), rabbit anti-phosphorylated N-methyl-D-aspartate (NMDA) receptor 1 (p-NR1) antibody (1:1000, Millipore), or rabbit anti-glyceraldehyde 3-phosphate dehydrogenase antibody (1:100,000, Millipore). Peroxidase-conjugated goat anti-mouse IgG, goat anti-rabbit IgG, and donkey anti-goat IgG (1:10,000, Jackson ImmunoResearch, West Grove, PA) were used as secondary antibodies. Membranes were incubated in enhanced chemiluminescence (Bio-Rad) and imaged by ImageQuant LAS 4000 (GE Healthcare Life Sciences). Protein band densities were analyzed with ImageJ 1.46a software.

Drugs and Intrathecal Injections

Minocycline from Tocris Bioscience (Bristol, UK) was dissolved in water to 25 mmol/L, separated into aliquots, and stored in tightly-sealed vials at –20°C. This stock solution was freshly diluted to the desired dosage with vehicle (saline) before use. Rats were briefly anesthetized in 2.0% isoflurane before being infused intrathecally with drug or vehicle *via* lumbar puncture [27]. CCI rats were randomized to receive a 15 µL intrathecal injection of vehicle ($n = 7$) or minocycline (1 µg, $n = 9$; 10 µg, $n = 10$; or 100 µg, $n = 9$) at day 18 post-CCI. PWT was tested 1 day before CCI, before intrathecal injection (pre-IT), and 30 min, 60 min, 120 min, 150 min, 180 min, and 240 min after injection (post-IT).

Data Analysis

To determine the PWT in animal behavior studies, we converted the pattern of positive and negative von Frey filament responses to a 50% threshold value using the formula provided by Dixon [25]. The PWT was compared

Table 1 Primers used for RT-PCR.

Gene	Forward primer (5'-3')	Reverse primer (5'-3')
Astrocyte marker		
GFAP	TCCTGGAACAGCAAAACAAG	CAGCCTCAGGTTGGTTCAT
Microglial marker		
OX42	CAGATCAACAATGTGACCGTATGGG	CATCATGTCCTTGTACTGCCGCTTG
M1 markers		
iNOS	CCCTTCAATGGTTGGTACATGG	ACATTGATCTCCGTGACAGCC
CD16	GCTTTCTACCGTGGCATCA	TCCAGTGAAGTTTGGGTTCC
CD32	TGAAGAAGGGGAAAACCATCA	GGCTTTGGGGATTGAAAAAT
M2 markers		
Arg1	TTAGCCAAGGTGCTTGCTGCC	TACCATGGCCCTGAGGAGGTTCC
CD163	TGGGCAAGAACAGAATGGTT	CCTGAGTGACAGCAGAGACG
TGF- β	GACCTGCTGGCAATAGCTTC	GACTGGCGAGCCTTAGTTTG
Pro-inflammatory cytokines		
TNF- α	TGAGCACTGAAAGCATGATCC	GGAGAAGAGGCTGAGGAACA
IL-1 β	CAGGAAGGCAGTGTCACTCA	AAAGAAGGTGCTTGGGTCTCT
Anti-inflammatory cytokines		
IL-4	CAGGGTGCTTCGCAAATTTTAC	CACCGAGAACCCCACTTGG
IL-10	TAAGGGTTACTTGGGTTGC	TATCCAGAGGGTCTTTCAGC
Control		
β -Actin	AGAAGGACTCCTATGTGGGTGA	CATGAGCTGGGTCATCTTTTCA

between the pre- and post-SCS conditions and between groups by using a two-way mixed model analysis of variance (ANOVA). In each study, we blinded the experimenter to the treatments (e.g., drug) to reduce selection and observation bias. Western blot and immunocytochemistry data were analyzed as described previously [28, 29]. The ipsilateral and contralateral spinal cord were analyzed separately, and results from different groups were compared. Statistica 6.0 software (StatSoft, Inc., Tulsa, OK) was used to conduct all statistical analyses. The Tukey honestly significant difference *post hoc* test was used to compare specific data points. Bonferroni correction was applied for multiple comparisons. Two-tailed tests were performed and numerical data expressed as the mean + SEM; $P < 0.05$ was considered statistically significant in all tests.

Results

SCS Induces Inhibition of Mechanical Hypersensitivity in CCI Rats

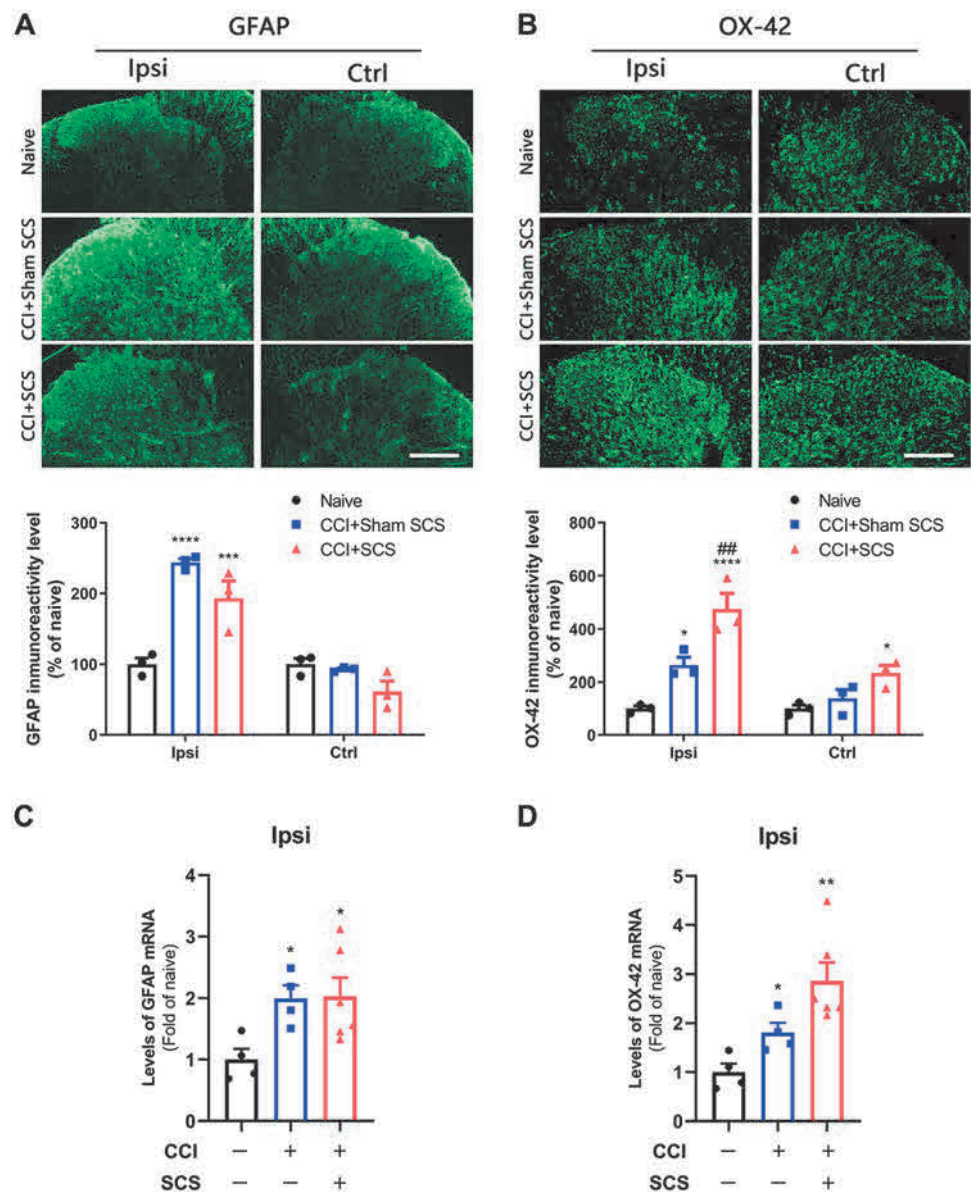
The PWT of the ipsilateral hind paw was significantly decreased from the pre-injury level in CCI rats before SCS treatment on day 18 post-CCI (Fig. 1C; $F = 201.1$, group; $F = 18.84$, time; $F = 6.66$, group–time interaction). SCS ($n = 15$) increased the ipsilateral PWTs of CCI rats from

the pre-SCS level on each of the treatment days. The pain-inhibiting effect started by 30 min intra-SCS and peaked ~60 min intra-SCS. Sham SCS ($n = 10$) did not significantly alter the PWT in CCI rats.

SCS Enhances Microglial Activation in the Spinal Cord of CCI Rats

Sham-stimulated CCI rats exhibited significantly greater immunoreactivity for both GFAP (an astrocyte-reactive marker) and OX-42 (a microglia-reactive marker) than did naïve rats (Fig. 2A, B). Repeated SCS treatment induced a downward trend in the GFAP immunoreactivity of CCI rats that was not seen in sham-stimulated rats ($P = 0.38$). GFAP immunoreactivity on the contralateral side was not significantly altered by CCI or SCS (Fig. 2A). In contrast, SCS produced a significant increase in OX-42 immunoreactivity in both the ipsilateral and contralateral dorsal horn of CCI rats, when compared to that in sham-stimulated rats (Fig. 2B). RT-PCR revealed that the levels of GFAP and OX-42 mRNA in the ipsilateral lumbar cord were approximately two-fold higher in sham-stimulated CCI rats than in naïve rats (Fig. 2C, D). CCI rats that received SCS showed a trend toward an additional increases in OX-42 mRNA ($P = 0.06$) but no change in GFAP mRNA (Fig. 2A: $F = 22.29$, ipsilateral; $F = 4.203$, control; Fig. 2B, $F = 23.10$, ipsilateral; $F = 6.64$, control; Fig. 2C: $F = 4.37$; Fig. 2D; $F = 9.52$).

Fig. 2 Changes in the immunoreactivity and mRNA levels of GFAP and OX-42 in the spinal cord after CCI and SCS. **A** Upper: representative images of GFAP staining in the dorsal horn ipsilateral (Ipsi) and contralateral (Ctrl) to the nerve injury. Lower: quantification of GFAP immunoreactivity in each group. **B** Upper: representative images of OX-42 staining. Lower: quantification of OX-42 immunoreactivity. Scale bars, 100 μ m. **C, D** Levels of GFAP mRNA (**C**) and OX-42 mRNA (**D**) in the ipsilateral cord of the different groups. $n = 3-6$ rats/group. Data are shown as the mean \pm SEM. * $P < 0.05$, ** $P < 0.01$, *** $P < 0.001$, **** $P < 0.0001$ vs naïve; ## $P < 0.01$ vs CCI + Sham SCS; one-way ANOVA, with Bonferroni *post hoc* test.



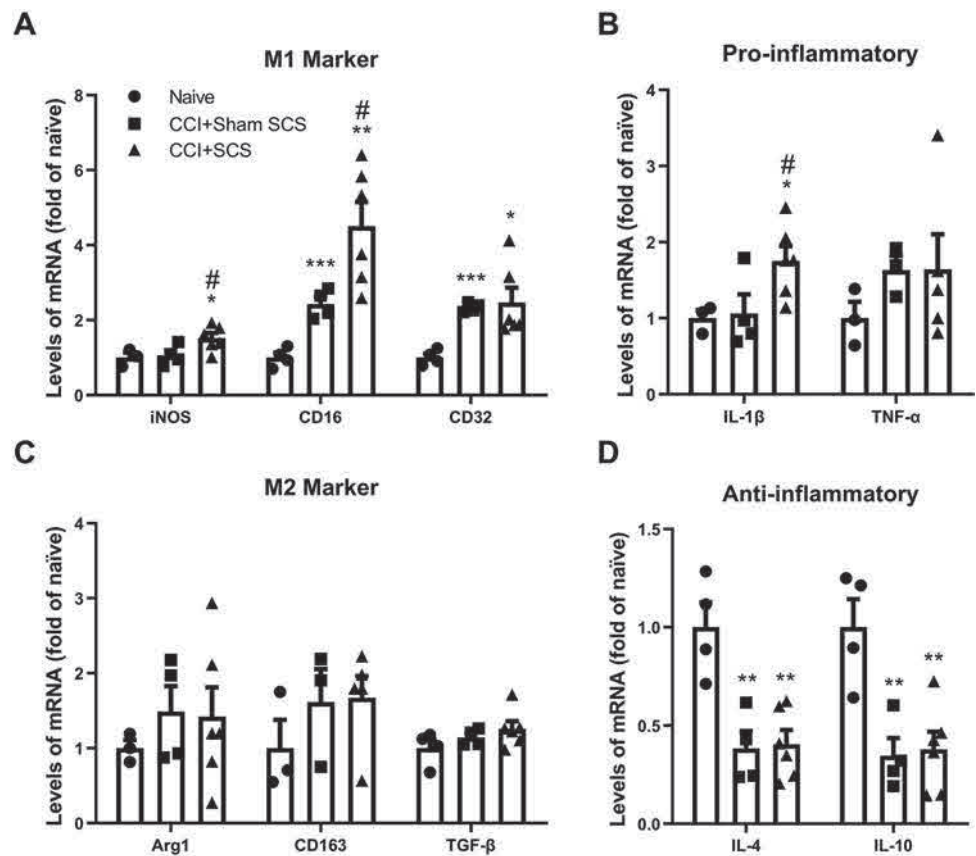
SCS Changes Microglial Phenotypic Markers and Cytokine Levels in the Spinal Cord of CCI Rats

RT-PCR of the ipsilateral dorsal horn showed that the mRNA levels of CD16 and CD32 (M1-like markers) were significantly higher in sham-stimulated CCI rats than in naïve rats (Fig. 3A). In addition, SCS significantly increased the mRNA levels of both CD16 and iNOS mRNA in CCI rats. The mRNA levels of the pro-inflammatory cytokines IL-1 β and TNF- α were similar in sham-stimulated CCI rats and naïve rats. However, the IL-1 β mRNA level was significantly increased in CCI rats after SCS (Fig. 3B). The mRNA levels of the M2-like markers Arg1, CD163, and TGF- β were not significantly changed by CCI or SCS (Fig. 3C). However, the mRNA levels of the anti-inflammatory cytokines

IL-4 and IL-10 were significantly lower in sham-stimulated CCI rats than in naïve rats. SCS did not significantly alter the IL-4 or IL-10 mRNA levels in CCI rats from those in sham-stimulated CCI rats (Fig. 3D; $F = 4.39$, iNOS; $F = 13.34$, CD16; $F = 6.625$, CD32; $F = 4.36$, IL-1 β ; $F = 0.74$, TNF- α ; $F = 0.39$, Arg1; $F = 1.01$, CD163; $F = 1.81$, TGF- β ; $F = 12.99$, IL-4; $F = 10.92$, IL-10).

Western blot analysis showed that the protein levels of iNOS, TNF- α , Arg1, and IL-10 did not differ significantly between sham-stimulated CCI and naïve rats. Repeated SCS in CCI rats upregulated iNOS expression (Fig. 4A), but did not change TNF- α , Arg1, or IL-10 expression (Fig. 4B–D), as compared to that in sham-stimulated rats ($F = 4.49$, iNOS; $F = 1.27$, TNF- α ; $F = 2.06$, Arg1; $F = 0.024$, IL-10).

Fig. 3 Changes in the mRNA levels of M1-like and M2-like microglia markers and related cytokines in the ipsilateral spinal cord after CCI and SCS. **A** Levels of iNOS, CD16, and CD32 mRNA. **B** Levels of IL-1 β and TNF- α mRNA. **C** Levels of Arg1, CD163, and TGF- β mRNA. **D** Levels of IL-4 and IL-10 mRNA. $n = 3$ –6 rats/group. Data are shown as the mean \pm SEM. * $P < 0.05$, ** $P < 0.01$, *** $P < 0.001$ vs naïve; # $P < 0.05$ vs CCI + Sham SCS; one-way ANOVA, with Bonferroni *post hoc* test.



Effects of SCS on the Expression of Pro-nociceptive Molecules in the Spinal Cord of CCI Rats

Phosphorylated (p-) forms of NR1 (p-NR1), GluR1 (p-GluR1^{ser831}), and extracellular signal-regulated kinase (p-ERK1/2) are neurochemical markers for central sensitization [30–32]. Thus, in addition to the M1-like markers associated with microglial polarization, we examined the protein levels of these pro-nociceptive molecules in the spinal cord. Western blot analysis showed that the p-ERK1/2 levels were significantly higher in the ipsilateral cord of sham-stimulated CCI rats than in that of naïve rats (Fig. 5A). However, the protein levels of c-Fos, BDNF, PKC- γ , p-NR1, and p-GluR1^{ser831} did not differ significantly between the two groups (Fig. 5B–F). Compared to sham stimulation, SCS significantly decreased the BDNF levels in CCI rats (Fig. 5C; $F = 12.31$, p-ERK1/2; $F = 0.61$, c-Fos; $F = 4.55$, BDNF; $F = 0.37$, PKC- γ ; $F = 0.39$, p-NR1; $F = 3.45$, p-GluR1).

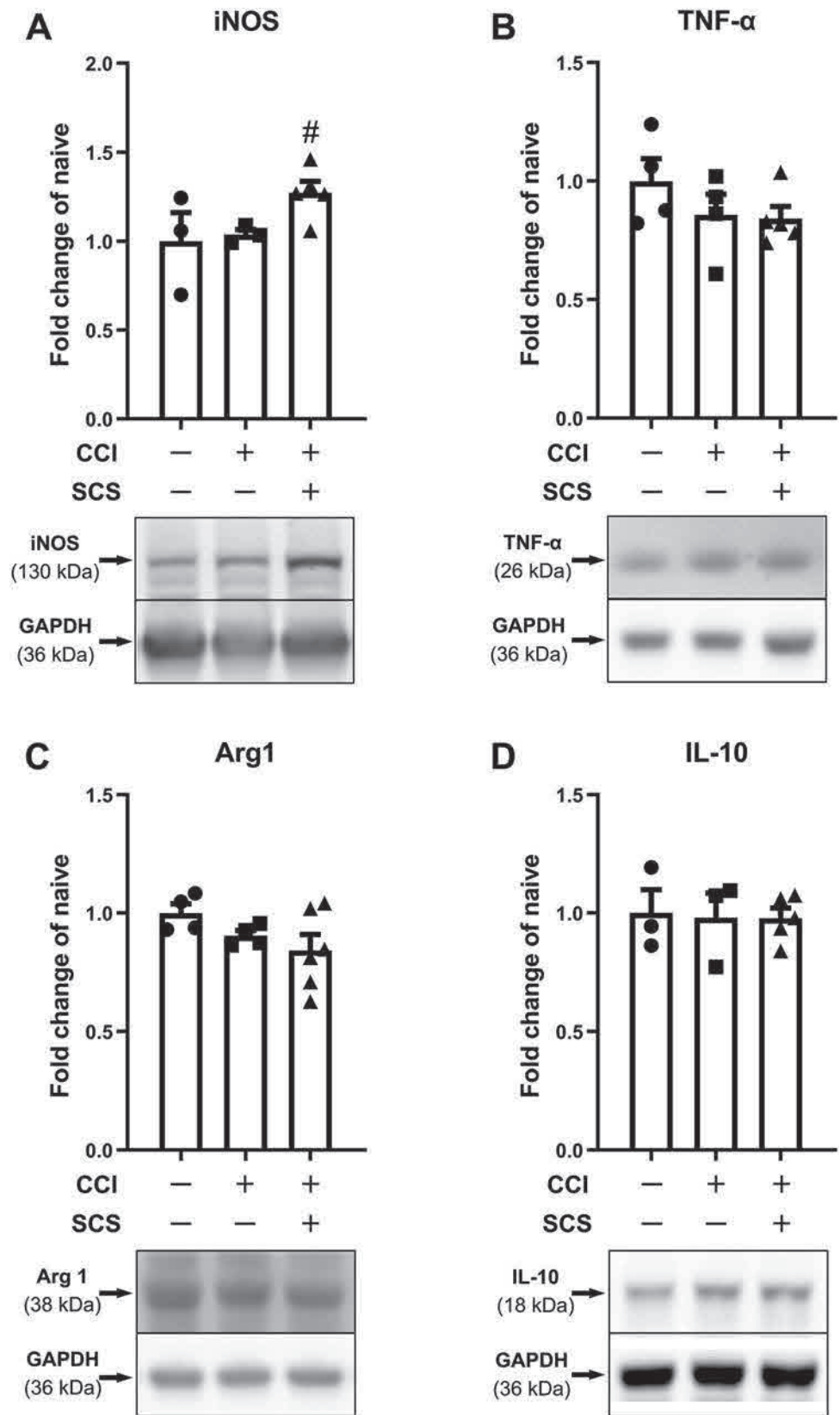
Intrathecal Injection of Minocycline Prolongs Pain Inhibition by SCS

Lastly, we determined whether inhibiting microglial activation in the spinal cord affects pain inhibition by SCS in CCI rats. Intrathecal administration of minocycline, a

microglial inhibitor, dose-dependently attenuated mechanical hypersensitivity in the ipsilateral hind paw of CCI rats (Fig. 6A; $F = 5.79$, group; $F = 228.7$, time; $F = 4.20$, group–time interaction). Based on previous studies [6, 33], we tested three minocycline doses (1 μ g, 10 μ g, 100 μ g/15 μ L). At the highest dose, the ipsilateral PWT was significantly increased from pre-drug baseline from 30 min–150 min post-drug; lower doses were not effective.

Based on these findings, we tested the combination of low-dose minocycline (1 μ g, i.t.) and SCS. Rats underwent CCI surgery and SCS electrode implantation on the same day and were randomized to receive SCS+minocycline ($n = 15$), SCS+vehicle ($n = 15$), or sham stimulation ($n = 7$) on day 18 post-CCI. SCS (50 Hz, 0.2 ms, biphasic, constant current, 80% MoT, 120 min) was delivered at 30 min after pretreatment with drug or vehicle. PWT was measured 1 day before CCI, before SCS and intrathecal injection (pre-SCS), during SCS (intra-SCS, 30 min, 60 min, and 120 min), and after SCS (30 min, 60 min, and 120 min). SCS increased the ipsilateral PWTs from pre-SCS levels in CCI rats that received either vehicle or minocycline, with a peak effect at \sim 60 min–120 min intra-SCS in both groups. The pain-inhibiting effect diminished quickly after SCS cessation in the vehicle-pretreated group. Notably, pretreatment with 1 μ g minocycline prolonged the SCS-induced pain inhibition, as

Fig. 4 Changes in the levels of M1-like and M2-like microglial markers and related cytokines in the ipsilateral spinal cord after CCI and SCS. Quantification (upper) and representative immunoblots (lower) of (A) iNOS, (B) TNF- α , (C) Arg1, and (D) IL-10 in different groups. $n = 3-6$ rats/group. Data are shown as the mean \pm SEM. # $P < 0.05$ vs CCI + Sham SCS; one-way ANOVA, with Bonferroni *post hoc* test.



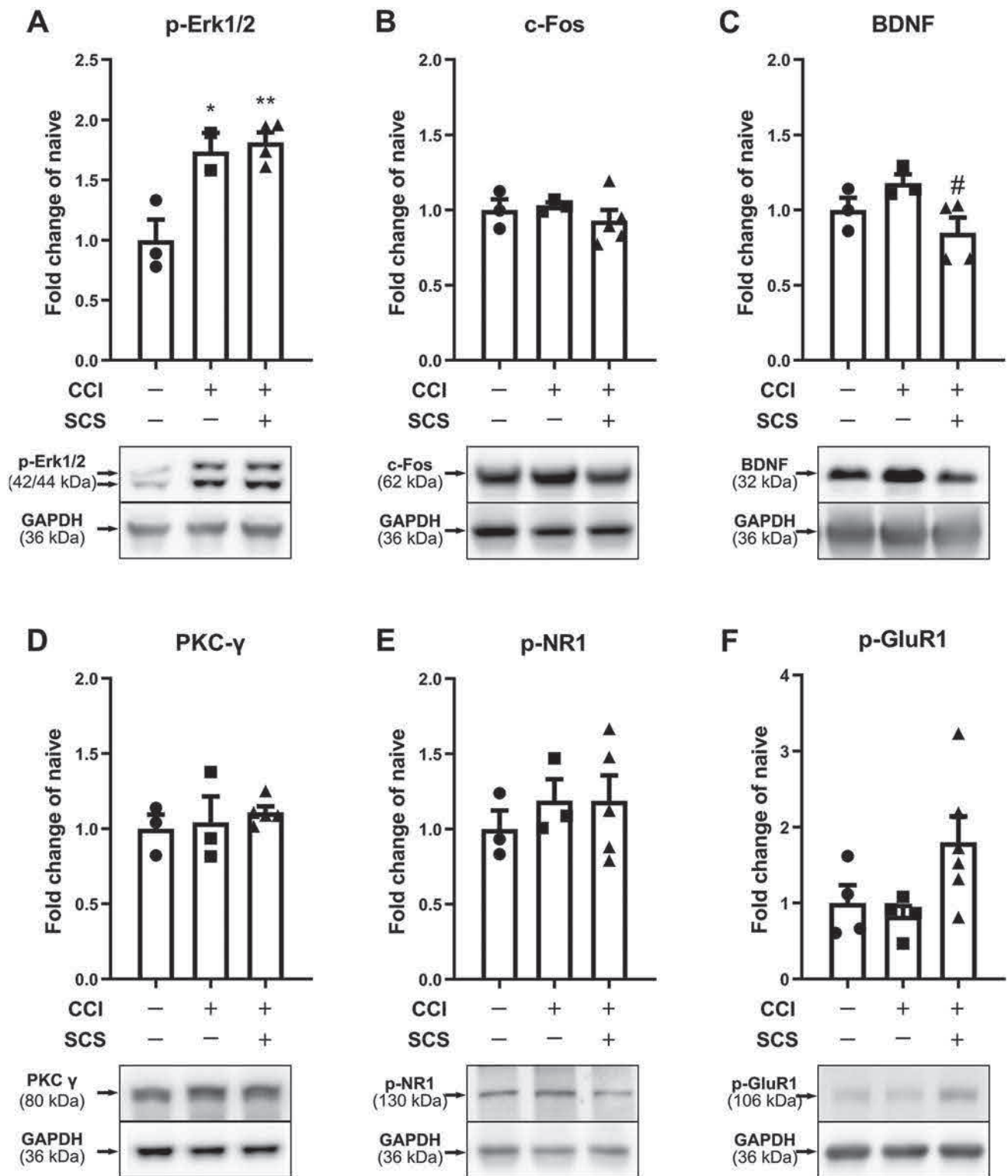


Fig. 5 Changes in the protein levels of pro-nociceptive factors in the ipsilateral spinal cord after CCI and SCS. Quantification (upper) and representative immunoblots (lower) of (A) p-ERK1/2, (B) c-fos, (C) BDNF, (D) PKC- γ , (E) p-NR1, and (F) p-GluR1^{ser831} in different

groups. $n = 3-6$ rats/group. Data are shown as the mean \pm SEM. * $P < 0.05$, ** $P < 0.01$ vs naive; # $P < 0.05$ vs CCI + Sham SCS; one-way ANOVA, with Bonferroni *post hoc* test.

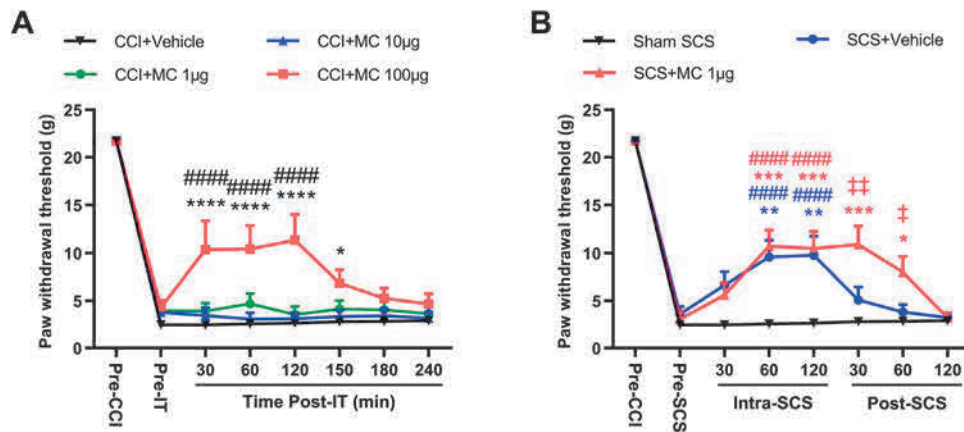


Fig. 6 Intrathecal administration of low-dose minocycline (MC) prolongs the pain inhibition induced by SCS in CCI rats. **A** Ipsilateral paw withdrawal thresholds (PWTs) of CCI rats after intrathecal injection of vehicle ($n = 7$) or minocycline (1 μg , 10 μg , or 100 μg , 15 μL , $n = 9$ or 10/dose). PWT was measured one day before CCI (Pre-CCI), before intrathecal injection (Pre-IT), and at 30 min, 60 min, 120 min, 150 min, 180 min, and 240 min post-injection (Post-IT) on day 18 post-CCI. Data are shown as the mean \pm SEM. * $P < 0.05$, **** $P < 0.0001$ vs CCI + Vehicle; ##### $P < 0.0001$ vs Pre-IT; two-way mixed model ANOVA, with Bonferroni *post hoc* test. **B** PWTs

after sham SCS ($n = 7$) or SCS in CCI rats pretreated (30 min) with an intrathecal injection of low-dose minocycline (1 μg , 15 μL , $n = 16$) or vehicle ($n = 15$). PWT was measured one day before CCI (Pre-CCI), before SCS and intrathecal injection (Pre-SCS), during SCS (Intra-SCS; 30 min, 60 min, and 120 min) and after SCS (Post-SCS; 30 min, 60 min, and 120 min) on day 18 post-CCI. Data are shown as the mean \pm SEM. * $P < 0.05$, ** $P < 0.01$, *** $P < 0.001$ vs Sham SCS; ##### $P < 0.0001$ vs Pre-SCS; † $P < 0.05$, †† $P < 0.01$ vs SCS + Vehicle; two-way mixed model ANOVA, with Bonferroni *post hoc* test.

compared to that with vehicle pretreatment (Fig. 6B; $F = 3.73$, group; $F = 101.4$, time; $F = 4.11$, group–time interaction).

Discussion

Both microglia and astrocytes in the spinal cord are thought to play an important role in neuropathic pain conditions [34, 35]. We found that at 3 weeks after rats underwent sciatic CCI, the ipsilateral lumbar spinal cord exhibited higher levels of OX-42 and GFAP immunoreactivity and mRNA than those of naïve rats, suggesting that both microglia and astrocytes remain activated at this maintenance phase of neuropathic pain. Repeated SCS did not significantly alter GFAP immunoreactivity or mRNA levels in the ipsilateral lumbar spinal cord of CCI rats. However, it further increased the immunoreactivity of OX-42, a marker of reactive microglia, in the bilateral dorsal horns of CCI rats. SCS also produced a trend toward increased OX-42 mRNA in the ipsilateral spinal cord. Thus, conventional SCS did not suppress the heightened astrocyte and microglial activation, but may have exacerbated microglial activation in the lumbar cord of CCI rats during the maintenance phase of neuropathic pain. This finding is in line with previous findings that continuous conventional SCS (72 h) in uninjured rats increases the GFAP and ITGAM (OX-42) genes in the lumbar cord, as

compared to sham stimulation, suggesting elevated glia-related mRNA in the spinal cord [36]. However, another study showed that 4 consecutive days of SCS attenuated glial activation in a spared nerve injury model of neuropathic pain, as indicated by decreased GFAP, MCP-1, and OX-42 immunoreactivity in the dorsal horn [19]. The reason for this discrepancy is unclear but may be due in part to differences in the animal models, post-injury time points, and SCS protocols between these studies.

How SCS increases OX-42 expression remains unclear. It is possible that conventional SCS may induce the release of ATP from neurons into the spinal cord, which would activate P2X7 and P2X4 receptors on microglial cells [37, 38]. Importantly, our RT-PCR study also showed that the SCS-induced increase in microglial activation was associated with differential changes in M1-like and M2-like phenotypic markers. Specifically, the mRNA levels of M1-like markers, such as iNOS and CD16, were significantly increased in CCI rats that received SCS, as compared to the levels in sham-stimulated rats. The increase in iNOS mRNA was also associated with increased protein expression. However, SCS did not alter the mRNA of some M2-like markers, such as Arg1, CD163, and TGF- β . In line with these findings, the mRNA levels of the pro-inflammatory cytokine IL-1 β was also increased in CCI rats after SCS, whereas the mRNA levels of the anti-inflammatory cytokines IL-4 and IL-10, which decreased after CCI, were not changed by SCS. These

findings suggest that SCS may promote the pro-inflammatory M1-like phenotype of microglia in the spinal cord after nerve injury. This notion supports findings in a recent RNA-sequencing study, which showed that repetitive SCS further increases the mRNA levels of many immune-related genes, including genes encoding markers for astrocytes (*Gfap* and *Ccl2*) and activated microglia (*Cd68* and *Itgam*) in the lumbar spinal cord of CCI rats [21].

Pro-inflammatory cytokines such as IL-1 β and TNF- α released from microglia can increase neural activity and activate neighboring glial cells. In addition, activated microglia may function to clear various neurotransmitters, including the pain-inhibitory gamma-aminobutyric acid (GABA) that is released during SCS [39, 40]. Hence, increased activation of M1-like microglia may compromise the pain-inhibiting actions of SCS. Nevertheless, the expression of c-Fos, PKC- γ , p-NR1, and p-GluR1^{ser831}, which are common markers of neuronal activation and sensitization, were not increased in CCI rats after SCS. In fact, SCS decreased the protein level of BDNF, which contributes to central sensitization by converting GABAergic inhibitory cells to excitation *via* TrkB-KCC2 [38] and by potentiating glutamatergic excitation *via* NMDA receptors. Thus, a decrease in BDNF expression may contribute to SCS-induced pain inhibition. Taken together, these findings suggest that conventional SCS induces a mixture of neurochemical changes in the spinal cord that involve immune and glial reactions.

Although microglia can be categorized into classically activated (M1-like) and alternatively activated (M2-like) states [41], *in vivo* these states may occur on a spectrum of functionality [41] that is context-dependent under different pathological conditions [42, 43]. Mounting evidence indicates that the net effect of microglial activation in the spinal cord contributes to neuropathic pain [44]. Minocycline is a tetracycline antibiotic that preferentially inhibits the proinflammatory actions of activated microglia, as neurons and astrocytes are more resistant to its metabolic effects. Minocycline has also been shown to inhibit chemotherapy-induced peripheral neuropathy and bone cancer pain by inhibiting the nuclear factor- κ B signaling pathway in astrocytes [45]. Besides inhibition of glial activation or function, minocycline can also alter spinal endocannabinoids [46], reduce the impairment of glial glutamate uptake [47], inhibit phosphorylation of neuronal ERK1/2 [48], and promote microglial M1-like to M2-like gene expression [33]. Indeed, intrathecal injection of minocycline dose-dependently inhibited the mechanical hypersensitivity in CCI rats. This finding supports previous observations [6, 49] and suggests that the net outcome of microglial activation may be pain facilitation at 3 weeks post-CCI. SCS increased the mechanical PWT in CCI rats from the pre-SCS level, but this effect was short-lived.

Importantly, pretreating rats with an intrathecal injection of a sub-effective minocycline dose prolonged the pain inhibition by SCS.

Clinically, pain relief by conventional, low-frequency (40 Hz–60 Hz) SCS often requires a high amplitude that elicits paresthesia (i.e., above the sensory threshold) in patients [11, 14]. Animal studies have also shown that decreasing the stimulation intensity to 20%–40% MoT markedly reduces the pain-inhibiting effect of conventional SCS [15–17]. The mode of action for conventional SCS involves feed-forward inhibition of dorsal horn neurons [10, 11, 16, 17]. Yet, whether it also depends on proper modulation or normalization of glial dysfunction and altered neuron-glia interactions is unclear. Collectively, the current findings suggest that SCS increases M1-like microglial activation in the spinal cord, which may counteract its pain inhibitory action. Recently, DTMP SCS was shown to induce greater pain inhibition than conventional SCS, perhaps owing to more effective modulation of gene expression and biological processes associated with glial function and neuron-glia interactions [18]. These findings suggest that the efficacy of SCS may be improved by developing new SCS paradigms that better modulate spinal glial function. As an anti-inflammatory drug, minocycline may also enhance SCS-induced pain inhibition through other neuronal mechanisms, such as by inhibiting sodium currents in dorsal root ganglion neurons [5]. However, the administration of low-dose minocycline alone did not inhibit pain, suggesting that this neuronal mechanism may not contribute to the enhancement of SCS-induced pain inhibition.

Our study has some limitations. First, we examined only the conventional SCS paradigm. Therefore, the effects of high-frequency, sub-sensory threshold SCS and burst SCS on spinal glial phenotypes and functions must still be studied. In addition, because of technical challenges, we used intermittent rather than continuous SCS (48–72 h), which is usually used in the clinic and has been tested in previous animal studies [18, 22, 36]. It is plausible that microglial modulation and its impact on pain may differ for different stimulation time schemes and paradigms. In addition, because tissues from CCI rats treated with minocycline and SCS were not harvested for RT-PCR and Western blotting, it remains to be determined whether the improvement in pain inhibition is attributable to enhanced inhibition of microglial activation.

SCS has more than 50 years of history as a useful non-pharmacological intervention for chronic pain. Although the clinical use of SCS continues to grow, studies of the biological and neurochemical mechanisms underlying SCS-induced analgesia have lagged behind. Most previous studies of SCS-induced analgesia have revolved around neuronal mechanisms in spinal and supraspinal structures,

and identified many neurochemical mechanisms, including serotonin, epinephrine, GABA, acetylcholine, adenosine, and endocannabinoids [10, 11, 50]. Comparatively, our knowledge about the roles of non-neuronal mechanisms in the therapeutic effects of SCS remains limited. Our current findings show that repeated SCS may increase M1-like microglial activation in the spinal cord of nerve-injured rats and suggest that inhibition of microglial activation or promotion of M2-like polarization with adjuvant pharmacotherapy may present an opportunity to prolong the pain inhibition of conventional SCS. Nevertheless, other M1- and M2-like polarization markers, and changes in the associated cytokines in the spinal cord after SCS warrant future investigation. This study represents a continuing effort toward understanding the non-neuronal modulatory actions of SCS [21, 22, 51], which may spur the clinical development of mechanism-based interventions to improve its therapeutic effects.

Acknowledgements We thank Claire F. Levine, MS, ELS (Scientific Editor, Department of Anesthesiology and Critical Care Medicine, Johns Hopkins University), for editing the manuscript and Medtronic, Inc. (Minneapolis, MN, USA) for generously providing the rodent electrodes for spinal cord stimulation. This work was supported by a grant from the Neurosurgery Pain Research Institute at the Johns Hopkins University and subsidized by the National Institutes of Health (Bethesda, Maryland, USA) (NS110598). The efforts of B.S. were supported by an award from the China Scholarship Council for Chinese PhD candidates to study abroad.

Conflict of interest Dr. Yun Guan received research grant support from Medtronic, Inc., Minneapolis, MN. However, none of the authors has a commercial interest in the material presented in this paper. There are no other relationships that might lead to a conflict of interest in the current study. The authors declare no competing interests.

References

- Watkins LR, Hutchinson MR, Ledeboer A, Wieseler-Frank J, Milligan ED, Maier SF. Norman Cousins Lecture. Glia as the “bad guys”: implications for improving clinical pain control and the clinical utility of opioids. *Brain Behav Immun* 2007, 21: 131–146.
- Crain JM, Nikodemova M, Watters JJ. Microglia express distinct M1 and M2 phenotypic markers in the postnatal and adult central nervous system in male and female mice. *J Neurosci Res* 2013, 91: 1143–1151.
- Nikodemova M, Watters JJ. Efficient isolation of live microglia with preserved phenotypes from adult mouse brain. *J Neuroinflammation* 2012, 9: 147.
- Inoue K, Tsuda M. Microglia in neuropathic pain: cellular and molecular mechanisms and therapeutic potential. *Nat Rev Neurosci* 2018, 19: 138–152.
- Mika J, Zychowska M, Popiolek-Barczyk K, Rojewska E, Przewlocka B. Importance of glial activation in neuropathic pain. *Eur J Pharmacol* 2013, 716: 106–119.
- Ledeboer A, Sloane EM, Milligan ED, Frank MG, Mahony JH, Maier SF, *et al.* Minocycline attenuates mechanical allodynia and proinflammatory cytokine expression in rat models of pain facilitation. *Pain* 2005, 115: 71–83.
- Chen G, Luo X, Qadri MY, Berta T, Ji RR. Sex-Dependent Glial Signaling in Pathological Pain: Distinct Roles of Spinal Microglia and Astrocytes. *Neurosci Bull* 2018, 34: 98–108.
- Tsuda M. Modulation of Pain and Itch by Spinal Glia. *Neurosci Bull* 2018, 34: 178–185.
- Kumar K, Taylor RS, Jacques L, Eldabe S, Meglio M, Molet J, *et al.* Spinal cord stimulation versus conventional medical management for neuropathic pain: a multicentre randomised controlled trial in patients with failed back surgery syndrome. *Pain* 2007, 132: 179–188.
- Barchini J, Tchachaghian S, Shamaa F, Jabbur SJ, Meyerson BA, Song Z, *et al.* Spinal segmental and supraspinal mechanisms underlying the pain-relieving effects of spinal cord stimulation: an experimental study in a rat model of neuropathy. *Neuroscience* 2012, 215: 196–208.
- Foreman RD, Linderth B. Neural mechanisms of spinal cord stimulation. *Int Rev Neurobiol* 2012, 107: 87–119.
- Sivanesan E, Maher DP, Raja SN, Linderth B, Guan Y. Supraspinal Mechanisms of Spinal Cord Stimulation for Modulation of Pain: Five Decades of Research and Prospects for the Future. *Anesthesiology* 2019, 130: 651–665.
- Huang Q, Duan W, Sivanesan E, Liu S, Yang F, Chen Z, *et al.* Spinal Cord Stimulation for Pain Treatment After Spinal Cord Injury. *Neurosci Bull* 2019, 35: 527–539.
- Sdrulla AD, Guan Y, Raja SN. Spinal Cord Stimulation: Clinical Efficacy and Potential Mechanisms. *Pain Pract* 2018, 18: 1048–1067.
- Yang F, Xu Q, Cheong YK, Shechter R, Sdrulla A, He SQ, *et al.* Comparison of intensity-dependent inhibition of spinal wide-dynamic range neurons by dorsal column and peripheral nerve stimulation in a rat model of neuropathic pain. *Eur J Pain* 2014, 18: 978–988.
- Shechter R, Yang F, Xu Q, Cheong YK, He SQ, Sdrulla A, *et al.* Conventional and kilohertz-frequency spinal cord stimulation produces intensity- and frequency-dependent inhibition of mechanical hypersensitivity in a rat model of neuropathic pain. *Anesthesiology* 2013, 119: 422–432.
- Guan Y. Spinal cord stimulation: neurophysiological and neurochemical mechanisms of action. *Curr Pain Headache Rep* 2012, 16: 217–225.
- Vallejo R, Kelley CA, Gupta A. Modulation of neuroglial interactions using differential target multiplexed spinal cord stimulation in an animal model of neuropathic pain. *Mol Pain* 2020, 16: 1744806920918057.
- Sato KL, Johaneck LM, Sanada LS, Sluka KA. Spinal cord stimulation reduces mechanical hyperalgesia and glial cell activation in animals with neuropathic pain. *Anesth Analg* 2014, 118: 464–472.
- Sivanesan E, Stephens KE, Huang Q, Chen Z, Ford NC, Duan W, *et al.* Spinal cord stimulation prevents paclitaxel-induced mechanical and cold hypersensitivity and modulates spinal gene expression in rats. *Pain Rep* 2019, 4: e785.
- Stephens KE, Chen Z, Sivanesan E, Raja SN, Linderth B, Taverna SD, *et al.* RNA-seq of spinal cord from nerve-injured rats after spinal cord stimulation. *Mol Pain* 2018, 14: 1744806918817429.
- Vallejo R, Tilley DM, Cedeno DL, Kelley CA, DeMaegd M, Benjamin R. Genomics of the Effect of Spinal Cord Stimulation on an Animal Model of Neuropathic Pain. *Neuromodulation* 2016, 19: 576–586.
- Bennett GJ, Xie YK. A peripheral mononeuropathy in rat that produces disorders of pain sensation like those seen in man. *Pain* 1988, 33: 87–107.

24. Chaplan SR, Bach FW, Pogrel JW, Chung JM, Yaksh TL. Quantitative assessment of tactile allodynia in the rat paw. *J Neurosci Methods* 1994, 53: 55–63.
25. Dixon WJ. Efficient analysis of experimental observations. *Annu Rev Pharmacol Toxicol* 1980, 20: 441–462.
26. Yang F, Xu Q, Shu B, Tiwari V, He SQ, Vera-Portocarrero LP, *et al.* Activation of cannabinoid CB1 receptor contributes to suppression of spinal nociceptive transmission and inhibition of mechanical hypersensitivity by Abeta-fiber stimulation. *Pain* 2016, 157: 2582–2593.
27. Mestre C, Pelissier T, Fialip J, Wilcox G, Eschaliere A. A method to perform direct transcutaneous intrathecal injection in rats. *J Pharmacol Toxicol Methods* 1994, 32: 197–200.
28. Liu S, Huang Q, He S, Chen Z, Gao X, Ma D, *et al.* Dermorphin [D-Arg2, Lys4] (1–4) amide inhibits below-level heat hypersensitivity in mice after contusive thoracic spinal cord injury. *Pain* 2019, 160: 2710–2723.
29. He SQ, Xu Q, Tiwari V, Yang F. Oligomerization of MrgC11 and μ -opioid receptors in sensory neurons enhances morphine analgesia. *Sci Signal* 2018, 11(535):eaa03134. <https://doi.org/10.1126/scisignal.aao3134>.
30. Ji RR, Befort K, Brenner GJ, Woolf CJ. ERK MAP kinase activation in superficial spinal cord neurons induces prodynorphin and NK-1 upregulation and contributes to persistent inflammatory pain hypersensitivity. *J Neurosci* 2002, 22: 478–485.
31. Zhuang ZY, Gerner P, Woolf CJ, Ji RR. ERK is sequentially activated in neurons, microglia, and astrocytes by spinal nerve ligation and contributes to mechanical allodynia in this neuropathic pain model. *Pain* 2005, 114: 149–159.
32. Woolf CJ, Mannion RJ. Neuropathic pain: aetiology, symptoms, mechanisms, and management. *Lancet* 1999, 353: 1959–1964.
33. Burke NN, Kerr DM, Moriarty O, Finn DP, Roche M. Minocycline modulates neuropathic pain behaviour and cortical M1-M2 microglial gene expression in a rat model of depression. *Brain Behav Immun* 2014, 42: 147–156.
34. Ji RR, Berta T, Nedergaard M. Glia and pain: Is chronic pain a gliopathy? *Pain* 2013, 154: S10–S28.
35. Raghavendra V, Tanga F, DeLeo JA. Inhibition of microglial activation attenuates the development but not existing hypersensitivity in a rat model of neuropathy. *J Pharmacol Exp Ther* 2003, 306: 624–630.
36. Tilley DM, Cedeño DL, Kelley CA, Benyamin R, Vallejo R. Spinal Cord Stimulation Modulates Gene Expression in the Spinal Cord of an Animal Model of Peripheral Nerve Injury. *Reg Anesth Pain Med* 2016, 41: 750–756.
37. Trang T, Beggs S, Wan X, Salter MW. P2X4-receptor-mediated synthesis and release of brain-derived neurotrophic factor in microglia is dependent on calcium and p38-mitogen-activated protein kinase activation. *J Neurosci* 2009, 29: 3518–3528.
38. Coull JA, Beggs S, Boudreau D, Boivin D, Tsuda M, Inoue K, *et al.* BDNF from microglia causes the shift in neuronal anion gradient underlying neuropathic pain. *Nature* 2005, 438: 1017–1021.
39. Stiller CO, Cui JG, O'Connor WT, Brodin E, Meyerson BA, Linderoth B. Release of gamma-aminobutyric acid in the dorsal horn and suppression of tactile allodynia by spinal cord stimulation in mononeuropathic rats. *Neurosurgery* 1996, 39: 367–374; discussion 374–365.
40. Cui JG, O'Connor WT, Ungerstedt U, Linderoth B, Meyerson BA. Spinal cord stimulation attenuates augmented dorsal horn release of excitatory amino acids in mononeuropathy via a GABAergic mechanism. *Pain* 1997, 73: 87–95.
41. Colonna M, Butovsky O. Microglia Function in the Central Nervous System During Health and Neurodegeneration. *Annu Rev Immunol* 2017, 35: 441–468.
42. Wes PD, Holtman IR, Boddeke EW, Moller T, Eggen BJ. Next generation transcriptomics and genomics elucidate biological complexity of microglia in health and disease. *Glia* 2016, 64: 197–213.
43. Zhang Y, Chen K, Sloan SA, Bennett ML, Scholze AR, O'Keefe S, *et al.* An RNA-sequencing transcriptome and splicing database of glia, neurons, and vascular cells of the cerebral cortex. 2014, 34: 11929–11947.
44. Cao H, Zhang YQ. Spinal glial activation contributes to pathological pain states. *Neurosci Biobehav Rev* 2008, 32: 972–983.
45. Song ZP, Xiong BR, Guan XH, Cao F, Manyande A, Zhou YQ, *et al.* Minocycline attenuates bone cancer pain in rats by inhibiting NF-kappaB in spinal astrocytes. *Acta Pharmacol Sin* 2016, 37: 753–762.
46. Guasti L, Richardson D, Jhaveri M, Eldeeb K, Barrett D, Elphick MR, *et al.* Minocycline treatment inhibits microglial activation and alters spinal levels of endocannabinoids in a rat model of neuropathic pain. *Mol Pain* 2009, 5: 35.
47. Nie H, Zhang H, Weng HR. Minocycline prevents impaired glial glutamate uptake in the spinal sensory synapses of neuropathic rats. *Neuroscience* 2010, 170: 901–912.
48. Cho IH, Lee MJ, Jang M, Gwak NG, Lee KY, Jung HS. Minocycline markedly reduces acute visceral nociception via inhibiting neuronal ERK phosphorylation. *Mol Pain* 2012, 8: 13.
49. Pu S, Xu Y, Du D, Yang M, Zhang X, Wu J, *et al.* Minocycline attenuates mechanical allodynia and expression of spinal NMDA receptor 1 subunit in rat neuropathic pain model. *J Physiol Biochem* 2013, 69: 349–357.
50. Meyerson BA, Linderoth B. Mode of action of spinal cord stimulation in neuropathic pain. *J Pain Symptom Manage* 2006, 31: S6–12.
51. Tilley DM, Lietz CB, Cedeno DL, Kelley CA, Li L, Vallejo R. Proteomic Modulation in the Dorsal Spinal Cord Following Spinal Cord Stimulation Therapy in an In Vivo Neuropathic Pain Model. *Neuromodulation* 2020. <https://doi.org/10.1111/ner.13103>.



Fine-Grained Topography and Modularity of the Macaque Frontal Pole Cortex Revealed by Anatomical Connectivity Profiles

Bin He^{1,2,3} · Long Cao^{2,5} · Xiaoluan Xia^{2,8} · Baogui Zhang^{2,3} · Dan Zhang¹⁰ · Bo You¹ · Lingzhong Fan^{2,3,4,7} · Tianzi Jiang^{2,3,4,5,6,7,9} 

Received: 31 March 2020 / Accepted: 30 July 2020 / Published online: 27 October 2020
© The Author(s) 2020

Abstract The frontal pole cortex (FPC) plays key roles in various higher-order functions and is highly developed in non-human primates. An essential missing piece of information is the detailed anatomical connections for finer parcellation of the macaque FPC than provided by the previous tracer results. This is important for understanding the functional architecture of the cerebral cortex. Here, combining cross-validation and principal component analysis, we formed a tractography-based parcellation scheme that applied a machine learning algorithm to divide the macaque FPC (2 males and 6 females) into eight subareas using high-resolution diffusion magnetic resonance imaging with the 9.4T Bruker system, and then

revealed their subregional connections. Furthermore, we applied improved hierarchical clustering to the obtained parcels to probe the modular structure of the subregions, and found that the dorsolateral FPC, which contains an extension to the medial FPC, was mainly connected to regions of the default-mode network. The ventral FPC was mainly involved in the social-interaction network and the dorsal FPC in the metacognitive network. These results enhance our understanding of the anatomy and circuitry of the macaque brain, and contribute to FPC-related clinical research.

Keywords Macaque · Frontal pole cortex · Anatomical connectivity profile · Parcellation · Neuroimaging · Principal component analysis

Electronic supplementary material The online version of this article (<https://doi.org/10.1007/s12264-020-00589-1>) contains supplementary material, which is available to authorized users.

- ✉ Bo You
youbu@hrbust.edu.cn
- ✉ Lingzhong Fan
lingzhong.fan@ia.ac.cn
- ✉ Tianzi Jiang
jiangtz@nlpr.ia.ac.cn

¹ School of Mechanical and Power Engineering, Harbin University of Science and Technology, Harbin 150080, China

² Brainnetome Center, Institute of Automation, Chinese Academy of Sciences, Beijing 100190, China

³ National Laboratory of Pattern Recognition, Institute of Automation, Chinese Academy of Sciences (CAS), Beijing 100190, China

⁴ Center for Excellence in Brain Science and Intelligence Technology, Institute of Automation, CAS, Beijing 100190, China

⁵ Key Laboratory for NeuroInformation of the Ministry of Education, School of Life Science and Technology, University of Electronic Science and Technology of China, Chengdu 610054, China

⁶ The Queensland Brain Institute, University of Queensland, Brisbane, QLD 4072, Australia

⁷ University of CAS, Beijing 100049, China

⁸ College of Information and Computer, Taiyuan University of Technology, Taiyuan 030600, China

⁹ Chinese Institute for Brain Research, Beijing 102206, China

¹⁰ Core Facility, Center of Biomedical Analysis, Tsinghua University, Beijing 100084, China

Abbreviations**Abbreviations of the Brain Regions**

10	Area 10 of cortex
11	Area 11 of cortex
13	Area 13 of cortex
23	Area 23 of cortex
25	Area 25 of cortex
30	Area 30 of cortex
31	Area 31 of cortex
32	Area 32 of cortex
35	Area 35 of cortex
44	Area 44 of cortex
10471	Area 9/32 of cortex
15584	Area 9/46 of cortex
10D	Area 10 of cortex, dorsal part
10M	Area 10 of cortex, medial part
10V	Area 10 of cortex, ventral part
11L	Area 11 of cortex, lateral part
11m	Area 11 of cortex, medial part
13a	Area 13a of cortex
13L	Area 13 of cortex, lateral part
13M	Area 13 of cortex, medial part
14M	Area 14 of cortex, medial part
14o	Area 14o
23a	Area 23a of cortex
23b	Area 23b of cortex
23c	Area 23c of cortex
24/23a	Area 24/23a of cortex
24/23b	Area 24/23b of cortex
24a	Area 24a of cortex
24b	Area 24b of cortex
24c	Area 24c of cortex
29a	Area 29a of cortex
45A	Area 45A of cortex
45B	Area 45B of cortex
46D	Area 46D of cortex
46V	Area 46V of cortex
47(12)	Area 47 (old 12) of cortex
47(12)L	Area 47 (old 12) of cortex, lateral part
47(12)O	Area 47 (old 12) of cortex, orbital part
6VR(F5)	Area 6 of cortex, rostral ventral part
8AD	Area 8 of cortex, anterodorsal part
8AV	Area 8 of cortex, anteroventral part
9/46D	Area 9/46 of cortex, dorsal part
9/46V	Area 9/46 of cortex, ventral part
9L	Area 9 of cortex, lateral part
9M	Area 9 of cortex, medial part
AA	Anterior amygdaloid area
Acb	Accumbens nucleus
AI	Agranular insular cortex
AO	Anterior olfactory nucleus

Apul	Anterior pulvinar
Atha	Anterior thalamic nucleus
BL#2	Basolateral amygdaloid nucleus
BLD	Basolateral amygdaloid nucleus, dorsal part
BM#3	Basomedial amygdaloid nucleus
BM#4	Basal nucleus (Meynert)
BST	Bed nucleus of the stria terminalis central division
BSTIA	Bed nucleus of the stria terminalis intraamygdaloid division
Cd	Caudate nucleus
Ce	Central amygdaloid nucleus
Cl#2	Centrolateral thalamic nucleus
CM#2	Central medial thalamic nucleus
CMnM	Centromedial thalamic nucleus, medial part
Den	Dorsal endopiriform nucleus
DI	Dysgranular insular cortex
GP	Globus pallidus
Gu	Gustatory cortex
HDB	Nucleus of the horizontal limb of the diagonal band
Hy	Hypothalamus
IAM	Interanteromedial thalamic nucleus
IMD	Intermediodorsal thalamic nucleus
IPro	Insular proisocortex
Ipul	Inferior pulvinar
La#3	Lateral amygdaloid nucleus
Ldsf	Lateral dorsal thalamic nucleus, superficial part
Lpul	Lateral pulvinar
LV	Lateral ventricles
MB	Midbrain
MD	Mediodorsal thalamic nucleus
Me	Medial amygdaloid nucleus
MPul	Medial pulvinar
OPAI	Orbital periallocortex
OPro	Orbital proisocortex
PaIL	Parainsular cortex
PaS	Parasubiculum
Pf#2	Parafascicular thalamic nucleus
PGM	Area PGM/31 of cortex
Pir	Piriform cortex
ProKM	Prokoniocortex, medial part
ProM	Area ProM (promotor)
ProST	Prostriate area
PrS	Presubiculum
Pu	Putamen
Pul#1	Pulvinar nuclei
Pvt	Paraventricular thalamus
R#4	Reticular thalamic nucleus
R36	The perirhinal cortex
Re	Reuniens thalamic nucleus
Se	Septum
SI	Substantia innominata

ST1	Superior temporal sulcus area 1
ST2	Superior temporal sulcus area
ST3	Superior temporal sulcus area 3
TAa	Temporal area TAa
TPPro	Temporopolar proisocortex
TTPAI	Temporopolar periallocortex
Tu	Olfactory tubercle
VA	Ventral anterior thalamic nucleus
VL	Ventral lateral thalamic nucleus
VP#3	Ventral pallidum

Other Abbreviations

ANTs	Advanced normalization tools
aspd	Anterior supraprincipal dimple
cgs	Cingulate sulcus
DMN	Default-mode network
dMRI	Diffusion magnetic resonance imaging
DTI	Diffusion tensor imaging
ESIN	Exclusively social interaction network
fMRI	Functional magnetic resonance imaging
MIPAV	Medical image processing, analysis, and visualization software
morbs	Medial orbital sulcus
MRI	Magnetic resonance imaging
PCA	Principal component analysis
ps	Principal sulcus
pspd	Posterior supraprincipal dimple
ROI	Region of interest
ros	Rostral sulcus
SIN	Social-interaction network

Introduction

The macaque frontal pole cortex (FPC) has a homotypical cytoarchitecture and a location relative to other prefrontal regions that is similar to that of humans [1], which means that it has the potential to be an excellent model for understanding the mechanisms of the human brain [2, 3]. As a portion of the prefrontal cortex, this area that has undergone more extensive evolution [4], and it is a late-developing area of the neocortex [5]. The FPC has a singularly high neuronal density and rich dendritic spines, which together suggest complex functions and multiple areas of cytoarchitectonic differentiation. In addition, the functional complexity of the FPC varies between species, which makes it a focal point for comparisons across species. Especially, as the core area involved in decision-making in the executive system [6, 7], the FPC has been pinpointed as a unique area that could separate humans from other primates with respect to higher cognitive powers [8, 9].

Although a variety of findings suggest that the macaque FPC can be divided into multiple functional subareas with different connectivity [10, 11], this area still lacks specialized research on its anatomical connections and a detailed parcellation map. Much of the previous work on this region primarily focused on cytoarchitecture and tract-tracing techniques [12–15]. The early researchers defined this area as Brodmann area (BA) 10 in humans and BA 12 in non-human primates [16]. Subsequently, this area was reclassified as BA 10 in non-human primates by Walker [17]. Recently, three primary studies have revealed markedly different cytoarchitectonic parcellation results [18–20], and many trace-injection experiments involving the FPC were based on previous rough maps of this area. In addition, the FPC has been suggested to be potentially associated with the default-mode network (DMN) [21, 22]. Statistical maps of enhanced activation have revealed that the FPC is involved in the social-interaction network (SIN) [23]. In macaque monkeys, Miyamoto, Setsuie, Osada, Miyashita [24] found that the FPC is recruited for the metacognitive judgment of non-experienced events by fMRI experiments. The inactivation of this area does not affect the detection of non-experienced events, but selectively impairs the metacognition of non-experienced events. From a different perspective, studies based on the diffusion tensor imaging (DTI) connectivity could further improve our understanding of the relationship between the macaque FPC and different functional networks, including the DMN, SIN, and metacognitive networks, but relevant studies are lacking. The above issues, which are both important and controversial, hint at the urgency of obtaining a detailed understanding of this region; however, to our knowledge, the macaque FPC remains one of the least understood brain areas [25]. Moreover, the traditional parcellation method based on cytoarchitectonics is not only limited to non-invasive approaches, but is also limited by the number of samples and lack of consideration of individual variation. Many trace-injection studies related to the FPC have been based on previous rough parcellation maps and relevant studies based on DTI are still a rarity.

In view of the importance of the diversity of functions of the monkey FPC and the lack of detailed anatomical connection information in comparison with the previous tracer results [19, 26, 27], as well as to pave the way for a systematic follow-up study using tracer injections, a study of the topological organization properties of the macaque FPC is necessary and attractive. Recently, connectivity-based parcellation (CBP) has been a powerful framework for mapping the human brain [28–30] and may provide a better picture of regional parcellation and anatomical connectivity information [31, 32] as well as allowing the target areas of tracer injections to be chosen less blindly. In this study, we provided a tractography-based parcellation

scheme that applied a machine-learning algorithm to obtain a fine-grained subdivisions of the macaque FPC, and then revealed their subregional connections. Exploring the modular structure of a community and the anatomical connectivity patterns of different functional networks could help understand brain mechanisms and evolution, which contributes to FPC-related clinical research.

Materials and Methods

To study the topological organization properties of the macaque FPC, three research objectives were established and the corresponding work was carried out. The overall workflow is shown in Fig. 1. First, we used DTI data to divide the macaque FPC into different subregions; then we explored the anatomical connectivity patterns of each subdivision. Furthermore, we proposed an improved hierarchical clustering algorithm to explore the modular structure of the community for the bilateral subregions.

Macaque Brain Specimens

The rhesus macaques (*Macaca mulatta*) were obtained from Kunming Institute of Zoology, Chinese Academy of Sciences [33] (details in Table 1). All experimental procedures were conducted according to the policies set forth by the National Institutes of Health Guide for the Care and Use of Laboratory Animals, and approved by the

Animal Care and Use Committee of the Institute of Automation, Chinese Academy of Sciences. They were judged by the veterinarian as appropriate subjects for euthanasia due to serious illnesses (acute gastroenteritis and enteritis). Each animal was intraperitoneally administered an overdose of pentobarbital [100 mg/kg, Sigma Aldrich (Shanghai) Trading Co., Ltd, Shanghai]. After verifying the status of deep anesthesia, they were transcardially perfused first with Phosphate-buffered saline (PBS) containing 1% heparin [pH 7.4, Sigma Aldrich (Shanghai) Trading Co., Ltd, Shanghai], followed by pre-cooled PBS containing 4% paraformaldehyde [Sigma Aldrich (Shanghai) Trading Co., Ltd, Shanghai]. Five minutes after starting the perfusion, the rate was lowered to 1 mL/min from an initial rate of 20 mL/min, and the entire perfusion lasted 2 h. The head was then removed and stored in PBS containing 4% paraformaldehyde. Then, the skull was carefully removed to expose the whole brain for MRI scanning. No apparent structural anomalies were found in any of the brains used in the present study.

MRI Acquisition

All the macaque MRI data were obtained using a 9.4T horizontal animal MRI system [Bruker Biospec 94/30 USR, with Paravision 6.0.1 (Ettlingen,Baden-Württemberg, Germany)]. Radiofrequency (RF) transmission and reception were achieved with a 154-mm inner-diameter quadrature RF coil. The SpinEcho DTI sequence used for

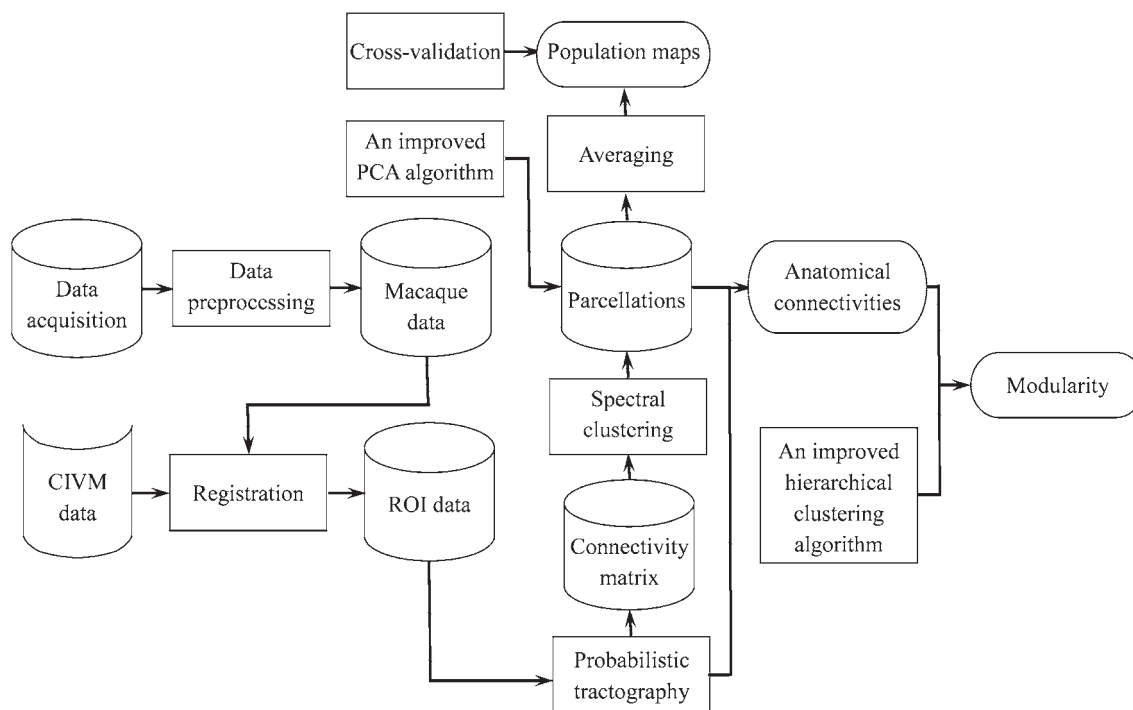


Fig. 1 The overall workflow of this study.

Table 1 Information about the eight monkey brains.

Perfusion date	Number	Gender	Age	Weight (kg)
2016/05/09	93310	Female	23	3.24
	08046	Female	8	3.58
	12027	Male	4	3.06
	12411	Male	4	2.89
2016/05/10	01006	Female	15	3.57
	04084	Female	12	4.23
	10427	Female	6	3.69
	11402	Female	5	2.9

the DTI data provided the main parameters: 74 slices, echo time (TE) = 22 ms, repetition time (TR) = 9800 ms, field of view (FOV) = $94 \times 66 \text{ mm}^2$, flip angle (FA) = 90° , acquisition matrix = 140×110 , and resolution = $0.6 \times 0.6 \times 0.6 \text{ mm}^3$ without gap. This sequence produced a complete set of 64 images, including 4 non-diffusion-weighted images ($b = 0 \text{ s/mm}^2$) and 60 images with non-collinear diffusion gradients ($b = 1000 \text{ s/mm}^2$) and required $\sim 115 \text{ h}$ of scanning time per specimen. T1-weighted data were acquired using a 2D IR-prepared RARE sequence with these main parameters: 74 slices, TE = 5.8 ms, TR = 4019 ms, inversion time = 750 ms, matrix = 280×220 , FA = 90° , resolution = $0.3 \times 0.6 \times 0.3 \text{ mm}^3$, FOV = $84 \times 66 \text{ mm}^2$, slice thickness = 0.6 mm, and no gap, requiring $\sim 55 \text{ min}$. T2-weighted data were obtained in a 2D Turbo RARE sequence with these main parameters: 86 slices, TE = 30.9 ms, TR = 8464 ms, FA = 90° , resolution = $0.3 \times 0.6 \times 0.3 \text{ mm}^3$, matrix = 280×220 , FOV = $84 \times 66 \text{ mm}^2$, slice thickness = 0.6 mm, and no gap, requiring $\sim 15 \text{ min}$.

Definition of Seed and Target Masks of Macaque FPC

The macaque FPC seed masks were extracted from a publicly-available post-mortem macaque brain atlas (CIVM, <https://scalablebrainatlas.incf.org/macaque/CBCetal15>) [34] and all regional names were found in the list of abbreviations. This atlas is largely consistent with that of Paxinos *et al.* [18] Nissl-based atlas and has become increasingly popular in macaque studies [35–37]. The mask occupied the most rostral portions of the prefrontal cortex; its dorsal extent was bounded posteriorly by the anterior supraprincipal dimple (aspd) and did not cross the posterior supraprincipal dimple (pspd). In addition, on the medial aspect of the hemisphere, the FPC mask posteriorly bordered the cingulate sulcus (cgs) and in the coronal plane, it was ventrally delimited by the anterior termination of the olfactory sulcus. For each subject, the standard seed mask was wrapped back into individual diffusion space using the

inverse of the deformations, and each resulting mask was visually inspected for possible errors and necessary modifications using ITK-SNAP (Philadelphia, Pennsylvania) [38]. To calculate the connectivity matrix and obtain the connectivity fingerprints, we extracted cortical regions and subcortical structures in the same hemisphere from the CIVM atlas as target regions [39]. The extraction approach for the target regions was the same as that for the FPC. Subsequently, we transformed them into individual diffusion space.

Diffusion MRI Data Preprocessing

The diffusion MRI (dMRI) data were preprocessed using the FMRIB Diffusion Toolbox (FSL version 5.0; <https://fsl.fmrib.ox.ac.uk/fsl/fslwiki/FSL>), the prominent Medical Image Processing, Analysis, and Visualization software (MIPAV, <https://mipav.cit.nih.gov/>), and Advanced Normalization Tools (ANTs, <http://www.picsl.upenn.edu/ANTs/>), which is a state-of-the-art medical image registration toolkit [40]. The main procedure included the following steps. First, for the CIVM template, we transformed the raw format to the available dMRI space with MIPAV, which enables the quantitative analysis and visualization of medical images in different formats. Second, in the diffusion data from each subject, distortions caused by eddy currents were corrected using the FSL tool [41]. Finally, after conversion into the standard available format with MIPAV, the b_0 image of the CIVM template space was co-registered to the individual non-diffusion-weighted images ($b = 0 \text{ s/mm}^2$) using ANTs. After the registration, an inverse transformation was performed to transform the seed and target masks for each subject's small cortical areas into native dMRI space.

Probabilistic Diffusion Tractography

After preprocessing, the macaque FPC was chosen as the seed and probabilistic tractography was carried out for the tractography-based parcellation. This process has been described in the toolbox for connectivity-based parcellation of the monkey brain [42] and is similar to that in another study [43]. Voxelwise estimates of the fiber orientation distribution were computed using Bedpostx. We calculated the probability distributions in two fiber directions at each voxel using a multiple fiber extension [44]. Based on the probability distributions, we then estimated the connectivity probability between each voxel in the seed region and every voxel of the whole brain using PROBTRACKX2 (Oxford, Oxfordshire). Probabilistic tractography was applied by sampling 15,000 streamline fibers per voxel and the step size was set to 0.2 mm [45, 46]. To exclude implausible pathways, we restricted how sharply pathways

could turn, and the default threshold was set to 0.2. To correct the path distribution for the length of the pathways, we introduced a distance correction. The connection probability between each voxel in the seed region and any other voxel in the brain was obtained by computing the number of traces arriving at the target site. To decrease the number of false-positive connections, we thresholded the path distribution estimates for each subject using a connection probability value $P < 20/15000$ (20 out of 15,000 samples). Information about the connectivity was stored in an M-by-N matrix, where M denotes the number of voxels in the seed mask and N the number of voxels in the native diffusion space. To de-noise the data and increase computational efficiency, the connectivity profiles for each voxel were down-sampled to 2-mm isotropic voxels [47].

Tractography-Based Parcellation of the Macaque FPC

Based on the connectivity patterns of all the voxels of the FPC, cross-correlation matrices were computed and fed into spectral clustering [28]. The maximum probability map (MPM) was computed by assigning each voxel of the standard space to the subarea in which it was most likely to be located [48]. First, we transformed the parcellation results from individual diffusion space to the CIVM template. Second, the MPM was computed according to the eight subjects' parcellation results in CIVM space.

After parcellation of the FPC using spectral clustering, the next step was to select the number of clusters. To avoid an arbitrary choice of this number, we used two prevailing validation methods, cross-validation indices to obtain a consistent segmentation for all eight subjects at the group level, and principal component analysis (PCA), to determine the optimal number of clusters across the subjects at the individual diffusion level [42].

Cross-Validation Indices

The cross-validation offered two indices, Cramer's V [49, 50] and topological distance (TpD) [51], for determining the optimal clustering number. Cramer's V, is an indicator of clustering consistency and has values in the interval [0, 1], high values indicating good consistency. The TpD index, which quantifies the similarity of the topological arrangement of putative homologous regions in the bilateral hemispheres across all specimens, further determined the cluster number. The TpD score ranges from 0 to 1; a score close to 0 suggests that the two hemispheres have similar topology. The clustering number of local extremum points (peaks and valleys) means better consistency than that of adjacent ones, and in general, the local

extrema are recommended as a good solution for each presumptive index [52, 53].

Principal Component Analysis

PCA, which requires no artificial hypothesis or prior knowledge, is a popular statistical framework for determining the clustering number [30, 54]. To ensure that the number of principal components to be chosen retain enough features and effectively represent the data, we proposed three criteria based on the literature [55, 56]. The first was the cumulative contribution, which means that a cumulative proportion of the variation could be explained by the eigenvalue obtained using the connection data. To obtain the cumulative proportion value (cpv), a threshold must be established. Generally, a sensible threshold is very often in the range 70% to 90%; it can sometimes be higher or lower depending on the practical details of a particular dataset. In our study, we thresholded the cpv at $> 80\%$. Taking into account individual variation, we allowed a lower limit change of no more than 1%. The second criterion was that only factors with eigenvalues > 1 or next closest to 1 were retained. Specifically, the latter weak criterion (values close to 1) is like a "factorial scree" for atypical individual variation. The third criterion is a scree test [30, 54]. Briefly, for each subject, a 'connectivity' matrix between the various seeds and the whole brain was derived from the data of the probabilistic tractography. This matrix consisted of columns that indicated the FPC subregion of interest and rows that represented the whole-brain regions. To estimate the number of principal components to extract from each subject, a power curve was plotted by fitting the data, the inflexion point was extracted using a homemade routine written in MatLab (Natick, Massachusetts) R2017b, and all subjects were averaged to obtain a mean cluster value for the left and right hemispheres separately. Meanwhile, we set the difference threshold between the inflection point value of each individual and the average value as 0.5 to ensure that the clustering number among individuals was stable.

Anatomical Connectivity Patterns

To explore the different anatomical connection patterns of the FPC subdivisions, we first drew 10^5 samples from the fiber orientation distribution for each voxel in the subdivisions to calculate the whole-brain probabilistic fiber tracking [44]. To form the seed mask, each subarea was extracted from the probability map of the FPC at 25% probability. To reduce the false-positive rate and facilitate the qualitative analysis, we thresholded the connectivity probability value at 3.08×10^{-5} at the individual level, which means that at least 3.08 of the 10^5 samples produced

from each seed voxel were connected [48]. Next, the identified fiber tracts were binarized and transformed into CIVM macaque template space. All the binarized results were averaged to obtain population maps with a threshold of 50% [39], which means that only those voxels that were present in at least 4 of 8 subjects were mapped, and were then transformed into F99 space for display.

Subsequently, to visualize the differences in the anatomical connectivity of each subarea, we further calculated the anatomical connectivity fingerprints between each subarea and each of the target regions in the CIVM atlas. For the eight subjects, these target brain regions, including the cortical areas and subcortical structures of each subject, were extracted from the CIVM atlas in the same hemisphere using the same method as used to extract the FPC and was subsequently transformed into individual dMRI space. Using their fingerprints, we were able to find the different connectivity properties for each subregion. In addition, we performed similarity analysis of the connections for these clusters to estimate the connection similarity between individuals. Briefly, we computed the correlation coefficients for the seed-to-target connections and obtained the P values for the hypothesis that there was no relationship between the observed phenomena. We defined the threshold of statistical significance as statistically highly significant at $P < 0.001$.

Furthermore, we also investigated and summarized other tract-tracing studies involving the macaque FPC to compare their consistency by assessing the repeatability of the connected areas that they identified. As a preliminary qualitative comparison, we collected the regions connected to the FPC from the CoCoMac database [57] and compared them with the regions connected to subdivisions of the FPC. The CoCoMac database provides convincing structural connectivity data for the macaque brain and was a remarkable effort by many researchers. Currently, it is the largest macaque connectivity study, with data extracted from > 400 published tract-tracing studies of the macaque brain. We also made a further comparison with some of the detailed trace-injection experiments.

Moreover, inspired by a human frontal pole study [50], to reveal a clearer picture of different functional networks from the perspective of anatomical connections, we analyzed the connections between the subregions and the regions of different functional networks. Specifically, we combined the regions that were connected to the DMN [21, 22], SIN [23], and metacognition network [24, 58] and estimated the linkages and differences between the subareas. Additional comparisons with other studies and findings are presented in the Discussion.

Mapping the Hierarchical Module Structure for FPC Subregions

Exploring the modular structure of a community and the connectivity patterns of different functional networks is important for understanding brain mechanisms and evolution. Many neuroscientific studies [59–61] have revealed that the brain networks share important organizational principles in common, such as modularity, and that topological modules often comprise anatomically neighboring cortical areas. In addition, the modules of brain networks contain both unilateral and bilateral areas [62], and a community structure in the brain can be correlated with functionally localized regions, such as visual, auditory, and central modules [63]. Here, we proposed an improved hierarchical clustering algorithm to examine the subregional members of the bilateral FPC and assign them to clusters. The correlation coefficient matrix of the native connectivity data was fed into the algorithm; as the number of clusters increased, those with high connection similarity were given priority and grouped together. Besides, we calculated the cophenetic correlation coefficient to evaluate and select the optimal clustering scheme. The hierarchical clustering method not only uncovered the modular community structure of the bilateral FPC, but also provided some methods that other researchers can use in making within-species comparisons. In particular, this method can be used for comparisons between parcellations with a greater number of subdivisions and those with fewer subdivisions that have been obtained from studies that use different methods. This approach can also be used to make heuristic comparisons between species, including comparisons of parcellation patterns and connectivity patterns involving different functional networks. Compared with previous studies [33, 43], the advantage of our method is that it is able to automatically select the optimal clustering by introducing the cophenetic correlation coefficient to compare the results of clustering the same data set using different distance calculation methods and clustering algorithms. The cophenetic correlation coefficient scores range from 0 to 1. The closer the value is to 1, the more accurately the clustering solution reflects the data.

Results

Connectivity-Based Parcellation and Subregional Anatomical Connectivity Patterns of the Macaque FPC

For the macaque FPC, the cross-validation of the spectral clustering data showed that the 8-cluster solution, as local extremum points of Cramer's V , was optimal for a fine

parcellation (Fig. 2A). The TpD index also selected the 8-cluster solution as optimal (Fig. 2B). These results of validity indices suggested the consistency of the parcellations across subjects and the similarity of the topological organization distribution of the parcellation results between the bilateral hemispheres at the group level [42]. In addition, at the individual diffusion space level, the index results of PCA also suggested a segregation of the FPC into an average of 8 subdivisions for each of the hemispheres (left hemisphere, 8.31, see Fig. 2E; right hemisphere, 8.27, see Fig. 2F).

The eight distinct subareas consisted of four components in the lateral section with the remaining four components in the medial section. These results were transformed and combined into F99 brain space [64] with Caret software [65] to create population-based parcellations of the FPC, and we further presented the probabilistic map for each subarea that could help to understand the consistency between subjects in the topography of the clusters (left hemisphere see Fig. 3; right hemisphere see Fig. S1). To facilitate understanding of the results, we determined the location of each subregion based on histologically defined cortical areas and a topologic map as well as on its anatomical connection information. In describing the location of these subregions, we refer to them with respect to the cgs, principal sulcus (ps), medial orbital sulcus (morbs), rostral sulcus (ros), aspd, and the adjacent areas. In the sagittal plane, a ventrolateral boundary along the direction of the ps separates C4 from C6, and another lateral boundary above the rostral ps distinguishes subareas C6 from C8. The dorsolateral boundary above the aspd separates subareas C8 from C7. In the medial FPC, a boundary along the anterior extension of the ros segregates subareas C3 from C2, and another boundary around the rostral cgs distinguishes subareas C1 from C2. Above the rostral cgs, a dorsomedial boundary separates subareas C5 from C1.

Furthermore, the anatomical connectivity patterns of each subregion were obtained from the whole-brain probabilistic tractography in native diffusion space by estimating the fiber orientations for each voxel. To minimize the effects of inter-individual variations, the probabilistic patterns of the fiber tracts were then transformed into CIVM space; then an averaged fiber tract map was calculated for each subdivision and displayed in the F99 surface. The anatomical connectivity fingerprints between the subdivisions and other brain structure areas of the CIVM atlas could identify the connectivity differences for each subarea (see Fig. 4, Fig. 5, S2, and S3 for details).

Cluster C1

C1 was located in the medial part of the FPC around the rostral tip of the anterior cingulate cortex (ACC), following a medial-to-lateral direction, gradually along the dorsal surface of area 32, then in front of areas 9/32 and 32. Following an anterior-to-posterior direction, with the extension of the ros, C1 extended dorsally to the cgs. Above it was Cluster C5, and its dorsal extent was limited by Cluster C8. Its ventral border was delimited by Cluster C2 just above the ros, while ventrally it was anteriorly delimited by Cluster C6. This subdivision also encompassed part of the anterior bank of the cgs. Tractography samples seeded from Cluster C1 to the cortex were mostly distributed in the medial frontal cortex, the adjacent ACC, and the posterior cingulate cortex, including areas 32, 24a, 24b, 9/32, 24/23a, 29, and 10M. At a longer distance, it connected with areas 31, 23, PGM, ProST, TTPA1, and TTPro. In the subcortical results, area C1 showed a stronger connection with Re, IMD, Cl#2, and Se.

Cluster C2

C2 was located in the medial part of the FPC just below Cluster C1. It lay anterior to area 32, followed a medial-to-lateral direction immediately in front of the rostral cgs and also encompassed part of the rostral bank of the cgs. In its dorsal rostral part, it extended to the most posterior part of Cluster C6. Its ventral extent was limited by Cluster C3, which was located in the orbital FPC. In the coronal plane, Cluster 2 was above the smooth extension line of the ps. The connectivity of Cluster C2 was predominantly with the medial frontal cortex and part of the lateral frontal lobe, including areas 24a, 32, the most anterior FPC, 24b, 24/23a, 14, and 10M. In addition, the subcortical structures, including Se, SI, BM#4, AA, and Re, shared a stronger connectivity seeded from area C2.

Cluster C3

C3 covered the medial orbital part of the FPC. Following a medial-to-lateral direction, its dorsal border was delimited by Clusters C2 and C6 and gradually continued along the ventral area of Cluster C4. Along the lateral extended direction, the morbs separated Cluster C3 from Cluster C4. C3 was heavily connected with the orbitofrontal cortex, temporal cortex, and LV, including areas 14, OPA1, 13a, and the anterior and ventral parts of area 10. This cluster had strong connections with the orbital periallocortex, the rostral part of area TL (area 36R), and the temporopolar periallocortex. Compared with the connection strength with subcortical structures, Cluster C3 shared stronger connections with SI, HDB, Se, and BST.

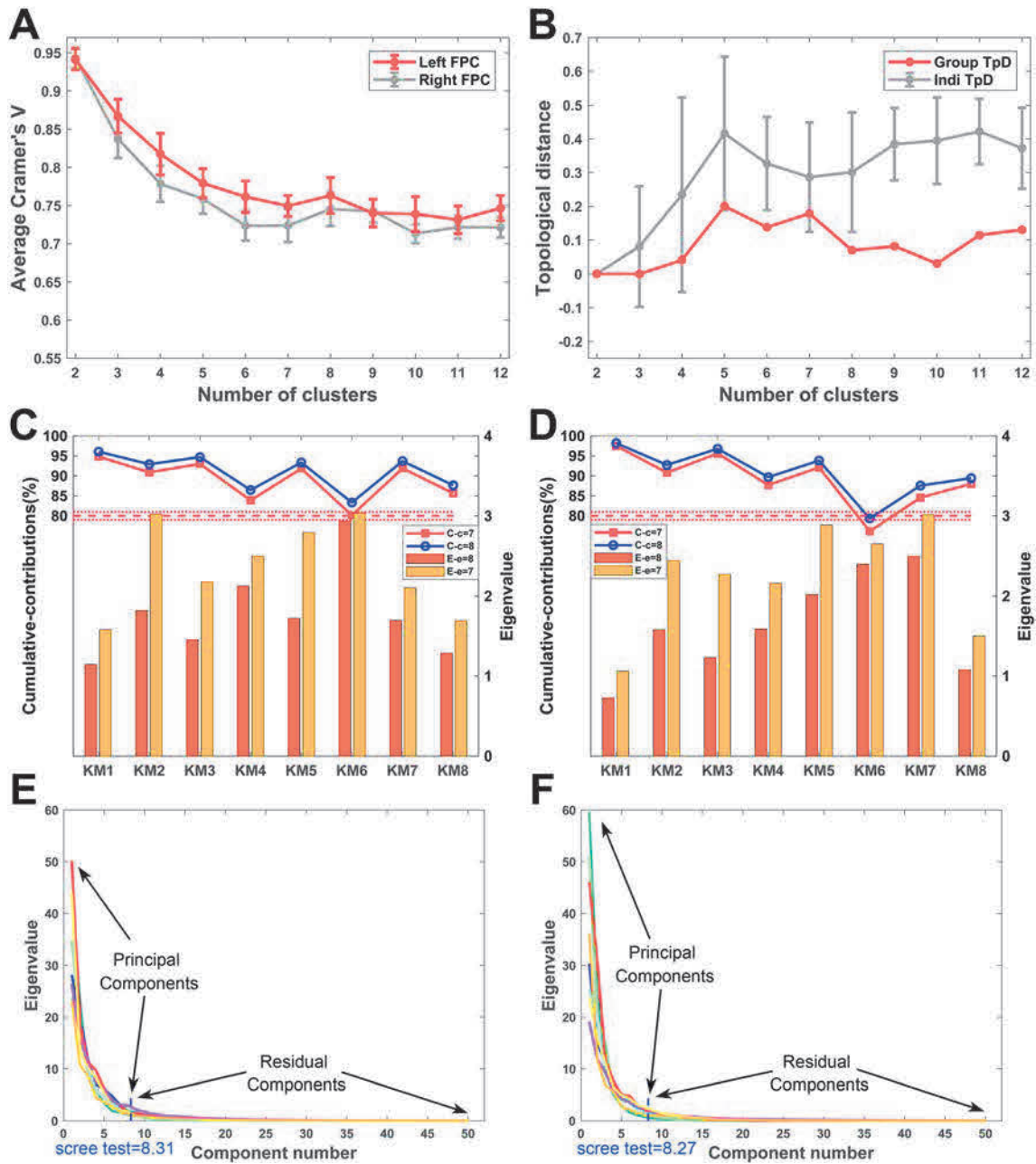


Fig. 2 Cross-validity indices of parcellation of the FPC. **A, B** Cluster number consistency and topological similarity indicated by the average Cramer's V (A) and TpD (B). The red/gray polyline of the average Cramer's V indicates the clustering consistency of the left/right brain across subjects. The red/gray polyline of the TpD denotes the similarity of the topological arrangement of presumptive homologous regions between hemispheres and across subjects (KM1, KM2, ..., KM8) at the group/individual level. **C, D** Cumulative contribution

rates and eigenvalues for the left (C) and right (D) hemisphere under criterion 1 and criterion 2. A comparison of the blue and red curves reveals that eight principal components (blue) are superior to seven (red). The bars represent the eigenvalues of the seventh (yellow) and eighth (brown) components. **E, F** Graph of principal components according to their eigenvalue sizes for the left (E) and right (F) hemispheres for all specimens.

Cluster C4

A distinct cluster, C4, occupied the lateral orbital part of the FPC. In the coronal plane, following an anterior-to-posterior direction, it was below Cluster C6 and its medial border was delimited by Cluster C3, gradually disappearing

with Cluster C6. Its lateral part was below the ps and extended medially above the ps near the interface of ps and ros from the sagittal section followed by its extension to the anterior of area 11 in the lateral orbitofrontal cortex. The connectivity of Cluster C4 was similar to that of cluster C3. The difference was that the former had stronger

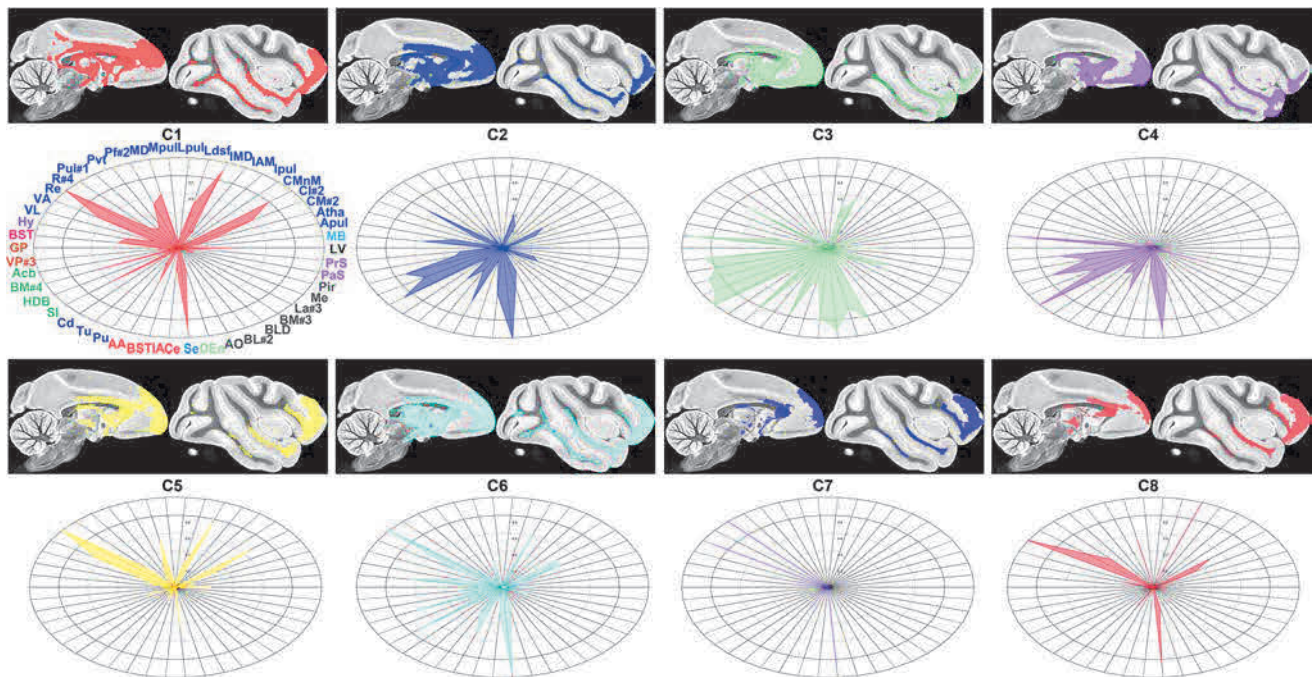


Fig. 5 Anatomical connectivity patterns between each subarea and subcortical structures (left hemisphere). Population maps of the whole brain anatomical connectivity patterns shown in CIVM space using MRIcron help to qualitatively identify differential connections, and the connection pattern of each area is colored differently. Anatomical connectivity fingerprints quantitatively identify the differences of the connectivity patterns between each subarea and the subcortical structures. For the fingerprints, we classified the connected regions on

the periphery of the ellipse based on the different structure to which they belong, and display them using different color fonts (starting from area LV, and anticlockwise, the brain regions with different color fonts belong to the lateral ventricles, midbrain, hypothalamus, central subpallium, pallium, paraseptal subpallium, striatum, subpallial amygdala, subpallial septum, lateral pallium, ventral pallium, and medial pallium). Each subarea is named C1, C2, ..., C8.

connections with the lateral and orbital frontal cortex than the latter. For instance, stronger connections with Cluster C4 were detected throughout area 11, the ventral part of area 10, and the orbital preisocortex. In contrast, the connections with subcortical structures, including SI, Se, BM#4, and BST, were similar but fewer than those for Cluster C3.

Cluster C5

C5 covered a small region, relative to the other subregions, in the medial dorsal part of the FPC. The distribution of Cluster C5 was mainly around the white matter above the cgs from the coronal plane. It exhibited strong connectivity with the dorsolateral frontal cortex and ProM, including areas 9/46D, 24a, 9/46D, and the dorsal and medial parts of area 10. It also had a stronger connection with 6VR than the other subareas. Some subcortical structures, i.e. Re, IMD, VA, and C1#2, had a strong connectivity with Cluster C5.

Cluster C6

C6, which was located in the lateral middle part of the FPC, was focused around the anterior of the aspd. It lay above

the ps and a portion of this subregion extended to the medial surface. Following a medial-to-lateral direction, its superior and posterior borders were delimited by Clusters C1 and C2, then, gradually, with the disappearance of these two subdivisions, its superior border was limited by Cluster C8. This subdivision was around the rostral part of the ps and covered part of its anterior bank. Its inferior adjacent subarea was Cluster C4. Cluster C6 was mainly connected to the anterior-most frontal cortex, 46, 47, and the orbital preisocortex. With respect to the subcortical structures, it had a strong connectivity with Re, Se, SI, BM#4, and BST.

Cluster C7

C7 occupied the dorsal lateral part of the FPC. It was delimited posteriorly by Cluster C5 near the medial surface, gradually limited by the adjacent area 9 and covered the posterior bank of the aspd following a medial-to-lateral direction. The ventral extension was limited by Cluster C8. It was characterized by a very strong connectivity with the dorsal and lateral frontal lobe, including the adjacent areas of 10D, 9/46D, 9/46V, 45, 46, and 9. In addition, the subcortical structures R#4 and VA shared a stronger connectivity seeded from area C7.

Cluster C8

C8 was located in the dorsal inferior part of the lateral FPC. It covered a large part above the most anterior limb of the ps. C8 occupied a small area near the medial surface, relative to the other clusters. Following a medial-to-lateral direction, it was gradually sandwiched between C7 and C6 and extended to the superior margin of area 46D near the most lateral surface. The connectivity patterns of Clusters C7 and C8 were very similar, but the latter had stronger connections with areas 9/46V, 46, 47, and ProM.

Similarity Analysis and Repeatability of Connected Brain Regions, and FPC Modularity Structure

After the connection differences between subdivisions were determined, the inter-individual correlation index revealed a high level of connection similarity for the eight clusters (Fig. 6A and S4A), which suggests that the connectivities of parcellation results are very consistent among the eight subjects. Using the CoCoMac data, we identified the areas derived from our connectivity data and theirs that were derived from the axonal tracer projections that originate in the FPC, and calculated an 88.24% coherence (Fig. 6B and S4B), which to some extent suggests repeatability of the connected areas and the reliability of our parcellation results.

Then, using the improved hierarchical clustering method, the eight subdivisions were grouped into three contiguous boundary connectivity families: medial FPC (MF; C1, C2, C3), dorsolateral FPC (DLF; C5, C6, C7, C8), and lateral orbital FPC (LOF; C4) (Fig. 6C and S4A). A dendrogram was constructed using the standardized Euclidean distance (seuclidean) and average linkage (average) method because this method led to the most faithful representation of the original distances based on their highest cophenetic coefficients (left brain, 0.92; right brain, 0.94). As a mediator of network modularity in the macaque [66], these FPC subregions connected to other regions with inter-area coordination; in detail, the MF mainly connected the “medial” brain network, the DLF connected to most of the regions of the dorsal brain network, and the LOF mainly connected to the orbital brain regions.

Further, based on the anatomical connections of each subarea and the modular analysis, we found that these subareas were collaboratively involved in the DMN, SIN (Fig. 6D and S4D), and metacognition network. First, previous studies have revealed that the macaque FPC is functionally correlated with the DMN [22, 67]. We found that the DLF, in conjunction with an extension to the medial part (C1, C2), had strong connection probabilities to areas of the DMN. In particular, areas C1, C5, and C7 had a strong connection with the DMN core. Second, our results

revealed that the orbital and medial FPC play an important role in connectivity to the SIN, and the medial FPC showed a stronger connection than other parts of the FPC with the exclusively SIN (ESIN) [23]. The medial FPC (areas C1, C2, and C5) had a strong connection with areas 32, 10M, 24b, 9M, 44, 6VR, and 24b. Areas C3, C4, and C6 showed a strong connection with areas 14, 47, OPro, 11L, 10o, R36, ST1, ST2, TAa, TPro, Cd. In addition, the dorsal FPC had strong connections with the regions involved in metacognition; in particular, subareas C5, C7, and C8 had a strong connection with the cortical region anterior to the pspd (aSPSD) and metamemory processing regions, including areas 9L, 9/46D, 46D, 8A, and 6VR. Besides, the regions of metacognitive performance for remote memory have mainly been identified in the dorsal frontal lobe; dorsal FPC showed strong connections with them. These dorsal FPC subareas mainly connected the memory retrieval regions, including the anterior bank of the frontal cortex (area 45B) and area 9/46V, but we found no connections between the FPC and the parietal cortex. Further, subarea C5 had a strong connection with the cortical network module of retrieval-related regions (area DI and 6VR).

Discussion

In this study, we performed a tractography-based parcellation and divided the macaque FPC into eight subregions, and then elucidated the anatomical connectivity patterns of the macaque FPC at the subregional level, and finally explored the modularity of the eight subareas. To more fully elucidate the reasonability of our parcellation results, we compared our parcellation and anatomical connectivity results from DTI data with previous relevant studies from a variety of perspectives, including the overlap between our boundaries and those from other parcellation results and between our connection results and those that were obtained using tracer injections.

First, the eight subregions were distinguished by different boundaries, some of which coincided well with those of other parcellation studies [30, 68]. The parcellation results of the macaque FPC have varied over the past few decades. Initially, the FPC was recognized as a single area; then it was subdivided into two areas by Carmichael, Price [20], who thought that the medial part of the FPC had a homogeneous granular structure. Subsequently, however, different connections of subareas in this area were found [19, 69, 70]. Here, we found that the orbital FPC can be further subdivided into two subregions (C3 and C4) and area 10m of Carmichael, Price [20] can be subdivided into a number of subregions (Fig. 7A). In addition, the dorsolateral boundary (G-b3) and another lateral boundary (G-

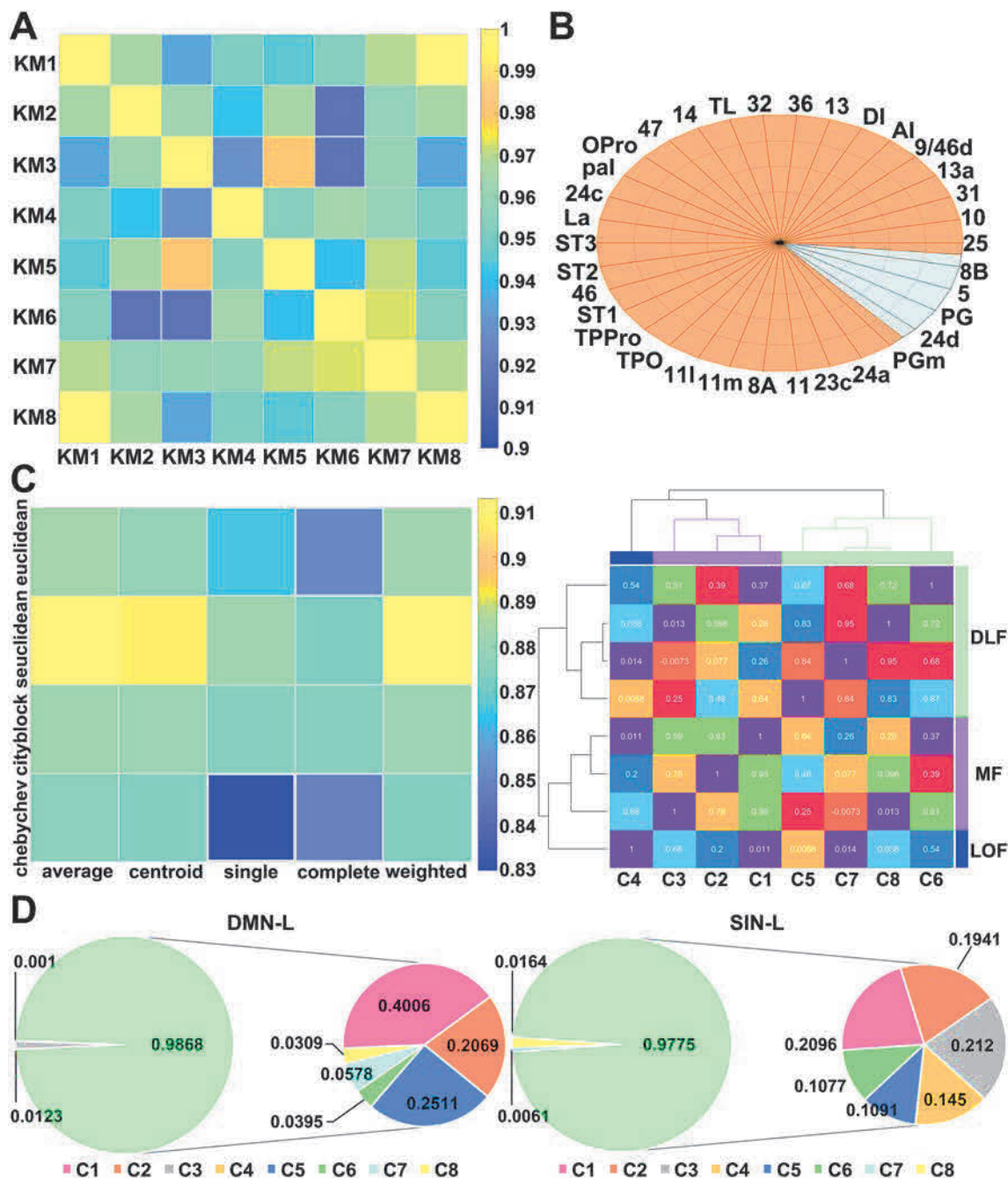


Fig. 6 Similarity analysis and repeatability of connected brain regions, and modularity analysis (left hemisphere). **A** The connectivity similarity matrix for all the subareas across different subjects (KM1, KM2, ..., KM8). **B** Consistency comparison between tracer projections of CoCoMac and the anatomical connections identified by our study. The areas around the outside edges of the ellipse are the tracer results from CoCoMac; the areas marked in orange are the anatomical connections we found, and the gray means that we did not find these connections. **C** Optimization cophenetic coefficient parameter selection, connectivity similarity matrix, and dendrogram

constructed on the basis of connectivity similarity for all the clusters. **D** Diagrammatic summary of the primary connections between the subdivisions and the regions of different functional networks. The connection probabilities involved in different functional networks for each subarea are normalized in this display. Each block of the pie chart represents the anatomical connection after normalization between each subarea and the regions of different functional networks. The green circles on the left represent the sum of the primary connections on the right.

b4) above the rostral ps in the macaque frontal cortex in another parcellation result [68] have positions similar to the boundaries between C7 and C8 (b3) and between C8 and

C6 (b4), respectively, in our parcellation results. The lateral boundary (b4) and another boundary (b5) along the anterior extension of the ros were approximately the

Table 2 Consistent cortical connections from our tractography compared with the data acquired in previous studies using tracer injection.

Experiments	Cases/case no.	Injection site(s)	Corresponding subregions	Projections found
Barbas and Mesulam [73]	Case V, (HRP)	Rostral principalis region (rostral 46 and 10)	C6, C8, C7	Dorsal and medial parts of the FPC, 14, 46, 12, 11, 9/46D, R36, TTPAI, ST1, ST2, ST3, TAa
Barbas and Pandya [27]	Case 1, (isotope injection)	OPro		C3, C4, C6, C7
	Case 3, (isotope injection)	14, 13		C3, C4
	Case 4, (isotope injection)	Orbital area 12		
	Case 6, (isotope injection)	46		
Barbas <i>et al.</i> [74]	Case ARb, (FB)	Medial area 10	C1, C5	9, 46, 24, 32, 12, 14, 11, 25, 8, 13, OPro, TTPAI, TPro
Germuska <i>et al.</i> [12]	Cases BA, (BDA)		C4	ST1, ST2, TTPAI, TPro
	Cases BC, BF, (BDA)		C7, C8	ST1, ST2, ST3
Parvizi <i>et al.</i> [75]	M1-BDA-23B, M1-FB-31, M2-BDA-23a/b, M3-BDA-29/30(23a)	23b, 31, 23a, 23b, 29/30(23a)		Dorsal and dorsomedial parts of the FPC (C1, C2, C5, C8)
Petrides and Pandya [76]	Case 4, (DY)	Lateral area 9		Dorsal subareas (C5, C7)
	Case 6, (FB)	9/46d		C1, C5
	Case 8, (FB)	Dorsal area 46 (close to FPC)		FPC
Petrides and Pandya [72]	Case 1, (isotope injection)	Area 10	FPC	9, 46, 32, 11, 13, 14, 8A, 47/12, 45, 23, 24, 25, 30, OPro, ST1, ST2, ST3, TAa, TPro, Pal, AI, DI
	Case 2, (isotope injection)	Ventral and orbital area 10	C4	46, 10, 11, 14, 47/12, 14, 13, 32, 25, TAa
Saleem <i>et al.</i> [26]	OM19 (FB)	10o	C3, C4	47/12(12o,12l), 10mr, 10o, 46(46d), 13(13b), 10mc, 11m, 14(14r/c), 32, AI, ST1, ST2, ST3
	OM69 (FB), OM64 (FB)	10mr	C1, C2, C6, C8	46(46d, 46v, 46f), 45(45a, 45b), 8A(8Ad), 10mr, 10o, 10mc, 9 (9d, 9m), 13(13m/l, 13a, b), 47/12(12o), 11m, 14(14r/c), 32, AI, 25, ST1, ST2, ST3, 24a, 24b, 24c, 23, 29, 30

facilitate functional studies of localized areas and help to understand brain mechanisms [62, 63, 83]. Our results from the hierarchical clustering for the connectivity-based parcellation revealed that the different subregions collaborate to connect different functional networks.

We found that the orbital FPC connected with most of the regions of the “orbital” prefrontal network; the medial FPC mainly linked to the “medial” prefrontal network, which is consistent with the descriptions of previous network partitions [84]. Subsequently, eight subareas are collaboratively involved in the DMN, SIN, and metacognition network. The FPC has a functional involvement with the SIN [23, 85], and the medial frontal regions around the rostral tip of the ACC show significant activity during interactive social communication [86]. Correspondingly, we found that area C1, which is located around the rostral tip of the ACC, had a strong connection with the regions of the SIN. The theory of mind (ToM) and the DMN intersectional regions in the human brain have a fairly plausible homology and locations similar to the ESIN

regions of the macaque brain. These macaque areas are in locations similar to the DMN and ToM intersectional regions in humans and share anatomical features with the human ToM and ESIN; these findings are confirmed by our results. With respect to the third function, metacognition, in macaque monkeys only the bilateral FPCs are enlisted for the metacognitive evaluation of non-experienced items, the dorsal FPC is only significantly correlated with metacognitive performance with respect to non-experienced items and serves as the neural substrate for awareness of one’s own ignorance in macaques [24]. The FPC is functionally connected with the aPSPD, which is essential for the metacognitive judgment of remote memory; in particular, there is a strong resting-state functional connectivity with area 9 that is related to metamemory processing [58]. Here, we found anatomical connections between the FPC and the aPSPD with particularly strong connections with area 9. For retrieval of remote memory, the FPC may be involved in metacognitive processing. Anatomical connections between the FPC and area 9 also

Table 3 Consistent subcortical connections from our tractography compared with the data acquired in previous studies using tracer injection.

Experiments	Cases/case no.	Injection site(s)	Corresponding subregions	Projections found
An <i>et al.</i> [69]	Case OM36, (BDA)	10m	C1, C2	dorsolateral midbrain PAG
	Case OM38, (BDA)	10o	C3	
	Case OM32, (FB)	Ventrolateral midbrain PAG		C1, C2, C5, C6, C7, C8
	Case OM35, (FB)	Dorsolateral midbrain PAG		
	Case OM36, (FB)	Rostral dorsolateral midbrain PAG		
	Case OM36, (CTb)	Lateral midbrain PAG		
Ferry <i>et al.</i> [77]	Case OM38, (BDA)	10m	C1, C2	Cd, Acb
	Case OM38, (BDA)	10o	C3, C4	Cd, Acb, Pu
Ghashghaei <i>et al.</i> [78]	Case BD_R_BDA	BM#3, BL#2, BLD, Me, Ce		C1, C2, C3, C4, C6
	Case BD_L_BDA			
Hsu and Price [79]	Case OM74, (FR)	10m	C1, C3	MITN, Re, CM#2, CMnM, Cl#2
	Case OM66, (FR)			
Ongur <i>et al.</i> [70]	Case OM26, (FB)	Lateral hypothalamus		FPC (10m, 10o)
	Case OM27, (FB)	Ventromedial hypothalamic nucleus		
	Case OM37, (FB)	Anterior hypothalamus		
Petrides and Pandya [72]	Case 1, (isotope injection)	Area 10	FPC	Lv, Cd, Pu, thalamus, Pul#1, IAM, IMD, Hy, amygdala, BL#2, BLD, BM#3, hypothalamus
Rempel-Clover and Barbas [80]	Case SF, (HRP)	Dorsal area 10	C6, C8	hypothalamus
Romanski <i>et al.</i> [81]	Case Fig. 7C, (WGA-HRP)	FPC	C1, C2, C4, C6	MPul, Pul#1
	Case 1, (WGA-HRP)	Medial pulvinar		C1, C4
	Case 2, (WGA-HRP)	Central/lateral PM		C4
	Case 3, (WGA-HRP)	Medial region of the PM (intruded on caudal, medial regions of the mediodorsal nucleus)		C1, C3,
Cho <i>et al.</i> [82]	Cases J12FR, J12LY, J16LY, J8LY, J12FS	BM#4		C1, C2, C3, C4

FB fast blue, *DY* diamidino yellow, *HRP* horseradish peroxidase, *BDA* biotinylated dextran amine, *CTb* cholera toxin subunit B, *WGA-HRP* wheat germ agglutinin-horseradish peroxidase, *FR* fluoro-ruby, *LY* Lucifer yellow, *FS* fluorescein.

suggested that these two regions work cooperatively to support metacognitive judgments in ecological situations. These findings suggested a consistent relationship between functional activation and connectivity fingerprints [87]. Previous studies have reported that the corresponding memory-related regions between humans and macaques have not been established. Consistent with the previous studies [6, 26, 72], we found no connections between the FPC and the parietal regions. Notably, the medial subareas C1 and C2 had rich connections with other regions of different functional networks, a finding which suggests that these two subareas play an important role in coordinating other subareas to participate in different network functions.

To sum up, the above comparative findings validate the reliability of our parcellation results and indicate that anatomical connections and tracer-injection studies provide consistent results. We need to mention that, although different studies [30, 68] have often disagreed about the definition of the borders of the subareas in the macaque frontal cortex, if a boundary near a similar position was found in other studies, we were more convinced of its authenticity. The anatomical connections estimated from diffusion tractography may susceptible to false positives (the tracking of pseudo-pathways) and false negatives (the inability to track pathways that have been found), and do not furnish the level of detail of the gold standard based on

invasive tract-tracing techniques, but DTI has proven to be an indispensable method and can offer invaluable insights for neuroscience [88] and neuroanatomy [89, 90], including the discovery of new pathways [31], the description of whole-brain connectivity information [32], and the refinement of brain regions [28].

The methods used in the current study are discussed below, along with their advantages, disadvantages, and problems of validation. First, previous studies have suggested that the CBP method can yield more fine-grained parcellations than traditional cytoarchitectonic mapping, and compared with other neuroimaging methods, it has the pivotal strength to actually map distinct brain regions without sample size restriction [33, 91]. Second, to some extent, challenges were raised in CBP studies because of the inter-individual variability, which made it difficult to relate the anatomical connectivity patterns of a region to its functional roles [29]. Third, in this study, the efficiency of the parcellation framework based on CBP and the parameters for parcellation have been validated by many studies [33, 43, 48, 92]. In general, it is worth noting that all the parameters must be reasonable, which means that they cannot be uncommon extreme values, otherwise wrong results will be tracked. One of the effective verification methods is to compare the results of the anatomical connections with those of tracer injection [93]. There are many parameters in tractography, and all of these affect the results of fiber tracking to different degrees, more or less (i.e., number of samples, distance correction, step length, curvature, exclusion mask, track style, number of steps per sample ...). In particular, some studies have reported the effects of these parameters [94–99]. However, in the current study, we mainly set two parameters (number of samples = 15000; step size = 0.2 mm), other parameters are based on the default values. All these parameters were based on previous studies [33, 42] and the official instructions of FSL. Tournier *et al.* have revealed that the dispersion in tractography is dependent on the step size; small step sizes reduce the spread of probabilistic tracking results [98]. Therefore, to explore the sensitivity of the parcellation results to the number of samples, here we used different samples of tractography and carried out repetitive parcellation experiments on the macaque FPC (left brain, see details in supplementary materials; the details of the experiment and the stability validation of the parcellation method have also been described in our previous study [42]). In addition, for CoCoMac, there are still some challenges in automatically extracting data from published studies [100]. The results of tracer experiments such as those obtained from the CoCoMac database or other databases [101] are not only limited to invasive approaches to some extent, but also limited to the number of samples and lack of consideration of individual variation. The data

may also miss tiny pathways and produce slightly different projections caused by individual differences, so we agree that the combination of tractography and the tracer injection results is an effective and complementary way to assess brain connectivity, which is crucial for accurately mapping structural connectivity [102]. Advances in MRI have made it increasingly feasible to calculate their connections [93], and DTI tractography is capable of providing inter-regional connectivity comparable to neuroanatomical connectivity [103]. In the current study, the consistency of the connectivity comparison with other relevant studies increases the confidence in the structural connectivity of the macaque FPC and is important for studying FPC-related networks of brain functions and their disorders [104, 105]. In future, we plan to conduct a tracer injection based on the parcellation results in the current study to explore the detailed connectivity of each subregion by a quantitative cytoarchitectonic analysis and evaluate the degree of consistency between anatomical connections and tracer injections in the same subjects. Furthermore, we have released the detailed parcellation pipeline and will then apply it to the whole macaque brain to obtain a fine-grained macaque brain atlas.

Besides, compared with other methods, the framework of CBP provided in the current study not only inherited the advantages of other classical CBP methods [48, 50] but also improved them in selecting the optimal clustering scheme and making them more adaptable to non-human primates [42]. The results of the modularity could heuristically facilitate functional studies of localized areas and exploration of the connectivity patterns of different functional networks is important for understanding brain mechanisms and evolution. Furthermore, based on previous studies [68], our proposed hierarchical clustering algorithm can automatically select the best clustering parameters to generate an optimal clustering result by calculating and comparing all the cophenetic correlation coefficients, which is helpful for users to group the clusters into different broad connectivity families.

Conclusions

In the present study, we used a CBP scheme for the macaque FPC and divided it into eight distinct subareas. As a powerful analytical framework, CBP not only reveals the spatial distribution of cytoarchitectural boundaries but also provides supplementary information related to the organization of anatomical and different functional networks among brain regions.

Furthermore, by using a hierarchical clustering algorithm, we identified the modularity of the bilateral FPC and found synergy related to the DMN, SIN, and metacognition

network among the subdivisions. We hope that all of the above information is helpful for understanding the anatomy and circuitry of related regions and can facilitate the use of available knowledge in FPC-related clinical research, especially in understanding the dysfunctions caused by complex diseases.

Acknowledgements We thank E. Rhoda and Edmund F. Peruzzi for constructive comments on the manuscript and great help with the English language. This work was supported by the National Natural Science Foundation of China (91432302 and 31620103905), the Science Frontier Program of the Chinese Academy of Sciences (QYZDJ-SSW-SMC019), the National Key R&D Program of China (2017YFA0105203), Beijing Municipal Science and Technology Commission (Z161100000216152, Z161100000216139, Z181100001518004 and Z171100000117002), the Beijing Brain Initiative of Beijing Municipal Science and Technology Commission (Z181100001518004), and the Guangdong Pearl River Talents Plan (2016ZT06S220).

Open Access This article is licensed under a Creative Commons Attribution 4.0 International License, which permits use, sharing, adaptation, distribution and reproduction in any medium or format, as long as you give appropriate credit to the original author(s) and the source, provide a link to the Creative Commons licence, and indicate if changes were made. The images or other third party material in this article are included in the article's Creative Commons licence, unless indicated otherwise in a credit line to the material. If material is not included in the article's Creative Commons licence and your intended use is not permitted by statutory regulation or exceeds the permitted use, you will need to obtain permission directly from the copyright holder. To view a copy of this licence, visit <http://creativecommons.org/licenses/by/4.0/>.

References

1. Tsujimoto S, Genovesio A, Wise SP. Evaluating self-generated decisions in frontal pole cortex of monkeys. *Nat Neurosci* 2010, 13: 120–126.
2. Passingham R. How good is the macaque monkey model of the human brain? *Curr Opin Neurobiol* 2009, 19: 6–11.
3. Gibbs RA, Rogers J, Katze MG, Bumgarner R, Weinstock GM, Mardis ER, *et al.* Evolutionary and biomedical insights from the rhesus macaque genome. *Science* 2007, 316: 222–234.
4. Gebhard R, Zilles K, Schleicher A, Everitt BJ, Robbins TW, Divac I. Parcellation of the frontal cortex of the New World monkey *Callithrix jacchus* by eight neurotransmitter-binding sites. *Anat Embryol (Berl)* 1995, 191: 509–517.
5. Fuster JnM. The prefrontal cortex—An update: Time is of the essence. *Neuron* 2001, 30: 319–333.
6. Rushworth MF, Noonan MP, Boorman ED, Walton ME, Behrens TE. Frontal cortex and reward-guided learning and decision-making. *Neuron* 2011, 70: 1054–1069.
7. Koechlin E, Hyafil A. Anterior prefrontal function and the limits of human decision-making. *Science* 2007, 318: 594–598.
8. Neubert FX, Mars RB, Thomas AG, Sallet J, Rushworth MF. Comparison of human ventral frontal cortex areas for cognitive control and language with areas in monkey frontal cortex. *Neuron* 2014, 81: 700–713.
9. Mansouri FA, Koechlin E, Rosa MGP, Buckley MJ. Managing competing goals—a key role for the frontopolar cortex. *Nat Rev Neurosci* 2017, 18: 645–657.
10. Tsujimoto S, Genovesio A, Wise SP. Frontal pole cortex: encoding ends at the end of the endbrain. *Trends Cogn Sci* 2011, 15: 169–176.
11. Bosch EA, Piekema C, Buckley MJ. Essential functions of primate frontopolar cortex in cognition. *Proc Natl Acad Sci U S A* 2015, 112: E1020–E1027.
12. Germuska M, Saha S, Fiala J, Barbas H. Synaptic distinction of laminar-specific prefrontal-temporal pathways in primates. *Cereb Cortex* 2006, 16: 865–875.
13. Joyce MKP, Barbas H. Cortical connections position primate pre 25 as a keystone for interoception, emotion, and memory. *J Neurosci* 2018, 38: 1677–1698.
14. Medalla M, Barbas H. Anterior cingulate synapses in prefrontal areas 10 and 46 suggest differential influence in cognitive control. *J Neurosci* 2010, 30: 16068–16081.
15. Medalla M, Lera P, Feinberg M, Barbas H. Specificity in inhibitory systems associated with prefrontal pathways to temporal cortex in primates. *Cereb Cortex* 2007, 17 Suppl 1: i136–i150.
16. Brodmann K. *Vergleichende Lokalisationslehre der Grosshirnrinde in ihren Prinzipien dargestellt auf Grund des Zellenbaues*. Barth, 1909.
17. Walker AE. A cytoarchitectural study of the prefrontal area of the macaque monkey. *Journal of Comparative Neurology* 1940, 73: 59–86.
18. Paxinos G, Huang XF, Toga AW. *The Rhesus Monkey Brain: in Stereotaxic Coordinates*. (2 ed.). 2009.
19. Saleem KS, Kondo H, Price JL. Complementary circuits connecting the orbital and medial prefrontal networks with the temporal, insular, and opercular cortex in the macaque monkey. *J Comp Neurol* 2008, 506: 659–693.
20. Carmichael ST, Price JL. Architectonic subdivision of the orbital and medial prefrontal cortex in the macaque monkey. *J Comp Neurol* 1994, 346: 366–402.
21. Mantini D, Vanduffel W. Emerging roles of the brain's default network. *Neuroscientist* 2013, 19: 76–87.
22. Mantini D, Gerits A, Nelissen K, Durand JB, Joly O, Simone L, *et al.* Default mode of brain function in monkeys. *J Neurosci* 2011, 31: 12954–12962.
23. Sliwa J, Freiwald WA. A dedicated network for social interaction processing in the primate brain. *Science* 2017, 356: 745–749.
24. Miyamoto K, Setsuie R, Osada T, Miyashita Y. Reversible silencing of the frontopolar cortex selectively impairs metacognitive judgment on non-experience in primates. *Neuron* 2018, 97: 980–989 e986.
25. Mansouri FA, Buckley MJ, Mahboubi M, Tanaka K. Behavioral consequences of selective damage to frontal pole and posterior cingulate cortices. *Proc Natl Acad Sci U S A* 2015, 112: E3940–E3949.
26. Saleem KS, Miller B, Price JL. Subdivisions and connective networks of the lateral prefrontal cortex in the macaque monkey. *J Comp Neurol* 2014, 522: 1641–1690.
27. Barbas H, Pandya DN. Architecture and intrinsic connections of the prefrontal cortex in the rhesus monkey. *J Comp Neurol* 1989, 286: 353–375.
28. Fan L, Li H, Zhuo J, Zhang Y, Wang J, Chen L, *et al.* The human brainnetome atlas: A new brain atlas based on connective architecture. *Cereb Cortex* 2016, 26: 3508–3526.
29. Eickhoff SB, Yeo BTT, Genon S. Imaging-based parcellations of the human brain. *Nat Rev Neurosci* 2018, 19: 672–686.
30. Cerliani L, D'Arceuil H, Thiebaut de Schotten M. Connectivity-based parcellation of the macaque frontal cortex, and its relation with the cytoarchitectonic distribution described in current atlases. *Brain Struct Funct* 2017, 222: 1331–1349.

31. Assaf Y, Johansen-Berg H, Thiebaut de Schotten M. The role of diffusion MRI in neuroscience. *NMR Biomed* 2019, 32: e3762.
32. O'Donnell LJ, Daducci A, Wassermann D, Lenglet C. Advances in computational and statistical diffusion MRI. *NMR Biomed* 2019, 32: e3805.
33. Xia X, Fan L, Hou B, Zhang B, Zhang D, Cheng C, *et al.* Fine-grained parcellation of the macaque nucleus accumbens by high-resolution diffusion tensor tractography. *Front Neurosci* 2019, 13: 709.
34. Calabrese E, Badea A, Coe CL, Lubach GR, Shi Y, Styner MA, *et al.* A diffusion tensor MRI atlas of the postmortem rhesus macaque brain. *Neuroimage* 2015, 117: 408–416.
35. Balbastre Y, Riviere D, Souedet N, Fischer C, Herard AS, Williams S, *et al.* A validation dataset for Macaque brain MRI segmentation. *Data Brief* 2018, 16: 37–42.
36. Haile TM, Bohon KS, Romero MC, Conway BR. Visual stimulus-driven functional organization of macaque prefrontal cortex. *Neuroimage* 2019, 188: 427–444.
37. Tasserie J, Grigis A, Uhrig L, Dupont M, Amadon A, Jarraya B. Pypreclin: An automatic pipeline for macaque functional MRI preprocessing. *Neuroimage* 2019: 116353.
38. Yushkevich PA, Piven J, Hazlett HC, Smith RG, Ho S, Gee JC, *et al.* User-guided 3D active contour segmentation of anatomical structures: significantly improved efficiency and reliability. *Neuroimage* 2006, 31: 1116–1128.
39. Xu J, Wang J, Fan L, Li H, Zhang W, Hu Q, *et al.* Tractography-based parcellation of the human middle temporal gyrus. *Sci Rep* 2015, 5: 18883.
40. Avants BB, Tustison NJ, Song G, Cook PA, Klein A, Gee JC. A reproducible evaluation of ANTs similarity metric performance in brain image registration. *Neuroimage* 2011, 54: 2033–2044.
41. Liang S, Wang Q, Kong X, Deng W, Yang X, Li X, *et al.* White matter abnormalities in major depression biotypes identified by diffusion tensor imaging. *Neurosci Bull* 2019, 35: 867–876.
42. He B, Yang Z, Fan L, Gao B, Li H, Ye C, *et al.* MonkeyCBP: A toolbox for connectivity-based parcellation of monkey brain. *Front Neuroinform* 2020, 14: 14.
43. Wang J, Zuo Z, Xie S, Miao Y, Ma Y, Zhao X, *et al.* Parcellation of macaque cortex with anatomical connectivity profiles. *Brain Topogr* 2018, 31: 161–173.
44. Behrens TE, Berg HJ, Jbabdi S, Rushworth MF, Woolrich MW. Probabilistic diffusion tractography with multiple fibre orientations: What can we gain? *Neuroimage* 2007, 34: 144–155.
45. Sani I, McPherson BC, Stemmann H, Pestilli F, Freiwald WA. Functionally defined white matter of the macaque monkey brain reveals a dorso-ventral attention network. *Elife* 2019, 8.
46. Takemura H, Caiafa CF, Wandell BA, Pestilli F. Ensemble Tractography. *PLoS Comput Biol* 2016, 12: e1004692.
47. Johansen-Berg H, Behrens TE, Robson MD, Drobniak I, Rushworth MF, Brady JM, *et al.* Changes in connectivity profiles define functionally distinct regions in human medial frontal cortex. *Proc Natl Acad Sci U S A* 2004, 101: 13335–13340.
48. Zhuo J, Fan L, Liu Y, Zhang Y, Yu C, Jiang T. Connectivity profiles reveal a transition subarea in the parahippocampal region that integrates the anterior temporal-posterior medial systems. *J Neurosci* 2016, 36: 2782–2795.
49. Fan L, Wang J, Zhang Y, Han W, Yu C, Jiang T. Connectivity-based parcellation of the human temporal pole using diffusion tensor imaging. *Cereb Cortex* 2014, 24: 3365–3378.
50. Liu H, Qin W, Li W, Fan L, Wang J, Jiang T, *et al.* Connectivity-based parcellation of the human frontal pole with diffusion tensor imaging. *J Neurosci* 2013, 33: 6782–6790.
51. Tungaraza RL, Mehta SH, Haynor DR, Grabowski TJ. Anatomically informed metrics for connectivity-based cortical parcellation from diffusion MRI. *IEEE J Biomed Health Inform* 2015, 19: 1375–1383.
52. Bzdok D, Heeger A, Langner R, Laird AR, Fox PT, Palomero-Gallagher N, *et al.* Subspecialization in the human posterior medial cortex. *Neuroimage* 2015, 106: 55–71.
53. Kelly C, Uddin LQ, Shehzad Z, Margulies DS, Castellanos FX, Milham MP, *et al.* Broca's region: linking human brain functional connectivity data and non-human primate tracing anatomy studies. *Eur J Neurosci* 2010, 32: 383–398.
54. Thiebaut de Schotten M, Urbanski M, Valabregue R, Bayle DJ, Volle E. Subdivision of the occipital lobes: an anatomical and functional MRI connectivity study. *Cortex* 2014, 56: 121–137.
55. Wold S. Cross-validatory estimation of the number of components in factor and principal components models. *Technometrics* 1978, 20: 397–405.
56. Kaiser HF. The application of electronic computers to factor analysis. *Edu Psychol Measur* 1960, 20: 141–151.
57. Bakker R, Tiesinga P, Kotter R. The scalable brain atlas: Instant web-based access to public brain atlases and related content. *Neuroinformatics* 2015, 13: 353–366.
58. Miyamoto K, Osada T, Setsuie R, Takeda M, Tamura K, Adachi Y, *et al.* Causal neural network of metamemory for retrospection in primates. *Science* 2017, 355: 188–193.
59. Xia X, Fan L, Cheng C, Cheng L, Cao L, He B, *et al.* Mapping connective differences between humans and macaques in the nucleus accumbens shell-core architecture. *bioRxiv* 2020: 2020.2006.2012.147546.
60. Suárez LE, Markello RD, Betzel RF, Misic B. Linking structure and function in macroscale brain networks. *Trends Cogn Sci* 2020, 24: 302–315.
61. Chen Y, Wang S, Hilgetag CC, Zhou C. Features of spatial and functional segregation and integration of the primate connectome revealed by trade-off between wiring cost and efficiency. *PLOS Computational Biology* 2017, 13: e1005776.
62. Hagmann P, Cammoun L, Gigandet X, Meuli R, Honey CJ, Wedeen VJ, *et al.* Mapping the structural core of human cerebral cortex. *PLoS Biol* 2008, 6: e159.
63. Chen ZJ, He Y, Rosa-Neto P, Germann J, Evans AC. Revealing modular architecture of human brain structural networks by using cortical thickness from MRI. *Cereb Cortex* 2008, 18: 2374–2381.
64. Van Essen DC. Windows on the brain: the emerging role of atlases and databases in neuroscience. *Curr Opin Neurobiol* 2002, 12: 574–579.
65. Van Essen DC, Drury HA, Dickson J, Harwell J, Hanlon D, Anderson CH. An integrated software suite for surface-based analyses of cerebral cortex. *J Am Med Inform Assoc* 2001, 8: 443–459.
66. Wu Z, Ainsworth M, Browncross H, Bell AH, Buckley MJ. Frontopolar cortex is a mediator of network modularity in the primate brain. *bioRxiv* 2019: 2019.2012.2020.882837.
67. Miranda-Dominguez O, Mills BD, Grayson D, Woodall A, Grant KA, Kroenke CD, *et al.* Bridging the gap between the human and macaque connectome: a quantitative comparison of global interspecies structure-function relationships and network topology. *J Neurosci* 2014, 34: 5552–5563.
68. Goulas A, Stiers P, Hutchison RM, Everling S, Petrides M, Margulies DS. Intrinsic functional architecture of the macaque dorsal and ventral lateral frontal cortex. *J Neurophysiol* 2017, 117: 1084–1099.
69. An X, Bandler R, Ongur D, Price JL. Prefrontal cortical projections to longitudinal columns in the midbrain periaqueductal gray in macaque monkeys. *J Comp Neurol* 1998, 401: 455–479.
70. Ongur D, An X, Price JL. Prefrontal cortical projections to the hypothalamus in macaque monkeys. *J Comp Neurol* 1998, 401: 480–505.

71. Ongur D, Ferry AT, Price JL. Architectonic subdivision of the human orbital and medial prefrontal cortex. *J Comp Neurol* 2003, 460: 425–449.
72. Petrides M, Pandya DN. Efferent association pathways from the rostral prefrontal cortex in the macaque monkey. *J Neurosci* 2007, 27: 11573–11586.
73. Barbas H, Mesulam M. Cortical afferent input to the principals region of the rhesus monkey. *Neuroscience* 1985, 15: 619–637.
74. Barbas H, Ghashghaei H, Dombrowski SM, Rempel-Clower NL. Medial prefrontal cortices are unified by common connections with superior temporal cortices and distinguished by input from memory-related areas in the rhesus monkey. *J Comp Neurol* 1999, 410: 343–367.
75. Parvizi J, Van Hoesen GW, Buckwalter J, Damasio A. Neural connections of the posteromedial cortex in the macaque. *Proc Natl Acad Sci U S A* 2006, 103: 1563–1568.
76. Petrides M, Pandya DN. Dorsolateral prefrontal cortex: comparative cytoarchitectonic analysis in the human and the macaque brain and corticocortical connection patterns. *Eur J Neurosci* 1999, 11: 1011–1036.
77. Ferry AT, Ongur D, An X, Price JL. Prefrontal cortical projections to the striatum in macaque monkeys: Evidence for an organization related to prefrontal networks. *J Comp Neurol* 2000, 425: 447–470.
78. Ghashghaei HT, Hilgetag CC, Barbas H. Sequence of information processing for emotions based on the anatomic dialogue between prefrontal cortex and amygdala. *Neuroimage* 2007, 34: 905–923.
79. Hsu DT, Price JL. Midline and intralaminar thalamic connections with the orbital and medial prefrontal networks in macaque monkeys. *J Comp Neurol* 2007, 504: 89–111.
80. Rempel-Clower NL, Barbas H. Topographic organization of connections between the hypothalamus and prefrontal cortex in the rhesus monkey. *J Comp Neurol* 1998, 398: 393–419.
81. Romanski LM, Giguere M, Bates JF, Goldman-Rakic PS. Topographic organization of medial pulvinar connections with the prefrontal cortex in the rhesus monkey. *J Comp Neurol* 1997, 379: 313–332.
82. Cho YT, Ernst M, Fudge JL. Cortico-amygdala-striatal circuits are organized as hierarchical subsystems through the primate amygdala. *J Neurosci* 2013, 33: 14017–14030.
83. Hilgetag CC, Burns GA, O'Neill MA, Scannell JW, Young MP. Anatomical connectivity defines the organization of clusters of cortical areas in the macaque monkey and the cat. *Philos Trans R Soc Lond B Biol Sci* 2000, 355: 91–110.
84. Carmichael ST, Price JL. Connectional networks within the orbital and medial prefrontal cortex of macaque monkeys. *J Comp Neurol* 1996, 371: 179–207.
85. Price JL, Carmichael ST, Drevets WC. Networks related to the orbital and medial prefrontal cortex; a substrate for emotional behavior? *Prog Brain Res* 1996, 107: 523–536.
86. Shepherd SV, Freiwald WA. Functional Networks for Social Communication in the Macaque Monkey. *Neuron* 2018, 99: 413–420 e413.
87. Mars RB, Passingham RE, Jbabdi S. Connectivity fingerprints: From areal descriptions to abstract spaces. *Trends Cogn Sci* 2018, 22: 1026–1037.
88. Jeurissen B, Descoteaux M, Mori S, Leemans A. Diffusion MRI fiber tractography of the brain. *NMR Biomed* 2019, 32: e3785.
89. Newcombe VF, Williams GB, Scoffings D, Cross J, Carpenter TA, Pickard JD, *et al.* Aetiological differences in neuroanatomy of the vegetative state: insights from diffusion tensor imaging and functional implications. *J Neurol Neurosurg Psychiatry* 2010, 81: 552–561.
90. Johansen-Berg H, Rushworth MF. Using diffusion imaging to study human connective anatomy. *Annu Rev Neurosci* 2009, 32: 75–94.
91. Eickhoff SB, Thirion B, Varoquaux G, Bzdok D. Connectivity-based parcellation: Critique and implications. *Hum Brain Mapp* 2015, 36: 4771–4792.
92. Rilling JK, Glasser MF, Preuss TM, Ma X, Zhao T, Hu X, *et al.* The evolution of the arcuate fasciculus revealed with comparative DTI. *Nat Neurosci* 2008, 11: 426–428.
93. van den Heuvel MP, de Reus MA, Feldman Barrett L, Scholtens LH, Coopmans FM, Schmidt R, *et al.* Comparison of diffusion tractography and tract-tracing measures of connectivity strength in rhesus macaque connectome. *Hum Brain Mapp* 2015, 36: 3064–3075.
94. Azadbakht H, Parkes LM, Haroon HA, Augath M, Logothetis NK, de Crespigny A, *et al.* Validation of high-resolution tractography against *in vivo* tracing in the macaque visual cortex. *Cereb Cortex* 2015, 25: 4299–4309.
95. Girard G, Descoteaux M. Anatomical Tissue Probability Priors for Tractography. 2012.
96. Shen K, Goulas A, Grayson DS, Eusebio J, Gati JS, Menon RS, *et al.* Exploring the limits of network topology estimation using diffusion-based tractography and tracer studies in the macaque cortex. *Neuroimage* 2019, 191: 81–92.
97. Sotiropoulos SN. Processing of diffusion MR images of the brain: from crossing fibres to distributed tractography. 2010.
98. Tournier J, Calamante F, Connelly A. Effect of step size on probabilistic streamlines: implications for the interpretation of connectivity analysis. *Proc Intl Soc Mag Reson Med* 2011, 19: 2019.
99. Tournier JD, Calamante F, Connelly A. MRtrix: Diffusion tractography in crossing fiber regions. *Int J Imaging Syst Technol* 2012, 22: 53–66.
100. Stephan KE. The history of CoCoMac. *Neuroimage* 2013, 80: 46–52.
101. Markov NT, Ercsey-Ravasz MM, Ribeiro Gomes AR, Lamy C, Magrou L, Vezoli J, *et al.* A weighted and directed interareal connectivity matrix for macaque cerebral cortex. *Cereb Cortex* 2014, 24: 17–36.
102. Thomas C, Ye FQ, Irfanoglu MO, Modi P, Saleem KS, Leopold DA, *et al.* Anatomical accuracy of brain connections derived from diffusion MRI tractography is inherently limited. *Proc Natl Acad Sci U S A* 2014, 111: 16574–16579.
103. Gao Y, Choe AS, Stepniewska I, Li X, Avison MJ, Anderson AW. Validation of DTI tractography-based measures of primary motor area connectivity in the squirrel monkey brain. *PLoS One* 2013, 8: e75065.
104. Jiang T. Recent progress in basic and clinical research on disorders of consciousness. *Neurosci Bull* 2018, 34: 589–591.
105. Song M, Zhang Y, Cui Y, Yang Y, Jiang T. Brain network studies in chronic disorders of consciousness: Advances and perspectives. *Neurosci Bull* 2018, 34: 592–604.



Genetic Evidence that Dorsal Spinal Oligodendrocyte Progenitor Cells are Capable of Myelinating Ventral Axons Effectively in Mice

Minxi Fang¹ · Qian Yu^{1,2} · Baiyan Ou¹ · Hao Huang¹ · Min Yi¹ · Binghua Xie¹ · Aifen Yang¹ · Mengsheng Qiu¹ · Xiaofeng Xu¹

Received: 15 January 2020 / Accepted: 30 June 2020 / Published online: 13 October 2020
© Shanghai Institutes for Biological Sciences, CAS 2020

Abstract In the developing spinal cord, the majority of oligodendrocyte progenitor cells (OPCs) are induced in the ventral neuroepithelium under the control of the Sonic Hedgehog (Shh) signaling pathway, whereas a small subset of OPCs are generated from the dorsal neuroepithelial cells independent of the Shh pathway. Although dorsally-derived OPCs (dOPCs) have been shown to participate in local axonal myelination in the dorsolateral regions during development, it is not known whether they are capable of migrating into the ventral region and myelinating ventral axons. In this study, we confirmed and extended the previous study on the developmental potential of dOPCs in the absence of ventrally-derived OPCs (vOPCs). In Nestin-Smo conditional knockout (cKO) mice, when ventral oligodendrogenesis was blocked, dOPCs were found to undergo rapid amplification, spread to ventral spinal tissue, and eventually differentiated into myelinating OLs in the ventral white matter with a temporal delay, providing genetic evidence that dOPCs are capable of myelinating ventral axons in the mouse spinal cord.

Keywords Dorsally-derived OPCs · OPC proliferation · Oligodendrocyte differentiation · Myelination

Introduction

Oligodendrocytes (OLs) myelinate axons in the central nervous system (CNS) of vertebrates, enabling the rapid transmission of action potentials and providing structural and metabolic support to neurons. The specification and differentiation of oligodendrocyte progenitor cells (OPCs) are controlled by a complex network of extracellular signals, transcriptional factors, and epigenetic regulators [1]. Elucidation of the signaling pathways that control OL differentiation and myelin formation is a crucial prerequisite for developing novel strategies for myelin repair in several neurological diseases [2].

During embryonic development, OPCs are generated from distinct neural epithelial cells in the spinal cord and brain. The diversity of OPCs based on their origins is known as developmental heterogeneity [3]. In the developing mouse spinal cord, most OPCs initially arise from the ventral ventricular zone (VZ) at embryonic day 12.5 (E12.5) under the influence of Sonic Hedgehog (Shh) signaling from the notochord and floor plate [4, 5]. At around E15.5, a minority of OPCs are generated from the dorsal VZ, independent of Shh signaling [6–8]. Most dorsally-derived OPCs (dOPCs) are confined to the dorsal half of the spinal cord, whereas ventrally derived OPCs (vOPCs) spread widely throughout the entire spinal cord [9, 10]. This raises the questions as to why there is developmental heterogeneity in the OL lineage, and whether different OPC populations fulfill different roles.

In the course of spinal cord development, the dorsal funiculus is initially populated by ventrally-derived OLs

Electronic supplementary material The online version of this article (<https://doi.org/10.1007/s12264-020-00593-5>) contains supplementary material, which is available to authorized users.

✉ Mengsheng Qiu
m0qiu001@yahoo.com

✉ Xiaofeng Xu
xuxf1988@gmail.com

¹ Institute of Life Sciences, Zhejiang Key Laboratory of Organ Development and Regeneration, College of Life and Environmental Sciences, Hangzhou Normal University, Hangzhou 310029, China

² CAS Center for Excellence in Brain Science and Intelligence Technology, Institute of Neuroscience, Chinese Academy of Sciences, Shanghai 200031, China

(vOLs), but by adulthood it comprises more than 80% dorsally-derived OLs (dOLs) [9]. The number of vOLs decreases after P13 while the number of dOLs stays constant, strongly suggesting that dOLs have a selective advantage in the dorsal funiculus. Notably, we and others have demonstrated that dOPCs exhibit distinct behavior under pathological conditions. In response to focal demyelination of the spinal cord and corpus callosum, dOPCs undergo enhanced proliferation and differentiation, making a proportionally larger contribution to remyelination than their ventral counterparts [10, 11], drawing attention to their developmental significance and remyelination capacity.

To investigate the developmental potential of dOPCs in the myelination of ventral axons, we utilized the *Nestin^{cre}*; *Smo^{fl/fl}* conditional knock-out (cKO) animal model, in which the ventral oligodendrogenesis is blocked [12]. Previous studies have demonstrated that *Smoothened* (*Smo*), a member of the frizzled family with seven transmembrane domain proteins, is essential for relaying the Hh signaling pathway across the plasma membrane [13]. Through analysis and comparison of OL development and myelin formation, we found that in the absence of vOPCs, dOPCs can undergo rapid proliferation, spread to ventral spinal tissue, and finally differentiate into myelinating OLs in the ventral white matter. These findings provide further genetic evidence that dOPCs are capable of myelinating ventral axons in the mouse spinal cord.

Materials and Methods

Mice

Animal housing and experiments were approved by the Institutional Animal Care and Use Committee at Hangzhou Normal University. *Smo^{fl}* (No. 004526), *tdTomato* (No. 007909) and *Nestin^{cre}* (No. 003771) mice were purchased from the Jackson Laboratory (Bar Harbor, ME, USA). *Smo^{fl}* mice were mated with *Nestin^{cre}* mice to obtain double heterozygous mice *Nestin^{cre}*; *Smo^{fl/+}* mice. The *Nestin^{cre}*; *Smo^{fl/fl}* conditional mutants were generated by intercrossing the *Nestin^{cre}*; *Smo^{fl/+}* and *Smo^{fl}* mouse lines. All mice were crossed and maintained on the C57BL/6 background. Animals of either sex were used for analyses. All efforts were made to minimize the number of animals and their suffering. Genomic DNA was extracted from embryonic tissues or tails and used for subsequent genotyping by PCR. Genotyping PCR was performed using primers as described by the Jackson Laboratory website (<https://www.jax.org/cn/>).

In situ RNA Hybridization (ISH)

After anesthesia, each mouse was perfused with 4% paraformaldehyde (PFA). The spinal cord was then dissected and postfixed in 4% PFA at 4°C overnight. It was subsequently immersed in 30% sucrose in PBS at 4°C overnight, and embedded in OCT medium (Thermo Fisher Scientific Inc., MA, USA, Cat# 6506M). The cord was sectioned on a cryostat at 16–18 µm. ISH procedures were performed as described previously [14–16]. The digoxin-labeled RNA probes used for ISH corresponded to nucleotides 59–862 of mouse *Mbp* mRNA (NM_001025254.2), nucleotides 1210–2178 of mouse *Plp1* mRNA (NM_011123.4), and nucleotides 1613–2463 of mouse *Pdgfra* mRNA (NM_011058.3).

Antibody Production

Antibodies against Sox10 were generated in guinea pigs against a purified bacterially-expressed protein consisting of amino-acids 181–233 and 308–400 of mouse Sox10 [17]. Similarly, antibodies against Myrf were generated in rabbits against a purified bacterially-expressed protein consisting of the N-terminus amino-acids of mouse Myrf. Both antisera were affinity-purified.

Immunofluorescence Staining

Spinal cords for immunofluorescence (IF) staining were sectioned at 14 µm on a cryostat. IF staining was performed as previously described [18]. The primary antibodies used were as follows: rabbit anti-Olig2 (Merck KGaA, Darmstadt, Germany, Cat# AB9610, 1:1000), mouse anti-Islet1 (Developmental Studies Hybridoma Bank (DSHB), Iowa City, IA, USA, Cat# 39.3F7, 1:50), mouse anti-MNR2 (DSHB, Cat# 81.5C10, 1:50), goat anti-ChAT (Merck KGaA, Cat# AB144P, 1:1000), guinea pig anti-Sox10 (Qiu Lab, 1:300), rabbit anti-Ki67 (Abcam, Cambridge, UK, Cat# AB15580, 1:1000), rabbit anti-Myrf (Qiu Lab, 1:300), and mouse anti-Nkx2.2 (DSHB, Cat# 74.5A5, 1:30). The secondary antibodies used were Alexa Fluor 488/594-conjugated antibodies (Invitrogen, Carlsbad, CA, USA). To enhance the fluorescence signals, the sections were incubated in 10 nmol/L sodium citrate buffer (Bio Basic Inc., Shanghai, China, Cat# 6132-04-3) for 30 min at 80°C before blocking for antigen retrieval.

Transmission Electron Microscopy

Transmission electron microscopy (TEM) was performed as previously described [19]. Briefly, after anesthesia mice were perfused with 2% PFA/4% glutaraldehyde/4% sucrose in 0.1 mol/L phosphate buffer, pH 7.4, and post-

fixed in 2% osmium tetroxide. The spinal cord was then removed from the vertebrae, re-fixed in 1% osmium tetroxide, dehydrated in ascending grades of acetone, and embedded in Epon. Ultrathin sections (50 nm) were stained with uranyl acetate and lead citrate, mounted on copper grids, and visualized with a TEM. Total axons per area in the ventral white matter of the thoracic spinal cord were counted in control and mutant mice at P21. ImageJ software (<https://imagej.nih.gov/ij/>) was used to calculate the g-ratio and axonal diameter.

Statistical Analyses

For each analysis, the results from independent animals were treated as biological replicates ($n \geq 3$). Quantitative data of the number of cells in mutant and control cords are presented as the mean \pm SEM with $n \geq 3$ embryos per experimental point. Statistical significance was evaluated by Student's *t*-test. Differences were considered statistically significant at $*P < 0.05$, $**P < 0.01$, and $***P < 0.001$, and n.s. was used to indicate no significant difference.

Results

Generation of vOPCs is Blocked in Nestin-Smo cKO Embryos

It is well documented that the Hh signaling pathway plays a crucial role in early oligodendroglial development. In *Shh*^{-/-} or *Smo*^{-/-} mutants, the spinal cord is dorsalized, and the majority of ventral structures including vOPCs are missing [6, 20–22]. However, as these conventional mutants die prenatally, it remains unclear whether dorsal OPCs are capable of migrating into the ventral region and myelinating ventral axons. To address this question, we used *Nestin*^{cre}; *Smo*^{fl/fl} conditional knockout mice (referred to as Nestin-Smo cKO mice) in which *Smo* was ablated in neural progenitor cells and their progeny. The efficacy of recombination was confirmed using *idTomato* reporter mice crossed with the Nestin-Smo cKO line (Fig. 1A). In agreement with the previous finding [12], the specification of vOPCs from the pMN domain at E12.5 was blocked in the spinal cord of Nestin-Smo cKO mice, as evidenced by the complete loss of Olig2+ (Fig. 1B, B') and *Pdgfra*+ cells (Fig. 1C, C').

Notably, Hh signaling has been demonstrated to play pivotal roles in the control of the MN-OPC switch, and *Nestin*^{cre}; *Smo*^{fl/fl} mice die at \sim P21 and exhibit apparent ataxia, prompting us to investigate the development of motor neurons (MNs) in Nestin-Smo cKO mice. First, we examined the expression of the MN markers *Islet1* and *MNR2* at E12.5. In comparison with that in control

embryos, the early generation of MNs in mutants appeared normal at E12.5 (Fig. 1D–E'). Quantitative analysis showed that the number of *Islet1*+ and *MNR2*+ MNs in Nestin-Smo cKO embryos was slightly but significantly higher than that in control embryos (Fig. 1F). These results confirmed and extended the previous data, suggesting that the generation of vOPCs is blocked in Nestin-Smo cKO embryos without changes in the identity of MNs. Further examination of the maturation of MNs by choline acetyltransferase (ChAT) immunostaining at P0 and P21 did not reveal any overt difference in the distribution or number of mature MNs between control and mutant spinal cords (Fig. S1). Taken together, conditional knockout of *Smo* did not affect the generation or maturation of MNs, and the death of the mutants may have been due to unknown developmental defects.

dOPCs Proliferate and Migrate more than Normal to Compensate for the Loss of vOPCs in the Nestin-Smo cKO Spinal Cord

We further compared the generation and proliferation of OPCs between control and mutant embryos during later stages. In Nestin-Smo cKO embryos, we did not detect any Olig2+ cells in the spinal cord before E14.5. At \sim E15.5, while dOPCs were detected in the dorsal half of the spinal cord in control embryos (Fig. 2A), a small number of Olig2+ cells were primarily found in the dorsal spinal cord in *Smo* mutant embryos (Fig. 2A'), providing strong evidence that these cells were generated from the dorsal VZ. As development proceeded, these Olig2+ dOPCs gradually spread to the lateral and ventral parts of the cord (Fig. 2B'). At P0, Olig2+ cells were evenly distributed throughout the spinal cord (Fig. 2C'), although there were still significantly fewer of these cells in mutant embryos than in control embryos (Fig. 2E). We did not detect any OPCs of ventral origin during early developmental stages. The uniform distribution of Olig2+ cells in *Smo* mutants indicated that dOPCs migrated into the ventral half, at least under conditions in which the generation of vOPCs was compromised. By P4, there was no significant difference in the number or distribution of Olig2+ cells between control and Nestin-Smo cKO mice (Fig. 2D, D', E).

In addition, we examined the effect of the expression of two oligodendrocytic markers, *Sox10* and *Pdgfra*, which are downstream of Olig2, in promoting OL differentiation [23, 24]. In the control spinal cord, the expression of *Sox10* was also restricted to OL-lineage cells (Fig. 2F–H). In contrast to Olig2+ cells, *Sox10*+ cells were not notably observed until birth in the Nestin-Smo cKO mice (Fig. 2F'). At P0, *Sox10*+ cells were evenly distributed in the gray matter of the mutant spinal cord, without accumulating in the white matter (Fig. 2G', I), indicating a

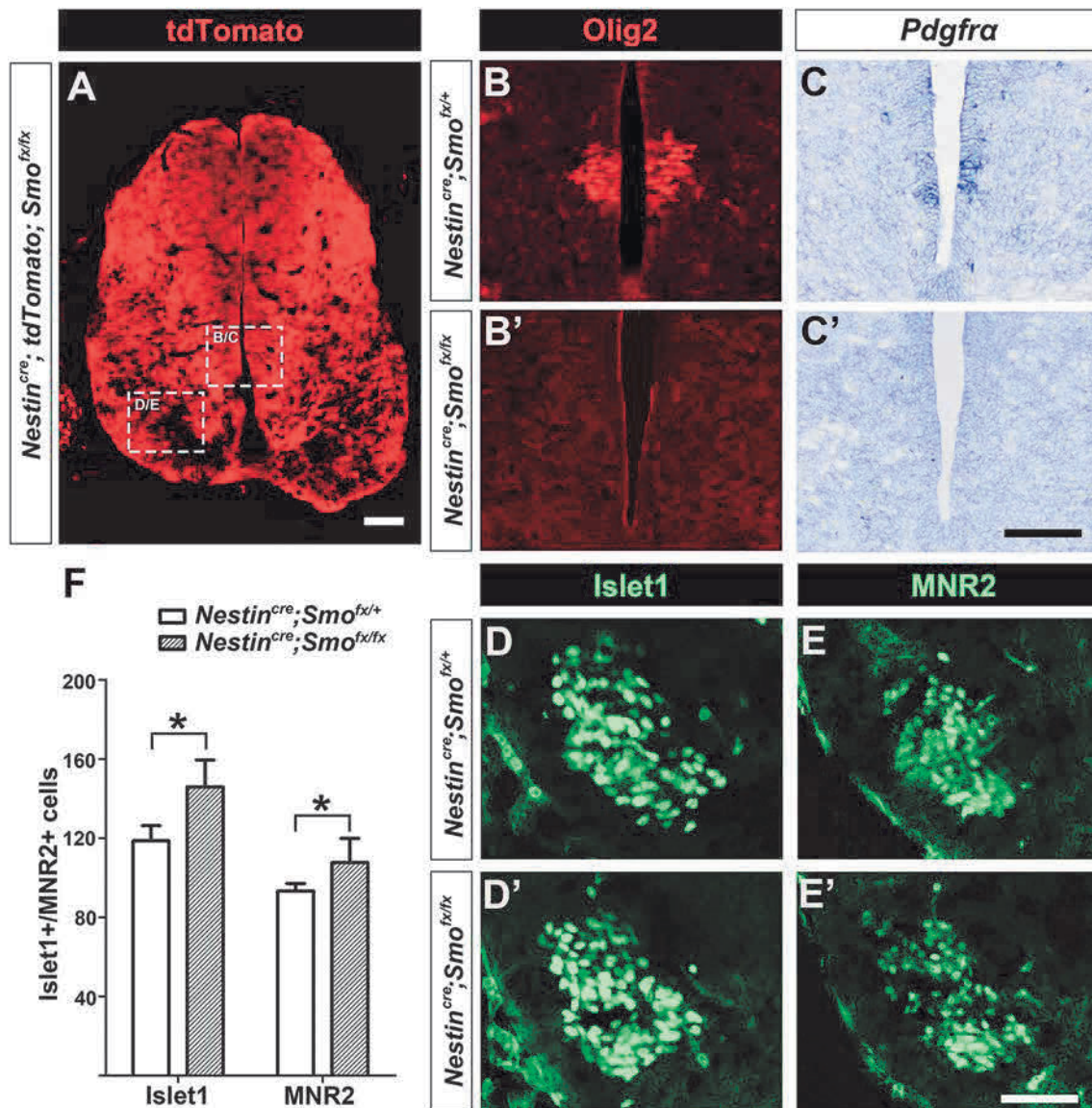


Fig. 1 Conditional ablation of Smo in neural progenitor cells blocks the generation of ventrally-derived OPCs (vOPCs), without affecting the differentiation of motor neurons. **A** tdTomato fluorescence in the spinal cord of a *Nestin^{cre}; tdTomato; Smo^{fx/fx}* embryo at E12.5. **B–E'** Representative images of spinal cord sections from *Nestin^{cre}; Smo^{fx/+}* (control) and *Nestin^{cre}; Smo^{fx/fx}* (Nestin-Smo cKO) embryos subjected

to Olig2 IF (**B, B'**), *Pdgfra* ISH (**C, C'**), Islet1 (**D, D'**), and MNR2 (**E, E'**) IF at E12.5. **B/B', C/C', D/D'** and **E/E'** are the higher magnifications of the boxed areas in **A** in each embryo. **F** Quantification of Islet1+ and MNR2+ cells per section in the spinal cords of control and Nestin-Smo cKO embryos at E12.5. Error bars indicated SEM. **P* < 0.05. Scale bars, 100 μ m.

significant delay of OPC differentiation. Afterwards, the number and distribution of Sox10+ cells recovered to normal levels at P4 (Fig. 2H', I). Unlike Olig2 and Sox10, *Pdgfra* was exclusively expressed in OPCs (Fig. S2A, B). At E16.5, fewer *Pdgfra*+ OPCs were detected in Smo mutants than controls and most of them were scattered around the spinal cord (Fig. S2A'). The expression of *Pdgfra* gradually increased and there was no significant difference in the distribution or number of *Pdgfra*+ cells between control and mutant embryos at P0 (Fig. S2B, B', C). In conclusion, after specification, dOPCs in the

cord of Nestin-Smo cKO mice quickly migrate outwards and ventrally and achieve a normal distribution and number in neonatal stages.

Cell proliferation was analyzed by assessing the nuclear antigen Ki67, which is expressed throughout all phases of the cell cycle except early G1/G0 (Fig. 3). Although the numbers of Ki67/Olig2 double-positive cells were comparable in both genotypes (Fig. 3A–C), the percentage of Ki67+/Olig2+ cells among all Olig2+ OPCs was significantly higher in mutants than in controls (Fig. 3D), indicating that a greater fraction of dOPCs are mitotically

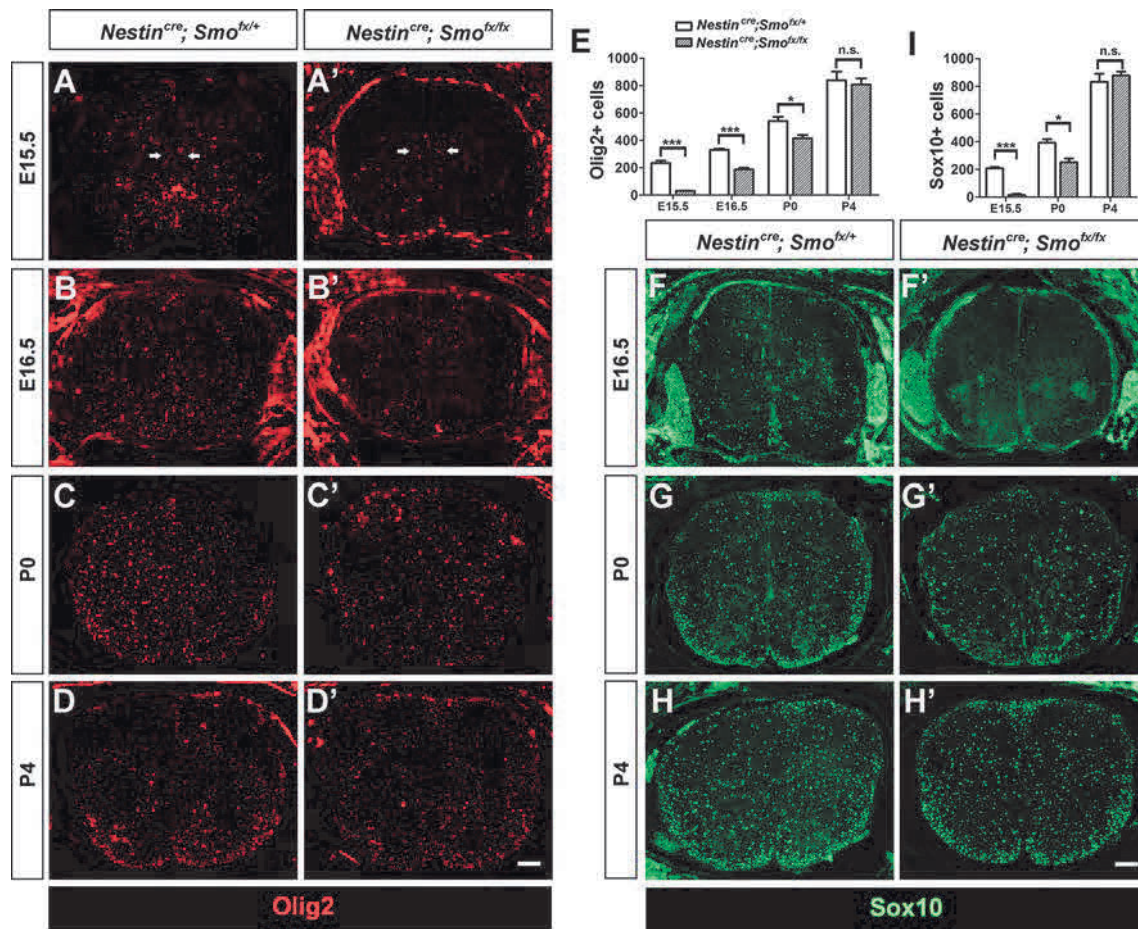


Fig. 2 The number and distribution of OPCs in Nestin-Smo cKO embryos recover to normal levels after birth. **A–D'** and **F–H'** Representative images of spinal cord sections from control and Nestin-Smo cKO embryos subjected to Olig2 (**A–D'**) and Sox10 (**F–H'**) IF at indicated stages. Dorsal towards the top. Arrows in **A** and **A'** indicate the origin site of dOPCs. **E** Quantification of Olig2+ cells per

section in the spinal cords of control and Nestin-Smo cKO embryos at indicated stages. **I** Quantification of Sox10+ cells per section in the spinal cords of control and Nestin-Smo cKO embryos at indicated stages. Error bars indicate SEM. * $P < 0.05$ and *** $P < 0.001$. n.s., no significant difference. Scale bars, 100 μm .

active in mutants than in their control counterparts and that the prominent recovery of dOPCs in Nestin-Smo mutant embryos is the result of an enhanced proliferative response. Together, these findings demonstrated that in Nestin-Smo mutants, dOPCs proliferate and migrate more than normal while vOPCs are absent, until a comparable OPC density is achieved.

Terminal Differentiation of dOPCs in the Spinal Cord of Nestin-Smo cKO Mice is Delayed, but also Triggered by Nkx2.2/Olig2 Co-expression

To evaluate the terminal differentiation of dOPCs in the ventral spinal cord, which they do not normally occupy in wild-type embryos, we first examined the expression of two mature OL markers, *Mbp* and *Plp1*. ISH analysis revealed the absence of *Mbp*+ (Fig. 4A', B') and *Plp1*+ (Fig. 4F', G') OLs from E16.5 to P0 in the Smo

cKO mice. At postnatal stages, the expression levels of *Mbp* and *Plp1* rapidly increased and were nearly indistinguishable from those in the control spinal cord from P4 to later stages (Fig. 4C–E', H–J', K). Similarly, *Myrf*, a regulatory transcription factor for myelin [25, 26], also displayed a temporal delay in expression in Nestin-Smo cKO embryos (Fig. 4L–N') but the expression of *Myrf* recovered to normal levels after P4 (Fig. 4O). Thus, these data implied that dOPCs are capable of terminal differentiation but with a temporal delay compared to vOPCs.

Our previous studies suggested that some vOPCs might be specified from the Nkx2.2+/Olig2+ progenitor cells [27], and that co-expression of Nkx2.2 and Olig2 might be the switch that initiates the terminal differentiation of OPCs [16, 24]. On the other hand, a lack of Nkx2.2-expressing OPCs in Nkx6 mutants [8] suggests that vOPCs and dOPCs have distinct molecular properties, and dOPCs might initiate terminal differentiation independent of

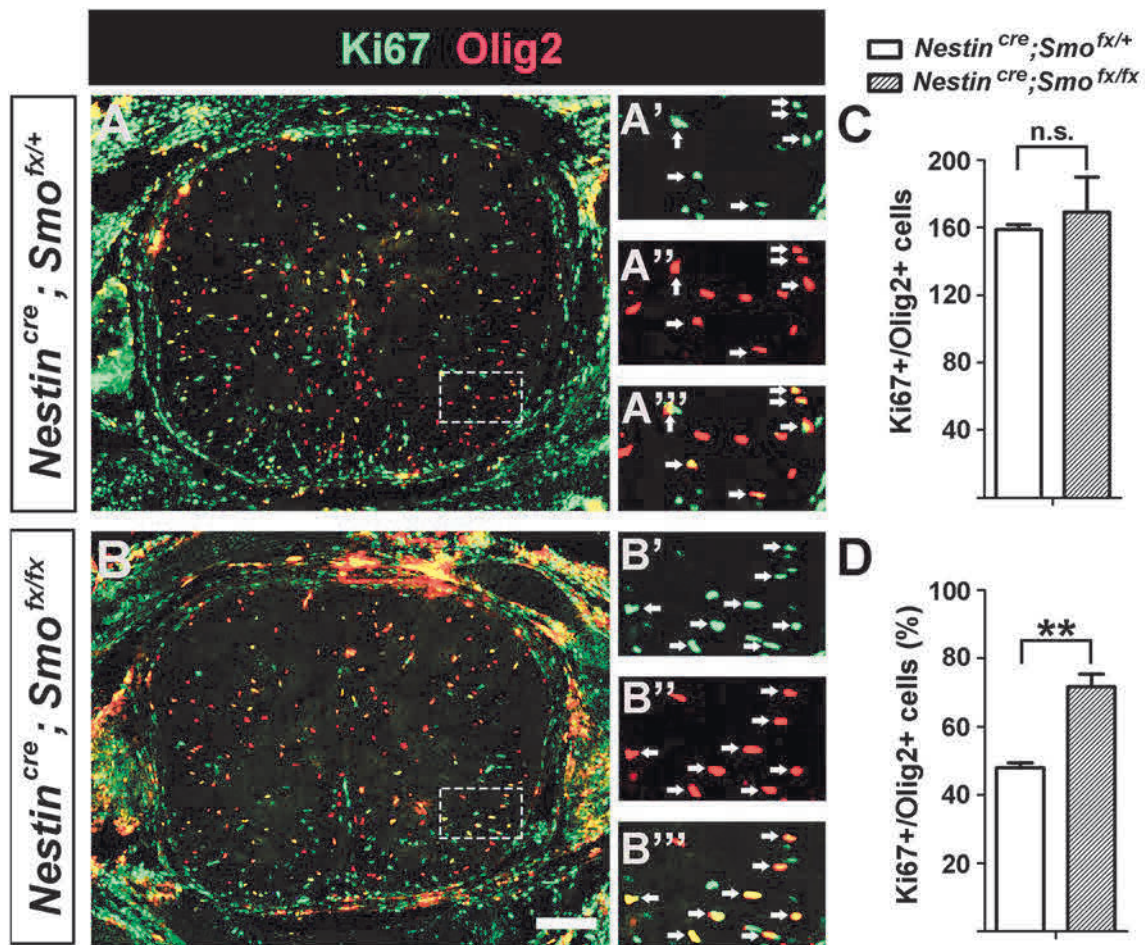


Fig. 3 dOPCs in Nestin-Smo cKO embryos exhibit enhanced proliferation. **A–B** Representative images of spinal cord sections from control and Nestin-Smo cKO mice subjected to Ki67 (green) and Olig2 (red) IF at E16.5. **A'–B'''** are higher magnifications of the boxed areas in **A** and **B**. Arrows indicate the coexpression of Ki67 and Olig2. **C** Quantification of Ki67/Olig2 double positive cells per

section in the spinal cords of control and Nestin-Smo cKO embryos at E16.5. **D** Quantification of the percentage of Ki67+/Olig2+ cells among all Olig2+ cells in the spinal cords of control and Nestin-Smo cKO embryos at E16.5. Error bars indicate SEM. ** $P < 0.01$. n.s., no significant difference. Scale bars, 100 μm .

Nkx2.2 expression. Therefore, we also analyzed the co-expression of Nkx2.2 and Olig2 at early postnatal stages when the terminal differentiation of OPCs occurs rapidly. At P0, Nkx2.2+ cells were detected throughout the entire spinal cord and most Nkx2.2+/Olig2+ cells were observed in the white matter of control and mutant spinal cords (Fig. 5A, B). At P4, Nkx2.2 staining in newly-differentiated OLs exhibited an oligodendrocyte-like morphology with numerous branching processes (Fig. 5C, D). Notably, at P0, the number of Nkx2.2+/Olig2 cells was significantly lower in Nestin-Smo cKO embryos than in control embryos, and recovered to normal levels at P4 (Fig. 5E), which is in agreement with the expression changes in *Mbp* and *Plp1*. Therefore, it is reasonable to speculate that the terminal differentiation of dOPCs in Nestin-Smo cKO mutants is also triggered by the co-expression of Olig2 and Nkx2.2.

dOLs in the Spinal Cord of Nestin-Smo cKO Mice are Able to Myelinate Ventral Axons and form Thicker Myelin than those in Control Mice

To assess whether dOPCs can myelinate ventral axons normally, we performed transmission electron microscopy (TEM) of the spinal cords of Nestin-Smo cKO mice and control littermates at P21. The majority of the axons in the ventral white matter were myelinated in Nestin-Smo cKO mice (Fig. 6C), and statistical analyses showed that the percentage of myelinated axons was comparable between control and Nestin-Smo cKO mice (Fig. 6F), indicating that dOPCs are able to myelinate ventral axons effectively. Unexpectedly, the overall thickness of myelin sheaths was significantly elevated in the mutants, as measured by the g-ratio (Fig. 6G, H). Meanwhile, the average diameter of

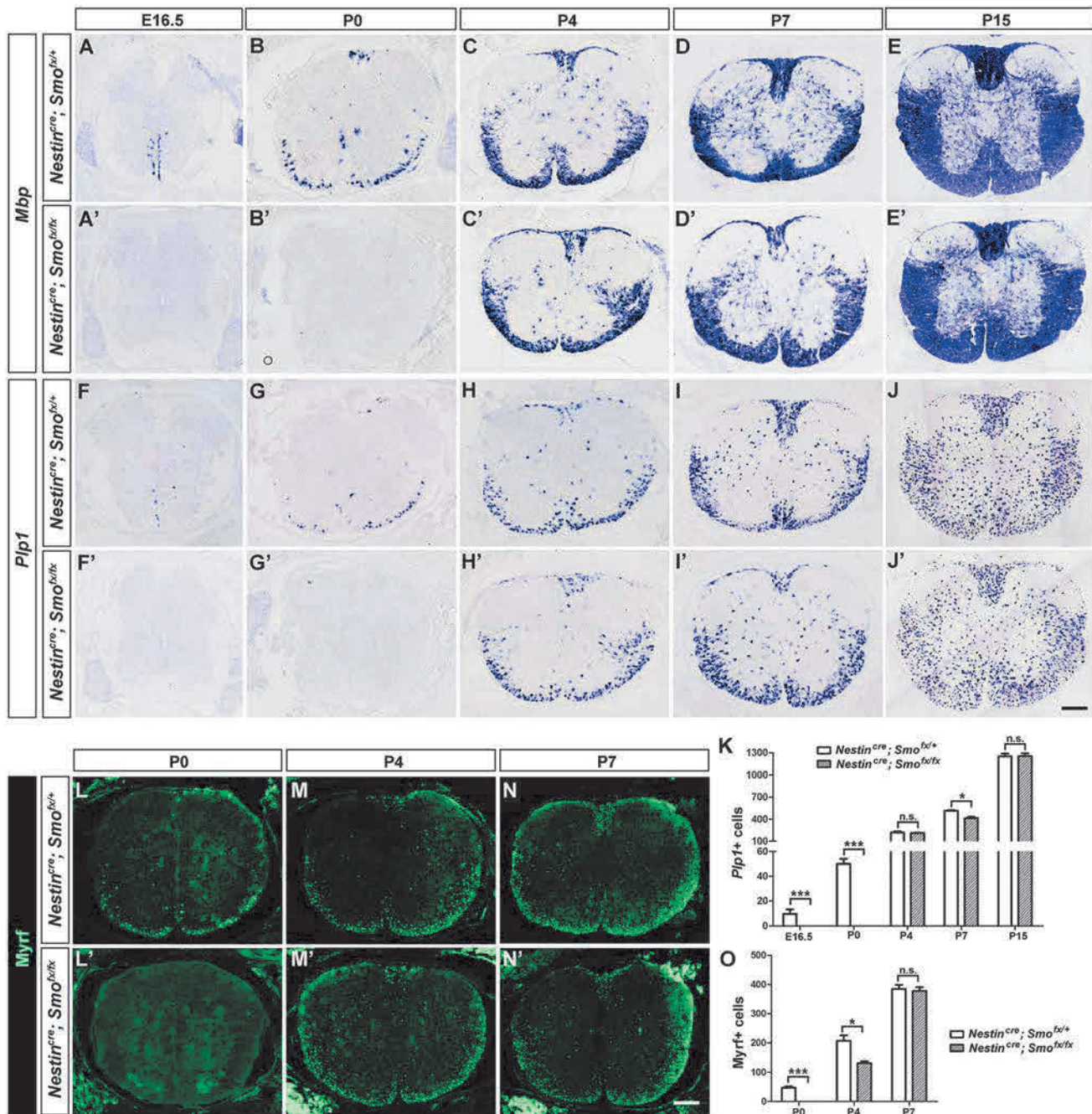


Fig. 4 The differentiation of dOLs in Nestin-Smo cKO mice is delayed but recovers to normal levels from P4. Representative images of spinal cord sections from control and Nestin-Smo cKO mice subjected to *Mbp* (A–E') and *Plp1* (F–J') ISH, and *Myrf* (L–N') IF at indicated stages. **K** Quantification of *Plp1*+ cells per section in the

spinal cords of control and Nestin-Smo cKO embryos at indicated stages. **O** Quantification of *Myrf*+ cells per section in the spinal cords of control and Nestin-Smo cKO embryos at indicated stages. Error bars indicate SEM. * $P < 0.05$ and *** $P < 0.001$. n.s., no significant difference. Scale bars, 100 μm .

myelinated axons was unchanged in *Smo* mutants compared to control mice (Fig. 6G), implying that the increase in myelin sheath thickness is unlikely to be a consequence of altered axon caliber. TEM and g-ratio analysis of the dorsal white matter also showed a significant increase in

myelin thickness in the mutants compared to the controls (Fig. 6I, J), implying that the thicker myelin sheath in Nestin-Smo cKO mice may have been caused either directly or indirectly by the genetic deletion of *Smo* rather than the regions where OPCs originated.

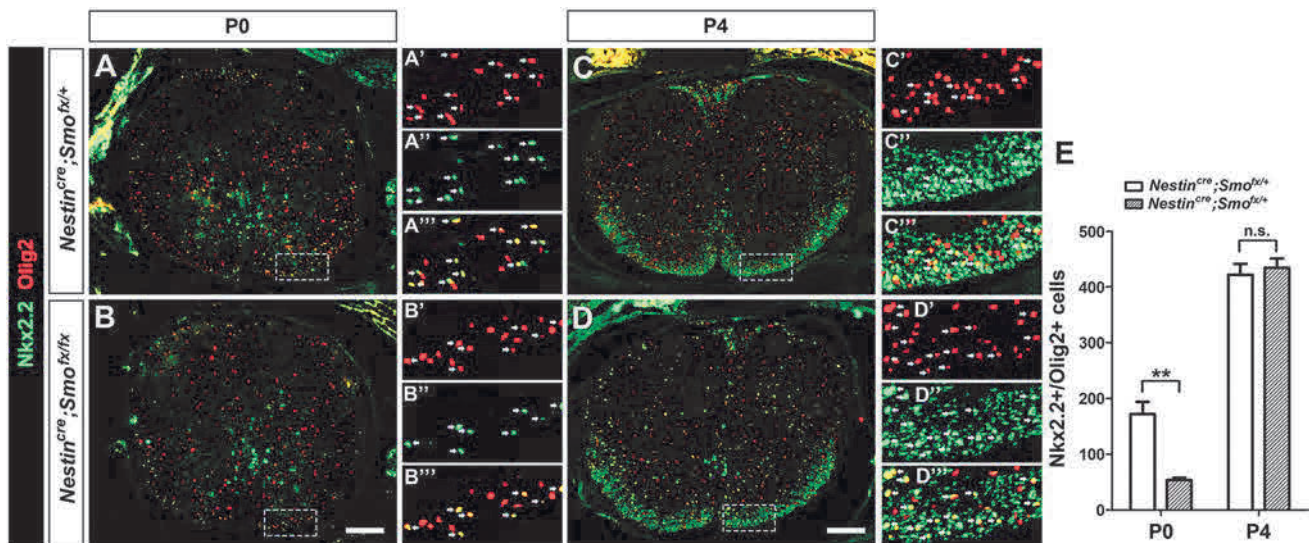


Fig. 5 The change of Nkx2.2 and Olig2 co-expression resembles that of OL differentiation in Nestin-Smo cKO embryos. **A–D** Representative images of spinal cord sections from control and Nestin-Smo cKO embryos subjected to Nkx2.2 (green) and Olig2 (red) IF at P0 and P4. **A'–D''** are higher magnification of the boxed areas in **A–D**. Arrows

indicate the coexpression of Nkx2.2 and Olig2. **E** Quantification of Nkx2.2/Olig2 double positive cells per section in the spinal cords of control and Nestin-Smo cKO embryos at P0 and P4. Error bars indicate SEM. * $P < 0.05$ and *** $P < 0.001$. n.s., no significant difference. Scale bars, 100 μm .

Discussion

To investigate the developmental potential of dOPCs in the developing spinal cord, we used the Nestin-Smo cKO mouse line to abolish the generation of vOPCs during early development. In the absence of vOPCs (Fig. 1B–C'), dOPCs started to emerge in the dorsal spinal cord on schedule at $\sim\text{E15.5}$ (Fig. 2A'), and the number of dOPCs increased rapidly with enhanced proliferation to compensate for the loss of vOPCs (Fig. 3). This finding is consistent with the previous finding that dOPCs are produced from the dorsal neuroepithelium independent of Shh signaling [6–8]. Despite the temporal delay in myelin gene expression in the spinal cords of Nestin-Smo cKO mice in neonatal stages, mature *Mbp+Plp1+* OL populations gradually recovered to normal levels at around P4 (Fig. 4). In wild-type embryos, dOPCs and vOPCs exhibit different migration and setting patterns. dOPCs are concentrated in the dorsal and dorsolateral funiculi, whereas vOPCs are distributed widely throughout the spinal cord [9, 10]. Thus, it is widely accepted that dOPCs are less migratory than their ventral counterparts. This could be either an intrinsic difference or could reflect the fact that dOPCs appear after vOPCs have already colonized the cord and that their migration and proliferation are constrained by vOPCs. These results demonstrate that when vOPCs are absent from Nestin-Smo cKO mutants, dOPCs spread uniformly throughout the cord, proliferate, and migrate at a higher rate, implying that the heterogeneity between dOPCs and vOPCs might be the

result of extrinsic factors rather than the intrinsic properties of the cells themselves.

In addition, our study confirmed that the initiation of dOPC terminal differentiation is also associated with the co-expression of Nkx2.2 and Olig2 (Fig. 5). It has been proposed that this co-expression is responsible for triggering the terminal differentiation of OLs in the embryonic spinal cord [16, 24, 27–29]. However, according to Vallstedt *et al.*, Olig2+ cells in dorsal explants initiate the differentiation of OLs in the absence of Nkx2.2 expression [8], implying that ventrally- and dorsally-derived OPCs might express distinct molecular properties to switch on terminal differentiation. In this study, we compared Nkx2.2 and Olig2 expression in control and Smo cKO mutants and demonstrated that their co-expression was closely associated with the differentiation of dOPCs in mutant embryos and vOPCs in control embryos. dOPC and vOPC lineage cells in the spinal cord might share the same molecular properties, at least at the initiation stages of terminal differentiation.

Since it has been demonstrated that there are both dorsally- and ventrally-derived populations of OPCs in the spinal cord and brain [30–32], an outstanding question is whether these are functionally identical or specified in some way. To analyze whether the lack of vOPCs affects axonal myelination, we harvested the spinal cords of control and mutant mice at P21 for electron microscopy. Detailed TEM analysis revealed that these dorsally-derived OLs were able to undergo axonal myelination in the ventral white matter (Fig. 6). Surprisingly, we found that the thickness of the myelin sheaths in Nestin-Smo cKO

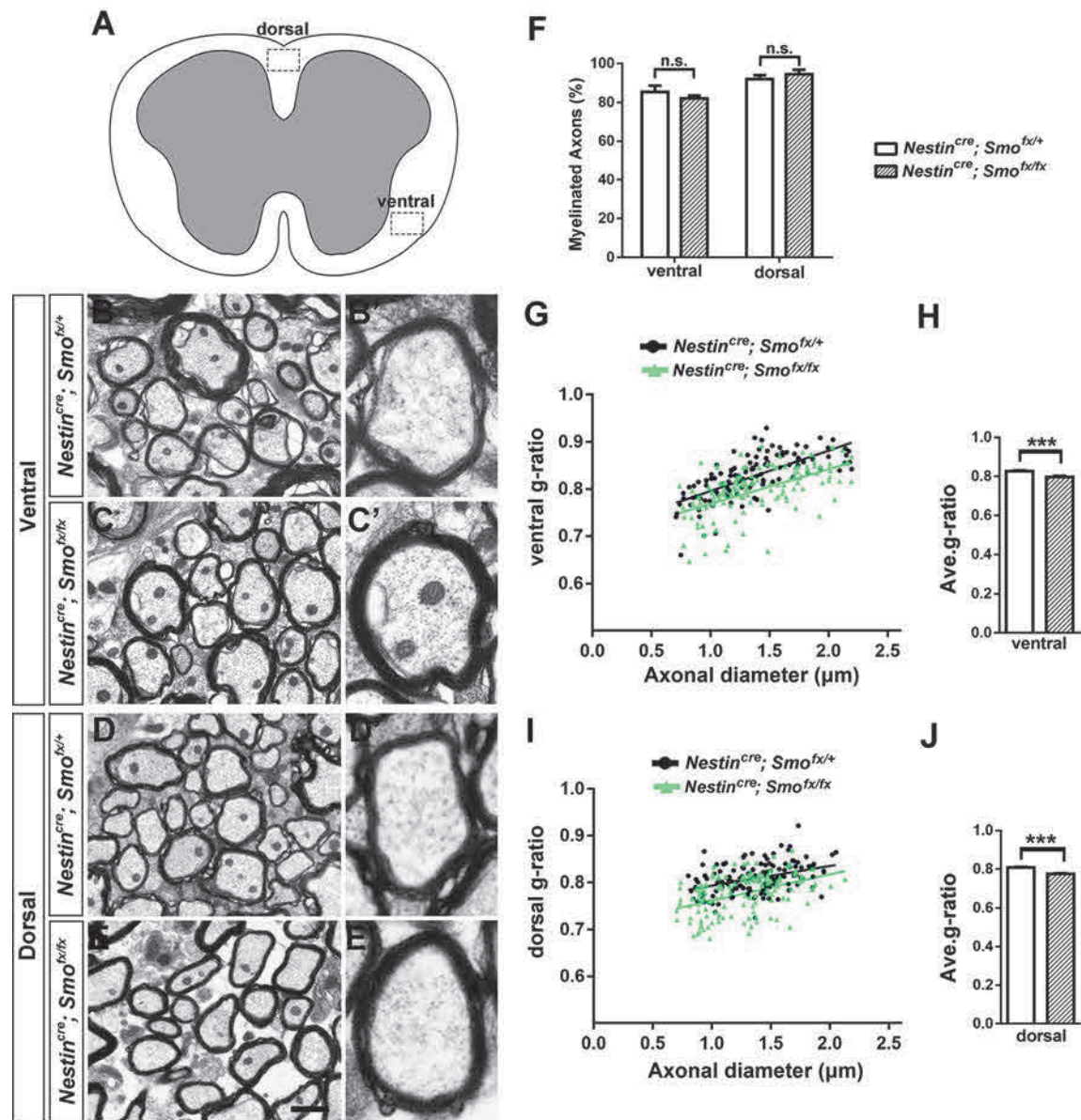


Fig. 6 dOLs in Nestin-Smo cKO mice are capable of myelinating ventral axons. **A** Schematic of the ventral and dorsal white matter areas in control and Nestin-Smo cKO mice at P21. **B–E** Transmission electron microscopy of ventral and dorsal spinal cords in control and Nestin-Smo cKO mice at P21. **B'–E'** are higher magnifications of **B–E**, respectively. **F** Quantification of the percentage of myelinated

axons per field in the spinal cords of control and Nestin-Smo cKO mice. **G, I** g-ratio analysis of ventral and dorsal white matter in the spinal cords of control and Nestin-Smo cKO mice at P21. **H, J** Quantification of the average g-ratio in ventral and dorsal white matter of control and Nestin-Smo cKO mice. Error bars indicate SEM. *** $P < 0.001$. n.s., no significant difference. Scale bar, 1 μ m.

mutants was significantly increased, prompting us to speculate that late-born dOLs possess a higher intrinsic capacity for axonal myelination. Consistent with this notion, in the developing cortex, vOLs are gradually replaced by later-born dOLs in postnatal stages [30]. In the spinal cord, the corticospinal and rubrospinal tracts are preferentially myelinated by dOLs, even though vOLs dominate these tracts during early postnatal stages [9, 10]. Furthermore, dOPCs make a proportionally larger contribution to remyelination than their ventral counterparts

following focal demyelination of the spinal cord and corpus callosum [10, 11]. Therefore, dOLs might have a competitive advantage over vOLs in developing myelination and myelin repair following demyelination. However, ultrastructure analysis of the dorsal white matter of Nestin-Smo cKO mice showed that myelin thickness was also increased with respect to that in controls, suggesting the alternative possibility that the thicker myelin sheath in *Smo* cKO embryos may result from the loss of the *Smo* gene in dorsal OPCs independent of their embryonic origins.

Taken together, our studies demonstrate that dorsally-derived OPCs in the spinal cord are capable of extensive proliferation and migration in the absence of vOPCs, leading to effective myelination of ventral axons. These findings provide further genetic evidence that dOPCs are capable of myelinating ventral axons in the mouse spinal cord.

Acknowledgements This work was supported by the Natural Science Foundation of Zhejiang Province, China (LQ17C040001, LQ20C090004, and LQ18C090005) and the National Natural Science Foundation of China (31871480, 81771028, and 31771621).

Conflict of interest All authors claim that there are no conflicts of interest.

References

- Emery B. Regulation of oligodendrocyte differentiation and myelination. *Science* 2010, 330: 779–782.
- Gallo V, Deneen B. Glial development: the crossroads of regeneration and repair in the CNS. *Neuron* 2014, 83: 283–308.
- Foerster S, Hill MFE, Franklin RJM. Diversity in the oligodendrocyte lineage: Plasticity or heterogeneity? *Glia* 2019, 67: 1797–1805.
- Pringle NP, Richardson WD. A singularity of PDGF alpha-receptor expression in the dorsoventral axis of the neural tube may define the origin of the oligodendrocyte lineage. *Development* 1993, 117: 525–533.
- Pringle NP, Yu WP, Guthrie S, Roelink H, Lumsden A, Peterson AC, *et al.* Determination of neuroepithelial cell fate: induction of the oligodendrocyte lineage by ventral midline cells and sonic hedgehog. *Dev Biol* 1996, 177: 30–42.
- Cai J, Qi Y, Hu X, Tan M, Liu Z, Zhang J, *et al.* Generation of oligodendrocyte precursor cells from mouse dorsal spinal cord independent of Nkx6 regulation and Shh signaling. *Neuron* 2005, 45: 41–53.
- Fogarty M, Richardson WD, Kessaris N. A subset of oligodendrocytes generated from radial glia in the dorsal spinal cord. *Development* 2005, 132: 1951–1959.
- Vallstedt A, Klos JM, Ericson J. Multiple dorsoventral origins of oligodendrocyte generation in the spinal cord and hindbrain. *Neuron* 2005, 45: 55–67.
- Tripathi RB, Clarke LE, Burzomato V, Kessaris N, Anderson PN, Attwell D, *et al.* Dorsally and ventrally derived oligodendrocytes have similar electrical properties but myelinate preferred tracts. *J Neurosci* 2011, 31: 6809–6819.
- Zhu Q, Whitemore SR, Devries WH, Zhao XF, Kuypers NJ, Qiu MS. Dorsally-derived oligodendrocytes in the spinal cord contribute to axonal myelination during development and remyelination following focal demyelination. *Glia* 2011, 59: 1612–1621.
- Crawford AH, Tripathi RB, Richardson WD, Franklin RJM. Developmental origin of oligodendrocyte lineage cells determines response to demyelination and susceptibility to age-associated functional decline. *Cell Rep* 2016, 15: 761–773.
- Yu K, McGlynn S, Matise MP. Floor plate-derived sonic hedgehog regulates glial and ependymal cell fates in the developing spinal cord. *Development* 2013, 140: 1594–1604.
- Zhang XM, Ramalho-Santos M, McMahon AP. Smoothed mutants reveal redundant roles for Shh and Ihh signaling including regulation of L/R symmetry by the mouse node. *Cell* 2001, 106: 781–792.
- Schaeren-Wiemers N, Gerfin-Moser A. A single protocol to detect transcripts of various types and expression levels in neural tissue and cultured cells: in situ hybridization using digoxigenin-labelled cRNA probes. *Histochemistry* 1993, 100: 431–440.
- Shen YT, Gu Y, Su WF, Zhong JF, Jin ZH, Gu XS, *et al.* Rab27b is involved in lysosomal exocytosis and proteolipid protein trafficking in oligodendrocytes. *Neurosci Bull* 2016, 32: 331–340.
- Xu X, Yu Q, Fang M, Yi M, Yang A, Xie B, *et al.* Stage-specific regulation of oligodendrocyte development by Hedgehog signaling in the spinal cord. *Glia* 2020, 68: 422–434.
- Stolt CC, Lommes P, Sock E, Chaboissier MC, Schedl A, Wegner M. The Sox9 transcription factor determines glial fate choice in the developing spinal cord. *Genes Dev* 2003, 17: 1677–1689.
- Jiang C, Yang W, Fan Z, Teng P, Mei R, Yang J, *et al.* AATYK is a novel regulator of oligodendrocyte differentiation and myelination. *Neurosci Bull* 2018, 34: 527–533.
- Ge X, Xiao G, Huang H, Du J, Tao Y, Yang A, *et al.* Stage-dependent regulation of oligodendrocyte development and enhancement of myelin repair by dominant negative Mastermind 1 protein. *Glia* 2019, 67: 1654–1666.
- Chiang C, Litingtung Y, Lee E, Young KE, Corden JL, Westphal H, *et al.* Cyclopia and defective axial patterning in mice lacking Sonic hedgehog gene function. *Nature* 1996, 383: 407–413.
- Tan M, Hu X, Qi Y, Park J, Cai J, Qiu M. Gli3 mutation rescues the generation, but not the differentiation, of oligodendrocytes in Shh mutants. *Brain Res* 2006, 1067: 158–163.
- Wijgerde M, McMahon JA, Rule M, McMahon AP. A direct requirement for Hedgehog signaling for normal specification of all ventral progenitor domains in the presumptive mammalian spinal cord. *Genes Dev* 2002, 16: 2849–2864.
- Stolt CC, Rehberg S, Ader M, Lommes P, Riethmacher D, Schachner M, *et al.* Terminal differentiation of myelin-forming oligodendrocytes depends on the transcription factor Sox10. *Genes Dev* 2002, 16: 165–170.
- Zhu Q, Zhao X, Zheng K, Li H, Huang H, Zhang Z, *et al.* Genetic evidence that Nkx2.2 and Pdgfra are major determinants of the timing of oligodendrocyte differentiation in the developing CNS. *Development* 2014, 141: 548–555.
- Emery B, Agalliu D, Cahoy JD, Watkins TA, Dugas JC, Mulinyawe SB, *et al.* Myelin gene regulatory factor is a critical transcriptional regulator required for CNS myelination. *Cell* 2009, 138: 172–185.
- Huang H, Teng P, Du J, Meng J, Hu X, Tang T, *et al.* Interactive repression of MYRF self-cleavage and activity in oligodendrocyte differentiation by TMEM98 protein. *J Neurosci* 2018, 38: 9829–9839.
- Fu H, Qi Y, Tan M, Cai J, Takebayashi H, Nakafuku M, *et al.* Dual origin of spinal oligodendrocyte progenitors and evidence for the cooperative role of Olig2 and Nkx2.2 in the control of oligodendrocyte differentiation. *Development* 2002, 129: 681–693.
- Qi Y, Cai J, Wu Y, Wu R, Lee J, Fu H, *et al.* Control of oligodendrocyte differentiation by the Nkx2.2 homeodomain transcription factor. *Development* 2001, 128: 2723–2733.
- Zhou Q, Choi G, Anderson DJ. The bHLH transcription factor Olig2 promotes oligodendrocyte differentiation in collaboration with Nkx2.2. *Neuron* 2001, 31: 791–807.
- Kessaris N, Fogarty M, Iannarelli P, Grist M, Wegner M, Richardson WD. Competing waves of oligodendrocytes in the forebrain and postnatal elimination of an embryonic lineage. *Nat Neurosci* 2006, 9: 173–179.
- Naruse M, Ishizaki Y, Ikenaka K, Tanaka A, Hitoshi S. Origin of oligodendrocytes in mammalian forebrains: a revised perspective. *J Physiol Sci* 2017, 67: 63–70.
- Richardson WD, Kessaris N, Pringle N. Oligodendrocyte wars. *Nat Rev Neurosci* 2006, 7: 11–18.



Connexin 36 Mediates Orofacial Pain Hypersensitivity Through GluK2 and TRPA1

Qian Li¹ · Tian-Le Ma¹ · You-Qi Qiu¹ · Wen-Qiang Cui^{1,2} · Teng Chen¹ ·
Wen-Wen Zhang¹ · Jing Wang³ · Qi-Liang Mao-Ying¹ · Wen-Li Mi¹ ·
Yan-Qing Wang¹ · Yu-Xia Chu¹

Received: 25 March 2020 / Accepted: 6 September 2020 / Published online: 16 October 2020
© Shanghai Institutes for Biological Sciences, CAS 2020

Abstract Trigeminal neuralgia is a debilitating condition, and the pain easily spreads to other parts of the face. Here, we established a mouse model of partial transection of the infraorbital nerve (pT-ION) and found that the Connexin 36 (Cx36) inhibitor mefloquine caused greater alleviation of pT-ION-induced cold allodynia compared to the reduction of mechanical allodynia. Mefloquine reversed the pT-ION-induced upregulation of Cx36, glutamate receptor ionotropic kainate 2 (GluK2), transient receptor potential ankyrin 1 (TRPA1), and phosphorylated extracellular signal regulated kinase (p-ERK) in the trigeminal ganglion. Cold allodynia but not mechanical allodynia induced by pT-ION or by virus-mediated overexpression of Cx36 in the trigeminal ganglion was reversed by the GluK2 antagonist NS102, and knocking down Cx36 expression in Nav1.8-expressing nociceptors by

injecting virus into the orofacial skin area of Nav1.8-Cre mice attenuated cold allodynia but not mechanical allodynia. In conclusion, we show that Cx36 contributes greatly to the development of orofacial pain hypersensitivity through GluK2, TRPA1, and p-ERK signaling.

Keywords Orofacial pain · Gap junction · Glutamate receptor ionotropic kainate 2 · Transient receptor potential A1

Introduction

Trigeminal nerve injury causes persistent orofacial neuropathic pain, and one of the prominent features of such injury is ectopic pain [1, 2]. Ectopic pain refers to the spread of pain from the area innervated by the injured nerve to the area innervated by the intact nerve [3]. The induction of trigeminal neuropathic pain, especially ectopic pain, seriously affects the quality of life in patients. The underlying mechanisms behind such pain remain unclear, but it has been proposed that primary sensory neurons become activated and sensitized following trigeminal nerve injury [4, 5] and that intact neurons and satellite glial cells (SGCs) then also become sensitized through nitric oxide released by the injured neurons [3] and through mutual information transmission between neurons in the trigeminal ganglion (TG) *via* calcitonin gene-related peptide (CGRP) [6] and various molecules such as Ca²⁺ and glutamate [7]. Therefore, the direct or indirect activation of adjacent neurons or SGCs by the injured cells might contribute greatly to the induction of ectopic orofacial pain.

Gap junctions (also known as electrical synapses) allow electrical signals and small cytoplasmic molecules that are no more than 1 kDa in size to pass quickly between cells [8]. Allodynia can be explained by the “ignition theory”

Qian Li, Tian-Le Ma and You-Qi Qiu contributed equally to this work.

Electronic supplementary material The online version of this article (<https://doi.org/10.1007/s12264-020-00594-4>) contains supplementary material, which is available to authorized users.

✉ Yu-Xia Chu
yuxiachu@fudan.edu.cn

¹ Department of Integrative Medicine and Neurobiology, Institutes of Integrative Medicine, School of Basic Medical Sciences, Institutes of Brain Science, Brain Science Collaborative Innovation Center, State Key Laboratory of Medical Neurobiology, and MOE Frontiers Center for Brain Science, Fudan University, Shanghai 200031, China

² Department of Pain Management, Shandong Provincial Qianfoshan Hospital, The First Hospital Affiliated with Shandong First Medical University, Jinan 250000, China

³ Department of Nephropathy, The Third Affiliated Hospital of Shenzhen University, Luohu Hospital Group, Shenzhen 518001, China

[9] in which the electrical communication depends on the transmission of chemicals between neurons [10, 11], and thus gap junctions might play a role in allodynia. Gap junctions are made up of connexins (Cxs), and among these the relationship between Cx43 and pain has been widely reported. Cx43 is distributed among SGCs, and contributes to the activation of glial cells [12, 13]. Peripheral nerve injury causes increased expression of Cx43 [14, 15], and blockade of Cx43 [16] or RNA interference of the *Gjal* gene [17] attenuates allodynia. The gap junctions between SGCs of the TG are mainly composed of Cx43, which plays an important role in the induction of ectopic orofacial pain [18]. In addition to the SGC-SGC coupling formed by Cx43, dual-cell patch clamp recordings have provided evidence of neuron-neuron and neuron-SGC electrical coupling in the TG [19], and the function of such connections in the induction and spread of orofacial pain is worth investigating.

There are at least four kinds of Cxs in the TG that are related to pain and inflammation: Cx36, Cx26, Cx40, and Cx43 [20]. Cx36 is the only subtype that is specifically expressed and widely distributed between neurons [21]. Cx36 contributes to the electrical coupling that plays a critical role in synchronizing rhythmic activity within the olivary nucleus [22], and the electrical synapses formed by Cx36 between intermediate neurons are essential for inhibitory γ oscillation [23]. However, few studies have investigated the function of Cx36 in the development of pain, especially orofacial pain. One report has shown that Cx36 in the medullary dorsal horn contributes greatly to mechanical allodynia through coupling GABAergic neurons [24]. The expression of Cx36 mRNA and protein is detectable in the TG, and Cx36 is distributed in neurons that express substance P, CGRP, and some temperature-sensitive transient receptor potential channels [25] that are closely related to pain production. Moreover, the expression of Cx36 and Cx40 in neurons is increased in animal models of inflammation, but there is no significant increase in Cx43 in astrocytes [26], and our previous study found significant upregulation of Cx36 following partial transection of the infraorbital nerve (pT-ION) [27].

From the above, we hypothesized that upregulated expression of Cx36 plays a vital role in the increased coupling between neurons, which then forms a more highly connected network for rapid signal exchange and thus lays the foundation for primary and secondary allodynia.

We therefore designed experiments to determine whether Cx36 expression would increase after pT-ION, whether functional blockade of Cx36 by the Cx36 inhibitor mefloquine could alleviate pT-ION-induced mechanical and cold allodynia, and whether the increase in the downstream molecules could be reversed. Moreover, we knocked down Cx36 expression using short hairpin RNA

(shRNA)-carrying viruses in Nav1.8-Cre transgenic mice to specifically examine the roles of Cx36 and its downstream molecules in Nav1.8-positive neurons in the pT-ION-induced pain-like behaviors.

Materials and Methods

Animals

All experiments conducted in the present work were approved by the Fudan University Institutional Animal Care and Use Committee and were performed according to the ethical standards of the International Association for the Study of Pain. Male C57Bl/6 mice 6–8 weeks of age and were obtained from the Shanghai Laboratory Animal Center of the Chinese Academy of Sciences. The mice were kept under fixed conditions of 23°C and 12 h of light/dark cycling with free access to food and water. A total of 4–8 animals were placed in a cage for acclimation at least 2 weeks before experiments. Nav1.8-Cre mice were a gift from Dr. Qiufu Ma (Harvard University, Boston, USA) with the permission of Dr. John Wood (University College London, London, UK). All surgery was performed under Avertin anesthesia. The experimenters tried their best to reduce the number and suffering of animals used.

pT-ION Surgery

Mice in the pT-ION group were subjected to pT-ION surgery, which has been shown to rapidly induce stable peripheral neuropathy in mice [27]. After anesthesia with Avertin [350 mg/kg, intraperitoneal (*i.p.*), T48402, Sigma-Aldrich, St. Louis, MO], a cavity was exposed in the left palate and the infraorbital nerve under the mucosa was exposed using angled clamps. The deep branch of the infraorbital nerve innervating the ventral edge of the left vibrissal pad and upper lip was tightly bound with 4.0 catgut, and the distal end was cut open to remove a 1–2 mm segment of the distal nerve. Tissue glue was used to close the incision. Mice in the sham group were anesthetized and the infraorbital nerve exposed as described above, but without nerve ligation or amputation.

Behavioral Testing

Mechanical Allodynia

The experimenters were blinded to the group assignments in the behavioral tests. The ipsilateral hairs in the V2 and V3 skin areas were removed using a hair clipper (HC1066, Philips, Netherlands) three days before the baseline behavioral tests. Mice were handled and conditioned once

a day for 3 days before the tests. During the tests of mechanical allodynia, the mice were placed on the palm of the experimenter's hand for 3 min of adaptation. When the head was stabilized, a set of von Frey fibers (Stoelting, Wood Dale, IL) were poked into its left face in the V2 and V3 skin areas. The bending force of the von Frey fibers varied from 0.07 to 2.0 g, and each fiber was bent to 90° in order to keep the stimulation consistent. A positive reaction was recorded when the mouse flicked its head quickly in response to a complete stimulation. The skin was stimulated five times with each fiber with 30-s intervals between stimulations. The force (g) of the von Frey fiber with three positive reactions among five stimulations was recorded as the threshold of mechanical allodynia. Mice were allowed to move freely during the whole process of behavioral testing.

Cold Allodynia

When we tried to perform the acetone test in the V2 area during the preliminary experiments, we found that it was difficult to avoid spraying acetone into the eyes, and this severely influenced the subsequent behavioral testing. Therefore, the acetone test was performed only in the V3 area. During the test, each mouse was held gently to keep the head fixed, and a 1 mL syringe (Hamilton, Reynolds, NV) was used to drip 50 μ L acetone onto the V3 area of the left side. We tried to protect the eyes by delivering all of the acetone quickly and evenly. Cold hypersensitivity induced by the evaporation of acetone was assessed by the mouse rubbing or grabbing the skin in the V3 region using its front or rear paws. The total duration of wiping caused by the acetone was recorded starting immediately after its application.

Open Field Test

The box for the test was 50 \times 50 \times 40 cm³ with a central zone of 25 \times 25 cm². We put each mouse in the central area and the monitor was started at the same time. The movement of the mouse within the box over the course of 5 min was recorded and calculated using video analysis software (Shanghai Mobile Datum Information Technology Co., Shanghai, China). All of the tests were conducted in a dim and quiet experimental room.

Immunofluorescence Staining

The removal and sectioning of the left TG and immunofluorescence staining were performed as described previously [27]. Briefly, mice were deeply anesthetized using Avertin (350 mg/kg, *i.p.*) and perfused with PBS followed by 4% paraformaldehyde (80096618, Hushi, Shanghai, China).

The TG sections were cut at 10 μ m on a microtome. The primary antibodies were as follows: mouse anti-Cx36 (1:50, sc398063, Santa Cruz Biotechnology, Dallas, TX), goat anti-CGRP (1:500, ab36001, Abcam, Cambridge, UK), mouse anti-neurofilament 200 (NF-200, 1:50, N5389, Sigma-Aldrich, St. Louis, MO), rabbit anti-TRPA1 (1:200, NB110-40763, Novus Biologicals, Centennial, CO), rabbit anti-GluK2 (1:400, AGC-009, Alomone Labs, Jerusalem, Israel), and mouse anti-Cre (1:1,000, MAB3120, Sigma-Aldrich). The mixed secondary antibodies included Alexa 488-conjugated, Alexa 594-conjugated, and Alexa 647-conjugated IB4 antibodies (1:1,000, Invitrogen, Rockford, IL). The sections were coverslipped with DAPI-Fluoromount-G and observed under a multiphoton laser point scanning confocal microscopy system (FV1000, Olympus, Tokyo, Japan). For each experiment, images were captured using same acquisition parameters, processed simultaneously, and analyzed using ImageJ (version 1.8.0; NIH). For single immunofluorescence, the optical density of immunoreactive (IR) staining for Cx36, GluK2, or TRPA1 was measured. The density of IR for each protein was determined by subtracting the background density, and six sections for each mouse were averaged to provide a mean density of IR ($n = 4$ /group). For double immunofluorescence, if the expression of Cx36 or GluK2 (green) in Nav1.8-positive neurons (Cre, red) increased, the area of the merged signal (yellow) was larger, and thus the area of the yellow signal was used to reflect the co-localization intensity. To compare the co-localization of Cx36 or GluK2 and Cre in different groups, six TG sections ($n = 4$ /group) were randomly selected, analyzed, and averaged to obtain the co-localization intensity.

Western Blotting

The treatment of the left TG samples and the following western blotting procedures were also the same as described in our previous work [27]. In brief, protein samples of the left TG were separated by SDS-PAGE and then transferred onto PVDF membranes, which were then blocked with 5% milk and incubated with primary antibodies at 4°C overnight and then incubated with the HRP-conjugated secondary antibody. Listed below are the primary antibodies used in the incubation: mouse anti-Cx36 (1:100, sc398063, Santa Cruz Biotechnology), rabbit anti-TRPA1 (1:500, NB110-40763, Novus Biologicals, CO, USA), rabbit anti-GluK2 (1:400, AGC-009, Alomone Labs), rabbit anti-ERK and anti-p-ERK (1:2,000, Cell Signaling Technology, Danvers, MA), HRP-conjugated mouse anti- β -actin (1:10,000, 4967, Cell Signaling Technology), and HRP-conjugated rabbit anti- β -tubulin (1:5000, 5346, Cell Signaling Technology). The secondary antibodies were HRP-conjugated goat anti-rabbit IgG

(H+L) (1:10,000, SA00001-2, Proteintech) or HRP-conjugated goat anti-mouse IgG (H+L) (1:10,000, SA00001-1, Proteintech). When necessary, western blot stripping buffer (21059, Thermo Fisher, Waltham, MA) was used to remove the combined primary and secondary antibodies of one protein from the PVDF membrane in order to re-detect the other proteins. The intensities of the bands were quantified using Quantity One analysis software (Version 4.6.2, Bio-Rad Laboratories, Hercules, CA) and normalized against the density of β -actin or tubulin.

Drug Administration

Mefloquine (M2319, Sigma-Aldrich), a specific inhibitor of Cx36 [28], was made up in suspension with Tween-80 and then dissolved and diluted in normal saline. Repeated *i.p.* injection of mefloquine was performed in each mouse at 20 or 30 mg/kg once a day from day 7 to day 13 after pT-ION. A single *i.p.* injection of the competitive GluK2 antagonist NS102 (N179, Sigma-Aldrich) was applied at 80, 40, or 8 $\mu\text{mol/L}$ in a volume of 0.1 mL per mouse on day 21 after pT-ION and on day 28 after AAV-Cx36-Ove virus injection. NS 102 was prepared as a stock solution in DMSO (D2650, Sigma-Aldrich) and diluted with DMSO at first and further diluted with normal saline before experiments. The concentration of DMSO in the drug solution was 5%.

Adeno-Associated Virus (AAV)-Mediated Gene Knockdown and Overexpression

For the Cx36 knockdown experiment, the vector-mediated miR30-based short hairpin RNA (shRNA) knockdown strategy was used. In detail, for Cre-dependent expression of shRNAs in transgenic mice, the shRNA coding sequence targeting mouse *Gjd2* (5-GCAGCACTCCACTATGATT-3) was cloned into the pAAV-CBG-LSL-EGFP-3xFLAG-WPRE vector (OBiO Technology Co., Ltd., Shanghai, China) using the *BsrGI*/*HindIII* restriction sites. AAV2/Retro-CBG-LSL-EGFP-miR30shRNA(*Gjd2*)-WPRE and its control AAV2/Retro-CBG-LSL-EGFP-3xFLAG-WPRE virus were packaged by OBiO Technology. *Gjd2* is the encoding gene of Cx36, and the above gene construction achieved the retrograde and Cre-dependent interference of *Gjd2* expression, and thus resulted in the downregulation of Cx36 in TG neurons after subcutaneous virus injection. For the Cx36 overexpression experiment, the coding sequence of mouse Cx36 (NC_000068.7) was designed and packaged as an AAV2/Retro virus (rAAV-CMV-*Gjd2*-P2A-EGFP-WPRE) by BrainVTA (Hubei, China). The control virus was constructed as rAAV-CMV-EGFP. Mice were deeply anesthetized by Avertin (350 mg/kg, *i.p.*), and 8 μL of virus was injected into four sites in the V2 and V3 areas for the Cx36 knockdown experiment while 6 μL of

virus was injected into three sites in the V2 area for the Cx36 overexpression experiment using a 10 μL syringe (Hamilton Co.). The rate of injection was 1 $\mu\text{L}/\text{min}$. The doses of AAV-Cx36-Interfering (AAV-Cx36-Int) virus and AAV-Cx36-Overexpressing (AAV-Cx36-Ove) virus were 3.80×10^{12} viral genomes (v.g.)/mL and 5.60×10^{12} v.g./mL, respectively. After injection into each site, the needle was retained for 1 min.

Statistical Analysis

The data were analyzed by GraphPad Prism 8 (GraphPad Software Inc., San Diego, CA) and are presented as means \pm SEM. One-way analysis of variance (ANOVA) followed by Tukey's test or Dunnett's multiple comparisons test and Student's *t*-test were used to compare the differences between two groups. The data from the behavioral tests were analyzed by two-way repeated-measures (RM) ANOVA followed by Sidak's test or Tukey's test. The linear correlation between data from two groups was analyzed using Pearson's correlation. $P < 0.05$ was adopted as the significance threshold for all analyses.

Results

The Cx36 Inhibitor Mefloquine Ameliorates the pT-ION-induced Primary and Secondary Orofacial Allodynia, Especially Cold Allodynia

We used the pT-ION mouse model of trigeminal neuralgia, which has been used in previous work [27]. This model was established by the ligation and subsequent partial transection of the infraorbital nerve. The V2 skin area was innervated by the injured nerve, and the allodynia in this area is referred to as primary allodynia, while that in the uninjured nerve-innervated V3 area is referred to as secondary allodynia. A lower threshold response upon mechanical stimulation from the von Frey filament compared to baseline or the sham group is defined as mechanical allodynia. From day 7 after the pT-ION surgery, the thresholds in response to von Frey hair stimulation in the V2 and V3 areas ipsilateral to the injured nerve were significantly reduced compared to the sham group and remained stable for the following 21 days (Fig. 1A, B). Cold allodynia in the V3 area was also induced compared to the sham group, with significantly prolonged duration of wiping time caused by acetone starting from day 7 after surgery and lasting for at least 21 days (Fig. 1C).

To ascertain the contribution of Cx36 to neuropathic orofacial allodynia, mice were injected *i.p.* with mefloquine, an inhibitor of Cx36, on day 7 after pT-ION.

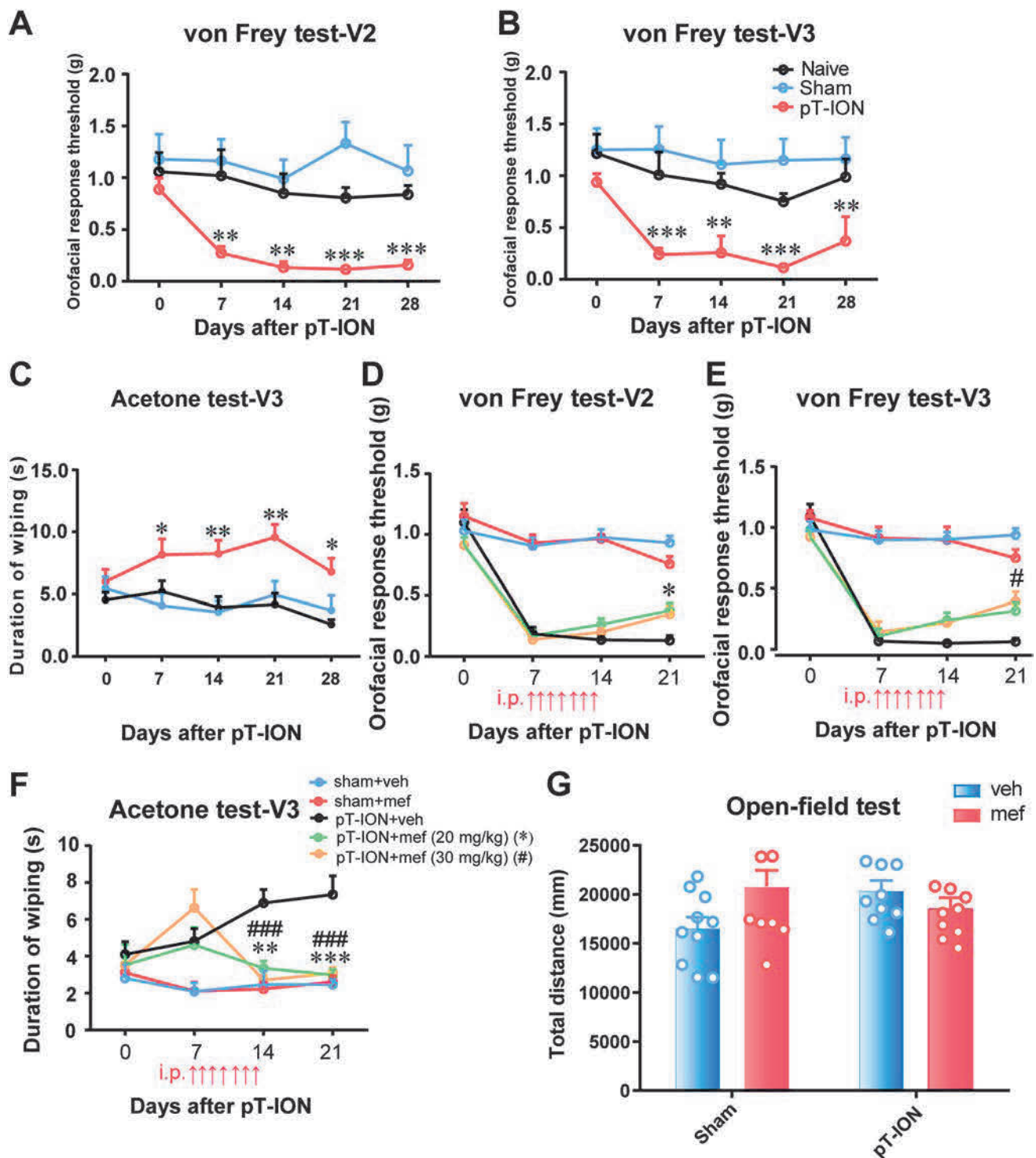


Fig. 1 Pharmacological inhibition of Cx36 reverses pT-ION-induced orofacial allodynia. **A–C** pT-ION leads to long-lasting primary (A) and secondary (B) mechanical allodynia in the ipsilateral V2 and V3 areas and to secondary cold allodynia (C) in the ipsilateral V3 area. Data are shown as means \pm SEM, $n = 8$ /group. $*P < 0.05$, $**P < 0.01$, and $***P < 0.001$ vs sham group (two-way RM ANOVA followed by Tukey's test). **D–F** Mefloquine (mef) at two doses for 7 consecutive days, significantly suppresses pT-ION-induced primary (D) and secondary (E) mechanical allodynia and secondary cold

allodynia (F) in the V2 and V3 areas (arrows, time points of mefloquine injection). Data are shown as means \pm SEM, $n = 10$ /group. $*P < 0.05$, $**P < 0.01$, and $***P < 0.001$, pT-ION+mef (20 mg/kg) vs pT-ION+veh; $*P < 0.05$ and $###P < 0.001$, pT-ION+mef (30 mg/kg) vs pT-ION+veh (two-way RM ANOVA followed by Tukey's test). **G** The open-field test shows no difference in total distance among the four groups at 20 mg/kg mefloquine ($n = 10$; two-way ANOVA followed by Sidak's test).

Because stable primary and secondary orofacial allodynia was established on day 7 after pT-ION, the effects of mefloquine on established allodynia were evaluated at that time point. The mefloquine was administered at either 20 or 30 mg/kg daily for 7 days. Compared to the pT-ION+veh group, both doses of mefloquine significantly reversed the mechanical allodynia in the V2 and V3 regions, and the effect was similar for both doses (Fig. 1D, E). It should be noted that while mefloquine only partially rescued the mechanical allodynia, it completely reversed the pT-ION-induced cold allodynia (Fig. 1F), which indicated that Cx36 is more involved in trigeminal nerve injury-induced cold pain. To test whether mefloquine had an effect on motor function, the open-field test was performed on day 21 after pT-ION. The total distance was measured and showed no significant difference when mefloquine was applied at 20 mg/kg in pT-ION mice (Fig. 1G). However, we found that the higher dose of mefloquine at 30 mg/kg resulted in movement deficiency (data not shown), so 20 mg/kg was chosen as the treatment dose in the subsequent experiments. In addition, mefloquine had no significant impact on movement in the sham groups (Fig. 1G).

Trigeminal Nerve Injury Induces Increased Cx36 Expression in the TG

Immunofluorescence staining images of Cx36 in the TG are shown in Fig. 2A. We measured the expression of Cx36 in the TG on days 1, 3, 5, 7, 14, 21, and 28 after pT-ION surgery. The level of Cx36 increased significantly from day 5 and lasted up to 28 days (Fig. 2B, C). If aberrant Cx36 expression really induces and mediates the primary and secondary orofacial allodynia in mice with trigeminal nerve injury, then changes in Cx36 expression in the ipsilateral TG should be correlated with the occurrence of orofacial allodynia behaviors. Linear regression analysis showed that the level of Cx36 expression in the ipsilateral TG was negatively correlated with the mechanical response thresholds in both the V2 and V3 areas (V2: $P = 0.1248$, $r = -0.7736$, $Y = -1.250 * X + 1.683$; V3: $P = 0.0311$, $r = -0.9117$, $Y = -1.493 * X + 1.864$; Fig. 2D, E) and was positively correlated with the duration of the wiping response to acetone in the V3 region ($P = 0.0476$, $r = 0.8823$, $Y = 0.3455 * X - 1.248$; Fig. 2F). The relationship between Cx36 upregulation in the TG and orofacial allodynia after pT-ION surgery suggested that Cx36 is critical in inducing orofacial allodynia.

We next determined the distribution of Cx36 in the TG-V2 and TG-V3 neurons of the pT-ION mice (Supplementary Fig. S1A). The TG mainly includes three types of neurons: peptidergic nociceptors (expressing the marker CGRP), non-peptidergic nociceptors (expressing the

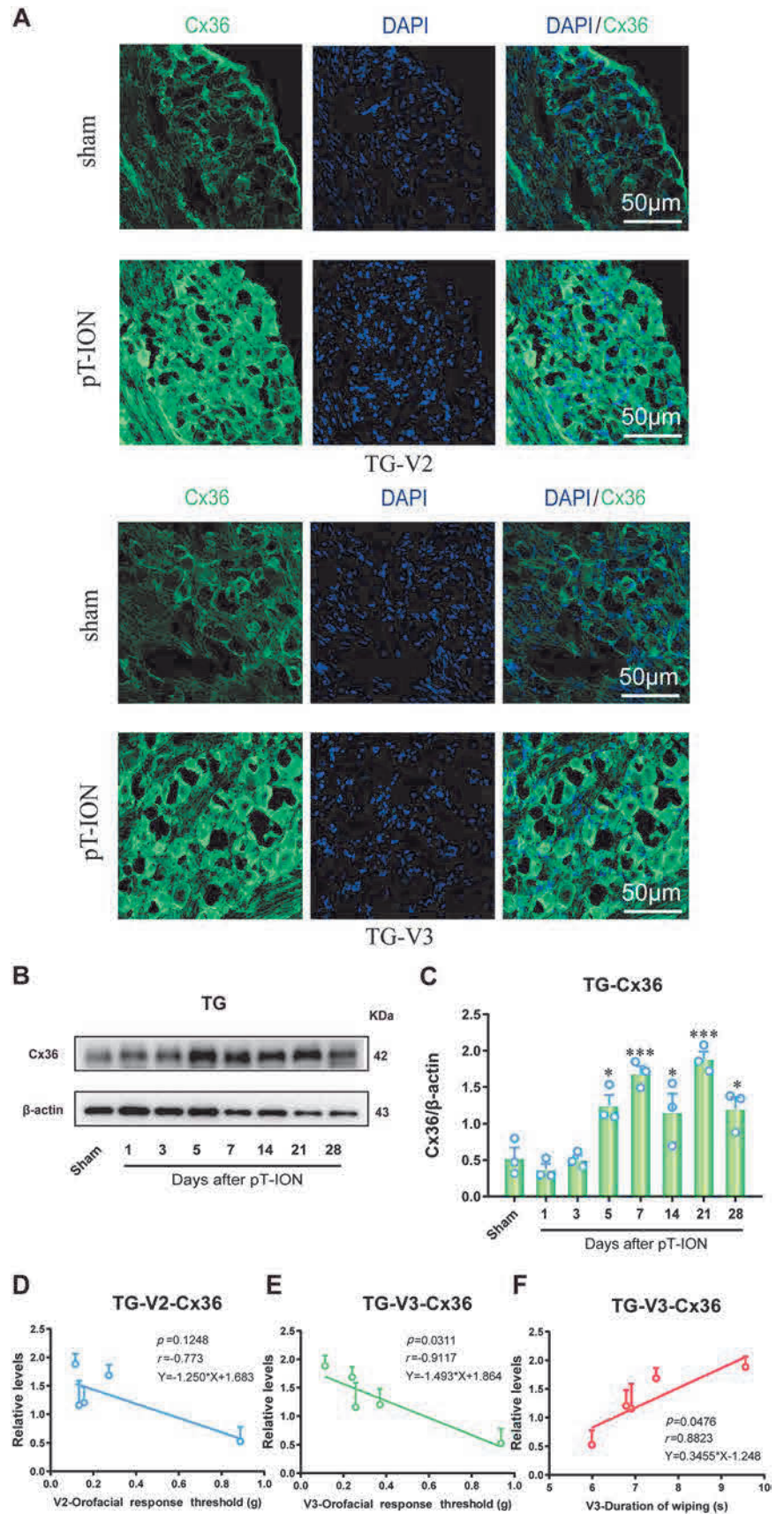
marker IB4), and large non-nociceptive neurons (expressing the marker NF200). Immunofluorescence staining showed that Cx36 was co-localized with CGRP (Fig. S1B), IB4 (Fig. S1C), and NF200 (Fig. S1D) in both TG-V2 and TG-V3 at 21 days after pT-ION. These results demonstrated that Cx36 is widely distributed in the TG but is not selectively expressed in nociceptors. Moreover, the pT-ION-induced increase in Cx36 expression was observed in both TG-V2 and TG-V3 neurons (Fig. S2), which provided anatomical support for the Cx36-mediated spread of pain.

The Cold Sensor GluK2 is a Potential Downstream Effector of Cx36 in Mediating pT-ION-induced Cold Allodynia

Given the significant alleviation of cold allodynia by mefloquine, we hypothesized that Cx36 blockade changes the expression or function of a cold sensor. A recent study showed that mouse GluK2 in peripheral sensory neurons is involved in mediating cold sensation [29], so we next determined whether GluK2 acts downstream of Cx36 in mediating pT-ION-induced cold allodynia. Immunofluorescence staining showed that GluK2 was expressed in both TG-V2 and TG-V3 neurons after pT-ION (Fig. 3A). GluK2 was upregulated in the ipsilateral TG starting from 7 days to at least 21 days after nerve injury (Fig. 3B). Moreover, the pT-ION-induced upregulation of GluK2 was positively correlated with the increased expression of Cx36 ($P = 0.0443$, $r = 0.9557$, $Y = 0.3781 * X + 0.4898$; Fig. 3C). Immunofluorescence staining also showed a pT-ION-induced increase in GluK2 expression in TG neurons (Supplementary Fig. S2)

To determine the role of GluK2 in mediating primary and secondary allodynia, NS 102, an antagonist of GluK2, was injected on day 21 after pT-ION. NS 102 was tested at 8, 40, and 80 $\mu\text{mol/L}$ in 0.1 mL was injected *i.p.*. The von Frey test and acetone test were carried out at 1, 2, 4, and 24 h after NS 102 injection. We found that blocking GluK2 with NS 102 did not reduce mechanical allodynia in the V2 or V3 areas regardless of the dose or time point (Fig. 4A, B). However, as is shown in Fig 4C, all three doses of NS 102 significantly reversed cold allodynia in the V3 area at 1 and 2 h after drug application. Western blotting showed that NS 102 caused a dose-dependent reduction in the phosphorylation of ERK at 2 h after NS 102 administration (Fig. 4D–F), which is critical in mediating the development of pain [30]. However, no difference in total ERK was shown in response to NS 102. The highest dose, 80 $\mu\text{mol/L}$, was used in the subsequent experiments. Therefore, the above results demonstrate that GluK2 contributes greatly to cold allodynia, but not mechanical allodynia, perhaps through downstream ERK activation.

Fig. 2 pT-ION induces upregulation of Cx36 in the TG. **A** Representative images of immunofluorescence staining of Cx36 in the TG on day 14 after surgery. **B, C** Time course of Cx36 expression in the ipsilateral TG after pT-ION. Data are shown as means \pm SEM, $n = 3/\text{group}$. * $P < 0.05$ and *** $P < 0.001$ vs sham (one-way ANOVA followed by Dunnett’s test). **D–F**, Linear correlation between Cx36 expression and orofacial response threshold (g) in the V2 and V3 and duration of wiping (s). (**D**: $P = 0.1248$, $r = -0.7736$; **E**: $P = 0.0311$, $r = -0.9117$; **F**: $P = 0.0476$, $r = 0.8823$).



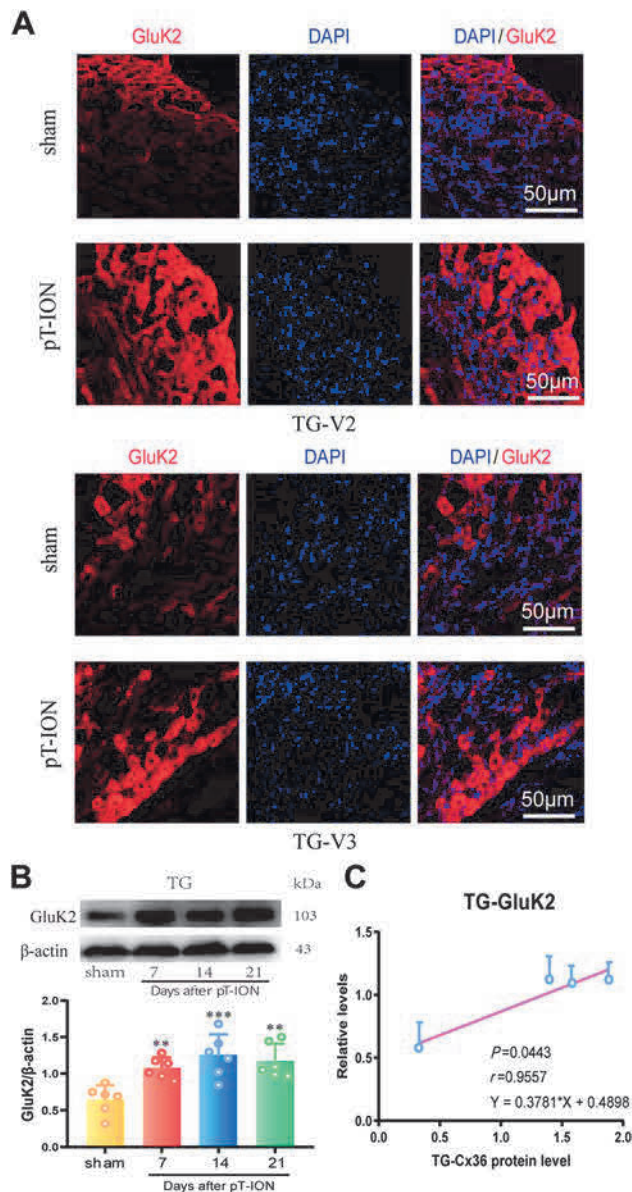


Fig. 3 pT-ION induces upregulation of GluK2. **A** Representative images of immunofluorescence staining of GluK2 in the TG. DAPI was used to stain the cell nuclei. **B** Time course of GluK2 expression in the ipsilateral TG after pT-ION (TGs from the sham group were obtained on day 7 after surgery). Data are shown as means \pm SEM, $n = 6/\text{group}$. $**P < 0.01$ and $***P < 0.001$ vs sham (one-way ANOVA analysis followed by Tukey's test). **C** pT-ION-induced increase in GluK2 expression is positively correlated with Cx36 expression in the ipsilateral TG ($P = 0.0443$, $r = 0.9557$).

The Cx36 Inhibitor Mefloquine Reverses the pT-ION-induced Upregulation of TRPA1 in Addition to GluK2 and p-ERK

Because Cx36 blockade alleviated not only cold allodynia, but also the mechanical allodynia induced by PT-ION, and because Cx36 overexpression induced both cold and mechanical allodynia, other molecules downstream of

Cx36 may mediate the induction of mechanical allodynia. Given that our previous study showed that the TRPA1 antagonist HC-030031 reverses pT-ION-induced mechanical and cold allodynia [27], TRPA1 might be this downstream molecule. Immunofluorescence staining showed that TRPA1 was co-localized with Cx36 in both the TG-V2 and TG-V3 neurons of pT-ION mice (Fig. 5A, B), and immunofluorescence staining showed a pT-ION-induced increase in TRPA1 expression in the TG-V2 and TG-V3 neurons (Fig. S2). Western blotting showed that pT-ION induced an increase in TRPA1 expression in the TG, and this increase was significantly reversed by repeated application of mefloquine at 20 mg/kg (daily from 7 to 13 days after pT-ION) at day 21 after pT-ION (Fig. 5C, F). Moreover, linear regression analysis showed that the downregulation of TRPA1 due to Cx36 blockade was positively correlated with the decreased expression of Cx36 protein (TRPA1-Cx36: $P = 0.0104$, $r = 0.8319$, $Y = 1.102 \cdot X + 0.01795$, Fig. 5J). In addition, the pT-ION-induced upregulation of GluK2 and p-ERK was also significantly reversed by repeated application of mefloquine, and the downregulation of both GluK2 and p-ERK was positively correlated with the decrease in Cx36 expression following mefloquine application (GluK2-Cx36: $P = 0.0208$, $r = 0.7856$, $Y = 1.198 \cdot X + 0.1418$; p-ERK-Cx36: $P = 0.0334$, $r = 0.7463$, $Y = 0.9241 \cdot X + 0.3188$) (Fig. 5C–E, G–J). No significant differences were seen after mefloquine treatment in mice from the sham groups. These results support the hypothesis that, in addition to GluK2, TRPA1 serves as another downstream effector of Cx36 in mediating trigeminal nerve injury-induced mechanical and cold allodynia.

The Cold Allodynia, but not the Mechanical Allodynia Induced by AAV-mediated Cx36 Overexpression is Reversed by the GluK2 Antagonist NS 102

To demonstrate whether upregulation of Cx36 in the V2 area is sufficient to induce orofacial allodynia, we induced AAV-mediated Cx36 overexpression in the TG-V2 neurons of naïve mice by injecting the virus subcutaneously. The AAV-Cx36-Ove virus or AAV-control virus was subcutaneously injected into three sites in the V2 skin area (Fig. 6A), and 2 μL of virus was injected into each site. This viral vector is retrogradely transported from the nerve endings to the somata and overexpress Cx36 specifically in TG-V2 neurons. This method allowed the virus to specifically target TG-V2 or TG-V3 neurons without infecting neurons in the adjacent TG areas (Fig. S3). The von Frey test and acetone test were carried out every week after viral injection, and the orofacial response thresholds of the ipsilateral V2 and V3 areas were significantly decreased 3

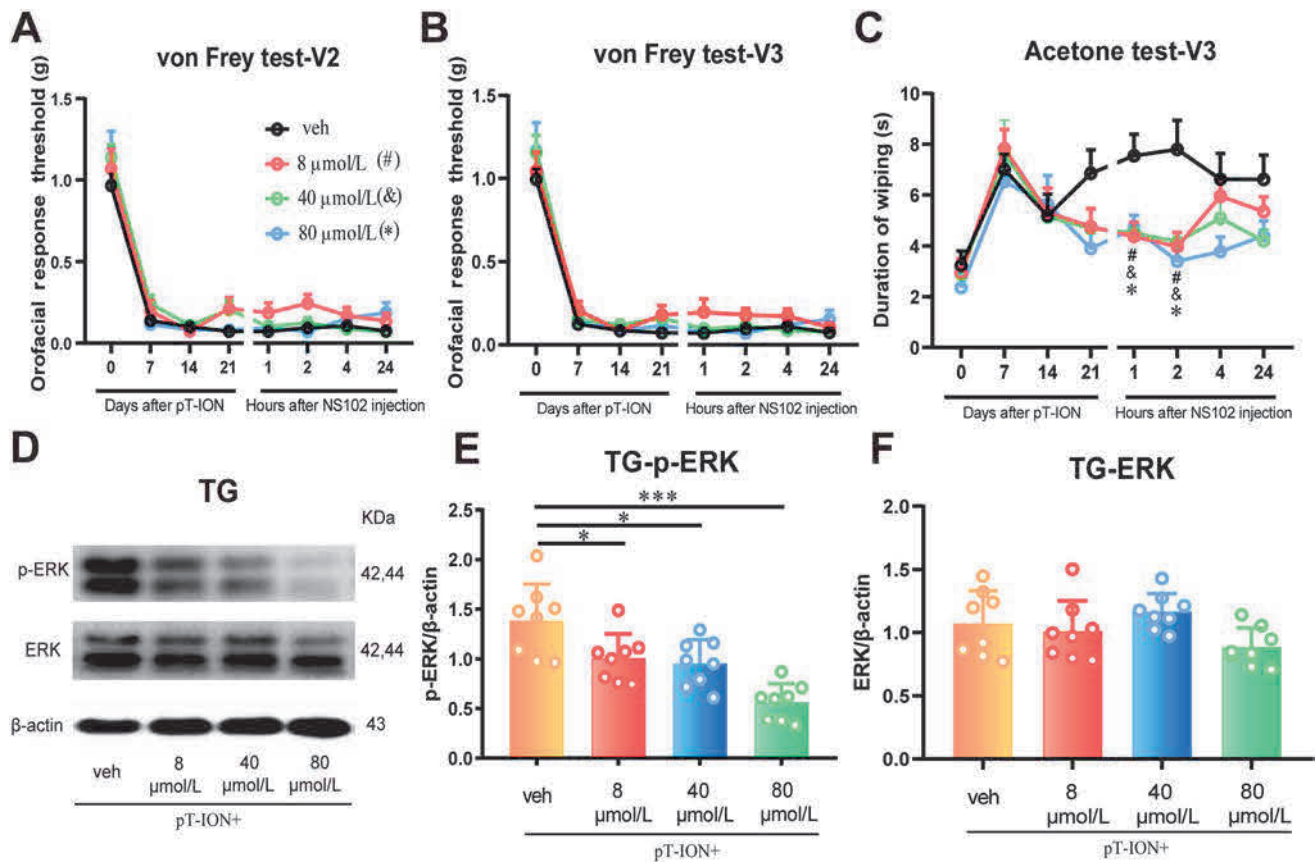


Fig. 4 The GluK2 antagonist NS 102 reverses pT-ION-induced cold allodynia and ERK activation but not mechanical allodynia. **A–C** At day 21 after pT-ION, *i.p.* injection of NS 102 at three doses attenuated cold allodynia in the V3 area (C), but not mechanical allodynia in either the V2 (A) or V3 (B) area at 1 or 2 h after injection. Data are shown as means \pm SEM, $n = 10$ /group. # $P < 0.05$ (8 $\mu\text{mol/L}$), & $P < 0.05$ (40 $\mu\text{mol/L}$), and * $P < 0.05$ (80 $\mu\text{mol/L}$) vs vehicle (veh) (two-way RM ANOVA followed by Tukey's test). **D–F** Activation of ERK in the ipsilateral TG is reversed by all three doses of NS 102 at 2 h after injection. Data are shown as means \pm SEM, $n = 10$ /group. * $P < 0.05$ and *** $P < 0.001$ vs veh (one-way ANOVA followed by Tukey's test).

weeks after injection of AAV-Cx36-Ove virus (Fig. 6B, C), and this effect lasted until the final day of the experiment (28 days after virus injection). At the same time, the duration of wiping increased significantly on day 28 after virus injection (Fig. 6D). NS 102 was administered to the mice on day 28 to see whether GluK2 blockade could rescue Cx36 overexpression-induced orofacial allodynia, and we found that the Cx36 overexpression-induced increase in the duration of wiping was significantly reversed (Fig. 6D). However, Cx36 overexpression-induced mechanical allodynia in the V2 and V3 regions was not affected (Fig. 6B, C). Western blots showed that overexpressing Cx36 in the TG-V2 neurons of naïve mice significantly enhanced the expression of GluK2, TRPA1, and p-ERK in the TG ipsilateral to the injury (Fig. 6E–K), and these increases were positively correlated with the upregulation of Cx36 (Fig. 6L). Moreover, the Cx36 overexpression-induced increase in p-ERK expression was reversed by the GluK2 antagonist NS 102 (Fig. 6I, J). These results suggested that upregulation of Cx36

overexpression is sufficient to induce both cold and mechanical allodynia and that GluK2, TRPA1, and p-ERK serve as the downstream effectors of Cx36 in mediating the induction of cold allodynia but not mechanical allodynia.

overexpression is sufficient to induce both cold and mechanical allodynia and that GluK2, TRPA1, and p-ERK serve as the downstream effectors of Cx36 in mediating the induction of cold allodynia but not mechanical allodynia.

Selective Knockdown of Cx36 in Nav1.8-expressing Nociceptors Reverses pT-ION-induced Cold Allodynia but not Mechanical Allodynia

It has been proposed that Nav1.8-expressing nociceptors are critical in mechanical and cold pain perception [31]. In addition, we showed above that Cx36 blockade alleviated pT-ION-induced cold allodynia more than mechanical allodynia. Therefore, we hypothesized that Cx36 expressed in the Nav1.8-expressing nociceptors of the TG contributes to pT-ION-induced cold allodynia. To this end, we first tested the changes of Cx36 expression in Nav1.8-positive neurons. Immunofluorescence staining showed that Cx36 was expressed in Nav1.8-positive neurons, and the

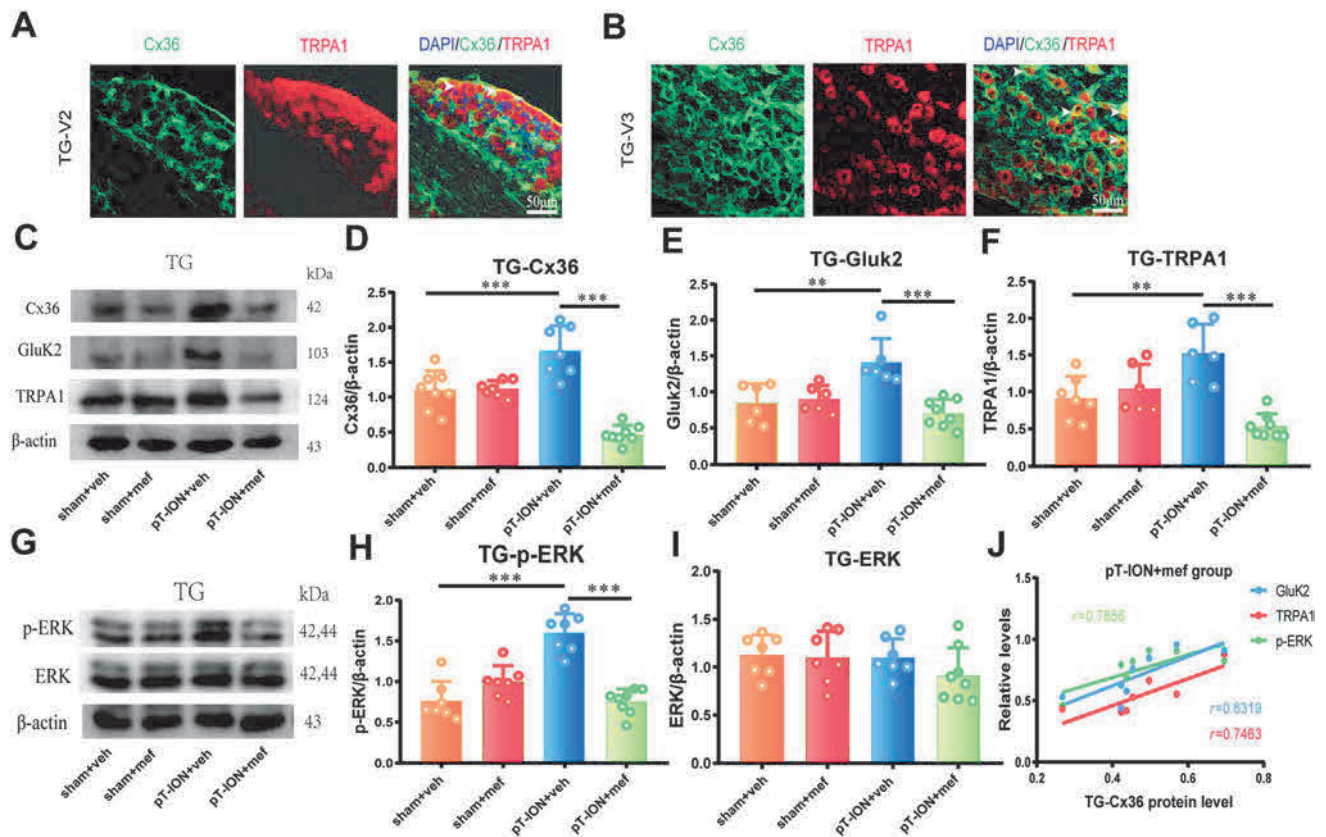


Fig. 5 The Cx36 inhibitor mefloquine reverses the pT-ION-induced increase in expression of Cx36, GluK2, TRPA1, and p-ERK. **A**, **B** Cx36 (green) is co-localized with TRPA1 (red) in both the TG-V2 (**A**) and TG-V3 (**B**) in pT-ION mice (scale bars, 50 μ m). DAPI was used to stain the cell nuclei. **C–I** The pT-ION-induced upregulation of Cx36, GluK2, TRPA1, and p-ERK in the ipsilateral TG is reversed by repeated application of the Cx36 inhibitor mefloquine (mef, 20 mg/kg, *i.p.*, once a day from day 7 to day 13 after pT-ION). Data are

shown as means \pm SEM, $n = 7$ /group. ** $P < 0.01$ and *** $P < 0.001$ (one-way ANOVA followed by Tukey's test). **J** The decrease in GluK2, TRPA1, and p-ERK expression by the Cx36 inhibitor mefloquine (20 mg/kg, *i.p.*) is positively correlated with the mefloquine-induced downregulation of Cx36 (GluK2-Cx36: $P = 0.0208$, $r = 0.7856$; TRPA1-Cx36: $P = 0.0104$, $r = 0.8319$; p-ERK-Cx36: $P = 0.0334$; $r = 0.7463$).

expression was significantly increased after pT-ION compared with the sham group (Fig. S4). The expression of GluK2 showed similar results. We then subcutaneously injected Cre-dependent AAV-Cx36-Int or AAV-control virus into Nav1.8-Cre mice to selectively knock down Cx36 expression in Nav1.8-expressing nociceptors. The virus was injected at four sites in the orofacial area with 2 μ L of virus in each site (Fig. 7A). This viral vector is retrogradely transported from the nerve endings into the somata of TG neurons to interfere with the expression of Cx36. The pT-ION surgery was performed immediately after virus injection in Nav1.8-Cre mice, and the virus was allowed 3 weeks to reach peak infection. As is indicated in Fig. 7D, the AAV-Cx36-Int virus, but not the AAV-control virus, completely reversed the pT-ION-induced cold allodynia in the V3 area, which started at day 21 after virus injection (the infection peak) and lasted for at least 7 days. However, no distinct alleviation of mechanical allodynia in the V2 or V3 regions was found (Fig. 7B, C). Western

blotting was used to explore the changes in Cx36 and the downstream molecules in TG samples on day 28 after virus injection. The AAV-Cx36-Int virus reversed the pT-ION-induced upregulation of Cx36, GluK2, TRPA1, and p-ERK, but no significant difference was found for total ERK expression (Fig. 7E–K). The downregulation of GluK2, TRPA1, and p-ERK was positively correlated with the downregulation of Cx36 in the AAV-Cx36-Int virus group (GluK2-Cx36: $P = 0.0093$, $r = 0.8387$, $Y = 0.8486 * X + 0.1443$; TRPA1-Cx36: $P = 0.0312$, $r = 0.7526$, $Y = 1.131 * X + 0.03634$; p-ERK-Cx36: $P = 0.0409$, $r = 0.7272$, $Y = 0.6553 * X + 0.2932$; Fig. 7L). Furthermore, immunofluorescence staining also showed the downregulation of Cx36 in Nav1.8-positive neurons (Fig. S5). These results support our hypothesis that Cx36 and the downstream pathway in Nav1.8-expressing nociceptors only contribute to the pT-ION-induced cold allodynia.

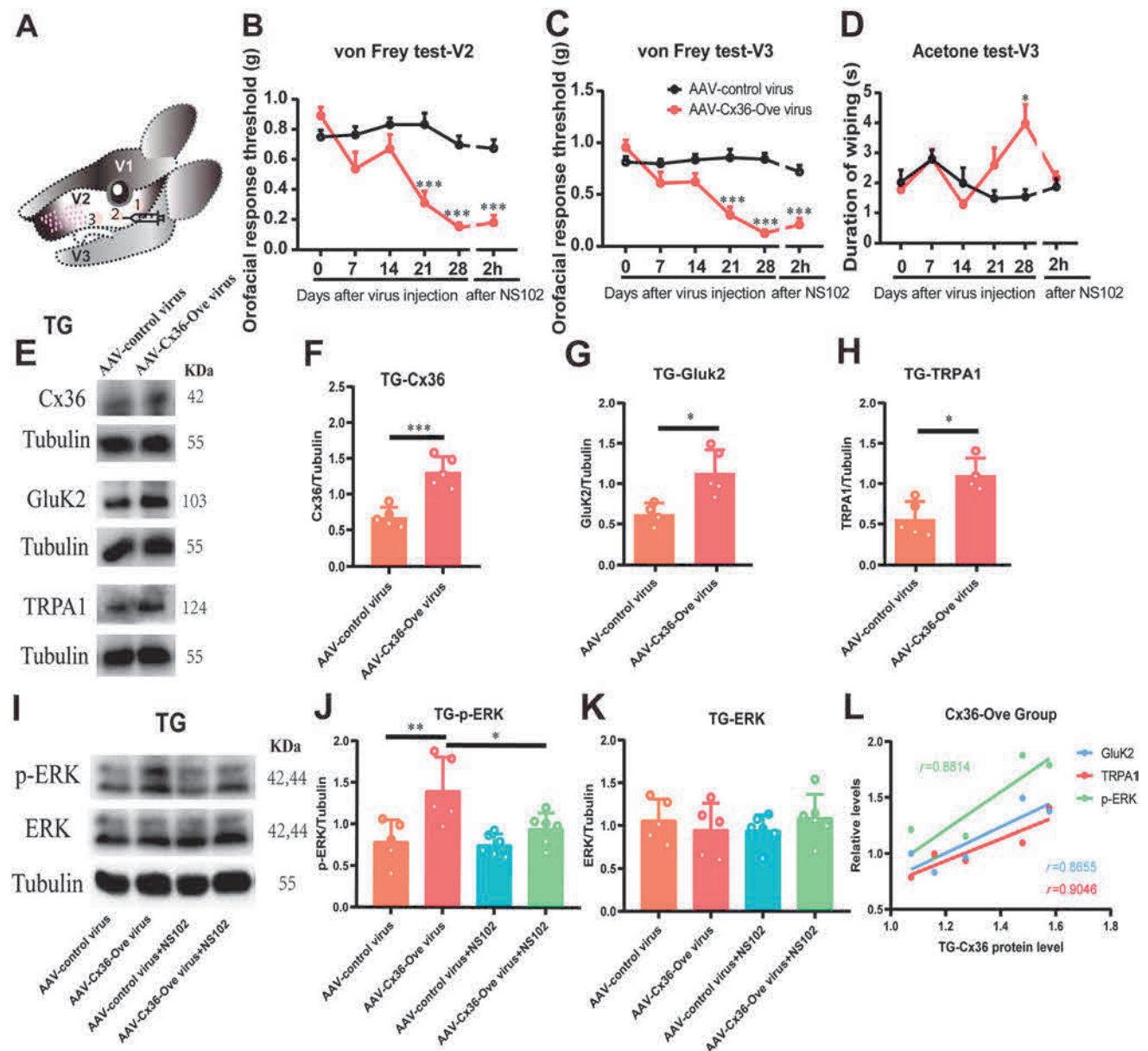


Fig. 6 The orofacial allodynia and the upregulation of GluK2 and TRPA1 induced by Cx36 overexpression in TG-V2 neurons and the effects of the GluK2 antagonist NS 102. **A** Schematic of the three injection sites in the V2 skin area. **B–D** Cx36 overexpression in TG-V2 neurons induces mechanical allodynia in both the V2 (**B**) and V3 (**C**) skin areas and cold allodynia in the V3 area (**D**). Data are shown as means \pm SEM, $n = 10$ /group. * $P < 0.05$ and *** $P < 0.001$ vs AAV-control virus (two-way RM ANOVA followed by Sidak's test). **E–H** The expression of Cx36, GluK2, and TRPA1 increases after Cx36 overexpression. **I–K** The upregulation of p-ERK induced by

Cx36 overexpression is reversed by the GluK2 antagonist NS-102. Data are shown as means \pm SEM, $n = 5$ for the AAV-control virus group and AAV-Cx36-Ove virus group, $n = 6$ for the AAV-control virus+NS102 group and AAV-Cx36-Ove virus+NS102 group. * $P < 0.05$, ** $P < 0.01$, *** $P < 0.001$ (one-way ANOVA followed by Tukey's test). **L** The increase in GluK2, TRPA1, and p-ERK expression induced by Cx36 overexpression is positively correlated with the upregulation of Cx36 (GluK2-Cx36: $P = 0.0580$, $r = 0.8655$; TRPA1-Cx36: $P = 0.0349$, $r = 0.9046$; p-ERK-Cx36: $P = 0.0482$; $r = 0.8814$).

Discussion

Trigeminal neuralgia is one of the most intractable diseases of the nervous system, and a lack of understanding of its underlying etiology has limited the development of treatments. Our study demonstrates that pT-ION results in

increased expression of Cx36 in the ipsilateral TG and that this upregulation is associated with mechanical and cold allodynia. Blocking Cx36 with mefloquine reversed the pT-ION-induced mechanical and cold allodynia and increased GluK2, TRPA1, and p-ERK expression. In addition, overexpressing Cx36 in TG-V2 neurons induced

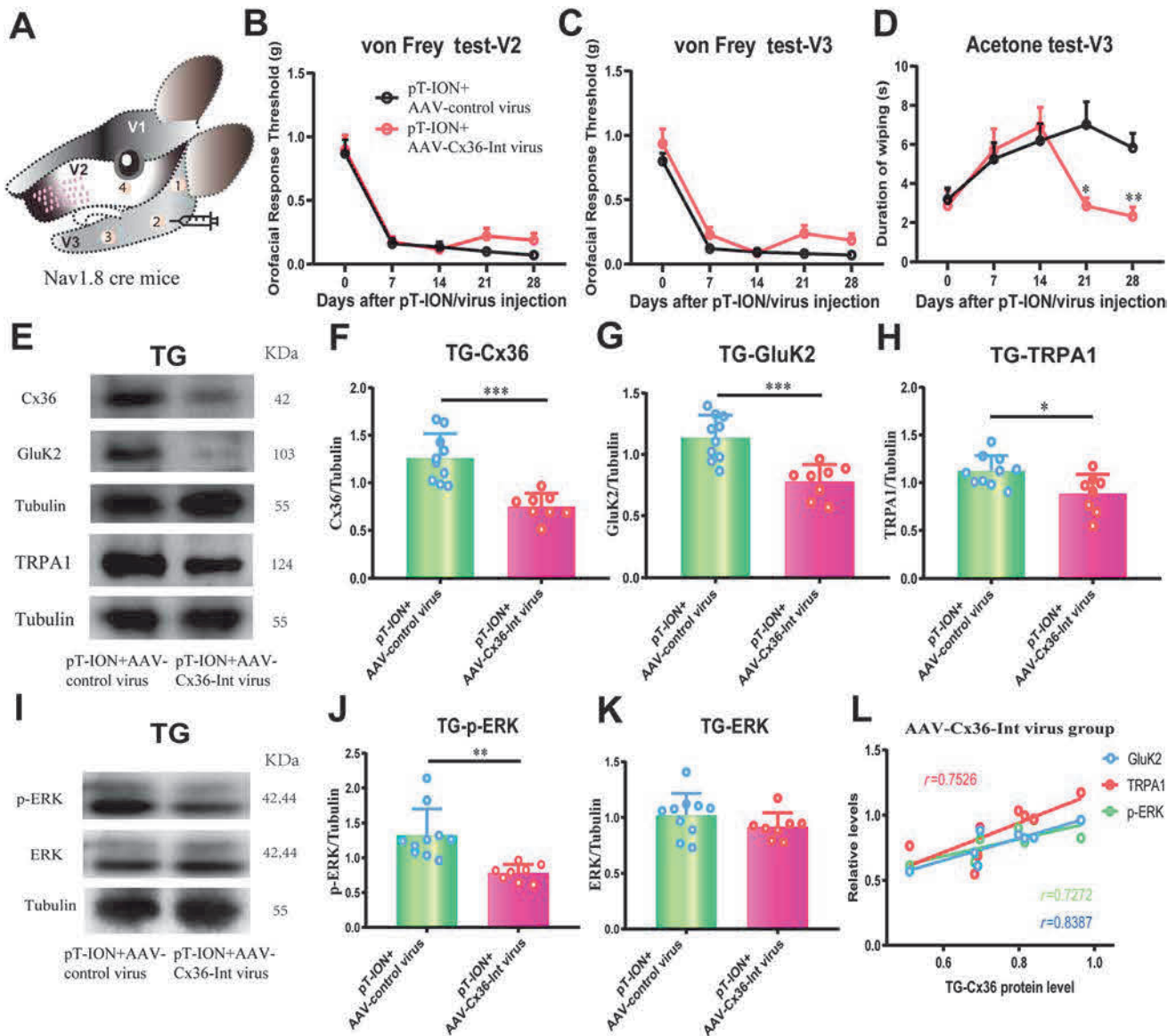


Fig. 7 The reversal of pT-ION-induced cold allodynia and the upregulation of Cx36, GluK2, TRPA1, and p-ERK by genetic inhibition of Cx36 expression in Nav1.8-Cre mice. **A** Schematic of the four injection sites in the V2 and V3 skin areas. **B–D** Cx36 knockdown in TG-V2 and TG-V3 neurons alleviates cold allodynia (**D**) in the V3 skin area but not mechanical allodynia in either the V2 (**B**) or V3 (**C**) areas starting from 21 days after pT-ION (*i.e.* 21 days after virus injection). Data are shown as means \pm SEM, $n = 10$ /group. * $P < 0.05$ and ** $P < 0.01$ vs AAV-control virus (two-way RM ANOVA followed by Sidak’s test). **E–K** The pT-ION-induced

upregulation of GluK2, TRPA1, and p-ERK is reversed by Cx36 knockdown through subcutaneous injection of AAV-Cx36-Int virus at 28 days after pT-ION (*i.e.* 28 days after virus injection). Data are shown as means \pm SEM, $n = 7$ /group. * $P < 0.05$, ** $P < 0.01$, and *** $P < 0.001$ (Student’s unpaired *t*-test). **L** The AAV-Cx36-Int virus-mediated decrease in GluK2, TRPA1, and p-ERK expression is positively correlated with the downregulation of Cx36 (GluK2-Cx36: $P = 0.0093$, $r = 0.8387$; TRPA1-Cx36: $P = 0.0312$, $r = 0.7526$; p-ERK-Cx36: $P = 0.0409$; $r = 0.7272$).

stable mechanical and cold allodynia in both the V2 and V3 areas, and the cold allodynia but not the mechanical allodynia was reversed by the GluK2 antagonist NS102. Specifically knocking down Cx36 expression in Nav1.8-expressing nociceptors suppressed cold allodynia but did not suppress mechanical allodynia. On the whole, we suggest that Cx36 in the TG mediates orofacial pain hypersensitivity through GluK2 and TRPA1 signaling, and

Cx36 in Nav1.8-expressing nociceptors in particular contributes to the induction of orofacial cold allodynia (Fig. 8).

We developed a mouse model of pT-ION that presents with stable primary allodynia in the V2 skin area and secondary allodynia in the V3 skin area. In the pT-ION model we cut off and removed a 1–2 mm segment of the distal infraorbital nerve, which causes a more rapid

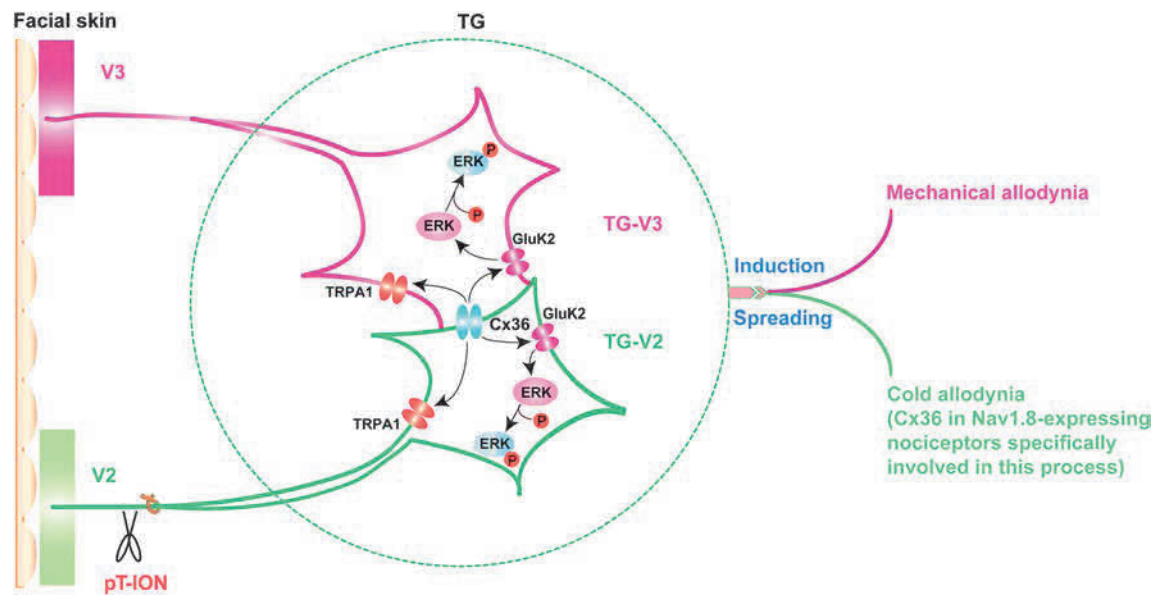


Fig. 8 Schematic of the proposed mechanism. pT-ION induces the upregulation of Cx36 and the downstream activation of GluK2, TRPA1, and ERK, which leads to hyperactivity of primary TG-V2 subdivision neurons. The sensitization of TG-V2 neurons subsequently activates the TG-V3 neurons through Cx36 gap junctions.

GluK2, TRPA1, and the downstream ERK are activated in TG-V3 neurons, resulting in the spread of behavioral hypersensitivity to nearby uninjured facial skin. pT-ION, spared nerve injury of the infraorbital nerve; TG, trigeminal ganglion; Cx36, connexin 36; GluK2, kainate receptor.

allodynia onset and stabilization than the traditional model of chronic constriction injury of the infraorbital nerve [32, 33]. The pT-ION model was established by the ligation and removal of the infraorbital nerve, which consists purely of sensory fibers. Consistent with previous reports [27, 34, 35], we found that trigeminal nerve injury leads to both mechanical and cold allodynia. In addition, the increased sensitivity to mechanical stimulation and cold has similarities with the clinical presentation of patients with trigeminal neuralgia [36].

Gap junctions play a critical role in the nervous system, and they have been shown to take part in neurogenesis, differentiation, and information transmission [37, 38]. It has been reported that electrical coupling contributes to the synchronous activation of adjacent neurons after nerve injury [39], which thus provides a new mechanism for the induction of pain hypersensitivity [40]. Several kinds of Cxs are expressed in the TG, including Cx26, which is located between neurons and SGCs, Cx36, which is specifically expressed between neurons, and Cx43, which is expressed between SGCs [26]. Here, we found that secondary orofacial allodynia occurred quite early, starting from 7 days after pT-ION and at almost the same time as primary allodynia. We assume that TG-V2 neurons rapidly activate TG-V3 neurons through gap junctions, and thus secondary allodynia in the V3 area is quickly induced. Spreading is quite common in persistent pain and is commonly considered to be associated with CNS activity [33], but our present work provides a possible peripheral

mechanism mediated by gap junctions. It has been reported that increased expression of Cx36 in the medullary dorsal horn contributes to trigeminal nerve injury-induced mechanical allodynia by coupling GABA cells [24]. We found that the expression of Cx36 was upregulated in the TG after nerve injury, but there are no GABA cells in the TG, so whether and how Cx36 in the TG is involved in the development of orofacial pain hypersensitivity is unknown.

We found that mefloquine, which is widely used to prevent malaria and acts as a specific Cx36 inhibitor [41], reduced chronic neuropathic pain and both primary and secondary allodynia. It should be noted that the cold allodynia was reversed immediately after the repeated injection of mefloquine for 7 consecutive days, while the alleviation of mechanical allodynia occurred 7 days after the last injection. This might be due to the cumulative effects of repeated injection of mefloquine, and the progressive suppression of TRPA1 or other unknown protein expression to a low level at 7 days after the last injection might lie behind the delayed alleviation of the mechanical allodynia. We found that repeated injection of mefloquine led to the downregulation of Cx36 in the TG and the alleviation of orofacial pain, which is consistent with a previous report that knocking down Cx36 expression in the anterior cingulate cortex (ACC) by RNA interference alleviates neuropathic pain [41]. Meanwhile, it should be noted that the effects of mefloquine on the ACC or other central nuclei cannot be excluded because of mefloquine's ability to cross the blood-brain barrier. However, in the

present study, the AAV-mediated Cx36 overexpression in the TG induced both mechanical and cold allodynia and thus strongly supports a significant contribution of Cx36 in the TG to the development of orofacial pain hypersensitivity. The low dose (20 mg/kg, *i.p.*) and high dose (30 mg/kg, *i.p.*) had similar effects in attenuating chronic neuropathic pain, but some mice in the high-dosage group demonstrated numbness and lethargy, which was not found in the low-dose group. Mefloquine has been reported to be a safe and effective antimalarial drug [42], but we assume that the numbness and lethargy are side-effects of mefloquine, and further pharmacological studies are needed to test this.

Subcutaneous AAV-Cx36-Int virus and AAV-Cx36-Ove virus injection in the V2 or V3 skin, which selectively targeted TG neurons, was a good tool for separately investigating the mechanisms of primary and secondary allodynia and allowed the model to be duplicated in the V2 and V3 area. We found that cold allodynia in the V3 area was induced upon acetone stimulation after pT-ION, which was consistent with previous reports [27, 34]. Also, we found that trigeminal nerve injury induced pain-like behaviors in mice, which was consistent with the pain and the highly sensitive cold sensation in patients suffering from trigeminal neuralgia [36]. The AAVs used in this study were subcutaneously delivered to infect TG neurons. At present, AAV is the only viral vector used in clinical research, and optimizing its mode of administration provides a useful approach that can be used for gene therapy for pain in humans.

In the present study, GluK2 was found to be widely expressed and to co-localize with Cx36, and GluK2 expression was increased in the TG after pT-ION. GluK2, which is a novel cold sensor [29], is more sensitive to temperature than TRPA1 and TRPV1. Also, as a subtype of kainate receptors, GluK2 has been shown to take part in both excitatory and inhibitory neurotransmission and to contribute to the development of synaptic plasticity [43]. Here, GluK2 was found to act downstream of Cx36 and to play a key role in mediating the cold allodynia induced either by trigeminal nerve injury or by Cx36 overexpression. Patients with trigeminal neuralgia are usually sensitive to cold stimulation such as a cold wind and cold water. The finding that GluK2 blockade significantly alleviated nerve injury-induced cold allodynia provides a GluK2-targeting approach for treating trigeminal neuralgia. However, until now there have been no reports of its involvement in allodynia induced by mechanical stimulation. Also, the present work does not support a potential contribution of GluK2 activation to the induction of pT-ION-induced mechanical allodynia. TRPA1 is reported to be located in nociception-specific neurons, and it has been proposed to mediate both mechanical allodynia and cold allodynia

[44–47]. Thus, we conclude that GluK2 specifically participates in cold allodynia and plays a role only as a cold sensor, rather than both a mechanical and cold sensor, and that activation of TRPA1 underlies the induction of mechanical allodynia upon Cx36 activation.

ERK belongs to a subfamily of the mitogen-activated protein kinases, and it plays a key role in transmitting extracellular signals to the nucleus [48]. It has been shown that ERK plays an important role in the process of peripheral allodynia and hypersensitivity after harmful stimulation [49, 50]. ERK is activated upon by being phosphorylated and then crosses the nuclear membrane to induce changes in the expression of specific proteins [30, 51, 52]. p-ERK occurs in dorsal root ganglion neurons and the trigeminal spinal nucleus caudalis in inflammatory pain [53, 54]. Our results showed that pT-ION induced an increase in p-ERK expression, which is consistent with a previous study showing that the activation of ERK mediates the development of neuropathic pain [55]. The Cx36 inhibitor mefloquine and the GluK2 antagonist NS 102 reversed the pT-ION-induced upregulation of p-ERK, and this may underlie the analgesic effects of the blockade of Cx36 or GluK2.

The Nav1.8 Na⁺ channel is considered to be specifically expressed in nociceptive neurons of medium and small diameters [56]. Nav1.8 is the dominant Na⁺ channel in the DRG of mice, and it is speculated to play a similar role in the TG [57]. *SCN10A* is the gene encoding the Nav1.8 channel, and gain-of-function mutations of *SCN10A* have been reported to induce peripheral neuropathic pain [58]. Also, pharmacological knockout of Nav1.8 in mice leads to a total lack of response to harmful mechanical and cold stimulation [31]. Although the role of Nav1.8 in inflammatory pain hypersensitivity seems to be limited, research into neuropathic pain suggests that it is critical for the induction of cold allodynia and not mechanical allodynia [59, 60]. Therefore, the nociceptors expressing Nav1.8 play a critical role in the induction and modulation of noxious and cold hypersensitivity in neuropathic pain. The mouse model of pT-ION is a typical trigeminal neuropathic pain model, and the present work found that specifically knocking down Cx36 in Nav1.8-expressing nociceptors only alleviated pT-ION-induced cold allodynia and not mechanical pain. Thus, we assume that activation of Cx36 and the downstream GluK2 may contribute to cold allodynia by changing the activity of Nav1.8-expressing nociceptors. It should be noted that TRPA1 expression was also decreased in the AAV-Cx36-Int virus group; however, the mechanical allodynia was not significantly alleviated. This might be because the decrease in TRPA1 expression was only slight and thus was not sufficient to rescue the decreased threshold in response to mechanical stimulation. The other hypothesis is that TRPA1 in Nav1.8-positive

neurons of the TG is predominantly involved in the induction of pT-ION-induced cold allodynia, while TRPA1 in Nav1.8-negative neurons might strongly contribute to the induction of pT-ION-induced mechanical allodynia.

In conclusion, our findings suggest that pT-ION surgery induces upregulation of Cx36 in the ipsilateral TG, which promotes the occurrence of mechanical and cold allodynia in both the V2 and V3 areas through the action of GluK2, TRPA1, and p-ERK as downstream proteins. Our results also indicate the potential of Cx36, GluK2, or TRPA1 antagonists in treating trigeminal neuralgia in clinical practice, which should be the focus of future studies.

Acknowledgements This work was supported by the National Natural Science Foundation of China (81971056, 31600852, 81771202, and 81873101), the Innovative Research Team of High-level Local Universities in Shanghai, the Foundation of Science, Technology and Innovation Commission of Shenzhen Municipality (JCYJ20180302153701406), the National Key R&D Program of China (2017YFB0403803), the Shanghai Municipal Science and Technology Major Project (2018SHZDZX01), and ZJLab.

Conflict of interest All authors claim that there are no conflicts of interest.

References

- Imbe H, Iwata K, Zhou QQ, Zou S, Dubner R, Ren K. Orofacial deep and cutaneous tissue inflammation and trigeminal neuronal activation. Implications for persistent temporomandibular pain. *Cells Tissues Organs* 2001, 169: 238–247.
- Zakrzewska JM, Wu J, Mon-Williams M, Phillips N, Pavitt SH. Evaluating the impact of trigeminal neuralgia. *Pain* 2017, 158: 1166–1174.
- Sugiyama T, Shinoda M, Watase T, Honda K, Ito R, Kaji K, *et al.* Nitric oxide signaling contributes to ectopic orofacial neuropathic pain. *J Dent Res* 2013, 92: 1113–1117.
- Campbell JN, Meyer RA. Mechanisms of neuropathic pain. *Neuron* 2006, 52: 77–92.
- Kim YS, Chu Y, Han L, Li M, Li Z, LaVinka PC, *et al.* Central terminal sensitization of TRPV1 by descending serotonergic facilitation modulates chronic pain. *Neuron* 2014, 81: 873–887.
- Shinoda M, Iwata K. Neural communication in the trigeminal ganglion contributes to ectopic orofacial pain. *J Oral Biosci* 2013, 55: 165–168.
- Jeon YH, Youn DH. Spinal gap junction channels in neuropathic pain. *Korean J Pain* 2015, 28: 231–235.
- Goldberg GS, Lampe PD, Nicholson BJ. Selective transfer of endogenous metabolites through gap junctions composed of different connexins. *Nat Cell Biol* 1999, 1: 457–459.
- Devor M, Amir R, Rappaport ZH. Pathophysiology of trigeminal neuralgia: the ignition hypothesis. *Clin J Pain* 2002, 18: 4–13.
- Rappaport ZH, Devor M. Trigeminal neuralgia: the role of self-sustaining discharge in the trigeminal ganglion. *Pain* 1994, 56: 127–138.
- Spray DC, Hanani M. Gap junctions, pannexins and pain. *Neurosci Lett* 2019, 695: 46–52.
- Chen MJ, Kress B, Han X, Moll K, Peng W, Ji RR, *et al.* Astrocytic CX43 hemichannels and gap junctions play a crucial role in development of chronic neuropathic pain following spinal cord injury. *Glia* 2012, 60: 1660–1670.
- Kang J, Kang N, Lovatt D, Torres A, Zhao Z, Lin J, *et al.* Connexin 43 hemichannels are permeable to ATP. *J Neurosci* 2008, 28: 4702–4711.
- Vit JP, Jasmin L, Bhargava A, Ohara PT. Satellite glial cells in the trigeminal ganglion as a determinant of orofacial neuropathic pain. *Neuron Glia Biol* 2006, 2: 247–257.
- Pannese E, Ledda M, Cherkas PS, Huang TY, Hanani M. Satellite cell reactions to axon injury of sensory ganglion neurons: increase in number of gap junctions and formation of bridges connecting previously separate perineuronal sheaths. *Anat Embryol (Berl)* 2003, 206: 337–347.
- Chen G, Park CK, Xie RG, Berta T, Nedergaard M, Ji RR. Connexin-43 induces chemokine release from spinal cord astrocytes to maintain late-phase neuropathic pain in mice. *Brain* 2014, 137: 2193–2209.
- Ohara PT, Vit JP, Bhargava A, Jasmin L. Evidence for a role of connexin 43 in trigeminal pain using RNA interference in vivo. *J Neurophysiol* 2008, 100: 3064–3073.
- Kaji K, Shinoda M, Honda K, Unno S, Shimizu N, Iwata K. Connexin 43 contributes to ectopic orofacial pain following inferior alveolar nerve injury. *Mol Pain* 2016, 12.
- Spray DC, Iglesias R, Shraer N, Suadicani SO, Belzer V, Hanstein R, *et al.* Gap junction mediated signaling between satellite glia and neurons in trigeminal ganglia. *Glia* 2019, 67: 791–801.
- Niederberger E, Kuhlein H, Geisslinger G. Update on the pathobiology of neuropathic pain. *Expert Rev Proteomics* 2008, 5: 799–818.
- Rash JE, Yasumura T, Dudek FE, Nagy JI. Cell-specific expression of connexins and evidence of restricted gap junctional coupling between glial cells and between neurons. *J Neurosci* 2001, 21: 1983–2000.
- Long MA, Deans MR, Paul DL, Connors BW. Rhythmicity without synchrony in the electrically uncoupled inferior olive. *J Neurosci* 2002, 22: 10898–10905.
- Deans MR, Gibson JR, Sellitto C, Connors BW, Paul DL. Synchronous activity of inhibitory networks in neocortex requires electrical synapses containing connexin36. *Neuron* 2001, 31: 477–485.
- Ouachikh O, Hafidi A, Boucher Y, Dieb W. Electrical synapses are involved in orofacial neuropathic pain. *Neuroscience* 2018, 382: 69–79.
- Nagy JI, Lynn BD, Senecal JMM, Stecina K. Connexin36 expression in primary afferent neurons in relation to the axon reflex and modality coding of somatic sensation. *Neuroscience* 2018, 383: 216–234.
- Garrett FG, Durham PL. Differential expression of connexins in trigeminal ganglion neurons and satellite glial cells in response to chronic or acute joint inflammation. *Neuron Glia Biol* 2008, 4: 295–306.
- Cui WQ, Chu YX, Xu F, Chen T, Gao L, Feng Y, *et al.* Calcium channel $\alpha 2\delta 1$ subunit mediates secondary orofacial hyperalgesia through PKC-TRPA1/gap junction signaling. *J Pain* 2020, 21: 238–257.
- Seemann N, Welling A, Rustenbeck I. The inhibitor of connexin Cx36 channels, mefloquine, inhibits voltage-dependent $\text{Ca}(2+)$ channels and insulin secretion. *Mol Cell Endocrinol* 2018, 472: 97–106.
- Gong J, Liu J, Ronan EA, He F, Cai W, Fatima M, *et al.* A cold-sensing receptor encoded by a glutamate receptor gene. *Cell* 2019, 178: 1375–1386.e1311.
- Ji RR, Gereau RWT, Malcangio M, Strichartz GR. MAP kinase and pain. *Brain Res Rev* 2009, 60: 135–148.

31. Abrahamsen B, Zhao J, Asante CO, Cendan CM, Marsh S, Martinez-Barbera JP, *et al.* The cell and molecular basis of mechanical, cold, and inflammatory pain. *Science* 2008, 321: 702–705.
32. Imamura Y, Kawamoto H, Nakanishi O. Characterization of heat-hyperalgesia in an experimental trigeminal neuropathy in rats. *Exp Brain Res* 1997, 116: 97–103.
33. Ringkamp M, Meyer RA. Injured versus uninjured afferents: Who is to blame for neuropathic pain? *Anesthesiology* 2005, 103: 221–223.
34. Lim EJ, Jeon HJ, Yang GY, Lee MK, Ju JS, Han SR, *et al.* Intracisternal administration of mitogen-activated protein kinase inhibitors reduced mechanical allodynia following chronic constriction injury of infraorbital nerve in rats. *Prog Neuropsychopharmacol Biol Psychiatry* 2007, 31: 1322–1329.
35. Guo QH, Tong QH, Lu N, Cao H, Yang L, Zhang YQ. Proteomic analysis of the hippocampus in mouse models of trigeminal neuralgia and inescapable shock-induced depression. *Neurosci Bull* 2018, 34: 74–84.
36. Scrivani S, Wallin D, Moulton EA, Cole S, Wasan AD, Lockerman L, *et al.* A fMRI evaluation of lamotrigine for the treatment of trigeminal neuropathic pain: pilot study. *Pain Med* 2010, 11: 920–941.
37. Eugenin EA, Basilio D, Saez JC, Orellana JA, Raine CS, Bukauskas F, *et al.* The role of gap junction channels during physiologic and pathologic conditions of the human central nervous system. *J Neuroimmune Pharmacol* 2012, 7: 499–518.
38. Akbarpour B, Sayyah M, Babapour V, Mahdian R, Beheshti S, Kamyab AR. Expression of connexin 30 and connexin 32 in hippocampus of rat during epileptogenesis in a kindling model of epilepsy. *Neurosci Bull* 2012, 28: 729–736.
39. Kim YS, Anderson M, Park K, Zheng Q, Agarwal A, Gong C, *et al.* Coupled activation of primary sensory neurons contributes to chronic pain. *Neuron* 2016, 91: 1085–1096.
40. Devor M, Wall PD. Cross-excitation in dorsal root ganglia of nerve-injured and intact rats. *J Neurophysiol* 1990, 64: 1733–1746.
41. Chen ZY, Shen FY, Jiang L, Zhao X, Shen XL, Zhong W, *et al.* Attenuation of neuropathic pain by inhibiting electrical synapses in the anterior cingulate cortex. *Anesthesiology* 2016, 124: 169–183.
42. Tine RC, Faye B, Sylla K, Ndiaye JL, Ndiaye M, Sow D, *et al.* Efficacy and tolerability of a new formulation of artesunate-mefloquine for the treatment of uncomplicated malaria in adult in Senegal: open randomized trial. *Malar J* 2012, 11: 416.
43. Evans AJ, Gurung S, Henley JM, Nakamura Y, Wilkinson KA. Exciting times: New advances towards understanding the regulation and roles of kainate receptors. *Neurochem Res* 2019, 44: 572–584.
44. Kwan KY, Allchorne AJ, Vollrath MA, Christensen AP, Zhang DS, Woolf CJ, *et al.* TRPA1 contributes to cold, mechanical, and chemical nociception but is not essential for hair-cell transduction. *Neuron* 2006, 50: 277–289.
45. Obata K, Katsura H, Mizushima T, Yamanaka H, Kobayashi K, Dai Y, *et al.* TRPA1 induced in sensory neurons contributes to cold hyperalgesia after inflammation and nerve injury. *J Clin Invest* 2005, 115: 2393–2401.
46. Trevisan G, Benemei S, Materazzi S, De Logu F, De Siena G, Fusi C, *et al.* TRPA1 mediates trigeminal neuropathic pain in mice downstream of monocytes/macrophages and oxidative stress. *Brain* 2016, 139: 1361–1377.
47. Moore C, Gupta R, Jordt SE, Chen Y, Liedtke WB. Regulation of pain and itch by TRP channels. *Neurosci Bull* 2018, 34: 120–142.
48. Lin MW, Lin CC, Chen YH, Yang HB, Hung SY. Celastrol inhibits dopaminergic neuronal death of Parkinson's disease through activating mitophagy. *Antioxidants (Basel)* 2019, 9: 37. <https://doi.org/10.3390/antiox9010037>.
49. Zhuang ZY, Xu H, Clapham DE, Ji RR. Phosphatidylinositol 3-kinase activates ERK in primary sensory neurons and mediates inflammatory heat hyperalgesia through TRPV1 sensitization. *J Neurosci* 2004, 24: 8300–8309.
50. Dai Y, Iwata K, Fukuoka T, Kondo E, Tokunaga A, Yamanaka H, *et al.* Phosphorylation of extracellular signal-regulated kinase in primary afferent neurons by noxious stimuli and its involvement in peripheral sensitization. *J Neurosci* 2002, 22: 7737–7745.
51. Impey S, Obrietan K, Storm DR. Making new connections: role of ERK/MAP kinase signaling in neuronal plasticity. *Neuron* 1999, 23: 11–14.
52. Cao H, Ren WH, Zhu MY, Zhao ZQ, Zhang YQ. Activation of glycine site and GluN2B subunit of NMDA receptors is necessary for ERK/CREB signaling cascade in rostral anterior cingulate cortex in rats: implications for affective pain. *Neurosci Bull* 2012, 28: 77–87.
53. Noma N, Tsuboi Y, Kondo M, Matsumoto M, Sessle BJ, Kitagawa J, *et al.* Organization of pERK-immunoreactive cells in trigeminal spinal nucleus caudalis and upper cervical cord following capsaicin injection into oral and craniofacial regions in rats. *J Comp Neurol* 2008, 507: 1428–1440.
54. Ji RR, Befort K, Brenner GJ, Woolf CJ. ERK MAP kinase activation in superficial spinal cord neurons induces prodynorphin and NK-1 upregulation and contributes to persistent inflammatory pain hypersensitivity. *J Neurosci* 2002, 22: 478–485.
55. Shao S, Xia H, Hu M, Chen C, Fu J, Shi G, *et al.* Isotalatizidine, a C19-diterpenoid alkaloid, attenuates chronic neuropathic pain through stimulating ERK/CREB signaling pathway-mediated microglial dynorphin A expression. *J Neuroinflammation* 2020, 17: 13.
56. Han C, Huang J, Waxman SG. Sodium channel Nav1.8: emerging links to human disease. *Neurology* 2016, 86: 473–483.
57. Chang W, Berta T, Kim YH, Lee S, Lee SY, Ji RR. Expression and role of voltage-gated sodium channels in human dorsal root ganglion neurons with special focus on nav1.7, species differences, and regulation by paclitaxel. *Neurosci Bull* 2018, 34: 4–12.
58. Faber CG, Lauria G, Merkies IS, Cheng X, Han C, Ahn HS, *et al.* Gain-of-function Nav1.8 mutations in painful neuropathy. *Proc Natl Acad Sci U S A* 2012, 109: 19444–19449.
59. Leo S, D'Hooge R, Meert T. Exploring the role of nociceptor-specific sodium channels in pain transmission using Nav18 and Nav19 knockout mice. *Behav Brain Res* 2010, 208: 149–157.
60. Foulkes T, Wood JN. Mechanisms of cold pain. *Channels (Austin)* 2007, 1: 154–160.



Dual Oxidase Mutant Retards Mauthner-Cell Axon Regeneration at an Early Stage via Modulating Mitochondrial Dynamics in Zebrafish

Lei-Qing Yang¹ · Min Chen¹ · Da-Long Ren^{1,2} · Bing Hu¹

Received: 5 April 2020 / Accepted: 25 July 2020 / Published online: 29 October 2020
© Shanghai Institutes for Biological Sciences, CAS 2020

Abstract Dual oxidase (*duox*)-derived reactive oxygen species (ROS) have been correlated with neuronal polarity, cerebellar development, and neuroplasticity. However, there have not been many comprehensive studies of the effect of individual *duox* isoforms on central-axon regeneration *in vivo*. Here, we explored this question in zebrafish, an excellent model organism for central-axon regeneration studies. In our research, mutation of the *duox* gene with CRISPR/Cas9 significantly retarded the single-axon regeneration of the zebrafish Mauthner cell *in vivo*. Using deep transcriptome sequencing, we found that the expression levels of related functional enzymes in mitochondria were down-regulated in *duox* mutant fish. *In vivo* imaging showed that *duox* mutants had significantly disrupted mitochondrial transport and redox state in single Mauthner-cell axon. Our research data provide insights into

how *duox* is involved in central-axon regeneration by changing mitochondrial transport.

Keywords *duox* · Zebrafish · Mauthner cell · Axon regeneration · Mitochondrial dynamics

Introduction

Reactive oxygen species (ROS) are chemically reactive molecules or free radicals containing oxygen, such as superoxide anion radicals (O_2^-) and hydrogen peroxide (H_2O_2) [1]. ROS were known to be inevitable and damage-inducing by-products of cellular respiration long before the discovery of nicotinamide adenine dinucleotide phosphate (NADPH) oxidase family members [2, 3]. The NADPH oxidase (NOX) family is involved in the production of ROS in response to various stages of cellular differentiation, growth, and maintenance [4–6]. Dual oxidase (Duox), a member of the NOX family, was originally identified as thyroid NADPH oxidase [7]. However recent studies have reported that Duox enzymes are also expressed in the salivary glands, rectum, trachea, and bronchium [8, 9]. In zebrafish, there is only a single *duox* gene, in contrast to the two *duox* genes in both humans and rodents, Duox1 and Duox2 [10]. Recently, it has been shown that Duox-generated H_2O_2 is critical for the recruitment of leukocytes to initiate inflammation in zebrafish larvae [11, 12]. Studies in zebrafish have also shown that Duox deficiency presents as congenital hypothyroidism [7, 13, 14].

In addition, Duox has been reported to be vital in heart regeneration [15] and sensory-axon regeneration [16]. However, little is known about its role in the regeneration of axons in the central nervous system (CNS). In mammals, axon regeneration in the CNS is extremely limited [17, 18],

Electronic supplementary material The online version of this article (<https://doi.org/10.1007/s12264-020-00600-9>) contains supplementary material, which is available to authorized users.

✉ Da-Long Ren
rendl@ustc.edu.cn

✉ Bing Hu
bhu@ustc.edu.cn

¹ Eye Center, The First Affiliated Hospital of USTC, Hefei National Laboratory for Physical Sciences at the Microscale, Chinese Academy of Sciences Key Laboratory of Brain Function and Disease, School of Life Sciences, Division of Biomedical Sciences, University of Science and Technology of China, Hefei 230026, China

² Anhui Province Key Laboratory of Local Livestock and Poultry Genetic Resource Conservation and Bio-breeding, College of Animal Science and Technology, Anhui Agricultural University, Hefei 230036, China

unlike in the peripheral nervous system (PNS) [19]. Conversely, several types of neurons have robust regenerative abilities in the CNS of zebrafish [20–24]. Recent studies in zebrafish have used laser axotomy to precisely damage single axons in the CNS, making it possible to explore the potential factors impacting axon regeneration [25, 26]. For example, miRNAs [27], mitochondria [28], and Ca^{2+} activity [29] have been demonstrated to be involved in Mauthner-cell axon regeneration after two-photon laser ablation. Hence, zebrafish have become an attractive vertebrate model for studying the impact of Duox on axon regeneration in the CNS.

In our study, we found that loss of Duox retarded Mauthner cell axon regeneration in zebrafish *in vivo*, and that this was due to disrupted mitochondrial transport and redox state.

Methods

Zebrafish Lines and Maintenance

Wild-type (WT), *duox*^{+/-} mutant, *duox*^{-/-} mutant, Tg (Tol-056) [30], Tg (Tol-056); *duox*^{+/-} mutant, and Tg (Tol-056); *duox*^{-/-} mutant zebrafish (*Danio rerio*) were used in this study. Zebrafish embryos were bred with a laboratory stock and maintained at 28.5°C with a 14/10 h light/dark cycle. Embryos were collected from natural spawning and staged by dpf (days post-fertilization) according to established criteria [31]. To prevent dark pigment formation, larvae were raised in embryo medium containing 0.2 mM N-phenylthiourea (Sigma). All animal manipulations in this study were conducted in strict accordance with the guidelines and regulations set forth by the University of Science and Technology of China (USTC) Animal Resources Center and the University Animal Care and Use Committee. The protocol was approved by the Committee on the Ethics of Animal Experiments of the USTC (Permit Number: USTCACUC1103013).

Design of Mutant Sites and Synthesis of Cas9 mRNA and sgRNA

The sgRNAs were designed to target the fifth exon of the *duox* gene by “SeqBuilder” software (DNASar, USA). The targeting sequences started with GG, ended with NGG (PAM), and contained the restrictive enzyme BamH-I site near the PAM for genotyping. The Cas9 mRNA and sgRNAs were synthesized with little modification as previously described [32]. In brief, the Cas9 mRNA was synthesized with a T7 mMESSAGE mMACHINE Kit (Promega, USA). The DNA fragments of the sgRNAs were amplified with pairs of primers (Table S1), and then

purified with phenol and chloroform. The sgRNAs were transcribed *in vitro* with T7 Riboprobe Systems (Promega, USA).

Construction and Identification of *duox* Mutants

Cas9 mRNA (250 ng/ μL) and sgRNAs (45 ng/ μL) were co-microinjected into one-cell zebrafish embryos. Genomic DNAs, which were extracted from the injected embryos at 20 h post-fertilization, were used as templates for the following identifications. DNA fragments containing the *duox* target sequences were amplified by PCR and digested with BamH-I restriction endonucleases (Takara, Japan) at 37°C for 0.5 h. The uncleaved bands were cleaned after gel electrophoresis and cloned into pMD-19T (Takara, Japan). Monoclonal colonies were picked up for PCR and restriction enzyme digestion and were then sequenced by Sanger sequencing (Genewiz, Inc.). Primers used in the experiment are listed in Supplementary Table S1.

The microinjected founder (F_0) larvae were raised to adulthood and then crossed with WT zebrafish to generate F_1 larvae. The F_1 larvae that carried heterozygous knockout alleles were raised to adulthood, and their genotypes were confirmed by PCR amplification and sequencing analysis of DNA from fin clippings. Homozygous knockout zebrafish were generated and selected by genotyping and then crossing male and female zebrafish carrying heterozygous knockout alleles.

Retro-complementation and Single-Cell Electroporation *In Vivo*

For *duox* gene retro-complementation, *duox* gene and *duox*^{-/-} mutant gene CDS sequences were cloned *via* primer (Table S1), then inserted into the plasmid UAS-mCherry to construct the retro-complementation plasmids UAS-*duox*-mCherry and UAS-*duox*^{-/-}-mCherry. Then the CMV-GAL4-VP16/UAS-mCherry plasmids (control group), CMV-GAL4-VP16/UAS-*duox*-mCherry plasmids (*duox* gene retro-complementation group), and CMV-GAL4-VP16/UAS-*duox*^{-/-}-mCherry plasmids (*duox*^{-/-} gene retro-complementation group) were co-transfected through single-cell electroporation into unilateral Mauthner cells at 4 dpf in *duox*^{-/-} mutant fish as described previously [33]. Different concentrations of rhodamine-dextran (a fluorescent dye that labels Mauthner cells), CMV-GAL4-VP16 (a plasmid that drives the expression of GAL4-VP16), UAS-mCherry/UAS-*duox*-mCherry/ UAS-*duox*^{-/-}-mCherry (plasmids that drive the expression of the red fluorescent protein, mCherry), UAS-mito-EGFP (a plasmid that labels mitochondria), and UAS-mito-roGFP2-Orp-1 (plasmids that drive expression of redox state probes; Addgene, no. 64997) were combined (using 100–200 ng/ μL of each

plasmid) and co-delivered into unilateral Mauthner cells. Zebrafish larvae were returned to embryo media containing N-phenylthiourea and allowed to recover. Two days after electroporation, morphologically normal and healthy larvae were selected for subsequent experiments.

Two-Photon Axotomy

Before axotomy, each 6-dpf zebrafish larva expressing mCherry/GFP fluorescence in unilaterally in Mauthner cells was anesthetized in MS222 (Sigma) and immobilized in 1% low-melting agarose. A Zeiss two-photon microscope (LSM710) was used to ablate Mauthner cell axons over the cloacal pores [26, 34]. We used a two-photon laser at 800 nm and an intensity of 16%–22% to ablate the Mauthner cell axons.

In Vivo Imaging of Axon Regeneration and Mitochondrial Movement

To observe Mauthner cell axon regeneration, anesthetized larvae were imaged at 2 days-post axotomy (dpa) with a confocal system (Olympus FV1000) and a water-immersion lens (40 \times , 0.85 numerical-aperture objective) at 2- μ m intervals. All of the images were spliced using Adobe Photoshop CS4. The point just above the cloacal pores was defined as the starting point of regrowth, and the axonal terminal of regeneration was defined as the end-point of regrown axons. All of the fluorescent live images and time-lapse movies show a lateral view of the spinal cord, with the anterior to the left and dorsal above. The regenerative length was calculated using Fiji-ImageJ.

To obtain static images of mitochondrial morphology in the axon terminal, larvae were screened for co-labeled mito-EGFP and rhodamine-dextran in Mauthner cells. We collected images of larval axonal terminals at 6, 7, and 8 dpf using an Olympus microscope equipped with a water-immersion lens (60 \times , 0.9 numerical-aperture objective) at 1- μ m intervals. Dynamic imaging and analysis of mitochondrial movement in axons *in vivo* were as described previously [28]. Mitochondrial motility was defined as the percentage of moving mitochondria. The speed of a mitochondrion was defined as the total distance moved divided by the time spent moving.

To image the redox state of mitochondria in Mauthner cells, Mauthner cell soma was scanned with a confocal system (Zeiss, LSM710). Biosensor fluorescence was excited using 405-nm and 488-nm lasers sequentially and *via* line-by-line scanning. Emission was detected at 500–570 nm. The fluorescent intensity of an Mauthner cell soma in a single horizontal plane was measured. The fluorescent ratio (405 nm/488 nm) of each Mauthner cell soma was calculated using Fiji-ImageJ.

RNA Extraction and qRT-PCR

Total RNAs were extracted from 50 larvae of the WT and *duox*^{-/-} lines using TRIzol (Takara, Japan) reagent. Quantitative real-time PCR (qRT-PCR) was performed with the SYBR green kit (Invitrogen, USA). qRT-PCR was performed in triplicate with three individual biological samples (nine replicates). The results were normalized to the expression level of the housekeeping gene β -actin and are shown as a relative expression level calculated using the $2^{-\Delta\Delta C_t}$ method [35].

Western Blotting

To examine the protein expression in *duox*^{-/-} mutant zebrafish, 5-dpf WT and *duox*^{-/-} mutant larvae were collected and lysed with RIPA buffer. Samples were boiled for 5 min and run on a 12% SDS-PAGE gel. Mouse monoclonal anti-Duox1 (Santa Cruz, USA) was used to assess the protein levels in each group.

Deep-Sequencing-Based Transcriptomic Analysis

Total RNAs were extracted from 4-dpf *duox*^{-/-} and WT zebrafish, and 3 g of RNA per sample was prepared for constructing a transcriptional library. Sequencing libraries were generated with an UltraTM RNA Library Prep Kit (NEB, USA) according to the manufacturer's instructions. Clustering of the index-coded samples was conducted with a cBot Cluster Generation System using a TruSeq PE Cluster Kit (Illumina, USA), per the instructions. After clustering, the library preparations were sequenced on an Illumina Hiseq 2000 platform. Perl scripts were used to remove the adapter for clean reads, calculating the Q20/Q30 duplicate data, and generating the raw reads. Transcriptomic assembly was performed according to a protocol described previously [36]. For the Gene Ontology (GO) enrichment assay, the differentially-expressed genes (DEGs) were identified using Wallenius' non-central hypergeometric distribution, implemented in the GOseq R packages [37]. KOBAS software was used to determine the statistical enrichment of DEGs in KEGG pathways to predict and classify the functions of the assembled sequences [38].

Transmission Electron Microscopy

Each larval zebrafish fixed in 2.0% formaldehyde and 2.5% glutaraldehyde solution (Electron Microscopy Sciences) overnight at 4 °C. Following washes, they were washed with 0.1 mol/L phosphate buffer (pH 7.4). Specimens were then incubated in post-fixation solution containing 1% osmium tetroxide for 2 h, washed with water, washed three

times with 0.1 mol/L phosphate buffer (pH 7.4) for 15 min each time. Next, specimens were washed with water, dehydrated with serial dilutions of ethanol in water (50%, 70%, 80%, 90%, 100%, 100%) and 100% acetone twice for 15 min each. The samples were then embedded in Epon/Araldite resin with surrounding support tissue and hardened for 2–3 days at 60°C. Ultrathin (80 nm) transverse sections of the brain from larvae were stained with uranyl acetate and lead citrate. Sections were viewed and photographed with an FEI Tecnai Spirit (120 kV) transmission electron microscope (TEM).

Statistical Analysis

All of the data are reported as the mean \pm SEM, or as relative proportions of 100%, as indicated in the figure legends. We used either Student's two-tailed t tests or one-way analyses of variance (ANOVAs) for all of analyses, as indicated in the figure legends. All graphs were constructed and statistical tests were performed in GraphPad Prism 7. We considered $P < 0.05$ statistically significant ($*P < 0.05$; $**P < 0.01$; $***P < 0.001$). We defined the length from the cloacal pore to the tail end as the whole length of the Mauthner cell, as the head end was too thick to sufficiently image *in vivo*.

Results

Generation and Identification of *duox* Mutant Zebrafish

To investigate the functions of *duox in vivo*, we attempted to obtain a *duox* mutant zebrafish line. We designed a CRISPR-Cas9-targeted site in the fifth exon of the zebrafish *duox* gene that contained a BamH-I restriction site for further identifying the resultant mutants (Fig. 1A). Cas9 mRNA and *duox* sgRNA were co-microinjected into one-cell embryos. To identify specific mutagenesis, a 440-bp DNA fragment was amplified by PCR from the genomic DNA and digested with a BamH-I restriction enzyme. The results of gel electrophoresis showed that F₂ zebrafish larvae were heritably homozygous mutants (Fig. 1B). Moreover, the representative sequencing results indicated that F₂ zebrafish had a two-bp deletion (Fig. 1C–E). Furthermore, bioinformatics analysis revealed that the functional sequence domains (HLH-PAS-PAS) of the F₂ zebrafish Duox protein were frame-shifted (Fig. 1F). Finally, we used Western blotting to determine whether our *duox* mutation was a null allele mutation. The results showed that the expression of Duox protein was completely abolished in *duox* mutant zebrafish (Fig. 1G and H). Taken

together, these results verified that we successfully generated a *duox* null-mutant zebrafish line.

Duox Deficiency Retards Mauthner-Cell Axon Regeneration at an Early Stage *In Vivo*

Duox is known to be required for promoting injury-induced peripheral sensory axon regeneration in zebrafish skin [16]. However, the *in vivo* role of Duox in CNS axon regeneration has remained unclear. Mauthner cells are a pair of myelinated hindbrain neurons projecting to the spina cord in zebrafish and have been demonstrated to exhibit a strong regenerative capacity in our previous studies [26–28]. To investigate the roles of Duox in Mauthner cell axon regeneration, we crossed the transgenic line Tg (T056: EGFP) with the *duox*^{-/-} mutant for two consecutive generations to obtain the Tg (T056: EGFP)/*duox*^{-/-} zebrafish line (Fig. 2A). We used two-photon laser axotomy to transect one of the Mauthner cell unilateral axons over the cloacal pores at 6 dpf (Fig. 2B). Furthermore, *in vivo* live imaging showed that homozygous and heterozygous *duox* mutant larvae displayed a reduced length of Mauthner cell axon regeneration compared with that of WT larvae (Fig. 2C and D). We analyzed the whole length of Mauthner cell axons and found no significant difference among WT, homozygous and heterozygous *duox* mutant larvae, indicating that the original length of Mauthner-cell axon was unaffected by *duox* mutant (Fig. 2E and F). For the retro-complementation experiment, we co-transfected CMV-GAL4-VP16/UAS-mCherry plasmids (*duox*^{-/-} mutant + UAS-mCherry group), CMV-GAL4-VP16/UAS-*duox*-mCherry plasmids (*duox*^{-/-} mutant + UAS-*duox*-mCherry group), and CMV-GAL4-VP16/UAS-*duox*^{-/-}-mCherry plasmids (*duox*^{-/-} mutant + UAS-*duox*^{-/-}-mCherry group) through single-cell electroporation into unilateral Mauthner cells at 4 dpf in *duox*^{-/-} mutant fish (Fig. 2G and H). Subsequently, we ablated red-fluorescent Mauthner cell axons at 6 dpf with a two-photon laser-scanning microscope and continued to image the regenerated length of Mauthner cells at 8 dpf (2 dpa) (Fig. 2I). Live imaging results showed that overexpression of the *duox* gene remarkably rescued the weak regenerative ability in *duox*^{-/-} mutant fish and *duox*^{-/-} gene retro-complementation had no significance impact on Mauthner cell axon regeneration (Fig. 2J and K). Taken together, these results suggest that Duox is required for Mauthner cell axon regeneration in zebrafish.

Duox Modulates Genes Associated with Mitochondrial Function

Robust Mauthner cell axon regeneration requires high mobility of mitochondrial transport along axons [28]. ROS

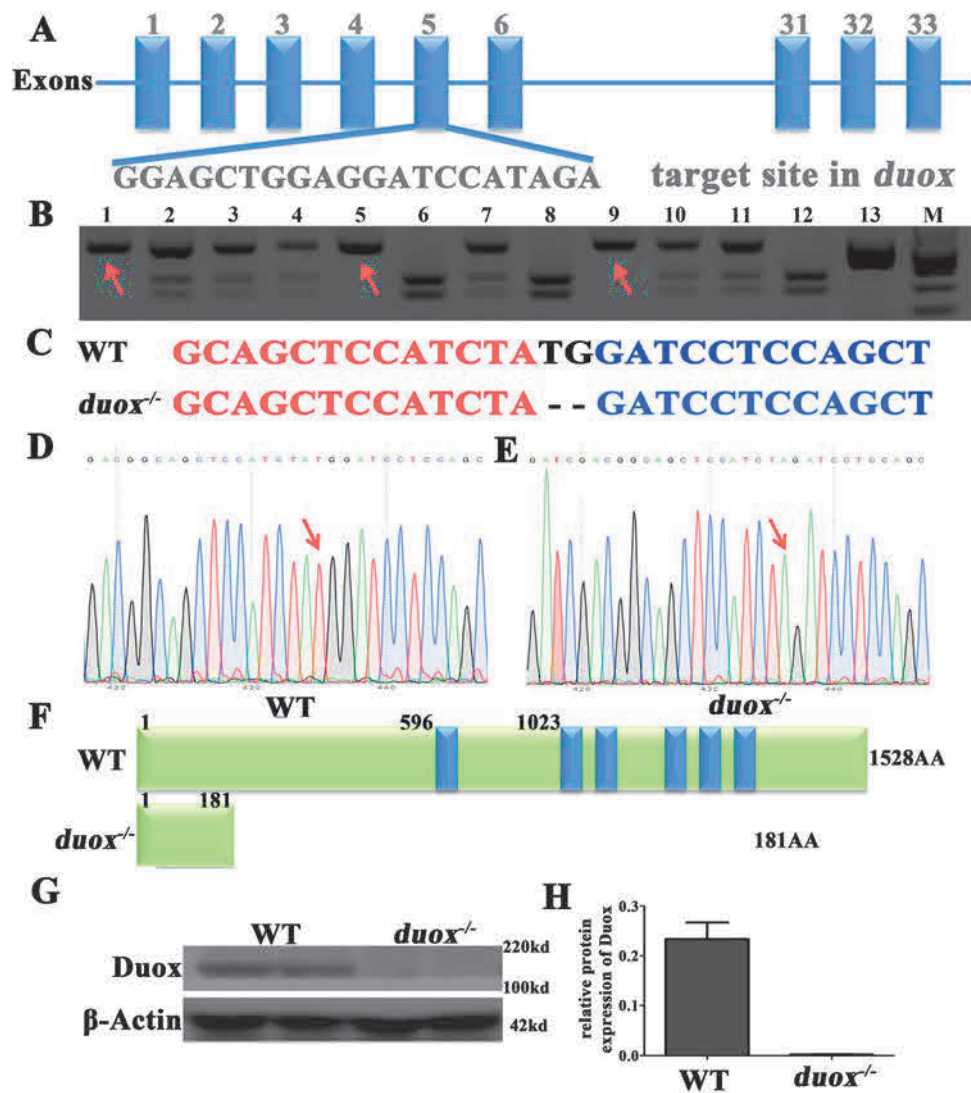
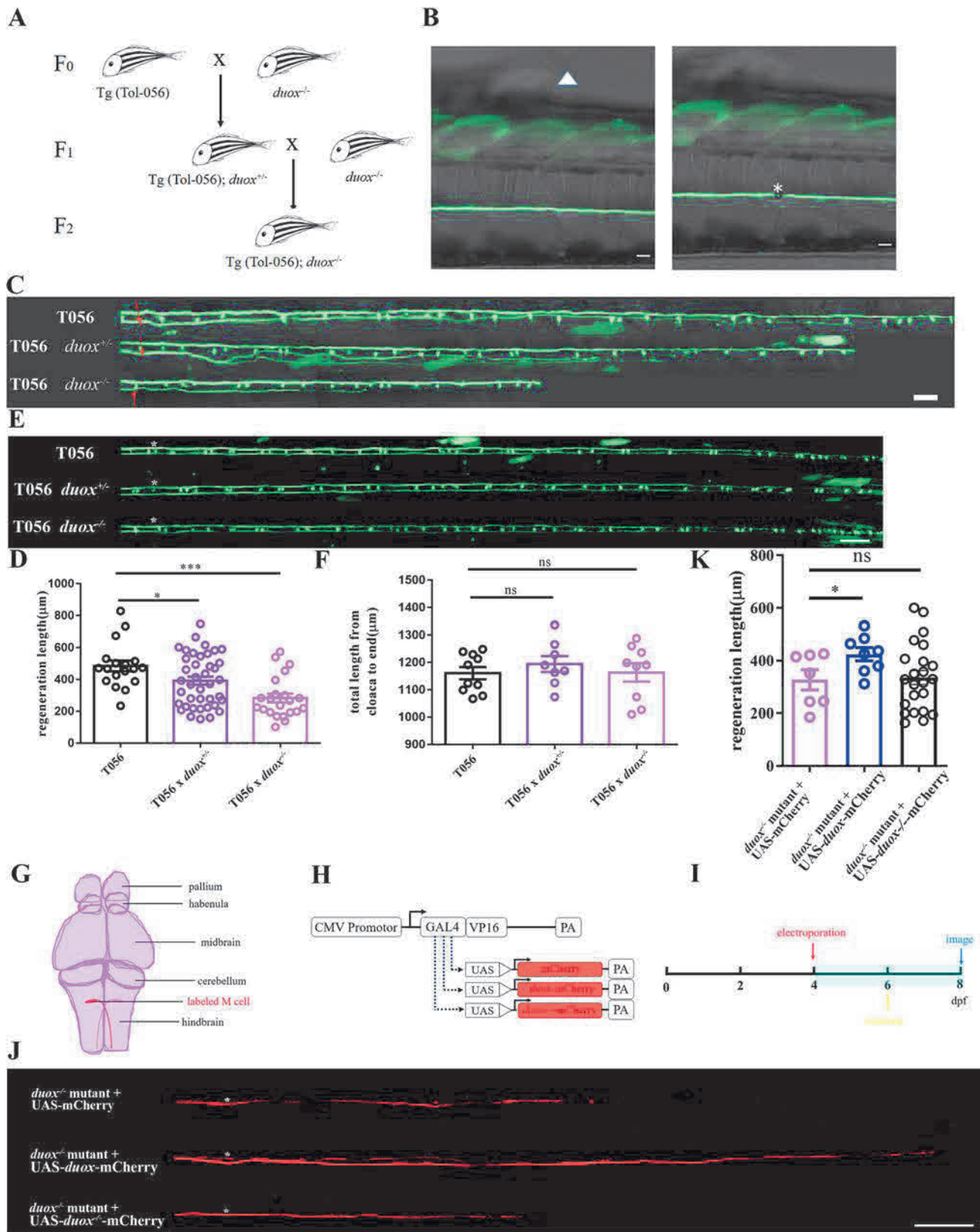


Fig. 1 Generation and characterization of *duox*-null mutant zebrafish. **A** Schematic of the Cas9-sgRNA-targeted site located at the fifth exon of *duox*. **B** The targeted fragment was amplified by PCR from genomic DNA of F₂ embryos and was then digested with BamH I. The uncleaved and cleaved PCR bands are indicated by red arrows. Lanes 1, 5, 9: *duox*^{+/+} enzyme-digested fragments; lanes 2–4, 7, 10–11: *duox*^{+/-} enzyme-digested fragments; lanes 6, 8, 12: WT enzyme-digested fragments; lane M: 600-bp ladder. **C–E** Representative sequencing results of mutated and WT zebrafish lines. The mutant

shows a two-bp base deletion, indicating a frameshift mutation that resulted in truncated proteins (lower). **F** Bioinformatics analysis indicating that the mutated region is located at the HLH-PAS-PAS functional domain of Duox. The mutant translated to only 181 normal amino-acids, whereas the WT expressed 1,528 amino-acids. **G, H** Western-blotting analysis showing that Duox protein expression is completely inhibited in the mutant group compared with that of the WT. The data were analyzed with unpaired *t* tests (**P* < 0.05; ***P* < 0.01; ****P* < 0.001). Error bars represent SEM.

is known to play important roles in both mitochondrial H₂O₂ generation and the electron transport chain [39]. To investigate the Duox-affected genes involved in mitochondria, we performed high-throughput RNA sequencing in *duox*^{-/-} mutant and WT larvae at 4 dpf. Transcriptomic analysis revealed that there were 360 down-regulated genes and 375 up-regulated genes in *duox*^{-/-} mutant fish (Fig. 3A and Table S2) (The data have been deposited in the NCBI Gene Expression Omnibus, GEO accession number GSE144689). Furthermore, GO analyses revealed

that these DEGs participated in rhythmic processes, responded to stimuli, and were involved in growth, antioxidant activity, catalytic activity, and transcription factor activity, and were significantly altered in *duox*^{-/-} mutants (Fig. S1). Importantly, genes related to mitochondria, such as *cyp2p9*, *alas2*, *cyp11a1*, *mfn2*, *opal*, *atp5f1b*, *cyp2x8*, *gpx4b*, and *gsr*, were also down-regulated (Fig. 3B), which was further corroborated via qRT-PCR (Fig. 3C). These results suggest that Duox plays an important role in mitochondria.



◀ **Fig. 2** Duox regulates Mauthner-cell axon regeneration *in vivo*. **A** Hybridization of the transgenic line: Tg (T056: EGFP) and *duox* mutants were crossed for two consecutive generations to obtain Tg (T056: EGFP)/*duox*^{+/-} and Tg (T056: EGFP); *duox*^{-/-} lines. **B** Representative images of an Mauthner-cell axon before (left) and after (right) ablations by a two-photon laser (asterisk, injury site; arrow-head, cloacal pore; scale bars: 20 μm). **C, D** Confocal imaging of Mauthner-cells in *duox* mutants at 8 dpf (**C**) and the regeneration length at 2 dpa (**D**) (red arrowheads, cloacal pores; scale bar, 20 μm). **E, F** Defined total lengths of Mauthner cell axons were not significantly different among WT (*n* = 10), homozygous (*n* = 9), and heterozygous (*n* = 8) larvae (scale bar, 50 μm). **G** Schematic of Mauthner cell soma electroporation. **H** Schematic of constructs CMV-GAL4-VP16/UAS-mCherry plasmids (*duox*^{-/-} mutant + UAS-mCherry group), CMV-GAL4-VP16/UAS-*duox*-mCherry plasmids (*duox*^{-/-} mutant + UAS-*duox*-mCherry group), and CMV-GAL4-VP16/UAS-*duox*^{-/-}-mCherry plasmids (*duox*^{-/-} mutant + UAS-*duox*^{-/-}-mCherry group) through single-cell electroporation in living zebrafish larvae. **I** Time-line of the time points of electroporation, axotomy, and imaging. **J, K** *duox* gene retro-complementation rescues the length of Mauthner cell axon regeneration and *duox*^{-/-} gene retro-complementation had no significance impact on Mauthner cell axon regeneration in 4 dpf *duox*^{-/-} mutant fish. (scale bar, 50 μm). The regenerated and total lengths of the axons were analyzed with unpaired *t* tests (**P* < 0.05; ***P* < 0.01; ****P* < 0.001); error bars represent SEM.

Duox Affects Mitochondrial Morphology and Dynamics

Considering our previous study showing that mitochondria play a crucial role in the process of Mauthner cell axon regeneration [28], we next investigated whether *duox*^{-/-} mutations also affect mitochondrial transport in zebrafish larvae. We hypothesized that Duox mutations impair Mauthner cell axon regeneration length *via* disrupting mitochondrial transport.

To test the above hypothesis, we used TEM to observe mitochondrial morphology in the zebrafish brain (i.e., the mitochondria in the Mauthner cell axon were difficult to localize *via* TEM). TEM imaging results showed that mitochondrial sizes in *duox*^{-/-} mutants had dramatically larger surface areas, perimeters, and Feret's diameters than those in the WT group (Fig. S2). Duox mutations disrupting mitochondrial fusion and fission processes due to harmful substance invasion or other unknown mechanisms may have participated in shaping the differences in mitochondrial sizes and morphology in *duox*^{-/-} mutants compared to those in WTs.

To further investigate the role of Duox in mitochondrial dynamics, we imaged mitochondrial movement in Mauthner cell axons (Fig 4A). Mitochondrial movement directly affects mitochondrial transport which has deleterious effects on the delivery of energy to the regeneration site [40, 41]. Mitochondrial motility was defined as the percentage of moving mitochondria. The speed of a moving mitochondrion was defined as the total distance that a mitochondrion moved divided by the time spent

moving. Mitochondrial speed was significantly slower in the Mauthner cell axons of *duox* mutants (in 12 fish; total: $0.3481 \pm 0.01513 \mu\text{m/s}$, *n* = 82 mitochondria; anterograde: $0.3307 \pm 0.01468 \mu\text{m/s}$, *n* = 73 mitochondria; retrograde: $0.4896 \pm 0.05067 \mu\text{m/s}$, *n* = 9 mitochondria) than that of the WT group (in 12 fish; total: $0.5743 \pm 0.02923 \mu\text{m/s}$, *n* = 54 mitochondria; anterograde: $0.5475 \pm 0.02838 \mu\text{m/s}$, *n* = 49 mitochondria; retrograde: $0.8364 \pm 0.0927 \mu\text{m/s}$, *n* = 5 mitochondria; Fig. 4B and D). However, mitochondrial motility in Mauthner cell axons of *duox* mutant larvae (in 12 fish; total: 30.72% ± 3.744%; anterograde: 24.01% ± 3.999%; retrograde: 6.879% ± 3.273%) was not significantly different from that in WT larvae (in 12 fish; total: 33.11% ± 4.593%; anterograde: 29.32% ± 4.229%; retrograde: 3.781% ± 1.704%; Fig. 4B and C). Taken together, although the ratio of mobile mitochondria was unaffected in *duox*^{-/-} mutants, *duox* gene deficiency affected the speed of mitochondria along axons, which may have disrupted the efficacy of mitochondrial transport for providing energy.

To further investigate the roles of Duox in mitochondrial function, we assessed the mitochondrial redox state in single unilateral Mauthner cell axons *via* redox-sensitive GFPs (roGFPs), which allow subcellular redox-coupled-specific *in vivo* imaging in model organisms [42–44]. Therefore, we recognized that roGFP2 could be converted into a specific probes for H₂O₂ *via* coupling it to the microbial H₂O₂ sensor, oxidant receptor peroxidase 1 (Orp1) [45].

Since H₂O₂ is the major oxidant species involved in protein thiol oxidation and redox regulation, we generated a UAS-mito-roGFP2-Orp1 plasmid for measuring H₂O₂ in the mitochondrial matrix. H₂O₂ levels in Mauthner cell mitochondria were lower in the *duox* mutant group (0.9358 ± 0.04672 , *n* = 8) than in the WT group (2.125 ± 0.2215 , *n* = 4; Fig. 4E and F). In addition, H₂O₂ levels and ROS levels in whole-mount larvae were also down-regulated due to *duox* gene deficiency (Fig. S3). Collectively, these results suggest that *duox* gene mutation induces a low level of H₂O₂ formation, thus implying that mitochondrial redox in Mauthner cell axons is unbalanced.

In summary, we observed that *duox* mutants have disrupted mitochondrial morphology and function, especially in terms of a slower speed of transport in Mauthner cells, which may contribute to the retarded Mauthner cell axon regeneration in *duox* mutants.

Duox Affects Mitochondrial Mobility and Speed During an Early Stage of Mauthner-Cell Axon Regeneration

To directly examine the role of Duox in mitochondrial transport in Mauthner cell axon regeneration, we measured

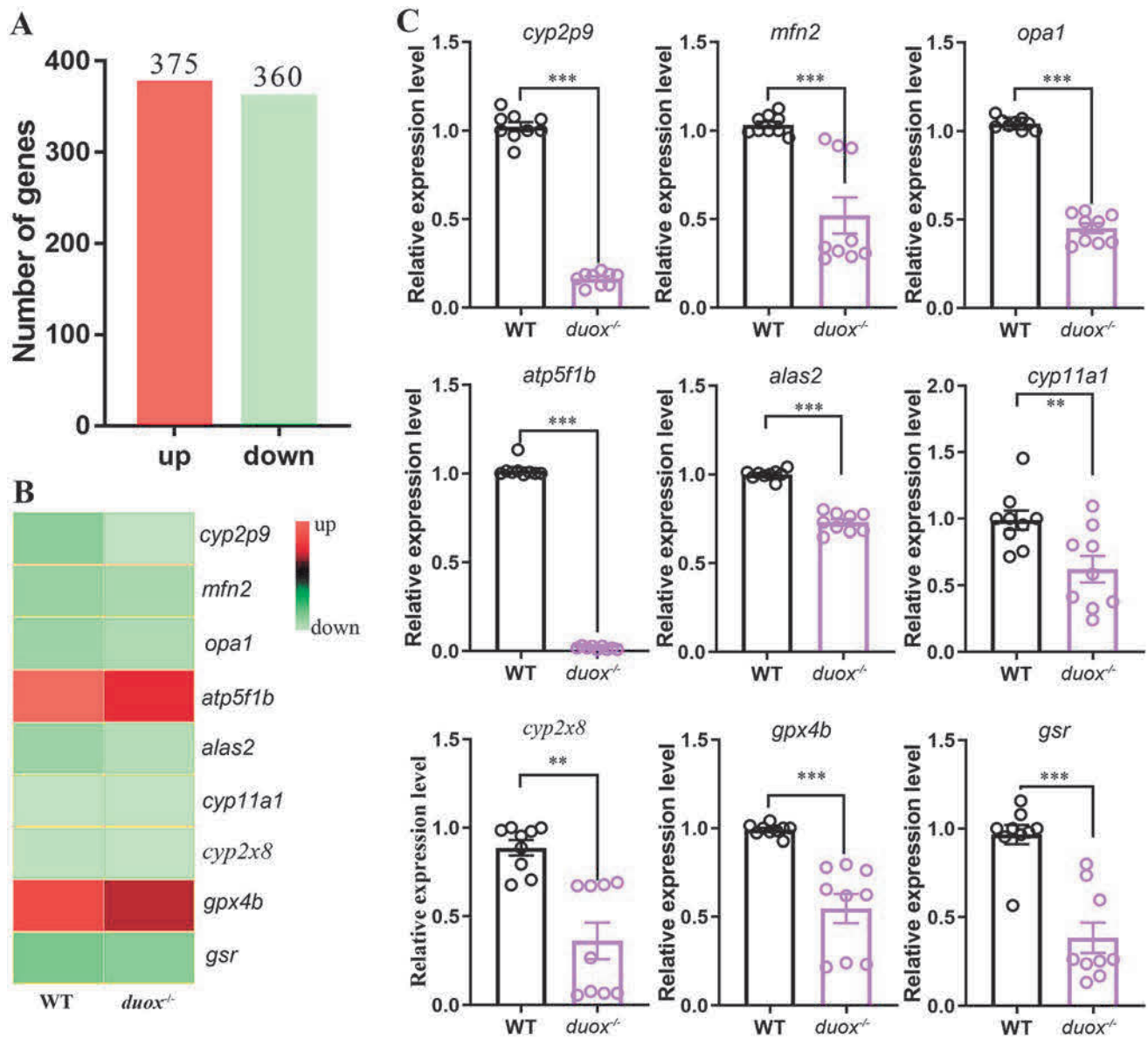


Fig. 3 Duox modulates genes associated with mitochondrial function. Transcriptomic sequencing to determine the downstream genes of *duox* that regulate axon regeneration. **A** Numbers of differentially-expressed genes (DEGs) in *duox*^{-/-} mutant zebrafish at 4 dpf, as revealed by transcriptomic analysis. **B** Histogram of 9 DEGs associated with mitochondria in *duox*^{-/-} mutant zebrafish (red,

upregulation; green, downregulation). **C** qRT-PCR analysis of nine down-regulated mitochondrial genes. Every group contains triplicate with three individual biological samples (nine replicates). The data were analyzed with unpaired *t* tests (**P* < 0.05; ***P* < 0.01; ****P* < 0.001). Error bars represent SEM.

mitochondrial mobility and speed at 24 h post-ablation (hpa) and 48 hpa. The results showed that in 24 hpa larvae, *duox* gene deficiency resulted in a slower mitochondrial speed (in 26 fish; total: $0.5313 \pm 0.01123 \mu\text{m/s}$, *n* = 208 mitochondria; anterograde: $0.524 \pm 0.01117 \mu\text{m/s}$, *n* = 186 mitochondria; retrograde: $0.5904 \pm 0.04542 \mu\text{m/s}$, *n* = 23 mitochondria) and lower mobility (in 26 fish; total: $25.22\% \pm 2.306\%$; anterograde: $22.09\% \pm 2.493\%$; retrograde: $3.121\% \pm 1.041\%$) than in the WT group (mitochondrial speed in 10 fish; total: $0.5814 \pm 0.01365 \mu\text{m/s}$, *n* = 56

mitochondria; anterograde: $0.576 \pm 0.014 \mu\text{m/s}$, *n* = 53 mitochondria; retrograde: $0.6764 \pm 0.02918 \mu\text{m/s}$, *n* = 3 mitochondria; Fig. 5A and B; mitochondrial mobility in 10 fish; total: $40.69\% \pm 3.422\%$; anterograde: $40.27\% \pm 3.307\%$; retrograde: $0.417\% \pm 0.417\%$; Fig. 5A and C). However, at 48 hpa, there was no significant difference in mitochondrial speed or mobility between the *duox*^{-/-} mutant and WT groups (Fig. 5B and C). Taken together, these results suggest that Duox mutants affect mitochondrial speed and motility in the early stages of regeneration,

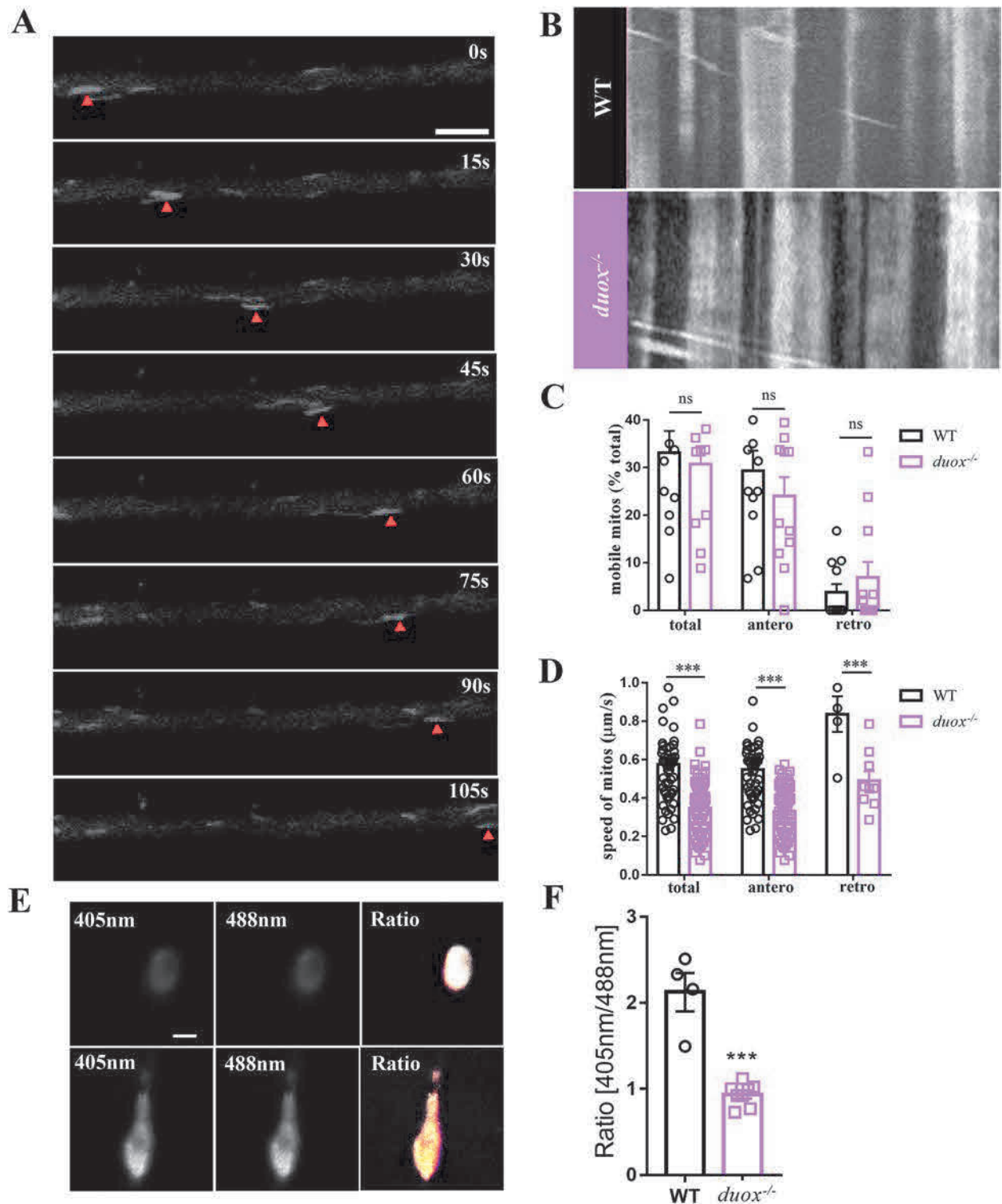


Fig. 4 Duox affects mitochondrial speed and redox in Mauthner-cell axons. **A** Representative images of moving mitochondria monitored *in vivo* by confocal time-lapse sequencing in a zebrafish Mauthner cell axon (arrowheads follow one such moving mitochondrion; scale bar, 5 μm). **B** Kymographs depict moving mitochondria in the Mauthner cell axons of WT and *duox*^{-/-} mutant fish at 6 dpf. **C**, **D** Mitochondrial motility and speed (showing total/antegrade/retrograde types) in

Mauthner cell axons of WT and *duox*^{-/-} mutant fish at 6 dpf. **E** Magnified images of the fluorescence ratios of Mauthner cell somata expressing mito-Orp-1-roGFP2 in WT and *duox*^{-/-} mutant larvae (scale bar, 10 μm). **F** Fluorescent ratios (405 nm/488 nm) of Mauthner cell somata expressing mito-Orp-1-roGFP2 in WT and *duox*^{-/-} mutant larvae. The data were analyzed with unpaired *t* tests (**P* < 0.05; ***P* < 0.01; ****P* < 0.001). Error bars represent SEM.

resulting in a lower energy supply for Mauthner cell axon regeneration.

Discussion

Duox, as a member of the NADPH oxidase family, was originally identified as thyroid NADPH oxidase, and has been demonstrated to be involved in the production of ROS in response to different extracellular signals. Studies of innate immunity have established Duox-generated H_2O_2 candidates for wound-to-leukocyte signaling in zebrafish [11]. Duox has been reported to play important roles in heart regeneration and sensory axon regeneration [15, 16], both of which are parts of the PNS. However, our previous work has shown that Mauthner cells have robust axon regeneration after two-photon axotomy, indicating that Mauthner cells are a promising model for studying CNS axon regeneration at single-cell resolution *in vivo*; in addition, Mauthner cells are large cells that can be viewed clearly and easily *in vivo* [26, 27]. Here, we found that Mauthner cell axon regeneration was inhibited in *duox*^{-/-} mutant zebrafish. This result was not likely due to a mere developmental delay because the whole length of the Mauthner cell axon in mutant larvae was not significantly different before ablation compared to that in WT. Our results are consistent with the above findings of PNS regeneration in that we also found that Duox plays a vital role in CNS regeneration due to H_2O_2 production.

In developing neurons, mitochondria are involved in many critical functions, including respiration/ATP production, Ca^{2+} buffering, apoptotic regulation, heme and Fe/S cluster biosynthesis, and ROS signaling/quenching [46, 47]. During the process of oxidative phosphorylation, mitochondria utilize oxygen to generate ATP from organic fuel molecules but in the process also produce ROS. H_2O_2 is a major type of ROS in organisms and is a central hub in redox signaling; H_2O_2 is mainly generated from NADPH oxidases or Complex III of the mitochondrial respiratory chain [48]. As mitochondria are the main source of cellular energy, we speculated that Duox affecting Mauthner cell axon regeneration was correlated with mitochondrial dynamics and H_2O_2 levels. To test this hypothesis, we investigated the effects of Duox mutations on mitochondrial motility and speed in Mauthner cell axons. We found that mitochondrial speed was slower in *duox*^{-/-} mutant larvae but that the mobility in Mauthner cell axons was unaffected. In addition, we used enzyme-coupled roGFP2-based probes to visualize chemically defined redox species *in vivo*. Orp-1-based probes specifically and reversibly report roGFP2 oxidation by H_2O_2 [43]. Our results showed that H_2O_2 levels were lower in *duox*^{-/-} mutant larvae than in

WTs. These results indicate that Duox induced a decrease in the amount of energy transported to axons and resulted in poor axon regeneration. Our results are consistent with findings from a previous study in giant pandas that used a mutation in the *duox* gene to allow them to have a lower metabolic rate through a lower level of thyroid hormone synthesis [49]. This study revealed that Duox deficiency inhibited Mauthner cell axon regeneration due to a lower metabolic rate through a lower level of mitochondrial energy production. However, these findings represented the Mauthner cell axonal state in *duox* mutants without laser ablation.

To further investigate the effect of Duox in Mauthner cell axon regeneration after laser ablation, we measured mitochondrial speed and mobility at 24 hpa and 48 hpa. We found that mitochondrial speed and mobility were both lower in *duox*^{-/-} mutant larvae than in WT larvae at 24 hpa, but there was no significant difference at 48 hpa; hence, we further focused on the changes at 24 hpa. Compared to non-ablation and 48 hpa results, we found that mitochondrial mobility played more vital roles at 24 hpa; we propose two possible accounts for this finding. First, mitochondria are mainly trafficked along microtubules by ATPase-dependent kinesin and dynein motor proteins and dendrite- and axon-specific adaptor proteins. In distal dendrites and the entire axon, the plus-end of microtubules is oriented toward the growth cone, and kinesins mediate anterograde transport while dyneins mediate retrograde transport [50]. In proximal dendrites, microtubule polarity is mixed, and motor proteins are not selective for either anterograde or retrograde transport [50]. After ablation, the growth cone was closer to our imaging position at the distal axonal area (Fig. 1A in our previous study) [28] compared to that during non-ablation conditions, so we speculated that Duox affects kinesin. Second, H_2O_2 is rapidly produced from axonal laser ablation; to avoid damage from high levels of H_2O_2 , Mauthner cell axons increase mitochondrial mobility to consume more H_2O_2 [51] in WT larvae. However, this mechanism is unnecessary in *duox*^{-/-} mutant larvae since H_2O_2 generation is inhibited. These findings collectively suggest that during axon regeneration, axons require highly integrated metabolic machinery and more anterograde trafficking of mitochondria for local ATP synthesis to meet the large energy demands of regeneration, but these processes appear to be impeded in *duox*^{-/-} mutant larvae.

In summary, we found that zebrafish Duox inhibited Mauthner cell axon regeneration *via* affecting mitochondrial mobility and speed. Our present study indicates that metabolic insufficiency induced by *duox* mutant may impair Mauthner cell regeneration due to impeded mitochondrial dynamics, which provides insight into the interactions among energy metabolism, mitochondrial trafficking, and axon regeneration in the CNS.

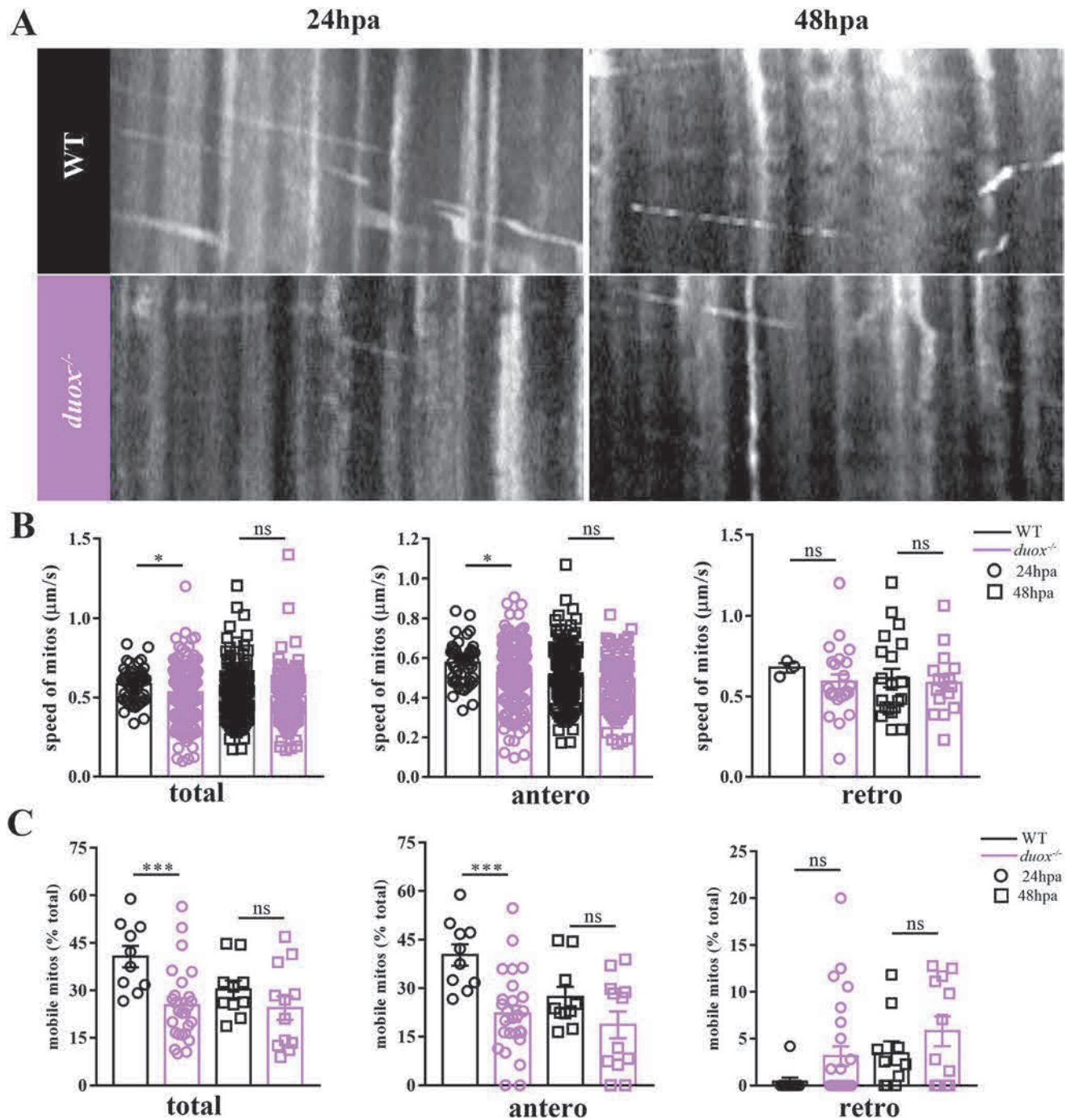


Fig. 5 Duox affects mitochondrial speed and motility during Mauthner-cell axon regeneration. **A** Kymographs depicting mitochondrial movement in Mauthner cell axons of WT (top) and *duox*^{-/-} mutant (below) fish at 24 hpa (left) and 48 hpa (right). **B** Comparison of mitochondrial speeds (showing total/anterograde/retrograde types) in

Mauthner cell axons of WT and *duox*^{-/-} mutant fish at 24 and 48 hpa. **C** Comparison of mitochondrial motility (showing total/anterograde/retrograde types) in Mauthner cell axons of WT and *duox*^{-/-} mutant fish at 24 and 48 hpa. The data were analyzed with unpaired *t* tests (**P* < 0.05; ***P* < 0.01; ****P* < 0.001). Error bars represent SEM.

Acknowledgements This work was supported by the National Natural Science Foundation of China (31771183 and 31701027) and the National Key Research and Development Program of China

(2019YFA0405603 and 2019YFA0405600). We thank LetPub (www.letpub.com) for its linguistic assistance during the preparation of this manuscript.

Data Availability The datasets generated during and/or analyzed during the current study are available from the corresponding author on reasonable request.

Conflict of interest The authors declare no competing financial interest.

References

- Bolduc JA, Collins JA, Loeser RF. Reactive oxygen species, aging and articular cartilage homeostasis. *Free Radic Biol Med* 2019, 132: 73–82.
- Buvelot H, Jaquet V, Krause KH. Mammalian NADPH Oxidases. *Methods Mol Biol* 2019, 1982: 17–36.
- Xu FF, Zhang ZB, Wang YY, Wang TH. Brain-derived glia maturation factor beta participates in lung injury induced by acute cerebral ischemia by increasing ROS in endothelial cells. *Neurosci Bull* 2018, 34: 1077–1090.
- Veith C, Boots AW, Idris M, van Schooten FJ, van der Vliet A. Redox imbalance in idiopathic pulmonary fibrosis: A role for oxidant cross-talk between NADPH oxidase enzymes and mitochondria. *Antioxid Redox Signal* 2019, 31: 1092–1115.
- Marrali G, Casale F, Salamone P, Fuda G, Ilardi A, Manera U, *et al.* NADPH oxidases 2 activation in patients with Parkinson's disease. *Parkinsonism Relat Disord* 2018, 49: 110–111.
- Ma MW, Wang J, Dhandapani KM, Wang R, Brann DW. NADPH oxidases in traumatic brain injury—Promising therapeutic targets? *Redox Biol* 2018, 16: 285–293.
- Park JS, Choi TI, Kim OH, Hong TI, Kim WK, Lee WJ, *et al.* Targeted knockout of duox causes defects in zebrafish growth, thyroid development, and social interaction. *J Genet Genomics* 2019, 46: 101–104.
- Geiszt M, Witta J, Baffi J, Lekstrom K, Leto TL. Dual oxidases represent novel hydrogen peroxide sources supporting mucosal surface host defense. *FASEB J* 2003, 17: 1502–1504.
- Sirokmany G, Donko A, Geiszt M. Nox/Duox family of NADPH oxidases: Lessons from knockout mouse models. *Trends Pharmacol Sci* 2016, 37: 318–327.
- Flores MV, Crawford KC, Pullin LM, Hall CJ, Crosier KE, Crosier PS. Dual oxidase in the intestinal epithelium of zebrafish larvae has anti-bacterial properties. *Biochem Biophys Res Commun* 2010, 400: 164–168.
- Niethammer P, Grabher C, Look AT, Mitchison TJ. A tissue-scale gradient of hydrogen peroxide mediates rapid wound detection in zebrafish. *Nature* 2009, 459: 996–999.
- Yoo SK, Starnes TW, Deng Q, Huttenlocher A. Lyn is a redox sensor that mediates leukocyte wound attraction in vivo. *Nature* 2011, 480: 109–112.
- Moreno JC, Bikker H, Kempers MJE, van Trotsenburg P, Baas F, de Vijlder JJM, *et al.* Inactivating mutations in the gene for thyroid oxidase 2 (THOX2) and congenital hypothyroidism. *N Engl J Med* 2002, 347: 95–102.
- Park KJ, Park HK, Kim YJ, Lee KR, Park JH, Park JH, *et al.* DUOX2 mutations are frequently associated with congenital hypothyroidism in the Korean population. *Ann Lab Med* 2016, 36: 145–153.
- Han P, Zhou XH, Chang N, Xiao CL, Yan S, Ren H, *et al.* Hydrogen peroxide primes heart regeneration with a derepression mechanism. *Cell Res* 2014, 24: 1091–1107.
- Rieger S, Sagasti A. Hydrogen peroxide promotes injury-induced peripheral sensory axon regeneration in the zebrafish skin. *PLoS Biol* 2011, 9: e1000621.
- Chen MF, Zheng BH. Axon plasticity in the mammalian central nervous system after injury. *Trends Neurosci* 2014, 37: 583–593.
- Becker T, Becker CG. Axonal regeneration in zebrafish. *Curr Opin Neurobiol* 2014, 27: 186–191.
- Li WY, Zhang WT, Cheng YX, Liu YC, Zhai FG, Sun P, *et al.* Inhibition of KLF7-targeting microRNA 146b promotes sciatic nerve regeneration. *Neurosci Bull* 2018, 34: 419–437.
- Taylor JSH, Jack JL, Easter SS. Is the Capacity for optic-nerve regeneration related to continued retinal ganglion-cell production in the frog—a test of the hypothesis that neurogenesis and axon regeneration are obligatorily linked. *Eur J Neurosci* 1989, 1: 626–638.
- Nagashima M, Fujikawa C, Mawatari K, Mori Y, Kato S. HSP70, the earliest-induced gene in the zebrafish retina during optic nerve regeneration: Its role in cell survival. *Neurochem Int* 2011, 58: 888–895.
- Saijilafu, Zhang BY, Zhou FQ. Signaling pathways that regulate axon regeneration. *Neurosci Bull* 2013, 29: 411–420.
- Vajn K, Plunkett JA, Tapanes-Castillo A, Oudega M. Axonal regeneration after spinal cord injury in zebrafish and mammals: differences, similarities, translation. *Neurosci Bull* 2013, 29: 402–410.
- Mu Z, Zhang S, He C, Hou H, Liu D, Hu N, *et al.* Expression of SoxC transcription factors during zebrafish retinal and optic nerve regeneration. *Neurosci Bull* 2017, 33: 53–61.
- Yanik MF, Cinar H, Cinar HN, Chisholm AD, Jin YS, Ben-Yakar A. Neurosurgery—Functional regeneration after laser axotomy. *Nature* 2004, 432: 822.
- Hu BB, Chen M, Huang RC, Huang YB, Xu Y, Yin W, *et al.* In vivo imaging of Mauthner axon regeneration, remyelination and synapses re-establishment after laser axotomy in zebrafish larvae. *Exp Neurol* 2018, 300: 67–73.
- Huang R, Chen M, Yang L, Wagle M, Guo S, Hu B. MicroRNA-133b Negatively regulates zebrafish single mauthner-cell axon regeneration through targeting tppp3 *in vivo*. *Front Mol Neurosci* 2017, 10: 375.
- Xu Y, Chen M, Hu B, Huang R, Hu B. *In vivo* imaging of mitochondrial transport in single-axon regeneration of zebrafish mauthner cells. *Front Cell Neurosci* 2017, 11: 4.
- Chen M, Huang RC, Yang LQ, Ren DL, Hu B. In vivo imaging of evoked calcium responses indicates the intrinsic axonal regenerative capacity of zebrafish. *FASEB J* 2019, 33: 7721–7733.
- Satou C, Kimura Y, Kohashi T, Horikawa K, Takeda H, Oda Y, *et al.* Functional role of a specialized class of spinal commissural inhibitory neurons during fast escapes in zebrafish. *J Neurosci* 2009, 29: 6780–6793.
- Kimmel CB, Ballard WW, Kimmel SR, Ullmann B, Schilling TF. Stages of embryonic-development of the zebrafish. *Dev Dyn* 1995, 203: 253–310.
- Jao LE, Wente SR, Chen WB. Efficient multiplex biallelic zebrafish genome editing using a CRISPR nuclease system. *Proc Natl Acad Sci U S A* 2013, 110: 13904–13909.
- Chen M, Xu Y, Huang RC, Huang YB, Ge SC, Hu B. N-cadherin is involved in neuronal activity-dependent regulation of myelinating capacity of zebrafish individual oligodendrocytes *in vivo*. *Mol Neurobiol* 2017, 54: 6917–6930.
- O'Donnell KC, Vargas ME, Sagasti A. WldS and PGC-1 alpha regulate mitochondrial transport and oxidation state after axonal injury. *J Neurosci* 2013, 33: 14778–14790.
- VanGuilder HD, Vrana KE, Freeman WM. Twenty-five years of quantitative PCR for gene expression analysis. *Biotechniques* 2008, 44: 619–626.
- Grabherr MG, Haas BJ, Yassour M, Levin JZ, Thompson DA, Amit I, *et al.* Full-length transcriptome assembly from RNA-Seq data without a reference genome. *Nat Biotechnol* 2011, 29: 644–652.

37. Young MD, Wakefield MJ, Smyth GK, Oshlack A. Gene ontology analysis for RNA-seq: accounting for selection bias. *Genome Biol* 2010, 11: R14.
38. Kanehisa M, Araki M, Goto S, Hattori M, Hirakawa M, Itoh M, *et al.* KEGG for linking genomes to life and the environment. *Nucleic Acids Res* 2008, 36: D480–D484.
39. Dan Dunn J, Alvarez LA, Zhang X, Soldati T. Reactive oxygen species and mitochondria: A nexus of cellular homeostasis. *Redox Biol* 2015, 6: 472–485.
40. Cartoni R, Norsworthy MW, Bei F, Wang C, Li S, Zhang Y, *et al.* The mammalian-specific protein *armacx1* regulates mitochondrial transport during axon regeneration. *Neuron* 2016, 92: 1294–1307.
41. Zhou B, Yu P, Lin MY, Sun T, Chen Y, Sheng ZH. Facilitation of axon regeneration by enhancing mitochondrial transport and rescuing energy deficits. *J Cell Biol* 2016, 214: 103–119.
42. Hanson GT, Aggeler R, Oglesbee D, Cannon M, Capaldi RA, Tsien RY, *et al.* Investigating mitochondrial redox potential with redox-sensitive green fluorescent protein indicators. *J Biol Chem* 2004, 279: 13044–13053.
43. Albrecht SC, Barata AG, Grosshans J, Teleman AA, Dick TP. *In vivo* mapping of hydrogen peroxide and oxidized glutathione reveals chemical and regional specificity of redox homeostasis. *Cell Metab* 2011, 14: 819–829.
44. Dooley CT, Dore TM, Hanson GT, Jackson WC, Remington SJ, Tsien RY. Imaging dynamic redox changes in mammalian cells with green fluorescent protein indicators. *J Biol Chem* 2004, 279: 22284–22293.
45. Gutsche M, Sobotta MC, Wabnitz GH, Ballikaya S, Meyer AJ, Samstag Y, *et al.* Proximity-based protein thiol oxidation by H₂O₂-scavenging peroxidases. *J Biol Chem* 2009, 284: 31532–31540.
46. Mattson MP, Gleichmann M, Cheng A. Mitochondria in neuroplasticity and neurological disorders. *Neuron* 2008, 60: 748–766.
47. McWilliams TG, Prescott AR, Allen GFG, Tamjar J, Munson MJ, Thomson C, *et al.* mito-QC illuminates mitophagy and mitochondrial architecture *in vivo*. *J Cell Biol* 2016, 214: 333–345.
48. Sies H. Role of metabolic H₂O₂ generation. *J Biol Chem* 2014, 289: 8735–8741.
49. Nie YG, Speakman JR, Wu Q, Zhang CL, Hu YB, Xia MH, *et al.* Exceptionally low daily energy expenditure in the bamboo-eating giant panda. *Science* 2015, 349: 171–174.
50. Baas PW, Deitch JS, Black MM, Banker GA. Polarity Orientation of microtubules in hippocampal-neurons—uniformity in the axon and nonuniformity in the dendrite. *Proc Natl Acad Sci U S A* 1988, 85: 8335–8339.
51. Treberg JR, Braun K, Selseleh P. Mitochondria can act as energy-sensing regulators of hydrogen peroxide availability. *Redox Biol* 2019, 20: 483–488.



METHOD

Quantitative Determination of Glymphatic Flow Using Spectrophotofluorometry

Yu Zhang¹ · Jian Song¹ · Xu-Zhong He¹ · Jian Xiong² · Rong Xue¹ ·
Jia-Hao Ge¹ · Shi-Yu Lu¹ · Die Hu¹ · Guo-Xing Zhang¹ · Guang-Yin Xu³ ·
Lin-Hui Wang¹

Received: 14 February 2020 / Accepted: 6 May 2020 / Published online: 25 July 2020
© Shanghai Institutes for Biological Sciences, CAS 2020

Abstract Following intrathecal injection of fluorescent tracers, *ex vivo* imaging of brain vibratome slices has been widely used to study the glymphatic system in the rodent brain. Tracer penetration into the brain is usually quantified by image-processing, even though this approach requires much time and manual operation. Here, we illustrate a simple protocol for the quantitative determination of glymphatic activity using spectrophotofluorometry. At specific time-points following intracisternal or intrastriatal injection of fluorescent tracers, certain brain regions and the spinal cord were harvested and tracers were extracted from the tissue. The intensity of tracers was analyzed spectrophotometrically and their concentrations were quantified from standard curves. Using this approach, the regional and dynamic delivery of subarachnoid CSF tracers into the brain parenchyma was assessed, and the clearance of tracers from the brain was also determined. Furthermore, the impairment of glymphatic influx in the brains of old mice was confirmed using our approach. Our method is more accurate and efficient than the imaging approach in terms of the quantitative determination of glymphatic activity, and this will be useful in preclinical studies.

Keywords Glymphatic system · Cerebrospinal fluid · Fluorescent tracer · Spectrophotofluorometry

Introduction

The glymphatic system/pathway is a brain-wide system for exchange between the cerebrospinal fluid (CSF) and the interstitial fluid (ISF). It is mediated by the aquaporin-4 (AQP4) densely expressed in astrocytic end-feet around the brain vasculature [1–3]. This system is proposed to function in the removal of toxic metabolic waste such as β -amyloid from the brain and the transport of CSF-derived molecules such as apoE into the brain [3–8]. The glymphatic system is composed of an influx (CSF inflow *via* the peri-arterial spaces) and an efflux (waste removal *via* the peri-venous spaces), which are functionally coupled by convective ISF flow from the arterial to the venous perivascular spaces [2, 9]. Accumulating studies have demonstrated that glymphatic activity is dramatically enhanced during sleep and anesthesia [10–12], while its function is seriously reduced in aging [13], Alzheimer's disease [14], traumatic brain injury [4], stroke [15], and hypertension [16, 17].

Multiple approaches have been developed to analyze the glymphatic pathway in animals and the human brain [2]. Among them, fluorescent tracers such as dextran, albumin, and ovalbumin with different molecular weights tagged with fluorophores are widely used to investigate CSF flow and the glymphatic pathway in the rodent brain [1, 13, 18, 19]. In addition, we recently found that cadaverine tagged with a fluorophore also delineates the movement of subarachnoid CSF into the brain and spinal cord of mice [20, 21]. Following intrathecal injection of tracers into the cisterna magna or lumbar spine, the

✉ Guang-Yin Xu
guangyinxu@suda.edu.cn

✉ Lin-Hui Wang
wanglinhui@suda.edu.cn

¹ Department of Physiology and Neurobiology, Medical College of Soochow University, Suzhou 215123, China

² Institute of Medical Biotechnology, Suzhou Vocational Health College, Suzhou 215009, China

³ Institute of Neuroscience, Soochow University, Suzhou 215123, China

dynamics of glymphatic flow has been successfully visualized *in vivo* and *ex vivo*. For *in vivo* imaging, two-photon optical imaging has been initially applied to characterize the detailed and rapid perivascular CSF–ISF exchange [1, 22, 23]. Transcranial macroscopic imaging through the intact skull has recently been used for more global observations of the mouse brain [24]. For *ex vivo* imaging, visualization is conducted on coronal and sagittal brain sections prepared from animals following the injection of fluorescent tracers [13, 25]. *Ex vivo* imaging, in combination with immunohistochemistry, provides detailed information on the perivascular distribution of CSF tracers in the whole brain, specific regions, and even at the cellular level [1, 13, 20, 21]. For quantitative analysis, tracer penetration into the central nervous system (CNS) can be quantified through image-processing [1, 13, 19, 20]. Usually under low power, a whole brain slice or an area of interest is chosen and the mean pixel intensity or the coverage area of the fluorescent tracer is manually analyzed in imaging software. However, the image-quantification method is time-consuming, laborious, and quite unreliable due to the many steps involved.

Spectrophotofluorometry is capable of measuring the content of fluorescent tracers in body fluids and tissues. For example, extravasated Evans blue dye has been quantified spectrophotometrically to assess protein leakage due to a damaged blood-brain barrier [26]. After intracisternal injection, the concentration of Evans blue-labeled albumin in serum and AlexaFluor488 goat-anti-rabbit IgG in plasma has been quantified on a microplate reader to assess the drainage of proteins from the subarachnoid space to the plasma [25, 27]. After gavaging, fluorescent tracers (MB-402 and MB-301) in urine have been analyzed spectrophotofluorometrically to identify intestinal injury in rats [28]. Therefore, determining the content of fluorescent tracers in brain tissues through spectrophotofluorometry could be used to evaluate glymphatic activity.

The goal of the present study was to establish a simple protocol for quantitative determination of glymphatic activity using spectrophotofluorometry. Using this approach, time–concentration curves were established to demonstrate the dynamic CSF inflow from the subarachnoid space to the CNS and the removal of solutes from the brain interstitium. Furthermore, we re-examined the impaired glymphatic inflow of old mice using this new approach. Our findings demonstrated that the glymphatic flow of fluorescent tracers can be accurately quantified by spectrophotofluorometry.

Materials and Methods

Animals

All our experimental protocols were approved by the Committee on Animal Resources of Soochow University, and conformed with the European Convention for the Protection of Vertebrate Animals used for Experimental and other Scientific Purposes. Male ICR mice and C57BL/6 mice were acquired from the Shanghai Laboratory Animal Center. The C57BL/6 mice (3–5 and 14–16 months old) were used to study the effect of aging on glymphatic activity, and ICR mice (3 months old) were used in the other experiments. ICR mice were used mainly because they are cheaper and more readily available than C57BL/6 mice. In all experiments, mice were anesthetized with a combination of xylazine (10 mg/kg) and ketamine (100 mg/kg) by intraperitoneal injection. During the whole process of tracer injection, body temperature was maintained at $37 \pm 0.5^\circ\text{C}$ by a heating pad.

Tracers

Fluorescein isothiocyanate–conjugated dextran (molecular weight, 3 kDa; Dex-3) and Alexa 555–conjugated ovalbumin (molecular weight, 45 kDa; OA-45) were from Invitrogen (D3306, O-34782, USA) [13, 29]. Tracers were diluted in RIPA lysis buffer (P0013C, Beyotime, China) [30] or artificial CSF (NaCl 7.247g, KCl 0.224g, NaHCO_3 2.184g, NaH_2PO_4 0.193g, MgSO_4 0.493g, CaCl_2 0.222g, $\text{C}_6\text{H}_{12}\text{O}_6$ 1.982g, for the volume of 1000 mL).

Establishing Standard Curves

A standard vial of tracer contained the volume of lysis buffer required to give a relative tracer concentration of 1×10^{10} pg/mL (1%). This stock solution was then used to generate a standard curve (Fig. 1A, B). Lysis buffer was used to make the dilutions as follows:

Ten test tubes #1–10 and “0 dose” were labeled, 270 μL of the lysis buffer was added to tubes #1–10 and 300 μL to the “0 dose” tube, and 30 μL of the stock solution was added to tube #1 and vortexed. This was Standard tube #1 with a concentration of 1×10^9 pg/mL (0.1%). Standards #2–10 were then prepared by performing a 1:10 dilution of the preceding standard. For example, to make Standard #2, 30 μL of Standard #1 was added to tube #2 and vortexed, and so on. No tracer was added to the “0 Dose” tube. In addition, two other standard tubes (2×10^7 and 5×10^7 pg/mL) were set for Dex-3 (Fig. 1B). Finally, 100 μL of solution was drawn from each tube and put into microplate

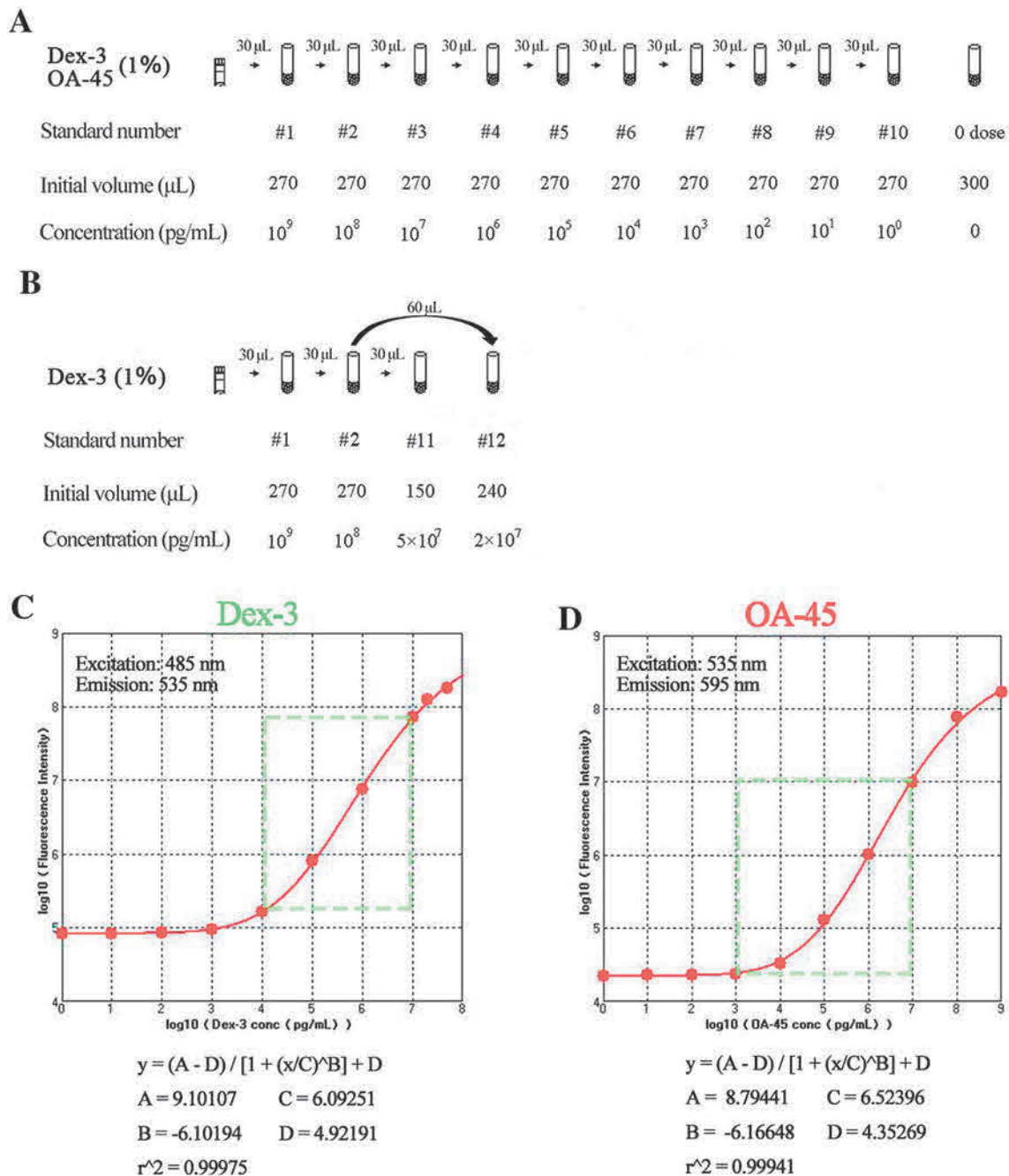
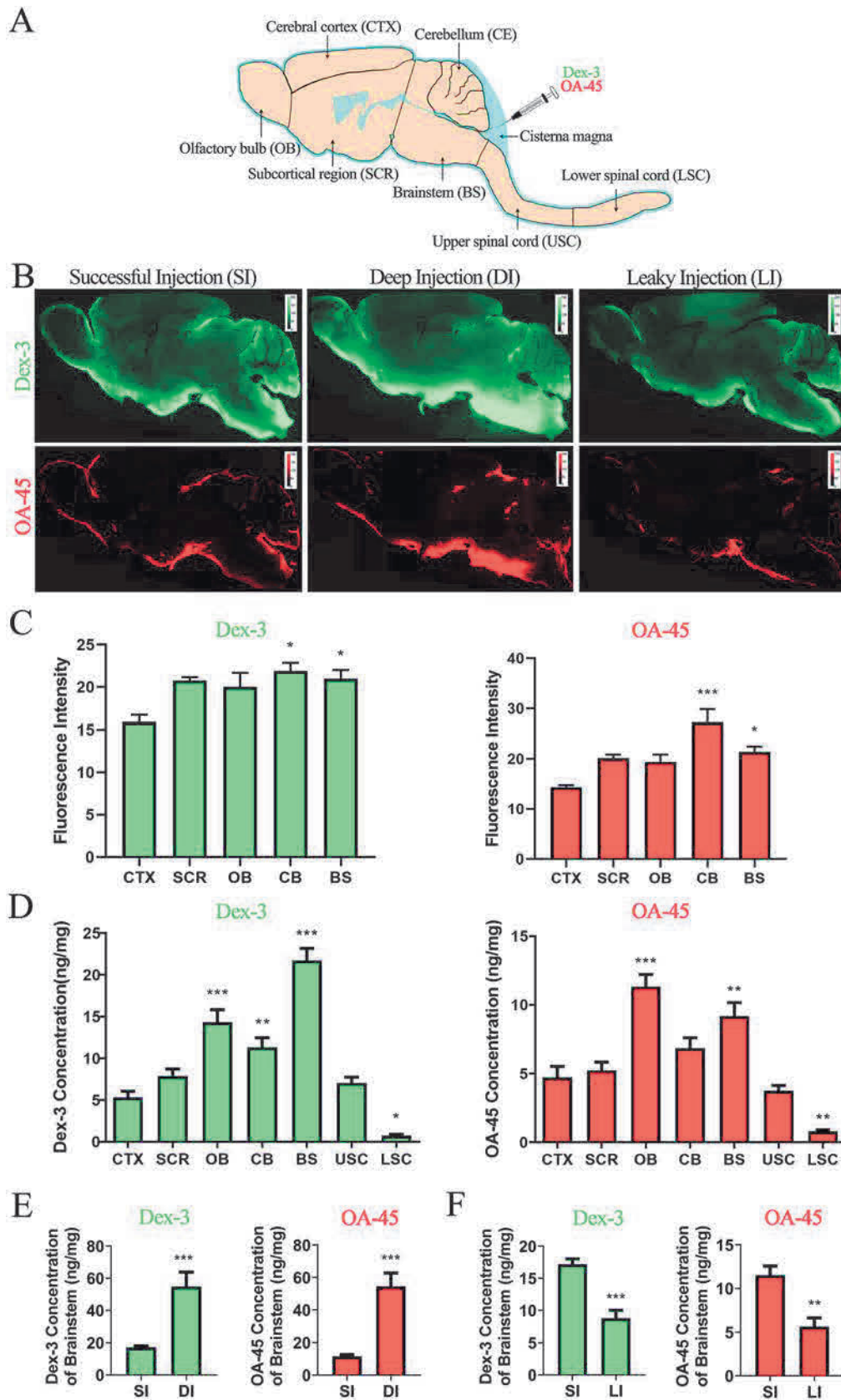


Fig. 1 Standard curves of fluorescent tracers. **A** Serial dilution of OA-45 and Dex-3 standards. **B** Serial dilution of the other two Dex-3 standards. **C** Standard curve of Dex-3. **D** Standard curve of OA-45.

containers. Three replicates were performed for each standard. The intensity of fluorescent tracers in the solutions was analyzed spectrophotofluorometrically at an excitation wavelength of 485 nm for Dex-3 and 535 nm for OA-45 and an emission wavelength of 535 nm for Dex-3 and 595 nm for OA-45 using a microplate reader (FilterMax F5, Molecular Devices). The fluorescence intensity of each standard (minus the fluorescence intensity of the “0

The area outlined by green dashed lines indicates the range of tracer intensity and their corresponding concentrations in the brain and spinal cord following tracer injection in this study.

Dose” tube) was processed by logarithmic transformation. Standard curves of the relationship between \log_{10} Fluorescence Intensity and \log_{10} Concentration (pg/mL) for OA-45 and Dex-3 were constructed (Fig. 1C, D). The limit of detection (LOD) was calculated using the equation $LOD = 3 SD/B$, where SD is the the standard deviation of the corresponding concentration in the blank tube and B is the slope of the linear equation.



◀ **Fig. 2** Regional distribution of tracers following intracisternal injection. **A** Schematic of intracisternal injection and region sampling. **B** Representative images showing the penetration of Dex-3 (green) and OA-45 (red) into the brain after successful and unsuccessful injections (deep insertion and leaky injection) (slices from lateral 0.36 mm). **C** Mean intensity of fluorescent tracer (mean pixel intensity) within defined ROIs following successful injection analyzed in ImageJ ($n = 4$, $*P < 0.05$, $***P < 0.001$ vs CTX, ANOVA followed by Dunnett's *t*-test). **D** Concentrations of fluorescent tracers (ng/mg tissue) in defined brain regions following successful injection assessed using a microplate reader ($n = 6$, $**P < 0.01$, $***P < 0.001$ vs CTX, ANOVA followed by Dunnett's *t*-test). **E** Concentrations of both tracers in the BS following deep injection are much higher than those of successful injection ($n = 4$, $***P < 0.001$, unpaired Student's *t*-test). **F** Concentrations of both tracers in the BS are significantly lower following leaky injection than those of successful injection ($n = 4$, $**P < 0.01$, $***P < 0.001$, unpaired Student's *t*-test). CTX, cerebral cortex; SCR, subcortical region; OB, olfactory bulb; CB, cerebellum; BS, brainstem; USC, upper spinal cord; LSC, lower spinal cord; SI, successful injection; DI, deep injection; LI, leaky injection.

Tracer Injection

Fluorescent tracer was diluted in artificial CSF to a final concentration of 0.5% and intracisternal tracer injection was done as previously described [13, 20, 21, 31]. Briefly, anesthetized mice were fixed in a stereotaxic frame and the dural membrane covering the cistern magna was carefully exposed and cannulated using a 30 G needle attached *via* PE-10 tubing to a Hamilton syringe. The needle was fixed to the dural membrane with a mixture of cyanoacrylate adhesive and dental cement. OA-45 and Dex-3 (10 μ L in total) were co-infused with a syringe pump (LSP01-1A, Longer Precision Pump, China), at 1 μ L/min for 10 min. Intrastratial tracer injection was performed as previously described with minor modifications [13]. Anesthetized mice were stereotaxically injected unilaterally into the right striatum. The coordinates for injection were antero-posterior +0.2 mm and mediolateral +2.0 mm relative to bregma, and dorsoventral -2.6 mm from the brain surface. Dex-3 (1 μ L in total) was injected at 0.25 μ L/min for 4 min. The needle was left in place for an additional 5 min and then removed. Normothermia was maintained with a heating pad and deep anesthesia was maintained throughout.

Tracer Assays

Mice were decapitated at specified time-points after intracisternal tracer infusion. After removing the brain and spinal cord, the meninges were carefully removed and the cerebral cortex, subcortical region, olfactory bulb, cerebellum, brain stem, upper spinal cord (cervical and thoracic segments), and lower spinal cord (lumbar and

sacral segments) were dissected (Fig. 2A). At 10, 60, and 90 min following intrastratial infusion, mice were decapitated and the specified brain regions (including the ipsilateral cortex and subcortex) were dissected (Fig. 4A). These tissues were weighed and then stored at -80°C until use. To demonstrate the accuracy of the separation procedure, the statistical results of tissue weights were recorded (Table 1). To measure the tracer content, these tissues were homogenized on ice with a volume of lysis buffer corresponding to their weights (200 mg/mL), then centrifuged at 12,000 g at 4°C for 20 min. Supernatant aliquots (100 μ L) were put into microplate containers and the intensity of fluorescent tracers was spectrophotofluorometrically assessed using the microplate reader. The concentration of tracer was quantified from the standard curves for Dex-3 and OA-45 and is expressed as ng/mg tissue.

Ex vivo Fluorescence Imaging

At specified time-points following intracisternal and intrastratial tracer infusion, mice were transcardially perfused with phosphate-buffered saline (PBS) and 4% paraformaldehyde (PFA). After post-fixation in 4% PFA overnight at 4°C , each brain was harvested and cut into 100 μ m sagittal or coronal sections on a vibratome. The distribution of fluorescent tracers within the slices was imaged under a fluorescence microscope (Eclipse TE 2000-U, Nikon, Japan). Whole-slice montages were integrated using the Virtual Slice module of Kolor Autopano Giga (V4.4), in which DAPI, green and red emission channels were included. Based on the un-injected control slices, exposure levels were determined and maintained constant throughout the study. The distribution of fluorescent tracer was quantified as previously described [18–21]. Based on the DAPI channel, the fluorescence channels were split and the region of interest (ROI) was defined for each slice. Under a $\times 4$ objective, the whole brain slice or defined ROI (Figs. 2A and 4A) was chosen and the mean pixel intensity of fluorescent tracer was quantified. Using ImageJ software (NIH), images were analyzed with a uniform threshold at pixel intensity from 50 to 255.

Statistical Analysis

All data are presented as the mean \pm SEM. All statistics were calculated with GraphPad Prism (La Jolla, CA). Analysis of variance (ANOVA) followed by Tukey's *post hoc* test was used for multiple comparisons. An unpaired Student's *t* test was used for comparison between two groups. $P < 0.05$ was considered to be statistically significant.

Results

Standard Curves of Fluorescent Tracers for Concentration Quantification

The standard curve of OA-45 demonstrated that the fluorescence intensity remained at the basal level and did not significantly change when the concentration ranged from 1 pg/mL to 100 pg/mL. Similarly, the standard curve of Dex-3 showed that the basal fluorescence intensity did not change when the concentration ranged from 1 pg/mL to 10 pg/mL. We then calculated the LOD for each tracer. Results showed that the LOD for OA-45 was 60.63 pg/mL, and that for Dex-3 was 5.79 pg/mL. Notably, the instrument saturated when the Dex-3 concentration reached 1×10^8 pg/mL, while it did not saturate when the OA-45 concentration reached 1×10^9 pg/mL (Fig. 1C, D), which was the highest concentration set in this experiment. Moreover, the fluorescence intensity of Dex-3 was markedly higher than that of OA-45 at the same concentration, mostly because Dex-3 conjugated more or brighter fluorophores per mg than OA-45. In all subsequent experiments, the fluorescence intensity of both tracers in CNS tissue following intracisternal or intraatrial injection was measured by the microplate reader, and the corresponding concentration was located in the middle of the standard curves (shown by the areas outlined by green dashed lines in Fig. 1C and D).

Delivery of Subarachnoid CSF Tracers into the Brain and Detection by the Microplate Assay

At 30 min following tracer injection, transport into the brain parenchyma was estimated *ex vivo* using the imaging approach and the microplate assay (Fig. 2A). Representative images showed that Dex-3 and OA-45 robustly accumulated at the pial surface, in several cisterns, and in the brain parenchyma. Dex-3 penetrated more deeply

than OA-45, mostly because the molecular weight of Dex-3 (3 kDa) is lower than OA-45 (45 kDa) (Fig. 2B). Next, we defined several brain ROIs – cerebral cortex (CTX), subcortical region (SCR), olfactory bulb (OB), cerebellum (CB), and brainstem (BS) (Fig. 2A) – and quantified the mean pixel intensity of tracer within these ROIs using ImageJ. The results showed that the fluorescence intensity of both tracers (mean pixel intensity) in the BS (Dex-3, 21.00 ± 1.02 ; OA-45, 21.45 ± 1.02) and CB (Dex-3, 21.90 ± 0.96 ; OA-45: 27.30 ± 2.57) were significantly higher than those in the CTX (Dex-3, 15.94 ± 0.82 ; OA-45, 14.34 ± 0.37). The intensity of both tracers in the SCR (Dex-3, 20.78 ± 0.40 ; OA-45, 20.20 ± 0.67) and OB (Dex-3, 20.01 ± 1.67 ; OA-45, 19.43 ± 1.44) were somewhat higher than those in the CTX but the difference was not significant (Fig. 2C).

The results of the microplate assays revealed that, after injection, the concentration of Dex-3 within each defined region was much higher than that of OA-45. Moreover, the concentration of both tracers (ng/mg tissue) in the BS (Dex-3, 20.93 ± 1.29 ; OA-45, 9.20 ± 0.96), CB (Dex-3, 11.83 ± 0.91 ; OA-45, 6.87 ± 0.74), and OB (Dex-3, 14.30 ± 1.50 ; OA-45, 11.31 ± 0.89) were much higher than those of CTX (Dex-3, 5.04 ± 0.80 ; OA-45, 4.74 ± 0.80). The concentrations of both tracers in the SCR (Dex-3, 7.55 ± 0.77 ; OA-45, 5.24 ± 0.60) and USC (Dex-3, 6.63 ± 0.91 ; OA-45, 3.77 ± 0.38) were similar to those of CTX, while those in the LSC (Dex-3, 0.82 ± 0.14 ; OA-45, 0.80 ± 0.12) were significantly lower than those in the CTX (Fig. 2D). These results on brain uptake of tracers are mostly in line with the results of the imaging-quantification approach.

In our experience, unsuccessful intracisternal injection may sometimes happen, especially for beginners. The failure is usually caused by tracer leakage during injection (leaky injection) or injecting into the tissue incautiously (deep injection). This is a significant source of data variability. To judge whether an injection was successful, we did the next experiments. PE-10 tubing was inserted

Table 1 Weights of tissue harvested from mice receiving intracisternal tracer injection (mg).

Mice	CTX	SCR	OB	CB	BS	USC	LSC
ICR	145.19 ± 2.22 (<i>n</i> = 30)	143.37 ± 3.30 (<i>n</i> = 30)	27.62 ± 0.72 (<i>n</i> = 30)	57.63 ± 1.02 (<i>n</i> = 30)	64.40 ± 1.34 (<i>n</i> = 42)	41.01 ± 1.87 (<i>n</i> = 30)	33.11 ± 1.48 (<i>n</i> = 30)
C57BL/6 (young)	147.44 ± 3.53 (<i>n</i> = 5)	146.96 ± 4.58 (<i>n</i> = 5)	23.36 ± 0.85 (<i>n</i> = 5)	50.50 ± 1.75 (<i>n</i> = 5)	65.36 ± 1.57 (<i>n</i> = 5)	41.20 ± 3.70 (<i>n</i> = 5)	33.64 ± 2.15 (<i>n</i> = 5)
C57BL/6 (old)	144.24 ± 4.75 (<i>n</i> = 5)	150.46 ± 4.36 (<i>n</i> = 5)	27.34 ± 0.52 (<i>n</i> = 5)	55.04 ± 5.15 (<i>n</i> = 5)	66.94 ± 2.25 (<i>n</i> = 5)	51.50 ± 4.75 (<i>n</i> = 5)	37.46 ± 2.47 (<i>n</i> = 5)

CTX, cerebral cortex; SCR, subcortical region; OB, olfactory bulb; CB, cerebellum; BS, brainstem; USC, upper spinal cord; LSC, lower spinal cord

into the brainstem, mimicking the situation of injecting too deep. In addition, a small volume of tracers (5 μ L, half of the normal volume) was injected intracisternally, mimicking the situation of leaky injection. Representative images showed that at 30 min following deep injection, large amounts of Dex-3 and OA-45 were found in the BS. In contrast, following leaky injection, the delivery of tracers into the BS and other regions was markedly reduced when compared with successful injection (Fig. 2B). Consistently, microplate assays revealed that, following injection, the concentration of tracer in the BS of mice receiving a deep injection dramatically increased to $318.4\% \pm 51.7\%$ (Dex-3) and $473.4\% \pm 70.8\%$ (OA-45) that of a successful injection (Fig. 2E). The tracer concentrations in the BS of mice receiving a leaky injection markedly decreased to $51.1\% \pm 7.0\%$ (Dex-3) and $49.0\% \pm 8.4\%$ (OA-45) that of a successful injection (Fig. 2F). Thus, we speculate that the tracer concentration in the BS can be used to judge whether an intracisternal injection is successful.

Next, we went further to explore the dynamic pattern of CSF tracer delivery into the CNS. At 10, 30, 60, and 120 min after injection into the cistern magna, tracer penetration into the CNS was evaluated *ex vivo* using the imaging approach and the microplate assay. Representative images

demonstrated that Dex-3 and OA-45 existed in the sagittal brain sections at all these time-points. In contrast, the un-injected control slices showed negligible fluorescence. The distribution of tracers in the sections varied largely with time (Fig. 3A). Evaluation of the delivery of tracers into the CNS at different time-points using the microplate assay revealed that the concentrations of both OA-45 and Dex-3 in the CTX and SCR reached a peak at 60 min, and declined at 120 min post-injection. The concentrations of both tracers in the OB reached a plateau at 30 min, and remained at the same level at 60 min, and then declined at 120 min post-injection. Interestingly, the concentrations of both tracers in the CB and BS peaked at 10 min and declined at later time points. This indicated that the transport of CSF tracers to the CB and BS is more rapid than other brain regions, mostly because these two regions are adjacent to the injection site. Moreover, both tracers in the LSC consistently remained very low at all time-points, mostly because the LSC is far from the injection site. In contrast, the concentrations of both tracers in the USC were much higher than those in the LSC at each time-point. They peaked at 60 min and then declined at 120 min post-injection (Fig. 3B, C).

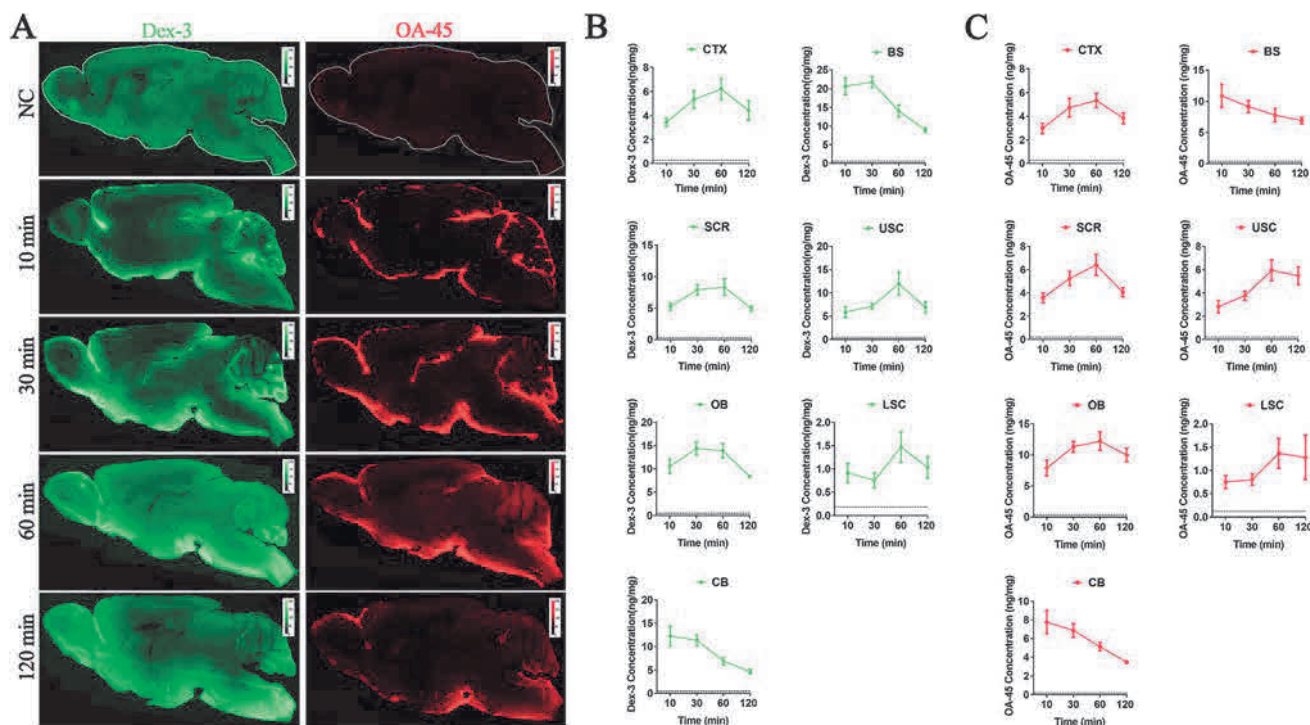
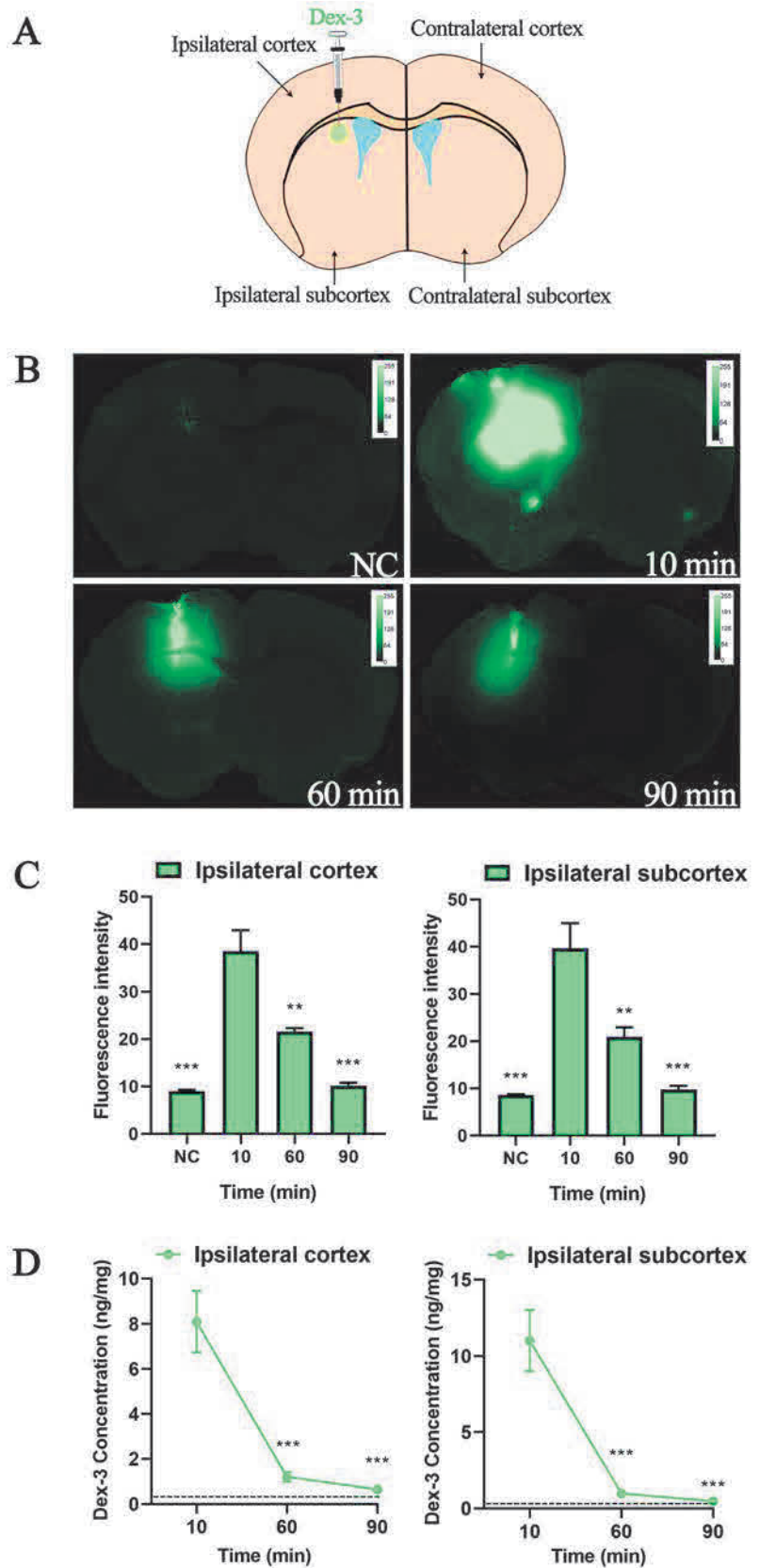


Fig. 3 Time-dependent inflow of CSF tracers into brain parenchyma. **A** Representative images showing that the distribution of fluorescent tracers in sagittal brain slices (at lateral 0.36 mm) varies with time (green, Dex-3; red, OA-45). Moreover, the un-injected control slices (NC) showed negligible fluorescence. **B**, **C** Time-dependent penetration of fluorescent tracers Dex-3 (**B**, $n = 6$) and OA-45 (**C**, $n = 6$)

quantified using microplate assays (dashed lines, virtual concentration of tracer (tissue autofluorescence) in defined brain regions from NC mice). CTX, cerebral cortex; SCR, subcortical region; OB, olfactory bulb; CB, cerebellum; BS, brainstem; USC, upper spinal cord; LSC, lower spinal cord.

Fig. 4 Clearance of fluorescent tracer from the brain detected by microplate assays. **A** Schematic of intrastriatal injection and regional sampling. **B** Representative images showing the distribution of Dex-3 (green) in brain over the first 90 min after tracer injection at bregma +1.10 mm. **C** Mean fluorescence intensity of tracer (mean pixel intensity) in specific brain regions quantified using ImageJ ($n = 3$; $**P < 0.01$, $***P < 0.001$ vs 10 min, ANOVA followed by Dunnett's *t*-test). **D** Concentration of tracer (ng/mg tissue) with time in specific brain regions using microplate assays (dashed lines, virtual tracer concentration (tissue autofluorescence) in defined brain regions from NC mice ($n = 6$; $***P < 0.001$ vs 10 min, ANOVA followed by Dunnett's *t*-test).



Clearance of Fluorescent Tracers from Brain Detected by Microplate Assay

We next explored whether the clearance of fluorescent tracers injected into the brain parenchyma can be detected by the microplate assay. The right caudate nucleus of anesthetized ICR mice was cannulated stereotaxically and then Dex-3 (1 μ L) was slowly injected. Notably, OA-45 was not used in this experiment due to its lower fluorescent sensitivity than Dex-3. At 10, 60, and 90 min following intrastriatal injection, the residual tracer in cortex and subcortex was estimated *ex vivo* by the imaging approach and the microplate assay (Fig. 4A). Representative images showed that robust Dex-3 intensity appeared in the ipsilateral cortex and subcortex, while the contralateral hemisphere was almost devoid of tracer following injection. Tracer accumulated in the injection site, radially spread to surrounding areas, and its signal declined sharply from 10 min to 90 min post-injection (Fig. 4B). Quantification showed that the pixel intensity in the ipsilateral cortex decreased to $65.6\% \pm 2.2\%$ (60 min) and $31.0\% \pm 1.7\%$ (90 min) of that at 10 min, and the tracer intensity in the ipsilateral subcortex decreased to $49.7\% \pm 4.7\%$ (60 min) and $23.1\% \pm 1.8\%$ (90 min) of that at 10 min (Fig. 4C).

Further, the ipsilateral cortex and subcortex were harvested and weighed (CTX: 64.09 ± 1.56 mg, $n = 15$; SCR: 73.29 ± 2.07 mg, $n = 15$), and tracers were detected by microplate assays. The results showed that the concentration of tracers in the ipsilateral cortex sharply decreased to $14.8\% \pm 2.8\%$ (60 min) and $8.0\% \pm 0.6\%$ (90 min) of that at 10 min, and those in the ipsilateral subcortex markedly declined to $8.9\% \pm 2.3\%$ (60 min) and $4.4\% \pm 0.4\%$ (90 min) of that at 10 min (Fig. 4D). The results were consistent with those with the imaging-quantification approach. Notably, the clearance measured by microplate assay was more rapid than that by the imaging approach, mostly because the overexposure of images reduced the difference in tracer intensity between the early and later time-points.

Reduced Glymphatic Inflow in the Aged Mouse Brain Confirmed by Microplate Assay

Evaluating CSF flow by *in vivo* two-photon optical imaging and *ex vivo* fluorescence imaging, Kress *et al.* reported that glymphatic activity is dramatically reduced in the aged mouse brain [13]. We next re-examined whether glymphatic influx was impaired in the aging brain using our microplate assay. In this experiment, young (3–5 months) and old (14–16 months) male C57Bl/6 mice were used. At 30 min after intracisternal injection, the transport of CSF tracer into the brain was estimated *ex vivo* by the

imaging approach and the microplate assay. Representative images showed that the signals of both Dex-3 and OA-45 in sagittal brain slices from old mice were weaker than those from young mice (Fig. 5A). Similarly, microplate assays demonstrated that the concentration of Dex-3 in the brain from old mice decreased to $49.3\% \pm 2.7\%$ (CTX) and $69.8\% \pm 4.9\%$ (SCR) that of young mice, and the concentration of OA-45 in the brain from old mice decreased to $59.0\% \pm 3.3\%$ (CTX) and $77.0\% \pm 5.4\%$ (SCR) that of young mice. In contrast, there was no significant difference between young and old mice in the other brain regions (Fig. 5B). These results are consistent with Kress's report using *in vivo* and *ex vivo* imaging [13].

Discussion

In the present study, two protocols were used to assess glymphatic activity (Fig. 6). At specific time-points following the injection of fluorescent tracers, their delivery into the brain parenchyma or removal from the brain was assessed *ex vivo* by the imaging approach and the microplate assay we developed here. The imaging approach refers to tracer distribution within brain sections imaged *ex vivo* under a fluorescence microscope and quantified using image-analysis software. This requires many manual operations such as myocardial perfusion with PBS and 4% PFA, overnight post-fixation, slicing on a vibratome, DAPI mounting, imaging under a microscope, acquiring images of whole-brain slices, and quantifying the mean pixel intensity or the coverage area of tracer using software. This approach has been widely used even though many steps are involved and much time is spent. In contrast, our microplate assay is time-saving and highly efficient in terms of the quantitation of glymphatic flow. After tracer injection, the subsequent steps only require sacrificing mice, dissecting brain regions, extracting tracers by homogenization and centrifugation, assessing the intensity of tracers using a microplate reader, and quantifying the concentrations of tracers from standard curves.

Here, five brain regions and the upper and lower spinal cord were separated. Among them, the weight of the OB was minimal (27.62 ± 0.72 mg for ICR mice), while the weight of the CTX was maximal (145.19 ± 2.22 mg for ICR mice) (Table 1). To minimize the influence of tissue weight on the results, these regions were precisely weighed on an electronic balance, and then homogenized with the corresponding volume of lysis buffer (200 mg/mL). Sometimes, small brain regions such as the hippocampus and hypothalamus, need to be separated for study [32]. For these smaller brain regions, we believe that our method is able to assess the concentrations of tracers within them if the proper volume of lysis buffer was used. For example, in

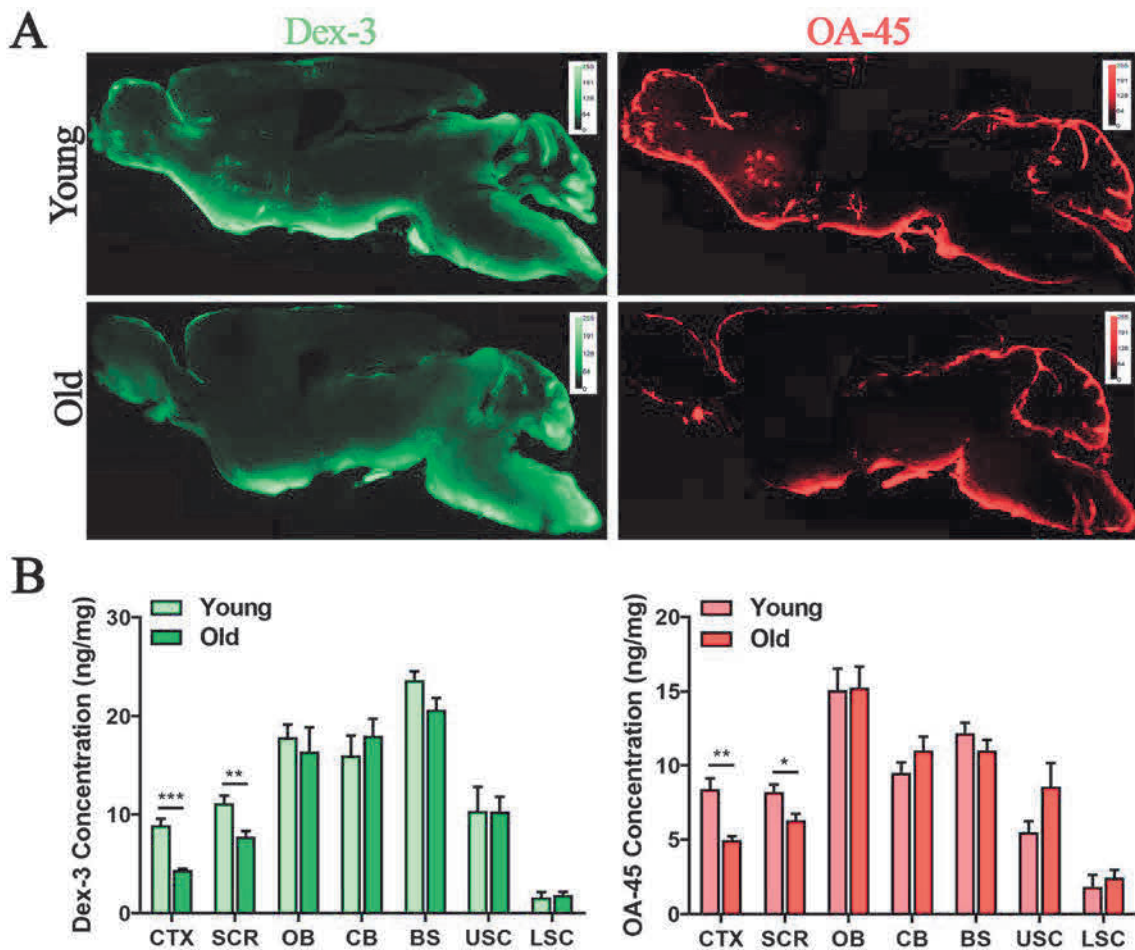


Fig. 5 The inflow of CSF tracers is markedly reduced in the brains of old mice. **A** Representative images showing the different tracer distribution in sagittal brain slices (at lateral 0.72 mm) in young and old mice (green, Dex-3; red, OA-45). **B** Concentrations of fluorescent tracers in defined brain regions using microplate arrays ($n = 6$; $*P <$

0.05, $**P < 0.01$, $***P < 0.001$ vs young mice, unpaired Student's *t*-test). CTX, cerebral cortex; SCR, subcortical region; OB, olfactory bulb; CB, cerebellum; BS, brainstem; USC, upper spinal cord; LSC, lower spinal cord.

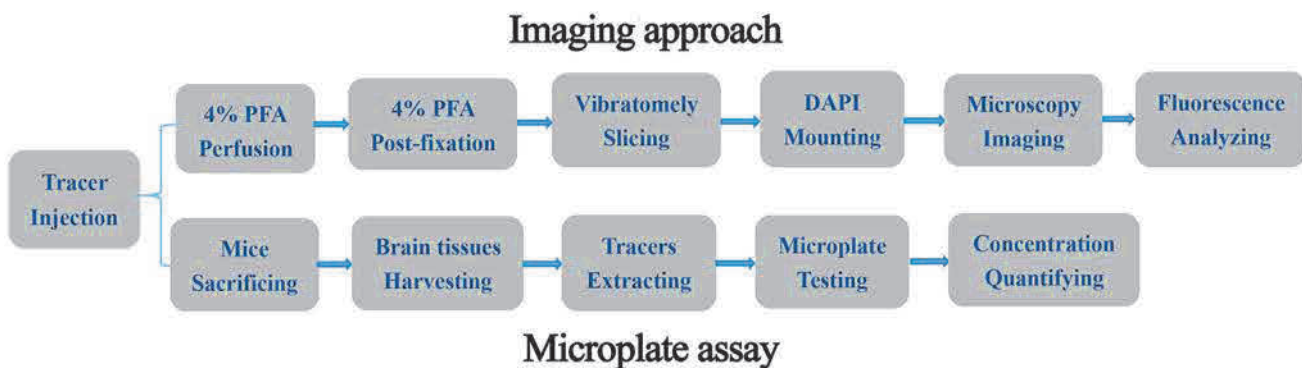


Fig. 6 Schematic of the imaging approach and microplate assay for the quantitation of glymphatic activity.

another project, the hippocampus of mice was separated at 30 min after intracisternal injection. After homogenization with a suitable volume of lysis buffer (100 mg/mL), the concentration of Dex-3 was successfully measured using

the microplate assay (~5 ng/mg). It is worth noting that more lysis buffer should be added when homogenizing smaller tissues in order to harvest sufficient supernatant.

Advantages of the Imaging Approach for Studies of the Glymphatic System

Apart from the outflow *via* arachnoid granulations and along cranial/spinal nerve sheaths, subarachnoid CSF can re-circulate into the brain along the peri-arterial space, exchange with brain ISF, and ultimately efflux *via* the perivenous space [2, 3]. The continuous and brain-wide CSF-ISF exchange is termed the glymphatic system, which is a novel concept in CSF studies and has received increasing attention recently [2, 9]. The role of the glymphatic system has been studied through injection with fluorescent, radiolabeled, and gadolinium-based tracers [2], among which fluorescent tracers are most extensively used to identify CSF flux and the glymphatic pathway in the rodent brain. Following intrathecal tracer injection, the dynamics of glymphatic flow has been imaged *in vivo* and *ex vivo*. *In vivo* imaging was initially conducted with two-photon optical imaging to demonstrate the detailed perivascular CSF-ISF exchange in rodents [1, 22, 23]. Transcranial macroscopic imaging is a less invasive approach due to imaging through the intact skull of mice, and such global observation has been used more recently [24]. Moreover, dynamic contrast-enhanced magnetic resonance imaging (MRI) and PET-CT scans, the least invasive approaches, have been used in both preclinical and clinical studies of glymphatic activity [25, 33–35].

Besides, *ex vivo* imaging has been widely used to study the glymphatic pathway. This is usually conducted on brain sections (20–100 μm thick) from mice or rats after tracer injection [13, 25]. The superiority of this approach is that it can provide detailed information on the brain-wide and regional distribution of CSF tracers in the glymphatic pathway. In combination with immunohistochemistry, the microscopic distribution of fluorescent tracers can be compared with the expression patterns of specific molecules, such as AQP4 expressed on astrocytic end-feet [1, 13], and demonstrate the uptake of CSF solutes by specific cells such as neurons and astrocytes [20, 21]. In addition, tracer penetration into the brain can be quantified through image-processing [1, 13, 19, 20]. Usually at low power, whole-brain slices or defined ROIs are chosen and the mean pixel intensity or the coverage area of fluorescent tracer is quantified. At least 3 slices per region per animal are quantified in the same manner and then averaged to produce a single value. By quantification of the mean pixel intensity or the coverage of tracers, previous studies have shown that glymphatic influx dramatically increases under anesthesia [12], low alcohol exposure [36], and voluntary running [37]. In contrast, glymphatic flux is seriously damaged in aging [13], Alzheimer's disease [14], traumatic

brain injury [4], deficiency of platelet-derived growth factor B [38], and under chronic stress [19, 39].

Comparison of Imaging Approach and Microplate Assay

Although the imaging-quantification approach has been widely used, it is worth noting that this method has some obvious limitations. First, the signal of fluorescent tracers under microscopy is highly dependent on the quality of tissue fixation, especially transcardial perfusion-fixation. Poor fixation leads to the loss of tracers from tissue and a weak fluorescence signal, which leads to a high degree of data inaccuracy. Second, imaging parameters are hard to set to avoid over- and under-exposure in all images. Third, sequential images must be quantified manually to reveal the distribution of tracers in the whole brain or specific brain regions. The ROIs outlined for tracer distribution and the minimum/maximum fluorescence intensity settings are subjective. Most seriously, the protocol is extremely time-consuming due to the many steps involved. What is more, the distribution of CSF tracers in histological sections following fixation does not always faithfully reflect their locations when the animals are alive. By using *in vivo* particle tracking in live mice, Mestre *et al.* showed that myocardial perfusion with 4% PFA causes retrograde CSF flow and collapses the perivascular space (PVS), significantly altering the distribution of tracers in the brain parenchyma [16]. Thus, it is desirable to establish a better method to quantify the glymphatic pathway in animal models.

In the present study, we described a simple protocol – the microplate assay – for the quantification of glymphatic flow following the injection of fluorescent tracers. The regional and time-dependent inflow of CSF tracer into the brain parenchyma following intracisternal injection was successfully detected by the microplate assay. Moreover, the clearance of CSF tracers from the brain following intrastriatal infusion was also successfully detected using this approach. The results were mostly in line with our observations using the imaging approach. Compared to the imaging-quantification approach, the main advantage of our protocol is time-saving due to elimination of the perfusion-fixation, overnight post-fixation, cutting, imaging, and the manual quantification of images. Moreover, the tissue-content of tracers is measured accurately by spectrophotofluorometry, which is more efficient and objective than manual quantification of images. In our view, the microplate assay is advantageous in quantitative determination, while the imaging approach excels in demonstrating detailed anatomical structure [40]. Thus,

following fluorescent tracer injection, the imaging approach is recommended to qualitatively visualize the detailed pathways of glymphatic flow, and the microplate assay is recommended to quantitatively assess changes in glymphatic activity for the whole brain or specific regions. Combination of the two approaches will enhance the study of glymphatic CSF inflow, ICF flow, and solute removal from the brain.

By using the approach described here, we found that following intracisternal injection, the concentrations of both OA-45 and Dex-3 in the CTX and OB reached a peak at 60 min, consistent with findings using *in vivo* transcranial macroscopic imaging [38]. Moreover, using dynamic contrast-enhanced MRI, Gaberel *et al.* revealed that DOTA-Gadolinium progressively enters the brain, and the contrast material reaches all the brain regions of Swiss mice at 60 min after intracisternal injection [15]. Similarly, Mestre *et al.* found that the signal of the contrast agent gadoteridol on coronal sections increased from 30 min to 60 min after intracisternal injection, whether in the whole brain or specific regions such as the cortex, subcortical regions, hippocampus, and third ventricle [41]. These findings with the imaging approach are in line with our data from the microplate assay.

Comparison of Radio-labeled Approach and Microplate Assay

Besides the imaging approaches discussed above, glymphatic flow has also been quantified using the radio-labeled approach. Radio-labeled tracers (e.g., ^3H -mannitol, ^3H -dextran-10, ^{125}I -A β 40, and ^{14}C -inulin) are intracisternally injected at very low concentrations. After a certain number of minutes, the mouse brain is quickly harvested and analyzed for radioactivity to quantify glymphatic influx [1, 14]. Moreover, the radioactive tracers are stereotaxically micro-injected into the frontal cortex or caudate nucleus of mice. Thirty minutes to 2 h after injection, tracer clearance is assessed by gamma counting or liquid scintillation counting to quantify solute clearance from the brain [1, 10, 13, 14]. Although it has greater resolution, the radio-labeled approach has the vital limitation of radioactive pollution. Since fluorescent tracers can be measured by microplate readers and are easily degraded, they seem to be an ideal replacement for radio-labeled tracers to study glymphatic flow. Our study showed that the concentration of fluorescent tracers even at rather low levels in the CNS after intracisternal or intrastriatal injection can be successfully determined by microplate assays. Compared to the radio-labeling approach, the method described here is minimally-polluting, relatively cheap, and accessible. Of note, the protocol we developed

is not applicable to clinical use because it is invasive and the fluorescent tracers are harmful.

Re-examination of Glymphatic Influx in the Aging Mouse Brain Using the Microplate Assay

Using *in vivo* and *ex vivo* fluorescence microscopy, Kress *et al.* found that aging leads to a significant reduction in glymphatic influx in mice [13]. Further, quantification of OA-45 penetration demonstrated that the age-related reduction of glymphatic activity is mainly restricted to the cortex [13]. In the present study, we confirmed the damaged glymphatic influx into the cortex of old mice using our microplate assay. Representative images showed that the difference in CSF tracers in cortex between young and old mice was not significant (Fig. 5), mostly because only the dorsal cortex was contained in the sagittal slices (at lateral 0.72 mm). Consistent with this, through quantification of tracer fluorescence in coronal brain slices, Kress *et al.* also found that the decline of glymphatic influx caused by aging was significant in the lateral and ventral cortex, but not in the dorsal cortex [13].

To evaluate the interstitial solute clearance from the brain, Kress *et al.* further stereotaxically injected radiotracers such as ^{125}I -A β 40 and ^{14}C -inulin into the mouse striatum [13]. After 60 min, the drainage of radiotracers was analyzed for radioactivity, showing that the clearance of ^{14}C -inulin and ^{125}I -A β 40 was markedly reduced in both the middle-aged and old mouse brains [13]. This approach has also been used by other groups to assess solute clearance from the brain [10, 14]. In the present study, the concentration of residual fluorescent tracer at 60 and 90 min following intrastriatal injection was also detected by our microplate assay. However, injection into cortex or striatum is invasive. Mestre *et al.* recently reported that the injection approach markedly suppresses CSF influx [41]. To avoid the acute damage caused by insertion, it is necessary to stereotaxically implant a cannula into the brain 18–24 h before tracer injection [42]. Even so, it is worth noting that glymphatic activity may be damaged by the chronic traumatic injury [4]. Thus, we did not use intraparenchymal tracer injection to investigate the glymphatic disorder in the old mouse brain in the present study.

Conclusion

To the best of our knowledge, we are the first to evaluate glymphatic inflow and the clearance of fluorescent tracers using spectrophotofluorometry. The content of fluorescent tracers in the CNS following intrathecal or intraparenchymal injection can be accurately measured using our microplate assay. Furthermore, the impairment of

glymphatic influx in aged mice was confirmed using our approach. In terms of quantitation, our protocol has advantages over the imaging approach due to the short time required and better accuracy. Compared to the radio-labeling approach, the main advantage of the protocol described here is minimal pollution and easy accessibility. The approach developed here is convenient and efficient for the quantitation of glymphatic activity.

Acknowledgements This work was supported by grants from the National Natural Science Foundation of China (31871167 and 81920108016), China Postdoctoral Science Foundation (2016M601882), Suzhou Science and Technology Research Project (SYS201669 and SYS201709), Postdoctoral Science Foundation of Jiangsu Province, China (1601083C), and Priority Academic Program Development of Jiangsu Higher Education Institutions.

References

- Iliff JJ, Wang M, Liao Y, Plogg BA, Peng W, Gundersen GA, *et al.* A paravascular pathway facilitates CSF flow through the brain parenchyma and the clearance of interstitial solutes, including amyloid beta. *Sci Transl Med* 2012, 4: 147ra111.
- Rasmussen MK, Mestre H, Nedergaard M. The glymphatic pathway in neurological disorders. *Lancet Neurol* 2018, 17: 1016–1024.
- Jessen NA, Munk AS, Lundgaard I, Nedergaard M. The glymphatic system: a beginner's guide. *Neurochem Res* 2015, 40: 2583–2599.
- Iliff JJ, Chen MJ, Plog BA, Zeppenfeld DM, Soltero M, Yang L, *et al.* Impairment of glymphatic pathway function promotes tau pathology after traumatic brain injury. *J Neurosci* 2014, 34: 16180–16193.
- Lundgaard I, Lu ML, Yang E, Peng W, Mestre H, Hitomi E, *et al.* Glymphatic clearance controls state-dependent changes in brain lactate concentration. *J Cereb Blood Flow Metab* 2017, 37: 2112–2124.
- Acharyar TM, Li B, Peng W, Verghese PB, Shi Y, McConnell E, *et al.* Glymphatic distribution of CSF-derived apoE into brain is isoform specific and suppressed during sleep deprivation. *Mol Neurodegener* 2016, 11: 74.
- Lundgaard I, Li B, Xie L, Kang H, Sanggaard S, Haswell JD, *et al.* Direct neuronal glucose uptake heralds activity-dependent increases in cerebral metabolism. *Nat Commun* 2015, 6: 6807.
- Rangroo Thrane V, Thrane AS, Plog BA, Thiyagarajan M, Iliff JJ, Deane R, *et al.* Paravascular microcirculation facilitates rapid lipid transport and astrocyte signaling in the brain. *Sci Rep* 2013, 3: 2582.
- Benveniste H, Lee H, Volkow ND. The glymphatic pathway: waste removal from the CNS via cerebrospinal fluid transport. *Neuroscientist* 2017, 23: 454–465.
- Xie L, Kang H, Xu Q, Chen MJ, Liao Y, Thiyagarajan M, *et al.* Sleep drives metabolite clearance from the adult brain. *Science* 2013, 342: 373–377.
- Lee H, Xie L, Yu M, Kang H, Feng T, Deane R, *et al.* The effect of body posture on brain glymphatic transport. *J Neurosci* 2015, 35: 11034–11044.
- Hablitz LM, Vinitzky HS, Sun Q, Staeger FF, Sigurdsson B, Mortensen KN, *et al.* Increased glymphatic influx is correlated with high EEG delta power and low heart rate in mice under anesthesia. *Sci Adv* 2019, 5: eaav5447.
- Kress BT, Iliff JJ, Xia MS, Wang MH, Wei HLS, Zeppenfeld D, *et al.* Impairment of paravascular clearance pathways in the aging brain. *Ann Neurol* 2014, 76: 845–861.
- Peng WG, Acharyar TM, Li BM, Liao YH, Mestre H, Hitomi E, *et al.* Suppression of glymphatic fluid transport in a mouse model of Alzheimer's disease. *Neurobiol Disease* 2016, 93: 215–225.
- Gabriel T, Gakuba C, Goulay R, Martinez De Lizarondo S, Hanouz JL, Emery E, *et al.* Impaired glymphatic perfusion after strokes revealed by contrast-enhanced MRI: a new target for fibrinolysis? *Stroke* 2014, 45: 3092–3096.
- Mestre H, Tithof J, Du T, Song W, Peng W, Sweeney AM, *et al.* Flow of cerebrospinal fluid is driven by arterial pulsations and is reduced in hypertension. *Nat Commun* 2018, 9: 4878.
- Nygaard Mortensen K, Sanggaard S, Mestre H, Lee H, Kostrikov S, Xavier ALR, *et al.* Impaired glymphatic transport in spontaneously hypertensive rats. *J Neurosci* 2019, 39: 6365–6377.
- Yang L, Kress BT, Weber HJ, Thiyagarajan M, Wang B, Deane R, *et al.* Evaluating glymphatic pathway function utilizing clinically relevant intrathecal infusion of CSF tracer. *J Transl Med* 2013, 11: 107.
- Wei F, Song J, Zhang C, Lin J, Xue R, Shan LD, *et al.* Chronic stress impairs the aquaporin-4-mediated glymphatic transport through glucocorticoid signaling. *Psychopharmacology (Berl)* 2019.
- Wei F, Zhang C, Xue R, Shan L, Gong S, Wang G, *et al.* The pathway of subarachnoid CSF moving into the spinal parenchyma and the role of astrocytic aquaporin-4 in this process. *Life Sci* 2017, 182: 29–40.
- Zhang C, Lin J, Wei F, Song J, Chen W, Shan L, *et al.* Characterizing the glymphatic influx by utilizing intracisternal infusion of fluorescently conjugated cadaverine. *Life Sci* 2018, 201: 150–160.
- Smith AJ, Yao X, Dix JA, Jin BJ, Verkman AS. Test of the 'glymphatic' hypothesis demonstrates diffusive and aquaporin-4-independent solute transport in rodent brain parenchyma. *Elife* 2017, 6.
- Schain AJ, Melo-Carrillo A, Strassman AM, Burstein R. Cortical spreading depression closes paravascular space and impairs glymphatic flow: implications for migraine headache. *J Neurosci* 2017, 37: 2904–2915.
- Plog BA, Mestre H, Olveda GE, Sweeney AM, Kenney HM, Cove A, *et al.* Transcranial optical imaging reveals a pathway for optimizing the delivery of immunotherapeutics to the brain. *JCI Insight* 2018, 3.
- Pizzo ME, Wolak DJ, Kumar NN, Brunette E, Brunnquell CL, Hannocks MJ, *et al.* Intrathecal antibody distribution in the rat brain: surface diffusion, perivascular transport and osmotic enhancement of delivery. *J Physiol* 2018, 596: 445–475.
- Saria A, Lundberg JM. Evans blue fluorescence: quantitative and morphological evaluation of vascular permeability in animal tissues. *J Neurosci Methods* 1983, 8: 41–49.
- Wolf MS, Chen Y, Simon DW, Alexander H, Ross M, Gibson GA, *et al.* Quantitative and qualitative assessment of glymphatic flux using Evans blue albumin. *J Neurosci Methods* 2019, 311: 436–441.
- Dorshow RB, Hall-Moore C, Shaikh N, Talcott MR, Faubion WA, Rogers TE, *et al.* Measurement of gut permeability using fluorescent tracer agent technology. *Sci Rep* 2017, 7: 10888.
- Wei F, Song J, Zhang C, Lin J, Xue R, Shan LD, *et al.* Chronic stress impairs the aquaporin-4-mediated glymphatic transport through glucocorticoid signaling. *Psychopharmacology (Berl)* 2019, 236: 1367–1384.
- Gao Y, Wang Z, Zhu Y, Zhu Q, Yang Y, Jin Y, *et al.* NOP2/Sun RNA methyltransferase 2 promotes tumor progression via its

- interacting partner RPL6 in gallbladder carcinoma. *Cancer Sci* 2019, 110: 3510–3519.
31. Dos Santos TG, Pereira MSL, Oliveira DL. Rat cerebrospinal fluid treatment method through cisterna cerebellomedullaris injection. *Neurosci Bull* 2018, 34: 827–832.
 32. Liu T, Li Z, He J, Yang N, Han D, Li Y, *et al.* Regional metabolic patterns of abnormal postoperative behavioral performance in aged mice assessed by (1)H-NMR dynamic mapping method. *Neurosci Bull* 2020, 36: 25–38.
 33. Iliff JJ, Lee H, Yu M, Feng T, Logan J, Nedergaard M, *et al.* Brain-wide pathway for waste clearance captured by contrast-enhanced MRI. *J Clin Invest* 2013, 123: 1299–1309.
 34. Ringstad G, Vatnehol SAS, Eide PK. Glymphatic MRI in idiopathic normal pressure hydrocephalus. *Brain* 2017, 140: 2691–2705.
 35. de Leon MJ, Li Y, Okamura N, Tsui WH, Saint-Louis LA, Glodzik L, *et al.* Cerebrospinal fluid clearance in Alzheimer disease measured with dynamic PET. *J Nucl Med* 2017, 58: 1471–1476.
 36. Lundgaard I, Wang W, Eberhardt A, Vinitzky HS, Reeves BC, Peng S, *et al.* Beneficial effects of low alcohol exposure, but adverse effects of high alcohol intake on glymphatic function. *Sci Rep* 2018, 8: 2246.
 37. von Holstein-Rathlou S, Petersen NC, Nedergaard M. Voluntary running enhances glymphatic influx in awake behaving, young mice. *Neurosci Lett* 2018, 662: 253–258.
 38. Munk AS, Wang W, Bechet NB, Eltanahy AM, Cheng AX, Sigurdsson B, *et al.* PDGF-B is required for development of the glymphatic system. *Cell Rep* 2019, 26: 2955–2969 e2953.
 39. Xia M, Yang L, Sun G, Qi S, Li B. Mechanism of depression as a risk factor in the development of Alzheimer's disease: the function of AQP4 and the glymphatic system. *Psychopharmacology (Berl)* 2017, 234: 365–379.
 40. Dai JK, Wang SX, Shan D, Niu HC, Lei H. Super-resolution track-density imaging reveals fine anatomical features in tree shrew primary visual cortex and hippocampus. *Neurosci Bull* 2018, 34: 438–448.
 41. Mestre H, Hablitz LM, Xavier AL, Feng W, Zou W, Pu T, *et al.* Aquaporin-4-dependent glymphatic solute transport in the rodent brain. *Elife* 2018, 7.
 42. Deane R, Wu Z, Sagare A, Davis J, Du Yan S, Hamm K, *et al.* LRP/amyloid beta-peptide interaction mediates differential brain efflux of Abeta isoforms. *Neuron* 2004, 43: 333–344.



Synaptic Adaptation Contributes to Stimulus-Specific Adaptation in the Thalamic Reticular Nucleus

Yu-Ying Zhai^{1,2} · Ryszard Auksztulewicz^{3,4} · Pei-Run Song^{1,2} · Zhi-Hai Sun⁵ ·
Yu-Mei Gong^{1,2} · Xin-Yu Du¹ · Jie He¹ · Xiongjie Yu^{1,2}

Received: 28 January 2020 / Accepted: 10 March 2020 / Published online: 18 June 2020
© Shanghai Institutes for Biological Sciences, CAS 2020

Dear Editor,

Stimulus-specific adaptation (SSA) is the process whereby a neuron responds more strongly to rare stimuli than to the same stimuli presented in a repetitive way. This phenomenon has been regarded as one of the mechanisms that give rise to novelty- or change-detection. SSA has been extensively investigated along the auditory pathway from the cochlear nucleus to the auditory cortex (AC) [1, 2] and in other sensory systems [3]. While the exact neuronal mechanisms underlying SSA are still poorly understood and may involve a range of effects including synaptic plasticity and intrinsic membrane dynamics (for a review, see [2]), the functional characteristics of SSA have been well described by computational models. One such model, the ‘adaptation in narrowly-tuned modules’ (ANTM)

model [4], is currently the most widely accepted model of auditory SSA in the frequency domain. Although it was first introduced to explain SSA in the AC, the principles of the model may also apply to other brain areas. This is indeed an important challenge, since SSA is a ubiquitous phenomenon in the brain, and computational models of SSA should capture the general mechanisms mediating SSA independent of brain region, stimulus type, or modality [4].

One of the paradoxical findings explained by the ANTM model is that SSA occurs in widely-tuned neurons in the AC, even though the physical differences between rare deviants and repetitive standards may be very narrow. The ANTM model postulates that SSA in widely-tuned neurons reflects adaptation specific to inputs from neurons narrowly tuned to the repetitive frequency [4], allowing adaptation to be frequency-specific. However, evidence for such frequency specificity from regions other than the AC is so far limited to subcortical regions such as the thalamus and inferior colliculus, with a large proportion of narrowly-tuned neurons [5]. It is therefore an open question whether areas with different tuning properties show frequency-specific adaptation. Here, we focus on the thalamic reticular nucleus (TRN), an area receiving multiple corticothalamic and thalamocortical collaterals and mostly populated by widely-tuned neurons [6].

Furthermore, as most of the previous SSA research mainly focused on comparing responses to the same stimuli between the rare presentation and the repetitive presentation, but not on the temporal evolution of SSA [1, 2, 7, 8], little direct analysis has been made to probe the frequency specificity of SSA during the entire adaptation process. In this report, we first demonstrate frequency-specific adaptation in widely-tuned neurons in the TRN in two regimes: during acoustic stimulation, and during direct electrical

Electronic supplementary material The online version of this article (<https://doi.org/10.1007/s12264-020-00536-0>) contains supplementary material, which is available to authorized users.

✉ Xiongjie Yu
yuxiongj@zju.edu.cn

¹ Department of Neurology, Second Affiliated Hospital of Zhejiang University School of Medicine, Interdisciplinary Institute of Neuroscience and Technology, College of Biomedical Engineering and Instrument Science, Zhejiang University, Hangzhou 310029, China

² Laboratory for Biomedical Engineering of the Ministry of Education, Zhejiang University, Hangzhou 310027, China

³ Department of Biomedical Sciences, City University of Hong Kong, Hong Kong SAR, China

⁴ Department of Neuroscience, Max Planck Institute for Empirical Aesthetics, 60322 Frankfurt am Main, Germany

⁵ School of Information and Engineering, Hangzhou Dianzi University, Hangzhou 310018, China

stimulation in monosynaptic inputs from the AC to the TRN. In both cases, we then characterize the dynamics of TRN adaptation and release over time. Finally, we interpret these findings in terms of synaptic adaptation in narrowly-tuned inputs from the AC to the TRN.

We used an oddball paradigm (a detailed description of the materials and methods is provided in Supplemental Materials) with a combination of two tones (Fig. 1A). Instead of a traditional analysis focusing on a comparison between deviant and standard responses, we analyzed neuronal firing during the switching period between the last standard stimulus and the deviant stimulus, to characterize the temporal evolution of SSA.

Single TRN neurons ($n = 44$) (an example location is shown in the left panel of Figure 1B) were isolated *in vivo* in 10 rats. The neurons were first tested by screening their responses to different tones (right panel in Fig. 1B). Two tones were then chosen to generate the oddball stimulus sequence. In this particular example, we presented a 2,150 Hz pure tone 6 times, followed by a deviant 3,096 Hz tone with an interstimulus interval (ISI) of 200 ms (Fig. 1C). There was a 2.8-s period of silence after each deviant tone for the recovery of the neuron before another stimulation block started. The 2,150 Hz pure tone elicited a response on first presentation; however, after 4–6 trials, the neuron adapted completely to the tone and stopped responding.

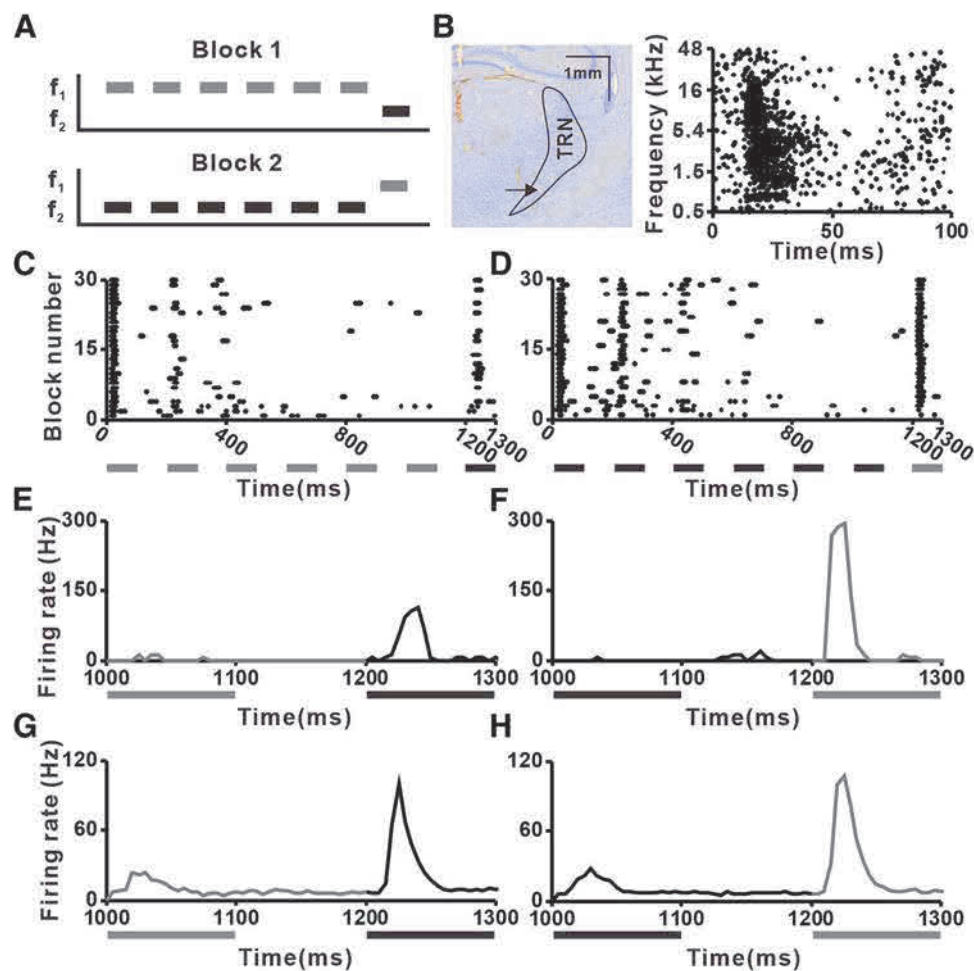


Fig. 1 Adaptation in the TRN is frequency-specific. **A** The oddball paradigm. Two tones with at least 0.53 octave separation were selected for subsequent oddball stimulation across two blocks. In one block, one tone (standard stimulus) was presented 6 times and followed by a single deviant tone (deviant stimulus), each separated by 200 ms; in the other block, the formed deviant became the new standard and *vice versa*. The two blocks were randomly presented at an inter-block interval of 4 s. **B** Left: Track of recording electrode, as shown by Nissl stain (arrow indicates the recording site; scale bar, 1 mm). Right: Raster plots of a representative example neuron as a

function of tone frequency. Pure tones (0.5–48 kHz) were randomly presented at 70 dB SPL. **C, D** Raster displays showing example single-trial responses during the entire block; acoustic stimulation is indicated by the filled bars below (black: 3,096 Hz tone; grey: 2,150 Hz tone). **E, F** Peristimulus time histograms (PSTHs) of the example neuron during the switching period from the last standard stimulation to the first deviant stimulation; stimuli indicated by the bars as in **C, D**. **G, H** Population PSTHs ($n = 44$) during the switching period. Bars indicate the two tones (grey: f1; black: f2; f1 < f2).

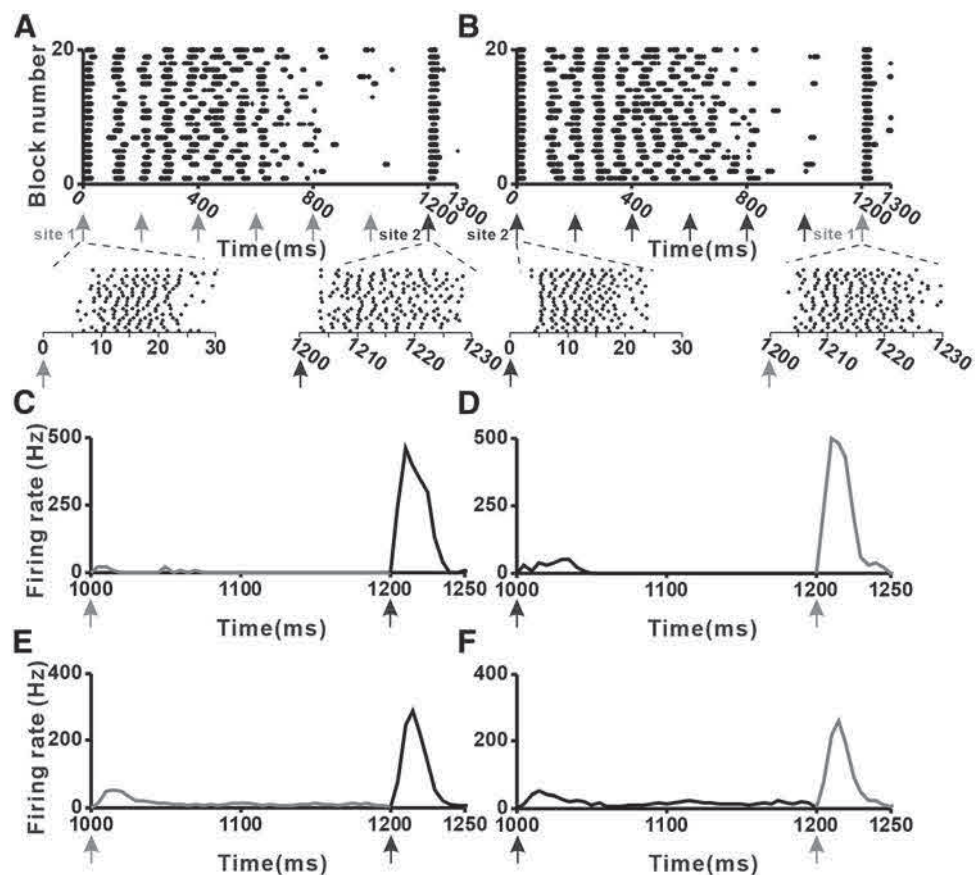
The subsequent introduction of the 3,096 Hz tone evoked a strong response (Fig. 1C), suggesting that complete adaptation to the 2,150 Hz (“standard”) tone did not apply to the 3,096 Hz (“deviant”) tone. Next, the standard and deviant stimuli were swapped (Fig. 1D). Again, the TRN neuron adapted completely to the 3,096 Hz tone by the 6th trial, but showed a robust response to the deviant 2,150 Hz tone, showing frequency-specific adaptation. The temporal dynamic of the neuron’s responsiveness during the switching period was evident in the peristimulus time histograms (PSTHs) (Fig. 1E–F). In both cases, we could easily detect the transformation of neuronal firing from silent to highly responsive when the stimulation changed from standard to deviant (Fig. 1E–F).

The population data showed similar results (Fig. 1G, H). During the first transition from standard to deviant, the mean firing rate increased from 10.8 Hz for the last standard presentation to 23.7 Hz for the deviant presentation (Fig. 1G, $P < 0.001$, paired t -test). During the reverse transition, the mean firing rate increased again from 11.8 Hz to 27.3 Hz (Fig. 1H, $P < 0.001$, paired t -test). Thus, even though the TRN neurons adapted to one specific tone, they demonstrated strong responses to novel tones at different frequencies (Fig. 1G, H), suggesting frequency-specific adaptation.

Having demonstrated the frequency-specific adaptation underlying SSA in TRN neurons, we explored the possible neuronal mechanisms underlying this phenomenon. The major inputs to the TRN are from the thalamus and cortex [9], with cortical inputs much stronger than thalamic inputs [10]. Since cortical inputs to the TRN follow the tonotopic organization in the AC [7, 10], we asked whether frequency-specific adaptation in the TRN could arise from the frequency-specificity of adaptation in tonotopic regions of the AC. Given the broad and unidirectional inputs from the AC to each individual TRN neuron [6, 11], we used direct electrical activation in the AC to test the hypothesis that frequency-specific adaptation in the TRN results from adaptation in its AC inputs. Instead of pure tones (Fig. 1A), the oddball stimulation formed a sequence of electrical stimulation at two sites in the AC with tentative monosynaptic projections to the TRN (see below).

Biphasic (0.5/0.5 ms) current at 50 μ A was applied at site 1 in the AC 6 times (Fig. 2A, grey arrows), followed by the deviant electrical stimulation at site 2 (black arrow), with an ISI of 200 ms. The stimulation at site 1 elicited a strong response in the example TRN neuron on the first trial. The short response latency (6.5 ms) suggested that the projection was monosynaptic, which is also consistent with previous results *in vitro* [10]. By trial 5, the neuron adapted

Fig. 2 TRN adaptation specificity to tonotopic inputs from the AC. **A, B** Raster displays showing responses during the entire block of an electrical oddball paradigm, based on electrical stimulation at two sites in the AC. Stimulation (0.5/0.5 ms biphasic) is indicated by the arrows (grey: site 1; black: site 2). Insets: short-latency responses relative to stimulation onset (30 ms) for the first trial and the deviant trial in each block. **C, D** PSTHs of a representative neuron during the switching period from the last standard to the deviant stimulation (grey arrow: site 1; black: site 2). **E, F** Population PSTHs ($n = 12$) during the switching period. Arrows below the PSTHs indicate electrical stimulation at two sites (grey: site 1; black: site 2; site numbers arbitrarily assigned).



completely to stimulation at site 1, suggesting that synaptic adaptation took place at the corticoreticular synapses. When the stimulation was switched to AC site 2, the TRN neuron recovered and responded, again with a short latency (4.9 ms), indicating a monosynaptic projection. The difference in TRN response latencies suggested that the two AC sites recruited different synapses. Next, the standard and deviant stimulation sites were swapped (Fig. 2B). The TRN neuron stopped responding to the stimulation at site 2 by the 6th trial, but showed a robust response to the deviant stimulation at site 1 (latency: 5.6 ms). The PSTHs (Fig. 2C, D) and population data (Fig. 2E, F) showed effects similar to those following auditory stimulation: in both cases, neuronal firing increased during both switching periods from standard to deviant stimulation (Fig. 2C, D), suggesting that frequency-specific adaptation in the TRN can be induced not only by acoustic stimulation, but also by electrical stimulation of different regions in the tonotopically-organized AC. Since we used the same settings for both electrical and sound oddball stimulation, the synaptic adaptation during the electrical stimulation may also occur in the sound stimulation. These results taken together suggest that synaptic adaptation in the tonotopically-organized AC (Fig. 2) is a plausible mechanism underlying frequency-specific adaptation in the TRN (Fig. 1).

We provide the first *in vivo* experimental evidence from TRN neurons that although some of their synaptic inputs adapt to the stimulation, other synaptic inputs can continue to evoke strong responses (Fig. 2). Synaptic adaptation may therefore contribute to adaptation specificity with respect to the frequency of acoustic stimulation (Fig. 1) and tonotopically-organized inputs (Fig. 2). Both of these effects are consistent with the hypothesis that SSA in broadly-tuned neurons is mediated by adaptation in their narrowly-tuned inputs [4]. Since SSA has been reported in a wide range of brain regions [1–3, 7, 8], and synaptic adaptation occurs throughout the brain and *in vitro* [12], we hypothesize that synaptic mechanisms also mediate SSA in other brain regions – possibly alongside other factors, such as circuit-level mechanisms [13] or network-wide inferential processes [14, 15]. Taken together, our findings provide direct evidence for the view that SSA in a single neuron may result from integration over distributed synaptic inputs.

Acknowledgements This work was supported by the National Natural Science Foundation of China (31671081 and 31872768).

Conflict of interest The authors declare no competing financial interests.

References

- Parras GG, Nieto-Diego J, Carbajal GV, Valdes-Baizabal C, Escera C, Malmierca MS. Neurons along the auditory pathway exhibit a hierarchical organization of prediction error. *Nat Commun* 2017, 8: 2148.
- Malmierca MS, Sanchez-Vives MV, Escera C, Bendixen A. Neuronal adaptation, novelty detection and regularity encoding in audition. *Front Syst Neurosci* 2014, 8: 111.
- Vinken K, Vogels R, Op de Beeck H. Recent visual experience shapes visual processing in rats through stimulus-specific adaptation and response enhancement. *Curr Biol* 2017, 27: 914–919.
- Mill R, Coath M, Wennekers T, Denham SL. A neurocomputational model of stimulus-specific adaptation to oddball and markov sequences. *PLoS Comput Biol* 2011, 7.
- Shen L, Zhao L, Hong B. Frequency-specific adaptation and its underlying circuit model in the auditory midbrain. *Front Neural Circuits* 2015, 9: 55.
- Pinault D. The thalamic reticular nucleus: structure, function and concept. *Brain Res Rev* 2004, 46: 1–31.
- Zhai YY, Sun ZH, Gong YM, Tang Y, Yu X. Integrative stimulus-specific adaptation of the natural sounds in the auditory cortex of the awake rat. *Brain Struct Funct* 2019, 224: 1753–1766.
- Rui YY, He J, Zhai YY, Sun ZH, Yu X. Frequency-dependent stimulus-specific adaptation and regularity sensitivity in the rat auditory thalamus. *Neuroscience* 2018, 392: 13–24.
- Jones EG. *The Thalamus*. 2nd ed. Cambridge; New York: Cambridge University Press, 2007.
- Golshani P, Liu XB, Jones EG. Differences in quantal amplitude reflect GluR4- subunit number at corticothalamic synapses on two populations of thalamic neurons. *Proc Natl Acad Sci U S A* 2001, 98: 4172–4177.
- Yu XJ, Meng XK, Xu XX, He J. Individual auditory thalamic reticular neurons have large and cross-modal sources of cortical and thalamic inputs. *Neuroscience* 2011, 193: 122–131.
- Wang H, Han YF, Chan YS, He J. Stimulus-specific adaptation at the synapse level *in vitro*. *PLoS One* 2014, 9: e114537.
- Natan RG, Briguglio JJ, Mwilambwe-Tshilobo L, Jones SI, Aizenberg M, Goldberg EM, *et al.* Complementary control of sensory adaptation by two types of cortical interneurons. *Elife* 2015, 4.
- Nieto-Diego J, Malmierca MS. Topographic distribution of stimulus-specific adaptation across auditory cortical fields in the anesthetized rat. *PLoS Biol* 2016, 14: e1002397.
- Chen Z, Parkkonen L, Wei J, Dong JR, Ma Y, Carlson S. Prepulse inhibition of auditory cortical responses in the caudolateral superior temporal gyrus in *Macaca mulatta*. *Neurosci Bull* 2018, 34: 291–302.



Iron Aggravates the Depressive Phenotype of Stressed Mice by Compromising the Glymphatic System

Shanshan Liang¹ · Yan Lu² · Zexiong Li¹ · Shuai Li¹ · Beina Chen¹ ·
Manman Zhang¹ · Binjie Chen¹ · Ming Ji¹ · Wenliang Gong¹ · Maosheng Xia³ ·
Alexei Verkhratsky^{1,4,5} · Xu Wu⁶ · Baoman Li¹

Received: 27 February 2020 / Accepted: 2 April 2020 / Published online: 24 June 2020
© Shanghai Institutes for Biological Sciences, CAS 2020

Dear Editor,

The pathophysiological mechanisms underlying mood disorders including major depressive disorder (MDD) remain to be fully characterized. Iron is a key component in the development of the central nervous system and iron deficiency has been linked to impairments of mood and cognition [1]. Recent studies have reported an inverse association between iron uptake and the risk of depression, as MDD patients have a reduced serum concentration of iron [2]. Moreover, few investigations have monitored the symptoms of MDD patients with iron supplementation. Evidence for effects of increased iron on cognitive disorders is scarce, although treatment of small group of psychiatric patients with an iron chelator apparently led to clinical improvement [3].

The function of the brain is to a large extent defined by blood circulation and the movements of cerebrospinal and

interstitial fluids (CSF and ISF). The glymphatic system is responsible for the brain-wide clearance of waste protein through a paravascular pathway and CSF–ISF exchange [4]. Operation of the glymphatic system is supported by perivascular astroglial endfeet [5]. Our previous studies demonstrated that chronic unpredictable mild stress (CUMS), a well-established model for inducing depressive-like phenotypes in rodents, partially inhibits the glymphatic system, impairing the clearance of endogenous and exogenous amyloid beta-42 from the cortex and hippocampus [6]. Exposure to CUMS does not affect motor functions, learning, or memory in mice [6]. However, it remains unknown whether iron overload impairs the operation of the glymphatic system.

It is well known that iron is a microelement essential for body growth and development and is also required for cellular metabolism. Iron can cross the blood-brain barrier (BBB) and binds to the transferrin receptors (TFRs) of endothelial cells through transferrin [7]. Iron is released into the brain parenchyma from vascular endothelial cells and is taken up by astrocytes and neurons [8]. Facing

Shanshan Liang and Yan Lu have contributed equally to this work.

Electronic supplementary material The online version of this article (<https://doi.org/10.1007/s12264-020-00539-x>) contains supplementary material, which is available to authorized users.

✉ Alexei Verkhratsky
Alexej.Verkhtratsky@manchester.ac.uk

✉ Xu Wu
xwu@cmu.edu.cn

✉ Baoman Li
bmli@cmu.edu.cn

¹ Practical Teaching Center, School of Forensic Medicine, China Medical University, Shenyang 110122, China

² Key Laboratory of the Ministry of Health in Congenital Malformation, The Affiliated Shengjing Hospital of China Medical University, Shenyang 110004, China

³ Department of Orthopedics, The First Hospital, China Medical University, Shenyang 110001, China

⁴ Faculty of Biology, Medicine and Health, The University of Manchester, Manchester, UK

⁵ Achucarro Center for Neuroscience, IKERBASQUE, 48011 Bilbao, Spain

⁶ Department of Forensic Pathology, School of Forensic Medicine, China Medical University, Shenyang 110122, China

excessive iron concentrations, neurons up-regulate the expression of TFRs and ferroportin, the latter exporting iron back to the extracellular space [9]. However, if the iron accumulation exceeds the neuronal metabolic capacity for protein storage, neurotoxicity and death are induced [8]. Little is known about the expression of both proteins in MDD patients or in mouse models of depression, hence we investigated how iron affects depressive phenotypes and the operation of the glymphatic system in the CUMS mouse model.

First, we found that iron overload aggravated the circulatory disturbance of the glymphatic system induced by CUMS. Experimental animals were divided into four groups (i) controls; (ii) iron-overloaded (Iron); (iii) exposed to CUMS (CUMS); and (iv) exposed to CUMS and iron overload (CUMS + Iron). An excessive iron load was induced by intraperitoneal injection of iron dextran for 6 days (see supplementary methods). The accumulation of iron in the brain tissue was measured by Perl's staining. As shown in Fig. S1A–E, compared to the control group, the staining ratios of Perl's-positive iron deposits in the Iron group were increased to $545.43\% \pm 54.00\%$ ($P < 0.001$, $n = 6$) in the cortex and $462.56\% \pm 68.27\%$ ($P < 0.001$, $n = 6$) in the hippocampus; in the CUMS + Iron group, the staining ratios were increased to $1310.54\% \pm 108.93\%$ ($P < 0.001$, $n = 6$) in cortex and $980.21\% \pm 161.97\%$ ($P < 0.001$, $n = 6$) in the hippocampus. We found no iron deposits in mice exposed to CUMS alone.

The activity of the glymphatic system was assessed by measuring the penetration of the red fluorescent tracer, OA555 (Fig. 1A). Compared with anterior slices from the control group, the penetration of OA555 was decreased to $71.33\% \pm 6.17\%$ ($P = 0.001$, $n = 6$) in the Iron group, to $67.83\% \pm 4.79\%$ ($P < 0.001$, $n = 6$) in the CUMS group, and to $47.33\% \pm 3.69\%$ ($P < 0.001$, $n = 6$) in the CUMS + Iron group (Fig. 1B). Compared with posterior slices from the control group, the penetration of OA555 was decreased to $71.12\% \pm 3.80\%$ ($P < 0.001$, $n = 6$) in the Iron group, to $72.89\% \pm 4.31\%$ ($P < 0.001$, $n = 6$) in the CUMS group, and to $52.70\% \pm 3.49\%$ ($P < 0.001$, $n = 6$) in the CUMS + Iron group (Fig. 1B). Furthermore, the penetration of tracer in the CUMS + Iron group was significantly different from both the Iron and CUMS groups (Fig. 1B).

Cortical astrocytic morphology was visualized by immunostaining with antibodies against glial fibrillary acidic protein (GFAP) (Fig. 1C). Compared with controls, iron increased the fluorescence intensity of GFAP to $156.29\% \pm 12.58\%$ ($P = 0.007$, $n = 6$), CUMS enhanced it to $143.33\% \pm 10.78\%$ ($P = 0.031$, $n = 6$), and in the CUMS + Iron group it was elevated to $198.03\% \pm 18.23\%$ ($P < 0.001$, $n = 6$) (Fig. 1D). The fluorescence intensity of GFAP in the CUMS + iron group was significantly

different from both the Iron and the CUMS groups (Fig. 1D).

Subsequently, we found that CUMS increased the expression of TFRs induced by iron overload (Fig. 2). We assessed the expression of TFRs in the cortex and hippocampus by immunocytochemistry (Fig. 2). In the cortex, compared to controls, the fluorescence intensity of TFR in the Iron group was increased to $159.93\% \pm 16.41\%$ ($P = 0.009$, $n = 6$), and in the CUMS + Iron group it was enhanced to $216.03\% \pm 15.89\%$ ($P < 0.001$, $n = 6$; Fig. 2C). Similar changes were found in the hippocampus: in the Iron group the TFR intensity was increased to $256.36\% \pm 14.81\%$ ($P < 0.001$, $n = 6$), while in the CUMS + Iron group it was increased to $365.09\% \pm 30.76\%$ ($P < 0.001$, $n = 6$; Fig. 2C). There was also a significant difference in TFR levels between the Iron and CUMS + Iron groups, both in cortex and hippocampus. However, exposure to CUMS alone did not change the intensity of TFR staining (Fig. 2C).

Meanwhile, CUMS increased the neuronal apoptosis induced by iron overload. The neuronal apoptosis in cortex and hippocampus was visualized with TUNEL assays (Fig. S2A, C). Compared with the control group, in the Iron group the neuronal apoptosis was increased to $169.25\% \pm 23.58\%$ ($P = 0.013$, $n = 6$) in cortex and to $173.82\% \pm 12.14\%$ ($P = 0.003$, $n = 6$) in the hippocampus, and in the CUMS + Iron group it increased to $222.66\% \pm 21.12\%$ ($P < 0.001$, $n = 6$) in cortex and to $232.08\% \pm 24.57\%$ ($P < 0.001$, $n = 6$) in the hippocampus (Fig. S2B, D). There was a significant difference in the apoptosis ratio between the Iron and CUMS + Iron groups (Fig. S2B, D). However, exposure to CUMS alone did not affect the apoptosis (Fig. S2B, D).

To further investigate the effects of iron overload on the behavioral phenotype of mice subjected to chronic stress, we ran depressive, locomotor, and cognitive behavioral tests. In the sucrose preference test, iron overload reduced the ratio of sucrose intake to $91.73\% \pm 3.01\%$ of control ($P = 0.154$, $n = 6$), but the difference was not significant (Fig. S3A). In the CUMS group, the preference was decreased to $72.80\% \pm 4.52\%$ ($P < 0.001$, $n = 6$), and in the CUMS + Iron group, it was reduced to $56.72\% \pm 2.57\%$ ($P < 0.001$, $n = 6$) (Fig. S3A). Sucrose preference was significantly different ($P = 0.009$; $n = 6$) between the CUMS and CUMS + Iron groups. In the tail-suspension test (TST) and forced-swimming test (FST), the behavioral manifestations demonstrated similar changes. Compared with the control group, iron overload insignificantly increased the immobility time to $154.07\% \pm 28.23\%$ ($P = 0.251$, $n = 6$) in the TST (Fig. S3B) and to $116.79\% \pm 12.13\%$ ($P = 0.354$, $n = 6$) in the FST (Fig. S3C). In the CUMS group the immobility time increased to $212.26\% \pm 22.76\%$ ($P = 0.023$, $n = 6$) in the TST (Fig. S3B) and to

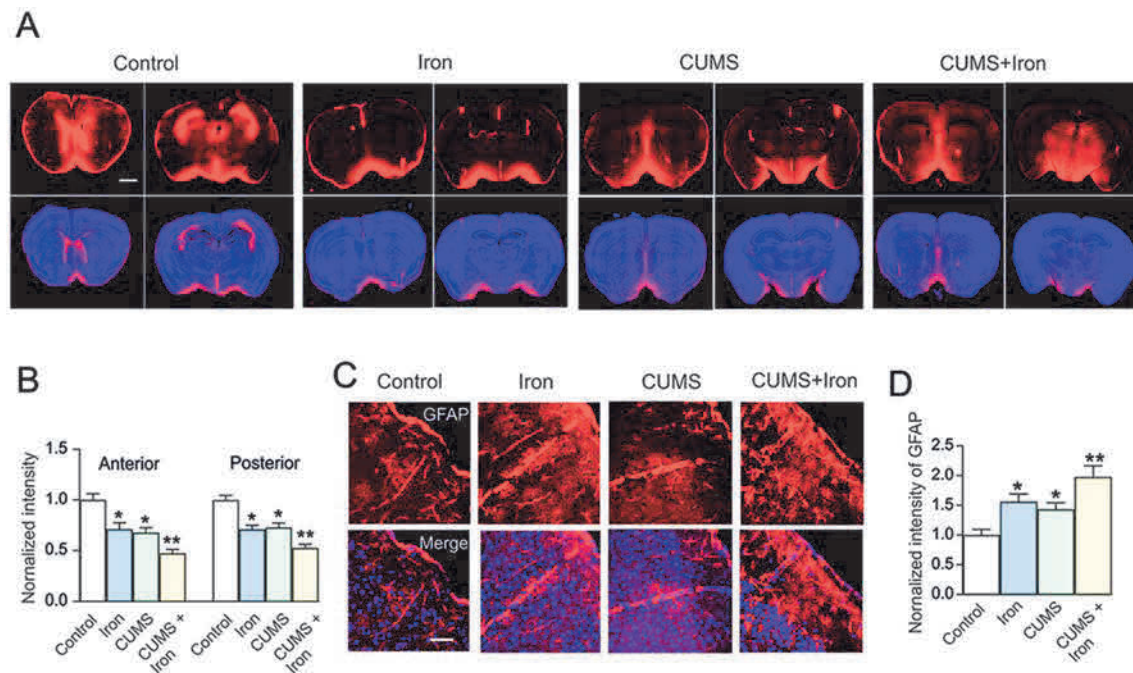


Fig. 1 Excess iron aggravates malfunction of the glymphatic system in mice exposed to CUMS. **A, B** Mice with or without exposure to CUMS for 6 weeks, in the last week were randomly selected to be injected with dextran or iron dextran for 6 days, then a fluorescent tracer (OA555, 45 kDa) was injected intracisternally. **A** Representative images showing penetration of the fluorescence tracer into the brain; OA555 (red) and DAPI (blue) are imaged simultaneously in anterior and posterior slices (scale bar, 1 mm). **B** Thirty minutes after

injection, the animals were perfusion-fixed and the whole-slice fluorescence was calculated. The fluorescence intensities of OA555 normalized to the intensity of the control group, were assessed in anterior and posterior slices. **C** Immunocytochemistry of GFAP (red) and staining with DAPI (blue) in cortex (scale bar, 50 μ m). **D** GFAP immunolabeling intensity normalized to the intensity in the control group. Data are presented as the mean \pm SEM, $n = 6$. * $P < 0.05$ versus controls; ** $P < 0.05$ vs any other group.

144.61% \pm 6.28% ($P = 0.020$, $n = 6$) in the FST (Fig. S3C). In the CUMS + Iron group the immobility time was further increased to 331.31% \pm 59.32% ($P < 0.001$, $n = 6$) in the TST (Fig. S3B) and to 184.60% \pm 8.25% ($P < 0.001$, $n = 6$) in the FST (Fig. S3C). Again, the difference in immobility time in both the TST and FST between the CUMS and CUMS + Iron groups was significant ($P = 0.024$, $n = 6$ and $P = 0.035$, $n = 6$, respectively).

In the pole test, exposure to CUMS did not change the movement time from the pole top to the floor (T-LA time) compared to the control group (Fig. S3D). In the Iron group however, the T-LA time was significantly increased to 142.87% \pm 9.37% of the control ($P = 0.025$, $n = 6$), and in the CUMS + Iron group, was further increased to 224.51% \pm 30.81% ($P < 0.001$, $n = 6$; Fig. S3D).

In the Morris water maze test, the time spent in the target quadrant and the escape latency were measured. Compared with the control group, exposure to CUMS did not affect these times. In the Iron group, the time spent in the target quadrant was decreased to 78.18% \pm 7.08% of control ($P = 0.031$, $n = 6$; Fig. S3E) and the escape latency was increased to 128.69% \pm 10.20% of control ($P = 0.033$, $n = 6$; Fig. S3F). In the CUMS + Iron group the time spent in the target quadrant was decreased to 56.11% \pm 4.63%

($P < 0.001$, $n = 6$; Fig. S3E) while the escape latency was increased to 170.62% \pm 10.55% ($P < 0.001$, $n = 6$; Fig. S3F). The times in the CUMS + Iron group were also significantly different from those in the Iron group ($P = 0.039$, $n = 6$ and $P = 0.004$, $n = 6$; Fig. S3E, F).

According to the above results, the excessive accumulation of iron in the brains of mice inhibits the functional activity of the glymphatic system. In this respect, the action of iron was similar to CUMS, which also triggers malfunction of the glymphatic system [11]. When CUMS was paired with iron overload, glymphatic function was suppressed even further, which arguably compromised the clearance of iron from the brain parenchyma. In response to iron overload, the expression of TFRs in neurons was up-regulated, and CUMS additionally enhanced TFR expression. At the same time, iron overload increased neuronal apoptosis, and this was increased even further by exposure to CUMS. At the behavioral level, iron overload exacerbated the depressive-like phenotype of stressed mice, and added motor and cognitive impairments that do not occur in mice exposed to CUMS alone.

Operation of the glymphatic system is supported by astrocytes, the principal homeostatic cells of the central nervous system [5, 10]. In particular, polarized expression

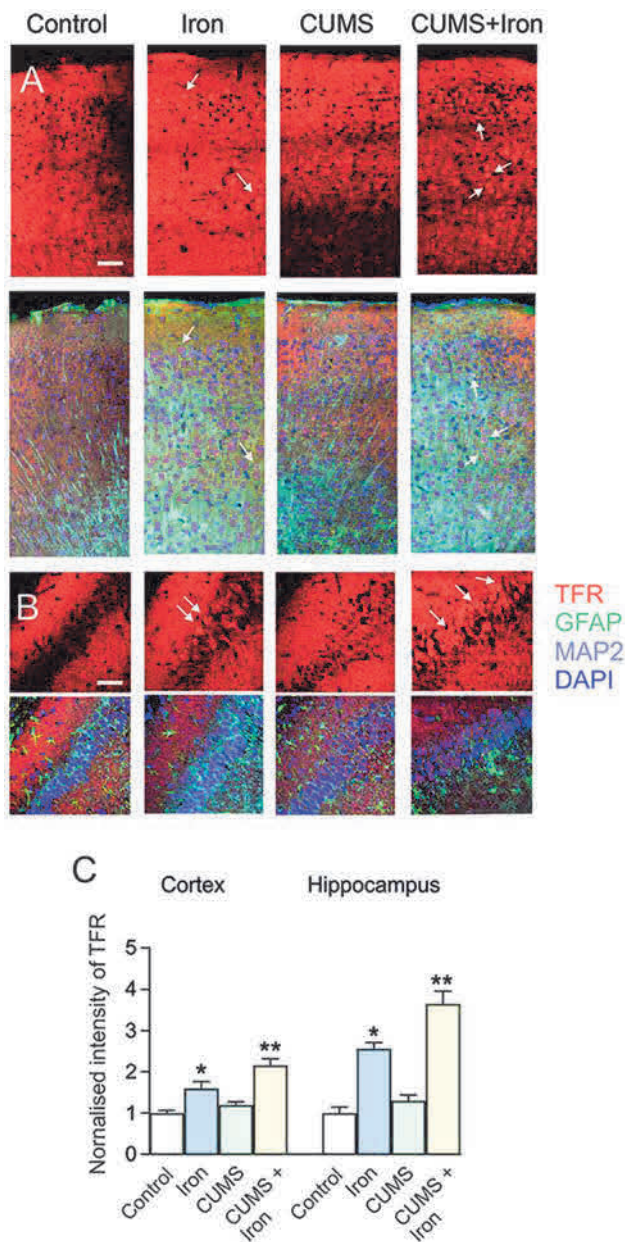


Fig. 2 Exposure to CUMS promotes neuronal expression of TFR stimulated by iron overload. **A, B** Representative images of immunohistochemistry of TFR (red) stained with MAP2 (cyan), GFAP (green), and DAPI (blue) in cortex (**A**) and hippocampus (**B**) (mice with or without exposure to CUMS for 6 weeks, in the last week were randomly selected to be injected with dextran or iron dextran for 6 days). **C** TFR immunolabeling intensity normalized to the intensity in the control group in cortex and hippocampus (scale bar, 50 μ m). Data are presented as the mean \pm SEM, $n = 6$. * $P < 0.05$ vs control; ** $P < 0.05$ vs any other group.

of the water channel aquaporin 4 (AQP4) in astroglial perivascular endfeet is required for the normal function of the glymphatic system [5, 6, 10]. We found that accumulation of iron in the brain parenchyma triggered reactive astrogliosis in the cortex and hippocampus, as indicated by

an increase in GFAP expression. Again, pairing iron overload with CUMS further increased GFAP expression, suggesting stronger reactivity of astrocytes.

Excess iron uptake can induce cellular death and this phenomenon is always considered to be a risk for neurodegenerative diseases, such as Alzheimer's disease or Parkinson's disease [11]. The accumulation of iron is reported to be associated with up-regulation of ferritin expression in the substantia nigra of aged animals [12]. The level of iron transport proteins holds promise as markers of MDD, especially in patients with suicidal tendencies [13]. In this study, we found that the pairing of iron with CUMS was accompanied by an elevation of TFR expression in neurons, as well as by increased neuronal apoptosis arguably induced by iron ion ($\text{Fe}^{2+}/\text{Fe}^{3+}$) dyshomeostasis. In consequence, Fe^{3+} transport into neurons could be increased through up-regulated TFRs. However, exposure to CUMS alone did not affect the neuronal levels of TFRs, neither did it influence neuronal apoptosis. At the same time, iron accumulation paired with chronic stress promoted new pathological phenotypes manifested by motor and cognitive impairments that did not occur in mice exposed to CUMS alone. In addition, the depressive-like behaviors and/or anhedonia induced by CUMS were significantly exacerbated by iron overload. In the clinical setting, not all MDD patients have cognitive or motor deficits [14], although depressive disorders are risk factors for the occurrence of neurodegenerative diseases [15]. Under exposure to CUMS, the circulatory functions of the AQP4-dependent glymphatic system are impaired and this is paralleled with anhedonia and depressive behaviours [6]. In addition, mice exposed to CUMS show decreased efficiency of exchange between the subarachnoid CSF and brain parenchyma, and the circulation of a paravascular fluorescent tracer is suppressed in anhedonic mice [6].

Our results demonstrate that excess iron aggravates malfunction of the glymphatic system, thus exacerbating the depressive and cognitive behavioral phenotypes induced by chronic stress. Increased iron intake could add to the pathophysiological evolution of MDD and hence we suggest that excess iron intake has to be considered as an additional risk factor for cognitive impairment in patients with depression. Meanwhile, iron chelation may be a potential therapeutic strategy for MDD patients with high serum iron.

Acknowledgements This work was supported by the National Natural Science Foundation of China (81871852, 81200935, 81671867 and 81971794), the Liaoning Revitalization Talents Program (XLYC1807137), the Scientific Research Foundation for Returned Scholars of the Ministry of Education of China (20151098), and the Natural Science Foundation of Liaoning Province, China (20170541030).

Conflict of interest The authors have no conflicts of interest to disclose.

References

1. Lomagno KA, Hu F, Riddell LJ, Booth AO, Szymlek-Gay EA, Nowson CA, *et al.* Increasing iron and zinc in pre-menopausal women and its effects on mood and cognition: a systematic review. *Nutrients* 2014, 6: 5117–5141.
2. Islam MR, Islam MR, Shalahuddin Qusar MMA, Islam MS, Kabir MH, Mustafizur Rahman GKM, *et al.* Alterations of serum macro-minerals and trace elements are associated with major depressive disorder: a case–control study. *BMC Psychiatry* 2018, 18: 94.
3. Cutler P. Iron overload and psychiatric illness. *Can J Psychiatry* 1994, 39: 8–11.
4. Iliff JJ, Nedergaard M. Is there a cerebral lymphatic system? *Stroke* 2013, 44: S93–S95.
5. Kress BT, Iliff JJ, Xia M, Wang M, Wei HS, Zeppenfeld D, *et al.* Impairment of paravascular clearance pathways in the aging brain. *Ann Neurol* 2014, 76: 845–861.
6. Xia M, Yang L, Sun G, Qi S, Li B. Mechanism of depression as a risk factor in the development of Alzheimer’s disease: the function of AQP4 and the glymphatic system. *Psychopharmacology (Berl)* 2017, 234: 365–379.
7. Jefferies WA, Brandon MR, Hunt SV, Williams AF, Gatter KC, Mason DY. Transferrin receptor on endothelium of brain capillaries. *Nature* 1984, 312: 162–163.
8. Leitner DF, Connor JR. Functional roles of transferrin in the brain. *Biochim Biophys Acta* 2012, 1820: 393–402.
9. Boserup MW, Lichota J, Haile D, Moos T. Heterogenous distribution of ferroportin-containing neurons in mouse brain. *Biometals* 2011, 24: 357–375.
10. Nedergaard M. Garbage truck of the brain Science. *Neuroscience* 2013, 340: 1529–1530.
11. Song N, Xie J. Iron, dopamine, and α -synuclein interactions in at-risk dopaminergic neurons in Parkinson’s disease. *Neurosci Bull* 2018, 34: 382–384.
12. Walker T, Michaelides C, Ekonomou A, Geraki K, Parkes HG, Suessmilch M, *et al.* Dissociation between iron accumulation and ferritin upregulation in the aged substantia nigra: attenuation by dietary restriction. *Aging (Albany NY)* 2016, 8: 2488–2508.
13. Dean B, Tsatsanis A, Lam LQ, Scarr E, Duce JA. Changes in cortical protein markers of iron transport with gender, major depressive disorder and suicide. *World J Biol Psychiatry* 2020, 21: 119–126.
14. Knight MJ, Lyrtzis E, Baune BT. The association of cognitive deficits with mental and physical quality of life in major depressive disorder. *Compr Psychiatry* 2019, 97: 152147.
15. Miebach L, Wolfgruber S, Frommann I, Fließbach K, Jessen F, Buckley R, *et al.* Cognitive complaints in memory clinic patients and in depressive patients: an interpretative phenomenological analysis. *Gerontologist* 2019, 59: 290–302.



Eye-Opening Alters the Interaction Between the Salience Network and the Default-Mode Network

Junrong Han¹ · Xuehai Wu² · Hang Wu¹ · Dong Wang¹ · Xuan She¹ · Musi Xie¹ · Fang Zhang³ · Delong Zhang¹ · Xilin Zhang¹ · Pengmin Qin^{1,4,5}

Received: 27 February 2020 / Accepted: 9 May 2020 / Published online: 17 July 2020
© Shanghai Institutes for Biological Sciences, CAS 2020

Dear Editor,

Brain networks consist of several long-distance regions that interact constantly with each other. Interactions between networks suggest that different brain functions are coordinated during complex cognitive tasks [1]. A triple-network mechanism underlying cognitive control has been found across task paradigms and stimulus modalities [2]. This triple-network mechanism includes the interactions among the salience network (SN), the default mode network (DMN), and the central executive network (CEN). The core regions of the SN include the anterior insula (AI), anterior cingulate cortex, and thalamus [3]; those of the DMN are the medial prefrontal cortex, posterior cingulate cortex, and lateral parietal cortex [3]; and for the CEN, the

dorsolateral prefrontal cortex, inferior parietal cortex, and precuneus are the key nodes [3]. Available evidence has shown increased activation in the CEN and SN, and decreased activation in the DMN during cognitive tasks [1, 2]. Furthermore, Sridharan *et al.* demonstrated that the SN initiates control signals to activate the CEN and deactivate the DMN during the resting state, providing a view of the network mechanism underlying endogenous cognitive control [1].

The network mechanism may vary under different conditions. For example, it can be influenced by important baseline conditions, such as the eyes-open (EO) and eyes-closed (EC) conditions. Riedl *et al.* and Xu *et al.* found that the SN exhibits increased glucose metabolism and altered functional connectivity of the blood oxygenation level-dependent (BOLD) signal with other areas during EO compared to EC [4, 5]. Moreover, the functional connectivity of the BOLD signal between the DMN and parts of both the SN and the CEN increases during EO [6]. However, how the triple-network mechanism is impacted by EO and EC has not been thoroughly investigated. The importance of the EO and EC conditions can be ascribed to their deep involvement in psychological experiments and psychiatric disorder studies [7]. They are commonly used as baseline conditions requiring participants to perform any cognitive task, but their spontaneous BOLD signals show distinct activity patterns. Therefore, in order to get a deeper understanding of the network mechanism underlying endogenous cognitive control, and help establish proper baseline conditions for future neuroscience experiments, it is necessary to clarify the influence of EC/EO on the three networks and their interactions.

Unlike electrophysiological methods, resting-state functional magnetic resonance imaging (fMRI) has the capacity to measure the neuronal activity in networks of interest in

Electronic supplementary material The online version of this article (<https://doi.org/10.1007/s12264-020-00546-y>) contains supplementary material, which is available to authorized users.

✉ Xilin Zhang
xlzhang@m.scnu.edu.cn

✉ Pengmin Qin
qin.pengmin@gmail.com

¹ Centre for Studies of Psychological Applications, Guangdong Key Laboratory of Mental Health and Cognitive Science, School of Psychology, South China Normal University, Guangzhou 510631, China

² Neurosurgical Department, Shanghai Huashan Hospital, Fudan University, Shanghai 200040, China

³ Department of Rehabilitation Medicine, The Third Affiliated Hospital, Sun Yat-sen University, Guangzhou 510630, China

⁴ Ministry of Education, Key Laboratory of Brain, Cognition and Education Sciences (South China Normal University), Guangzhou 510631, China

⁵ Pazhou Lab, Guangzhou 510335, China

deep brain regions with high spatial resolution. Moreover, resting-state fMRI can capture stable coupling between networks with a sufficiently long segment of data. Therefore, based on resting-state fMRI data, we were able to detect reliable network-wise changes in correlation between EC and EO using functional connectivity (FC) analysis.

Besides FC analysis, dynamic causal modeling (DCM), a nonlinear system identification procedure, is a useful tool for inferring how the coupling among areas is influenced by experimental inputs [8], such as EC and EO. DCM is able to infer hidden neuronal activity from the recorded BOLD signal with posterior estimates of neurobiological features, such as the connection strength of synapses among neuronal populations and modulation by experimental inputs [8]. Thus, DCM basically estimates the parameters of effective connectivity at the neuronal level, which may reduce the influence of the slow temporal resolution of fMRI signals, and was used to investigate the modulation of the network mechanism by EC and EO in our experiments.

The objectives of this study were to: (1) determine the differences in the correlations among the three networks (SN, DMN, and CEN) between EC and EO; and (2) investigate how the causality between these three networks is influenced by EC and EO. In the first experiment, 22 healthy participants (12 males; average age, 20.31 years) were recruited, and their resting-state fMRI data were obtained under EO and EC conditions (resting-state dataset 1). Adopting the regions of interest (ROIs) from a previous study, the ROI-based FCs were calculated (Fig. 1A) [3]. We compared the differences of FC among the three networks between EC and EO in this dataset, and examined the change in the FC pattern in an open resting-state dataset (resting-state dataset 2, http://fcon_1000.projects.nitrc.org/indi/retro/BeijingEOEC.html) (details in supplementary material). Paired *t*-testing of resting-state dataset 1 showed decreased FC between the SN and the DMN during EO compared to EC ($P < 0.005$ Bonferroni-corrected), while that of resting-state dataset 2 suggested reduced FC in two pairs of networks: SN–DMN ($P < 0.005$, Bonferroni-corrected) and DMN–CEN ($P < 0.001$, Bonferroni-corrected) (Fig. 1B). There was no significant difference in FC between the SN and the CEN during EO and EC in the two datasets (Fig. 1B). These results were replicated with network components extracted by spatially-constrained independent component analysis (Fig. S3).

To further explore the causality changes among the three networks from EC to EO, 32 healthy participants (24 males; average age, 28.09 years) were enrolled. Each participant attended one fMRI run, which included 17 EC conditions (duration, 16 s) and 16 EO conditions (duration, 12 s). In order to find out which network was the input

network modulated by the driving inputs (EC and EO) for the subsequent DCM analysis, we first estimated the coefficients (beta values) of BOLD signals for the EC and EO conditions in each network using a general linear model, and compared the beta values of the networks between the two conditions using the paired *t*-test (details in supplementary material). The result showed significant BOLD signal changes in the SN between the two conditions ($P < 0.001$, Bonferroni-corrected), while no significant difference was found in the other two networks (Fig. 1C). These results suggested that the SN would be the input network in the subsequent DCM model.

The stochastic DCM was then used to estimate the modulation of network causality by EC and EO. The stochastic DCM, an extension of the DCM, includes the random fluctuations of BOLD signals in the state equation [9]. According to a previous study, the reproducibility of the stochastic DCM is excellent as it showed consistent results across three datasets (each with 60 participants) [10]. Based on the data from the first experiment, decreased SN–DMN FC was found in both resting-state datasets, while decreased DMN–CEN FC was seen only in resting-state dataset 2. We concluded that EO might modulate the bidirectional or unidirectional connection between the SN and the DMN, and could affect the bidirectional, unidirectional, or no extrinsic connection between the DMN and the CEN. As a result, 12 hypothesized network models were constructed for each participant (Fig. 2A).

Random-effects Bayesian model selection (BMS), which accounts for between-subjects heterogeneity, was used to select the optimal model across all candidates [11]. In order to show that the optimal model did not stem from the specific method of model selection, we followed the approach of a previous study by using another model-selection algorithm, the fixed-effects BMS, to enhance the reproducibility of the optimal model [12]. The fixed-effects BMS, assuming the model is homogeneous across subjects, can provide complementary information to the random-effects BMS [12] (details in supplementary material). The results of random-effects BMS demonstrated that Model 10 (M10) was optimal, with the highest model exceedance probability (0.5355) (Fig. 2B), which shows that the SN receives its driving inputs from EC and EO, and EO modulates the signals transmitted from the SN to the DMN. The same optimal model was selected using the fixed-effects BMS (Fig. S4), suggesting that the model we found is reliable.

In summary, we conducted two fMRI experiments, and investigated how the interactions among the three large-scale networks were modulated by the EO and EC conditions. The results from resting-state datasets showed lower FC between the SN and the DMN in EO than EC. Furthermore, the results from the block-design dataset

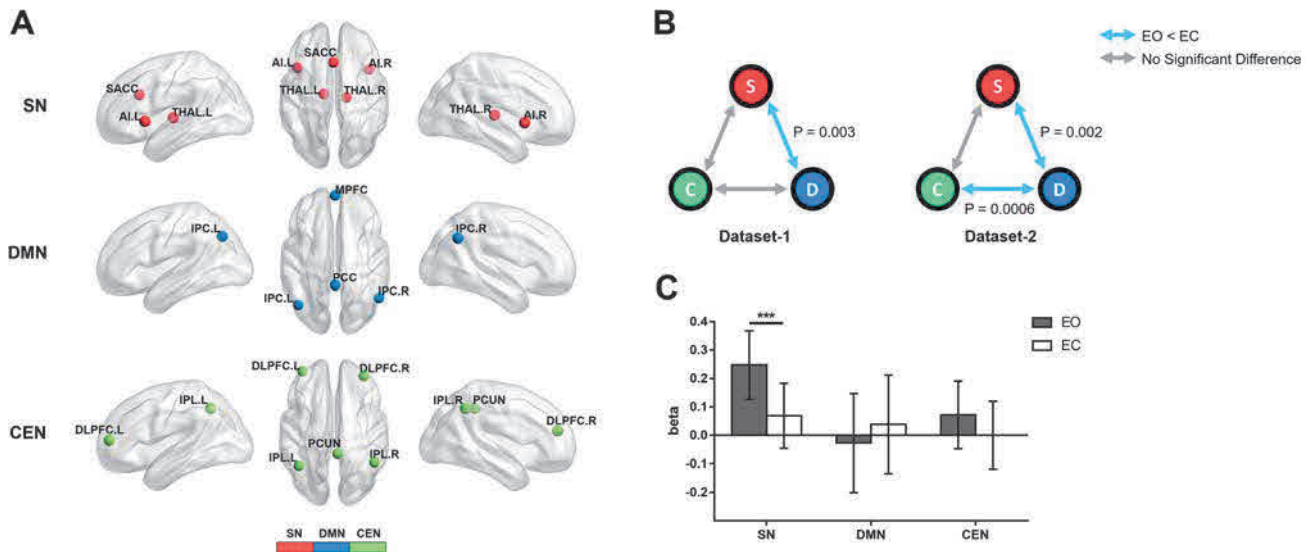


Fig. 1 Difference of functional connectivity (FC) and beta value in the three networks between eyes open (EO) and eyes closed (EC). **A** Plots of the three networks rendered on the cortical surface [red , regions specific to the salience network (SN); blue , regions specific to the default mode network (DMN); green, regions specific to the central executive network (CEN); anterior insula (AI), subgenual anterior cingulate cortex (SACC), thalamus (THAL), medial prefrontal cortex (MPFC), posterior cingulate cortex (PCC), lateral

parietal cortex (LPC), dorsolateral prefrontal cortex (DLPFC), inferior parietal cortex (IPL), precuneus (PCUN); L/R, left/right]. **B** FC differences among the three networks in the two resting datasets (color coding as in **A**; S, SN; D, DMN; C, CEN; blue arrows, significantly decreased FC during EO *versus* EC; gray arrows, no significant difference). **C** Paired *t*-test results of the beta value comparisons between EO and EC within each network in block-design experiments (***) $P < 0.001$.

suggested significantly greater activation in the SN during EO than EC, and we proposed an optimal DCM model demonstrating that EO modulates the signals transmitted from the SN to the DMN.

Opening the eyes is a basic behavior to direct attention to the external world, and changes our brain from an internal to an external state [5, 6]. The SN may be responsible for processing the external information during this switch. The SN assigns saliency to various stimuli, segregating the most relevant signals among internal and external stimuli in order to guide behavior [2]. A previous study suggested that EO leads to higher regional properties (nodal degree, efficiency and betweenness centrality) in exteroceptive-related networks, including regions of the SN, to allocate more resources for exteroceptive processing compared to EC [5]. Moreover, the SN is able to affect the activity of the DMN and its interactions with other networks [2]. The DMN is associated with internal information processing [13], so the decreased FC between the SN and the DMN during EO suggests that attentional resources are directed to external processing from internal processing to a larger extent in the EO than in the EC condition.

In the block-design experiments, the increased activation in the SN during EO further suggested that the SN assigns saliency to external stimuli when our eyes are open. This result is supported by previous reports. For example, a simultaneous FDG-PET/fMRI study found an increase in

glucose metabolism within the SN during EO compared to EC [4]. This result not only supports the idea that more attentional resources are allocated for external processing during EO, but also suggests that the SN may be the input network for model construction in DCM analysis.

The optimal model (M10), derived from DCM analysis, showed that EO modulates the signals from the SN to the DMN and provides a potential explanation for the decreased FC between the SN and the DMN. Previous studies have suggested that the SN initiates cognitive control signals to the DMN [1, 12]. Moreover, a special class of neurons, von Economo neurons, are exclusively found within the SN and may relay signals from the SN to other parts of the brain [14]. And an anatomical study has also shown that the structural integrity of the SN predicts the efficient regulation of activity in the DMN [15]. Taken together, it is reasonable to conclude that the SN transmits internal signals to the DMN. As revealed by our model, this signaling would be modulated by EO, possibly leading to decreased coupling between the SN and the DMN. This suggests that EO might disrupt the control signal from the SN to the DMN in order to assign more attentional resources to the external world.

Although the SN and the DMN have been considered to be involved in self-processing, a meta-analysis revealed that the SN, specifically the AI, is activated during self-related stimuli (not non-self-related stimuli), while the DMN, centered on cortical midline structures including the

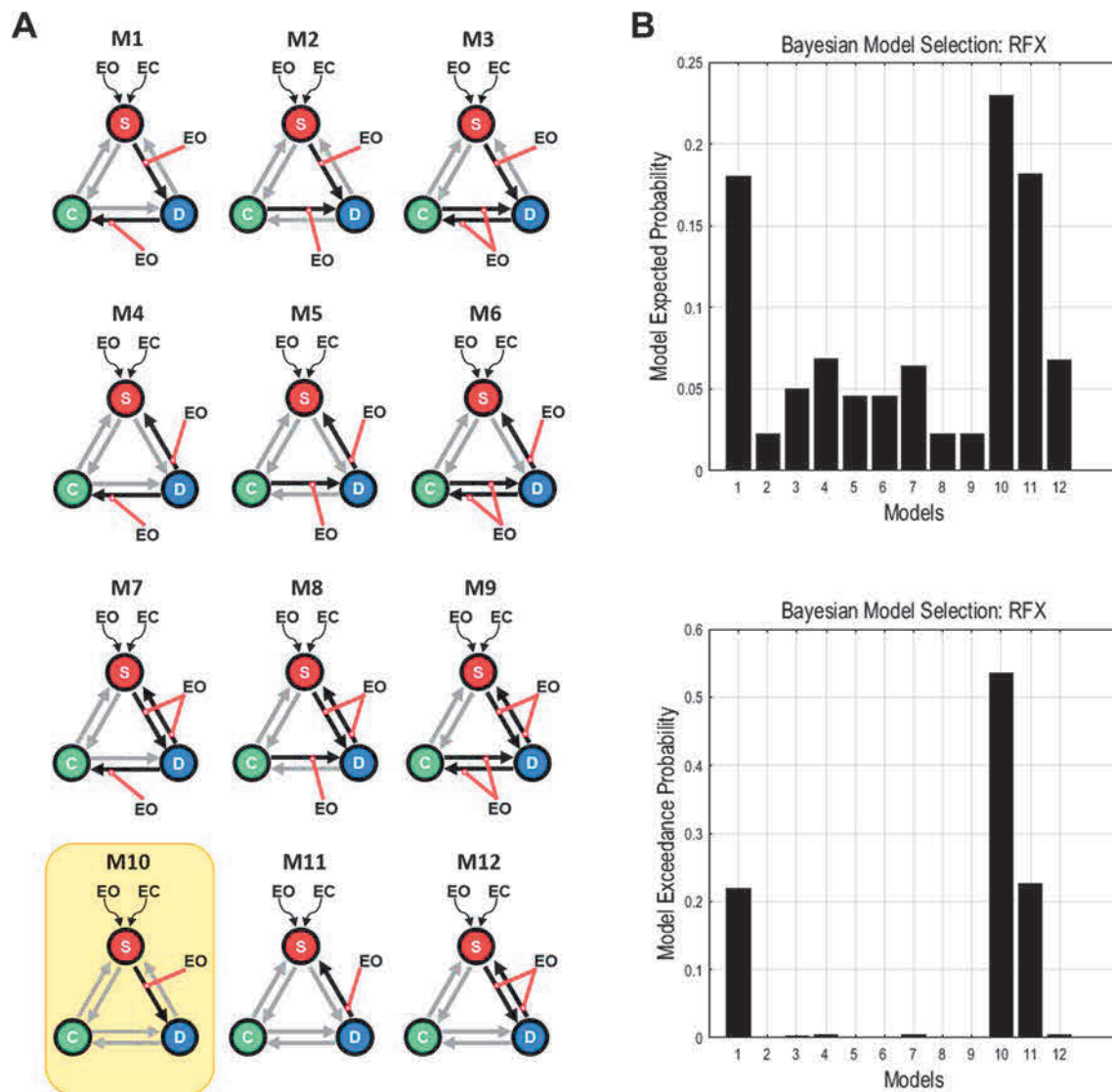


Fig. 2 Model spaces of dynamic causal modeling (DCM) and the results of random-effect Bayesian model selection (BMS) for the block-design experiments. **A** Twelve hypothesized models estimated with DCM. Each model contains bidirectional connections among the three networks and two driving inputs (EC and EO) to the SN (red lines, modulatory effects of EO; black arrows, connections influenced

medial prefrontal cortex and posterior cingulate cortex, shows activation during both self- and non-self-related stimuli [16]. These results demonstrate that the SN plays a more special role in self-related processing than the DMN, while the DMN could be involved in more general functions, such as social cognition and monitoring the environment. Accordingly, our findings further suggest that the SN assigns self-specificity to an external stimulus, and changes the external stimulus into a self-related stimulus. However, the exact mechanism deserves further investigation.

A novel theory has recently been proposed that neural activity and mental features (e.g. self, consciousness, and

perception of the passage of time) are connected into an intrinsic relationship by the dynamics of “inner time and space”, which suggests that neural dynamics are mental dynamics [17]. The dynamics of inner time and space has been proposed to be constructed by the spatiotemporal dynamics of spontaneous activity in the brain. In contrast, the dynamics of “outer time and space” describe the spatiotemporal dynamics of the outside world. Following this theory, the present study, which showed an altered dynamic interaction between two self-related networks (SN and DMN) at the neuronal level, suggests that self-processing changes along with the switch from EC to EO. We have further assumed that the spatiotemporal

dynamics of the self-related mental feature would change with the dynamic interaction between the SN and the DMN. This offers a new perspective to expand our understanding of the self-processing in different conditions besides EC and EO.

In some recent studies, the SN has been divided into dorsal and ventral regions [18]. The dorsal SN, which includes the bilateral dorsal AI and part of the subgenual anterior cingulate cortex (SACC), plays an important role in attention and switching between cognitive resources, and a causal control role in the DMN and the CEN [12]. The ventral SN, consisting of the bilateral ventral AI and part of the SACC, is thought to be crucial during emotions [18]. Thus, the dorsal AI and SACC were included in the current study, whereas the ventral AI was excluded. Our results further expand the understanding of the dorsal SN by showing that the control signal from the dorsal SN to the DMN can be influenced by EO.

One issue in this study should be mentioned. Functional brain networks are usually dynamic and time-varying, even at rest. However, due to the low temporal resolution of our fMRI dataset, it was difficult to investigate the dynamic characteristics of functional brain networks in the current study. Thus, the impact of EC/EO on the dynamic interactions among the three networks could be further explored using measurements with high temporal resolution, such as magnetoencephalography or electroencephalography in further studies.

In summary, our results demonstrate that the triple-network mechanism changes once we open our eyes. Specifically, the coupling between the SN and the DMN decreased and activation of the SN increased during EO rather than EC, and EO modulated the signaling from the SN to the DMN. These findings show that the network mechanism underlying endogenous cognitive control is influenced by the eyes. Our study lays a foundation for the design of psychological experiments and the interpretation of results under different conditions.

Acknowledgements This work was supported by the National Natural Science Foundation of China (31771249 and 31971032), the Major Program of the National Social Science Fund of China (18ZDA293), the Basic and Applied Basic Research Foundation of Guangdong Province, China (2020A1515011250), Guangdong-Hong Kong-Macao Greater Bay Area Center for Brain Science and Brain-Inspired Intelligence Fund (2019023), Key Realm R&D Program of Guangdong Province (2019B030335001), Key Realm R&D Program of Guangzhou (202007030005), and the National Natural Science Foundation of China (31871135).

Conflict of interest The authors claim that there are no conflicts of interest.

References

1. Sridharan D, Levitin DJ, Menon V. A critical role for the right fronto-insular cortex in switching between central-executive and default-mode networks. *Proc Natl Acad Sci U S A* 2008, 105: 12569–12574.
2. Menon V, Uddin LQ. Saliency, switching, attention and control: a network model of insula function. *Brain Struct Funct* 2010, 214: 655–667.
3. Qin PM, Wu XH, Huang ZR, Duncan NW, Tang WJ, Wolff A, *et al.* How are different neural networks related to consciousness? *Ann Neurol* 2015, 78: 594–605.
4. Riedl V, Bienkowska K, Strobel C, Tahmasian M, Grimmer T, Forster S, *et al.* Local activity determines functional connectivity in the resting human brain: a simultaneous FDG-PET/fMRI study. *J Neurosci* 2014, 34: 6260–6266.
5. Xu P, Huang R, Wang J, Van Dam NT, Xie T, Dong Z, *et al.* Different topological organization of human brain functional networks with eyes open versus eyes closed. *Neuroimage* 2014, 90: 246–255.
6. Jao T, Vertes PE, Alexander-Bloch AF, Tang IN, Yu YC, Chen JH, *et al.* Volitional eyes opening perturbs brain dynamics and functional connectivity regardless of light input. *Neuroimage* 2013, 69: 21–34.
7. Zhong Y, Wang C, Gao W, Xiao Q, Lu D, Jiao Q, *et al.* Aberrant resting-state functional connectivity in the default mode network in pediatric bipolar disorder patients with and without psychotic symptoms. *Neurosci Bull* 2018, 35: 581–590.
8. Friston KJ, Harrison L, Penny W. Dynamic causal modelling. *Neuroimage* 2003, 19: 1273–1302.
9. Daunizeau J, Stephan KE, Friston KJ. Stochastic dynamic causal modelling of fMRI data: should we care about neural noise? *Neuroimage* 2012, 62: 464–481.
10. Bernal-Casas D, Balaguer-Ballester E, Gerchen MF, Iglesias S, Walter H, Heinz A, *et al.* Multi-site reproducibility of prefrontal-hippocampal connectivity estimates by stochastic DCM. *Neuroimage* 2013, 82: 555–563.
11. Rigoux L, Stephan KE, Friston KJ, Daunizeau J. Bayesian model selection for group studies - revisited. *Neuroimage* 2014, 84: 971–985.
12. Chand GB, Wu J, Hajjar I, Qiu D. Interactions of the salience network and its subsystems with the default-mode and the central-executive networks in normal aging and mild cognitive impairment. *Brain Connect* 2017, 7: 401–412.
13. Hassabis D, Maguire EA. Deconstructing episodic memory with construction. *Trends Cogn Sci* 2007, 11: 299–306.
14. Allman JM, Watson KK, Tetreault NA, Hakeem AY. Intuition and autism: a possible role for Von Economo neurons. *Trends Cogn Sci* 2005, 9: 367–373.
15. Bonnelle V, Ham TE, Leech R, Kinnunen KM, Mehta MA, Greenwood RJ, *et al.* Salience network integrity predicts default mode network function after traumatic brain injury. *Proc Natl Acad Sci U S A* 2012, 109: 4690–4695.
16. Qin P, Northoff G. How is our self related to midline regions and the default-mode network? *Neuroimage* 2011, 57: 1221–1233.
17. Northoff G, Wainio-Theberge S, Evers K. Is temporo-spatial dynamics the “common currency” of brain and mind? In *Quest of “Spatiotemporal Neuroscience”*. *Phys Life Rev* 2019.
18. Touroutoglou A, Hollenbeck M, Dickerson BC, Feldman Barrett L. Dissociable large-scale networks anchored in the right anterior insula subserve affective experience and attention. *Neuroimage* 2012, 60: 1947–1958.



Pgant4 and Tango1 Mediate Anoxia and Reoxygenation Injury

Qingqing Du^{1,2} · Nastasia K. H. Lim^{3,4,5} · Yiling Xia^{1,2} · Wangchao Xu⁶ ·
Qichao Zhang^{4,7} · Liyao Zhang^{4,7} · Fude Huang^{4,5,7} · Wenan Wang^{1,2,5}

Received: 16 April 2020 / Accepted: 8 June 2020 / Published online: 16 August 2020
© Shanghai Institutes for Biological Sciences, CAS 2020

Dear Editor,

Diseases caused by ischemia, including coronary artery disease and stroke, are a leading cause of death worldwide [1]. Restoration of the blood and oxygen supply after restriction also causes tissue damage by activating a number of pathological pathways, such as inflammatory, oxidative stress, and cell death pathways that are mediated by microRNAs and hypoxia-inducible factors [1, 2]. In recent years, thrombolytic and surgical treatments for patients with acute stroke or coronary artery disease have improved and are effective, but currently there is no approved therapy for use after an ischemic stroke [3]. This lack of effective neuroprotective drugs suggests a shortage of proper therapeutic targets for treating ischemia-reperfusion injury. Thus, to uncover new molecules that regulate or mediate ischemia-reperfusion injury, it is necessary to identify novel targets for drug development.

Qingqing Du, Nastasia K. H. Lim, Yiling Xia, Wangchao Xu have contributed equally to this work.

Electronic supplementary material The online version of this article (<https://doi.org/10.1007/s12264-020-00562-y>) contains supplementary material, which is available to authorized users.

✉ Fude Huang
huangfd@nuo-beta.com

✉ Wenan Wang
wangwenan@hotmail.com

¹ Department of Neurology, Xinhua Hospital Affiliated to Shanghai Jiaotong University School of Medicine, Shanghai 202150, China

² Department of Neurology, Xinhua Hospital Chongming Branch Affiliated to Shanghai Jiaotong University School of Medicine, Shanghai 202150, China

The genetic basis of anoxia tolerance is not well understood. Using an anoxia- or hypoxia-tolerant animal model to find new genes involved in such resistance may uncover new pathways for further investigation. One such model is *Drosophila*, which has been used to investigate the susceptibility or tolerance to anoxia or hypoxia [4, 5]. An estimated 75% of known human disease genes are matched in the genetic code of *Drosophila*, thus it has frequently been used to model human diseases and these models have been successfully used to study the interactions between disease-related molecules and to screen for disease-modifying drugs and genes [6]. Using a *Drosophila* model of Alzheimer's disease [7], we previously conducted a genetic screen for modifiers and identified some genes as novel regulators or mediators of intraneuronal A β ₄₂ accumulation and its associated neural degeneration [8]. Importantly, genetic reduction of a mouse homologue of one of these modifiers found in *Drosophila* (eighty-five requiring 3 protein in mice and rolling blackout in flies) also suppresses the neurodegeneration in a mouse model of Alzheimer's disease [9]. Thus, genetic screening for modifiers of disease phenotypes in *Drosophila* is a reliable means of discovering novel mediators of pathogenesis.

³ Shanghai Institute of Materia Medica, University of the Chinese Academy of Sciences, Shanghai 201203, China

⁴ Shanghai Advanced Research Institute, University of the Chinese Academy of Sciences, Shanghai 201210, China

⁵ Nuo-beta Pharmaceutical Technology (Shanghai) Co. Ltd, Shanghai 201210, China

⁶ Institute of Neuroscience, University of the Chinese Academy of Sciences, Shanghai 200031, China

⁷ Sino-Danish College, University of the Chinese Academy of Sciences, Beijing 100049, China

Previously, we established an efficient and reliable assay for studying the mortality and motor impairment caused by anoxia-reoxygenation in flies [10]. Flies subjected to an extended period of anoxia can recover and become active again when placed in a normoxic environment. Nevertheless, anoxia-reoxygenation stress induces damage in flies such as motor deficits, increased caspase-3 staining in the brain, and increased mortality [10]. If the duration of anoxia is > 1 h, flies will die in the following days, and the cumulative death rate on day 5 is linearly and positively correlated with the duration of anoxia [10]. Here, using this anoxia assay, we conducted a genetic screen and isolated several lines with increased tolerance to anoxia-reoxygenation.

Pgant4 is a well-conserved O-glycosyltransferase that glycosylates transport and Golgi organization protein 1 (Tango1) and protects it from degradation by cleavage from Furin, a peptidase [11]. Tango1 (melanoma inhibitory activity 3, MIA3, in mammals), *via* interaction with multiple proteins, organizes endoplasmic reticulum exit sites (ERES), mediates cargo-sorting and the formation of large secretory vesicles, and controls or influences the secretion of large vesicles (*e.g.* collagens, lipoproteins, and other molecules), as well as the general secretion of small molecules in all tissues of both flies and mammals [12]. Further analysis has shown that both Pgant4 and Tango1 mediate anoxia-reoxygenation damage in *Drosophila*. Our study suggests that the Pgant4/Tango1-controlled ER-Golgi pathway, along with the molecules being transported, is a novel and important mechanism underlying ischemia-reperfusion injury.

To screen for genes involved in the damage caused by anoxia-reoxygenation in *Drosophila*, mutant flies with different identified deletions of DNA segments on the 3rd chromosome or a few on the 2nd chromosome (Fig. 1A) were separately crossed for 10 generations to an isogenic wild-type strain, w^{1118} . The progeny containing the chromosome deficiencies and control w^{1118} (Ctrl) flies were exposed to anoxia for 3 h, then transferred to a normoxic condition and the cumulative death rate for each genotype was calculated in the following 5 days and compared to that of the Ctrl flies. Three deficient lines, BL stock # 6965, 7675, and 7681, were found to be more resistant to anoxia-reoxygenation (Fig. 1A and data not shown). To determine the specific genes involved in anoxia-reoxygenation injury, line 6965 and another three lines with overlapping deficiency, 9599, 6507, and 7787, were tested again for resistance to anoxia-reoxygenation (Fig. 1B). Lines 6965, 7787, and 6507, but not 9599, were more resistant to anoxia-reoxygenation (Fig. 1C), demonstrating that the affected gene or genes were located between the break points at 2L:3466844 and 3473493 (~6 kb), which covered 5 genes: *mssl-2*, *ND-PDSW*, *CG3238*, *CG31776*,

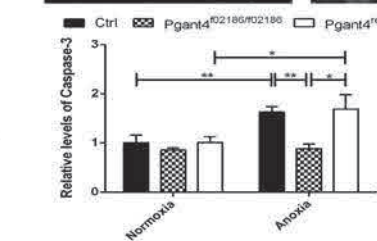
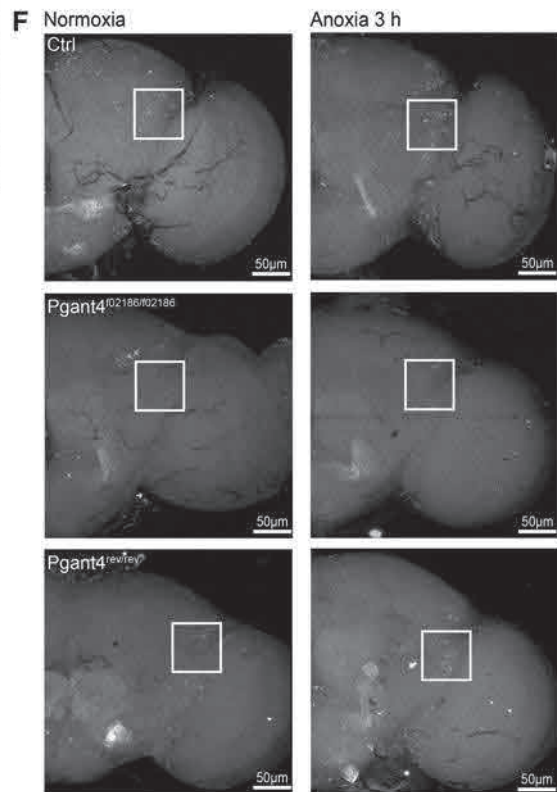
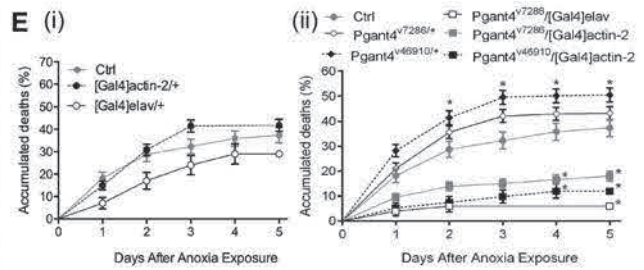
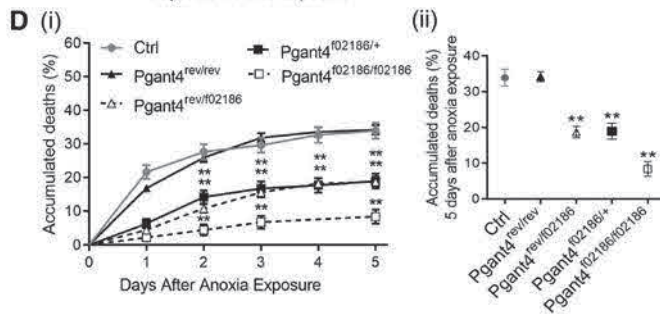
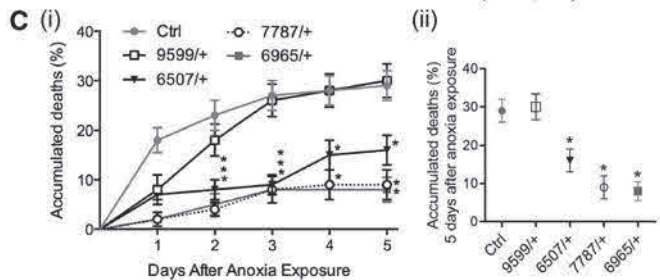
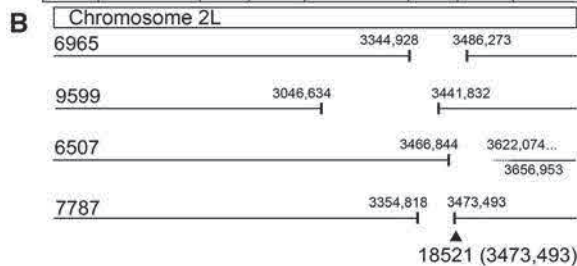
and *Pgant4*. Testing the available temporary mutants of these genes (see supplementary materials for method) in the anoxia-reoxygenation assay showed that the transposon-insertion mutation, PBac{WH}*Pgant4*^{f02186} (*Pgant4*^{f02186/f02186} or *Pgant4*^{f02186/+}) was more resistant to anoxia-reoxygenation (Fig. 1D). To confirm that this increased resistance was due to the genetic reduction of Pgant4, we precisely removed the transposon insertion in *Pgant4* with a transposase-expressing transgene, P{Δ2-3}99B, which generated the revertant chromosome and obtained 2 groups of flies: *Pgant4*^{rev/rev} and *Pgant4*^{rev/f02186}, which we then tested in the anoxia-reoxygenation assay. As shown in Fig. 1D, the revertant chromosome acted just like a wild-type chromosome. Therefore, down-regulation of the Pgant4 protein level increases the resistance to anoxia-reoxygenation, or Pgant4 mediates the anoxia-reoxygenation damage. This was further confirmed by the increased resistance to anoxia-reoxygenation in flies with *Pgant4* knocked down either ubiquitously or in neurons alone (Fig. 1E).

To investigate the effect of Pgant4 reduction on the neural damage caused by anoxia-reoxygenation, we analyzed the active caspase-3 levels in the brains of flies. Previously, we showed that flies exposed to the anoxia assay have increased caspase-3 staining in the brain [10]. Under normoxic conditions, the levels of active caspase-3 were comparable in Ctrl, *Pgant4*^{f02186/f02186}, and *Pgant4*^{rev/rev} flies, as assessed using immunofluorescence (Fig. 1F). After exposure to anoxia for 3 h, followed by 3 h of recovery in normoxia, the active caspase-3 level was significantly increased in Ctrl and *Pgant4*^{rev/rev} flies, but unchanged in *Pgant4*^{f02186/f02186} flies, when compared with flies without anoxia exposure (Fig. 1F), further confirming the protective effect of Pgant4 reduction.

Tango1 is a substrate of Pgant4 and its o-glycosylation by Pgant4 protects it from degradation by cleavage from Furin, a peptidase [11]. To examine the downstream consequences of Pgant4 reduction in anoxia-reoxygenation, we analyzed the o-glycosylated and total levels of Tango1 with an antibody recognizing o-glycosylated Tango1 and an antibody against Tango1 in Ctrl and *Pgant4*^{f02186/f02186} flies after exposure to anoxia (Fig. 2A). First, the specificity and recognition of the *Drosophila* Tango1 by the antibody against mammalian MIA3 were assessed (Fig. 2A), and the band in the immunoblot recognized by the anti-MIA3 antibody displayed the correct molecular weight. Furthermore, the density of the band decreased when Pgant4 was reduced or Tango1 was knocked down in neurons, and increased when Tango1 was overexpressed. Then, Ctrl and *Pgant4*^{f02186/f02186} flies were exposed to 0, 1, or 3 h of anoxia and collected immediately after exposure or allowed to recover for 3 h in normoxia before analysis. In Ctrl flies, the level of glycosylated

A

BL stock #	Deleted segment	Location	BL stock #	Deleted segment	Location	BL stock #	Deleted segment	Location
6965	23E5–23F5	2L	7929	65F7–66A4	3L	24955	79B2–79F5	3L
8836	28F5–29B1	2L	24412	66A8–66B11	3L	8089	79C2–80A4	3L
3129	33A1–33B2	2L	9070	66D12–66E6	3L	5951	79D3–79F6	3L
2577	61A–61D3	3L	9194	66D12–66E6	3L	4787	82F3–82F11	3R
8047	61B1–61C1	3L	8066	66D12–67B3	3L	5694	82F8–83A3	3R
23674	61F6–62A9	3L	9221	66E1–67B1	3L	7623	88F1–88F7	3R
9693	62A11–62B7	3L	4499	66E3–4–66F1–2	3L	4562	93B3–92F13	3R
7566	62A2–62A6	3L	9295	66E5–66F6	3L	24993	94F3–95D1	3R
2400	62B7–62E6	3L	4500	66E–66F	3L	4940	95A5–95C11	3R
7571	62F5–63A3	3L	7079	66F1–67B3	3L	2585	95A5–95D11	3R
26523	63A2–63B11	3L	9561	66F4–67A1	3L	7992	95B1–95D1	3R
26524	63A7–63B12	3L	24414	66F4–67B2	3L	4939	95B–95C	3R
24392	63F1–64A4	3L	8975	67B11–67C5	3L	*7675	95C12–95D8	3R
24395	64C1–64E1	3L	24416	67C4–67D1	3L	28827	95C8–95E1	3R
7585	64D6–64E2	3L	8072	69C4–69F6	3L	4432	95D7–D11.95F15	3R
7586	64E5–64F5	3L	8097	70A3–70C10	3L	7676	95D8–95E1	3R
24914	64E7–65B3	3L	8099	73D5–74E2	3L	26531	96B20–96C2	3R
24915	65A2–65C1	3L	6411	74D3–75B5	3L	27403	96C7–96D1	3R
4393	65A2–65E1	3L	6754	75F10–76A5	3L	27923	96C8–96D1	3R
6867	65D4–65E6	3L	9697	75F1–76A1	3L	*7681	96D1–96E2	3R
9701	65D5–65E6	3L	6646	76A7–B1;76B4–5	3L	25050	96D1–96E3	3R
8974	65E9–65F5	3L	8101	78D5–79A2	3L	27360	96E1–96E3	3R



Tango1 was unchanged after exposure to anoxia for 1 h, but increased by ~ 4-fold after exposure for 3 h and by ~ 6-fold after 3 h of anoxia and 3 h of recovery in normoxic conditions (Fig. 2B, upper left). Consistent with this, the total amount of Tango1 was unchanged, or increased by ~ 4- and ~ 8-fold at the corresponding time points (Fig. 2B, lower left). In the *Pgant4*^{f02186/f02186} flies, the total amount of Tango1 was markedly lower than that in Ctrl flies; note that the densities of Tango1 and tubulin in the immunoblots of both Ctrl and *Pgant4*^{f02186/f02186} flies in Fig. 2B are consistent with a previous report that loss of

Pgant4 reduces total Tango1 [11]. Importantly, in the *Pgant4*^{f02186/f02186} flies, both o-glycosylated and total levels of Tango1 remained unchanged or had much less of an increase at the corresponding time points (Fig. 2B, upper and lower right).

To test whether the protective effect of *Pgant4* reduction is mediated by the downregulation of Tango1, we knocked down Tango1 in neurons (*Tango1*^{RNAi}) and measured its effects on the mortality and active caspase-3 level in the anoxia-reoxygenation assay. *Tango1*^{RNAi} flies indeed showed a significant reduction in both mortality and active

◀ **Fig. 1** Genetic reduction of *Pgant4* increases anoxia resistance and decreases active caspase-3 levels in the brain of *Drosophila* exposed to anoxia-reoxygenation. **A** List of *Drosophila* deficiency lines in a genetic screen for increased resistance to anoxia-reoxygenation. The Bloomington (BL) stock number and the deleted region in the chromosome are indicated. BL stock numbers 6965, 7675, and 7681 (indicated by asterisks) exhibit reduced mortality in the anoxia-reoxygenation assay. A hundred flies were screened for each line. **B** Relative chromosomal map of four deficient lines used to identify the *Pgant4* gene. **C** (i) Deficient lines BL numbers 6965, 7787, and 6507, but not 9599, show increased resistance to anoxia-reoxygenation, compared with *w¹¹¹⁸* flies (Ctrl). (ii) Cumulative deaths 5 days after anoxia exposure (for clearer comparison between groups). **D** (i) Cumulative death rates of Ctrl and flies with different combinations of the *Pgant4^{f02186}* allele and *Pgant4^{rev}*. (ii) Cumulative deaths 5 days after anoxia exposure. **E** (i) Cumulative death rates of Ctrl and Gal4 flies ([Gal4]actin-2/+ and [Gal4]elav/+) just expressing the transcription factor Gal4, and (ii) Ctrl (as in E i) and flies with *Pgant4* knocked down ubiquitously (*Pgant4^{v7286}/[Gal4]actin-2* and *Pgant4^{v46910}/[Gal4]actin-2*) or just in neurons (*Pgant4^{v7286}/[Gal4]elav*), and UAS-transgenic control flies (*Pgant4^{v7286/+}* and *Pgant4^{v46910/+}*). The UAS flies harbor the transgene for expressing double-stranded RNA against *Pgant4*, but this expression requires Gal4. Notably, the cumulative death rate of [Gal4]actin-2/+ is significantly higher than that of Ctrl; this might be due to the homozygous lethal insertion of the [Gal4]actin-2 transgene into a locus unrelated to *Pgant4*. In C–E, the cumulative death rates of flies exposed to 3 h of anoxia before recovery in normoxic conditions are analyzed over the next 5 days (represented as cumulative death percentage). Error bars, \pm SEM; $n = 100$ – 200 flies/group; * $P < 0.05$, ** $P < 0.01$ vs Ctrl. **F**, Above, representative images of active caspase-3 immunofluorescence in Ctrl, *Pgant4* homozygous mutants (*Pgant4^{f02186/f02186}*), and revertant *Pgant4* (*Pgant4^{rev/rev}*) flies after 3 h of anoxia exposure and 3 h recovery (white squares, areas used to quantify the active caspase-3 level in each hemisphere of the fly brain; images represent 5–10 fly heads/group; scale bars, 50 μ m). Below, fluorescence intensity relative to Ctrl, Error bars, \pm SEM; * $P < 0.05$, ** $P < 0.01$, one-way ANOVA

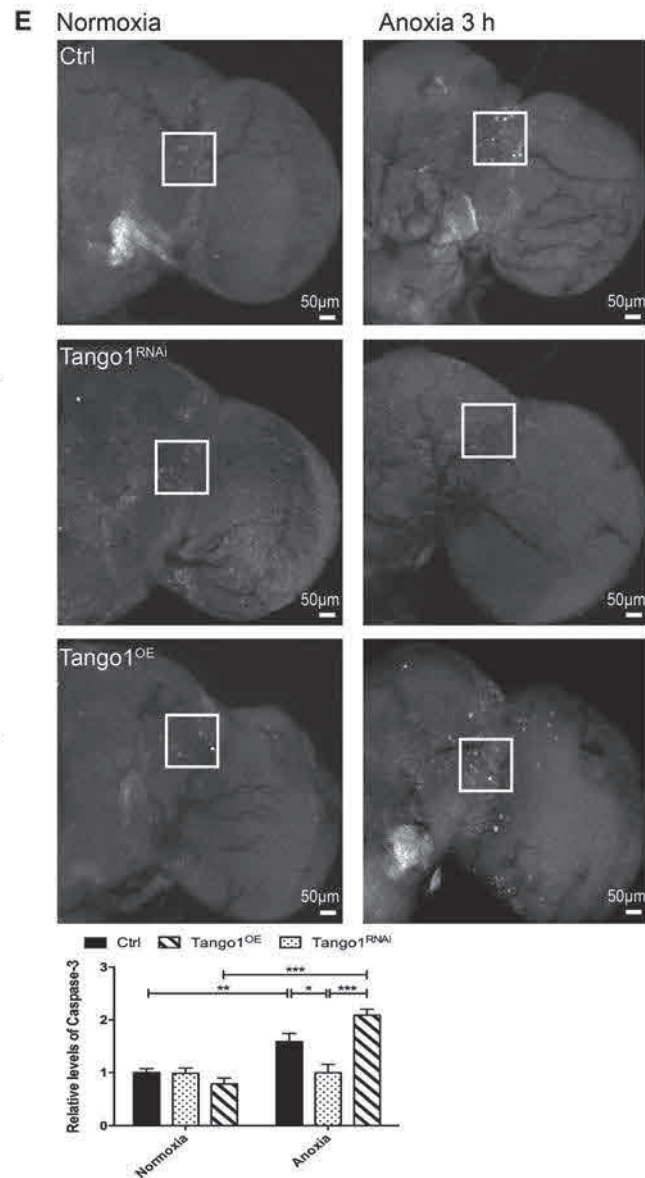
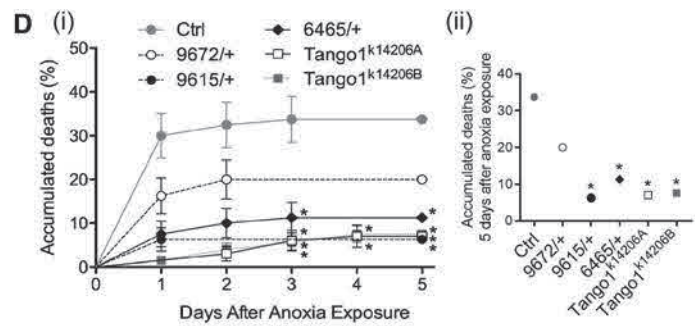
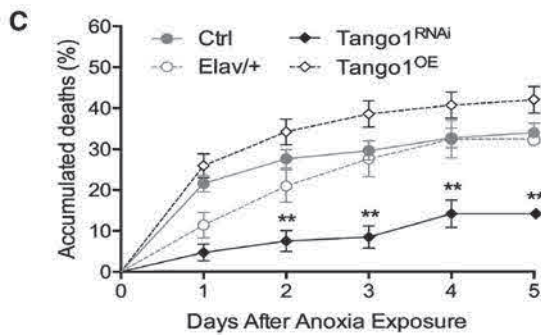
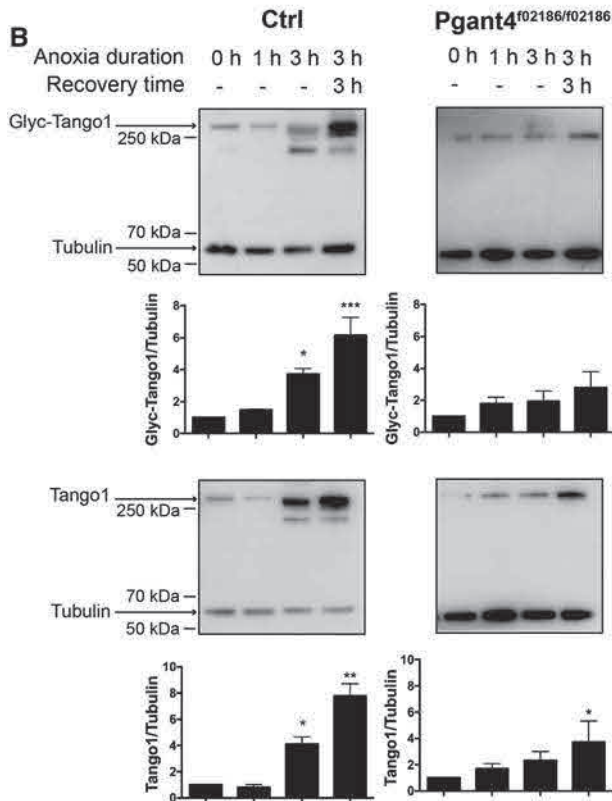
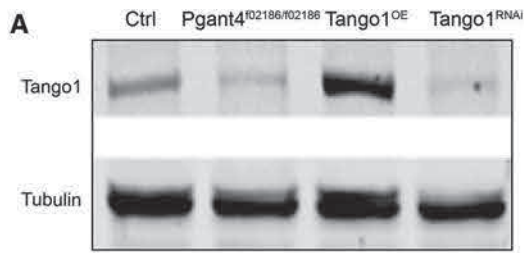
caspase-3 in the brain (Fig. 2C, E). Consistent with this, chromosome deficiencies and transposon-insertion mutations of *Tango1* also increased the resistance to anoxia-reoxygenation (Fig. 2D). To further test the role of *Tango1* in anoxia-reoxygenation damage, we investigated the effect of its upregulation in flies overexpressing *Tango1* in neurons (*Tango1^{OE}*). As expected, *Tango1^{OE}* flies exhibited an increased cumulative death rate and showed increased active caspase-3 levels after exposure to anoxia (Fig. 2C, E). Thus, the ability to tolerate anoxia, anoxia-reoxygenation, or both is inversely controlled by the level of *Tango1* protein.

Using a newly developed anoxia-reoxygenation assay and an unbiased genetic screen followed by identification and characterization of isolated mutants with increased resistance to anoxia-reoxygenation, we obtained conclusive evidence showing that the expression levels of both *Pgant4* and *Tango1* inversely determine the ability to tolerate anoxia or anoxia-reoxygenation in *Drosophila*. First, downregulation of *Pgant4*, either ubiquitously or just in

neurons, decreased the mortality and active caspase-3 levels in the brain after exposure to anoxia-reoxygenation. Second, in control flies, prolonged anoxia robustly increased the glycosylated and total levels of *Tango1*, and this upregulation continued to increase even after removal from anoxic conditions and may contribute to reperfusion injury. Third, the upregulation of *Tango1* caused by anoxia-reoxygenation was dramatically suppressed by the downregulation of *Pgant4*. Fourth, *Tango1* knockdown or overexpression alone improved or worsened the mortality and activation of caspase-3 respectively in anoxia-reoxygenation exposure.

Pgant4 belongs to the UDP-GalNAc:polypeptide N-acetylgalactosaminyltransferase superfamily that catalyze the transfer of a GalNAc sugar onto the hydroxyl groups of serine and threonine in secreted or membrane-bound proteins [13]. *Pgant4* glycosylates *Tango1* and protects it from Furin-mediated proteolysis in *Drosophila* [11]. *Pgant4* is orthologous to mammalian GALNT10 and GALNTL6 (flybase.org), both of which are ubiquitously expressed in the mammalian body, and GALNTL6 is especially enriched in human heart (Genecards). *Tango1*/MIA3 mediates cargo sorting and the formation of large ER transport vesicles, as well as organizing ERES in both flies and mammals, directly controlling the bulk secretion of large proteins such as collagens and lipoproteins, and indirectly influencing the general secretion of small molecules [12]. Down regulation of *Tango1* reduces ERES and impairs not only the secretion of collagen and large extracellular matrix proteins, but also general secretion, whereas overexpression of *Tango1* or even truncated *Tango1* missing the cargo-binding domain greatly increases ERES and general secretion. In our study, anoxia-reoxygenation induced a ~ 4 – 8 -fold elevation of *Tango1*, and presumably markedly increased the secretion of both large extracellular matrix proteins and small secretory molecules or membrane-bound proteins. The nature of these secreted or transported molecules *via* the *Pgant4*/*Tango1*-ER Golgi pathway and their roles in anoxia-reoxygenation or ischemia-reperfusion require further study.

A previous study suggested that flies less susceptible to protein unfolding are more tolerant of anoxia, but a genetic basis for this response to anoxia had not been found [4]. Furthermore, in a genome-wide association analysis of flies exposed to anoxia, there were no change in heat shock proteins (Hsps), chaperones that repair or protect unfolded proteins in response to stress, suggesting an upstream or downstream regulator may be involved [4]. Our study revealed that *Pgant4*/*Tango1* may be this regulator, particularly as the Src homology 3 domain of *Tango1* interacts with Hsp47 to package collagens into vesicles for transport [14]. Proteins, after correct folding and post-translational



modification, are shuttled between the ER and Golgi to undergo additional modifications for maturation before transport to the plasma membrane, organelles, or extracellular space [15]. Tango1 directly and indirectly binds to many proteins to form macromolecular complexes at

ERES, including the subunits of coat protein complex II (COPII), which are required for the transport of most secretory proteins and transmembrane proteins [12]. The up to 8-fold increase of Tango1 in anoxia-reoxygenation might have hijacked too many COPII and other common

◀ **Fig. 2** Anoxia-reoxygenation markedly increases the glycosylated and total Tango1, which is suppressed by downregulation of *Pgant4*. **A** Immunoblots showing the specificity and recognition of *Drosophila* Tango1 by anti-MIA3 antibody. The anti-MIA3 antibody detects a band at 250 kDa, the correct molecular weight for Tango1, but with a different density in control *w¹¹¹⁸* (Ctrl) flies, *Pgant4* homozygous mutants (*Pgant4^{f02186/f02186}*), with *Tango1* knocked down in neurons (*Tango1^{RNAi}*), and flies with Tango1 overexpression (*Tango1^{OE}*). Tubulin served as loading control; $n = 30\text{--}40$ fly heads/group. **B** Representative immunoblots and levels of o-glycosylated Tango1 (Glyc-Tango1) and total Tango1 (Tango1) in Ctrl (left) and *Pgant4^{f02186/f02186}* (right) flies after exposure to anoxia for 0, 1, or 3 h, or exposure to 3 h of anoxia before recovery in 3 h under normoxic conditions. Tubulin served as loading control. Each experiment was repeated at least three times; $n = 30\text{--}40$ fly heads/group. **C** Cumulative death rates of Ctrl, [Gal4]elav (Elav/+), *Tango1^{RNAi}*, and *Tango1^{OE}* flies. Data for Ctrl flies is the same as in Fig. 1D. **D** (i) Cumulative death rates of Ctrl, deficient (9672/+, 9615/+, and 6465/+) and transposon-insertion mutants of *Tango1* (*Tango1^{k14206A/+}* and *Tango1^{k14206B/+}*). (ii) Cumulative deaths 5 days after anoxia exposure. In C and D, $n = 100\text{--}200$ flies/group. **E** Above, representative images of active caspase-3 immunofluorescence after 3 h of anoxia and 3 h recovery in Ctrl, *Tango1^{RNAi}*, and *Tango1^{OE}* flies (white squares, areas used to quantify caspase-3 levels in each hemisphere; scale bars, 50 μm), Below, fluorescence intensity relative to Ctrl. $n = 5\text{--}10$ fly heads/group; error bars, \pm SEM; * $P < 0.05$, ** $P < 0.01$, *** $P < 0.001$, one-way ANOVA

players along the ER-Golgi pathway, and greatly inhibited other *Pgant4*/*Tango1*-independent transport.

Our study opens a new pathway to investigate the mechanisms underlying anoxia-reoxygenation or ischemia and reperfusion injury, and this may have implications for therapeutic strategies for diseases and conditions such as coronary artery disease and stroke. Our study provides a working model that involves partially reducing either *Pgant4* or *Tango1* to dramatically inhibit anoxia-reoxygenation damage, indicating that regulating or managing the *Pgant4*/*Tango1*-mediated secretion or transport of molecules that mediate ischemia and reperfusion, rather than targeting these molecules individually, may be a much more efficient therapeutic strategy for treating ischemia and reperfusion injury.

Acknowledgements This work was supported by the National Natural Science Foundation of China (81771416, 81650110527 and 8197100), Shanghai Municipal Commission of Health and Family Planning (201740153) and Key Discipline of Chongming District, Shanghai, China, 2018.

Conflict of interest Fude Huang's research in this study received financial support from Nuo-Beta Pharmaceutical Technology (Shanghai) Co., Ltd (Nuo-Beta), Fude Huang and Wenan Wang have share holdings in Nuo-Beta. The other authors declare no competing financial interests.

References

- Eltzschig HK, Eckle T. Ischemia and reperfusion—from mechanism to translation. *Nat Med* 2011, 17: 1391–1401.
- Mo JL, Pan ZG, Chen X, Lei Y, Lv LL, Qian C, *et al.* MicroRNA-365 knockdown prevents ischemic neuronal injury by activating oxidation resistance 1-mediated antioxidant signals. *Neurosci Bull* 2019, 35: 815–825.
- Karsy M, Brock A, Guan J, Taussky P, Yashar M, Park MS. Neuroprotective strategies and the underlying molecular basis of cerebrovascular stroke. *Neurosurg Focus* 2017, 42: E3. <https://doi.org/10.3171/2017.1.focus16522>.
- Campbell JB, Overby PF, Gray AE, Smith HC, Harrison JF. Genome-wide association analysis of anoxia tolerance in *Drosophila melanogaster*. *G3 Genes Genomes Genet* 2019, 9: 2989–2999.
- Zhou D, Visk DW, Haddad GG. *Drosophila*, a golden bug, for the dissection of the genetic basis of tolerance and susceptibility to hypoxia. *Pediatr Res* 2009, 66: 239–247.
- Pandey UB, Nichols CD. Human disease models in *drosophila melanogaster* and the role of the fly in therapeutic drug discovery. *Pharmacol Rev* 2011, 63: 411–436.
- Zhao XL, Wang WA, Tan JX, Huang JK, Zhang X, Zhang BZ, *et al.* Expression of $\text{A}\beta$ induced age-dependent presynaptic and axonal changes in *Drosophila*. *J Neurosci* 2010, 30: 1512–1522.
- Liu H, Han M, Li Q, Zhang X, Wang WA, Huang FD. Automated rapid iterative negative geotaxis assay and its use in a genetic screen for modifiers of $\text{A}\beta_{42}$ -induced locomotor decline in *Drosophila*. *Neurosci Bull* 2015, 31: 541–549.
- He Y, Wei M, Wu Y, Qin H, Li W, Ma X, *et al.* Amyloid β oligomers suppress excitatory transmitter release via presynaptic depletion of phosphatidylinositol-4,5-bisphosphate. *Nat Commun* 2019, 10: 1193.
- Xia Y, Xu W, Meng S, Lim NKH, Wang W, Huang FD. An efficient and reliable assay for investigating the effects of hypoxia/anoxia on *Drosophila*. *Neurosci Bull* 2018, 34: 397–402.
- Zhang L, Ali Syed Z, Van Dijk H'rd I, Lim JM, Wells L, Ten Hagen KG. O-Glycosylation regulates polarized secretion by modulating Tango1 stability. *Proc Natl Acad Sci U S A*. 2014, 111: 7296–7301.
- Saito K, Chen M, Bard F, Chen S, Zhou H, Woodley D, *et al.* TANGO1 facilitates cargo loading at endoplasmic reticulum exit sites. *Cell* 2009, 136: 891–902.
- Ten Hagen KG, Tran DT, Gerken TA, Stein DS, Zhang Z. Functional characterization and expression analysis of members of the UDP-GalNAc: polypeptide N-acetylgalactosaminyltransferase family from *Drosophila melanogaster*. *J Biol Chem* 2003, 278: 35039–35048.
- Ishikawa Y, Ito S, Nagata K, Sakai LY, Bächinger HP. Intracellular mechanisms of molecular recognition and sorting for transport of large extracellular matrix molecules. *Proc Natl Acad Sci U S A* 2016, 113: E6036–E6044.
- Sicari D, Iqbaria A, Chevet E. Control of protein homeostasis in the early secretory pathway: current status and challenges. *Cells* 2019, 8: 1347. <https://doi.org/10.3390/cells8111347>.



Complement Factor H Displays Opposite Expression Patterns Under Two Situations of Methamphetamine Administration: Acute Exposure and Chronic Dependence

Ming Lin^{1,2} · Jiamin Xu^{1,2} · Zhimin Liu³ · Liang Qin^{4,5} · Xiaodong Wang^{4,5} · Xiaoping Pu^{1,2}

Received: 8 April 2020 / Accepted: 9 June 2020 / Published online: 7 September 2020
© Shanghai Institutes for Biological Sciences, CAS 2020

Dear Editor,

Methamphetamine (METH) is a highly addictive central nervous system stimulant that has severe physical and psychological side-effects, including loss of appetite, hyperactivity, dysphoria, and depression [1]. Due to its illegal production, distribution, sale, and possession it has become a worldwide burden. METH is directly toxic to dopaminergic and serotonergic neurons, resulting in excitotoxicity, oxidative stress, and other processes [2]. Research on biomolecules associated with these processes will be useful for identifying potential markers, exploring the mechanism of METH dependence, and even developing prevention and treatment strategies.

The authors Ming Lin and Jiamin Xu are co-first authors and contributed equally to this work.

Electronic supplementary material The online version of this article (<https://doi.org/10.1007/s12264-020-00576-6>) contains supplementary material, which is available to authorized users.

✉ Xiaodong Wang
xiaodong@muc.edu.cn

✉ Xiaoping Pu
pxp123@bjmu.edu.cn

- ¹ National Key Research Laboratory of Natural and Biometric Drugs, Peking University, Beijing 100191, China
- ² Department of Molecular and Cellular Pharmacology, School of Pharmaceutical Sciences, Peking University, Beijing 100191, China
- ³ National Institute on Drug Dependence, Peking University, Beijing 100191, China
- ⁴ Centre for Imaging and Systems Biology, Minzu University of China, Beijing 100081, China
- ⁵ College of Life and Environmental Sciences, Minzu University of China, Beijing 100081, China

Complement factor H (CFH) is one of these potential METH-dependence-related molecules; it is a 155-kDa glycoprotein comprised of 20 contiguous complement control protein modules [3]. It can be secreted by several types of cells, including monocytes, fibroblasts, endothelial cells, platelets, and retinal pigment epithelial cells, but it is mainly secreted by the liver [3]. CFH is the major soluble regulator of the complement alternative pathway due to its ability to recognize related biomolecules to inhibit the activation and amplification of the complement system on host surfaces. Mutations of CFH can lead to autoimmune inflammatory and thrombotic disorders, such as age-related macular degeneration and atypical hemolytic uremic syndrome [3].

Our previous studies found that CFH is strongly associated with METH administration. Using two-dimensional gel electrophoresis to investigate protein expression in METH abusers and control serum, CFH has been found to be stably up-regulated after chronic METH abuse/dependence [4]. Moreover, the up-regulation of CFH has also been reported in the serum and the ventral tegmental area and hippocampus (HPC) of the METH-induced conditioned place preference (CPP) rat, a model of chronic METH dependence [5], *via* ELISA and western blot [4]. Recently, the up-regulation of CFH was demonstrated in the serum and HPC of a mouse model of behavioral METH sensitization using ELISA and immunofluorescence, respectively [6]. However, the approaches using ELISA and western blot only reflect the expression changes of CHF indirectly. Alternatively, MALDI-MSI (matrix-assisted laser desorption ionization – mass spectrometry imaging) has been developed into a powerful molecular imaging method for simultaneous detection and characterization of the spatial distribution and relative abundance of various compounds, including proteins, peptides, lipids,

and metabolites, directly from the surface of biological tissue sections [7]. It has been applied to a wide range of research, for example, biology [7] and medical science [8]. Many reports have demonstrated that MALDI-MSI can provide direct evidence for both untargeted and targeted analysis [9, 10]. The investigation of CFH *via* MALDI-MSI is promising.

Here, we performed comparative analysis to study the relationship between CHF and METH abuse/dependence *via* both indirect and direct approaches. The detailed information of the materials and methods can be found in the supplemental file. According to the immunofluorescence results, acute METH exposure in cell cultures and animal experiments showed that acute METH treatment down-regulated the expression of CFH in the cell line and the rat HPC, while CFH up-regulation was detected *via* both immunofluorescence and MALDI-MSI in METH-induced CPP rat HPC. Moreover, CFH was up-regulated in METH abuser serum using ELISA again in this study, but a statistical difference was only found in the group with < 200 days of abstinence. Taken together, CFH showed opposite expression patterns under these two METH situations, indicating that CFH plays different roles after acute METH exposure and during chronic METH dependence. The successful *in situ* detection of the CFH fragment using MALDI-MSI can be helpful for mechanism research in future.

The cell line SH-SY5Y is a type of dopaminergic neuron that is commonly used for toxicology tests. Compared to the control, 0.1 mmol/L METH exposure did not affect the expression of CFH (Fig. 1A), but the fluorescent CFH signal in SH-SY5Y cells clearly decreased ($P < 0.05$), after 24 h incubation with 2 mmol/L METH (Fig. 1A). There was no difference between the two METH groups in CFH expression (Fig. 1A).

A description of the animal experiments can be found in the supplemental file. In the animal models, we focused on the HPC, which plays an important role in the establishment of memory and is a region of interest in studies of psychosis [11]. In the rat brain acutely exposed to METH, down-regulated CFH expression was found in CA1 (Fig. 1B), CA2/3 (Fig. 1C), and the dentate gyrus (DG) (Fig. 1D) 24 h after administration of 20 mg/kg METH. But the expression of CFH recovered to normal in these areas after 7 days (Fig. 1B–D).

In the METH-induced CPP model, the expression change of CFH was first analyzed *via* immunofluorescence. The expression of CFH in this model differed from that in the acute exposure model (Fig. 2). The CFH fluorescence signal increased in CA1 (Fig. 2A), CA2 (Fig. 2B), CA3 (Fig. 2C), and the DG (Fig. 2D), after establishment of the CPP model.

Then, the up-regulated expression of CFH was detected using MALDI-MSI (Fig. 2E). Due to the large molecular weight of CFH, a 155-kDa glycoprotein, it is difficult to directly map the whole CFH protein in rat brain using MALDI-MSI. Here, MALDI-MSI was used to detect the fragments of CFH after *in situ* enzyme digestion on brain slices as described in the supplemental methods. One peptide fragment (NGFYPATR, 925.479 m/z) generated from CFH was mapped (Fig. 2E) and confirmed by MALDI-TOF/TOF MS/MS (matrix-assisted laser desorption ionization – time of flight/time of flight – mass spectrometry/mass spectrometry) (Fig. 2E). The CFH signal was significantly higher in the HPC of METH-treated rats than in controls (Fig. 2E).

Furthermore, we measured the CFH concentration in serum from 54 METH abusers and 44 healthy controls using ELISA and found that the level in chronic METH abusers was significantly higher than that in the controls (Fig. 2F). Due to the unavailability of human samples at different stages of withdrawal, no previous reports have analyzed the effect of abstinence range on CFH expression. However, in order to explore how long the CFH expression changes last, we roughly divided the METH abusers into three groups (< 200 days, 210–365 days, > 365 days). In detail, up-regulated CFH was only evident in METH abusers within 200 days of the abstinence period, while there was no difference between the other abusers with > 210 days of abstinence and the controls (Fig. 2G).

Our previous research revealed a close relationship between CFH expression changes and METH dependence, especially in the HPC [4]. We used imaging techniques to investigate the changes of CFH expression in this study and found that CFH displayed opposite expression patterns under two different situations of METH administration: acute exposure and chronic dependence.

Down-regulation of CFH is generally associated with excessive inflammation, and miRNA-146a down-regulates the expression of CFH to initiate a cascade of inflammation in ROS-stressed human neural cells and in a rat model of chronic temporal lobe epilepsy [12]. Moreover, down-regulated expression of CFH has also been reported participated in the removal of apoptotic cells by binding to nucleosomes in ARPE-19 cells under oxidative stress [13]. METH activates dopaminergic neurons to acutely release a large amounts of dopamine, which leads to oxidative stress and neurotoxic effect [2]. In sum, the down-regulated expression of CFH in both the cell line acutely exposed to METH and rat the model was likely to be caused by the oxidative stress induced by METH administration. This expression change of CFH may indicate activation of the complement system by acute high-dose METH exposure. However, further investigation

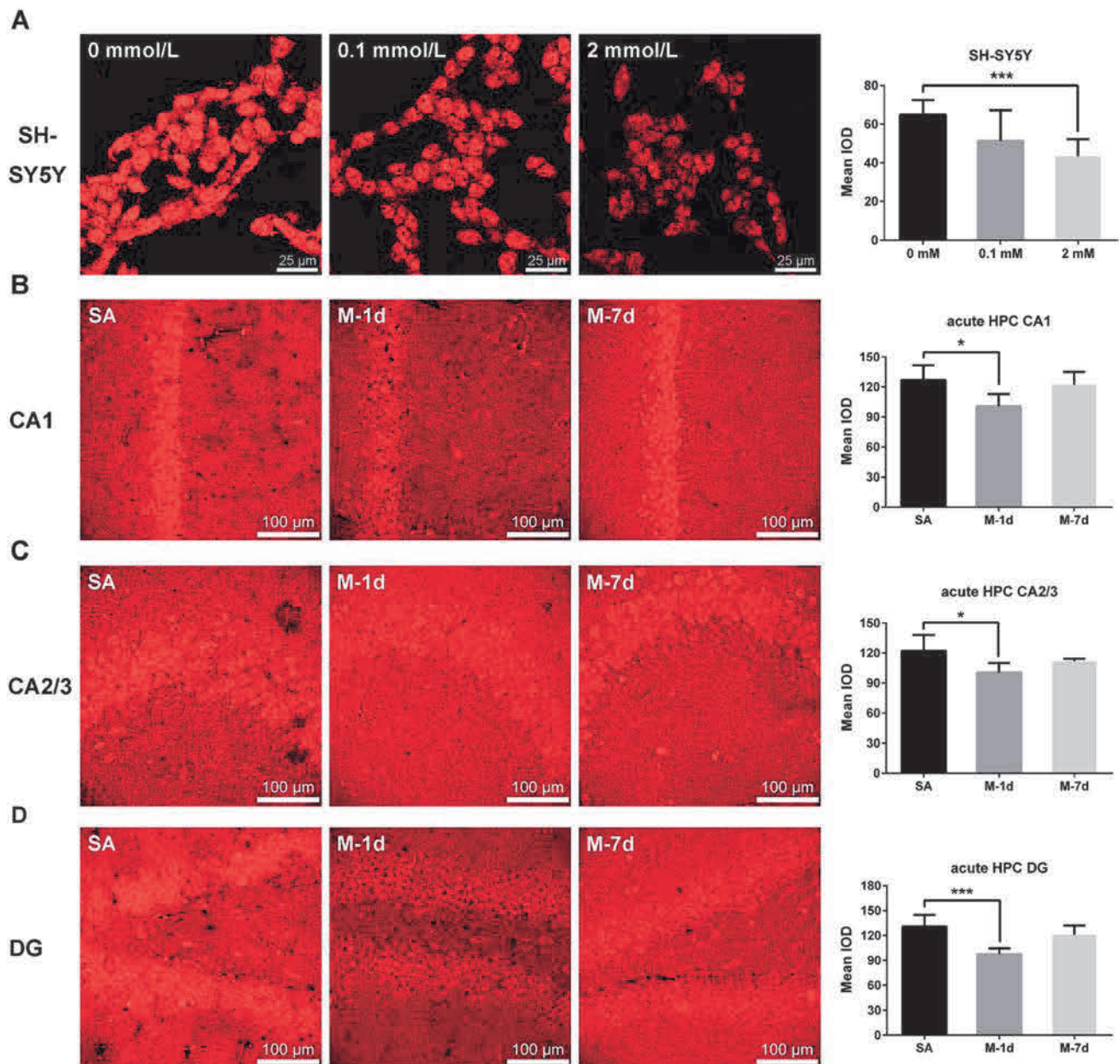


Fig. 1 Acute METH exposure induces down-regulation of CFH. **A** METH down-regulates CFH expression in SH-SY5Y cells (control, 64.96 ± 7.48 ; 0.1 mmol/L, 51.29 ± 15.94 ; 2 mmol/L, 43.34 ± 8.90). $n = 3$. **B** METH down-regulates CFH expression in CA1 of rats with acute METH exposure (SA, 126.9 ± 14.74 ; M-1d, 100.8 ± 12.07 ; M-7d, 122.5 ± 12.77). **C** METH down-regulates CFH expression in CA2/3 of rats with acute METH exposure (SA,

122.2 ± 15.87 ; M-1d, 100.5 ± 9.376 ; M-7d, 111.9 ± 2.337). **D** METH down-regulates CFH expression in the DG of rats with acute METH exposure (SA, 130.8 ± 14.08 ; M-1d, 97.42 ± 6.862 ; M-7d, 120.7 ± 11.30). SA, saline controls; M-1d, 24 h after 20 mg/kg METH; M-7d, 7 days after 20 mg/kg METH; SA and M-1d, $n = 4$; M-7d, $n = 3$; mean \pm SD; * $P < 0.05$, *** $P < 0.001$.

is required to test our hypothesis and to study the dynamic changes of CFH in this model to understand the mechanism of METH dependence.

The up-regulation of CFH detected by western blot in our previous study was confirmed here by *in situ* imaging of immunofluorescence and MALDI-MSI. The CPP rat is commonly used as a classic drug addiction model for the study of addiction-related memory establishment [5],

which is a result of context-induced retrieval of addiction memory [14]. HPC plays an important role in the formation of addiction by transferring short term to long term memory [15]. Along with the research that uncovered the role of the complement system in memory formation, we hypothesized that the CFH up-regulation in the HPC of the CPP rat is related to neuronal activity in context-induced memory retrieval. Anyway, much more work is needed to

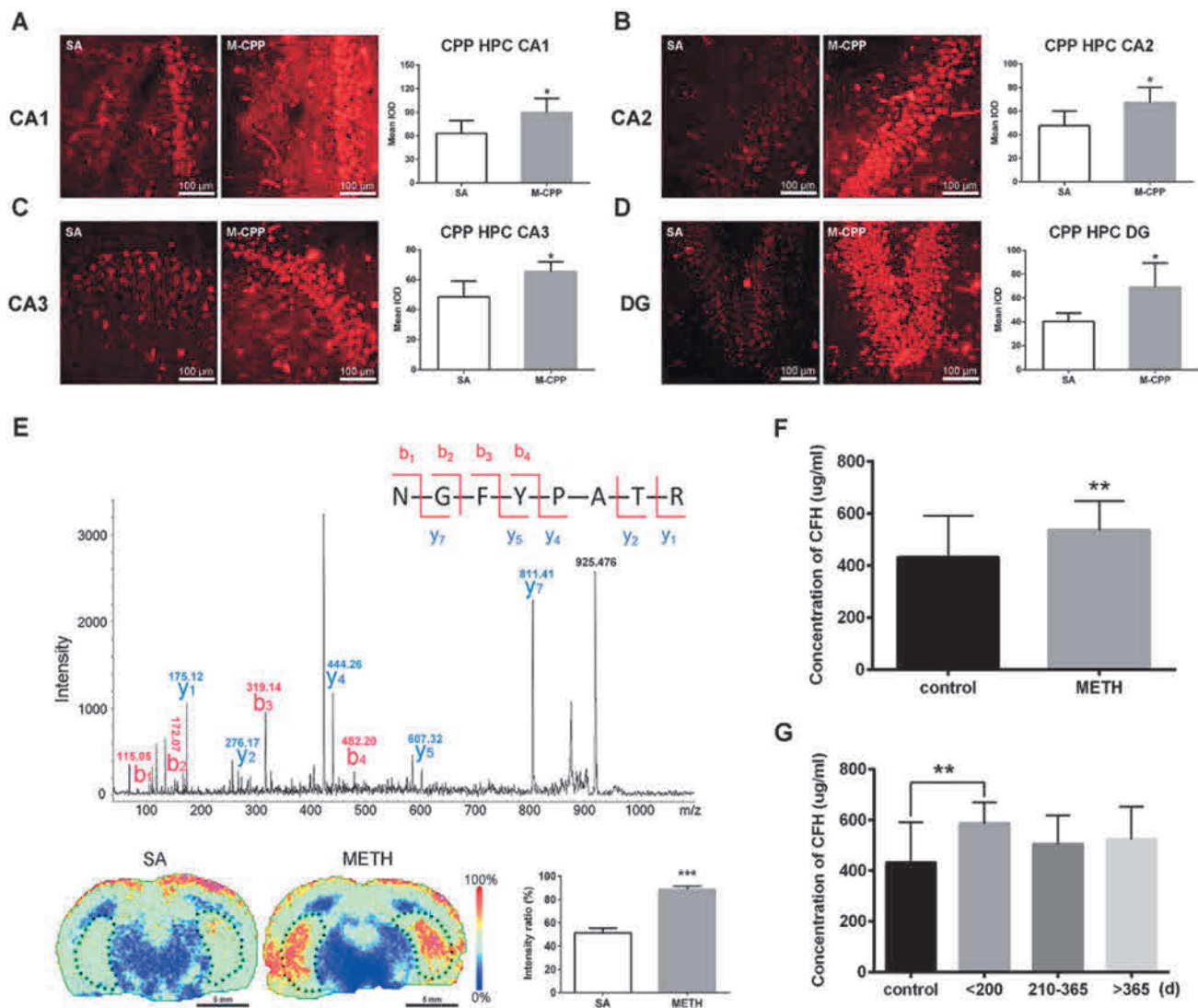


Fig. 2 Chronic METH dependence induces up-regulation of CFH. **A–D** METH up-regulates CFH expression in CA1 (**A**: SA, 63.22 ± 16.39 ; M-CPP, 89.66 ± 18.27), in CA2 (**B**: SA, 47.70 ± 10.80 ; M-CPP, 67.36 ± 12.95), in CA3 (**C**: SA, 48.40 ± 9.393 ; M-CPP, 65.46 ± 6.537), and in the DG (**D**: SA, 40.10 ± 6.307 ; M-CPP, 69.07 ± 20.29) of METH-induced CPP rats (SA, saline controls; M-CPP, METH-induced CPP rats; $n = 5$). **E** MALDI-MSI showing up-regulation of a CFH fragment

(NGFYPATR, 925.479 m/z) in the HPC of a METH-induced CPP rat ($n = 3$). **F** Up-regulation of CFH in the METH group ($n = 44$, $536.4 \pm 111.5 \mu\text{g/mL}$) versus controls ($n = 54$, $432.6 \pm 159.3 \mu\text{g/mL}$). **G** Up-regulation of CFH only occurs in the METH group within 200 days of abstinence ($n = 15$, $587.1 \pm 83.36 \mu\text{g/mL}$), but not at 210–365 days ($n = 21$, $504.9 \pm 113.7 \mu\text{g/mL}$) and > 365 days ($n = 8$, $523.8 \pm 129.9 \mu\text{g/mL}$) (mean \pm SD; * $P < 0.05$, ** $P < 0.01$, *** $P < 0.001$).

clarify the mechanism of CFH up-regulation after chronic METH dependence.

A high-quality antibody is needed to investigate the changes of CFH using immunohistochemistry, ELISA, or western blots. Among these methods, the intensities of color or fluorescent products are measured to reflect the content of specific targeted molecules of CFH. Obviously, the signals obtained *via* these immune-affinity methods are not detected directly from CFH. However, MALDI-MSI can directly detect the molecules of interest. The molecular weight of CFH is 155 kDa, which makes it hard to ionize

and map *via* MALDI-MSI, so we used an *in-situ* digestion strategy. The distribution of a peptide (NGFYPATR), a fragment of CFH, was successfully detected and mapped using MALDI-MSI. This is the first report of the successful detection of a CFH fragment in rat brain using MALDI-MSI, and this was also confirmed by MS/MS. This *in-situ*-digested peptide fragment had a direct mapping relationship with CHF. The changes of the fragment detected by MALDI-MSI directly reflected the level of intact CFH. Moreover, compared with traditional detection methods such as ELISA and western blots, MALDI-MSI can be

used to investigate the spatial distribution and relative abundance of various compounds simultaneously. The establishment of CFH mass spectrometry imaging is useful for further study of its function in METH dependence, and other CFH-related diseases.

We were unable to clarify the biological significance of different levels of CFH expression under different conditions in this study. But our findings revealed again the association between METH administration and CFH, and identified the different expression patterns of CFH under different METH situations for the first time. Acute METH exposure or long-term METH administration leads to the CFH down-regulation or up-regulation, respectively. There is no doubt that METH disturbs the expression of CFH, or even the whole complement system, and CFH plays different roles under the two situations studied here. The expression changes of CFH were associated with METH abuse/dependence, while the mechanism of action of CFH in METH dependence needs further research. MALDI-MSI provides a new way to study the expression and distribution of CFH *in situ*.

Acknowledgements This work was supported by the National Natural Science Foundation of China (81801364 and 81571354), the China Postdoctoral Science Foundation (2018M631277), and the Huayi Technology Innovation Center for Research Resources (HTIC P01 RR2018001M). We are grateful to all the participants in this study. We thank Zhenfeng Dai and Xi Liu for the collection of human serum.

Conflict of interest The authors claim that there are no conflicts of interest.

References

- Liang Q, Lin J, Yang J, Li X, Chen Y, Meng X, *et al.* Intervention effect of repetitive TMS on behavioral adjustment after error commission in long-term methamphetamine addicts: evidence from a two-choice oddball task. *Neurosci Bull* 2018, 34: 449–456.
- Moratalla R, Khairnar A, Simola N, Granado N, Garcia-Montes JR, Porceddu PF, *et al.* Amphetamine-related drugs neurotoxicity in humans and in experimental animals: main mechanisms. *Prog Neurobiol* 2017, 155: 149–170.
- Parente R, Clark SJ, Inforzato A, Day AJ. Complement factor H in host defense and immune evasion. *Cell Mol Life Sci* 2017, 74: 1605–1624.
- Shi WL, Zhao X, Liu ZM, Zhang M, Zhou BY, Pu XP. Serum proteomics of methamphetamine addicts and up-regulation of complement factor H related to methamphetamine addiction. *Neurosci Lett* 2012, 525: 23–28.
- Xue YX, Deng JH, Chen YY, Zhang LB, Wu P, Huang GD, *et al.* Effect of selective inhibition of reactivated nicotine-associated memories with propranolol on nicotine craving. *JAMA Psychiatry* 2017, 74: 224–232.
- Xu J, Zhang Z, Liu R, Sun Y, Liu H, Nie Z, *et al.* Function of complement factor H and imaging of small molecules by MALDI-MSI in a methamphetamine behavioral sensitization model. *Behav Brain Res* 2019, 364: 233–244.
- He H, Qin L, Zhang Y, Han M, Li J, Liu Y, *et al.* 3,4-Dimethoxycinnamic acid as a novel matrix for enhanced *in situ* detection and imaging of low-molecular-weight compounds in biological tissues by MALDI-MSI. *Anal Chem* 2019, 91: 2634–2643.
- Wang X, Han J, Hardie DB, Yang J, Borchers CH. The use of matrix coating assisted by an electric field (MCAEF) to enhance mass spectrometric imaging of human prostate cancer biomarkers. *J Mass Spectrom* 2016, 51: 86–95.
- Tucker LH, Hamm GR, Sargeant RJE, Goodwin RJA, Mackay CL, Campbell CJ, *et al.* Untargeted metabolite mapping in 3D cell culture models using high spectral resolution FT-ICR mass spectrometry imaging. *Anal Chem* 2019, 91: 9522–9529.
- Liu Y, Chen L, Qin L, Han M, Li J, Luo F, *et al.* Enhanced *in situ* detection and imaging of lipids in biological tissues by using 2,3-dicyanohydroquinone as a novel matrix for positive-ion MALDI-MS imaging. *Chem Commun (Camb)* 2019, 55: 12559–12562.
- Luo H, Liu Z, Liu B, Li H, Yang Y, Xu ZD. Virus-mediated overexpression of ETS-1 in the ventral hippocampus counteracts depression-like behaviors in rats. *Neurosci Bull* 2019, 35: 1035–1044.
- Pogue AI, Li YY, Cui JG, Zhao Y, Kruck TP, Percy ME, *et al.* Characterization of an NF-kappaB-regulated, miRNA-146a-mediated down-regulation of complement factor H (CFH) in metal-sulfate-stressed human brain cells. *J Inorg Biochem* 2009, 103: 1591–1595.
- Marazita MC, Dugour A, Marquioni-Ramella MD, Figueroa JM, Suburo AM. Oxidative stress-induced premature senescence dysregulates VEGF and CFH expression in retinal pigment epithelial cells: implications for age-related macular degeneration. *Redox Biol* 2016, 7: 78–87.
- Wang X, Liu Y, Jia M, Sun X, Wang N, Li Y, *et al.* Phosphorylated SNAP25 in the CA1 regulates morphine-associated contextual memory retrieval via increasing GluN2B-NMDAR surface localization. *Addict Biol* 2018, 23: 1067–1078.
- Lv XF, Sun LL, Cui CL, Han JS. NAc shell Arc/Arg3.1 protein mediates reconsolidation of morphine CPP by increased GluR1 cell surface expression: activation of ERK-coupled CREB is required. *Int J Neuropsychopharmacol* 2015, 18: 1–10.



Image-Forming Visual Basis of Empathy for Pain in Mice

Kai-Wen Geng^{1,2,4,5} · Rui Du^{1,2} · Na Wei^{1,2} · Chun-Li Li^{1,2} · Yan Wang^{1,2} · Wei Sun^{1,2} · Tao Chen³ · Dong-Yu Wei³ · Yang Yu^{1,2} · Ting He^{1,2} · Wen-Jun Luo^{1,2} · Rui-Rui Wang^{1,2} · Zhou-Feng Chen^{4,5,6,7} · Jun Chen^{1,2}

Received: 3 February 2020 / Accepted: 8 March 2020 / Published online: 20 June 2020
© Shanghai Institutes for Biological Sciences, CAS 2020

Dear Editor,

Empathy for distress refers to the highly evolutionarily-conserved ability of humans and other social animals to feel, recognize, and understand others' painful conditions (pain, fear, and catastrophe) [1, 2] and even benefit others by releasing distress through sharing, caring, and cooperation [1]. In the past decade, several types of lower empathic response have been gradually identified and characterized in laboratory rodents (rats and mice), referred to as empathic contagious pain [3–5], observational fear learning [2], and contagious itch [6]. Moreover, empathic consolation with allogrooming and/or allogrooming toward the injury site and/or the body or head of a distressed conspecific, a much higher form of empathy, has also been

identified in observers of both laboratory rodents [4, 5] and prairie voles [7] during social interactions.

Empathy for distress is a complicated process that may involve multiple sensory modalities. However, in human neuroimaging studies, it has been demonstrated that visual cue-based images of pain-like hurting can cause increased neuronal activity in the anterior cingulate cortex (ACC), which is known to be a critical region associated with empathy for pain, in witness subjects [8]. These results strongly imply that visual information plays a critical role in the development of empathy in humans. Furthermore, some studies have also demonstrated that visual cues play a principal role in both contagious pain [3, 5] and contagious itch [6]. However, sensory sources other than visual input have also been suggested in relation to the social transfer of pain although the experimental paradigm used was quite different from the above [9]. Nonetheless, direct experimental evidence was not provided by either of the above studies associated with sensory inputs required for empathy for pain.

The visual system is generally considered to perform two major functions: an image-forming visual (IFV)

Kai-Wen Geng, Rui Du and Na Wei have contributed equally to this work.

Electronic supplementary material The online version of this article (<https://doi.org/10.1007/s12264-020-00528-0>) contains supplementary material, which is available to authorized users.

✉ Jun Chen
junchen@fmmu.edu.cn

✉ Zhou-Feng Chen
chenz@wustl.edu

¹ Institute for Biomedical Sciences of Pain, Tangdu Hospital, The Fourth Military Medical University, Xi'an 710038, China

² Key Laboratory of Brain Stress and Behavior, People's Liberation Army, Xi'an 710038, China

³ Center of Clinical Aerospace Medicine, The Fourth Military Medical University, Xi'an 710032, China

⁴ Center for the Study of Itch, Washington University School of Medicine, St. Louis, MO 63110, USA

⁵ Department of Anesthesiology, Washington University School of Medicine, St. Louis, MO 63110, USA

⁶ Department of Psychiatry, Washington University School of Medicine, St. Louis, MO 63110, USA

⁷ Department of Developmental Biology, Washington University School of Medicine, St. Louis, MO 63110, USA

function [10] and a non-image-forming visual (NIFV) function [11]. The IFV function (patterned vision) is mainly mediated by the classical visual pathway from rod and cone photoreceptors to retinal ganglion cells and then to higher brain structures (retinogeniculate–V1 cortex) [10], while the NIFV function is mainly mediated by intrinsically photosensitive retinal ganglion cells (ipRGCs) which express the photopigment melanopsin and send projections to the superior chiasmatic nucleus of the hypothalamus (SCN) and participate in regulation of the circadian rhythm but not IFV function [11]. However, some recent findings in rodents suggest that ipRGCs are involved in spatial vision and brightness discrimination when rod and cone photoreceptors are lost [11–13]. In one line of evidence, observational contagious itch behavior has been shown to be mediated by gastrin-releasing peptide and its receptor in the SCN that may involve the ipRGC–SCN pathway [6]. Thus, both the retinogeniculate–V1 and the ipRGC–SCN pathways may be primarily involved in encoding social information that is finally sent to higher-order cortical visual areas and other cerebral cortical areas (such as the ACC and insular cortex) to motivate empathy for distress [6, 8, 10–14]. Accordingly, to address whether and how the visual system is involved in the induction of empathy for pain, we examined the roles of both the IFV and NIFV systems using a mouse model of empathy for pain in which both empathic observational contagious pain (OCP) and consolation behavior could be qualitatively identified and quantitatively rated in the mouse observer during and after social interaction with a familiar conspecific in pain [4]. The mouse observers used in this study had visual deficits due to experimental ablation of rod and cone photoreceptors of melanopsin-containing ipRGCs.

In this study, adult male C57BL/6J mice (7–14 weeks old) were used in all experiments. Bilateral intravitreal injections of N-methyl-N-nitrosourea (MNU) or saline were performed to ablate IFV functions through rod and cone photoreceptor degeneration, while melanopsin-saporin (Mel-sap) or control IgG-sap was injected to ablate NIFV functions through ablation of the melanopsin-containing ipRGCs (see Supplementary Methods for details). The experimental paradigm, procedures, and techniques for the establishment and quantitative assessment of the mouse model of empathy for pain have recently been published [4] and the specifications for this study are also provided in the Supplementary Methods.

We first investigated the effects of retinal photoreceptor ablation on the consolation behavior and the results showed that the total time and bouts of allogrooming and allolicking (AGAL) behavior were significantly reduced, along with prolongation of the latency in the MNU-treated observers compared with vehicle controls (Fig. 1A, C, D, Tables S1 and S3). It was also revealed that the significant

reduction of AGAL behaviors occurred distinctly in the first 15-min period of the time course (Fig. 1B, Table S2). However, in contrast, no significant difference was found in the total time and bouts of mouth-sniffing (MS), tail-sniffing (TS), and self-grooming (SG) between the MNU-treated and vehicle control although differences in latency were found in TS and SG (Fig. 1A, C, D, Tables S1 and S3). Then we assessed the effects on OCP behavior and found that the MNU-treated observers did not show any changes in mechanical threshold 1, 2, 4, and 8 h after 30-min priming dyadic social interaction (PDSI) compared to the baseline threshold. However, the vehicle-treated observers did show a distinct and significant reduction in mechanical threshold at 1 and 2 h after the PDSI (Fig. 1E, F, Tables S2 and S4). Electroretinography (ERG) showed complete loss of the waveforms evoked by scotopic and photopic stimuli in the MNU-treated observers, while the waveforms remained intact in both intact and vehicle-treated observers (Fig. 1G–I, Table S1). Moreover, the retinal hematoxylin/eosin (HE) staining showed complete loss of the outer nuclear layer (ONL), outer plexiform layer, and inner and outer segments in the MNU-treated observers, while these layers remained intact in both intact and vehicle-treated observers (Fig. 1J). The ONL/inner nuclear layer (INL) ratio was significantly lower in the MNU-treated than in the intact and vehicle-treated observers (Fig. 1K, Table S1). We also examined the effects of darkness on the consolation behavior and OCP in observers with intact IFV functions, and found complete loss of the OCP and reduction of the total time in AGAL in darkness, although latency and bouts were not significantly different from observers with intact IFV functions in the light (Tables S3 and S4).

No significant changes were revealed in the total time, time course, bouts, and latency of AGAL, MS, TS, and SG between observers treated with Mel-sap and IgG-sap (Fig. 2A–D, Tables S1 and S2). Moreover, the 8-h time course measurements showed a parallel and overlapping change (reduction and recovery) in mechanical threshold after the PDSI in observers treated with Mel-sap and IgG-sap (Fig. 2E, F, Table S2). Melanopsin immunohistochemical labeling showed almost complete loss of ipRGCs in the Mel-sap-treated observers, while they remained unchanged in both intact and IgG-sap control (Fig. 2G, H, Table S1). Meanwhile, retinal HE staining and the ONL/INL ratio showed no difference in retinal histological organization between Mel-sap- and IgG-sap-treated and intact observers (Fig. 2I, J, Table S1).

Here, we used the chemical lesion approach to investigate the potential roles of the two visual pathways in the development of empathy for pain. Our results indicated that the observers deprived of rod and cone photoreceptors behaved abnormally in both the empathic contagious pain

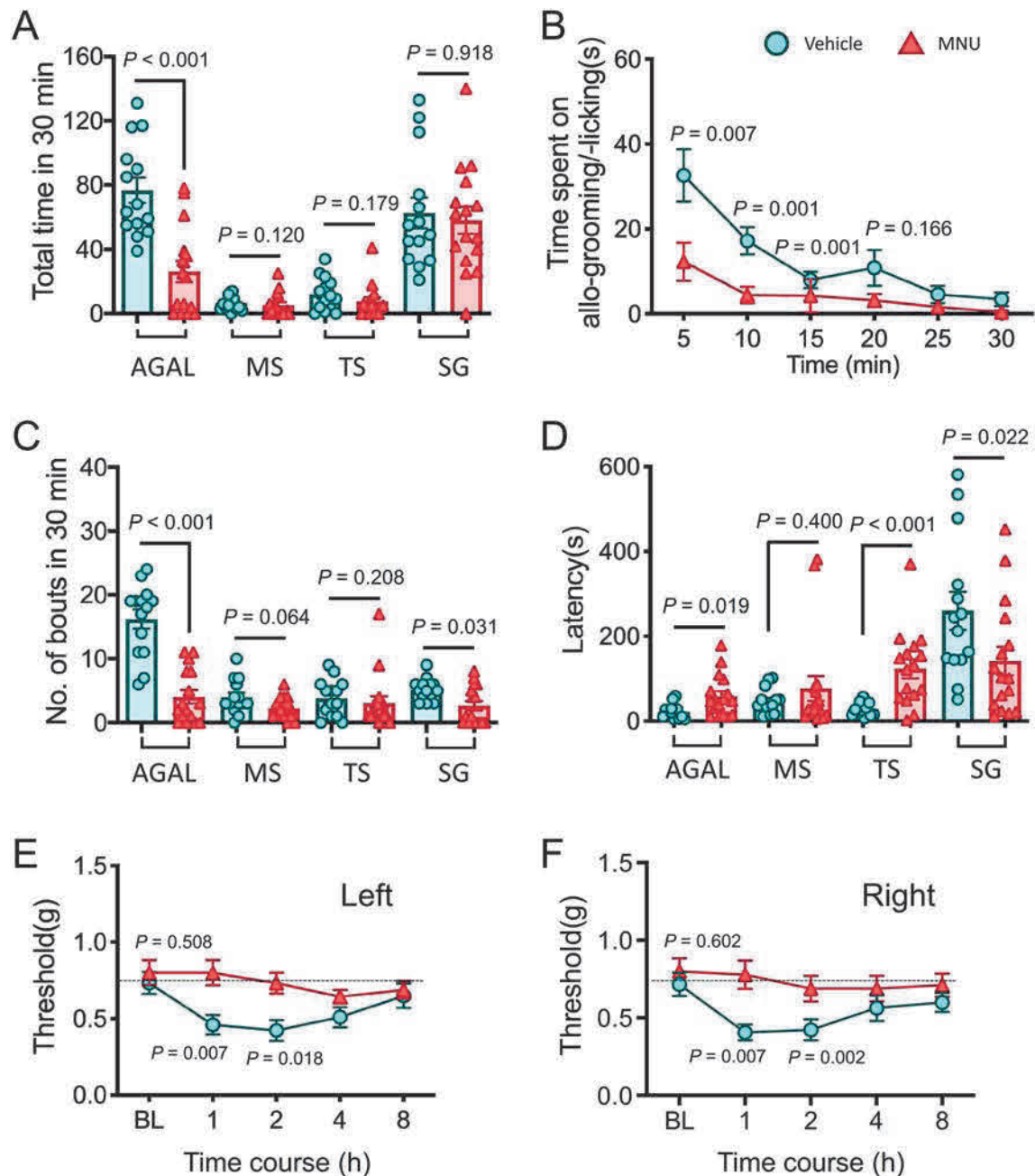


Fig. 1 Both consolation behavior and observational contagious pain are impaired in mouse observers with an image-forming visual deficit caused by ablation of rods and cones with MNU. **A–D** Total time, time course, number of bouts, and latency of allogrooming and allolicking (AGAL), mouth-sniffing (MS), tail-sniffing (TS), and self-grooming (SG) behaviors during 30-min dyadic social interaction with a familiar conspecific in pain. **E, F** Time courses of paw-withdrawal mechanical threshold in MNU-treated and vehicle-treated observers after the dyadic social interaction. **G** Representative scotopic and photopic waveforms from intact, vehicle- and MNU-treated observers. **H, I** B-wave amplitudes of scotopic and photopic waveforms in intact, vehicle- and MNU-treated

observers. **J** Representative images of retinal HE staining of intact, vehicle- and MNU-treated observers. **K** ONL/INL ratios of intact, vehicle- and MNU-treated observers. Mean \pm SEM, two-tailed Mann-Whitney *U*-test for **A** and **C–F**; two-way ANOVA RM with Bonferroni *post hoc* correction for **B**; Kruskal-Wallis one-way ANOVA with Bonferroni *post hoc* correction for **H** and **K**; and one-way ANOVA with Bonferroni *post hoc* correction for **I**; details in **Tables S1, 2**. ns, not significant. GCL, ganglionic cell layer; INL, inner nuclear layer; IPL, inner plexiform layer; IS, inner segment; ONL, outer nuclear layer; OPL, outer plexiform layer; OS, outer segment.

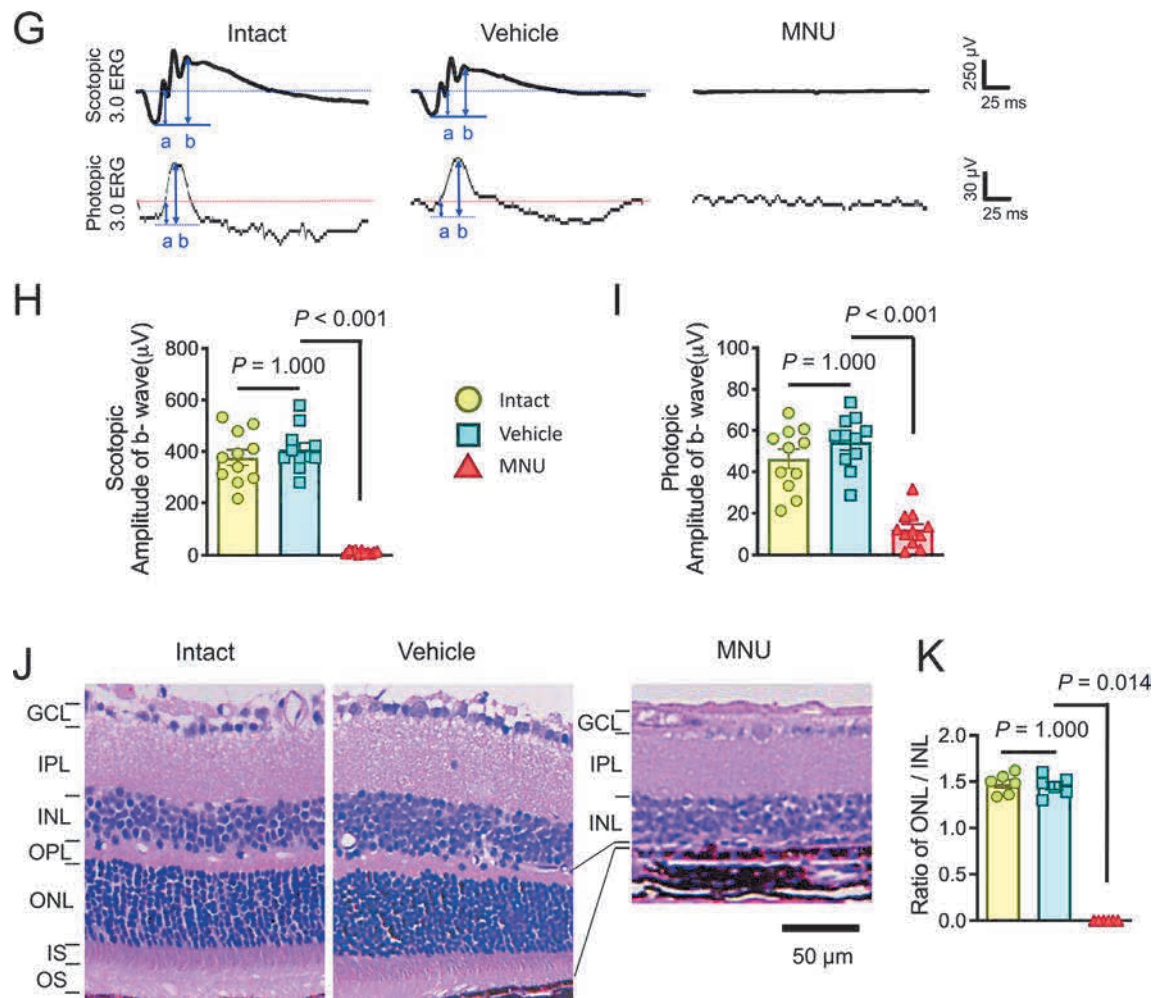


Fig. 1 continued

and consolation tests, while other general social (MS and TS) and nonsocial (self-grooming) behaviors remained almost intact. In contrast, the observers lacking ipRGCs did not show any differences from controls in either empathic contagious pain or consolation behavior.

Empathy has been proposed to be hierarchical in mammals according to the Russian-doll model, including the lower stage (emotional contagion and motor imitation), the intermediate stage (empathic concern and consolation), and the highest stage (perspective-taking, theory of mind, and targeted help) [1]. Thus, the empathic OCP and consolation experimentally observed in rodents [3–5] are theoretically assigned to the lower and intermediate stages, respectively. For emotional contagion, especially that of pain, visual cue-based information is essential to activate the neuronal activity of empathy representation in the brain (e.g., the ACC) in humans [8]. This implies that vicariously-felt pain can be obtained through the activation of brain regions related to negative emotions by visual inputs in humans. Similarly, several studies in rodents have shown

that preventing visual cues by an opaque partition, inactivation of the ACC, or chemical lesioning of the medial prefrontal cortex (mPFC) significantly reduce the emotional contagion induced by the observation of conspecifics in pain [2, 3, 5]. More notably, a recent study has identified emotional mirror neurons in the rat ACC and found most of them respond to both experiencing and witnessing pain [15]. These emotional mirror neurons in the ACC of a rat observer respond maximally to salient jumping behavior, a dramatic pain response, of the demonstrator, which further supports the involvement of visual cues in the empathy for pain response [15]. As for consolation in rodents, there is much less literature discussing the potential sensory input modalities, only one study reporting that the ACC, apart from its engagement in pain contagion, also plays a crucial role in mediating consolation behavior [7]. In consideration of this, it is highly likely that visual functions are involved in pain-associated empathic consolation behavior. In the current study, we provide strong evidence supporting

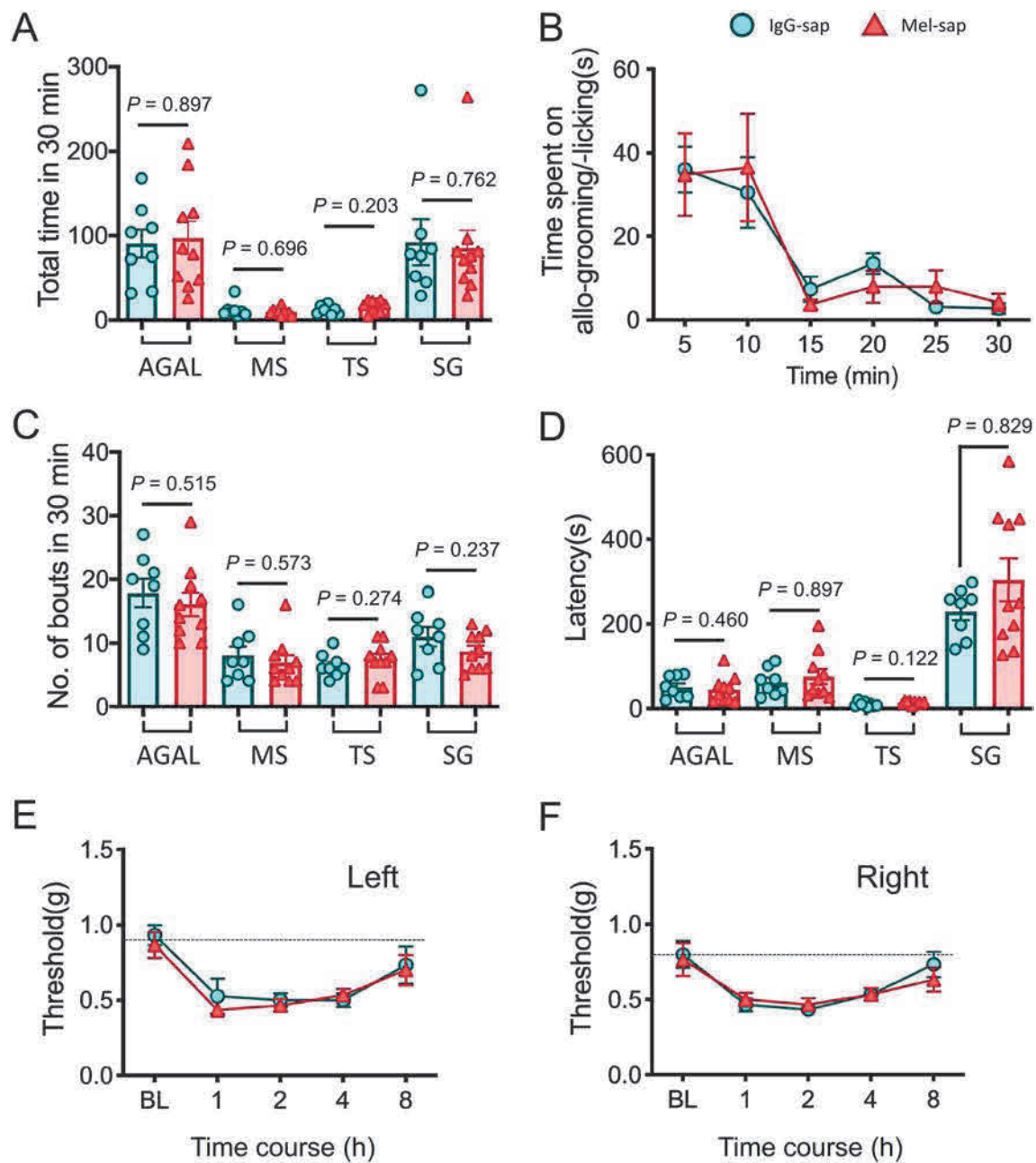


Fig. 2 Neither consolation behavior nor observational contagious pain is affected in mouse observers with deficient non-image-forming visual function caused by ablation of melanopsin-containing, intrinsically photosensitive retinal ganglion cells with intravitreal injection of melanopsin-saporin (Mel-sap). **A–D** Total time, time course, number of bouts, and latency of allogrooming and allolicking (AGAL), mouth-sniffing (MS), tail-sniffing (TS), and self-grooming (SG) behaviors during 30-min dyadic social interaction with a familiar conspecific in pain in observers with Mel-sap and IgG-sap controls. **E, F** Time courses of paw-withdrawal mechanical threshold after the dyadic social interaction in observers with Mel-sap and IgG-sap controls. **G** Immunohistochemical labeling of melanopsin-

positive retinal ganglion (MPRG) neurons is successfully ablated in observers with Mel-sap, while those of intact and IgG-sap-treated observers remain intact. **H** Numbers of MPRG neurons in observers of the intact, IgG-sap- and Mel-sap-treated groups. **I** Representative images of retinal HE staining in observers of intact, IgG-sap- and Mel-sap-treated groups. **J** ONL/INL ratios in observers of intact, IgG-sap- and Mel-sap-treated groups. Mean \pm SEM, two-tailed *t*-test for **A, C, and D**; two-way ANOVA RM with Bonferroni *post hoc* correction for **B, E, and F**; Kruskal-Wallis one-way ANOVA test with Bonferroni *post hoc* comparison for **H**; and one-way ANOVA with Bonferroni *post hoc* comparison for **J**; details in **Tables S1 and S2**; ns, not significant. Abbreviations as in Fig. 1.

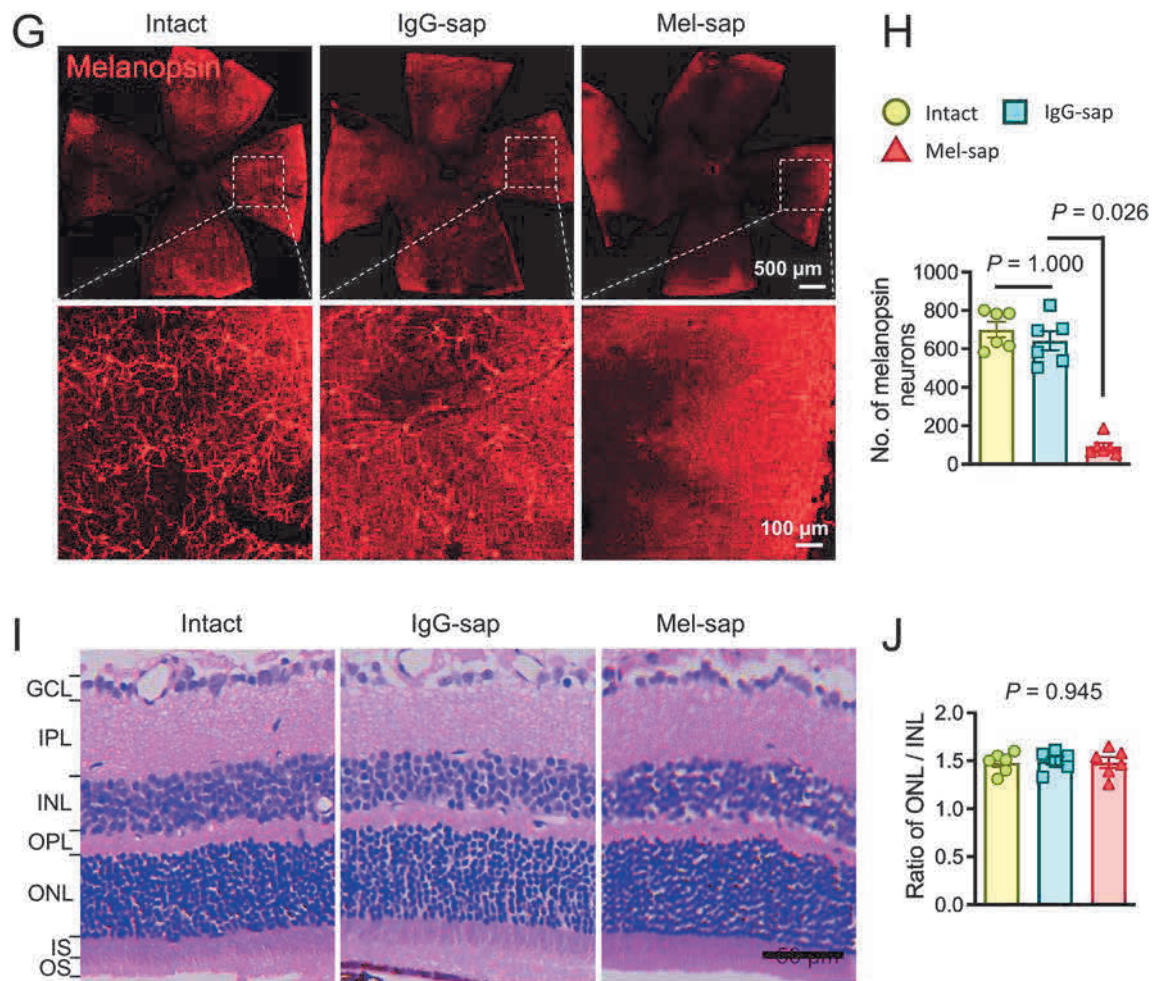


Fig. 2 continued

direct involvement of the IFV, but not the NIFV, pathway in the mediation of both empathic OCP and consolation in mouse observers.

Is vision the only sensory source for mediating empathy for pain? In a previous study [3], the authors investigated the roles of visual, olfactory, and auditory sensory inputs in the social contagion of pain by chemical lesioning of auditory or olfactory afferents, or by an opaque partition separating the dyadic mice from the visual cue-based social interaction. The results showed that only visual blockade eliminates the emotional contagion of pain [3]. However, a debate has been raised by another report showing potential involvement of olfactory cues in the social transfer of pain from conspecifics with chronic pain to bystander mice [9]. The experimental paradigm designed for that study was that mice were not allowed to socially interact in a physical contact environment, but instead, they were housed and tested in the same bedding space in which conspecifics with inflammatory or morphine/alcohol withdrawal pain had been housed. Moreover, at least 24 h of exposure to the

bedding from hyperalgesic mice was shown to be essential for the social transfer of pain to bystander mice, implying the potential involvement of an olfactory mechanism as well [9]. In our current study, the empathic OCP was completely eliminated in observers with an IFV functional deficit by ablating both rod and cone photoreceptors that had been confirmed by both ERG and retinal histology, fully supporting the role of visual information in the induction of empathic OCP. The current results of the darkness test in observers with intact IFV functions also supported the above conclusion. As another line of evidence, we have previously demonstrated that the timing of social transfer of pain is dependent on the visual salience of pain expression in the demonstrators [5]. Namely, the more visually salient the pain-related behavior (e.g., injured paw flinching, licking, and lifting) produced in the demonstrators (e.g., by intraplantar injection of bee venom or formalin), the earlier and easier the OCP can be identified in the observers. In sharp contrast, demonstrators without visually salient pain-related behaviors in models

such as complete Freud's adjuvant and spared nerve injury (only with evoked hyperalgesia) are not effective in inducing OCP in observers after initial 30-min PDSI but are effective after long-term co-housing of dyads for several days [5]. We still do not know what happens in the long-term co-housing paradigm due to the lack of time-consuming VCR recordings and shortage of experimental data from tests of observers with the IFV deficit. Nonetheless, based on the results of our current study, it can be concluded that visual cue-based information is the primary sensory input for observers to perceive the pain of others in a social physical contact paradigm.

Regarding the sensory inputs for induction of consolation behaviors, so far no data are available. In our current study, we found that the observers' AGAL behaviors toward a distressed conspecific were greatly reduced by chemical ablation of rods and cones; however, the effect was not complete due to minimal remaining behavior. This suggests that the consoling behavior of observers is predominantly driven by immediate/early visual cues (the first glance) of the demonstrator's injury and painful signs that later help recruit other sensory inputs. This assumption is fully supported by the results of our more recent study in both naive mouse and rat observers [4]. Namely, the latency for an observer to perform AGAL behaviors toward a distressed conspecific is much shorter than that for olfaction-based MS and TS (Tables S1 and S2) [4]. Taken together with our current results of the darkness test, we conclude that, unlike the OCP, consolation behavior may also require other sensory information besides visual cues to engage AGAL behaviors.

Which visual input pathway is involved? Rods, cones, and ipRGCs are the three major types of photoreceptive neurons in the retina, and primarily implement IFV functions (patterned vision) and NIFV functions (circadian photoentrainment and pupillary reflexes) [10–13]. Since it has recently been noted that rods and cones can signal light information through ipRGCs to the brain due to functional heterogeneity of the five subtypes of ipRGC [11–13], it becomes intriguing to determine whether the ipRGC–SCN pathway plays a role in the induction of empathy for pain. Here, we demonstrated that social distress information passes through the classical IFV pathway, not the melanopsin-containing ipRGC pathway, to induce empathic responses in the brain. Future efforts are needed to identify which population of conventional RGCs and which level of the retinogeniculate–V1–higher-order cortical visual areas pathway are involved in the induction of empathy for pain, finally dissecting the underlying structural and functional interconnectivity between visual input and other higher cortical regions (e.g., the mPFC and insular cortex) for the development of empathic responses at the molecular, cellular, and circuit levels [14].

In summary, the present study revealed that the IFV system is essential for driving empathic consoling behaviors as well as empathic OCP in mouse observers witnessing a conspecific in pain.

Acknowledgments We are grateful to YQ Yu, YJ Yin, Y Yang, and F Yang for cooperation and XL Wang for animal support. This work was supported by grants from the National Natural Science Foundation of China (81571072 and 31600855) and the Military Laboratory Animal Project (SYDW[2017]14 and SYDW[2018]07).

Conflict of interest The authors have no conflicts of interest to declare.

References

1. de Waal FBM, Preston SD. Mammalian empathy: behavioural manifestations and neural basis. *Nat Rev Neurosci* 2017, 18: 498–509.
2. Chen J. Empathy for distress in humans and rodents. *Neurosci Bull* 2018, 34: 216–236.
3. Langford DJ, Crager SE, Shehzad Z, Smith SB, Sotocinal SG, Levenstadt JS, *et al.* Social modulation of pain as evidence for empathy in mice. *Science* 2006, 312: 1967–1970.
4. Du R, Luo WJ, Geng KW, Li CL, Yu Y, Wei N, *et al.* Empathic contagious pain and consolation in laboratory rodents: species and sex comparisons. *Neurosci Bull* 2020. <https://doi.org/10.1007/s12264-020-00465-y>.
5. Li CL, Yu Y, He T, Wang RR, Geng KW, Du R, *et al.* Validating rat model of empathy for pain: effects of pain expressions in social partners. *Front Behav Neurosci* 2018, 12: 242.
6. Yu YQ, Barry DM, Hao Y, Liu XT, Chen ZF. Molecular and neural basis of contagious itch behavior in mice. *Science* 2017, 355: 1072–1076.
7. Burkett JP, Andari E, Johnson ZV, Curry DC, de Waal FBM, Young LJ. Oxytocin-dependent consolation behavior in rodents. *Science* 2016, 351: 375–378.
8. Lamm C, Decety J, Singer T. Meta-analytic evidence for common and distinct neural networks associated with directly experienced pain and empathy for pain. *Neuroimage* 2011, 54: 2492–2502.
9. Smith ML, Hostetler CM, Heinricher MM, Ryabinin AE. Social transfer of pain in mice. *Sci Adv* 2016, 2: e1600855.
10. Grimes WN, Songco-Aguas A, Rieke F. Parallel processing of rod and cone signals: retinal function and human perception. *Annu Rev Vis Sci* 2018, 4: 123–141.
11. Spitschan M, Lucas RJ, Brown TM. Chromatic clocks: color opponency in non-image-forming visual functions. *Neurosci Biobehav Rev* 2017, 78: 24–33.
12. Allen AE, Storchi R, Martial FP, Bedford RA, Lucas RJ. Melanopsin contributions to the representation of images in the early visual system. *Curr Biol* 2017, 27: 1623–1632.e4.
13. Sonoda T, Lee SK, Birnbaumer L, Schmidt TM. Melanopsin phototransduction is repurposed by ipRGC subtypes to shape the function of distinct visual circuits. *Neuron* 2018, 99: 754–767.e4.
14. Glickfeld LL, Olsen SR. Higher-order areas of the mouse visual cortex. *Annu Rev Vis Sci* 2017, 3: 251–273.
15. Carrillo M, Han YY, Migliorati F, Liu M, Gazzola V, Keysers C. Emotional mirror neurons in the rat's anterior cingulate cortex. *Curr Biol* 2019, 29: 1301–1312.e6.



RESEARCH HIGHLIGHT

New Insights into the Dysfunctions of Pericytes and Neurovascular Units in Neurodegenerative Diseases

Qiang Liu¹ · Wei-Jye Lin² · Yamei Tang¹

Received: 4 March 2020 / Accepted: 30 April 2020 / Published online: 3 August 2020
© Shanghai Institutes for Biological Sciences, CAS 2020

The neurovascular unit (NVU) is an essential anatomical and physiological entity for the maintenance of brain homeostasis and function; it is composed of endothelial cells, pericytes, astrocytes, neurons, vascular smooth muscle cells, microglia, and oligodendroglia [1]. The NVU regulates important brain vessel properties such as the integrity of the blood-brain barrier (BBB) and cerebral blood flow (CBF). Considerable efforts have been made to investigate the cerebral microcirculatory dysfunction in ageing and Alzheimer's disease (AD) [2].

Pericytes are perivascular mural cells that wrap processes around and along brain capillaries. They have come into focus in recent years for their regulatory roles in cerebrovascular integrity and CBF [3, 4]. Dysfunction or ablation of pericytes results in a series of pathological changes, including reduced pericyte coverage of the capillary wall, capillary constriction, BBB leakage, white matter dysfunction, synaptic loss, neuronal degeneration, and cognitive deficits [3–5]. Pericyte degeneration leads to metabolic stress, neurovascular uncoupling, and impaired neuronal excitability [6]. Moreover, pericyte loss reduces the clearance of A β peptides from brain interstitial fluid and accelerates amyloid angiopathy and cerebral amyloidosis in mouse models of AD [7].

Although there is increasing evidence of a tight relationship between pericytes and neurovascular endothelial cells in BBB function, the regulatory roles of pericytes in AD and other neurodegenerative diseases remained largely unknown. Recently, two studies have revealed the emerging links between pericytes, NVUs, and neurodegeneration, in which pericytes are involved in oligomeric A β -induced cerebral vascular constriction and CBF reduction, and pericyte-derived pleiotrophin (PTN) is identified as a neurotrophic factor required for neuronal survival and cognitive functions [8, 9].

Using two-photon *in vivo* microscopy and acute brain slices to directly visualize and measure vascular changes in the brain, Attwell and colleagues from University College London have demonstrated that oligomeric A β alters CBF and neurovascular coupling at the very early stages of AD progression [8]. They measured the diameters of cerebral capillaries near the pericyte soma in humans and mice that had shown the pathological hallmark of AD (A β deposition). Their results revealed the surprising fact that, in human patients depositing A β and tau, the cerebral capillaries were constricted specifically at pericyte locations. In biopsies of living AD patients' brains, the capillary diameters at pericyte locations were significantly smaller than at a distance from the pericyte soma. Moreover, increased accumulation of A β was associated with greater constriction of the capillaries. The same constriction was found in a mouse model of AD, in which capillaries in the cerebellum, which lacks A β deposition, were not constricted, suggesting that A β may trigger the constriction. This constriction was predicted to reduce CBF by ~50% in the AD mice, similar to the 42% decrease in the gray matter of AD patients.

To determine whether A β is mechanistically associated with this phenomenon, live cortical slices, resected from

✉ Yamei Tang
tangym@mail.sysu.edu.cn

¹ Department of Neurology, Sun Yat-Sen Memorial Hospital, Sun Yat-Sen University, Guangzhou 510120, China

² Guangdong Provincial Key Laboratory of Malignant Tumor Epigenetics and Gene Regulation, Medical Research Center, Sun Yat-Sen Memorial Hospital, Sun Yat-Sen University, Guangzhou 510120, China

glioma patients who underwent surgery to remove tumors, were used to study the acute effects of A β . When oligomeric A β (a soluble species of A β found in AD brains that correlates better with cognitive decline than amyloid plaques) was applied to the capillaries in these slices, it evoked constriction (based on measurement of the capillary diameter near the pericyte soma), while arterioles and venules were unchanged in diameter. In a manner similar to the human brain slices, both oligomeric A β_{1-40} and A β_{1-42} evoked capillary constriction in rat brain slices after 1 h of exposure.

The authors went further to explore the mechanisms of how A β oligomers interact with pericytes to constrict cerebral capillaries. They found that pericytes, but not resident microglia or perivascular macrophages, were the main cell type that generated reactive oxygen species (ROS) after A β stimulation (Fig. 1). Endothelin-1, which was released after ROS stimulation, perhaps from the pericytes, acted on ET_A receptors to induce pericyte constriction. A β -evoked pericyte constriction can be halted by blocking NADPH oxidase 4 (which is expressed in pericytes) as well as by blocking ET_A receptors, or reversed by applying the vasodilator C-type natriuretic peptide, which blocks Ca²⁺ release from internal stores in pericytes and activates myosin light chain phosphatase, thus inhibiting constriction of capillaries by these cells.

In addition to capillary constriction, Zlokovic and colleagues from the University of Southern California have reported an unexpected but critical role of pericytes in regulating neuronal survival and cognitive function. Notably, they generated a pericyte-specific, double-Cre driver system, which used control by the *Pdgfrb* and *Cspg4* promoters, two genes that encode the pericyte-expressing proteins PDGFR β and NG2 [9]. After cross-breeding with a Cre-dependent tdTomato reporter mouse line, this triple transgenic mouse model expresses inducible fluorescent protein tdTomato only in capillary pericytes and not in smooth muscle cells on the arterioles. The same double-Cre driver system was also used to generate pericyte-specific iDTR transgenic mice to specifically ablate nearly 60% of the CD13-positive pericytes in the adult mouse brain at 3 and 15 days after diphtheria toxin injection. Reduced CBF and decreased capillary diameter, followed by tissue hypoxia and edema, were found in the pericyte-ablated mice, and loss of pericytes also led to pronounced BBB breakdown, reduced tight junctions, and increased plasma protein leakage [9].

Accelerated loss of neurons and cognitive deficits were also found after pericyte ablation. A loss of 20%–25% of NeuN-positive neurons and 35%–40% of SMI12-positive neuritic density occurred in the cortex and hippocampus of these pericyte-ablated mice. The neuronal loss was

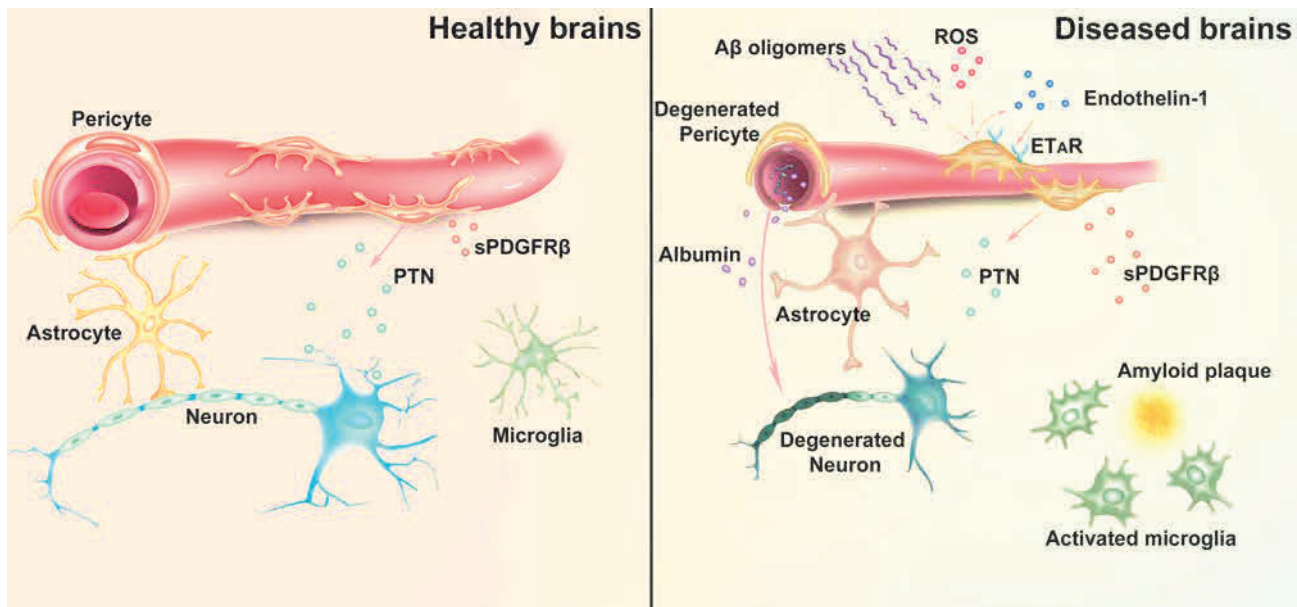


Fig. 1 Schematic of the roles of pericytes in neurovascular interactions in healthy and diseased brains. Left: in the healthy brain, pericytes maintain the integrity of the blood-brain barrier (BBB) and regulate cerebral blood flow. Pericytes secrete pleiotrophin (PTN) to support neuronal growth. Right: in Alzheimer's disease, A β oligomers stimulate ROS generation and endothelin-1 release (possibly from pericytes), which in turn activates pericyte ET_A receptors

(ET_AR), leading to capillary constriction and cerebral blood flow reduction. Degeneration of pericytes causes BBB breakdown, plasma leakage, and deprivation of PTN, which result in neurodegeneration. An increase of pericyte-derived soluble PDGFR β (sPDGFR β) in the CSF is also associated with early cognitive impairment and BBB breakdown.

attributed to both BBB breakdown and a lack of pericyte-derived PTN, a neurotrophic factor that is only expressed in pericytes and not in other cell types in the brain [Fig. 1]. Pericyte ablation led to a >60% reduction of PTN protein in brain capillaries and ~65% reduction of PTN in the cerebrospinal fluid (CSF) at day 15 after diphtheria toxin injection. A loss of function study of PTN by siRNA silencing in mice with intact pericyte coverage revealed neuronal vulnerability to circulatory stress. Conversely, continuous infusion of PTN into the cerebral ventricles rescued the neuronal loss and attenuated the cognitive impairment in pericyte-ablated mice, implying a critical regulatory role of pericyte-secreted PTN in cognitive function in healthy and diseased brains.

Another recent work by Zlokovic and colleagues also revealed an elevated level of soluble PDGFR β (sPDGFR β) in the CSF of patients with early cognitive dysfunction. Changes in the sPDGFR β level correlated with increased BBB dysfunction, independent of changes in biomarkers like A β and/or hyper-phosphorylated tau protein [10], indicating that sPDGFR β could be an early biomarker for detecting BBB breakdown and human cognitive dysfunction independent of A β and tau accumulation.

Together, these findings highlight the novel roles of pericytes in the physiological and pathological states of the NVU. In brains affected by AD, A β oligomers can induce capillary constriction through pericytes and result in a long-term reduction of CBF. In the case of pericyte loss, as in the brains of AD patients or genetic ablation in mouse models, pericyte degeneration results in neurovascular uncoupling and BBB breakdown. Reduction of pericyte-derived PTN also results in neuronal loss and cognitive impairment. These new findings on pericytes in pathological conditions reaffirm their critical roles in the context of neurodegenerative disease.

Future studies in the search for disease-associated pericyte biomarkers and elucidation of the complicated properties of pericytes regarding the crosstalk of NVUs in healthy and diseased brains should provide more information on the pathological roles played by pericytes. Identifying novel pericyte biomarkers associated with AD may shed new light on potential therapeutic targets to restore the function of NVUs, as indicated by recent work that shows a high correlation of increased pericyte-derived sPDGFR β in the CSF of patients with BBB leakage and early cognitive impairment [10]. Single-cell transcriptome analysis may

also provide novel insight into the heterogeneous properties of pericytes at different stages of disease progression and the mechanistic understanding of neurovascular uncoupling in neurodegenerative diseases.

Acknowledgements This highlight was supported by grants from the National Key R&D Program of China (2017YFC1307500 and 2017YFC1307504), the National Natural Science Foundation of China (81925031, 81972967 and 81820108026), and Science and Technology Program of Guangzhou Municipality, China (202007030001).

Conflict of interest The authors declare no potential conflicts of interest.

References

1. Zlokovic BV. Neurovascular pathways to neurodegeneration in Alzheimer's disease and other disorders. *Nat Rev Neurosci* 2011, 12: 723–738.
2. Sun BL, Li WW, Zhu C, Jin WS, Zeng F, Liu YH, *et al.* Clinical research on Alzheimer's disease: Progress and perspectives. *Neurosci Bull* 2018, 34: 1111–1118.
3. Bell RD, Winkler EA, Sagare AP, Singh I, LaRue B, Deane R, *et al.* Pericytes control key neurovascular functions and neuronal phenotype in the adult brain and during brain aging. *Neuron* 2010, 68: 409–427.
4. Montagne A, Nikolakopoulou AM, Zhao Z, Sagare AP, Si G, Lasic D, *et al.* Pericyte degeneration causes white matter dysfunction in the mouse central nervous system. *Nat Med* 2018, 24: 326–337.
5. Hall CN, Reynell C, Gesslein B, Hamilton NB, Mishra A, Sutherland BA, *et al.* Capillary pericytes regulate cerebral blood flow in health and disease. *Nature* 2014, 508: 55–60.
6. Kisler K, Nelson AR, Rege SV, Ramanathan A, Wang Y, Ahuja A, *et al.* Pericyte degeneration leads to neurovascular uncoupling and limits oxygen supply to brain. *Nat Neurosci* 2017, 20: 406–416.
7. Sagare AP, Bell RD, Zhao Z, Ma Q, Winkler EA, Ramanathan A, *et al.* Pericyte loss influences Alzheimer-like neurodegeneration in mice. *Nat Commun* 2013, 4: 2932.
8. Nortley R, Korte N, Izquierdo P, Hirunpattarasilp C, Mishra A, Jaunmuktane Z, *et al.* Amyloid β oligomers constrict human capillaries in Alzheimer's disease *via* signaling to pericytes. *Science* 2019, 365: eaav9518.
9. Nikolakopoulou AM, Montagne A, Kisler K, Dai Z, Wang Y, Huuskonen MT, *et al.* Pericyte loss leads to circulatory failure and pleiotrophin depletion causing neuron loss. *Nat Neurosci* 2019, 22: 1089–1098.
10. Nation DA, Sweeney MD, Montagne A, Sagare AP, D'Orazio LM, Pachicano M, *et al.* Blood–brain barrier breakdown is an early biomarker of human cognitive dysfunction. *Nat Med* 2019, 25: 270–276.



RESEARCH HIGHLIGHT

A Novel Potassium Nanosensor Powers up the Detection of Extracellular K^+ Dynamics in Neuroscience

Ying Wang¹ · Qingyu Wang² · Xia Zhang¹

Received: 29 March 2020 / Accepted: 18 May 2020 / Published online: 1 September 2020
© Shanghai Institutes for Biological Sciences, CAS 2020

Potassium ions (K^+), the pivotal cations for membrane potential, are particularly important for maintaining the physiological function of neurons [1]. When the concentration of extracellular K^+ ($[K^+]_o$) is pathologically changed, the intrinsic neuronal excitability and synaptic transmission are also altered, which have profound implications for many neurological disorders such as epilepsy, Parkinson's disease, and emotional disorders [2–4]. Moreover, K^+ channels, exchangers, and pumps, used for the flux and transport of K^+ , have emerged as promising drug targets for a variety of diseases [5]. Therefore, the development of K^+ sensors, which detect dynamic changes in K^+ levels, is potentially important not only for revealing the mechanism underlying neurological disorders, but also for enabling highly localized and on-demand drug release. However, most currently available K^+ sensors cannot work precisely due to many limitations, particularly in freely-moving animals. K^+ -selective electrodes have been the gold standards for the quantitative measurement of $[K^+]$, but they are invasive and not able to achieve the spatiotemporal imaging of dynamic K^+ variations [6]. Fluorescent K^+ sensors have been developed to image K^+ fluctuations using fluorescence microscopy, but they respond over a narrow dynamic range and have limited specificity for K^+ with interference from Na^+ when the efflux of K^+ is preceded by an influx of Na^+ during action potential generation [7]. Recently, as reported in *Nature*

Nanotechnology, a new, highly sensitive and specific nanosensor for monitoring $[K^+]_o$ levels in the brain of the freely-moving mouse has been developed by researchers at the Institute for Basic Science in South Korea and Zhejiang University in China [8].

The device was created by embedding a commercially-available K^+ indicator (Asante Potassium Green-2 tetramethylammonium salt) into mesoporous silica nanoparticles (MSNs), which are subsequently shielded by an ultrathin layer of a K^+ -specific filter membrane. The researchers first verified the performance of the new K^+ nanosensor in solution. They found that, compared with previous K^+ sensors, the shielded nanosensor has superior K^+ selectivity, which is attributed to the filter membrane that excludes the passage of ions other than K^+ . The pore size and composition of the filter membrane improve the attractive force for K^+ , but not Na^+ . Moreover, electrostatic attraction and inward diffusional force facilitate the influx of K^+ into the MSNs and the negatively-charged mesopores in the nanosensors enrich the $[K^+]$ in the MSNs ($[K^+]_{in}$) with respect to the $[K^+]$ of the solution ($[K^+]_{out}$), which significantly enhances the sensitivity of the nanosensors with a detection limit as low as 1.3×10^{-6} mol/L and the capability of accommodating sub-millimolar variations. Notably, the shielded nanosensor also proves to be fully reversible when the K^+ -saturated shielded nanosensors are re-dispersed in deionized water and it can be recycled 20 times, which is important for neural investigations. However, it is noteworthy that negative electrostatic attraction of the nanosensors not only improves the sensitivity to K^+ , but also traps the K^+ inside of the nanosensors. Then how does the absorbed K^+ escape from the negative electrostatic attraction and the binding energy, and fully desorb in response to the decreasing $[K^+]_{out}$? The researchers did not

✉ Ying Wang
wangying_199110@163.com

¹ Institute of Brain Science and Disease, Qingdao University, Qingdao 266071, China

² Department of Anesthesiology, Affiliated Hospital of Qingdao University, Qingdao 266000, China

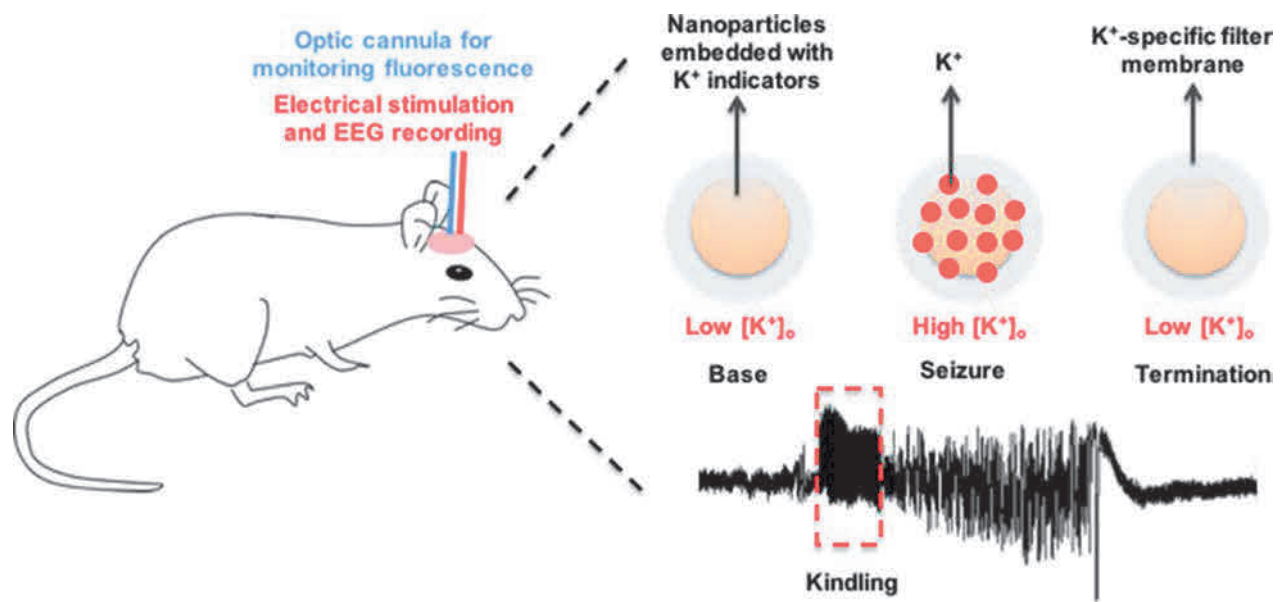


Fig. 1 Shielded K^+ nanosensors monitor the concentration of extracellular K^+ in freely-moving epileptic mice. Left panel, seizure activity is induced by hippocampal electrical stimulation and the optic cannula is used for acquisition of the fluorescence signal; right panel,

the concentration of extracellular K^+ increases during seizure activity, and the shielded K^+ nanosensors dynamically monitor its concentration.

propose any mechanistic hypothesis and we anticipate further investigations.

It is generally acknowledged that seizure activity results in an increase of $[K^+]_o$ [9]. Then, the researchers further verified the performance of the shielded K^+ nanosensor in *in vitro* and *in vivo* seizure models. First *in vitro*, the *Coriaria* lactone-induced $[K^+]_o$ increase was detected by the shielded K^+ nanosensors, but not free indicators and unshielded nanosensors. Moreover, the researchers modified the surface of the shielded nanosensors with glutathione and cysteamine (designated Glu/Cys-nanosensors) so that the nanosensors were anchored firmly on the plasma membrane, and they are effective for map the spatial K^+ release from different compartments of a single cultured hippocampal neuron during kainic acid-induced seizure-like activity. They found that compared with the soma, a higher $[K^+]_o$ was recorded in axons during seizure-like activity. Similarly, the spatiotemporal changes of $[K^+]_o$ in electrically-stimulated brain slices were also detected by the shielded nanosensors and Glu/Cys-nanosensors. However, in most experiments, the performance of the shielded K^+ nanosensors was only compared with free indicators and unshielded nanosensors, but not the K^+ -selective microelectrodes that are the gold standards to measure $[K^+]_o$ with high accuracy. Thus, whether the accuracy of the shielded K^+ nanosensors is better than K^+ -selective microelectrodes remains a question. Moreover, it is noteworthy that the shielded K^+ nanosensors may be phagocytized by cells during a long period of incubation. If so, the measurement of $[K^+]_o$ would be significantly affected

by the highly enriched intracellular K^+ after phagocytosis. Therefore, the measurement accuracy of the shielded K^+ nanosensor needs further verification (Fig. 1).

Further, in freely-moving epileptic mice, the researchers successfully achieved single-point and multipoint monitoring of the dynamic $[K^+]_o$ changes evoked by seizures with shielded K^+ nanosensors. They found that the response magnitude and signal duration gradually increased as the seizure stages progressed. Moreover, a temporal spread in $[K^+]_o$ increase from hippocampus to amygdala and cortex occurs in a focal seizure, while the $[K^+]_o$ increase happens almost at the same time in a generalized seizure. These results are in good agreement with the widely-accepted view of seizure propagation. To sum up, this study demonstrated the feasibility of the new K^+ nanosensor for monitoring seizures and its higher sensitivity and specificity in the spatiotemporal measurement of dynamic $[K^+]_o$ in freely-moving epileptic mice. However, the seizures induced by hippocampal electrical stimulation were acute, but not chronic spontaneous seizures. Thus, we anticipate verification of the performance of the new K^+ nanosensor in chronic models and evaluation of the sensitivity, selectivity, accuracy, and biocompatibility in the long-term, which is important for future applications in neurobiological disease models other than epilepsy.

The new K^+ nanosensor is a precision tool for neuroscience. This study not only provides a new idea for the design and preparation of minimally-invasive ion-specific probes with shielded nanoparticles, but also opens up a new strategy for exploring the spatiotemporal patterns

of pathological mechanisms underlying various neurological disorders which involve impaired homeostasis of [K⁺]_o, such as epilepsy, depression, and Parkinson's disease. Although the current Ca²⁺ probes can also test abnormal neuronal activity by assessing the intracellular [Ca²⁺], calcium ions may not be directly involved in the generation of action potentials. In pre-clinical experiments, the new K⁺ nanosensor can probably be combined with optogenetics or chemogenetics to achieve on-demand closed-loop control of specific neural circuits [10], which will make breakthroughs in the dissection of the neural networks underlying neurological disorders. Looking further ahead in the clinic, the optic cannula, although minimally-invasive, still limits the application of the new K⁺ sensor to humans and the whole-brain imaging cannot be achieved with the current device. Therefore, the development of a tissue-penetrating near-infrared emission-based K⁺ sensor and combining it with functional magnetic resonance imaging would be more useful to achieve whole-brain imaging in humans to detect the pathological changes in neurological disorders. Moreover, if loaded with drugs and coated with nanocomposites that can be disrupted by elevated K⁺ levels, these nanosensors could allow for highly-localized and on-demand drug release at the point of a focus [11], which would enhance the efficacy of drugs and reduce the side-effects on healthy tissue. Certainly, there is room for improvement in the new K⁺ nanosensor. The major limitation of the new K⁺ nanosensor is the lack of cell-type specificity which restricts its application in cell-type-specific or circuit-specific research. They measure the total extracellular [K⁺] which may come from both neuronal and glial sources. We expect it to be combined with cre-loxp technology to achieve cell-type specificity in the future. Above all, the new K⁺ nanosensor has great application potential in neuroscience: we expect it to be widely used in the treatment and assessment of neuropsychiatric diseases.

Acknowledgements This research highlight article was supported by the National Natural Science Foundation of China (81830035) and the China Postdoctoral Science Foundation (2019M662290).

Conflict of interest The authors declare that they have no conflict of interest.

References

1. Palmer BF, Clegg DJ. Physiology and pathophysiology of potassium homeostasis: core curriculum 2019. *Am J Kidney Dis* 2019, 74: 682–695.
2. Larson VA, Mironova Y, Vanderpool KG, Waisman A, Rash JE, Agarwal A, *et al.* Oligodendrocytes control potassium accumulation in white matter and seizure susceptibility. *Elife* 2018, 7.
3. Chen X, Xue B, Wang J, Liu H, Shi L, Xie J. Potassium channels: A potential therapeutic target for Parkinson's disease. *Neurosci Bull* 2018, 34: 341–348.
4. Cui Y, Yang Y, Ni Z, Dong Y, Cai G, Foncelle A, *et al.* Astroglial Kir4.1 in the lateral habenula drives neuronal bursts in depression. *Nature* 2018, 554: 323–327.
5. Yeh CY, Bulas AM, Moutal A, Saloman JL, Hartnett KA, Anderson CT, *et al.* Targeting a potassium channel/syntaxin interaction ameliorates cell death in ischemic stroke. *J Neurosci* 2017, 37: 5648–5658.
6. van de Velde L, d'Angremont E, Olthuis W. Solid contact potassium selective electrodes for biomedical applications - a review. *Talanta* 2016, 160: 56–65.
7. Bischof H, Rehberg M, Stryeck S, Artinger K, Eroglu E, Waldeck-Weiermair M, *et al.* Novel genetically encoded fluorescent probes enable real-time detection of potassium in vitro and in vivo. *Nat Commun* 2017, 8: 1422.
8. Liu J, Li F, Wang Y, Pan L, Lin P, Zhang B, *et al.* A sensitive and specific nanosensor for monitoring extracellular potassium levels in the brain. *Nat Nanotechnol* 2020, 15: 321–330.
9. Antonio LL, Anderson ML, Angamo EA, Gabriel S, Klafit ZJ, Liotta A, *et al.* In vitro seizure like events and changes in ionic concentration. *J Neurosci Methods* 2016, 260: 33–44.
10. Grosenick L, Marshel JH, Deisseroth K. Closed-loop and activity-guided optogenetic control. *Neuron* 2015, 86: 106–139.
11. Brudno Y, Mooney DJ. On-demand drug delivery from local depots. *J Control Release* 2015, 219: 8–17.



RESEARCH HIGHLIGHT

SCGN-regulated Stage-wise SNARE Assembly: Novel Insight into Synaptic Exocytosis

Ying Lv¹ · Sunmin Xiang² · Renxian Cao² · Li Wu² · Jing Yang² 

Received: 21 June 2020 / Accepted: 19 July 2020 / Published online: 6 October 2020
© Shanghai Institutes for Biological Sciences, CAS 2020

In neuroendocrine cells, hormones and neuropeptides stored in secretory granules are released in response to various stimuli in a highly concerted process, including the sequential actions of vesicle trafficking, docking, fusion, and unloading. In this process, the crucial step of vesicle fusion requires the formation of a soluble N-ethylmaleimide-sensitive factor attachment protein receptor (SNARE) complex, comprising primarily SNAP-25, syntaxin 1, and synaptobrevin 2 [1, 2]. After synaptic exocytosis, the SNARE complex is disassembled for another round of fusion, and the assembly and recycling of SNARE complex components are orchestrated by a cascade of regulators, including N-ethylmaleimide-sensitive factor (NSF), soluble NSF adaptor proteins (SNAPs), Munc18-1, Munc13-1, and others [1, 3]. NSF and the SNAPs disassemble the SNARE complex to recycle SNARE components for subsequent rounds of fusion, whereas Munc18-1 and Munc13-1 facilitate SNARE complex assembly in an NSF-SNAP-resistant manner [3, 4]. In addition to these well-recognized regulators, several proteins that chaperone components for SNARE complex formation remain to be discovered.

Secretagogin (SCGN), an EF-hand Ca²⁺-sensor hexamer protein expressed mainly in pancreatic islets, brain

cells, and gastrointestinal endocrine cells, has recently been identified as a crucial player in the regulation of exocytosis [5]. Studies have shown that the secretion of insulin, corticotropin-releasing hormone, glucagon-like peptide-1 (GLP-1), and matrix metalloproteinase-2 is regulated by SCGN [5–7]. It is generally accepted that SCGN modulates hormone exocytosis by interacting with cytoskeletal actin proteins and the SNARE complex. However, the precise mechanisms by which SCGN interacts with the SNARE complex and facilitates synaptic exocytosis are still unclear.

Recently, Qin *et al.* [8] published a report in *PNAS* revealing that SCGN interacts directly with SNAP-25 in complex with Ca²⁺ but not with the assembled SNARE complex. Crystal structure experiments further indicated that the SNAP-25 peptide specifically binds to a relatively small fragment within domain III of SCGN through hydrophobic interactions and multiple hydrogen bonds. Moreover, SCGN facilitates the accumulation of SNAP-25 at the plasma membrane (PM) by functioning as an intimate chaperone and inhibits the assembly of the SNARE complex by competitively binding to SNAP-25. However, a striking reduction in docosahexaenoic acid-mediated GLP-1 release was identified in SCGN-knockout STC-1 cells, and this decrease in GLP-1 release was reversed by SCGN re-expression, which indicates that SNAP-25 located in the PM can be released from SCGN to participate in the formation of the SNARE complex. These findings illustrate that the PM localization of SNAP-25 and the assembly of the SNARE complex are precisely regulated by SCGN and that SCGN acts as initially an inhibitor and then an activator of SNARE assembly and vesicle exocytosis.

Currently, two phases of exocytosis behavior have been reported for a great number of neuronal and

Ying Lv and Sunmin Xiang have contributed equally to this work.

✉ Jing Yang
yangjing9803@hotmail.com

¹ Department of Metabolism and Endocrinology, The Second Affiliated Hospital of the University of South China, Hengyang 421001, China

² Department of Metabolism and Endocrinology, The First Affiliated Hospital of the University of South China, Hengyang 421001, China

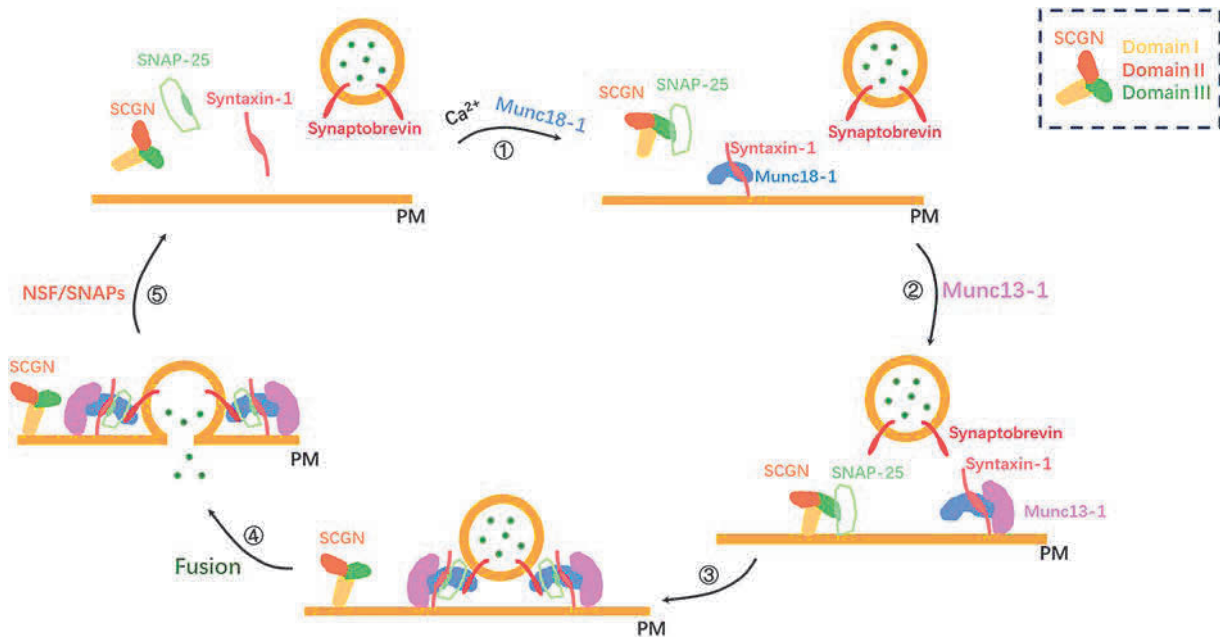


Fig. 1 The regulatory mechanism of SCGN/SNAP-25 during exocytosis. Step 1. Stimulus-triggered Ca^{2+} influx changes the conformational status of SCGN, which facilitates domain III of the C-terminus binding to SNAP-25 through hydrophobic interactions and hydrogen bonds in competition with syntaxin-1. Free syntaxin-1 binds to Munc18-1, thus forming a template to assemble the SNARE complex. Step 2. The SCGN/SNAP-25 complex migrates to the plasma membrane (PM), and Munc13-1 facilitates SNARE assembly

by catalyzing the activity of syntaxin-1. Step 3. With further changes to the redox state or spatial conformation of SCGN, SNAP-25 is released from SCGN and participates in the formation of the SNARE complex. Step 4. SNARE proteins mediate intracellular membrane fusion and exocytosis. Step 5. Following exocytosis, SNAPs bind NSF on the SNARE complex and initiate complex disassembly, freeing SNARE components for another round of exocytosis.

neuroendocrine hormones: an initial rapid release followed by a relatively slow release. Regarding insulin secretion, a small amount of insulin granules docked on the PM constitute first-phase secretion, whereas second-phase secretion depends on the translocation of a large number of insulin granules from intracellular storage pools to the PM with which they fuse. Intriguingly, silencing SCGN in islet β cells specifically suppressed second-phase insulin secretion but did not affect first-phase secretion [5]. Moreover, SCGN was shown to be a redox-responsive Ca^{2+} -sensor protein, and Ca^{2+} binding to the EF-hands of SCGN results in significant structural changes that expose the functional domain and affects its redox state, thereby promoting Ca^{2+} -mediated exocytosis [9, 10]. In addition, the sub-molecular structures of SCGN have been demonstrated to play distinct roles in cellular processes. As explained above, domain III in the C-terminal region regulates insulin release [8], whereas the N-terminal domain modulates insulin stability and preserves insulin sensitivity [11].

Based on this evidence, it is reasonable to speculate that the stage-wise steps of SNARE assembly and granule fusion are regulated by SCGN and that the regulatory effects are realized in a secretory phase- and spatial conformation-dependent manner. SCGN chaperones

localize SNAP-25 to the PM, where it transiently inhibits SNARE assembly during the rapid-release phase. However, with the increase in intracellular free Ca^{2+} concentration, the spatial conformation of SCGN changes and the PM-located SNAP-25 may be liberated from SCGN, and the subsequent steps of SNARE complex formation, vesicle fusion, and exocytosis during second-phase secretion are thus initiated (Fig. 1). However, the dual functional roles of SCGN in regulating the two phases of exocytosis are mainly logical speculations based on existing facts, and they should be verified by more experiments. In addition, it will be interesting to carry out clinical studies to determine whether genetic mutations in the C-terminal domain of SCGN are causative factors of insulin secretion insufficiency in diabetic patients.

Acknowledgements The work was supported by the Clinical Medical Technology Innovation Project of Hunan Province, China (2018SK51607) and the Scientific Research Project of the Health Commission of Hunan Province, China (B2019125).

Conflict of interest The authors declare that they have no conflict of interest.

References

1. Rizo J. Mechanism of neurotransmitter release coming into focus. *Protein Sci* 2018, 27: 1364–1391.
2. Mirza FJ, Zahid S. The Role of Synapsins in Neurological Disorders. *Neurosci Bull* 2018, 34: 349–358.
3. Ma C, Su L, Seven AB, Xu Y, Rizo J. Reconstitution of the vital functions of Munc18 and Munc13 in neurotransmitter release. *Science* 2013, 339: 421–425.
4. Prinslow EA, Stepien KP, Pan YZ, Xu J, Rizo J. Multiple factors maintain assembled trans-SNARE complexes in the presence of NSF and alpha SNAP. *Elife* 2019. <https://doi.org/10.7554/elife.38880>.
5. Yang SY, Lee JJ, Lee JH, Lee K, Oh SH, Lim YM, *et al.* Secretagogen affects insulin secretion in pancreatic beta-cells by regulating actin dynamics and focal adhesion. *Biochem J* 2016, 473: 1791–1803.
6. Hanics J, Szodorai E, Tortoriello G, Malenczyk K, Keimpema E, Lubec G, *et al.* Secretagogen-dependent matrix metalloprotease-2 release from neurons regulates neuroblast migration. *Proc Natl Acad Sci U S A* 2017, 114: E2006–E2015.
7. Romanov RA, Alpar A, Zhang MD, Zeisel A, Calas A, Landry M, *et al.* A secretagogen locus of the mammalian hypothalamus controls stress hormone release. *EMBO J* 2015, 34: 36–54.
8. Qin J, Liu Q, Liu Z, Pan YZ, Sifuentes-Dominguez L, Stepien KP, *et al.* Structural and mechanistic insights into secretagogen-mediated exocytosis. *Proc Natl Acad Sci U S A* 2020, 117: 6559–6570.
9. Khandelwal R, Sharma AK, Chadalawada S, Sharma Y. Secretagogen Is a Redox-Responsive Ca(2+) Sensor. *Biochemistry* 2017, 56: 411–420.
10. Lee JJ, Yang SY, Park J, Ferrell JE, Jr., Shin DH, Lee KJ. Calcium ion induced structural changes promote dimerization of secretagogen, which is required for its insulin secretory function. *Sci Rep* 2017, 7: 6976. <https://doi.org/10.1038/s41598-017-07072-4>.
11. Sharma AK, Khandelwal R, Kumar MJM, Ram NS, Chidananda AH, Raj TA, *et al.* Secretagogen Regulates Insulin Signaling by Direct Insulin Binding. *iScience* 2019, 21: 736–753.

Neuroscience Bulletin Copyright Transfer Statement and Submission Form

We submit this type of article (√):

- Original Article
- Review
- Research Highlight
- Insight
- Letter to the Editor
- Method

Title of article:

Words: Figures: (Color figures:); Tables:

A signature below certifies compliance with the following statements

Copyright Transfer Statement: The copyright to this article is transferred to *Neuroscience Bulletin*, Shanghai Institutes for Biological Sciences, CAS and Springer (respective to owner if other than Shanghai Institutes for Biological Sciences, CAS and Springer and for U.S. government employees: to the extent transferable) effective if and when the article is accepted for publication. The author warrants that his/her contribution is original and that he/she has full power to make this grant. The author signs for and accepts responsibility for releasing this material on behalf of any and all co-authors. The copyright transfer covers the exclusive right and license to reproduce, publish, distribute and archive the article in all forms and media of expression now known or developed in the future, including reprints, translations, photographic reproductions, microform, electronic form (offline, online) or any other reproductions of similar nature. An author may self-archive an author-created version of his/her article on his/her own website. He/she may also deposit this version on his/her institution's and funder's (funder designated) repository at the funder's request or as a result of a legal obligation, including his/her final version, provided it is not made publicly available until after 12 months of official publication. He/she may not use the publisher's PDF version which is posted on www.springerlink.com for the purpose of self-archiving or deposit. Furthermore, the author may only post his/her version provided acknowledgement is given to the original source of publication and a link is inserted to the published article on Springer's website. The link must be accompanied by the following text: "The original publication is available at www.springerlink.com". The author is requested to use the appropriate DOI for the article. Articles disseminated *via* www.springerlink.com are indexed, abstracted and referenced by many abstracting and information services, bibliographic networks, subscription agencies, library networks, and consortia.

After submission of this agreement signed by the corresponding author, changes of authorship or in the order of the authors listed will not be accepted by *Neuroscience Bulletin*, Shanghai Institutes for Biological Sciences of Chinese Academy of Sciences and Springer.

Authorship responsibilities

I/We confirm that:

- (1) The work described has not been published before in any language or in any journal or media; that it is not under consideration for publication elsewhere; that its publication has been approved by all co-authors, if any, as well as (tacitly or explicitly) by the responsible authorities at the institution where the work was carried out.
- (2) We also give an assurance that the material will not be submitted for publication elsewhere until a decision has been made as to its acceptability for *Neuroscience Bulletin* in 2 months, then declare this statement becomes null and void.
- (3) I am/We are responsible for obtaining permission for the use of any material in the manuscript that may be under copyright to my/our employer(s) or other party(ies).
- (4) I have read the complete manuscript and accept responsibility for the content and completeness.
- (5) I have made a significant contribution to this work and am familiar with the contents.

Author (1) signed: Date: Author (2) signed: Date:

Author (3) signed: Date: Author (4) signed: Date:

Author (5) signed: Date: Author (6) signed: Date:

Author (7) signed: Date: Author (8) signed: Date:

Author (9) signed: Date: Author (10) signed: Date:

Corresponding author signed: Date:

Corresponding author address:

Tel: E-mail:

Neuroscience Bulletin

Editors-in-Chief

Shumin Duan, Zhejiang University, Hangzhou, China
Ru-Rong Ji, Duke University, Durham, USA

Consulting Editors

Yizhang Chen, Second Military Medical University, Shanghai, China
Muming Poo, Institute of Neuroscience, CAS, Shanghai, China
Larry R. Squire, University of California, San Diego, USA
Charles F. Stevens, The Salk Institute, San Diego, USA
Xiongli Yang, Fudan University, Shanghai, China

Executive Associate Editors

Iain C. Bruce, Zhejiang University, Hangzhou, China
Guangyin Xu, Institute of Neuroscience, Soochow University, Suzhou, China

Associate Editors

Zhong Chen, Zhejiang University, Hangzhou, China
Tianming Gao, South Medical University, Guangzhou, China
Shihui Han, Peking University, Beijing, China
Cheng He, Second Military Medical University, Shanghai, China
Tianzi Jiang, Institute of Automation, CAS, Beijing, China
Weidong Le, Dalian Medical University, Dalian, China
Tao Li, West China Hospital, Sichuan University, Chengdu, China
Mengsheng Qiu, Hangzhou Normal University, Hangzhou, China
Fu-Dong Shi, St. Joseph's Hospital and Medical Center, Phoenix, USA

You Wan, Peking University, Beijing, China
Jian-Zhi Wang, Huazhong University of Science and Technology, Wuhan, China
Yanjiang Wang, Daping Hospital, Third Military Medical University, Chongqing, China
Longjun Wu, Mayo Clinic, Rochester, USA
Zhi-Ying Wu, Huashan Hospital, Shanghai Medical College, Fudan University, Shanghai, China
Tianle Xu, Shanghai Jiaotong University, Shanghai, China
Dai Zhang, Peking University, Beijing, China
Hanting Zhang, West Virginia University Health Sciences Center, Morgantown, USA
Chunjiu Zhong, Fudan University, Shanghai, China

Editorial Board

Philippe Ascher, Paris Diderot University, Paris, France
George Baillie, Institute of Cardiovascular and Medical Sciences, University of Glasgow, UK
Guo-Qiang Bi, University of Science and Technology of China, Hefei, China
Junli Cao, Xuzhou Medical College, Xuzhou, China
L. Judson Chandler, Medical University of South Carolina, USA
Jun Chen, The Fourth Military Medical University, Xi'an, China
Qing-Hui Chen, Michigan Technological University, Houghton, USA
Isaac M. Chiu, Harvard Medical School, Boston, USA

Yiru Fang, Shanghai Mental Health Center, Shanghai Jiaotong University School of Medicine, Shanghai, China
Richard S. Frackowiak, University of Lausanne, Lausanne, Switzerland
Tamás F. Freund, Institute of Experimental Medicine of the Hungarian Academy of Sciences, Budapest, Hungary
Yongjing Gao, Institute of Nautical Medicine, Nantong University, Nantong, China
Charles Gilbert, The Rockefeller University, New York, USA
Xiaosong Gu, Nantong University, Nantong, China
Junhai Han, Southeast University, Nanjing, China
Philip G. Haydon, Tufts University, Boston, USA
Joe Herbert, University of Cambridge, Cambridge, UK
Gregg E. Homanics, University of Pittsburgh, USA

- Zhi-An Hu**, Third Military Medical University, Chongqing, China
- Kazuhide Inoue**, Kyushu University, Fukuoka, Japan
- Yong-Hua Ji**, Shanghai University, Shanghai, China
- Helmut Kettenmann**, Max-Delbrück Center for Molecular Medicine, Berlin, Germany
- O.A. Krishtal**, Bogomoletz Institute of Physiology, Kiev, Ukraine
- Robert H. LaMotte**, Yale University School of Medicine, New Haven, USA
- Pierre Lavenex**, University of Fribourg, Fribourg, Switzerland
- C. Justin Lee**, Korea Institute of Science and Technology, Korea
- Juan Lerma**, Instituto de Neurociencias de Alicante, Alicante, Spain
- Bao-Ming Li**, Nanchang University, Nanchang, China
- Wolfgang Liedtke**, Duke University School of Medicine, Durham, USA
- David J. Linden**, Johns Hopkins University, Baltimore, USA
- Stuart A. Lipton**, Sanford-Burnham Medical Research Institute and University of California at San Diego, San Diego, USA
- Tong Liu**, Institute of Neuroscience, Soochow University, Suzhou, China
- Lin Lu**, Peking University Sixth Hospital, Beijing, China
- Bridget Lumb**, University of Bristol, Bristol, UK
- Benyan Luo**, Zhejiang University School of Medicine, China
- Jian-Hong Luo**, Zhejiang University School of Medicine, China
- Zhen-Ge Luo**, ShanghaiTech University, China
- Lan Ma**, Fudan University, Shanghai, China
- Qiufu Ma**, Dana-Farber Cancer Institute, Boston, USA
- Quanhong Ma**, Institute of Neuroscience, Soochow University, Suzhou, China
- Robert C. Malenka**, Stanford University, Stanford, USA
- Manuel S. Malmierca**, Universidad de Salamanca, Salamanca, Spain
- John H.R. Maunsell**, Harvard Medical School, Houston, USA
- Earl K. Miller**, Massachusetts Institute of Technology, Cambridge, USA
- Enrico Mugnaini**, Northwestern University, Feinberg School of Medicine, Chicago, USA
- Vladimir Parpura**, University of Alabama at Birmingham, Birmingham, USA
- Jos Prickaerts**, School for Mental Health and Neuroscience, Maastricht University, the Netherland
- Bruce R. Ransom**, University of Washington, Seattle, USA
- Tom E. Salt**, University College London, London, UK
- Joshua R. Sanes**, Harvard University, Boston, USA
- Michael N. Shadlen**, Columbia University, New York, USA
- Morgan Sheng**, Genentech, Inc., South San Francisco, USA
- Yousheng Shu**, Beijing Normal University, Beijing, China
- Sangram S. Sisodia**, The University of Chicago, Chicago, USA
- Peter Somogyi**, University of Oxford, Oxford, UK
- Feng-Yan Sun**, Fudan University, Shanghai, China
- Dick F. Swaab**, Netherlands Institute for Neuroscience, Amsterdam, Netherlands
- Keiji Tanaka**, RIKEN Brain Science Institute, Tokyo, Japan
- Xiaoqing Tang**, University of South China, Hengyang, China
- Yong Tang**, Chengdu University of TCM, Chengdu, China
- Makoto Tsuda**, Kyushu University, Fukuoka, Japan
- Alexej Verkhratsky**, The University of Manchester, Manchester, UK
- Steven R. Vincent**, University of British Columbia, Vancouver, Canada
- Guanghui Wang**, Soochow University, Suzhou, China
- Jian-Jun Wang**, Nanjing University, Nanjing, China
- Yun Wang**, Neuroscience Research Institute, Peking University, Beijing, China
- Xu-Chu Weng**, Hangzhou Normal University, Hangzhou, China
- William Wisden**, Imperial College London, London, UK
- Jun-Xia Xie**, Qingdao University, Qingdao, China
- Lin Xu**, Kunming Institute of Zoology, CAS, Kunming, China
- Xiao-Hong Xu**, Institute of Neuroscience, CAS, Shanghai, China
- Ying Xu**, School of Pharmacy & Pharmaceutical Sciences, University at Buffalo, The State University of New York, USA
- Yun Xu**, Nanjing Drum Tower Hospital, Nanjing, China
- Fengwei Yu**, National University of Singapore, Singapore
- Shanping Yu**, Emory University School of Medicine, Atlanta, USA
- Hong Zhang**, The Second Affiliated Hospital of Zhejiang University School of Medicine, Hangzhou, China
- Xiaohui Zhang**, Beijing Normal University, Beijing, China
- Xu Zhang**, Institute of Neuroscience, CAS, Shanghai, China
- Yong Zhang**, Peking University, Beijing, China
- Yu-Qiu Zhang**, Fudan University, Shanghai, China
- Zhi-Jun Zhang**, Zhongda Hospital, Southeast University, Nanjing, China
- Ping Zheng**, Fudan University, Shanghai, China
- Jiang-Ning Zhou**, University of Science and Technology of China, Hefei, China
- Libin Zhou**, Joint Laboratory for Brain Function and Health, Jinan University and The University of Hong Kong, Guangzhou, China
- Richard E. Zigmond**, Case Western Reserve University, Cleveland, USA
- Yimin Zou**, University of California-San Diego, USA

Neuroscience Bulletin

Copyright Information

For Authors

As soon as an article is accepted for publication, authors will be requested to assign copyright of the article (or to grant exclusive publication and dissemination rights) to the publisher (respective the owner if other than Springer Nature). This will ensure the widest possible protection and dissemination of information under copyright laws.

More information about copyright regulations for this journal is available at www.springer.com/12264

For Readers

While the advice and information in this journal is believed to be true and accurate at the date of its publication, neither the authors, the editors, nor the publisher can accept any legal responsibility for any errors or omissions that may have been made. The publisher makes no warranty, express or implied, with respect to the material contained herein.

All articles published in this journal are protected by copyright, which covers the exclusive rights to reproduce and distribute the article (e.g., as offprints), as well as all translation rights. No material published in this journal may be reproduced photographically or stored on microfilm, in electronic data bases, on video disks, etc., without first obtaining written permission from the publisher (respective the copyright owner if other than Springer Nature). The use of general descriptive names, trade names, trademarks, etc., in this publication, even if not specifically identified, does not imply that these names are not protected by the relevant laws and regulations.

Springer Nature has partnered with Copyright Clearance Center's RightsLink service to offer a variety of options for reusing Springer Nature content. For permission to reuse our content please locate the material that you wish to use on link.springer.com or on springerimages.com and click on the permissions link or go to copyright.com and enter the title of the publication that you wish to use. For assistance in placing a permission request, Copyright Clearance Center can be contacted directly via phone: +1-855-239-3415, fax: +1-978-646-8600, or e-mail: info@copyright.com

© Shanghai Institutes for Biological Sciences, CAS 2020

Journal Website

www.springer.com/12264

For the actual version of record please always check the online version of the publication.

Subscription Information

Volume 36 (12 issues) will be published in 2020.

ISSN: 1673-7067 print
ISSN: 1995-8218 electronic

For information on subscription rates please contact Springer Nature Customer Service Center: customerservice@springernature.com

The Americas (North, South, Central America and the Caribbean)
Springer Nature Journal Fulfillment,
Harborside Plaza II,
200 Hudson Street, Jersey City,
NJ 07302, USA
Tel. 800-SPRINGER (777-4643);
212-460-1500 (outside
North America)

Outside the Americas

Springer Nature Customer Service
Center GmbH, Tiergartenstr. 15,
69121 Heidelberg, Germany
Tel.: +49-6221-345-4303

Advertisements

E-mail contact: advertising@springer.com
or anzeigen@springer.com (Germany)

Disclaimer

Springer Nature publishes advertisements in this journal in reliance upon the responsibility of the advertiser to comply with all legal requirements relating to the marketing and sale of products or services advertised. Springer Nature and the editors are not responsible for claims made in the advertisements published in the journal. The appearance of advertisements in Springer Nature publications does not constitute endorsement, implied or intended, of the product advertised or the claims made for it by the advertiser.

Office of Publication

Springer Nature Singapore Pte Ltd.
152 Beach Road, #21-01/04
Gateway East, Singapore 189721,
Singapore



Impact Factor

4.326

2019 Journal Citation Reports: Q2
(CLARIVATE ANALYTICS, 2020)

NEUROSCIENCE BULLETIN 神经科学通报 (Monthly)

Vol. 36 No. 12 December 15, 2020

Sponsored by: Shanghai Institutes for Biological Sciences, Chinese Academy of Sciences
Chinese Neuroscience Society
Second Military Medical University

Editors-in-Chief: Shumin Duan, Ru-Rong Ji

Edited by: Editorial Board of *Neuroscience Bulletin*

319 Yueyang Road, Building 31 B, Room 405, Shanghai 200031, China

Phone: +86-21-54922863; Fax: +86-21-54922833

E-mail: nsb@sibs.ac.cn; <http://www.neurosci.cn>

Editors: Bin Wei, Zhi-Rui Liu

Published by: Shanghai Institutes for Biological Sciences, Chinese Academy of Sciences (320 Yueyang Road, Shanghai)

Printed by: Shanghai Shengtong Times Printing Co., Ltd (A6, No. 2888, Caolang Highway, Jinshan District, Shanghai)

Overseas Distributed by: Springer Nature

Home Distributed by: Local Post Offices

ISSN 1673-7067

CN 31-1975/R

Post Office Code Number: 4-608

Permit of Ad. Number: 3100420130051

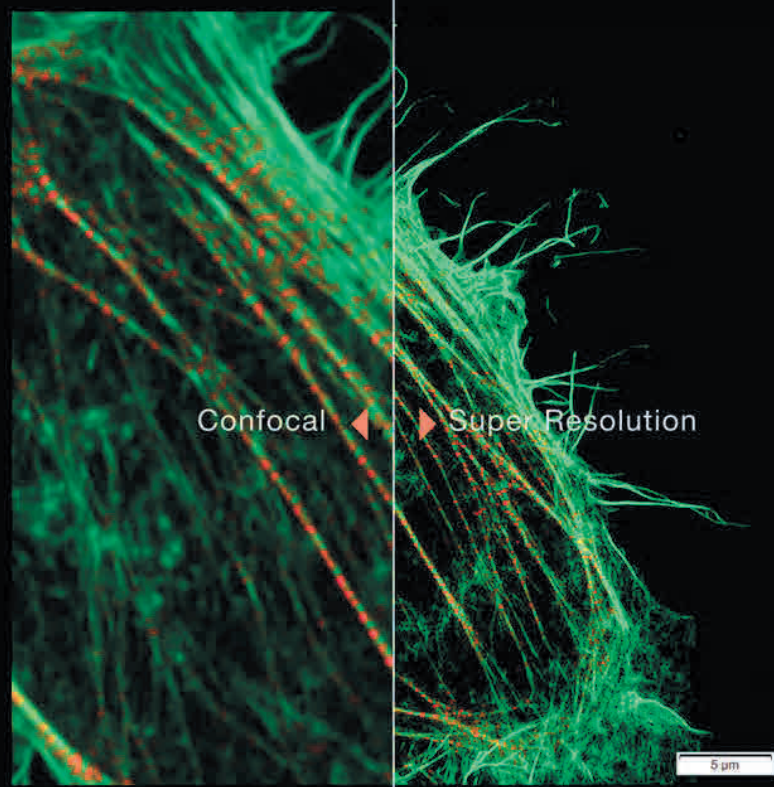
Price: ¥ 100.00

ISSN 1673-7067



兼顾分辨率和速度的

转盘共聚焦活细胞超分辨系统 SpinSR10



- 分辨率高达110nm的实时超分辨率成像
- 专有反卷积算法进一步提升图像质量
- 宽视野成像，速度高达 200fps
- 特色硅油物镜可以实现活细胞深层成像
- 宽场、共聚焦、超分辨率模式自由切换
- 功能强大的智能cellSens软件平台



奥林巴斯（北京）销售服务有限公司

北京朝阳区酒仙桥路10号恒通商务园B12C座2F (北京) 010-59756006
上海市徐汇区淮海中路1010号嘉华中心11楼 (上海) 021-51582084
广州市环市东路403号广州电子大厦16楼 (广州) 020-61227171

陕西省西安市新城区尚德路85号太平洋保险大厦8F

湖北省武汉市江岸区中山大道1628号武汉天地企业中心5号7楼701单元
四川省成都市人民南路四段三号来福士广场T1-11楼
辽宁省沈阳市沈河区友好街10号新地中心1号楼3501室

(西安) 029-87206108

(武汉) 027-82718838

(成都) 028-86703700

(沈阳) 024-23342084